Technical and Economic Performance Assessment of Pd/Alloy Membrane Reactor Technology Options in the Presence of Uncertainty

By

Reyyan Koc

A PhD thesis proposal

Submitted to the faculty of the

Worcester Polytechnic Institute

In fulfillment of the requirement for the

Degree of Doctor of Philosophy

In Chemical Engineering

By

<u>   </u>

May 2012

APPROVED BY:

<u>   </u>   <u>   </u>

Dr. Yi Hua Ma, Advisor   Dr. Nikolaos K. Kazantzis, Advisor

Dr. David DiBiasio, Head of Department   <u>   </u>

Dr. John M. Sullivan, Committee Member   <u>   </u>

Dr. William M. Clark, Committee Member   <u>   </u>

To my mother BAHAR…

Acknowledgements

Before anything else, I would like to thank Prof. Yi Hua Ma for his omniscient point of view, infinite patience and his scientific and emotional support. His consistent and determined professional style has become a role model for my own carrer. Seeing him working hard like an ant all day in his office and seeing him riding his boat during the get together days in his summer house during the leasure times made me learn how to work effectively and at the same time enjoy life . I hope that I and our entire research group could do well to fulfill his expectations. Hearing praises about him from people including not only WPI high level managers but also business people I met during the conferences that he sent us in places ranging from Washington, DC to Amsterdam/ Holland, made me proud to be one of his students. I wouldn't even dream about studying in the USA without the help of a tiny portion of the million dollar projects he brought to the CIMS group.

Prof. Kazantzis has an exceptionally high emotional intelligence and also a brilliant brain. I was extremely lucky to have him as one of my advisors. The combined guidance of Prof. Ma amd Prof. Kazantzis matched perfectly like puzzle pieces to see the whole picture and they were also very helpful to understand the challenging and effective assignments during the last four and a half years. It is impossible to not to admire his rare character and cultured personality.

I would like to present my sincere thanks to my committee members, Prof. John M. Sullivan and Prof. William M. Clark for their advice, insightful suggestions and encouragement. Moreover, the word "thank you" would be insufficient to express my gratefulness to Prof. Sullivan in return to his efforts to teach me some of the key points of my reaserch and also his sincere support in life.

The Center for Inorganic Membrane Studies (CIMS) group including Dr. Ivan Mardilovich, Dr. Federico Guazzone, Dr. Jacopo Catalano, Dr. Rajkumar Bhandari, Dr. Chao-Huang Chen, Dr Natalie Pomerantz, Alex Augustine and Pei-Shan Yen deserves special thanks. I

am grateful to them for their time, helping me to overcome the technical difficulties, sharing their expertise and more importantly for their friendship.

I am also thankful to the faculty of Chemical Engineering Department at WPI and the administrative assistants Paula Moravek, Felicia Vidito and Tiffany Royale. The technical help provided by Doug White and Jack Ferraro is also highly appreciated.

I would also like to thank Professor Sam Mannan and his Associates at the MKOC Process Safety Center, College Station-TX for their insightfull reviews/comments during the development of the HAZOP analysis and the economic evaluation framework for inherently safe membrane reactor module design. In addition, all of the invaluable technical support about the economic evaluation framework provided by Prof. William J. Nuttall from Judge Business School and Department of Engineering University of Cambridge/UK is highly appricated.

When I felt like time was flowing slower than usual in bad days and also when times flyes in a second of a blink during the joyful times, my family: my mother *Bahar*, my brother *Bahadir* and my husband *Suat* were always with me. Thanks for their unshakable support and love! To my mother *Bahar*: you were all we had in our childhood; sometimes a friend in the playground and sometimes a crazy teenager in a summer day, you were strong and unbreakable like a stone statute when you were defending us, you were soft and vulnerable when you saw the tears on our eyes, you were everything we had…

Last but not the least, Suat: You always liked to be called as my *life coach*. Thanks for being in my life in the last 12 years. I wouldn't be able to survive in this wild life without your advices and guidance. My love to you has been growing exponentially with time.

Abstract

A comprehensive process intensification analysis was performed for the integration of the Pd-based membrane reactor technology into IGCC power plants by designing effective process control strategies as well as identifying and optimally characterizing inherently safe operational conditions to achieve the most favorable economic outcomes. Experimental results indicated that Pd-based composite membranes supported on porous stainless steel tubes, fabricated with H_2 permeance values as high as ˜50 $m^3/[m^2.h.atm^{0.5}]$ at 450°C were capable of extra purity H_2 production (≥99.99%). Two illustrative process control and performance monitoring cases namely, process regulation and servo mechanism, were considered and quite satisfactory process control was attained by maintaining CO conversion at levels higher than 95% so that the retentate stream could become suitable for high pressure CO_2 sequestration. From a process safety standpoint, process parameters and operating conditions were identified and optimized to achieve the target performance level of 98% CO conversion and 95% H_2 recovery and at the same time to prevent conditions which could potentially induce hazards and thus compromise process system safety.

Furthermore, the average total product cost of a water-gas shift membrane reactor module including manufacturing costs and general expenses was carefully estimated by taking into account the full cost structure and found to be 1464 $/ft^2$. Moreover, a comprehensive economic assessment was performed for composite Pd/Alloy membrane reactor technology options integrated into IGCC power plants in the presence of market and regulatory uncertainty (possible regulatory action on CO_2 emissions) as well as technology risks with the aid of Monte-Carlo simulation techniques. Within such a context, it was demonstrated that an IGCC plant with embedded Pd-based membrane reactors and a stream of revenues coming from electricity and H_2 selling (IGCC co-production mode), represented an economically attractive and advantageous option when comparatively assessed against its main competitors namely, an IGCC plant with shift reactors and double stage Selexol units as well as the more traditional supercritical pulverized coal power plant option with an Econamine unit installed for CO_2 capture purposes.

Executive Summary

The Pd/alloy-based membrane reactor performance both for laboratory and industrial scale applications were assessed with the aid of membrane reactor simulations and a process intensification methodology for the water gas shift membrane reactor in three main areas namely process enhancement, control, safety and economics was proposed.

A process control system design was proposed to control CO conversion of the membrane reactor by manipulating the inlet steam flow rate. Although there is, in principle, a plethora of different scenarios relevant to process control studies, two main illustrative cases were considered, namely the process regulation and servo mechanism. In both control structures, quite satisfactory process control was attained maintaining CO conversion at levels higher than 95% so that the retentate stream could become suitable for high pressure CO_2 sequestration.

Throughout the performance enhancement and safety analysis, the preferred reaction conditions for the Pd/alloy based membrane reactor were determined with the aid of a non-isothermal membrane reactor model. In particular, the effect of variations in the total feed flow rate and temperature, catalyst loading, H_2O:CO ratio, reaction and permeate side pressures and purity of the feed on the process state was evaluated and desired membrane reactor operating conditions were determined to achieve the target performance levels of 98% CO conversion and 95% H_2 recovery. Either the total reaction side pressure was determined to be at least 35 atm at a fixed permeate side pressure of 1 atm or the permeate side pressure has to equal or be lower than 0.6 atm (with vacuum) at a fixed total reaction side pressure of 30 atm, to attain the performance target levels of $X_{CO} = 98\%$ and $R_{H2} = 95\%$, by using a feed temperature of 350°C, permeate pressure of 1 atm, H_2O:CO ratio of 4.5 and 50% $\rho_{Bulk,max}$ for an adiabatic membrane reactor. In addition, Hazard and Operability (HAZOP) analysis was pursued to identify potential hazards as well as failure modes and hopefully prevent potential risks to personnel, environment, equipment and/or process efficiency and performance. Detailed HAZOP worksheets were tabulated to be used as a reference source.

The membrane reactor model was modified by including multi-component gas diffusion (DGM) through the defects of the membrane. The purity levels of the H_2 separated through membranes with various selectivity values were successfully estimated with the modified model. Thus, the Pd-based membrane reactor model including the multi component gas diffusion through the defects could be used to identify the purity levels prior to actual testing. More importantly, both H_2 purity of 99.99% and flux target specified by the DOE could be easily achieved by using a Pd-based membrane having ~39 $m^3/[m^2$-h-atm$^{0.5}]$ H_2 permeance and ~8000 ideal H_2/He selectivity.

A two dimensional membrane reactor model was also developed and used to assess the total Pd/Au-based membrane reactor area and reactor dimensions for industrial conditions to achieve the performance target levels of $X_{CO} = 98\%$ and $R_{H2} = 95\%$. Furthermore, a comprehensive economical analysis was performed for the Pd/Au-based membrane reactor integrated into an Integrated Gasification Combined Cycle (IGCC) plants (IGCC-MR). In particular, a detailed Net Present Value (NPV) model has been developed to evaluate the economic viability of an IGCC-MR plant. The project value of the IGCC-MR was compared with the other options such as Supercritical Pulverized Coal, baseline IGCC and IGCC with traditional shift reactors with and without CO_2 capture systems. Moreover, sources of irreducible uncertainty were explicitly recognized such as the power plant capacity factor, Pd/Au price, membrane life time and CO_2-taxes due to future regulatory policies by the use of the Monte-Carlo simulation technique.

The static NPV analysis framework, based on "averages" or "best guesses" for the values of the pertinent NPV-model (inherently uncertain) inputs, suggested that the IGCC-MR technology option started appearing attractive under the scenario of a 25 $/ton tax imposed on CO_2 emissions starting in 2015. The IGCC-MR was predicted to provide the highest NPV of 0.44 B$, compared to the NPV values of IGCC-PBR and SC-PC with CO_2 capture plants when the above regulatory action on carbon emissions is introduced.

Investment decision making under uncertainty could be reliably informed through a methodologically careful integration of Monte Carlo techniques into the aforementioned detailed NPV-model. In particular, the various input uncertainties (mathematically realized by meaningful/realistic probability distributions) were propagated through the NPV-model using

rigorous and computationally powerful Monte Carlo techniques, eventually generating a distribution of the project's economic performance (a statistically characterized NPV distribution profile) in the presence of (operational, economic and regulatory uncertainty).

In particular, the main uncertainty drivers/inputs associated with the membrane reactor module cost that were explicitly considered in the present study were the Pd price, support price and also membrane lifetime. The expected total capital investment for the membrane reactor module consisting of 10 μm thick Pd-based membrane tubes (13043 m^2) was estimated to be 15750 US\$/m^2 (1464 US\$/ft^2) with a minimum and maximum value (reported in the pertinent literature) of 6681 US\$/m^2 (621 US\$/ft^2) and 36073 US\$/m^2 (3353 US\$/ft^2), respectively.

The rest of uncertain inputs to the NPV model explicitly accounted for in the research study were the plant capacity factor, initial CO_2 tax, CO_2 tax growth rate , nominal discount rate, inflation rate, electricity selling price, Pd price, support price and membrane life. In a future where CO_2 emissions were regulated through taxation, an IGCC plant with embedded Pd-based membrane reactors was shown as the economically advantageous option against its rivals namely, IGCC plant with shift reactors and double stage Selexol units as well as the more traditional supercritical pulverized coal power plant option with an Econamine unit installed for CO_2 capture purposes.

In addition, the uncertainty/risk in plant safety (realized as an additional random variable that follows a simple Bernoulli distribution to describe the possibility of the occurrence of an industrial accident) was explicitly considered for an IGCC-MR plant. A comparatively more attractive NPV distribution profile was obtained when concrete safety risk-reducing measures were taken into account through pre-investment in process safety, giving credence to the thesis that process safety investments may result in enhanced economic performance in the presence of irreducible uncertainties.

Table of contents

xi

List of Tables

List of Figures

1. INTRODUCTION

Hydrogen is being produced mostly from conventional sources (steam reforming of natural gas and partial oxidation of hydrocarbons) whereas 4% is being produced from renewable energy sources (solar photovoltaic power for direct conversion, wind power, hydropower) (Kothari et al. 2008b). As an alternative, hydrogen production from coal represents a promising option for the near to medium future (Miller et al., 2009). It is worth noting that coal reserves constitute 65% of the world's main fossil fuel reserves and North America (28%), Russia (25%) and China (13%) enjoy the lion's share of the world's coal reserves (Shafiee and Topal 2009). Furthermore, the development of technologies for pre-combustion CO_2 sequestration and economical hydrogen production is quite important to the hydrogen economy and environmental protection (Veziroglu and Barbir 1998). Indeed, one is reminded that the leading industrial countries that ratified the Kyoto Protocol are bound to set the CO_2 emission target levels at 6% below the 1990 ones for the time period 2008-2012 (Sirikitputtisak et al. 2009). As a result, research activity increasingly focuses on the development of new technology options or the modification of existing ones that would lead to cost-effective strategies for the reduction of CO_2 emissions while maximizing H_2 production (Tarun et al. 2007). Within such a context, the integrated gasification combined cycle (IGCC) process is a way to co-produce synthesis gas, electricity, hydrogen, fuels and chemicals from coal and coal/biomass-mix in an environmentally responsible manner. The production of hydrogen via the water-gas shift reaction (WGSR) represents a key part of this process and hydrogen of various purities can be produced in an IGCC plant. Notice that the application of hydrogen separation technology to promote the WGSR is a promising way of making hydrogen from coal and coal/biomass-mix for fuel cell applications. In addition, the CO_2 produced from the WGS shift membrane reactor is under high pressure and suitable for sequestration or tertiary oil recovery.

In particular, the WGSR represents one of the oldest catalytic reactions used in many industrial processes to produce H_2 or ammonia synthesis gas, and is a well known exothermic reaction (Basile et al. 1996a):

$$CO + H_2O \leftrightarrow CO_2 + H_2 \qquad \Delta H^0_{298\,K} = -41.2\ kj\ mol^{-1}$$

The maturation of the pertinent catalyst technology and the simplicity of the nature of the reaction (such as a no change in the total number of moles combined with a moderate heat of reaction), make the WGSR attractive for applications in the above context (Basile et al. 1996a; Barbieri et al. 2005; Basile et al. 2001; Basile et al. 1996b; Brunetti et al. 2009a). In a membrane reactor, as the WGSR proceeds, H_2 is removed from the gas mixture of the reaction side continuously. Thus, conversion of the reactants (CO, H_2O) can exceed substantially the thermodynamic equilibrium conversion. Notice that the separation of H_2 through the utilization of a membrane which has a very high selectivity of H_2 with respect to other gases is a prerequisite in order to be able to advantageously use high-purity H_2 in a fuel cell system. In addition, the outlet stream of the reaction side consists of mostly H_2O and CO_2 under high pressure making it amenable to capture after condensation of the steam (Basile et al. 2001; Basile et al. 1996b; Brunetti et al. 2009a; Criscuoli et al. 2000; Tosti et al. 2003; Uemiya et al. 1991b). WGSR is of course only one of the many possible applications such as hydrogenation and dehydrogenation reactions like dehydrogenation of ethylbenzene to styrene, propane dehydrogenation to propylene, dehydrogenation of alcohols and most prominently methane steam reforming (Dixon 2003).

The selection of the particular membrane type for pure H_2 production via WGSR represents the most important decision step in the overall process design. Compared to the conventional hydrogen-permeable membranes, mesoporous ceramic membranes (low selective), microporous ceramic membranes (low selective & permeable), dense ceramic membranes (low permeable) and Pd-based membranes (highly hydrogen permeable and selective towards hydrogen) are the best candidates for catalytic membrane reactors used in reforming and other reactions associated with hydrogen generation (Lukyanov et al. 2009). The high efficiency H_2 production is possible if a membrane is endowed with the following properties: high permeability and selectivity, cost effective fabrication and maintenance, resistance to feed components/impurities that attenuate H_2 permeance (CO, H_2S, etc), usability at high temperature (400-600ºC) and pressure (20-50 atm) (The membrane should tolerate the reaction conditions of industrial applications such as dehydrogenation, steam reforming and high temperature WGSRs (Armor 1998)), easiness in scale up, practical assembly/disassembly for both small and large

scale industrial applications, long term durability (5 years, 2015 DOE target (US DOE-Hydrogen from coal, 2011)).

The application of Pd/Pd-alloy composite membranes supported on porous metals, such as porous stainless steel, Inconel or Hastelloy, holds the promise of offering all the advantages associated with the features outlined above. Pd/Pd-Alloy membranes supported on porous metal (stainless steel, Hastelloy or Inconel) porous cylindrical tubes and welded to both ends of the non-porous stainless steel tubes (Ayturk et al. 2006b; Mardilovich et al. 1997; Mardilovich et al. 2002; Pomerantz and Ma 2009; Chen and Ma 2010b) were considered in the present study. The palladium membranes supported on porous substrates have several advantages such as very thin Pd layer (3-20 µm), good mechanical strength and quite high H_2 fluxes. Furthermore, the porous metal supports can be integrated into the process easily, while resistance to mechanical cracking and simplicity of the module construction are additional benefits associated with porous metal supports (Ma et al. 2003).

A notable challenge in the design and development of membrane reactor systems is the poisoning of the Pd/Pd-alloy membranes by some of the feed impurities such as CO and H_2S. However, Pd/alloy membranes like Pd/Cu and Pd/Au, have shown to have less permeance decline in the presence of H_2S (Chen and Ma 2010b; Chen and Ma 2010a; Kulprathipanja et al. 2005; Pomerantz et al. 2010b; Way et al. 2008). The effect of CO on the H_2 permeation is strongly dependent on reaction temperature and the reduction in the permeation rate could be neglected at temperatures higher than ˜350°C (Hara et al. 1999; Gallucci et al. 2007; Nguyen et al. 2009).

All major bench-scale performance assessment studies involving Pd/Pd-alloy based composite membranes emphasize certain advantages of scaling up to industrial scale applications. Consequently, many research efforts are now increasingly focusing on process intensification concepts and methods allowing improvements in process economics, environmental performance and process safety through the design of cheaper processes, smaller in size equipment/plant, inherently safe process design, efficiency-focused energy management, waste/by-products minimization and risk (Stankiewicz and Moulijn 2004). Within such a context, membrane reactor technology nicely exemplifies the above possibilities since it is

inherently aligned with and amenable to basic process intensification and inherently safe process design principles (Ayturk et al. 2009; Koc et al. 2011).

The integration of Pd-based membrane reactors into coal-fired power represents a new technology option which has neither been fully tested nor yet demonstrated at a commercial scale. The lack of operating experience associated with membrane reactor technology options integrated into IGCC power plants on the commercial scale inevitably produces a lack of actual data related with performance levels, process safety and economics.

Commercial scale conditions, determined based on simulation and bench scale experimental results, are perhaps favorable to evaluate inherent safety design prospects and hopefully demonstrate that the inherent process safety does not only undermine the economic viability of such a plant, but in an uncertain world it actually enhances the value of engineering design and the project itself in concrete economic terms (Mannan, 2011). In addition, any economic performance evaluation at this early stage would be driven by reasonable yet theoretical estimates, but methodologically should acknowledge irreducible (market, regulatory, technological) uncertainties in an explicit manner (Savage 2003; Savage 2002).

The main objective of the research conducted within the context of the present dissertation was to assess the Pd-based membrane reactor performance both for laboratory and industrial scale applications and to propose a process intensification methodology for the water gas shift membrane reactor in three main areas namely process enhancement, safety and economics. In summary, the specific objectives of this study were:

- Develop a process dynamic modeling framework in order to analyze and characterize the transient behavior of a Pd/alloy-based (Pd/Au or Pd/Cu) water gas shift (WGS) membrane reactor.

- Apply simple process control ideas into the dynamic model to enhance process system performance by inducing the desirable dynamic characteristics in the response of the controlled process during start-up as well as in the presence of unexpected adverse disturbances (process upset episodes) or operationally favorable set-point changes that reflect new hydrogen production requirements.

- Develop a systematic non-isothermal modeling framework under steady state conditions to identify process parameters and operating conditions which may induce hazards and compromise process safety during the operation of a catalytic high temperature water-gas shift reaction in a Pd-based membrane reactor.

- Compose Hazard and Operability (HAZOP) tables (Khan and Abbasi 1997; Kothari et al. 2008a) by following the standard principles of HAZOP analysis to identify incidents where process safety could be compromised.

- Develop a membrane reactor modeling framework that explicitly takes into account the multi-component gas diffusion through the defects in a Pd-based composite membrane.

- Assess the industrial scale Pd-based composite membrane reactor performance by using higher dimensional (two dimensional) simulation methods.

- Propose a comprehensive process economic assessment framework for a Pd/alloy-based membrane reactor integrated into an IGCC plant (IGCC-MR). In particular, develop a detailed Net Present Value (NPV) model to evaluate the economic viability of an IGCC-MR plant.

- Propose options for the integration of Pd-based membrane reactors into coal-fired power plants such as IGCC plants and find the optimum design conditions which would result into the maximum net plant efficiency and lowest plant cost and operating and maintenance costs.

- Perform economical risk analysis by taking into account the effect of the uncertainty drivers on the project's/plant's value by a Monte-Carlo simulation technique that enables the propagation of the above uncertain inputs through the NPV-model.

- Compare the economic feasibility of the IGCC-MR with other technology options such as relatively new IGCC power plants involving traditional sour shift reactors and pulverized coal power plants with extensive operational experience.

- Show as a part of risk assessment efforts, that if the required process safety investment is made (as part of the initial capital expenditure) at the construction stage of an IGCC

plant, process safety investment strategies can save money by preventing or minimizing the effects of accidents and possibly catastrophic events.

2. LITERATURE REVIEW

2.1. Palladium membranes

The word "membrane" was first used by Abbot J.A. Nollet in 1748 (it means pellicle, capsule, diaphragm, thin parchment in Latin). Palladium is one of the six transition metals which are also referred as "platinum metals" (Lewis 1967) and it is used as an attractive hydrogenation catalyst and hydrogen separation membrane because of its high hydrogen solubility (Bose 2009). Since Graham (1866) first separated H_2 by thin palladium tubes, the number of research and development efforts on the hydrogen separation and production by membranes and membrane reactors at high temperature and pressure, is continuing to increase.

Inorganic membranes are divided into metallic (solid phase) and ceramic (porous and non-porous) membranes. A porous (composite, asymmetric) membrane consists of a support made of ceramics, carbon, polymers, glass, stainless steel and a thin selectively permeable layer of Pd, Pd/alloy or zeolite (Lukyanov et al. 2009) and a composite membrane could be dense depending on the fabrication method.

The selection of the particular membrane type for pure H_2 production/separation represents the most important decision step in the overall process design. Compared to the conventional hydrogen-permeable membranes, mesoporous ceramic membranes (low selectivity), microporous ceramic membranes (low selectivity & permeablility), dense ceramic membranes (low permeability) and Pd-based membranes (highly hydrogen permeability and hydrogen selectivity) are the best candidates for catalytic membrane reactors of reforming and other reactions associated with hydrogen generation (Lukyanov et al. 2009). High efficiency H_2 production is possible if a membrane is endowed with the following properties: high permeability and selectivity, economical fabrication and maintenance, resistance to feed components/impurities that attenuate H_2 permeance (CO, H_2S, etc), usability at wide range of

temperature (200-600ºC) and pressure (1-50 atm), easiness in scale up, practical assembly/disassembly for both small and large scale industrial applications, long term durability. The membrane should tolerate the reaction conditions of industrial applications such as dehydrogenation, steam reforming and high temperature water gas shift reactions (Armor 1998). Notice that if the membrane is desired to be used in a GE IGCC plant, the pressure of the gas stream of 53 atm at the scrubber outlet (Haslbeck et al. 2010) should cause no problem in terms of membrane integrity.

The application of Pd/Pd-Alloy composite membranes supported on porous metals, such as porous stainless steel, Inconel or Hastelloy, holds the promise of offering all the advantages associated with the features outlined above. Pd/Pd-Alloy membranes supported on stainless steel or Inconel porous cylindrical tubes and welded to both ends of the non-porous stainless steel tubes were considered in this study. The palladium membranes supported on porous substrates have several advantages such as very thin Pd layer (3-20 µm), good mechanical strength and quite high H_2 fluxes. Furthermore, the porous metal supports can be integrated into the process easily, while resistance to mechanical cracking and simplicity of the module construction are additional benefits associated with porous metal supports (Ayturk et al. 2006b; Mardilovich et al. 1997; Mardilovich et al. 2002; Pomerantz and Ma 2009; Ma et al. 2003; Ma et al. 2000; Ma et al. 2003; Ma et al. 2004; Ma et al. 2007a; Chen and Ma 2010b).

2.1.1 Pd-H system: thermodynamics and hydrogen permeation

The detailed investigation of H_2 solubility in Pd bulk helps to illuminate the advantages of Pd as well as its limitations. The pressure-concentration isotherms shown in Figure 2-1 represent the relationship between H_2 pressure and H/Pd ratio at various temperatures. If the Palladium is exposed to H_2 atmosphere at $T \leq 298°C$ and $P \leq 2MPa$, β-phase hydride will form as shown in Figure 2-1. The β-phase hydride has a considerably expanded lattice compared with α-phase palladium hydride. The transition to β-phase hydride causes splitting of the membrane known as H_2 embrittlement. As long as a pure palladium membrane is operated at temperatures above the critical temperature of 300°C and not very low pressures, the H_2 embrittlement would be avoided. Fortunately, the α-β phase transition problem was solved by alloying the membrane with I-B metal (Shu et al. 1991).
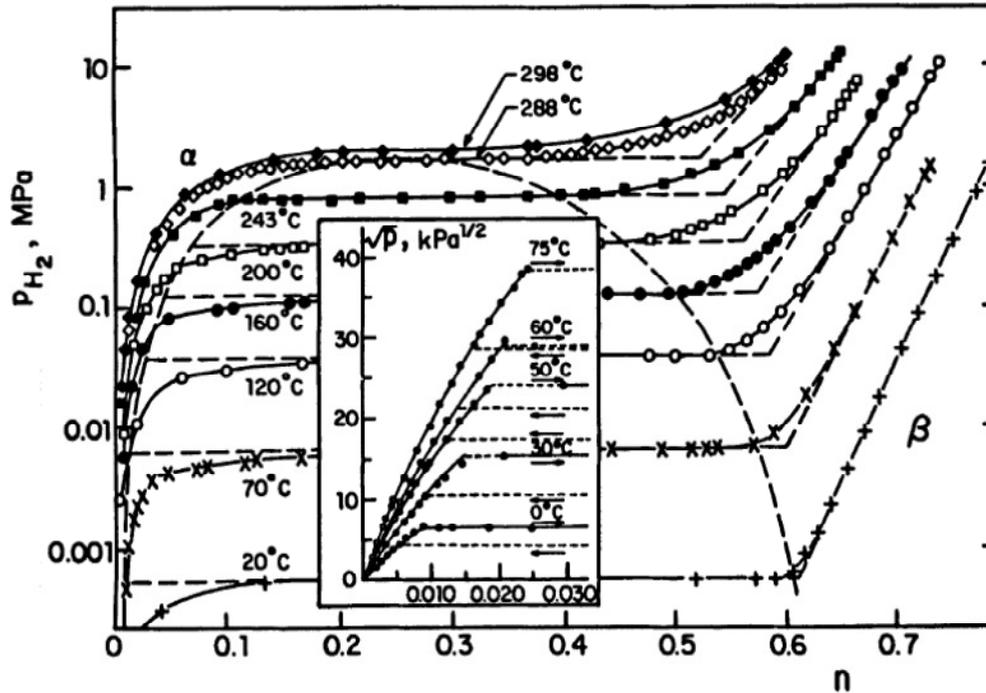
Figure 2-1. Equilibrium solubility isotherms of PdH_n for bulk Pd at different temperatures (inset figure: low pressure region) (Graham 1866; Frieske and Wicke 1973; Wicke and Nernst 1964).

The permeation of H_2 through metals is a complex multistep process (Shu et al. 1991). The major steps involved in the H_2 permeation through Pd are: (i) adsorption and dissociation of H_2 molecules to H atoms at the membrane surface of the high pressure side, (ii) diffusion of the H atoms through the bulk of the Pd layer, and (iii) re-association of H atoms and desorption of H_2 molecules at the membrane surface of the low pressure side (Bose 2009; Ward and Dao 1999). The model of Ward and Dao (1999) which accounted for all kinetic steps in the permeation process demonstrated that diffusion through the Pd layer is the rate limiting step in the absence of external mass transfer resistance at moderately high temperatures ($\geq$300°C). Desorption of H_2 molecules at the membrane surface of the low pressure side was indicated to be the rate-limiting process at low operating pressures. Adsorption step was predicted only to be important at very low H_2 partial pressures or in the presence of substantial surface contamination (Ward and Dao 1999). If the hydrogen permeation is assumed to be controlled by the hydrogen diffusion through the Pd layer and no phase transformation between α and β occurs, the hydrogen flux (J_{H_2}) is as follows:

$$J_{H_2} = -D \cdot \Delta C / \Delta x = D \cdot (C_{HP} - C_{LP}) / \delta \qquad (2.1)$$

$C = k.P^{0.5}$ is a good approximation for low H/Pd ratios within the α-phase region of Figure 2-2. Equation (2.1) can be rewritten as:

$$J_{H_2} = k \cdot D \, (P_{HP}^{0.5} - P_{LP}^{0.5}) / \delta \qquad (2.2)$$

where J_{H_2}: hydrogen flux [m^3/(m^2.s)] or [kmole/(m^2.s)], k: Henry's law constant [kmole/(m^3.atm$^{0.5}$)], D: diffusivity [m^2/s], δ: thickness of the membrane, HP and LP: high and low pressure sides, respectively. The values of k and D are dependent on temperature and the term $k \cdot D$ is the permeability. The membrane thickness is difficult to determine, thus permeance, $k \cdot D / \delta$, is a very convenient term. Equation (2.2) is commonly referred as Sieverts' Law. The derivation of the Sieverts' Law and the H$_2$ transport mechanism through the Pd layer is detailed in other studies (Ward and Dao 1999; Caravella et al. 2008; Chen et al. 2008a; Kajiwara et al. 2000a; Jewett and Makrides 1965; Caravella et al. 2010b). The exponent of pressure in the Sieverts' Law may deviate from 0.5 depending on the non-linearity of the pressure-concentration isotherms, surface reactions and presence of mass transfer resistances (Bose 2009; Ward and Dao 1999; Gabitto and Tsouris 2008). Therefore, it would be practical to express Equation (2.2) as:

$$J_{H_2} = k \cdot D \, (P_{HP}^{n} - P_{LP}^{n}) / \delta \qquad (2.3)$$

where $1 \geq n \geq 0.5$. n = 0.5 for the Sieverts' Law (Bose 2009).

Not all of the Pd-based membranes are perfect and may have leaks. The undesired leak growth on the surface of composite Pd membranes over a long period of time was characterized as the result of pinhole formation by Guazzone (2006b). The sintering of Pd grains would lead to the formation of pinholes, the release of stresses and the growth of Pd grains (Guazzone and Ma 2008; Guazzone et al. 2006a). The n-value of Pd-based composite membranes, (thickness ≥ 15 µm) prepared by Guazzone (2006), decreased from 0.7 to 0.5 as temperature was raised from 300 to 500°C and this decrease was explained as the result of the removal of contaminants and the increase of the linearity region of the isotherm of the P$^{1/2}$ versus n (H/Pd) with increased temperature. Defects in the dense Pd layer caused the n-value to increase as high as 0.75 at 500°C. In addition, the porous support which had large resistance was found to increase the exponents of the hydrogen partial pressure (Guazzone et al. 2006b; Guazzone and Ma 2008).

10

Thus, it is important to introduce "separation factor and ideal separation factor (selectivity)" at this point. Assuming that gas A separated from the gas mixture A,B and C separation factor (S_F) is the ratio of the compositions of components A and B+C in the permeate relative to the composition ratio of these components in the retentate (Koros et al. 1996).

$$S_F = [X_A/(X_B + X_C)]_{Permeate}/[X_A/(X_B + X_C)]_{Retentate} \tag{2.4}$$

Ideal separation factor or selectivity is commonly used for quantification of leak. The leak could be measured by determining the inert gas (He, N_2, Ar, etc.) permeance. The selectivity ($\alpha_{H_2/He}$) is defined by the ratio of the H_2 flux and the He flux at the same temperature and the pressure difference (Guazzone 2005).

$$\alpha_{H_2/He} = J_{H_2}/J_{He} \tag{2.5}$$

The H_2 permeation can be calculated with Equation (2.2) for the Pd membranes with infinite selectivity. However; if the membrane has defects, the transport mechanism will be different and the H_2 permeation through the defects will involve Knudsen diffusion (J_k) and viscous or Poiseuille flow (J_v) in addition to the solution diffusion (SD) term (Mardilovich et al. 1997; Guazzone et al. 2006b; Schramm and Seidel-Morgenstern 1999). The H_2 flux of membranes with leaks could be expressed as:

$$J_{H_{2,Total}} = J_{H_2,SD} + J_k + J_v \tag{2.6}$$

2.1.2 Pd/alloy-H system

Pd/alloy membranes have prominent properties compared to pure Pd membranes such as reduced critical temperature for the H_2 embrittlement, enhanced H_2 permeability at certain compositions, resistance to impurities (i.e., H_2S) and reduced cost when cheaper metals like Ag and Cu is used (Ma et al. 2003; Lewis 1967; Shu et al. 1991; McKinley 1966; Knapton 1977a).

In particular, an alloy of Pd-23 atom % Ag is preferred to be used in commercial membrane hydrogen purifier than a pure Pd membrane since the critical temperature and pressure for the α→β transition is decreased upon alloying Pd with Ag (Shu et al. 1991). Additionally, Pd/Ag alloys have higher hydrogen permeability compared to pure Pd. As the hydrogen solubility increases with the subsequent decrease in the diffusivity as a function of the

11

Ag content, a maximum in the hydrogen permeability for 20-25 wt% Ag is observed; which is 1.6-1.8 times of the permeability of the pure Pd (McKinley 1966).

Pd/Cu alloys do not exhibit hydrogen embrittlement as severe as pure Pd and the β-hydride phase formation of a Pd-40% Cu alloy occurs even below the room temperature (Karpova and Tverdovskii 1959). Thus, Pd/Cu alloys are good candidates for low temperature hydrogen production/purification processes. The body-centered cubic (bcc) Pd/Cu alloys has a peak in permeability at a Cu content of 40% and this permeability is only 6% higher than permeability of the pure Pd as shown in Figure 2-2. The diffusion coefficient of Pd/Cu alloys is very sensitive to the crystal structure. For instance, as the Pd-40% Cu alloy has similar diffusivity values with Cu if it is quenched to face-center cubic (fcc) structure, the bcc structure has an increase in hydrogen diffusivity by two orders of magnitude (McKinley 1966). Pd/Cu alloys are also known to have more resistant to H_2S poisoning than pure Pd for the fcc structure. Particularly, the sulfur tolerance of any membrane would be beneficial for the coal gasification process due to high sulfur content of the feed gas (Maurstad, 2005). Even though sulfur contamination at various concentrations causes a decline in hydrogen permeance of the fcc Pd/Cu alloy, the fcc structure has shown to have more tolerance compared to bcc Pd/Cu alloy and pure Pd (Kulprathipanja et al. 2005; McKinley 1967; Mundschau et al. 2006). Pomerantz and Ma (2009) were able to fabricate composite palladium membranes with a thin top Pd/Cu protective layer against sulfur poisoning and without greatly reducing the permeance. They were able to recover 65% of the permeance of a Pd-18% Cu membrane after exposure to 54.2 ppm H_2S/H_2 for 120 h at 450°C (Pomerantz and Ma 2009).

Pd/Au alloys showed higher hydrogen permeability than pure Pd for the Au contents below 20 wt% and also higher sulfur tolerance compared to other Pd alloys (Knapton 1977a; McKinley 1967; Gryaznov 2000). The permeability measurements of the Pd/Au alloys taken by McKinley (1966) and Knapton (1977b) contradicts with the results of Gryaznov (2000). According to Knapton (1977b), the permeability of the Pd/Au alloy up to 20 wt% Au was almost the same as the permeability of pure Pd. In contrary to Knapton (1977b), the permeability of Pd/Au alloy for the Au content range of 10-30 wt% was twice of the permeability of pure Pd as measured by Gryaznov (2000). Chen and Ma (2010a) performed the poisoning experiments by

using a 18.1 μm thick Pd/Au composite membrane with 8 wt% Au in 54.8 ppm H_2S/H_2 at 400°C for 4 hours and then recovered in H_2 at 500°C to 100% of the permeance prior to H_2S poisoning.

The normalized permeability values of various binary Pd alloys (such as Y, Ce, Rh, Pt, Au, Ag, Cu) with respect to pure Pd foil are presented as a function of alloying metal content in Figure 2-2. The selection of the alloying metal and composition should be done based on the peaks in the relative permeability values and also feasibility of the fabrication method to obtain the exact composition. The trends for H_2 permeability shown in Figure 2-2 were explained by the average bond distance of the Pd-alloys (Yun and Oyama 2011). The hydrogen permeation is controlled by the diffusion of atomic hydrogen through the metal lattice (Holleck 1970) and the larger atomic distances promote the atomic hydrogen diffusion. The H_2 permance was generally proportional to the average bond distance of the binary palladium alloys as shown in Figure 2-3.

For instance, rare-earth alloys of palladium such as yttrium and cerium alloys have excellent hydrogen permeability values as shown in Figure 2-2. The H_2 solubility of Pd-Y and Pd-Ce is higher than pure Pd because their atomic size is 30% larger than Pd, consequently, the hydrogen permeance is higher even though the diffusion coefficients in the rare-earth element alloys is smaller than that of Pd (Doyle and Harris 1988). The phase equilibrium restricts the Y content to 12 atom % (Shu et al. 1991). Both Y and Ce alloys are harder to form than Pd-23 % Ag and should be utilized in the processes operated at high pressures (Shu et al. 1991; Fort et al. 1975). The estimated solubility values for $PdAg_{30wt\%}$ and for $PdAu_{20wt\%}$ calculated using density functional theory are 10 times and 12 times higer, respectively, than that of pure Pd at 456 K, while the solubility of H atoms in pure Pd is 5 times larger than the one for $PdCu_{20wt\%}$ (Sonwane et al. 2006a). Furthermore, multi component alloys such as Pd/Ag/Pt, Pd/Au/Ru, Pd/Ag/Ni, Pd/Ag/Rh, Pd/Ag/Au/Ru and etc., were also tested to evaluate the separation performances (Shu et al. 1991; Knapton 1977a; Gryaznov 2000).
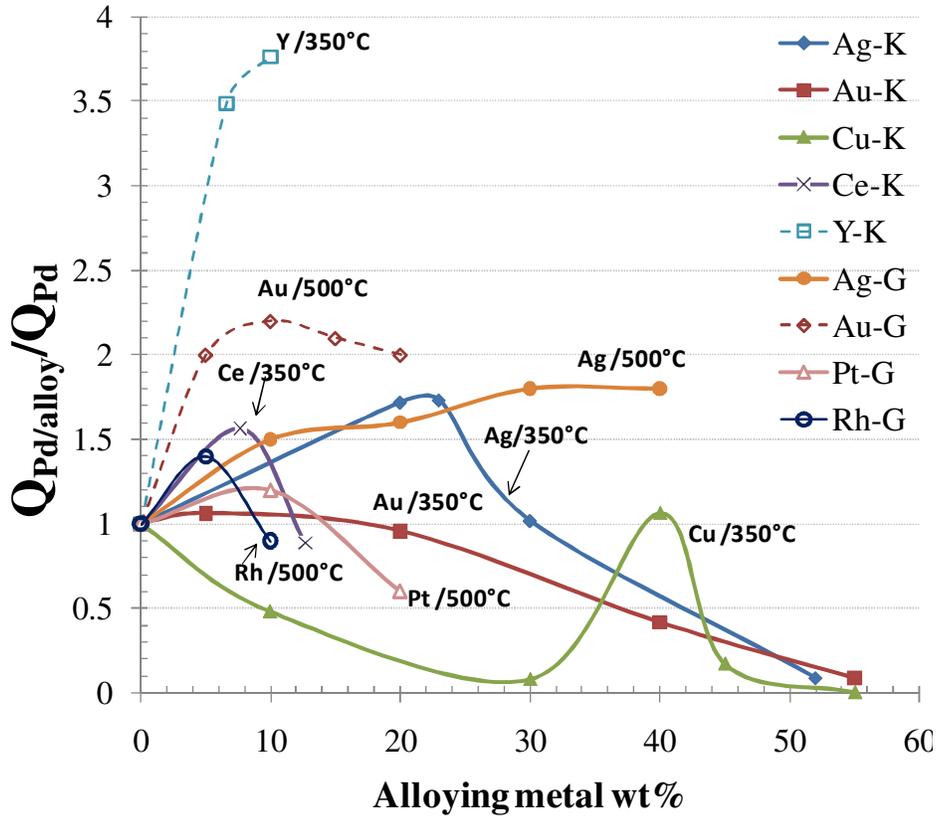
Figure 2-2. Relative coefficients of hydrogen permeation of Pd/alloy to the pure Pd. (Legend abbreviations; K: 350°C and 20.4 atm (Knapton 1977a) and G: 500°C (Gryaznov 2000).
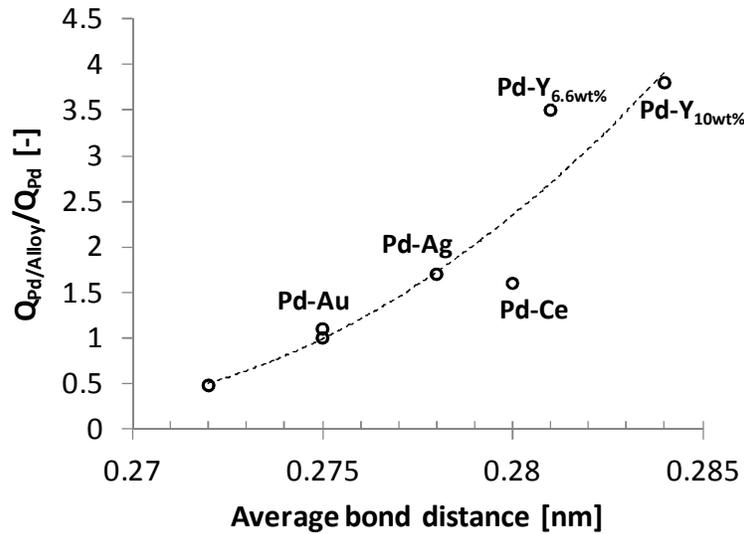
Figure 2-3. Relative coefficients of hydrogen permeation of binary Pd alloys to the pure Pd as a function of average bond distance (Yun and Oyama 2011).

14

2.2. Methods of Pd deposition on porous substrates

The basic requirements from a Pd membrane are its thickness and selectivity. The manufacturing techniques will be explained briefly by the definition of the method, advantages and disadvantages specifically for the Pd membrane fabrication. Conventional cold rolling and four other thin-film deposition techniques namely chemical vapor deposition (CVD), magnetron sputtering, electro plating and electroless plating will be introduced in the Chapter 2.2.

Conventional cold rolling involves melting the raw materials with the desired compositions, ingot casting, high-temperature homogenization, hot and cold forging and pressing, followed by consecutive cold rolling and annealing until the required thickness is achieved. One of the most important aspects of the alloy casting is the contamination as the metal becomes thinner. The mechanical properties of thin foils are strongly dependent on traces of specific elements (C, S, Si, Cl, O, etc.). The original purity of the ingot, cleanliness during forming and annealing are the parameters which would determine the thickness limit of the foil (Shu et al. 1991). Cold-rolling can be used to coat porous substrates with Pd to be used in membrane reactors (Tosti et al. 2002; Tosti et al. 2000). Tosti (2002) prepared 50 μm thick Pd and Pd/Ag composite membranes by following several steps of cold-rolling and annealing on ceramic porous tubes. Then the rolled thin foils were round-wrapped and arc-welded, using a tungsten electrode under inert gas atmosphere (Tosti et al. 2000). However, there are many other ways of coating porous supports with Pd less than 20 μm thickness which would result in higher permeance and more economical membrane fabrication.

The thin-film deposition technologies can be classified as:

- Evaporative methods including
  - Vacuum evaporation, e.g. electron-beam evaporation

- Glow-discharge processes
  - Sputtering, e.g. reactive sputtering, magnetron sputtering, ion beam deposition
  - Plasma processes, e.g. plasma oxidation, cathodic arc deposition

- Gas-phase chemical processes

    o Chemical vapor deposition (CVD), e.g. atmospheric-pressure CVD, metalorganic CVD.

    o Thermal forming processes, e.g. thermal oxidation

- Liquid-phase chemical techniques

    o Electro processes, e.g. electro plating, electroless plating

    o Mechanical techniques, e.g. spray pyrolysis

Generally three major techniques used to coat Pd thin films on porous metallic or ceramic supports are: CVD, physical sputtering and electroless plating (Lu et al. 2007).

2.2.1 Chemical vapor deposition (CVD)

CVD is a materials synthesis process where constituents of the vapor phase react chemically near or on a substrate surface to form a solid product. The main feature of CVD is its versatility for synthesizing both simple and complex compounds with relative ease at generally low temperatures. Both chemical composition and physical structure can be tailored by control of the reaction chemistry and deposition conditions. Liquid and solid reactants must be vaporized without decomposition at suitable temperatures and transported with a carrier gas through heated tubes to the reaction chamber, which complicates processing, especially in the case of reduced-pressure systems (Seshan, 2002). Thus, the application of CVD for the industrial scale productions would be difficult and probably impractical.

Xomeritakis and Lin (1996) prepared a 0.5 μm thick and fairly gas-tight Pd membranes inside pores of a supported γ-$A1_20_3$ membrane by a counter-diffusion CVD using $PdCl_2$ and H_2 as precursors. Their experimental results showed that the membranes had $0.5\text{-}1.0 \times 10^{-6}$ mol/[m^2.s.Pa] H_2 permeance at 350-450°C but the H_2/N_2 selectivity was unclear because of difficulties in sealing the disk-shaped membranes using graphite gaskets and predicted to be in the range of 100-1000. The rate of H_2 transport through such thin membranes was suggested to be controlled by surface reaction steps in that temperatures range (Xomeritakis and Lin 1996). Kikuchi et al. (2000) compared an electroless-plating Pd membrane with CVD Pd, Pt and Ru

membranes. An 8 μm thick Pd membrane supported on alumina tubes and prepared by electroless plating had the same permeance of 0.35 mol/[m^2.s.atm] with the CVD membrane, but the methane conversion of CVD membrane was 16% less than the electroless-plated membrane and also the CVD membrane had a low 280 H_2/N_2 selectivity compared to the infinite selectivity of the electroless-plated Pd membrane (Kikuchi et al. 2000). Some other publication on membrane preparation by CVD, e.g. Jun and Lee (2000), Kajiwara et al. (Kajiwara et al. 2000a; Kajiwara et al. 2000b; Kajiwara et al. 1999) would be useful sources to elucidate the characterization and performance of CVD membranes.

2.2.2 Magnetron Sputtering

The electrode and gas-phase phenomena in various kinds of glow discharges represent a rich source of processes used to deposit and etch thin films. Sputtering involves, diode-, reactive, bias-, magnetron- and ion-beam-sputtering. Magnetron sputtering attracted attention for Pd deposition due to its compatibility for a wide range of support materials. Magnetron sputtering uses a transverse magnetic field and produces several important modifications of the basic processes. Target-generated secondary electrons do not bombard substrates because they are trapped in cycloidal trajectories near the target, and thus do not contribute to increased substrate temperature and radiation damage. This allows the use of substrates that are temperature-sensitive (for example, plastic materials) and surface sensitive (for example, metal-oxides-semiconductor devices) with minimal adverse effects (Seshan, 2002). However, the advanced technology required for the magnet adds economic disadvantage. In addition, the direction of atom bombardment to the desired section of the target is still not very well controlled and causes difficulties for the large scale applications.

Asymmetric polymer membranes, porous metal sheets and oxide plates were used as support to prepare Pd and Pd/alloy (Mn, Co, Ru and Sn) membranes by magnetron sputtering (Gryaznov et al. 1993). A 10 μm thick Pd- 6% Ru membrane supported on porous stainless steel sheet was modified with an intermediate 0.8 μm tungsten layer to prevent the intermetallic diffusion. The latter membrane had a H_2 flux of 120 m^3/[m^2.h] at 800°C and pressure difference of 20 atm (Gryaznov et al. 1993). Tucho et al. (2009) prepared 5 and 10 μm Pd-23 wt% Ag self-supported membranes by magnetron sputtering onto single crystal Si-wafers. An average

permeability of 2.6±0.4 mol/[m.s.Pa$^{0.5}$] was obtained at a very low transmembrane pressure difference of 0.5 atm at 300°C (Tucho et al. 2009). Since the membranes prepared by Tucho et al. (2009) were self-supported, these membranes would not resist high pressure application which will improve the H$_2$ separation efficiency. The earliest work on Pd membrane preparation by magnetron sputtering done by Gryaznov (1993) and also one of the latest work done by Tucho et al. (2009) were mentioned here and more details can be obtained from the related literature (Bryden and Ying 1995; Zhao et al. 1999; Zhao et al. 2000; Checchetto et al. 2004; Huang and Dittmeyer 2007).

2.2.3 Electroplating

The growth of inorganic thin films from liquid phases by chemical reactions can be accomplished primarily by electrochemical processes and by chemical deposition processes which include electroless plating. In electroplating a metallic coating is electrodeposited on the cathode of an electrolytic cell consisting of a positive electrode (anode), a negative electrode (cathode), and an electrolyte solution (containing the metal ions) through which electric current flows. The quantitative aspects of the process are governed by Faraday's laws. Important electroplating variables include current efficiency, current density, current distribution, pH, temperature, agitation, and solution composition. Numerous metals and metal alloys have been successfully electroplated from aqueous solutions. The technically most useful electroplated metals are chromium, copper, nickel, silver, gold, rhodium, zinc, and a series of binary alloys including chromium/nickel composites (Seshan, 2002). Electroplating is widely used in industry and can produce deposits that range from very thin films to very thick coatings (electroforming). However, the control on large domains of the alloy composition is not easy since the relative deposition of two metals simultaneously from the same solution depends on the ease of controlling chemical complexing in the bath (Shu et al. 1991). The electroplating of Pd could not escape from the attention of the membrane researchers and Shu et al. (1991) summarized the early attempts.

Nam et al. (1999) employed the vacuum electrodeposition and managed to prepare defect free 1 µm thick Pd-22% Ni membrane supported on a 316L stainless steel porous disk. The highest permeance and H$_2$/N$_2$ selectivity that they achieved were 5.48×10-2 cm^3/cm^2.cm Hg.s

and 4700, respectively (Nam et al. 1999). However, Nam et al. (2000) did not include the total testing time which may change the membrane selectivity. Unlike the electroless plating in which hydrogen coverage takes place from solution to substrate, hydrogen evolution during electroplating initiates right on the substrate surface by the electron attraction of proton onto the electrode/substrate. Thus, the hydrogen blocking or encapsulation during electroplating is much severe, and this has stalled electroplating of palladium membrane from commercial development so far due to the hydrogen embrittlement from the dissolution of this surface hydrogen (Rei 2009). The problem of the hydrogen embrittlement could be solved by alloying Pd with Cu and Ni (Nam et al. 1999; Nam and Lee 2000; Nam and Lee 2000). In the new approach of Chen et al. (2008a; 2008b) the deposition of Pd-cations and hydrogen evolution was controlled by the proper choice of the current density and rpm of the substrate so that the hydrogen blockage during electroplating was prevented.

2.2.4 Electroless plating

Electroless plating processes differ from electroplating processes in that no external current source is required (Bunshah, 1994). Autocatalytic or electroless plating is a selective deposition plating process in which metal ions are reduced to a metallic coating by a reducing agent (R.A.) in solution. Plating takes place only on suitable catalytic surfaces, which include substrates of the same metal being plated, hence the definition autocatalysis (Seshan, 2002). Metal coatings are produced by the chemical reduction with electrons supplied by a reducing agent present in the solution:

$$M^{+n} + ne^- (supplied\ by\ R.A.)$$
$$\xrightarrow{Catalytic\ surface} M^0 (+reaction\ products) \tag{2.7}$$
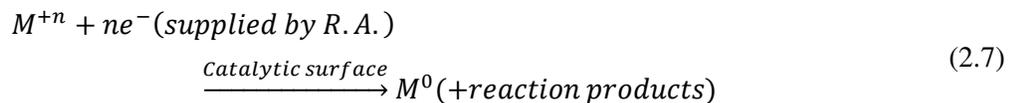
Even though the costs of the complexing and reducing agents used in electroless plating solutions make them non-competitive with electroplating processes for the industrial scale metal coating application, electroless plating fits perfectly for the fabrication of ultra thin Pd membranes. Electroless (or electrodeless) plating offers a number of advantages over electroplating, such as selective (patterned) deposition, but is limited to a few metals and some alloys (Seshan, 2002). More over the electroless plating is preferred due to the following reasons (Bunshah, 1994):

19

- Deposits are very uniform without excessive build-up on corners or projections or insufficient thickness in recessed areas. Internal surfaces are also evenly coated. The uniformity is limited only by the ability of the solution to contact the surface and be replenished at the surface.

- Deposits are usually less porous and more corrosion resistant than electroplated deposits (of equal thickness).

- Almost any metallic or non-metallic, non-conducting surfaces, including polymers (plastics), ceramics, glasses can be plated.

- Those materials which are not catalytic (to the reaction) can be made catalytic by suitable sensitizing and nucleation treatments

- Electrical contacts are not required.

- The deposits have unique chemical, mechanical, physical and magnetic properties.

The deposition of alloys at exact compositions is the main challenge of electroless plating because the controlled co-deposition of two metals is difficult. For composite Pd/alloy membranes, metals are deposited sequentially on the support and heat-treated at high temperatures to obtain the Pd alloy. Uemiya et al. (1991d) applied this method to prepare Pd- 6 wt % Cu and Pd- 7 wt% Ag composite membranes supported on porous glass and then in their following study they were able to fabricate ultra-thin (5 µm) Pd/Ag membranes with the Ag content range of wt% 11-31 (Uemiya et al. 1991c). They referred this method as "coating and diffusion treatment".

The first successful preparation of defect-free composite palladium membrane by electroless plating was reported by Prof. Ma's group (Mardilovich et al. 1997): the first composite palladium membrane ever reported in the literature which was pinhole-free and had high permselectivity (Mardilovich et al. 1997, Rei 2009). At 350°C and $\Delta P = 1$ atm, H_2 fluxes up to 4 m^3/ [m^2.h] and H_2/N_2 selectivity as high as 5000 was observed at the end of 1100 h of testing time. In their following study in 2002 (Mardilovich et al. 2002), it was demonstrated that the thickness of the membrane therefore the H_2 permeance was dependent on the size of the largest pore of the support. The minimum Pd thickness to obtain a dense membrane by electroless plating was approximated three times the diameter of the largest pores in the support

(Mardilovich et al. 2002). Moreover, Ma's group published the performance results of their first Pd/alloy membrane supported on porous stainless steel (PSS) in 2003 (Ma et al. 2003). The Pd/Cu membrane with an oxide layer as the intermetallic diffusion barrier (Ma et al. 2000), with a thickness of 34 μm, had constant H_2 flux of 1.31 m^3/ [m^2.h] for more than 50 hours and H_2/He selectivity of 100 at 350°C and $\Delta P = 1$ atm (Ma et al. 2003).

The popular substrate in the literature appears to be ceramic and Vycor glass. Ceramic supports have the advantages of having very uniform small pore systems which will enable to prepare very thin Pd membranes (1-6 μm), there is no intermetallic diffusion between the ceramic support and Pd and uniform alloys can be formed at higher temperatures. However, PSS supports dominated over the ceramic support due to the following properties: better mechanical strength, operability at high pressures, resistance to cracking, practical module fabrication and sealing and more importantly similar thermal expansion coefficient with Pd which would improve the mechanical strength during the temperature cycling of the Pd membrane (Ma et al. 2004). The solution of the intermetallic diffusion problem between the metallic (PSS) support and Pd layer could be easily solved as mentioned in the previous paragraph. Ma et al. (2003; 2004) investigated the formation of intermetallic diffusion barrier layer by the controlled in-situ oxidation of Pd, Pd/Cu and Pd/Ag-based composite membranes supported on porous stainless steel tubes. The existence of the oxide layer was shown by the SEM and EDS results at temperatures 600°C and higher. Furthermore, following the annealing of a Pd/alloy-based membranes at 600°C, the efficiency of the oxide layer as a diffusion barrier was proven with no intermetallic diffusion of support elements (particularly Fe) to the Pd layer (Ma et al. 2004).

A novel method to fabricate Pd-based membranes, having high tamman temperature intermediate layers, supported on metal substartes was proposed by Ma et. al (2007a). As an illustrative example: first a 0.1 media garde Hastelloy porous support was oxidezed at 700°C, then the support was graded with a slurry containing 4.6 g/L tungsten powder (<1μm particles) and 0.4 g/L silver powder (0.2-0.6 μm particles), and then a porous Pd/Ag/Pd/Ag/Pd layer (12μm) was plated on the support by electroless plating sequentially. Finally, a final Pd layer of 9.3 μm was applied over the porous Pd/Ag layer (Ma et al. 2007a). The H_2 permance of the membrane with the Pd/Ag barrier was 21.8 [m^3/m^2-h-atm$^{0.5}$]$_{STP}$ at the end of 96 hours of testing at 500°C without any sign of intermetallic diffusion of the support elements.

The same method which was also called bi-metal multi-layer (BMML) deposition technique for the formation of Pd/Ag intermetallic diffusion barrier was tested by Ayturk and Ma (2009) and Ayturk et al. (2008). A porous Pd/Ag composite layer was formed by consecutive deposition of Pd and Ag layers, and then a gas tight Pd layer was applied upon the BMML to produce a dense membrane. The permeance of a 23μm thick Pd/PSS membrane without the BMML declined from 8 to 6.5 $m^3/$ [$m^2.h.atm^{0.5}$] in 20 hours. Another 85μm thick Pd/PSS membrane having the Pd/Ag barrier was tested for more than 80 hours and its permeance remained constant at 8 $m^3/$ [$m^2.h.atm^{0.5}$] at 500°C indicating the efficiency of the BMML technique to prevent intermetallic diffusion (Ayturk et al. 2006b). Additionally, porous Pd/Ag diffusion barrier (BMML) was proven to be extremely effective against the intermetallic diffusion of PSS components (Fe, Cr and Ni) with the aid of microstructure analysis through SEM and EDS (Ayturk et al. 2007). The reader is refered to Ayturk et al. (2008) for the isothermal nucleation and growth kinetics of Pd/Ag alloy phase and electroless Pd and Ag deposition kinetics of the composite Pd and Pd/Ag membranes (Ayturk and Ma 2009).

The latest publications of Ma's group, on Pd and Pd/alloy membranes supported on porous metals (PSS, Inconel, etc.), showed the drastic improvement in the composite Pd-based membranes in terms of high permeance and selectivity. When the grading methods developed by Ma's group (Ma et al. 2007a; Ma and Guazzone 2010) were combined with the intermediate Pd/Ag porous metal layers, the fabrication of very thin (3-20 μm) Pd-based membranes having long term selectivity stability was possible (Ma et al. 2007a; Ma and Guazzone 2010; Guazzone and Ma 2006). The porous metal substrate could be graded with a powder having a Tamman temperature higher than the porous metal support prior to plating (Ma et al. 2007a). The purpose of the grading was to obtain a smooth surface for plating so that the support surface would be a good template to have a thin Pd layer on the top independent of the pore size distribution of the original porous metal support. While the grading method provided a smooth template without increasing the mass transfer resistance of the support, the intermediate porous Pd/Ag layer acted as a trap for the diffusing elements from the metal support. Moreover, Pd/Cu and Pd/Au composite membranes were also fabricated with the same method and tested for H_2S resistance (Pomerantz and Ma 2009; Chen and Ma 2010b). A 16.5 μm thick Pd- wt% 18 Cu membrane had a H_2 flux of 15 $m^3/$ [$m^2.h$] at 450°C and ΔP=2.24 bar (40% less than the pure Pd membrane due to the FCC phase structure of Pd-Cu membrane). The H_2/He selectivity of the same Pd/Cu

membrane decreased from 1770 to 220 over a period of 300 h (Pomerantz et al. 2010a). Due to the advantages and promising results provided in the previous three paragraphs, Pd and Pd/alloy membranes supported on porous metal substrates will be the focus of the work discussed in the following Chapters.

Among the composite Pd/Cu membranes that were fabricated via electroless plating by Way's group in 2003 (Roa et al. 2003), a Pd- 9wt% Cu membrane supported on asymmetric zirconia with a 12 µm thickness measured by SEM was better than the other membranes in their study in terms of H_2 flux and selectivity. This Pd-Cu membrane had a H_2 flux of 0.8 mol/ $[m^2.s]$ at 500°C and $\Delta P = 344.7$ kPa with a H_2/N_2 selectivity of 1400 at the end of 25 days (Roa et al. 2003). Later on, Roa and Way (2005) investigated the effect of air exposure on Pd-Cu membranes on ceramic supports. They observed a quasi-reversible change for the H_2 flux (a substantial increase immediately after the air exposure and decrease to a new steady state value); in contrast, the membranes lost their selectivity due to the irreversible defect formation on the surface. The $\alpha \rightarrow \beta$ phase transition was found to be induced faster in air than it was in inert or H_2 flow (Roa and Way 2005). Gade et al. (2009) tested Pd/Ru membranes to obtain membranes with greater mechanical strength and increased H_2 permeability at high temperatures. Their best membrane was a 3 µm thick Pd- 5wt% Ru membrane supported on a Pall AccuSep zirconia-coated stainless steel and had a H_2 flux of 0.9 mol/ $[m^2.s]$ at 500°C and $\Delta P = 78$ kPa. The initial H_2/N_2 selectivity of this membrane was 35000, however the testing time and the selectivity of this membrane at the end of testing was not reported. Most importantly, it was shown that the hardness, consequently the tensile strength of a Pd/Ru alloy membrane was 80% higher than the pure Pd membrane. Thus, Pd/Ru membranes would have higher strength at tough operating conditions (Gade et al. 2009). Recently, Hatlevik et al. (2010) reported the performances of pure Pd and Pd/Ag and Au membranes on stainless steel tubes coated with yttria-zirconia intermetallic diffusion barrier layer and also prepared by electroless plating. The most promising membrane, a 2.3 µm thick Pd-5wt% Au, had a H_2 flux of 1.01 mol/ $[m^2.s]$ at 400°C and $\Delta P = 1.38$ bar and a stable H_2/N_2 selectivity of 82000 and 10 before and after testing, respectively.

2.3. The water-gas shift reaction

The water-gas shift is a reversible and exothermic chemical reaction, usually assisted by a catalyst. Steam and carbon monoxide react to produce carbon dioxide and hydrogen gases:

$$CO_{(g)} + H_2O_{(g)} \leftrightarrow CO_{2(g)} + H_{2(g)} \qquad \Delta H_{(298\ K)} = 41.2\ kJ/mole \qquad (2.8)$$
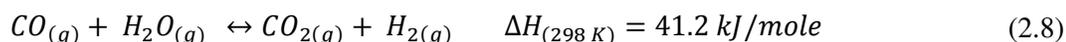
The WGS reaction is a step in many industrial processes like ammonia and hydrogen production. The demand for hydrogen, a product of WGS reaction, is increasing due to the numerous uses of hydrogen such as coal liquefaction and gasification, hydrotreating of ever heavier petroleum and shale oil liquids and use as a direct fuel (Newsome 1980).

The WGS equilibrium shifts to the left of Equation (2.8) at higher temperatures, limiting the complete conversion of CO. Even though the equilibrium favors the formation of products at lower temperatures, the reaction rate is faster at elevated temperatures. The Gibbs free energy is increasing and the equilibrium constant is decreasing as the temperature is increasing as shown in Figure 2-4. The equilibrium constant calculations are detailed in Appendix A. The reaction pressure does not have any significant effect on the equilibrium constant because the WGS reaction is equimolar.

The first ammonia synthesis plants included coupled multiple beds of iron oxide/chromium oxide catalyst with the aid of interbed cooling and 1% exit carbon monoxide levels were achieved. In the early 1960s, the previous system was replaced by two separate catalyst beds one containing iron oxide/ chromium oxide catalyst and the other copper-containing catalyst and the exit CO levels were reduced to 0.1 mol % (Twigg 1989). The WGS reaction is limited by equilibrium, thus the catalytic WGS reaction is typically performed in two steps: high-temperature shift (HTS) and low temperature shift (LTS). The first stage of the sequential WGS reactors is the HTS and it is operated at 350-550°C. The HTS is followed by the LTS with a temperature range of 150-300°C. The structure of the catalyst and the mechanism of WGS reactions will be examined briefly in the following Chapters to be utilized in the process intensification efforts.
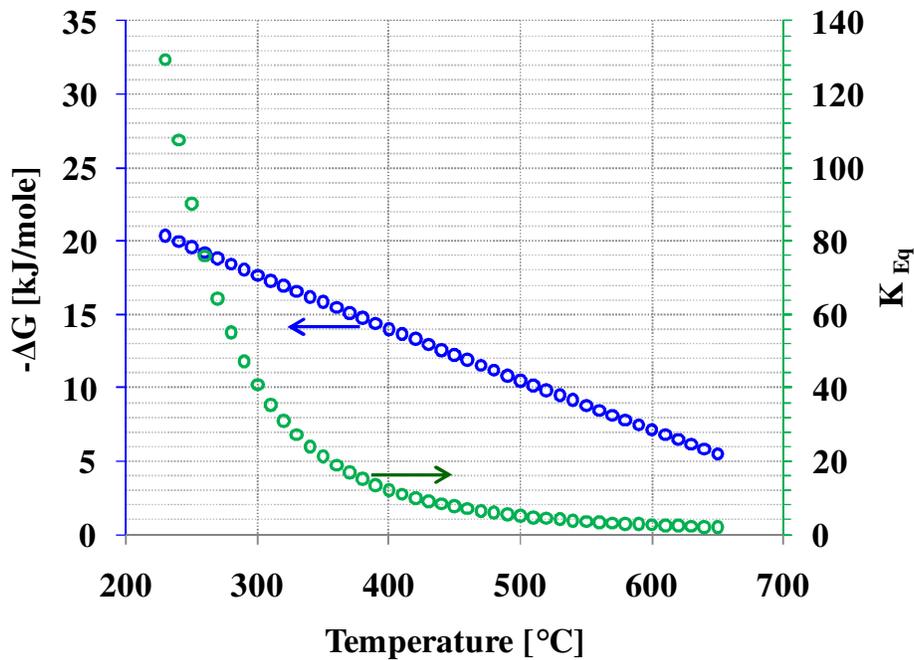
Figure 2-4. Thermodynamic equilibrium of the WGS reaction as described by the equilibrium constant (KEq) and Gibbs free energy (ΔG) as a function of temperature.

2.3.1 High-temperature shift catalyst (Iron-based)

The original catalyst was first used by BASF starting in 1915 (Newsome 1980), and its composition has not been changed much since. The catalyst is basically Fe_3O_4, the stable iron phase under reaction conditions, plus some chromia that is generally believed to act as a stabilizer rather than a promoter and prevents high temperature sintering and loss of surface area (Newsome 1980; Satterfield 1996). A typical composition contains about 55 wt% Fe and 6% Cr. The exact composition varies with the vendor and the typical compositions of two commercial HTS catalyst are listed in Table 2-1. The catalyst is supplied with a low sulfur content (for example, < 0.07%) when the high temperature converter is followed by the low temperature reactor in which the catalyst used is highly sensitive to low concentrations of sulfur compounds. The catalyst is unsupported, usually prepared by a precipitation process, and is available in the form of pellets (6×6 mm in size, for example) or rings (OD×ID×h = 10×4×8 mm) (Satterfield 1996).

25

Table 2-1. Specifications of commercial Fe-based HTS catalysts (Hla et al. 2009).

Catalyst	HTC1	HTC2
Composition		
Fe_2O_3	80-90%	80-95%
Cr_2O_3	8-13%	5-10%
CuO	1-2%	1-5%
Shape	Pellet	Pellet
Size [D×h]	6×6 mm	6×6 mm

The inlet temperatures 305°C and higher must be attained to achieve sufficient reaction rates and the maximum temperature is limited to about 530 to 550°C. Since the WGS is exothermic, the reactor temperature may vary considerably depending on the feed gas composition (Satterfield 1996).

The iron oxide WGS catalyst requires careful reduction before use. The hematite (Fe_2O_3) is partially reduced to magnetite (Fe_3O_4) in situ using process gas mixtures of H_2, N_2, CO, CO_2 and steam as indicated in Equation (2.9) and (2.10) (Rhodes et al. 1995).

$$3Fe_2O_3 + H_2 \rightarrow 2Fe_3O_4 + H_2O \qquad \Delta H = -16.3 \ kJ/mol \tag{2.9}$$

$$3Fe_2O_3 + CO \rightarrow 2Fe_3O_4 + CO_2 \qquad \Delta H = +24.8 \ kJ/mol \tag{2.10}$$
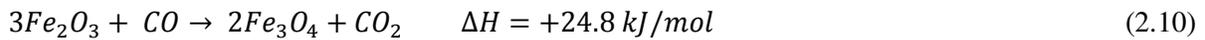
The over-reduction of the magnetite active material to lower oxides, carbides, or metallic iron species should be avoided. Metallic iron species are active catalyst for methanation and the Fischer-Tropsch processes. The Fischer-Tropsch processes will consume H_2 and cause hot spots due to the highly exothermic reaction (ΔH = -206.2 kJ/mol). Furthermore, over-reduction can cause pellet degradation which could cause significant pressure drop across the reactor (Rhodes et al. 1995). The reliable operation of iron oxide WGS catalyst can be ensured by using an empirical formula which is dependent of gas compositions and developed based on plant operation (Lywood and Twigg 1990). The formula for the reduction factor (R_F) is as follows:

$$R_F = [\{f_{CO} + f_{H_2}\}/\{f_{CO_2} + f_{H_2O}\}] \tag{2.11}$$

Plants operating with $R_F < 1.2$ can experience little difficulty associated with catalyst over-reduction. The difficulties caused by over-reduction will be serious if $R_F > 1.6$ (Rhodes et al. 1995).

The conditions that will allow the undesired carbide formation can be predicted with the aid of thermodynamic calculations. For the WGS reaction, the phase boundary calculations for the iron system indicated that the formation of Fe_3O_4 is favored thermodynamically at the operating temperatures of 400-500°C and $H_2O/CO \geq 1$ (Schechter and Wise 1979).

Even though there are many kinetic expressions for the WGS reaction over iron-based catalyst, some of which are extensively different and even conflicting, a generally accepted kinetic expression does not exist (Newsome 1980; Hla et al. 2009; Bohlbro 1961). Impurities in the reacting gases such as H_2S, diffusional limitations or the method of catalyst preparation are believed to be the possible reasons of the discrepancy in the kinetic expressions (Bohlbro 1961). The various derivatives of the mechanistic pathways are based on two main mechanisms (a) associative (adsorptive) and (b) regenerative (oxidation-reduction cycles) (Rhodes et al. 1995). Regenerative mechanisms consist of two sub-systems: steam oxidizes a site on the catalyst surface in one system and carbon monoxide reduces a previously oxidized site on the catalyst surface. The simplest redox-type mechanism could be written by Equations (2.12) and (2.13) (Van Natter et al. 2008). It should be noted that this simple two step mechanism is not the elementary steps of the WGS reaction over the iron-based catalyst and may involve species such as formates and bicarbonates as reactive surface intermediates (Van Natter et al. 2008; Lund 2001; Tinkle and Dumesic 1987).

$$CO + O.* \leftrightarrow * + CO_2 \qquad\qquad (2.12)$$

$$H_2O + * \leftrightarrow O.* + H_2 \qquad\qquad (2.13)$$

Some of the extensively studied WGS mechanisms on the Iron-based catalysts are listed in Table 2-2 and Table 2-3. More comprehensive information could be obtained from the 20 mechanisms derived from combinations of 60 elementary reaction steps reported by Callaghan (2006). Callaghan (2006) applied the Reaction Route (RR) Graph Theory, which incorporates fundamental elements of graph theory and electrical network theory to graphically depict and analyze reaction mechanisms, to the WGS reaction (Callaghan 2006). A simplified model which consisted of 11-steps, 3- route reduced mechanism, was simulated for the Iron-based catalyst and compared with the experimental results. The simplified microkinetic model did not match the experimental data as well as was the case for the Cu-based catalyst. Callaghan (2006) attributed the difference between the microkinetic model prediction and the experimental results to the uncertainties related with the calculated activation energies and the catalyst properties provided by the manufacturer.

It should be pointed out that the mechanism of the reaction would be different during the transient stage. Salmi et al. (1988) and Tinkle and Dumesic (1987) had shown that H_2 is liberated slower than CO_2 at the reaction start-up and pretreatment of the catalyst with steam had a delaying effect on the formation of H_2 (Keiski et al. 1996). Thus, the mechanisms IV and V listed Table 2-3 would express the transient kinetics more accurately.

Compared to the reaction rate equations derived from detailed and specific reaction mechanisms, the empirical power-law models are often used as a relatively simple way to calculate the approximate reaction rate. However, the power-law rate expressions are valid only for specific reaction conditions. The general form of the power law rate expressions is as follows:

$$r_{CO} = k.P_{CO}^a.P_{H_2O}^b.P_{CO_2}^c.P_{H_2}^d.(1-\beta) \tag{2.14}$$

$$\beta = P_{CO_2}.P_{H_2}/[P_{CO}.P_{H_2O}.K] \tag{2.15}$$

where r_{CO} = reaction rate (mol/[gcat.s]); a,b,c,d = reaction order of CO, H_2O, CO_2 and H_2, respectively; k = rate constant = A.exp(-E_a/[R_g.T]); A = pre-exponential factor; R_g = universal gas constant (kJ/[mol.K]); E_a = activation energy (kJ/mol); T = reaction temperature (K); K = equilibrium constant (Foggler 1999).

The details of some of the empirical rate expressions reported in the literature are listed in Table 2-4. The differences between the pellet sizes were reflected in the measured activation energies. The smallest particles give the highest activation energy. The activation energies measured using small catalysts are in the range of 110-113 kJ/mol (Keiski et al. 1992). The low activation energies would be caused by diffusional limitations due to utilization of the large catalyst pellets. The variation in the experimentally determined values of pre-exponential factor is acceptable (Moe 1962).

Table 2-2. Possible mechanisms for the WGS reaction on Fe-based HTS catalyst_1

Adsorptive Mechanism		
I. Langmuir-Hinshelwood type (L-H) (Keiski et al. 1996)	II. Eley-Rideal type (E-L) (Keiski et al. 1996)	III. (Oki and Mezaki 1973)
$H_2O + * \leftrightarrow H_2O.*$ (1) $CO + * \leftrightarrow CO.*$ (2) $CO.* + H_2O.* \leftrightarrow CO_2 + H_2 + 2*$ (3)	$CO + * \leftrightarrow CO.*$ (1) $CO.* + H_2O \leftrightarrow CO_2 + H_2 + *$ (2)	$CO + * \leftrightarrow CO.*$ slow (1) $H_2O + 3* \leftrightarrow 2H.* + O.*$ (2) $CO.* + O.* \leftrightarrow CO_2.* + *$ (3) $CO_2.* \leftrightarrow CO_2 + *$ (4) $2H.* \leftrightarrow H_2 + 2*$ slow (5)

Table 2-3. Possible mechanisms for the WGS reaction on Fe-based HTS catalyst_2

Regenerative Mechanism		
IV. (Tinkle and Dumesic 1987)	V. (Salmi et al. 1988)	VI.(Lund 2001)
$CO + *^1 \leftrightarrow COO.*$ slow (1)	$CO + O.*^a \leftrightarrow CO_2.*^a$ slow (1)	$CO + 2O.* \leftrightarrow CO_3.*_2$ (1)
$COO.* \leftrightarrow CO_2 + *^2$ slow (2)	$CO_2.*^a \leftrightarrow CO_2 + *^a$ slow (2)	$CO_3.*_2 \leftrightarrow CO_3.* + *$ (2)
$H_2O + *^2 \leftrightarrow H_2O.*^2$ (3)	$H_2O + *^b \leftrightarrow H_2O.*^b$ (3)	$CO_3.* \leftrightarrow CO_2 + *$ (3)
$H_2O.*^2 + *^1 \leftrightarrow 2H.*^1$ (4)	$H_2O.*^b + *^b + *^a \leftrightarrow 2H.*^b + O.*^a$ slow (4)	$H_2O + * \leftrightarrow H_2O.*$ (4)
$2H.*^1 \leftrightarrow H_2 + 2 *^1$ slow (5)	$2H.*^b \leftrightarrow H_2 + 2 *^b$ slow (5)	$H_2O.* + O.* \leftrightarrow 2HO.*$ (5)
		$2HO.* \leftrightarrow 2O.* + H_2$ (6)
		$H_2O.* + * \leftrightarrow OH.* + H.*$ (7)
		$2H.* \leftrightarrow H_2 + 2 *$ (8)

(*) active site, (*[1]): active site bonded with two Oxygen, (*[2]): active site bonded with one Oxygen, (*[a]): active site selective to adsorption of Oxygen atom, (*[b]): active site selective to adsorption of Hydrogen atom, X.*: species X adsorbed on the surface.

Steps 7 and 8 of mechanism VI add a route for initially generating surface oxygen from steam over a completely vacant surface.

Table 2-4. Activation energies and reaction orders of the power-law model for Fe-based catalysts

a [CO]	b [H₂O]	c [CO₂]	d [H₂]	Eₐ [kJ/mol]	ln(A)	Source
0.9 ∓ 11.1%	0.28 ∓ 27.3%	-0.58 ∓ 13%	0	114.48	8.59	(Bohlbro 1961)
1	1	0	0	48.95	0.093	(Moe 1962)
0.81 ∓ 6.1%	-0.024 ∓ 2.4%	-0.16 ∓ 2.6%	-0.044 ∓ 2.3%	118.8	7.61	(Podolski and Kim 1974)
0.74 ∓ 2.5%	0.47 ∓ 10.1%	-0.18 ∓ 25%	0	79.79	11.67	(Keiski et al. 1992)
1.1 ∓ 11.6%	0.53 ∓ 24.5%	0	0	95.0	26.1	(Keiski et al. 1996)
0.84	0.08	-0.4	0	122	8.52	(Koukou et al. 1998)
1	1	0	0	112	11.7	(Rhodes et al. 2002; Rhodes et al. 1995)
1.1 ∓ 11.6%	0	-0.36 ∓ 11.9%	-0.09 ∓ 7.8%	111 ∓ 2.5%	6.55	(Hla et al. 2009)
0.9 ∓ 4.6%	0.31 ∓ 18.1%	-0.156 ∓ 50%	-0.05 ∓ 12%	88 ∓ 2.5%	1.52	(Hla et al. 2009)

In an IGCC plant, the syngas is desulphurised to H_2S levels as low as 20 ppmv to prevent the corrosion and fouling of the downstream equipment (Maurstad, 2005). The catalyst activity is reduced by the presence of H_2S in the feed stream and the reaction orders of the other species might be affected (Bohlbro 1963; Xue et al. 1996; Boon et al. 2009). The effect of the H_2S concentration can be included in the power rate law expression as shown in Equation (2.16).

$$r_{CO} = k.P_{CO}^a.P_{H_2O}^b.P_{CO_2}^c.P_{H_2}^d.P_{H_2S}^e(1-\beta) \tag{2.16}$$

The activation energies and reaction orders of the WGS reaction over iron-based catalyst in the presence of trace or significant amount of H_2S are listed in Table 2-5. The experimental results of Bohlbro et al. (1963) showed that H_2S did not form metal sulphides, but adsorbed on the surface and the presence of even 10-15 ppm H_2S in the feed would decrease the CO conversion.

Table 2-5. Activation energies and reaction orders of the power-law model for Fe-based catalyst with H_2S

H_2S [ppmv]	a [CO]	b [H_2O]	c [CO_2]	d [H_2]	e [H_2S]	E_a [kJ/mol]	ln(A)	Source
11-35	0.84	1.17	-0.36	0.09	-0.3	112	0.31	(Boon et al. 2009)
75	0.75-0.8	0.5	-0.1	-0.15	-0.35	94	6.8	(Bohlbro 1963)
2000	0.85	0.4	-0.1	-0.1	-	92	4.6	(Bohlbro 1963)

2.3.2 Low temperature shift catalyst (Copper-based)

In earlier WGS processes, carbon monoxide and dioxide were removed by scrubbing with cupper liquor (e.g., an aqueous solution of copper ammonium formate). The development of low temperature shift catalyst for commercial applications in 1962 was a substantial improvement to convert the remaining CO from the HTS reactor (Satterfield 1996). The typical compositions of the commercial Cu-based catalyst are given in Table 2-6. In the absence of poisonous gases, the Al_2O_3-based catalysts have higher activities and greater resistance to deactivation with time than do Cr_2O_3-based catalysts (Lloyd et al. 1989). The activity and the stability to aging might be affected by the method of precipitation of the catalyst. Hence, the copper crystallites must be as small as possible and separated from one another by the zinc oxide and alumina particles to achieve the maximum activity and stability. The reduction of the copper-based catalyst is usually carried out in dilute H_2 stream. Over-reduction is not a problem for copper-based catalysts; however, hot spots on the catalyst surface might cause sintering of

the active Cu metal due to exothermic reduction represented by the Equation (2.17) (Rhodes et al. 1995).

$$CuO + H_2 \rightarrow Cu + H_2O \qquad \Delta H = -80.8 \, kJ/mol \qquad\qquad (2.17)$$
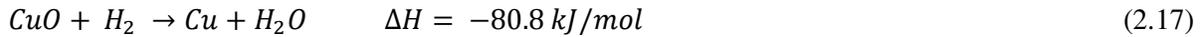
The catalyst was poisoned by sulfur and chloride compounds at concentrations in the range of 1 ppm. The copper metal acted as the active species and the role of the zinc oxide was to protect the copper from poisoning by adsorbing traces of sulfur compounds and reacting with them. Since copper had a relatively low melting point (1084°C), the copper-based catalyst was more benign to thermal sintering than the iron-based catalyst (Satterfield 1996).

Table 2-6. Compositions of the Cu-based LTS catalysts

$CuO[\%]$	$ZnO[\%]$	$Al_2O_3[\%]$	$Cr_2O_3[\%]$	Mn, Al, Mg oxides	Source
32-33	34-53	15-33	-	-	(Satterfield 1996)
33	34	33	-	-	
24	52	-	24	2-5	(Bohlbro 1961)

The most popular reaction mechanisms of WGS reaction on Cu-based catalysts are listed in Table 2-7. The associative mechanism VII (L-H process) shown in Table 2-7 for copper chromite was described by Yur'eva et al. (1969). However, the number of studies, which claimed that the WGS reaction proceeded via the redox mechanism over Cu-based catalyst, was increasing. The cyclic reduction-oxidation reactions must be allowed on the catalyst to prove the validity of the redox mechanism (mechanism VIII in Table 2-7). While it was well documented that the Cu-based catalyst surface could be reduced by carbon monoxide and hydrogen (Salmi et al. 1988), it was still uncertain whether Cu could be oxidized by water rapidly enough to account for the observed reaction rates (Rhodes et al. 1995).

Ovesen et al. (1996) studied the WGS reaction under industrial conditions over three different Cu-based catalysts ($Cu/ZnO/Al_2O_3$, Cu/Al_2O_3, Cu/SiO_2). The redox mechanism was used by them and there was a good agreement with the calculated and measured values of the exit mole fraction of CO for the pressures of 5 and 20 bars and T=180-220°C.

Callaghan et al.(2003) employed 70 possible overall reaction routes (RR) into the microkinetic model and concluded that the WGS kinetics over C was dominated by only three RR shown in Table 2-3 (mechanism IV). The formate and associative mechanisms that they proposed was shown to be dominant at low temperatures (100-200°C). The third one, modified redox mechanism, was predicted to be dominant at both low and high temperatures (100-300°C). Their experimental results at 200°C and 1.5 atm matched well with the results of the microkinetic model.

Gokhale et al. (2008) proposed a new mechanism for the WGS reaction on Cu(111) which involved a highly reactive surface intermediate, carboxyl (COOH). They were able to reproduce the experimental data covering a wide range of temperature, pressure and feed composition by the microkinetic model. In their DFT investigations, the dominant WGS reaction path went through the formation of the carboxyl intermediate, followed by its decomposition via disproportionation with adsorbed OH. More importantly, they claimed that the role of the commonly used redox mechanism was not significant.

The power law type models also appeared to work well to express reaction kinetics of WGS reaction over Cu-based catalysts. The activation energies and reaction orders used in some of the power-law expressions for Cu-based catalysts are listed in Table 2-8. The first expression came from Bohlbro et al. (1970) back in 1970s. Ovesen et al (1996) determined the parameters of the power–law model for $Cu/ZnO/Al_2O_3$ and Cu /Al_2O_3 at industrial conditions. They included the fudge factor (γ) by multiplying the reaction rate with the factor of P_T^γ to correct the pressure dependency and also they took into account the correction of the catalyst deactivation by time (Ovesen et al. 1996). In addition to the experimentally determined parameters for the power-law models, Gokhale et al. (2008) was able to predict and verify the parameters with the aid of the their microkinetic model based on carboxyl mechanism. Consistent with the experimental data, the calculated values of the negative CO_2 and H_2 reaction orders suggested that the WGS reaction on Cu-based catalysts was inhibited by its products (Gokhale et al. 2008).

Table 2-7. Possible mechanisms for the WGS reaction on Cu-based catalyst

VII. (Yur'eva et al. 1969)		VIII.(Ovesen et al. 1992)		IV.(Callaghan et al. 2003) (†i. Formate RR, ii. Associative RR, iii. Modified RR)		V.(Gokhale et al. 2008)	
$CO + * \leftrightarrow CO.*$	(1)	$CO + * \leftrightarrow CO.*$	(1)	$CO + * \leftrightarrow CO.*$	(1)	$CO + * \leftrightarrow CO.*$	(1)
$H_2O + * \leftrightarrow H_2O.*$	(2)	$H_2O + * \leftrightarrow H_2O.*$	(2)	$H_2O + * \leftrightarrow H_2O.*$	(2)	$H_2O + * \leftrightarrow H_2O.*$	(2)
$H_2O.* + CO.* \leftrightarrow * \leftrightarrow$	(3)	$H_2O.* + * \leftrightarrow H.* + OH.*$	(3)	$H_2O.* + * \leftrightarrow H.* + OH.*$	(3)	$H_2O.* + * \leftrightarrow H.* + OH.*$	(3)
$CO_2.* + H_2.*$		$OH.* + * \leftrightarrow O.* + H.*$	(4)	$CO.* + OH.* \leftrightarrow HCOO.* + *$	(4)	$CO.* + OH.* \leftrightarrow COOH.* + *$	(4)
$CO_2.* \leftrightarrow CO_2 + *$	(4)	$OH.* + OH.* \leftrightarrow H_2O.* + O.*$	(5)	$HCOO.* + * \leftrightarrow CO_2.* + H.*$	(5)	$COOH.* + * \leftrightarrow CO_2.* + H.*$	(5)
$H.* + H.* \leftrightarrow H_2 + 2*$	(5)	$CO.* + O.* \leftrightarrow CO_2.* + *$	(6)	$CO.* + OH.* \leftrightarrow CO_2.* + H.*$	(6)	$COOH.* + * \leftrightarrow CO_2.* + H_2O.*$	(6)
		$CO_2.* \leftrightarrow CO_2 + *$	(7)	$OH.* + H.* \leftrightarrow O.* + H_2.*$	(7)	$CO_2.* \leftrightarrow CO_2 + *$	(7)
		$H.* + H.* \leftrightarrow H_2 + 2*$	(8)	$CO.* + O.* \leftrightarrow CO_2.* + *$	(8)	$H.* + H.* \leftrightarrow H_2 + 2*$	(8)
				$CO_2.* \leftrightarrow CO_2 + *$	(9)		
				$H.* + H.* \leftrightarrow H_2.* + *$	(10)		
				$H_2.* \leftrightarrow H_2 + *$	(11)		

† The black reaction steps are common for all three mechanism, the colored steps indicates the differences of the mechanisms.

36

Table 2-8. Activation energies and reaction orders of the power-law model for Cu-based catalysts

a [CO]	b [H₂O]	c [CO₂]	d [H₂]	γ [P_T]	E_a [kJ/mol]	Specifications	Source
0.8	0.5	0	-0.15	-		Large pellets of Cu/Zn/Cr (4.5×4.5mm)	(Bohlbro 1970)
1	1.4	-0.7	-0.9	-0.4	86.5	Cu/ZnO/Al₂O₃ at P_T = 5 bar	(Ovesen et al. 1996)
1	1.5	-0.7	-0.7	-0.4	78.2	Cu/ZnO/Al₂O₃ at P_T = 20 bar	(Ovesen et al. 1996)
1	1.9	-1.4	-0.9	-0.4	59.3	Cu /Al₂O₃ at P_T = 20 bar	(Ovesen et al. 1996)
0.9	0.85	-0.55	-0.7	-	67-70	Modeling results for Cu(111) at P_T = 1 bar	(Gokhale et al. 2008)

2.4. Pd-based membrane reactors for hydrogen production/separation

The complexity of a petroleum refinery contains a vast amount of reactions. Membrane reactors can match easily with many of these reactions for the production of valuable products. The immense need for H_2 in refineries led researchers to new technologies such as the state of the art membrane reactor applications. Dehydrogenation reactions, oxydehydrogenation, catalytic decomposition of H_2S, hydrogenation reactions, steam reforming, water gas shift reaction, conversion of remote natural gas to syngas and liquid fuels are several examples for the membrane reactor applications (Armor 1998). Dixon's review (2003) on catalytic membrane

reactors provides an informative prospect particularly for the application of membrane reactors into dehydrogenation and hydrogenation reactions. Membrane science has focused mainly on selective H_2 separation due to the prominent H_2 separation feature of the Pd-based membrane reactors.

The decision on which process the Pd-based composite membranes would be used is dependent on many parameters such as reaction conditions, the type, availability and amount of the feedstock. By considering the fact that the world still has sufficient amount of coal reserves; mostly shared by US, China and Russia (Rosenberg et al. 2005), syngas as an ultimate product of the coal gasification process appears to be a good fit for the membrane reactor application. The water gas shift reaction can be carried out in a Pd-based membrane reactor to provide reaction and separation simultaneously. Thus, the remaining parts of this study will be devoted mainly on the utilization of the Pd-based composite membranes in the water gas shift reaction. The strengths and features needed to be improved of the WGS Pd-based membrane reactors were reviewed with the aid of the findings reported in the literature in two main categories: 1. experimental studies and numerical calculations to interpret the Pd-based membrane reactor results, 2. the modeling studies at the steady state and dynamic conditions and also process intensification endeavors to enhance the membrane reactor performance.

2.4.1 Pd-based membrane reactors applied for the WGS reaction

Kikuchi et al. (1989) fabricated a 20 μm thick composite Pd membrane on a microporous glass tube (with an average pore size of 300 nm) by electroless plating. This composite membrane was used in the water gas shift reaction membrane reactor and the effect of time factor (catalyst weight/CO feed flow rate), reaction pressure and mole fraction of hydrogen were tested. The CO conversion level was 98% at 400ºC and 5 atm reaction pressure by using a 50 ml/ min feed mixture of CO and H_2O in a molar ratio of 1 by using co-current 400 ml/min argon sweep at 1 atm pressure. Most of the previous studies on pertinent membrane reactor modeling focus on a one- or two-dimensional mathematical representation of the membrane reactor in isothermal or adiabatic operating mode at steady state conditions. In the later study of Uemiya and coworkers (1991a), a one-dimensional steady state model of an isothermal double tubular type of reactor was used to support their experimental results. Also, it was assumed that the H_2

permeation was not affected by any of the coexisting gases and the reaction occurred only on the catalyst, not on the palladium membrane. The physical properties of a composite palladium membrane, consisting of a 20 μm Pd film supported on the outer surface of a porous-glass tube (average pore size of 310 nm), were explicitly used in the simulations. On the basis of the simulation results presented, the high reaction efficiency was credited to the thickness of the Pd film.

The inner surface of a multilayer composite porous alumina tube (γ-Al_2O_3/α-Al_2O_3) was coated with 0.2 μm thick Pd with the co-condensation technique by Basile et al. (1996a) to fabricate an ultrathin palladium membrane. They experimentally demonstrated that a maximum CO conversion of 99.89% could be achieved using a counter-current N_2 sweep at a flow rate of 28 ml/min. They only focused on high CO conversion levels and did not report the H_2 recovery levels. It can be judged easily that the purity of the permeated H_2 was very low due to the poor H_2/N_2 selectivities as low as 2.1. Furthermore, Basile et al. (1996b) tested three Pd-based membranes supported on the multilayer composite porous ceramic supports prepared by three different techniques, namely the magnetron sputtering, physical vapor deposition (PVD) and the co-condensation or solvated metal atom deposition methods. The membrane prepared by the magnetron sputtering technique had a total thickness of 10 μm of 77% Pd and 23% Ag alloy. The thickness of the PVD membrane was not reported. Both of the magnetron sputtering and PVD membranes did not have a uniform thin layer and average pore size of the outer surface of the membrane were estimated to be greater than 10μm. As a result of using macroporous membranes, the CO conversion of these two membranes were below the equilibrium conversion at 322ºC and 1 atm reaction side pressure for the H_2O:CO ratio range of 1-3. The last membrane prepared by deposition of 0.1 μm Pd on the inner surface of the ceramic support via co-condensation technique was able to achieve the equilibrium conversion at 342ºC. However, the membrane lost its stability after 20 hours of operation and had a N_2 permeance of 0.5 mol/[m^2.s.kPa] at 322ºC.

Criscuoli et al. (2000) used the results of a steady state model for a one dimensional isothermal membrane reactor to determine the kinetic rate expression of the low temperature shift that fits the experimental results best. The membrane considered in their work was a 70-75μm Pd film folded into a cylindrical shape. It was assumed that the kinetics of a membrane reactor would be different than the one for a packed bed reactor because of the changes of the

type of the contact between catalyst and reactants, contact time and of the concentrations of the species. They showed that for a fixed-bed reactor, the Langmuir-Hinshelwood kinetics was in agreement with the experimental data; whereas for the use of a membrane reactor, the Temkin model appeared to be in better agreement with the experimental results reported. A similar and more extensive study was conducted by Basile et al. (2001) except that the mathematical model was developed by considering the significance of the diffusive mass transfer (or longitudinal-dispersion term). Rolled membranes obtained by a cold rolling and annealing of Pd and Pd/Ag sheets on ceramic supports were used by Basile et al. (2001). They performed the WGS reaction by using a 70 μm thick Pd and 50 μm thick Pd/Ag membranes. The main function of their ceramic support was to separate the Pd or Pd/Ag membrane from the catalyst bed. The WGS reaction was carried out by varying the CO, N_2 and CO_2 molar flow rates in the feed, total feed flow rate, sweep flow rate and reaction temperature (327-407ºC). Both experimental and simulations results showed an agreement on the possibility to shift towards a 100% CO conversion level (Basile et al. 2001). In the later work of Tosti et al. (2003), they used the same type of membrane (50 μm thick Pd/Ag) and membrane reactor configuration to test the low temperature shift reaction again. In the latter study, they tested the "pilot scale membrane reactor" with the dimensions of 150mm length and 10 mm internal diameter. Prior to the reaction tests, a rolled membrane with a thickness of 68 μm was operated with a pure H_2 feed for 6 months and maintained its infinite H_2 selectivity. The rolled membrane could achieve 98.9-95.4% CO conversion but the H_2 recovery levels were in the range of 83-14% depending on the feed flow rate in reaction temperature range of 325-330ºC and at 1 atm feed pressure (Tosti et al. 2003).

Ma and Lund (2003) developed a two-step microkinetic model to be able to assess the performance of the adiabatic membrane reactor, as well as to describe the kinetics of the high-temperature WGSR in a membrane reactor. A 10μm palladium membrane supported on a porous alumina or glass substrate was considered in their study. The model could also reflect the inhibiting effect of CO_2 on the ferrochrome high-temperature WGS catalyst. On the basis of the simulations conducted, the authors concluded that excess steam, although not necessary to further push equilibrium conversion to higher levels, was still beneficial to control the adiabatic temperature rise.

In the work by Barbieri et al. (2005), a one-dimensional isothermal reactor model under steady state conditions was considered to evaluate the membrane reactor's performance by following basic principles of process intensification. The model was able to capture the effect of operating conditions (temperature, pressure, feed flow rate, etc) on reactor performance and also the catalyst efficiency in terms of the Thiele module. Moreover, the model results were compared with the reaction data measured with a silica membrane on an alumina support. The required membrane area in order to carry out the WGSR was calculated by using the permeation parameters of a tubular Pd/Ag membrane (60µm thick). Based on space time analysis, a very low space time ratio (1/3) between the membrane reactor and a traditional reactor suggests that the volume required by a membrane reactor is significantly lower than that required by a tubular packed bed reactor for achieving the same conversion level.

Even though the self-supported membranes would not be applicable for large scale applications which require membrane durability at high transmembrane pressure differences, the WGS membrane reactor experiments done by Arstad et al. (2006) by using self-supported 1.6 µm Pd/23 wt% Ag membrane would help to explain the fundamentals of the membrane reactor performance. The Pd/Ag films were deposited by magnetron sputtering method and sealed between two steel plates, each with a 17.5 mm drilled hole. The reactions were performed in the temperature range of 190-275ºC with the low temperature Cu/ZnO/support methanol synthesis catalyst. The most important part of their work was the effect of CO on H_2 permeation at low reaction temperatures. The H_2 permeation during the WGS reaction declined 20% over 10 days of experiment. Fortunately, the original permeability of the membrane was restored by regeneration in N_2 flow at 190 ºC at the end of 3 days indicating that CO blocked the specific adsorption/dissociation sites on the surface and did not penetrate severely into the bulk (Arstad et al. 2006). Thus, operating the Pd-based membranes for WGS reaction at low temperatures (190-275ºC) would not be favorable due to the lowered H_2 permeation rate.

The performance of a pilot-scale WGS membrane reactor which consisted of 3-tube module with 1.27 cm OD× 30.5 cm L membranes mounted in a 6.4 cm ID × 105 cm L stainless steel shell casing was tested by Damle et al. (2008). They used a 4 µm thick Pd/Ag composite membrane on yittria stabilized zirconia coated porous stainless steel. The feed composition was H_2:CO:CO_2:CH_4 = 75.2%:15.6%:7.1%:2.1% with the H_2O/CO ratio of 1.2. At 550ºC and 10 atm

shell side pressure, the CO conversion was 65% (47% higher than the equilibrium conversion at the given reaction conditions) with 84% H_2 recovery.

The valuable studies done by Drioli's group for the experimental and theoretical understanding of the catalytic membrane reactors since 90's should be considered as a master guide. Barbieri et al. (2008a) proposed an innovative membrane reactor configuration to use the whole Pd-based membrane surface efficiently. Their reactor consisted of a traditional catalytic bed followed by a typical membrane reactor. Therefore, only reaction took place in the first zone and, in the second zone permeation and reaction took place simultaneously. The main reason of this configuration was the absence of H_2 in the feed which was only CO and H_2O. It was claimed that this novel configuration was necessary when no sweep gas was used to prevent back permeation. The new configuration was 8 cm traditional PBR followed by 9.5 cm in length membrane reactor. The membrane that they used was a 60 μm thick Pd-Ag commercial (Johnsonn-Matthey) membrane with a surface area of 2 cm^2. The WGS reaction was carried out by using a CuO/CeO_2 catalyst at 280-320ºC and up to 6 atm reaction side pressure. The highest CO conversion was 93% at 300ºC and 6 atm at 2000 h^{-1} and 70% of the H_2 produced by reaction was collected as pure permeate stream. In one of their recent work (Brunetti et al. 2009b), a syngas mixture of 33% H_2O, 33% CO, 29% H_2 and 4% CO_2 with balance N_2 was upgraded using a 60 μm thick Pd/Ag membrane on ceramic support by means of the WGS reaction. The membrane reactor was operated at 280-320 ºC and up to 6 atm without using a sweep and the permeate pressure was 1 atm. The highest CO conversion of their MR was 90% which was 2.5 times higher than equilibrium conversion of 36% at the aforementioned reaction conditions (Brunetti et al. 2009b). In their latest study (Brunetti et al. 2011), an integrated membrane plant consisting of a Pd-Ag membrane reactor and a commercial proton exchange membrane fuel cell (PEMFC) was evaluated and the special attention was focused on the effect of changes in the operating condition of the membrane reactor on the whole system performance. Exactly the same membrane as their previous studies was used in the WGS reaction by using a feed of $H_2:CO:CO_2:H_2O = 29\%:33\%:4\%:33\%$ at 290ºC , at the reaction side pressure range of 2-7 atm and at the permeate side pressure of 1 atm without sweep. The best output in terms of electric performance (power ~ 1900 mW and current density ca 210 $mA.cm^{-2}$) was obtained when the membrane reactor was operated at 5.5 atm reaction side pressure and 3200 h^{-1} GHSV. A strong dependence of the integrated system on the Pd/Ag membrane reactor operating conditions was

observed. The PEMFC and membrane reactor requirements were found to be compromised in order to reduce the H_2 loss and crossover and at the same time to maximize the electric performance. The theoretical studies of Drioli's group on membrane reactor modeling and thermodynamic calculations will be discussed in the following Chapter 2.4.1.1.

The carbon molecular sieve membrane reactor performance with the syngas feed containing H_2S was investigated by Abdollahi et al. (2010) from Tsotsis's group. A sulfur tolerant $Co/Mo/Al_2O_3$ catalyst and carbon molecular sieve membrane, which was believed to perform better than the Pd-based composite membrane reactor in the WGS reaction, was used in their study. The highest CO conversion and H_2 recovery were ~64 and 47%, respectively by using the dry syngas composition of $H_2:CO:CO_2:CH_4:H_2S$ = 39.5%:15.2%:32.4%:12.2%:0.7% with H_2O/CO = 1.2 at 250ºC at 5 atm reaction side pressure and sweep ratio of 0.1. The one dimensional steady state model at isothermal conditions was compared with the lab scale membrane reactor results and matched very well. Since their model fitted the experimental results, they also used the same model to predict the large scale (0.0057m O.D. × 1m L) membrane reactor performance in the pressure range of 20-30 atm and at 300ºC. Even though the isothermal model represented the membrane reactor performance fairly well for the lab scale, there might be significant discrepancy between the real performance and the model prediction in terms of temperature rise in the reaction side and hydrogen recovery due to dispersion effects. Thus, at least a two dimensional and non-isothermal model would give better approximations for industrial scale membrane reactor performance. Moreover, the CO content of the permeate flow was predicted to be around 0.3% which would be detrimental for the current PEM fuel cell applications.

2.4.1.1 Modeling of Pd-based membrane reactors for the WGS reaction

There is limited experience mainly clustered around lab scale and none for the industrial scale applications of the Pd-based membrane reactors included into the refinery products. Thus, the design tools such as mathematical models are extremely helpful guide for further technology development. Koukou et al. (1998) used two models of different complexity for the design and optimization of microporous silica membrane reactors used in an Integrated Gasification Combined Cycle (IGCC) plant for better energy efficiency and control of CO_2 emissions. A

simplified model which provided quick predictions for the preliminary reactor design and a detailed computational fluid dynamics (CFD) model both at adiabatic operation were investigated in their work. The materials and energy balances of the microporous silica membrane reactor were identical with the Pd-based dense composite membranes except the H_2 flux equation expressed with the Fick's Law. The permeation properties of a microporous silica membrane which had a H_2 permeability of 2×10^{-6} mol/[m^2.s.Pa] and permselectivity of 15 (H_2/other gases) were utilized in the models. The water gas shift reaction conditions were 325ºC, 36 bar reaction side pressure, H_2O/CO ratio of 1.28 with a steam sweep ratio of 0.92. The target values of the CO conversion and H_2 recovery were set as 90 and 80%, respectively, at the beginning of the simulations to achieve the optimum operation of the WGS membrane reactor. At first, the sensitivity analysis by varying Dahmköhler (Da) number, Péclet number (Pe), feed side pressure, sweep ratio and H_2O/CO ratio, was performed in order to narrow the process configuration and operating condition options. The Da-number, which compares reaction rate and flow rate, is the ratio of the rate of reaction of limiting reactant to the convective transport of the same reactant at the entrance of the reactor (Foggler 1999). According to Koukou's (1998) preliminary modeling results, the increase in the Da-number resulted in a higher CO conversion as would be expected. The H_2 recovery was strongly influenced by Da, increased as the Da-number was increased and the optimum value was fixed as 3.6 for their point of interest. The Pe-number is the ratio of rate of transport by convection and the rate of transport by diffusion or dispersion (Foggler 1999). Koukou et al. (Koukou et al. 1998) showed by modeling that the effect of Pe-number on CO conversion was insignificant and the H_2 recovery was rising with decreased Pe-number. The CFD model indicated that the reaction side temperature would increase from 327ºC to ˜713ºC at the first 25% of the reactor volume. Additionally, it was shown that the temperature increase became less steep at higher inlet flow rates because of lower heat production per gas volume passing through the reaction feed side. The membranes used in the simulation had low H_2 selectivities of 15 and 40. When they simulated the membrane with higher selectivity, the same performance levels were achieved at almost half of the reactor length of the low selectivity membrane (Koukou et al. 1998).

In the following study of Koukou et al. (2001), the effect of non-ideal flow on the performance of industrial scale membrane reactors was emphasized by comparing a plug flow assumption model with an advanced model including dispersion effects. A microporous silica

membrane with a H_2/CO_2 selectivity of 15 and a H_2 permeability of 2×10^{-6} mol/[m^2.Pa.s]. The reactions conditions were as follows: 36 bars feed side pressure, 21 bars permeate side pressure, and inlet temperature of the feed and separation sides was 325ºC. The feed consisted of H_2:CO:CO_2:H_2O:N_2= 38.73%:12.88%:24.31%:22.73%:1.35% and a sweep which was a mixture of 11.3% H_2O and 88.7% N_2 was utilized. The geometry of the membrane was 1.4 cm OD×0.8 cm ID×2 m L with 6 cm distance between the membrane tubes. The H_2 partial pressure profiles on the membrane wall in the reaction side calculated with these two models were compared in Figure 2-5. The maximum in the H_2 partial pressure in the simplified model was not observed in the dispersion model and the dispersion model predicted a steep initial decrease of H_2 partial pressure. Thus, the comparison shows that the driving force for H_2 permeation in the industrial scale membrane reactors would be reduced by the effect of dispersion. In brief, the membrane reactor conversion and H_2 recovery predicted by the dispersion model were lower than the respective values calculated by the simplified model.
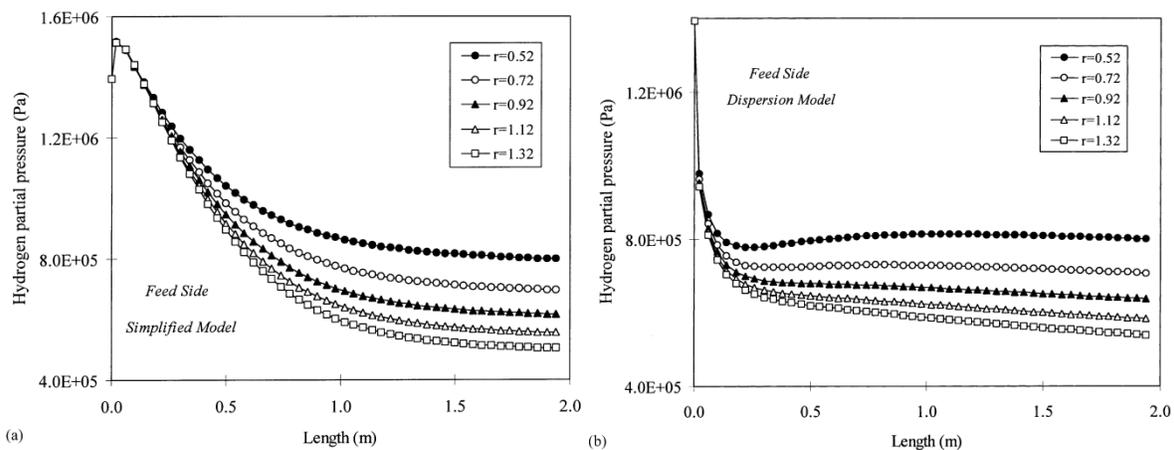
Figure 2-5. Axial profiles of H_2 partial pressure on the feed side membrane surface for various sweep ratios (feed rate = 1.0 kg.m^{-2}.s^{-1}) (Koukou et al. 2001).

In another interesting piece of research work, the performance of a WGSR process system involving a Pd-alloy membrane reactor was analyzed by means of a non-isothermal steady state model developed by Brunetti (2007) and co-workers. The model incorporated Ergun's law to account for the pressure drop on the feed side and an energy balance equation encompassing the heat production by the chemical reaction, the convective flux of energy and

the heat exchange between the furnace and the permeation side. A 60 μm thick self-supported Pd-Ag membrane with a permeability constant of 970 nmol/[m.s.Pa$^{0.5}$] and activation energy of 25.8 kJ/mol were used in the modeling efforts. The membrane reactor that they simulated had geometric characteristics of 1 cm OD× 50 cm L in a shell casing with 2 cm ID. The operating conditions were varied for the temperature range of 220-320ºC, the feed pressure range of 2-30 atm with a H_2O/CO ratio of 1 of the feed. Two mixture compositions were considered in the simulations; mixture 1: 50% CO and 50% H_2O and mixture 2: $H_2:CO:CO_2:H_2O$ = 50%:20%:10%:20%. Brunetti et al. (2007) used the Da number as the main parameter to identify the conditions that assure an improved membrane reactor performance without sweep gas. The solution of their one dimensional mass and energy balances together with the help of Da number analysis indicated that a Da number of 1 for a membrane reactor gives a better use of the catalytic bed and, thus, a better reactant management. The predictions showed that up to 95% CO conversion and 95% H_2 recovery could be achieved at high reaction side pressure (1500kPa). Moreover, the membrane reactor volume to reach 90% CO conversion was compared with the one required from a traditional packed bed reactor (PBR). At 15 atm reaction side pressure and 1 atm tube side pressure, a reduction of reaction volume by a factor of 4 was calculated in the case of the membrane reactor. Therefore, the necessary amount of catalyst to attain the target conversion level was significantly reduced and plant size reduction was an obvious gain particularly for the process economics. Furthermore, of notable insightfulness was the two dimensional reactor model developed by Chiappetta et al. (2008) which explicitly introduced a convective term in the axial direction and a diffusive one in the radial direction. The proposed modeling framework allowed choosing the appropriate feed pressure, sweep gas flow rate and temperature, the amount of catalyst along the length of the reactor to optimize conversion, as well as the temperature profile to mitigate potentially dangerous operational problems due to hot spot formation or prevent thermal runaway incidents. The most interesting part of Chiappetta's work (2008) was the effect of catalyst mass distribution. Three different catalyst distributions namely constant, linearly increasing and exponentially increasing were considered to prevent hot zones which would be detrimental for the membrane integrity. A catalyst mass increased linearly along the membrane reactor was found to be more efficient than an exponentially increased distribution to control the hot spots.

A multi-tubular membrane reactor with the catalyst in the shell side and co-current flow of the permeate side was selected as the focus of the theoretical work done by Adrover et al. (2009a). The reactor was assumed as globally adiabatic with respect to the environment without external coolant. The permeation properties of a 60 μm thick membrane tested by Criscuoli et al. (2000) with the dimensions of 13.4 mm OD× 8 mm ID × 26.8 mm L was used in their one dimensional model at steady state conditions. The feed composition was H_2:CO:CO_2:H_2O:CH_4 = 43.48%:7.97%:10.99%:31.88%:5.28%. The total area of the multi-tubular membranes was varied by changing the number of tubes which was selected as 63 to reach ˜60% H_2 recovery. The highest CO conversion based on the simulation results was 85% at 7 atm shell side pressure without sweep and the extent of temperature rise was 80ºC with the feed temperature and flow rate of 300ºC and 345 mol/h, respectively. Moreover, the stability analysis of the same type of membrane reactor by using the same one dimensional steady state model under non-isothermal conditions was investigated to find out the multiplicity of the steady states in the next study of Adrover et al. (2009b). In particular, the thermal effects of the inlet temperature of the sweep, flow rate of the sweep and configuration of the sweep gas as co-current and counter-current on the membrane reactor performance were examined with the aid of the simulations. The counter-current operation showed multiplicity of steady states for the operating conditions Adrover et al. (2009b) selected. The stability of the membrane reactor increased and, thus, the extinction temperature decreased, as the sweep gas flow and the inlet temperature were decreased. When the conventional packed bed reactors were compared with the membrane reactor, it was shown that the multiple steady state regions were wider for the membrane reactor. This high instability was attributed to the H_2 permeation which was magnifying the thermal effects. On the other hand, the co-current configuration did not exhibit steady state multiplicity and led to lower parametric sensitivity together with more isothermal axial profiles.

Although the pertinent body of literature encompasses many studies that rely on steady state mathematical models of membrane reactors, Pd-based membrane reactor studies for analysis and control purposes conducted with the aid of a comprehensive, insightful and computationally tractable unsteady state (dynamic) process modeling framework (Raich and Foley 1995; Fu and Wu 2008) remain relatively limited and deserve further attention. Within such a context, cyclohexane dehydrogenation was compared with isobutene dehydrogenation in a palladium membrane by Raich and Foley (1995). It was predicted that the reactor volume

required for isobutane dehydrogenation would need to be at least 750 times larger than that required for cyclohexane based upon published kinetics for commercial catalysts. Using a transient CSTR-CSTR modeling approach, Raich and Foley (1995) studied the coking and deactivation processes of the catalyst and the membrane noting that deactivation could occur in the hydrogen deficient reaction zone of the palladium reactor. On the membrane reactor dynamic analysis front, a non-isothermal unsteady-state model was developed to simulate methanol steam reforming using a double-jacketed Pd-based membrane reactor introduced by Fu and Wu (2008). Since various species concentration variations as well as reformer temperature fluctuations were difficult to measure and characterize experimentally during transient periods in the reactor's operational life, the proposed transient reactor model was used to determine the optimum operating strategy at the start-up stage.

The systematic dynamic modeling and optimization studies of the methanol synthesis conducted by Parvasi et al. (2009) and, Rahimpour and Behjati (2009) included a Pd/Ag membrane in the synthesis loop. The detailed dynamic model encompassing all basic equipments (mixer, heat exchanger, reactor and separator) in the methanol synthesis loop was used to predict the characteristics of the overall process (Parvasi et al. 2009). It was shown that increased production rates through the use of Pg/Ag membranes were balanced by the reduction of the production rates due to catalyst deactivation. A similar approach was followed to optimize the Pd/Ag membrane dual-type methanol reactor performance in the presence of catalyst deactivation with the aid of a dynamic model (Rahimpour and Behjati 2009). The primary dynamic optimization objective was to maximize methanol production by identifying the optimum membrane thickness, the temperatures of feed (cooling gas), cooling saturated water and the processing gas. It should be pointed out that the optimum membrane thickness was found to be only 0.3µm, and fabrication of highly selective membranes with such a thickness would be certainly challenging.

2.5. Process intensification (PI) for membrane reactors

In the scientific literature, the term *process intensification* started to appear in the mid-1960s and early '70s, mostly in East European publications concerning metallurgical processing (Chvatal 1965; Chervotkin et al. 1969; Grekov 1970; Kolpakov et al. 1971). The *process*

intensification at that time was understood as simply equivalent to *process improvement*. Also, in the first chemical industry–oriented articles (all of East European origin, by the way), the term *process intensification* had that same meaning (Leszczynski 1973; Kleemann et al. 1978). The birth of process intensification as a chemical engineering discipline came several years later in the United Kingdom and was marked by the paper published in 1983 by Colin Ramshaw from the ICI New Science Group, who described their studies on the application of centrifugal fields (so-called "HiGee") in distillation processes (Ramshaw 1983). The end of the 20th century and the beginning of the 21st have seen a fast growth in PI-related activities in both industry and academia (Stankiewicz and Moulijn 2004).

The philosophy of process intensification has been traditionally characterized by four words: *smaller, cheaper, safer, slicker*. This general philosophy of process intensification follow concrete opportunities, such as cheaper processes, smaller equipment/plant, safer processes, less energy consumption, shorter time to the market, less waste/by-products and better company image, that PI offers to chemical enterprises (Stankiewicz and Moulijn 2004). The development of the membrane reactors is an evident outcome of the ongoing process intensification efforts. Since the performance of the Pd-based membrane reactors has not been evaluated at industrial conditions, there is still a vast lack of information particularly on the safety aspects and economics of the Pd-based membrane reactors.

Many process intensification studies on membrane reactors clustered particularly about the performance enhancement of water-gas shift and methane steam reforming (MSR) membrane reactors. Thus, previous publications on performance enhancement, safety aspects and economical evaluation of (WGS or MSR) membrane reactors will be summarized in order to classify already accomplished tasks and improvements/unknowns waiting to be identified about the membrane reactor technology.

2.5.1 Performance enhancement

Sun and Khang (1990) compared the performance of a catalytic membrane reactor (CMR) with three different reactor type: the inert membrane reactor with catalysts packed in the feed side of the membrane (IMRCF), the plug flow packed bed reactor (PFR), and the mixed flow reactor in which catalyst pellets are well-mixed with reactants (MFR). Moreover, three

general reaction categories were also considered for all types of reactors: 1) the volume is increased after reaction (gas phase reaction), 2) the volume remains constant after reaction (liquid or gas phase reaction), 3) the volume is decreased after the reaction. The mathematical model offered by Sun and Khang (1990) included a microporous membrane where gas diffusion followed Knudsen diffusion. The simulation results of Sun and Khang (1990) indicated that both types of membrane reactors performed better than the traditional PFR and MFR. Between two membrane reactors, the performance of the IMRCF was better than that of the CMR at high space times for the reaction where no volume change occured like the water-gas shift reaction.

The review article by Hughes (2001) summarizes the preparation methods, configuration options of the membrane reactors, means of increasing flux and advantageous operating conditions of the composite palladium membrane reactors. Hughes pointed out one of the most important design criteria for the performance enhancement part of the process intensification of membrane reactors: the balance between the feed rate, reaction rate and permeation rate. The membrane reactor performance could be quantified via the comparison of the Dahmkohler-Peclet (Da.Pe) number product, where Da number expressed as the reaction rate divided by feed rate and Pe number which is the ratio of the feed rate to the permeation rate. The range of the product Da.Pe should lie between 0.1-10 to achieve optimum membrane reactor performance. Additionally, an innovative way of process intensification namely controlled addition of hydrogen through Pd membranes was suggested by Hughes (2001). According to Hughes (2001) theoretical claim, controlled H_2 addition could provide similar benefits to the controlled oxygen addition in partial oxidation and oxidative processes. Some advantages for the Pd membrane reactors include: the subsequent separation of unreacted H_2 is avoided, the reaction rate is controlled by H_2 pressure and hence so is the permeation rate, commercial H_2 can be used without poisons, and hydrogenation would be more selective because of less frequent side reactions at lower H_2 pressures, desired hydrogen concentrations could be maintained along the permeater length.

An interesting process intensification work was published by Wieland et al. (2002) on a membrane reactor in which methanol steam reforming reaction took place to supply H_2 to a fuel cell. The H_2 permeation characteristics and performances during reaction of three different membranes, a coated 40 µm thick vanadium membrane (Pd/V/Pd), 25 µm thick $Pd_{60}Cu_{40}$ and 25 µm thick $Pd_{75}Ag_{25}$ membranes, were compared. Even though the permeance of the Pd/V/Pd

membrane was 1.7 times higher than the permeance of the $Pd_{75}Ag_{25}$ membrane, the Pd/V/Pd membrane lost its stability at partial pressures higher than 4.2 bara. While the conversion levels of both Pd/Cu and Pd/Ag membranes were almost identical 99-100%, the H_2 recovery levels of Pd/Cu membrane was ~50% less than those of the Pd/Ag membrane.

Pioneering work of Drioli's group on both theory and practice has been providing inspiration and guidance to many other researchers on the membrane reactor area. One of their works, theoretical study of Barbieri et al. (2005) concentrated on the process intensification strategies only for performance enhancement of a lab-scale low-temperature WGS membrane reactor without the safety and economics aspects. The mathematical model was evaluated at the reaction conditions of T = 210-350°C, $P_{reaction}$ = 1-5 bars, R_{H2} = 0-100%, which would completely be different than the industrial WGS reaction conditions. The H_2 permeation properties of a 60 µm thick Pd/Ag membrane were used. The advantage of using a membrane reactor was more evident at higher H_2 recovery levels and increased as the temperature was increased at a fixed H_2 recovery level as seen in Figure 2-6.
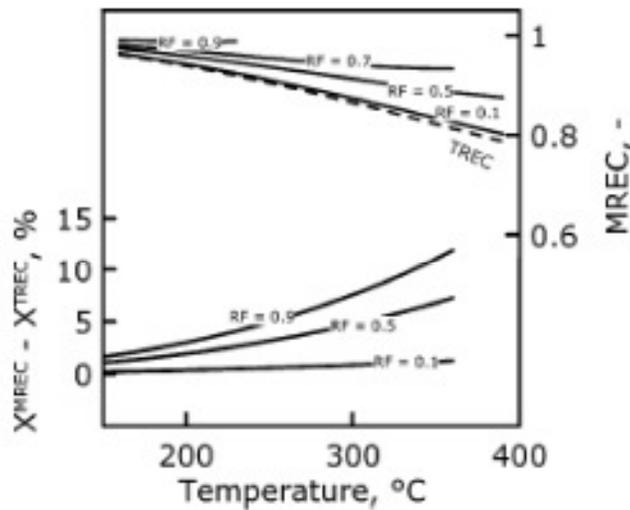
Figure 2-6. X^{MREC} - X^{TREC} and MREC as a function of temperature at different RF values. $P_{Reaction}$ = 1 bar. Solid lines: model results, Dashed line: TREC. (MREC: membrane reactor equilibrium conversion, TREC: traditional packed bed reactor equilibrium conversion, RF: Hydrogen recovery factor)

One of the most interesting features of membrane reactors is the positive effect of increased pressure difference between the reaction and permeate sides on the performance, particularly for reactions without volume change. As the pressure difference was increased the maximum possible CO conversion could be achieved at shorter-space times. The pressure acts in a traditional packed bed reactor only on kinetics, while in a membrane reactor it enables H_2 permeation through the membrane, which induces further product formation, having a positive effect on thermodynamics (Barbieri et al. 2005).

The aim of the work of Chiappetta et al. (2006b) was the theoretical analysis of the combination of both polymeric and palladium (Pd) separators as well as Pd-based membrane reactors for the recovery of extra purity H_2 production (CO content of the permeate < 10 ppm). The integrated membrane systems were compared to determine the lowest total membrane area and compression costs while meeting the H_2 separation target of 90%. Screening of the sequences was performed by considering the higher cost of Pd membranes compared to polymeric membranes, compression power and H_2 losses. For the syngas composition that Chiappetta et al. (2006b) considered (the syngas composition was not specified), the combination of Pd-based separation followed by a Pd-based membrane reactor operating at 25 atm was found to be more appropriate than the reverse sequence. When the driving force for H_2 permeation was low (5 atm feed side pressure), the syngas mixture was first fed to the two-stage polymeric membrane, then the re-compressed permeate stream was directed to a Pd-based separation unit while the retentate streams were processes in two Pd-based membrane reactors. However, the compression cost Chiappetta et al. (2006b) considered originated from the syngas compression which would be an unnecessary assumption. The most significant source of syngas is the coal gasification plants and the gasifiers already work at high pressures (24-50 atm, (US DOE-Hydrogen from coal, 2011; 2007)). The syngas stream leaving the gasifier will already be at high pressure without an extra compression cost. Moreover, the Pd-based separation units and reactors used in the work of Chiappetta et al. (2006b; 2006)were Pd foils having Pd thicknesses higher than 50 µm which would lead the economic analysis to the wrong direction. The current Pd membrane technology enables the fabrication of membranes with Pd thicknesses as low as 10 µm with very high H_2 selectivities (Mardilovich et al. 1997; Collins and Way 1993).

Since methane steam reforming is another important area of the membrane reactor application, the process improvement studies on the membrane reactor for methane steam

reforming has to be taken into consideration. A thoroughly studied example published by Drioli's group (Marigliano et al. 2001) involved the analysis of the energy transport in an annular and also tubular membrane reactor. The membrane tube which had an active 7.5 µm thick Pd/Ag layer on the outer surface of an Al_2O_3 porous support was the inner tube and the stainless steel shell casing was considered as the outer tube. Thus, two different catalyst packing options were available: packing the catalyst inside the membrane tube or inside the annulus between the shell casing and the membrane tubes. When the reaction took place in the annulus, the rate of heat transfer was high and the reaction side temperature reached the oven temperature which was set to the target reaction side temperature for the endothermic methane steam reforming. In contrast, the heat transfer resistance was high in the tubular membrane reactor, thus, the reaction side temperature remained lower than the oven temperature. The results of a one-dimensional mathematical model showed that the overall conversion of the membrane reactor was an increasing function of temperature, sweep factor and overall heat transfer coefficient. A lab-scale annular membrane reactor was found to have better thermal performance and higher conversion than the tubular membrane reactor for the methane steam reforming (Marigliano et al. 2001).

The best combination of all of the parameters, e.g. reaction temperature, pressure, feed flow rate, steam to limiting reactant ratio and etc, and could be determined by screening one by one or using an optimization code to maximize the overall conversion and H_2 recovery levels. A steady state, non-isothermal, non-isobaric and one dimensional model was first compared with experimental results of (Shu et al. 1994) and used as the basis of the optimization routine by Silva et al. (2008). The influence of inlet reactor pressure, methane feed flow rate, sweep gas flow rate, external reactor temperature and steam to methane feed flow ratio on methane conversion and H_2 recovery was analyzed. The objective function of the constraint optimization problem was the summation of methane conversion and H_2 recovery. The optimization results of Silva et al. (2008) showed that high levels of CH_4 conversion and H_2 recovery, 99.4% and 98.19%, respectively, could be achieved for the lab-scale methane steam reforming membrane reactor. However, one should keep in mind that while optimization of lab-scale membrane reactor parameters would be helpful for further steps of performance enhancement, the socio-economic conditions of the time of interest might cause the optimization results deviate significantly from the expected performance of an industrial scale membrane reactor. Thus,

economic analysis together with the performance enhancements efforts would result in more meaningful performance predictions.

As Bhat and Sadhukhan (2009) pointed out that recent emphasis on membrane reactor technology was on the development of better membranes, more efficient reactor configurations and better modeling approaches for analysis and optimization. More importantly, the process performance needs to be optimized specifically with respect to the two most important factors: the membrane area and the energy consumption in an integrated industrial scale framework. In the light of previous studies, the outlines of the performance enhancement of the membrane reactors could be listed as follows: The nature of the reaction (volume change, reversible-irreversible, endo-exothermic) is one of the key design considerations to improve the membrane reactor performance.

2.5.2 Process safety

Process safety is an indispensable part of the entire process intensification practice, as mentioned earlier. "No technology is absolutely safe!" (Winter 2009). Each technology including energy sector has its specific safety standards, and hydrogen energy does not differ from others in this context. In this Chapter 2.5.2, the basic definitions and principles, methodology of the safety analysis will be explained. Further, some illustrative examples from the existing literature about the hydrogen and Pd-based membrane reactor safety will be mentioned shortly.

Hazard or hazardous event or incident is defined as: an inherent chemical or physical characteristic that has the potential for causing damage to people, property, or the environment. In general, most hazards that arise in a system are thought to be due primarily to defects in design, material, workmanship, or human error (Nolan 1994). Widely used methodologies to identify hazards are (Hyatt 2003):

- Preliminary Hazards Analysis (PrHA). Also known as Screening Level Risk Analysis (SLRA)

- Hazard and Operability Analysis (HAZOP)

- Failure Mode and Effects Analysis (FMEA)

- What If Analysis

- Checklist

- What If + Checklist

Among all, HAZOP is the most widely used methodology in the world today as a tool for hazards identification. The advantage of HAZOP is that it is very thorough because most of the aspects are examined meticulously. On the other hand, HAZOP is very time consuming and costly. If not set up correctly and managed properly, it can be ineffective. An expert in the field of HAZOP has to lead the team. The keystones of the HAZOP analysis are basically (Hyatt 2003):

- Analyze the potential hazards and deficiencies.

- Indicate the cause mechanisms.

- Indicate potential consequences.

- Identify potential safeguards & redeeming features.

- Provide recommendations for any fix-it/remedial type solutions.

A worksheet (data base spreadsheet) form is used to collect and collate the process hazard analysis review data (Nolan 1994). The steps that have to be followed systematically during the HAZOP analysis are listed below (Hyatt 2003):

1. Collect applicable documents and drawings, e.g., process flow diagrams, piping and instrument diagrams, plot plans, etc.

2. Break facility down into manageable Chapters ("**Nodes**").

3. Prepare list of **Parameters** and **Operations** to be examined, composition, pressure, temperature, flow, etc. For batch operations list specific operations, e.g., transfer feed charge to reactor.

4. Apply **Guidewords** to **Parameters** and **Operations**.

- Main **Guidewords** (GW)

   o Words that imply an excess: **More** or **High** or **Higher** or **Greater** than the design intent.

- o Words that imply insufficiency: **No**, **None**, **Less** or **Low** or **Lower** or **Reduced** than the design intent.

- o Words that imply incompleteness: **Part of** or **Not all of** or **Partially** of the design intent.

- o Words that imply additional things occurring: **As well as** or **In addition** to the design intent.

- o Words that imply the reverse of something happening: **Reverse** or **Opposite to** or **Instead of** the design intent.

- o Words that imply something may have been overlooked: **Other than** or **What else** the design intent.

The design intent reflects the specific purpose for an item of equipment, piping, etc.

- • **Parameters** and **Operations**

  - o Applicable parameters typically include pressure, temperature, flow, composition, level, reaction rate, viscosity, pH

  - o Applicable operations typically include filling, transferring, purging, emptying, draining, venting, maintenance, start-up, shut-down.

5. For each **Node** create **Deviations**, e.g., High pressure, High temperature, High flow, Low pressure, Low temperature, Low flow, Reverse flow, etc.

6. List and record **Causes** for each **Deviation**.

7. List and record **Consequences** associated with each **Cause**.

8. List and record **Safeguards** or Controls that may prevent the **Cause** and for the **Consequences**. Safeguards are measures taken to prevent or mitigate the risk of accidents (operator surveillance, instrumentation, ESD, blowdown, etc.) (Nolan 1994).

> **Severity (S):** The magnitude of physical or intangible loss consequences (qualitative measure of consequences compared to industry experience).

> **Likelihood (L):** A measure of the expected frequency of an event's occurrence (qualitative measure of probability based on historical data or theoretical estimate).

Ranking (R): The qualitative estimation of risk from severity and likelihood levels, in order to provide a prioritizing of risk based its magnitude (refer to corporate risk matrix for ranking based on severity and likelihood levels).

9. List any future **Actions** or **Recommendations** that is thought to be implemented.

A typical HAZOP worksheet consists of the above titles indicated by bold letters and a suggested arrangement is shown in Table 2-9.

Table 2-9. Suggested HAZOP worksheet arrangement (Nolan 1994)

GW	Dev.	Causes	Consequence	Safeguards	S	L	R	Recs	Remarks	Comments

As mentioned in Chapter 2.4, the integration of Pd-based membranes into the coal gasification plants will be considered as the case study. Since the coal-fired power plants have being operated since 1920s (WRI-Pulverized Coal Power, 2011), there is enough operating confidence and most of the safety procedure are already established. Thus, in the case of Pd-based membrane reactor integration into coal-fired power plants; membrane reactor module needs to be considered as a new "node" and the HAZOP analysis has to be updated. The integration of Pd-based membrane reactors into coal-fired power plants is a mint new technology and the implementation of inherent safety for new plants is simpler and cheaper because the design exists only on paper (Mannan, 2011). In addition to membrane reactor safety analysis, the next obvious safety concern arises from extra purity H_2 production. In terms of the use of membrane reactors in electricity production plants, one important difference of H_2 is its capability of energy storage and transportation unlike electricity. Thus, if H_2 is not used directly for power generation it can be stored and transported for later use and necessary safety regulations have to be followed.

Selected safety related data for hydrogen and methane in comparison to gasoline are shown in Figure 2-7. The most distinguished four characteristics are as follows: 1) the diffusivity of hydrogen in air is very high, 2) the ignition energy of an ignitable hydrogen/oxygen mixture is very low, 3) the ignition range is wide, 4) carbon compound in hydrogen as well as radioactivity and radio-toxicities are inexistent.

Hydrogen quickly disperses vertically upwards into the air environment and, thus this feature could be thought as a safety element if the presence of an ignition element is prevented. However, the frictional electric potential on human skin or a micro-arc from an electric switch might be suffice to ignite the hydrogen/oxygen mixture. Furthermore, no risk can be treated lightly, but if the safety rules and regulations are strictly adhered to, hydrogen systems are safer than hydrocarbon systems based on the experience of engineers working with hydrocarbon and hydrogen (Peschka et al. 1992).
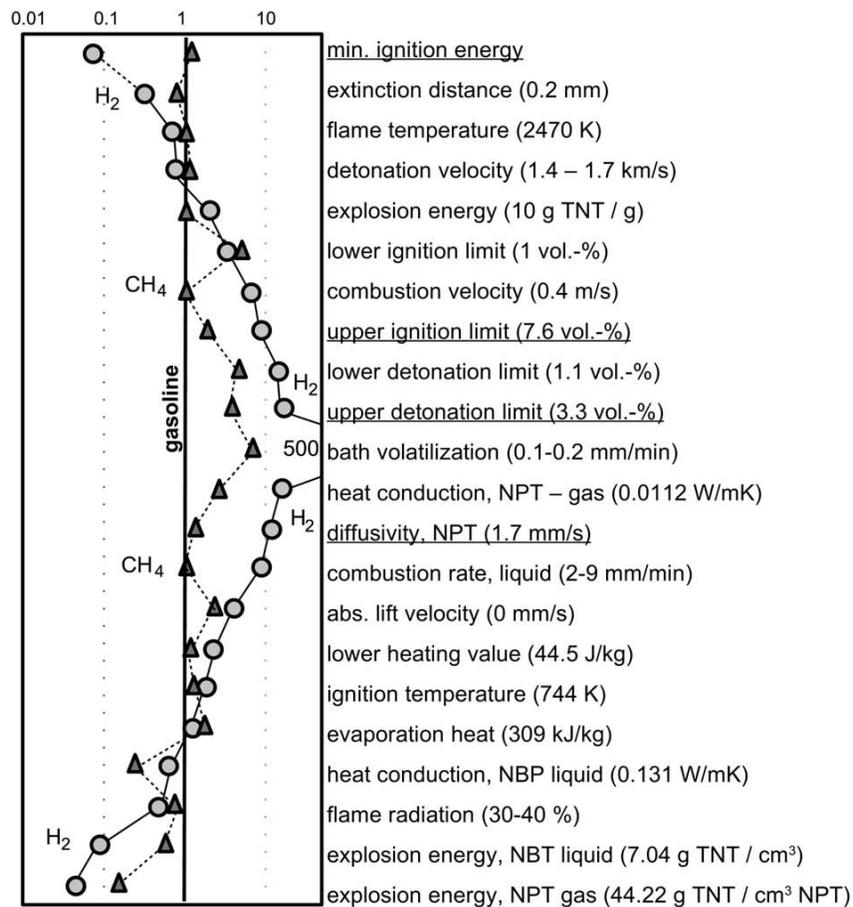
Figure 2-7. Safety data of hydrogen and methane compared to gasoline Data in brackets for gasoline; TNT: Tri-Nitro-Toluene; NPT: normal pressure and temperature (gas); NBT: normal boiling temperature (liquid) (Peschka et al. 1992).

The first analysis on Pd-based membrane reactor safety aspects was from Drioli's group by Chieppetta et al. (2006a). A two-dimensional–axial and radial directions- mathematical model was simulated at non-isothermal and steady state conditions. The membrane reactor was used as

the "node" by following the HAZOP logic. The parameters which would cause deviations from the intended design levels were reaction side temperature, pressure, sweep flow rate, molar feed ratio and feed flow rate. The behavior of a lab-scale membrane reactor was simulated for the range of each parameter and the conditions potential to cause hazards for personnel, environment, and reactor performance were identified. The utilization of sweep gas was found useful for both enhancing the hydrogen driving force and controlling the temperature profile inside the catalytic bed to prevent hot spots. Even though increased molar $H_2O:CO$ ratios lead to increased conversion levels in isothermal membrane reactors, the same effect was not observed in non-isothermal reactors due to lowering of the reaction side temperatures as the $H_2O:CO$ ratio was increased.

2.6. Economics of Pd-based membrane reactors

In the United States, coal resources are larger than remaining natural gas and oil resources. Coal-fired plants continue to lead the electricity output of the US by constituting 45% of the total electricity generation in 2009. The share of coal-fired power plants may remain as the dominant portion, 43%, by 2035 according to *AEO2011* reference case (EIA-U.S. Coal Reserves Current and Back Issues, 2011). Based on the projections of *AEO2011* up to 2035, the total energy supply will dominantly be dependent on dry natural gas and coal as shown in Figure 2-8. Coal is expected to remain as one of the essential sources due to its low cost and broad availability.

The challenge in the coal-fired systems is to achieve the highest thermodynamic efficiency with the lowest emissions of pollutants and greenhouse gases (Beér 2000). The most problematic emissions include sulfur dioxide (SO_2), nitrogen oxides (NO_x), particulate matter (PM), mercury (Hg) and carbon dioxide. The improvements of the thermodynamic efficiency would also result in reducing pollutant emissions from electric power plants. The Integrated Gasification Combined Cycle (IGCC) plants have achieved the lowest levels of critical pollutant air emissions (NO_x, SO_x, CO, PM10) of any coal-fired power plants in the world (Ratafia-Brown et al. 2002). In terms of emission performances, traditional pulverized coal plants have the highest air pollutant emission and the new generation IGCC power plant emissions are very close

to those of Natural Gas Combined Cycle (NGCC) which releases the lowest level of air pollutants (Rosenberg et al. 2005).
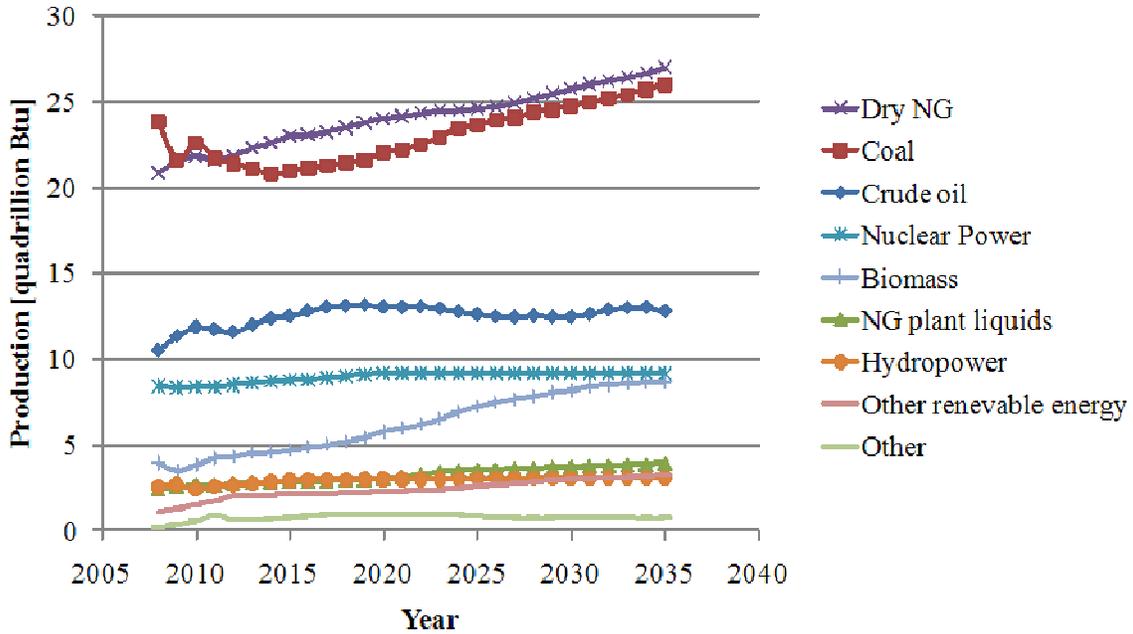
Figure 2-8. Total energy supply summary (EIA-U.S. Coal Reserves Current and Back Issues, 2011)

The modern coal gasification technology is combined with both gas turbine (Brayton cycle) and steam turbine (Rankine cycle) power generation in an IGCC plant. The net efficiency (% LHV) of the IGCC plants is very close to the traditional systems. The demonstration plants in Europe (one in Buggenum, Netherlands and the other in Spain) are between 43-45% which is very close to the efficiency of the generally accepted pulverized coal (PC) combustion in super critical steam boiler in a Rankine cycle (Beér 2000). Moreover, the cycle efficiency could approach 60% in a plant configuration where hydrogen is also produced in the gasification process and Brayton-Rankine cycles are combined with fuel cells. In addition to the advantages of the IGCC plant in terms of environmental performance and efficiency, IGCC provides feedstock flexibility: coal, refinery waste, or biomass could be used as fuel.

The share of coal related sources in the total carbon dioxide emission in the US is 35% in 2011 and expected to increase slightly to 37% by 2035 in the case of no regulatory action on

carbon emissions (AEO, 2011). The need for the development of technologies for pre-combustion CO_2 sequestration and economical co-production of hydrogen and electricity in coal-fired power plants is quite important in order to potentially address some of the key issues that the global energy economy is facing (Veziroglu and Barbir 1998). In an IGCC plant, the high pressure flue gas enables a more efficient CO_2 removal system compared to the other gasifiers working at lower pressures. The only drawback of the IGCC plants currently is their higher installation cost compared to other advanced coal burning systems such as supercritical PC plants (Beér 2000).

Many processes have been proposed for CO_2 recovery from flue gas such as Econamine FG^{SM}, Selexol, hot potassium carbonate or "Hot pot", CO_2 separation membranes and sterically hindered amines. Current commercial trends show that Econamine and Selexol systems are the most economical methods for CO_2 recovery. The full commercial advantage of the Econamine FG lies in atmospheric pressure applications. However, the Econamine FG is not applicable for streams containing large amounts of carbon monoxide and hydrogen, on streams containing more than 1 ppm H_2S, or on streams having less than 1vol% O_2. In the Selexol system, the CO_2 recovery is directly proportional to the partial pressure of CO_2 in the feed gas. The gasifiers working at higher pressure are suitable candidates for the CO_2 recovery by the Selexol system. For both systems, the drawbacks are less energy efficiency due to cooling of the feed stream, limited CO_2 recovery levels, up to 95% and penalty for waste disposal (absorbent) (Chapel and Mariz, C.L and Ernest, J. 1999). Another promising technology option is the oxycombustion concept. The coal is combusted in an enriched oxygen environment by using pure oxygen diluted with recycled flue gas in the oxygen-fired combustion systems. As a result, the flue stream is primarily CO_2 and H_2O and concentrated CO_2 is produced by condensing the steam in the exhaust gas. In addition, the levels of trace species such as NO_x, SO_x and CO are below the limits in oxycombustion plants. The main challenges in the oxycombustion are: i) the combustion temperature in pure O_2 is too high for the existing boiler and turbine materials, ii) the current capital and operating costs of the Air Separation Unit (ASU) is too high (Haslbeck et al. 2010). Thus, the oxycombustion system will be in stand-by mode until the required technological improvements are accomplished.

Catalytic membrane reactors assume a prominent role in a multitude of processes and associated application fields such as dehydrogenation, hydrogenation and oxidation reaction

systems (Takht Ravanchi et al. 2009). Furthermore, energy supply security considerations, growing environmental concerns and developments in the global fuel markets provide ample motivation to the examination of: i) the possibility of hydrogen production, a valuable energy carrier and feed to the petrochemical and chemical processing industries, from coal which, along with natural gas, represents the favorite fuels for electric power generation, and ii) within the Integrated Gasification Combined Cycle (IGCC) context, the possibility of co-production of electricity and hydrogen (as well as other valuable chemicals). From an environmental performance standpoint however, one of the primary environmental concerns related to coal combustion and gasification in coal-fired power plants is the significant amount of CO_2 emissions, coupled with the production of air pollutants (nitrogen and sulphur oxides) as well as toxic substances such as mercury. In light of the above remarks, the need for the development of technologies for pre-combustion CO_2 sequestration and economical co-production of hydrogen and electricity in coal-fired power plants is therefore well justified and quite important in order to potentially address some of the key issues that the global energy economy is facing (Veziroglu and Barbir 1998). Since carbon dioxide represents a key greenhouse gas (Amelio et al. 2007), Pd-based composite membrane reactor technology could provide the means for the simultaneous CO_2 capture and extra purity H_2 production in coal-fired power plants realized in a single process unit. Consequently, research activity focuses increasingly on the development of new technology options or the modification of existing ones that would provide cost-effective strategies for the reduction of CO_2 emissions through pre-combustion capture and removal, while enhancing H_2 production and, in particular, the technical feasibility of projects involving co-production of hydrogen, valuable chemicals and electricity via coal gasification (Tarun et al. 2007). Within the aforementioned context, the integrated gasification combined cycle (IGCC) process naturally represents a key option to co-produce synthesis gas, electricity, hydrogen, fuels and chemicals from coal and coal/biomass-mix in an environmentally responsible scenario (Beér 2000; Ratafia-Brown et al. 2002).

In an IGCC plant, after sulfur and mercury removal from the syngas exiting the gasifier, the water-gas shift reaction and H_2 separation take place simultaneously in a Pd-based membrane reactor. The outlet stream of the reaction side consists of mostly H_2O and CO_2 under high pressure. Please notice that after the condensation of steam, CO_2 at high pressure (˜25 atm) would result in a significant reduction in the compression costs associated with the operation of

the sequestration units downstream (Basile et al. 2001; Basile et al. 1996b; Brunetti et al. 2009a; Criscuoli et al. 2000; Tosti et al. 2003; Uemiya et al. 1991b).

The Pd-alloy supported on metal substrates and fabricated through electroless plating exhibits many advantages such as: high permeability and selectivity, cost-effective fabrication and maintenance, resistance to usability at high temperature (400-600 °C) and pressure (20-50 atm) (reaction conditions of industrial applications such as dehydrogenation, steam reforming and high temperature WGSRs are used from (Armor 1998)), easiness in scale up, practical assembly/disassembly for both small and large scale industrial applications, long term durability (5 years, 2015 DOE target (US DOE-Hydrogen from coal, 2011)). It should be pointed out that the poisoning of the Pd/Pd-alloy membranes by some of the feed components/impurities such as CO and H_2S is a notable challenge in the design and development of membrane reactor systems. However, Pd/alloy membranes like Pd/Cu and Pd/Au, have shown promising results in the presence of H_2S (Chen and Ma 2010b; Chen and Ma 2010a; Kulprathipanja et al. 2005; Pomerantz et al. 2010b; Way et al. 2008). The effect of CO on the H_2 permeation is strongly dependent on reaction temperature and the reduction in the permeation rate could be neglected at temperatures higher than ˜350°C (Hara et al. 1999; Gallucci et al. 2007; Nguyen et al. 2009).

Besides the technical advantages of the Pd-based membrane reactors, the economic viability of the Pd/Pd-alloy based composite membrane reactor technology has to be proven for large scale applications. One of the earliest economic analyses involving a two-step adiabatic WGS-MR system for CO_2 removal in an IGCC plant was conducted by Bracht et al. (1997). The characteristics of micro-porous silica membranes were explicitly taken into account in the economic evaluation efforts. The water gas shift membrane reactor concept was found to result in higher efficiencies coupled with lower costs when compared to more conventional options (low temperature wet gas cleaning) for CO_2 removal. In another study performed by Criscuoli et al. (2001), the costs related to a water gas shift membrane reactor such as energy requirements, catalyst and palladium costs were calculated based on the feed composition of the industrial scale oxo-synthesis gas plant in Augusta (Italy). A significant reduction in capital and operating costs for the membrane reactor module was shown for Pd thicknesses of 20 µm and lower. The effect of an H_2 permeability falling within the range of 1-10 mol.m/[m^2.s.$Pa^{0.5}$] on the membrane reactor module cost was also evaluated (Criscuoli et al. 2001). More importantly, the authors' calculations demonstrated that there was a limit value both for the permeability and Pd thickness

(high permeability and low thickness). According to Criscuoli et al. (2001), the membrane module cost does not vary noticeably with H_2 permeability and Pd thickness because the reaction rate becomes slower than the permeation rate, and thus, the rate controlling step. A membrane reactor module with 75 µm thick Pd layer was found to be more expensive compared to the conventional reactors with high and low shift reactors and separation devices. Criscuoli et al. (2001) concluded that the preparation of defect-free Pd membranes with selective layer of ≤20 µm would make the Pd-based membrane technology competitive with conventional technologies for CO_2 separation.

The coal fired IGCC systems with CO_2 capture using physical absorption, membrane reactors and chemical looping were compared by Rezvani et al. (2009). Conventional physical absorption, water gas shift reactor membranes and two chemical looping combustion cycles (CLC), which employ single and double stage reactors, were considered (Rezvani et al. 2009). Particularly in the membrane reactor case, the IGCC system was configured with a water gas shift membrane reactor (WGSMR) and an oxygen transport membrane (OTM) system instead of a physical absorption unit to increase the power plant efficiency and to improve process economics. The OTM unit displayed the capacity to convert the remaining combustibles in the gas coming from the retentate side of a WGSMR. Consequently, the membrane based technologies resulted in the lowest breakeven electricity selling price (levelized cost of energy) at a fuel cost of €3/GJ (€65.98/MWh at 8% discounted cash flow rate).

In the insightfully investigated work of Dolan et al. (2010), the estimated capital cost of the membrane reactor module was $US~180 million, much higher than the capital cost of a unit including high and low temperature shift reactors, amine-based CO_2 capture and PSA-based H_2 separation ($US~55 million). Dolan et al. (2010) emphasized that the membrane thickness had to be lower than 20 µm, with a plant cost of $US ~55 million and total membrane area of 13000 m^2, to meet the 2015 US DOE cost and flux target levels. Dijkstra et al. (2011) tested a bench scale multi-tube membrane reactor and performed a techno-economic evaluation. Interestingly, the results of the techno-economic analysis indicated that membrane water gas shift systems had better prospects for CO_2 capture than membrane reforming. The combination of a membrane water-gas shift reactor with gas heated reforming resulted in higher efficiencies and CO_2 avoidance costs that were found to be lower than in a conventional pre-combustion CO_2 capture system using a Selexol unit.

Frey et al. (1994) developed a stochastic modeling capability for the ASPEN chemical process simulator which enables the representation of uncertainties using probability distributions in any process technology. Their probabilistic process modeling approach was applied to an IGCC plant with hot-gas cleanup. More than 20 uncertainties related with the specific performance and cost parameters were used to determine meaningful distributions for plant net heat rate, total capital cost and levelized cost of electricity and these probability distributions were compared with the deterministic (point-estimate) results. There was more than a 75% probability that the levelized cost of electricity of the IGCC system with hot-gas cleanup would be higher than the deterministic estimate. In a recent study of Chen and Rubin (2009), a comprehensive performance and cost analysis of an IGCC system employing a GE quench gasifier with WGS reactors and a Selexol system for CO_2 capture was performed. According to the uncertainty distributions, the cost of electricity varied from 72 to 144 \$/MWh with a 69% likelihood of exceeding the deterministic estimate of 95.8 \$/MWh. In addition, the mean value of the COE distribution was 102.8 \$/MWh, which was 7 \$/MWh higher than the deterministic result.

All major bench-scale performance assessment studies involving Pd/Pd-alloy based composite membranes do highlight certain advantages of scaling up to industrial scale applications. Consequently, many research efforts are now increasingly focusing on process intensification concepts and methods allowing improvements in process economics, environmental performance and process safety through the design of cheaper processes, smaller in size equipment/plant, inherently safe process design, efficiency-focused energy management, waste/by-products minimization and risk (Stankiewicz and Moulijn 2004). Within such a context, membrane reactor technology nicely exemplifies the above possibilities since it is inherently aligned with and amenable to basic process intensification and inherently safe process design principles (Ayturk et al. 2009; Koc et al. 2011).

Considerable attention is now increasingly concentrated on the utilization of membrane reactors for large scale hydrogen production (Wieland et al. 2002; Amelio et al. 2007; Bracht et al. 1997; Roy et al. 1998; Aasberg-Petersen et al. 1998; Middleton et al. 2002; Bredesen et al. 2004; Diniz da Costa et al. 2009). In particular, a membrane reactor configuration with CO_2 capture may lead to a significant reduction in capital plant cost due to the reduced equipment size resulting from the elimination of the traditional two step water-gas shift reactors and amine

scrubbing units as well as reduced compression-related costs due to the high pressure thermodynamic state of the retentate stream. Two important findings of recent research studies on the process intensification prospects of membrane reactors are:

1) membrane (Pd) thickness values lower than 20 µm result in quite competitive economic outcomes compared to more conventional systems (Criscuoli et al. 2001; Dolan et al. 2010; Middleton et al. 2002),

2) the combination of membrane separation systems with water-gas shift reaction offers significant operatinal, economic and environmental advantages than membrane reforming systems in the case of a plant with a CO_2 capture unit (Dolan et al. 2010; Dijkstra et al. 2011; Li et al. 2010). In light of the above considerations, ultra thin (5-10µm) Pd/Au membranes supported on metal substrates and the assorted membrane reactor module represent the process system of the present study.

As Pd-based membrane technology matures, even more promising results under reaction conditions related to durability/reliability and long term behavior of Pd-based membranes appear in the pertinent literature (Ayturk et al. 2009; Augustine et al. 2011; Catalano et al. 2011; Shirasaki et al. 2009; Andrés et al. 2011; Li et al. 2011). The integration of Pd-based membrane reactors into coal-fired power represents a new technology option which has neither been fully tested nor yet demonstrated at a commercial scale. The lack of operating experience associated with membrane reactor technology options integrated into IGCC power plants on the commercial scale inevitably produces a lack of real data pertinent to process economics. Consequently, any economic performance evaluation at this early stage would be driven by reasonable yet theoretical estimates, but methodologically should acknowledge irreducible (market, regulatory, technological) uncertainties in an explicit manner (Savage 2003; Savage 2002).

3. Membrane Reactor Model Derivations

3.1. Unsteady-state membrane reactor model

In the present Chapter 3, a one dimensional dynamic process modeling framework is presented to analyze, characterize and eventually induce the desirable dynamic characteristics through feedback control action in the behavior of a catalytic Pd/Alloy-based water-gas shift (WGS) membrane reactor currently used in our laboratory for the production and separation of pure hydrogen. The composite Pd/Alloy-based membrane is mounted at the center of a stainless steel shell casing as shown in Figure 3-1. The Pd/Alloy-based membrane was on one side of the inner stainless steel tube and the entrance of the inner tube at the membrane side is blocked with a cap, while the other side is located at the reactor exit. The annular space between the shell casing and the membrane is filled with high temperature water gas shift catalyst and the remaining space of the reactor is filled with inert packing material such as glass beads. In Figure 3-1, radial direction and axial directions are denoted by x and y, respectively

The membrane reactor model was set up to characterize reactor transient (dynamic) behavior under the following standard assumptions: constant total pressure and temperature, ideal gas behavior, plug flow, no mass transfer limitations in the catalytic zone, no poisoning of the catalyst under the reaction conditions, and very high selectivity of the membrane. In addition, the Pd/Pd-Alloy membrane was assumed to be already characterized in pure H_2 prior to reaction. Thus, the membrane had a stable H_2 flux before the reactants were admitted into the reactor. The H_2 permeation through the Pd-Pd/Alloy membrane was assumed to follow Sieverts' Law (Sieverts 1907). Hydrogen separation by Pd-Pd/Alloy membranes based on the solution-diffusion transport mechanism had been studied thoroughly by Gryaznov (1986), Shu et al. (1991), Ward and Dao (1999), Caravella et al. (2008; 2010b), Iwuchukwu and Sheth (2008) elucidated the details of the multiple step H_2 transport mechanism through the Pd foils and Pd-based composite membranes thoroughly.
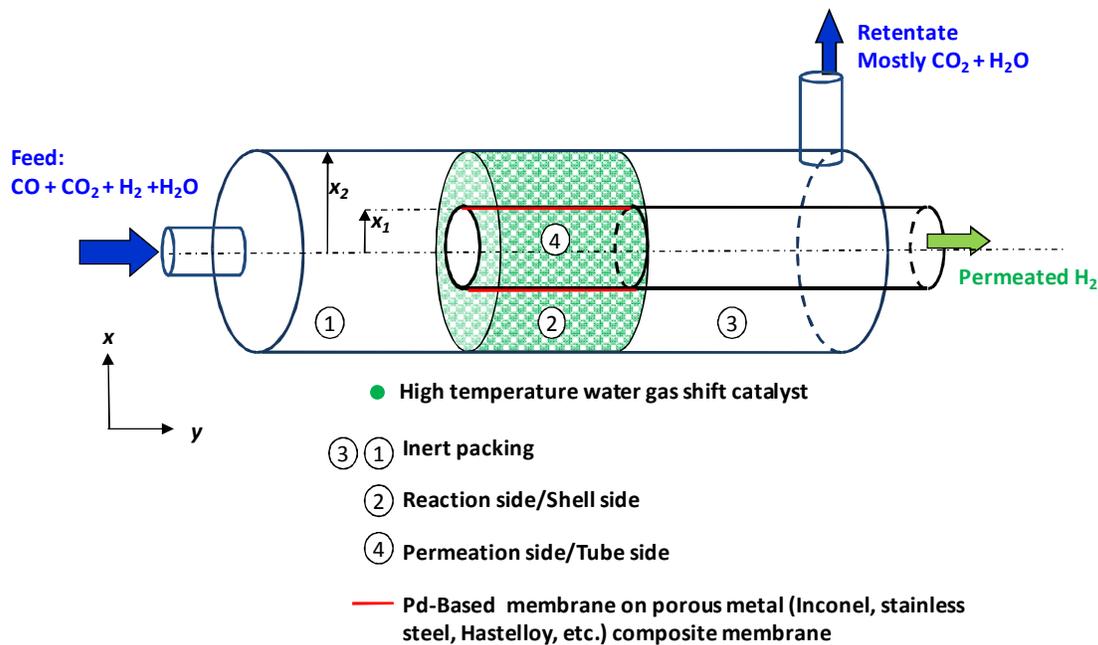
Figure 3-1. Schematic diagram of a membrane reactor

The parameters of the membrane reactor that were used in the simulations are shown in Table 3-1. The effects of WGS-component gases on the H_2 permeation properties of Pd and Pd/alloy membranes with various thicknesses ˜0.5-80 µm have been investigated extensively (Nguyen et al. 2009; Sonwane et al. 2006a; Li et al. 2010; Barbieri et al. 2008b; Caravella et al. 2010a; Mejdell et al. 2010; Scura et al. 2008; Gielens et al. 2006; Sonwane et al. 2006b). Furthermore, the diminishing effect of CO and H_2O on H_2 permeation was found to be negligible at temperatures above 350°C (Nguyen et al. 2009; Gielens et al. 2006). Thus, a reaction temperature of 450°C would be quite effective in practically reducing the effect of CO and H_2O.

More importantly, two challenges associated with the use of pure Pd membranes, namely H_2 embrittlement and poisoning by impurities such as H_2S, could be overcome by the utilization of Pd/alloy membranes. Pd/Cu alloys do not exhibit hydrogen embrittlement as severe as pure Pd and the β-hydride phase formation of a Pd-40% Cu alloy occurs even below the room temperature (Karpova and Tverdovskii 1959). Thus, Pd/Cu membranes would be durable if the process required temperature cyclings. Additionally, the body-centered cubic (bcc) Pd/Cu alloy has a peak in permeability at a Cu content of 40% and this permeability is only 6% higher than the permeability of pure Pd (Knapton 1977b). Pomerantz and Ma (2009) were able to fabricate a

68

16.5 μm thick composite palladium membrane with a thin top Pd/Cu protective layer against sulfur poisoning and without greatly reducing the permeance compared to pure Pd. The composite Pd-18 wt% Cu membrane lost 80% permeance after exposure to 54.2 ppm H_2S/H_2 for 120 h at 450°C, but they were able to recover 65% of the initial permeance in pure H_2 (Pomerantz and Ma 2009). Another promising candidate for processing feeds with sulfur impurities is a Pd/Au membrane. Pd/Au alloys showed higher hydrogen permeability than pure Pd for Au contents below 20 wt% and also higher sulfur tolerance compared to other Pd alloys (Knapton 1977a; McKinley 1967; Gryaznov 2000). Chen and Ma (2010b) conducted poisoning experiments by using a 18.1 μm thick Pd/Au composite membrane with 8 wt% Au in 54.8 ppm H_2S/H_2 at 400°C for 4 hours and managed to recover 100% of the permeance in H_2 at 500°C. Furthermore, the optimum Au composition to attain maximum performance in the presence of H_2S up to 5 ppmv was determined to be in the range of 10 – 30 wt% by Chen and Ma (2010a). In addition, a 17 μm thick Pd-based membrane with 12.3 wt% Au retained 61% of its permeance after exposure to 2 ppmv H_2S for 24 hours but 100% of the permeance was recovered in H_2 at 500°C. These results indicate that until a membrane which is tolerant to high concentrations of sulfur containing gases is developed, advanced sulfur removal units are indispensible at the upstream of the Pd or Pd/Alloy-based membrane reactors.

The expression below, namely Eq (3.1) , was determined via linear regression analysis by Ayturk et al. (2009) for the average H_2 permeability of H_2 in Pd foils and used to estimate the H_2 permeability. Only 30% of the resulting permeance was used to calculate the H_2 flux in Eq (3.2), in order to quantitatively capture the adverse effect of mechanisms such as poisoning into account.

$$Q = Q_0 e^{\frac{-E_p}{R_g.T}} = 6322.7 e^{\frac{-15630}{R_g.T}} \tag{3.1}$$

$$J_{H_2} = 0.3 \frac{Q.\Delta P_{H_2}^{0.5}}{l} \tag{3.2}$$

If the partial pressure of H_2 in the reaction side at the inlet is at least equal to or higher than the permeate side pressure, the membrane area would be used more efficiently. Otherwise the membrane area would not be used for permeation to the tube side until the reaction side H_2 partial pressure exceeds the permeate side pressure. A moderate reaction side total pressure of 15 atm would be sufficient enough to provide adequate driving force for H_2 permeation at the

reactor inlet ($\sqrt{P_{H_2}^{Shell}}\Big|_{y=0} - \sqrt{P_{H_2}^{tube}}\Big|_{y=0} = 2\ atm$). The permeation of H$_2$ through Pd is an Arrhenius type relation as shown in Eq (3.1) and the permeation rate increases as the temperature increases. Besides the increased permeation rates, the forward WGS reaction rate will increase with increased temperature and since the membrane reactor selectively removes H$_2$ the CO conversion would not be limited thermodynamically. Thus, a reaction at 450°C was considered in the model which was high enough for increased permeation as well as reaction rates while at the same time low enough to ensure membrane integrity. Augustine et al. (2009; 2010) worked with exactly the same type of lab-scale membrane reactor to test the performance of composite Pd-based membranes supported on metal substrates for the WGS reaction. The same reactor dimensions as the one used in the above experimental investigations (Augustine et al. 2009; Augustine et al. 2010) were considered in the ensuing dynamic simulations.

Table 3-1. Constants used in the dynamic model

Operating conditions and reactor dimensions	
Reaction temperature [°C]	450
Shell side total pressure, $P^{Shell,T}$ [atm]	15
Tube side total pressure, $P^{Tube,T}$ [atm]	1
I.D. of the shell casing, x_2 [m]	2.54×10^{-2}
O.D. of the membrane tube, x_1 [m]	1.27×10^{-2}
The total length of the membrane [m]	6.35×10^{-2}
Bulk catalyst density, $\rho_{Bulk,cat}$ [kg/m^3]	$1075.3 \pm \%13$
Bed porosity, ε [-]	0.5
Properties of the Pd-based composite membrane	
H$_2$ permeability constant, Q_o [m^3.μm/(m^2.h.atm$^{0.5}$)]	6322.7
Activation energy, E_p [kJ/mol]	15.63
Pd thickness, l [μm]	10

The membrane reactor modeling framework was realized by a comprehensive mathematical model structurally consisting of a system of material balance equations written component-wise for all species involved. In particular, partial differential equations representing

mass balances for each species on the shell and tube sides can be derived on the basis of first-principles and are provided below (Bird et al. 1990):

Shell side:

$$\frac{\partial}{\partial t}\left(\frac{F_{H_2}}{F_{Total}}\right) = \frac{1}{C_{Total}^{Shell}}\left[-\frac{\partial F_{H_2}}{\partial v^{Shell}} + \frac{1}{\Delta v^{Shell}}\int_{W_y}^{W_{y+\Delta y}} r_{H_2} dw - \frac{Q \cdot A_m}{l \cdot \Delta v^{Shell}} \cdot \Delta P_{H_2}^{0.5}\right] \tag{3.3}$$

i = CO, CO_2 and H_2O

$$\frac{\partial}{\partial t}\left(\frac{F_i}{F_{Total}}\right) = \frac{1}{C_{Total}^{Shell}}\left[-\frac{\partial F_i}{\partial v^{Shell}} + \frac{1}{\Delta v^{Shell}}\int_{W_y}^{W_{y+\Delta y}} r_i dw\right] \tag{3.4}$$

$$\frac{\partial}{\partial t}\left(\frac{F_{inert}}{F_{Total}}\right) = -\frac{1}{C_{Total}^{Shell}} \cdot \frac{\partial F_{inert}}{\partial v^{Shell}} \tag{3.5}$$

Tube side:

$$\frac{\partial}{\partial t}\left(\frac{F_{H_2}}{F_{Total}}\right) = \frac{1}{C_{Total}^{Tube}}\left[-\frac{\partial F_{H_2}}{\partial v^{Tube}} + \frac{Q \cdot A_m}{l \cdot \Delta v^{Tube}} \cdot \Delta P_{H_2}^{0.5}\right] \tag{3.6}$$

The following reaction rate equation for the WGS reaction over iron–chromium based commercial catalysts expressed through a power-law model was used in the simulation studies (Hla et al. 2009; Adams and Barton 2009). The thermodynamic properties listed in the NIST Chemistry Web Book (NIST Chemistry WebBook, 2011) for all gas species involved were used for the equilibrium constant calculation:

$$r = 10^{2.845\pm0.03} \cdot e^{\left(\frac{-111\pm2.63}{R_g \cdot T}\right)} \cdot P_{CO}^{1.0\pm0.031} \cdot P_{CO_2}^{-0.36\pm0.043} \cdot P_{H_2}^{1-0.09\pm0.007} \cdot \beta \tag{3.7}$$

where

$$\beta = \left[1 - \frac{1}{K}\frac{P_{CO_2} \cdot P_{H_2}}{P_{CO} \cdot P_{H_2O}}\right] \tag{3.8}$$

3.1.1 Lumped-parameter finite-dimensional process model approximation

The transient stage considered in the present study was specified as the time period between the occurrence of an external load/disturbance (e.g. introducing the reactants into the reactor or any unexpected changes in the inlet stream variables, pressure, temperature etc.) and

the final steady state reached by the process. Notice that the partial pressure of hydrogen on both shell and tube sides varies along the length of the reactor during the transient stage, and therefore, an equation describing the dependence of H_2 partial pressure on the length of the reactor is necessary for the Sieverts' law expression in Eq (3.3) & (3.6). Furthermore, the reaction rate expression in Eq (3.7) is highly nonlinear and the system of governing equations involves two independent variables (time and length) as well as an integral term for the reaction under consideration. Therefore, given the above observations on the structure of the mathematical model, finding/computing a solution can be computationally challenging and expensive. Furthermore, process control and monitoring systems involving sensors and actuators placed at certain locations along the process spatial domain are physically realizable and meaningfully designed once a spatial discretization of the above model is performed. Notice however, that the original partial differential equation-based infinite-dimensional reactor model can be accurately approximated by a finite-dimensional lumped-parameter dynamic model if the membrane reactor is partitioned into N zones/compartments/segments each one of them viewed and modeled as a standard continuous stirred-tank reactor (CSTR). This approximation procedure gives rise to a dynamic membrane reactor model that is comprised of a system of ordinary differential equations mathematically representing component mass balance equations written for each zone and solved simultaneously using an appropriately selected numerical method (Reyes and Luyben 2000).

Eq (3.9) through (3.14) form the basis of the aforementioned finite-dimensional lumped-parameter membrane reactor dynamic model-approximant. Each segment/zone of the lumped reactor model introduces 6 ordinary differential mass balance equations for species CO, CO_2, H_2O, H_2 and N_2 in the shell side respectively and for H_2 in the tube side. The full set of ordinary differential equations consisted of 120 nonlinear dynamic mass balance equations for a total of 20 lumps/zones (N × Number of equations for each segment = 20×6) and was numerically solved by using the MATLAB toolbox (ode45). MATLAB solver-ode45 computes the model state at the next time step using an explicit Runge-Kutta (4,5) formula (the Dormand-Prince pair) for numerical integration and more details about the solution method can be found in Mathworks (Mathworks, 2010).

Shell side:

$$\frac{df_{H_2}\big|_{y+\Delta y}}{dt} = \frac{1}{C_{Total}^{Shell}.\Delta v^{Shell}}\left[f_{H_2}\big|_y . F_{Total}^{Shell}\big|_y - f_{H_2}\big|_{y+\Delta y}.F_{Total}^{Shell}\big|_{y+\Delta y}\right.$$
$$\left. + r_{H_2}\big|_{y+\Delta y}.\Delta w - \frac{Q.A_m}{l}.\Delta P_{H_2}^{0.5}\right] \tag{3.9}$$

i = CO, CO$_2$ and H$_2$O

$$\frac{df_i\big|_{y+\Delta y}}{dt} = \frac{1}{C_{Total}^{Shell}.\Delta v^{Shell}}\left[f_i\big|_y . F_{Total}^{Shell}\big|_y - f_i\big|_{y+\Delta y}.F_{Total}^{Shell}\big|_{y+\Delta y} + r_i\big|_{y+\Delta y}.\Delta w\right] \tag{3.10}$$

$$\frac{df_{inert}\big|_{y+\Delta y}}{dt} = \frac{1}{C_{Total}^{Shell}.\Delta v^{Shell}}\left[f_{inert}\big|_y . F_{Total}^{Shell}\big|_y - f_{inert}\big|_{y+\Delta y}.F_{Total}^{Shell}\big|_{y+\Delta y}\right] \tag{3.11}$$

$$F_{Total}^{Shell}\big|_{y+\Delta y} = F_{Total}^{Shell}\big|_y - \frac{Q.A_m}{l}.\Delta P_{H_2}^{0.5} \tag{3.12}$$

Tube side:

$$\frac{df_{H_2}\big|_{y+\Delta y}}{dt} = \frac{1}{C_{Total}^{Tube}.\Delta v^{Tube}}\left[f_{H_2}\big|_y . F_{Total}^{Tube}\big|_y - f_{H_2}\big|_{y+\Delta y}.F_{Total}^{Tube}\big|_{y+\Delta y} + \frac{Q.A_m}{l}.\Delta P_{H_2}^{0.5}\right] \tag{3.13}$$

$$F_{Total}^{Tube}\big|_{y+\Delta y} = F_{Total}^{Tube}\big|_y + \frac{Q.A_m}{l}.\Delta P_{H_2}^{0.5} \tag{3.14}$$

If the length of the reactor volume, on which the mass balance equation was based, is assumed to be very small, then the average of the H$_2$ partial pressures at the inlet and at the outlet of the control volume can be used in the Sieverts' law expression in order to explicitly quantify the driving force for H$_2$ permeation through the Pd-based membrane layer as in Eq (3.15). At the end, the CO conversion and hydrogen recovery levels were found by using Eq (3.16) and (3.17).

$$\Delta P_{H_2}^{0.5} = \sqrt{\frac{P_{H_2}^{Shell}\big|_y + P_{H_2}^{Shell}\big|_{y+\Delta y}}{2}} - \sqrt{\frac{P_{H_2}^{Tube}\big|_y + P_{H_2}^{Tube}\big|_{y+\Delta y}}{2}} \tag{3.15}$$

$$X_{CO} = \left[F_{CO}^{Shell}\big|_{y=0} - F_{CO}^{Shell}\big|_y\right]/F_{CO}^{Shell}\big|_{y=0} \tag{3.16}$$

73

$$R_{H_2} = F_{H_2}^{Tube}\big|_y \Big/ \Big[F_{CO}^{Shell}\big|_{y=0} + F_{H_2}^{Shell}\big|_{y=0} \Big] \qquad (3.17)$$

The particular set of boundary conditions and initial condition for a well-posed problem formulation and the computation of the solution of the system of Eq (3.3) to (3.6) are as follows:

<u>Boundary condition at the inlet:</u> The molar flow rates of each gaseous species at the inlet stream of the catalytic zone remain constant for all times.

$$F_i\big|_{y=0} = \text{Constant} \qquad (3.18)$$

<u>Boundary condition at the exit:</u> At the interface between the porous part and the catalytic area, species entering the control volume exit it with no further change.

$$\partial F_i / \partial y = 0 \qquad (3.19)$$

<u>Initial conditions:</u> Two different initial conditions for the start-up and for the dynamic behavior of the membrane reactor in the presence of unexpected disturbances were considered. During the start-up stage of the reactor, only steam and H_2 are flowing through the reactor before admitting the reactants into the reactor: 47.6 % H_2O and 52.4% H_2. In the second case, the initial condition is the process nominal steady state just before the occurrence of a process upset episode whereby an unexpected disturbance strikes driving the process away from the nominal steady state.

3.2. Steady-state one dimensional membrane reactor model

A steady state process modeling framework for a catalytic high temperature water-gas shift Pd-based membrane reactor used for hydrogen production and separation has been developed at non-isothermal conditions in order to identify and characterize potentially hazardous conditions and key factors that could compromise process safety. The proposed membrane reactor modeling framework has been developed under the following assumptions: isobaric conditions on both reaction and permeate sides, ideal gas behavior, no membrane and/or catalyst poisoning, practically infinite selectivity of the membrane and no significant mass or heat dispersion effects. In addition reactor shell was assumed as adiabatic for the non-isothermal

case and the reaction and permeation side temperatures were assumed as same and constant for the isothermal case. Since no significant pressure drop across the membrane reactor was observed in the experimental studies reported in (Augustine et al. 2011) under the same type of Pd-based membrane and set of reaction conditions; the pressure drop across the catalyst region and on the permeate side was not considered given the specific dimensions of the lab-scale Pd-based membrane reactor (Brunetti et al. 2007; Hermann et al. 1997). The Pd-based membrane reactor considered in this part was a shell and tube configuration as the one described in greater detail in Chapter 3.1, Figure 3-1. The mass and energy balance equations at steady and also unsteady state conditions were derived by using the principles of conservation of mass and energy (Bird et al. 1990). The geometry of the membrane reactor and the properties of the composite Pd membrane which were used in the model are listed in Table 3-1. The H_2 flux was calculated with 100% of the Pd foil permeance by assuming either the feed is sulfur free or the membrane is resistant to sulfur containing components. Under steady state conditions and the aforementioned assumptions, the following mass balance equations naturally arise:

(i)   Mass balance equations for gas phase species in the reaction side (shell):

$$\frac{dF_{H_2}^{Shell}}{d\bar{y}} = \rho_{Bulk}.A_c.L.r_{H_2} - A_m.J_{H_2} \tag{3.20}$$

$$\frac{dF_i^{Shell}}{d\bar{y}} = \rho_{Bulk}.A_c.L.r_i \tag{3.21}$$

where i = CO, H_2O and CO_2

$$J_{H_2} = \frac{Q}{l}.\left(\sqrt{P_{H_2}^{Shell}} - \sqrt{P_{H_2}^{Shell}}\right) \text{ by Sieverts' Law} \tag{3.22}$$

(ii)   Mass balance equation for H_2 in the permeate side (tube):

$$\frac{dF_{H_2}^{Tube}}{d\bar{y}} = A_m.J_{H_2} \tag{3.23}$$

Furthermore, an energy balance equation in the reaction side takes the following form:

$$\frac{dT^{Shell}}{d\bar{y}} = \frac{(-r_i.\rho_{Bulk}.V_{An.})(-\Delta H_{Rxn}) - U.A_m\left(T^{Shell} - T^{Tube}\right)}{\left.\sum F_i C_{pi}\right|^{Shell}} \tag{3.24}$$

where i = CO, H_2O, CO_2 and H_2 Notice that the reaction side energy balance equation consists of the heat of reaction term, the term capturing the amount of heat being exchanged with the permeation side as well as the convective flux of energy in Eq (3.24). The amount of energy associated with the permeating H_2 was neglected compared to the heat of reaction.

Finally, an energy balance equation in the permeate side can also be explicitly developed:

$$\frac{dT^{Tube}}{d\bar{y}} = \frac{A_m . J_{H2}\left(H_{H_2}^{Shell} - H_{H_2}^{Tube}\right) + U.A_m\left(T^{Shell} - T^{Tube}\right)}{F_{H_2} C_{p,H_2}\big|^{Tube}} \tag{3.25}$$

Notice that both the amount of energy associated with the permeating H_2 and the heat exchange with the reaction side have been included in the above permeate side energy balance equation (Eq (3.25)). The system of equations from Eq (3.20) to (3.23) for the isothermal conditions and the systems of equations from Eq (3.20) to (3.25) for the non-isothermal conditions were numerically integrated with the aid of MATLAB solver-ode23s.

The effective radial heat conductivity and the wall heat transfer coefficients were calculated by using the correlations reported by Dixon and Cresswell (1979). The improved equation for the overall heat transfer coefficient proposed by Dixon (1996) was used in the model. Furthermore, heat transfer resistance overall heat transfer coefficient (U) calculations follow the method proposed in (Madia et al. 1999) for methane steam reforming in a membrane reactor.

Boundary condition at the inlet: The molar flow rates of each gaseous species at the inlet stream of the catalytic zone are constant at all times.

$$F_i|_{y=0} = \text{Constant and } T|_{y=0} = T_{Feed} \tag{3.26}$$

Boundary condition at the exit: At the interface between the porous part and the catalytic area, species that enter the control volume exit it with no further change.

$$\partial F_i/\partial y = 0 \text{ and } \partial T/\partial y = 0 \tag{3.27}$$

3.3. The integration of the Dusty-Gas Model (DGM) into the membrane reactor model

The Pd/Pd-alloy based membranes supported on porous metal substrates may have different selectivity values. The selectivity of the membrane is dependent on the flux of H_2 and other impurities in the permeation side. Defects like pinholes or cracks in the dense Pd/Pd-alloy layer of a composite membrane cause selectivity decline. Non-uniform grading and/or Pd deposition during the synthesis and pinhole formation due to incoherent sintering of the small (100nm) Pd crystallites (Guazzone 2005; Ma et al. 2007) are several reasons for selectivity decline. The low selectivity values may decrease the CO conversion and H_2 purity from the permeate side. Thus, the objective was to develop a mathematical model which takes the multi-component gas diffusion through the defects in the membrane into account. The one dimensional isothermal steady state mathematical model for the Pd-based membrane reactors was enhanced with the addition of the multi-component gas diffusion through the defects on the membrane. The multi component gas diffusion through the defects was described by the Dusty-Gas Model (Mason and Malinauskas 1983) and the model was able to predict the H_2 purity of the permeate flow. The Dusty-Gas Model has been discovered independently by at least five different scientists in five different periods (Cunningham and Williams 1980). The permeation of H_2 was described by two transport mechanisms; the diffusion in the porous parts of the Pd layer (defects) and the solution diffusion in the dense Pd layer. Since the water-gas shift reaction was assumed to be taking place at 400-450°C, the contribution from the surface flow for He, CO and CO_2 was neglected.

The corrected version (Krishna 1987; Taylor and Krishna 1993) of the Dusty Gas Model which was first proposed by Mason and Malinauskas (1983) was used in the simulation efforts. The Dusty Gas Model (DGM) allows a successful differentiation of the mass fluxes of all components though a porous material due to the incorporation of mutual interactions (Mason and Malinauskas 1983). It is based on the combination of the Stefan-Maxwell diffusion equations and the characteristics of mass transfer in porous solids. For a single species i in an n-component mixture the following equation of the DGM was used to describe the fluxes in the defected Pd layer:

$$\sum_{j=1, j \neq i}^{n} \frac{f_i.J_j - f_j.J_i}{D_{ij}^e} - \frac{J_i}{D_{iK}^e} = \frac{P}{R.T}\nabla f_i + \frac{f_i \nabla P}{R.T}\left(\frac{B_o.P}{\eta.D_{i,k}^e} + 1\right)$$

(3.28)

Where y is the mole fraction, J is the flux (mol/[m²-s]), D_{ij}^e is the effective binary diffusion coefficient (m²/s), D_{iK}^e is the effective Knudsen diffusion coefficient (m²/s), R is the ideal gas constant, T is temperature (K), P is total pressure (atm), B_o is the geometrical factor (m²), η is viscosity (μP). All of the parameters such as viscosity and diffusion coefficients are detailed in Appendix B.

$$\frac{f_1.J_2 - f_2.J_1}{D_{12}^e} + \frac{f_1.J_3 - f_3.J_1}{D_{13}^e} + \frac{f_1.J_4 - f_4.J_1}{D_{14}^e} - \frac{J_1}{D_{1K}^e} = \frac{P_{Total}^{Shell}.\nabla f_1}{R.T} + \left(1 + \frac{B_o.P_{Total}^{Shell}}{D_{1K}^e.\eta}\right)\frac{f_1.\nabla P}{R.T}$$

(3.29)

$$\frac{f_2.J_1 - f_1 J_2}{D_{21}^e} + \frac{f_2.J_3 - f_3.J_2}{D_{23}^e} + \frac{f_2.J_4 - f_4.J_2}{D_{24}^e} - \frac{J_2}{D_{2K}^e} = \frac{P_{Total}^{Shell}.\nabla f_2}{R.T} + \left(1 + \frac{B_o.P_{Total}^{Shell}}{D_{2K}^e\eta}\right)\frac{f_2 \nabla P}{R.T}$$

(3.30)

$$\frac{f_3.J_1 - f_1 J_3}{D_{31}^e} + \frac{f_3.J_2 - f_2.J_3}{D_{32}^e} + \frac{f_3.J_4 - f_4.J_3}{D_{34}^e} - \frac{J_3}{D_{3K}^e} = \frac{P_{Total}^{Shell}.\nabla f_3}{R.T} + \left(1 + \frac{B_o.P_{Total}^{Shell}}{D_{3K}^e\eta}\right)\frac{f_3 \nabla P}{R.T}$$

(3.31)

$$\frac{f_4.J_1 - f_1 J_4}{D_{41}^e} + \frac{f_4.J_2 - f_2.J_4}{D_{42}^e} + \frac{f_4.J_3 - f_3.J_4}{D_{43}^e} - \frac{J_4}{D_{4K}^e} = \frac{P_{Total}^{Shell}.\nabla f_4}{R.T} + \left(1 + \frac{B_o.P_{Total}^{Shell}}{D_{4K}^e\eta}\right)\frac{f_4 \nabla P}{R.T}$$

(3.32)

Where $B_o = \frac{\varepsilon\, d_p^2}{32\, \tau}$

(3.33)

$$\nabla f_i = \frac{f_i^{Shell} - f_i^{Tube}}{\Delta x} = \frac{f_i^{Shell} - f_i^{Tube}}{L_{Wall}}$$

(3.34)

$$\nabla P = \frac{P_{Total}^{Shell} - P_{Total}^{Tube}}{\Delta x} = \frac{P_{Total}^{Shell} - P_{Total}^{Tube}}{L_{Wall}}$$

(3.35)

The Eq (3.29) through (3.32) were re-organized to obtain a single vector of fluxes with known coefficients as follows:

$$\begin{bmatrix} -\dfrac{f_2}{D_{12}^e}-\dfrac{f_3}{D_{13}^e}-\dfrac{f_4}{D_{14}^e}-\dfrac{1}{D_{1K}^e} & \cdots & \dfrac{f_1}{D_{14}^e} \\ \vdots & \ddots & \vdots \\ \dfrac{f_4}{D_{41}^e} & \cdots & -\dfrac{f_1}{D_{41}^e}-\dfrac{f_2}{D_{42}^e}-\dfrac{f_3}{D_{43}^e}-\dfrac{1}{D_{4K}^e} \end{bmatrix}\begin{bmatrix} J_1 \\ J_2 \\ J_3 \\ J_4 \end{bmatrix} = \begin{bmatrix} \dfrac{P_{Total}^{Shell}.\nabla f_1}{R.T}+\left(1+\dfrac{B_o.P_{Total}^{Shell}}{D_{1K}^e.\eta}\right)\dfrac{f_1.\nabla P}{R.T} \\ \dfrac{P_{Total}^{Shell}.\nabla f_2}{R.T}+\left(1+\dfrac{B_o.P_{Total}^{Shell}}{D_{2K}^e\eta}\right)\dfrac{f_2\nabla P}{R.T} \\ \dfrac{P_{Total}^{Shell}.\nabla f_3}{R.T}+\left(1+\dfrac{B_o.P_{Total}^{Shell}}{D_{3K}^e\eta}\right)\dfrac{f_3\nabla P}{R.T} \\ \dfrac{P_{Total}^{Shell}.\nabla f_4}{R.T}+\left(1+\dfrac{B_o.P_{Total}^{Shell}}{D_{4K}^e\eta}\right)\dfrac{f_4\nabla P}{R.T} \end{bmatrix}$$

Two important physical properties namely, the geometrical factor B_o and the ratio of porosity over turtuosity (ε/τ) of the defects in the Pd layer are required to be determined experimentally. Thus, the Eq (3.28) was organized for single component system as shown in Eq (3.36) to determine the values of B_o and ε/τ (Uhlhorn et al. 1989).

$$\frac{J}{\Delta P} = \alpha + \beta.P_{ave} = \frac{1}{3}\sqrt{\frac{8}{\pi}}\frac{\varepsilon.d_{pore}}{L_{Wall}.\tau\sqrt{R.T.MW}} + \frac{1}{32}\frac{\varepsilon.d_{pore}^2}{L_{Wall}.\tau.\theta_k.\mu.R.T}P_{ave} \tag{3.36}$$

where $\alpha.\Delta P$ is the Knudsen flow (mol/[m^2.s.Pa]), $\beta.P_{ave}.\Delta P$ is the viscous flow(mol/[m^2.s.Pa]), L_{Wall} is the membrane wall thickness (m) (Pd layer+support wall thickness), d_{pore} is the pore diameter of the defects (m), MW is the molecular weight (kg/mol), $.\theta_k$ is the reflection factor and assumed as 1, μ is the gas viscosity (Pa.s). The pore diameter (d_{pore}) could be estimated by using the α/β ratio given in Eq (3.37) (Guazzone and Ma 2008).

$$\frac{\beta}{\alpha} = \theta_k.\frac{3}{32}.\sqrt{\frac{\pi}{8}}.\frac{1}{\sqrt{R.T}}.\frac{\sqrt{M}}{\mu}d_{pore} \tag{3.37}$$

The one dimensional membrane reactor with the multi component gas diffusion model was developed by assuming the following conditions: isobaric and isothermal on both reaction and permeate sides, ideal gas behavior, no membrane and/or catalyst poisoning and no significant mass or heat dispersion effects.

(i)   Mass balance equations for gas phase species in the reaction side (shell):

$$\frac{dF_{H_2}^{Shell}}{d\bar{y}} = \rho_{Bulk}.A_c.L.r_{H_2} - \Phi_{defect}.A_m.J_{H_2,defect}$$
$$- (1 - \rho_{defect}).A_m.J_{H_2} \tag{3.38}$$

$$\frac{dF_i^{Shell}}{d\bar{y}} = \rho_{Bulk}.A_c.L.r_i - \Phi_{defect}.A_m.J_{i,defect} \tag{3.39}$$

$$\rho_{defect=}\frac{Pe_{He,2}}{Pe_{He,1}} \tag{3.40}$$

(ii)   Mass balance equation for H_2 in the permeate side (tube):

$$\frac{dF_{H_2}^{Tube}}{d\bar{y}} = \Phi_{defect}.A_m.J_{H_2,defect} + (1 - \Phi_{defect}).A_m.J_{H_2} \tag{3.41}$$

$$\frac{dF_i^{Tube}}{d\bar{y}} = \Phi_{defect}.A_m.J_{i,defect} \tag{3.42}$$

where i = CO, H_2O and CO_2, $J_{H_2,defect}$ (mol/[m^2-s])is the H_2 flux trough the defects, Φ_{defect} (Schramm and Seidel-Morgenstern 1999) is the ratio of the defected area to the total area, $Pe_{He,2}$ is the He permeance of the defected membrane and $Pe_{He,1}$ is the He permeance of the support before the dense Pd layer deposition.

The ideal selectivity of Pd/Pd-alloy composite membranes would be insufficient in the presence of large defects on the membrane surface for comparison purposes. Thus, separation factor (S_F) (Koros et al. 1996) was used in the analysis of the membrane reactor model with the DGM and expressed with the formula:

$$S_F = \frac{[X_{H_2}/X_{(CO+CO_2+H_2O)}]_{Permeate}}{[X_{H_2}/X_{(CO+CO_2+H_2O)}]_{Retentate}} \tag{3.43}$$

Since CO will also present in the permeate side, the expression for the CO conversion (Eq (3.16) needs to be updated for the membranes with defects. The updated expression for the CO conversion for the defected membranes is given in Eq (3.44)

$$X_{CO} = \left[F_{CO}^{Shell} \Big|_{y=0} - \left(F_{CO}^{Shell} \Big|_{exit} + F_{CO}^{Tube} \Big|_{exit} \right) \right] / F_{CO}^{Shell} \Big|_{y=0} \qquad (3.44)$$

3.4. Two-dimensional membrane reactor model

In particular, a comprehensive first principle-based two dimensional (2D) membrane reactor modeling framework has been developed to take into account the radial concentration gradients and pressure drop of the Pd-based membrane reactor. The main objective of the 2D model was to reliably address the problem of possibly overestimating H_2 recovery levels and the calculated membrane areas, which were less than the actual required ones as calculated through the traditional simple one-dimensional (1D) model.

Even though the one-dimensional (1D) model provides useful information for quick estimations of membrane reactor performance, it is very limited to predict the behavior of large-scale membrane reactors, particularly for the estimation of hydrogen recovery and membrane area. A good demonstration of the difference between one (axial) and two dimensional (axial and radial) models is presented in Figure 3-2. Thus, the mass and momentum balance equations in the radial and axial coordinates were simulated to characterize the membrane reactor performance at isothermal and steady state conditions. In addition, axial dispersion and radial convection was neglected, the ideal selectivity of the membrane was assumed to be infinite and neither vacuum nor sweep was used in the permeate side. The detailed partial differential equations and boundary for the WGS membrane reactor are:
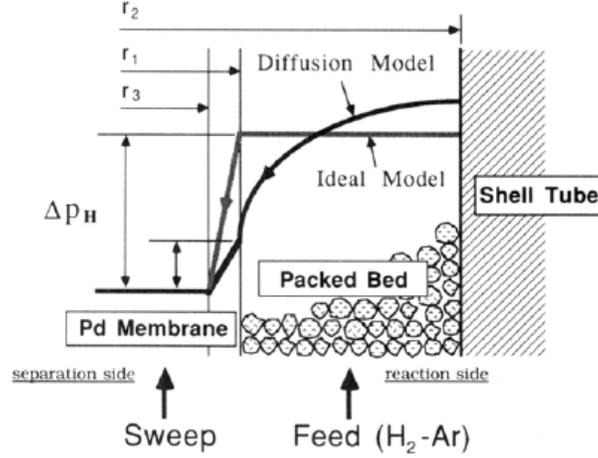
Figure 3-2. Models for hydrogen in a packed bed reactor (Itoh et al. 1994)

(i)   Mass balance equation for all gas phase species in the reaction side (shell) i=CO, H_2O, CO_2, H_2:

$$\frac{\partial(u.C_i)}{\partial y} - \frac{D^e_{i-mix}}{u}\left[\frac{\partial^2(u.C_i)}{\partial x^2} + \frac{1}{x}\frac{\partial(u.C_i)}{\partial x}\right] + \rho_{Bulk}.r_i = 0 \qquad (3.45)$$

(ii)   Momentum balance in the reaction side (shell):

$$\frac{dP^{Shell}_{Total}}{dy} = \left(150 + 1.75\frac{Re}{(1-\varepsilon)}\right).\frac{G.\mu_{mix,g}.(1-\varepsilon)^2}{\rho_{mix,g}.d^2_{particle}.\varepsilon^3} \qquad (3.46)$$

$$G = \rho_{mix,g}.u \qquad (3.47)$$

The linear gas velocity along the length of the reactor was evaluated by using Eq (3.48) through (3.50) with the sequence given below:

$$U_i(x,y) = u(y).C_i(x,y) = \frac{\bar{V}_{Total}(y)}{A_c}.C_i(x,y) = \frac{F^{Shell}_i(x,y)}{A_c} \qquad (3.48)$$

$$U_{Total}(x,y) = \sum_{j=1}^{i} U_j(x,y) \qquad (3.49)$$

$$u(y) = \frac{\bar{V}_{Total}(y)}{A_c} = \frac{U_{Total}(x,y).R.T}{P^{Shell}_{Total}} \qquad (3.50)$$

Boundary condition 1 (BC1), at the reactor inlet for i=CO, H_2O, CO_2, H_2 , $y = 0$:

$$u.C_i|_{y=0} = u^0 C_i^0 \tag{3.51}$$

Boundary condition 2 (BC2), at the shell casing surface for $i=CO$, H_2O, CO_2, H_2, $x = x_2$:

$$\partial(u.C_i)/\partial x = 0 \tag{3.52}$$

Boundary condition 3 (BC3), at the membrane surface for $i=CO$, H_2O, CO_2 except H_2, $x = x_1$:

$$\partial(u.C_i)/\partial x = 0 \tag{3.53}$$

Boundary condition 4 (BC4), at the membrane surface for H_2, $x = x_1$:

$$\frac{d_{particle}}{Pe} \frac{\partial(u.C_{H_2})}{\partial x} = J_{H_2} \tag{3.54}$$

Finite difference method was used to solve the systems of equations expressed by the Eq (3.45) and (3.46). A simple representation of the solution of the membrane reactor system with the finite difference method is shown in Figure 3-3. Forward difference for the axial direction (y) and central difference for the radial direction (x) were used. The finite difference approximation of the Eq (3.45) is given in Eq (3.55).

$$\frac{U_i(x, y+1) - U_i(x, y)}{\Delta y} \tag{3.55}$$

$$- \frac{D^e_{i-mix}}{u} \left[\frac{U_i(x+1, y) - 2U_i(x, y) + U_i(x-1, y)}{\Delta x^2} \right.$$

$$\left. + \frac{1}{r} \frac{U_i(x+1, y) - U_i(x-1, y)}{2\Delta x} \right] + \rho_{Bulk}.r_i(x, y) = 0$$
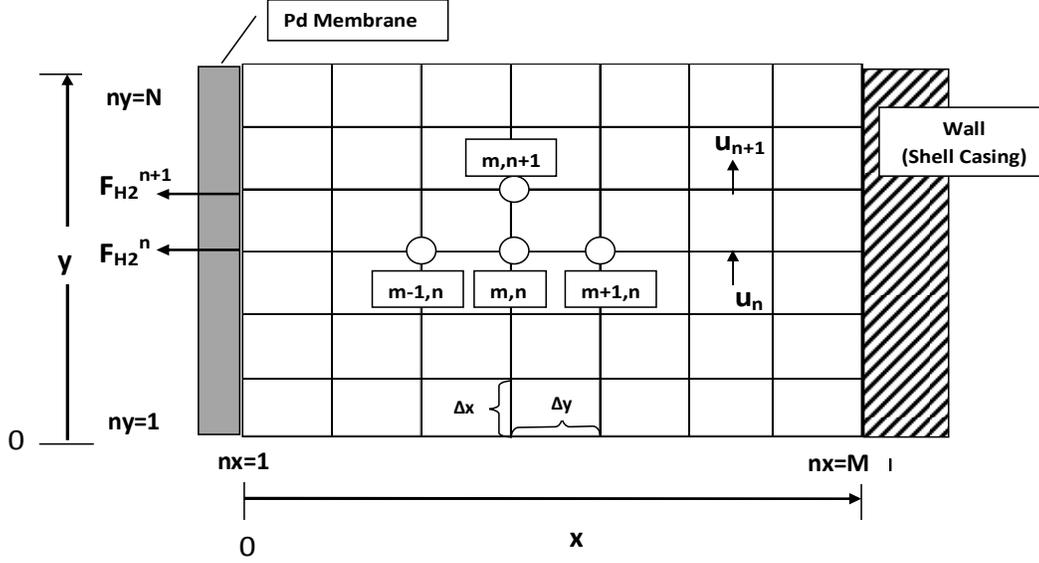
Figure 3-3. Representation of the membrane reactor with the finite difference method (nx: number of nodes in the radial direction, ny: the number of nodes in the axial direction)

After the Eq (3.55) is organized to combine dependent variables for the same location and the formula valid for interior nodes are:

$$U_i(x, y + \Delta y) = M_1 . U_i(x + \Delta x, y) + M_2 . U_i(x, y) + M_3 . U_i(x - \Delta x, y) - \Delta y . \rho_{Bulk} . r_i(x, y) \quad (3.56)$$

$$M_1 = \frac{\Delta y . D^e_{i-mix}}{\Delta x^2 . u} + \frac{D^e_{i-mix}}{2 . u . r . \Delta x} \quad (3.57)$$

$$M_2 = 1 - \frac{2 . \Delta y . D^e_{i-mix}}{\Delta x^2 . u} \quad (3.58)$$

$$M_3 = \frac{\Delta y . D^e_{i-mix}}{\Delta x^2 . u} - \frac{D^e_{i-mix}}{2 . u . r . \Delta x} \quad (3.59)$$

BC2 at the shell casing surface for i=CO, H_2O, CO_2, H_2, $x = x_2$:

$$\left. \frac{\partial (u . C_i)}{\partial x} \right|_{x=x_2} = \frac{U_i(x_2 + \Delta x, y) - U_i(x_2 - \Delta x, y)}{2\Delta x} = 0 \quad (3.60)$$

84

$$U_i(x_2 + \Delta x, y) = U_i(x_2 - \Delta x, y)^* \tag{3.61}$$

The E (3.56) is re-written at the shell casing surface for $i =$ CO, H_2O, CO_2 and H_2, $x = x_l$:

$$U_i(x_2, y + \Delta y) = M_2.U_i(x_2, y) + M_4.U_i(x_2 - \Delta x, y) - \Delta y.\rho_{Bulk}.r_i(x, y) \tag{3.62}$$

BC3 at the membrane surface for $i=$CO, H_2O, CO_2 except H_2, $x = x_l$:

$$\frac{\partial (u.C_i)}{\partial x}\bigg|_{x=x_1} = \frac{U_i(x_1 + \Delta x, y) - U_i(x_1 - \Delta x, y)}{2\Delta x} = 0 \tag{3.63}$$

$$U_i(x_1 + \Delta x, y) = U_i(x_1 - \Delta x, y)^\dagger \tag{3.64}$$

The Eq (3.56) is re-written at the membrane surface for $i=$CO, H_2O, CO_2 except H_2, $x = x_l$:

$$U_i(x_1, y + \Delta y) = M_4.U_i(x_1 + \Delta x, y) + M_2.U_i(x_1, y) - \Delta y.\rho_{Bulk}.r_i(x, y) \tag{3.65}$$

$$M_4 = \frac{2.\Delta y.D_{i-mix}^e}{\Delta x^2.u} \tag{3.66}$$

BC4 at the membrane surface for H_2, $x = x_l$:

$$\frac{\partial (u.C_{H_2})}{\partial x}\bigg|_{x=x_1} = \frac{U_{H_2}(x_1 + \Delta x, y) - U_{H_2}(x_1 - \Delta x, y)}{2\Delta x} = \frac{Pe.J_{H_2}}{d_{particle}} \tag{3.67}$$

$$U_{H_2}(x_1 - \Delta x, y) = U_{H_2}(x_1 + \Delta x, y) - \frac{2.\Delta x.Pe.J_{H_2}}{d_{particle}} \tag{3.68}$$

The Eq (3.56) is re-written at the membrane surface for H_2, $x = x_l$:

$$U_{H_2}(x_1, y + \Delta y) = M_4.U_i(x_1 + \Delta x, y) + M_2.U_i(x_1, y) + M_5 - \Delta y.\rho_{Bulk}.r_i(x, y) \tag{3.69}$$

$$M_5 = \left(\frac{\Delta y.D_{i-mix}^e}{\Delta x^2.u} + \frac{D_{i-mix}^e}{2.u.r.\Delta x}\right).\left(\frac{2.\Delta x.Pe.J_{H_2}}{d_{particle}}\right) \tag{3.70}$$

The definitions of the dimensionless numbers used in the model are:

---

* $x_2 + \Delta x$ is a shadow node
† $x_1 - \Delta x$ is a shadow node

$$\text{Peclet Number } (Pe) = 8.8 \left[2 - \left(1 - \frac{2.d_{particle}}{x_2 - x_1} \right)^2 \right] \text{ if } Re \geq 1000 \text{ (De Falco et al. 2007)} \tag{3.71}$$

$$\frac{1}{\text{Peclet Number } (Pe)} = \frac{0.4}{(Re.Sc)^{0.8}} + \frac{0.09}{\{1 + 10/(Re.Sc)\}} \text{ if } Re \leq 1000 \text{ (Wen and Fan 1975)} \tag{3.72}$$

$$\text{Reynolds Number } (Re) = \frac{d_{particle}.u.\rho_{mix,g}}{\mu_{mix,g}} \tag{3.73}$$

$$\text{Schmidt Number } (Sc) = \frac{\mu_{mix,g}}{\rho_{mix,g}.D^e_{i-mix}} \tag{3.74}$$

$$D^e_{i-mix} = \frac{1 - f_i}{\sum_{j \neq i} f_i / D^e_{ij}} \text{ (Adams and Barton 2009)} \tag{3.75}$$

4. Technical Performance Assessment and Economic Analysis Framework for Industrial Scale Pd/Alloy-based Membrane Reactors

4.1. Integration of Pd/Au-Based Membrane Reactors into IGCC Plants: Technical Performance Assessment

The configuration of the membrane reactor into coal-fired power plants has to be determined to achieve the maximum net plant efficiency. One of the most important parameters which affect the net plant efficiency for the membrane reactor integration is the type of the sulfur and mercury removal systems. Even though the utilization of the hot gas desulfurization (Gangwal et al. 1998) and the removal of trace metal contaminants (i.e., mercury, arsenic, selenium and cadmium) at elevated temperatures (Alptekin, Lind and Amalfitano, R. and Copeland, R., TDA Research, Inc.1917) has the potential to decrease the waste heat, the operational experience of these systems are limited. Conventional gas cleaning systems such as the combination of Selective Catalytic Reaction (SCR), fabric filters and Flue Gas Desulfurization (FGD) or Selexol units were considered in this study because of the sufficient technical information provided, particularly by the US Department of Energy.

The goal of co-production of hydrogen and electric power using a high temperature hydrogen separation system (Case 6 – Mitretek technical report (Gray and Tomlinson 2002)) underlies the integration option idea of Pd-based membrane reactors into a coal gasification – combined cycle power block (traditional IGCC) system. The key unit such a process system is the gasifier and auxiliary equipment. Three companies GE, Shell and ConocoPhillips dominate the gasification business through the introduction of advanced technology options bound to play

a major role in future IGCC demonstration projects (Maurstad, 2005). Requirements associated with a high operating pressure regime, $H_2O:CO$ mole ratio and low concentrations of impurities (H_2S, COS, etc) of the syngas make the GEE gasifier quite attractive when Pd-based membrane reactors are to be integrated into IGCC power plants. Therefore, in the present study, the GE Energy gasifier has been selected for the ensuing technical and economic performance assessment.

The detailed flow diagram of the GEE IGCC plant with CO_2 capture via conventional packed bed shift reactors (IGCC-PBR) reported in DOE/NETL report (Haslbeck et al. 2010) was compared with the target flow diagram of a Pd-based membrane rector embedded into the IGCC plant (IGCC-MR). The detailed block flow diagrams of the two cases are shown in Figure 4-1 and Figure 4-2. In a conventional IGCC plant with CO_2 separation, the coal is converted to hydrogen in five main steps: the first process is the air separation in the ASU unit, the second is the coal gasification by using oxygen feed, the third and forth steps are the hydrogen production in the shift reactors and H_2/CO_2 separation in the Selexol units and the final step is the combined cycle electricity generation as shown Figure 4-1(Haslbeck et al. 2010; Winter 2009). Since reaction and separation would take place in the Pd/alloy-based membrane reactor, the high and low temperature shift reactors and also the Selexol unit for H_2 separation were removed from the flow diagram as shown in Figure 4-2. The membrane reactor was placed after the gas clean-up step to prevent membrane poisoning by sulfur-containing gases.

The use of hydrogen is mostly dependent on the separation quality. The Pd-based membrane with high selectivity values would produce extra purity H_2 (99.9999%). In contrast, the utilization of Pd-based membranes which have leaks and thus low selectivity values could result in the production of low purity H_2 (<99%). Consequently, low purity H_2 (>94%) could still be used to generate electricity and extra purity H_2 (99.9999%) could be sold for other purposes such as de-hydrogenation/ hydrogenation reactions. All of the separated H_2 with the membrane reactor was assumed to be used for electricity generation to make a fair comparison with the other power plant options. However, the membrane reactor integration introduces an energy penalty at the inlet of the advanced F-class gas turbine (Haslbeck et al. 2010): the separated H_2 coming from the permeate side of the membrane reactor at 1 atm pressure has to be compressed to the working pressure of the gas turbine (~30 atm).

The specific performance target levels for the Pd/alloy-based membrane reactor were set as 98% CO conversion and 95% H_2 recovery. Thus, the exit stream of the membrane reactor at the retentate side would consist of mostly H_2O and CO_2. After condensation of the steam, the retentate stream which is comprised of mainly CO_2 at high pressure (˜25 atm if the gasifier pressure is ˜50 atm) would be ready for sequestration. In addition, separating CO_2 at high pressure through the membrane reactor generates substantial energy savings in terms of CO_2 compression costs as opposed to separating CO_2 at atmospheric pressure via a conventional Selexol unit.
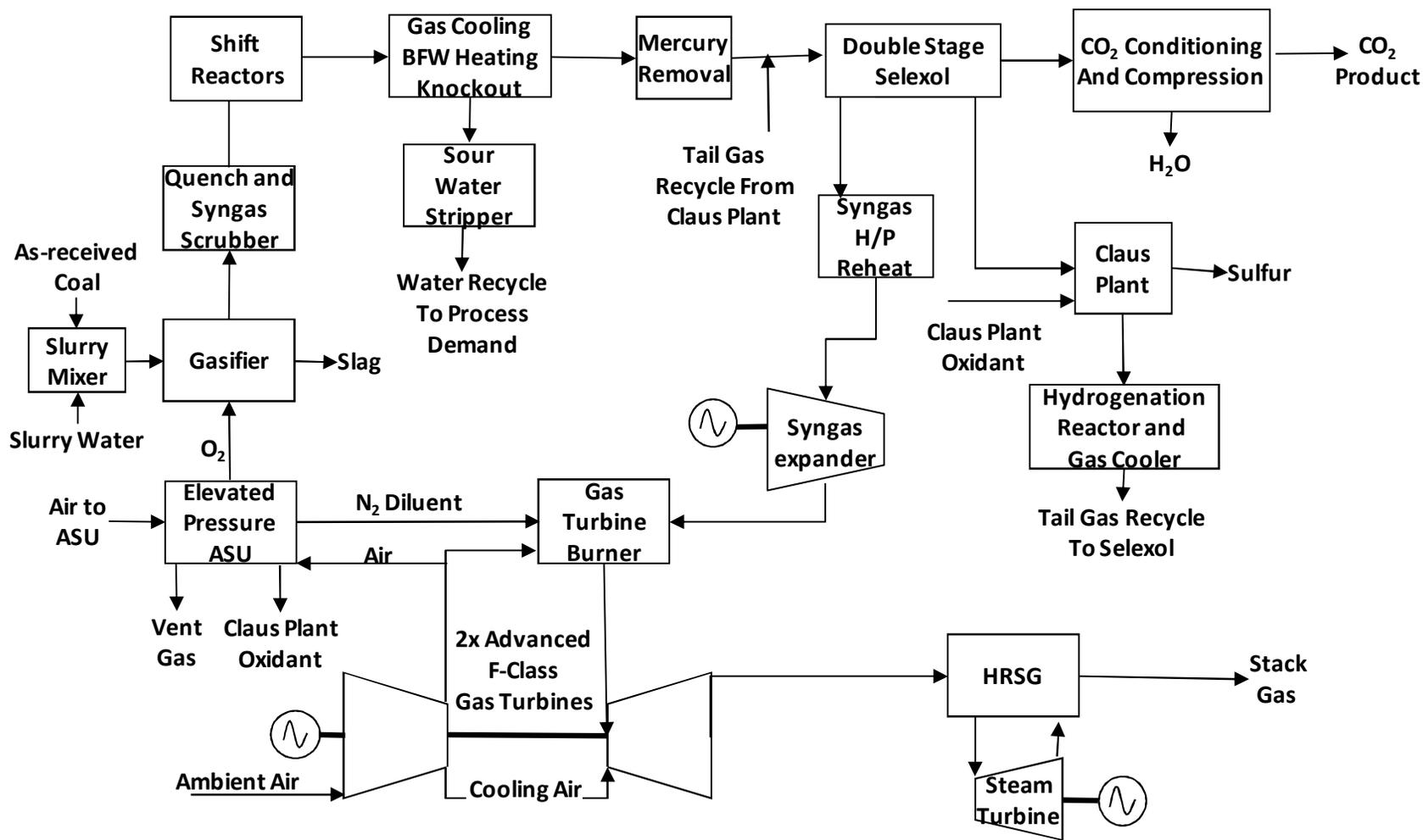
Figure 4-1. Schematic block flow diagram of the GEE IGCC with CO_2 capture using conventional packed bed reactors (Haslbeck et al. 2010)
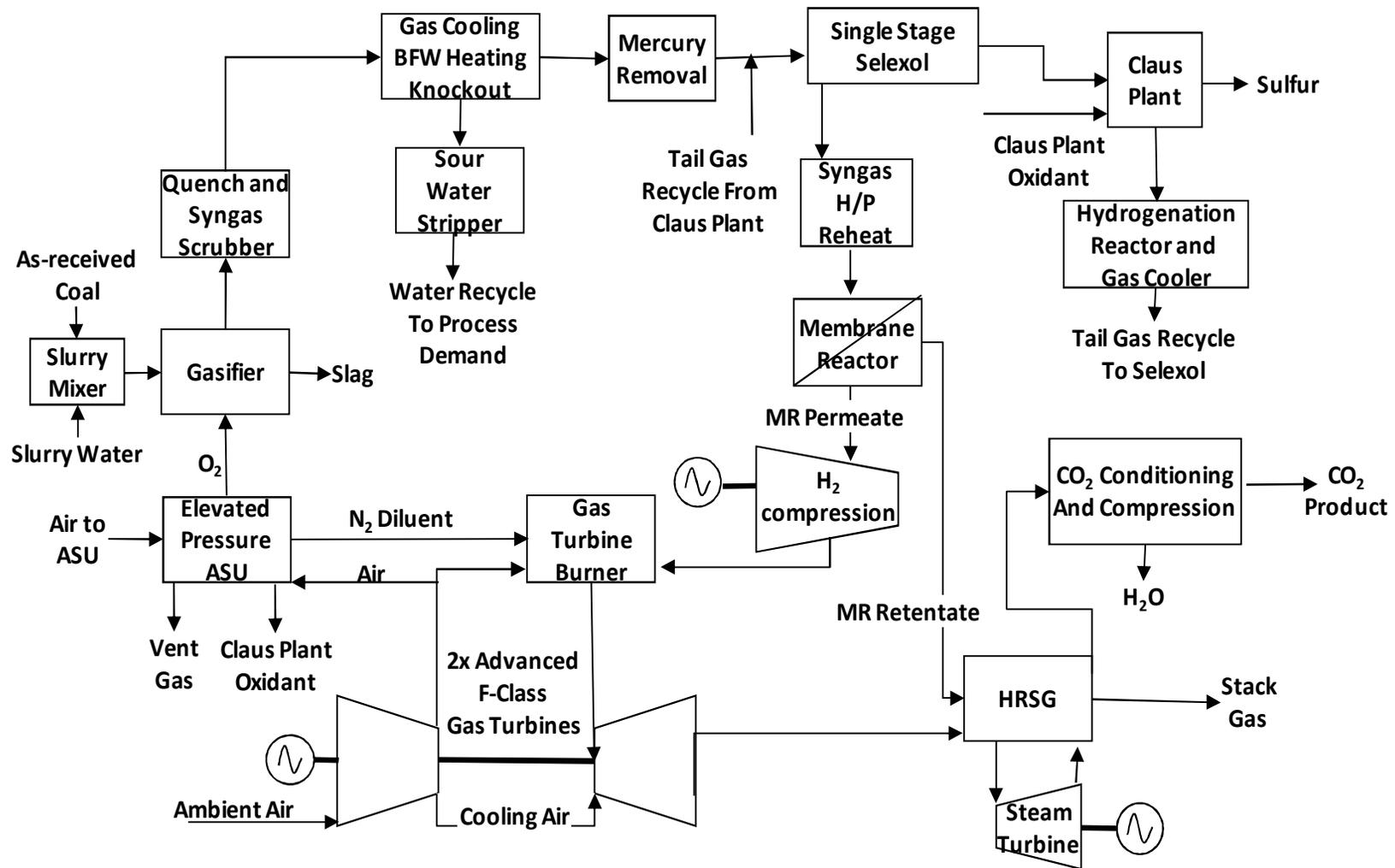
Figure 4-2. Schematic block flow diagram of the GEE IGCC with CO_2 capture using Pd-based membrane reactors

4.2. Economic Analysis Framework

The IGCC-MR economics were compared with:

- Baseline IGCC (without CO_2 capture)

- IGCC including traditional packed bed reactors with CO_2 capture (IGCC-PBR)

- Super critical pulverized coal plant (SCPC) with and without CO_2 capture

The cost figures of the water gas shift reactor and catalyst as well as the assorted equipment were adopted from the detailed block flow diagram of the GEE baseline IGCC and IGCC with CO_2 capture (with traditional PBR- Plant 4) in the DOE/NTEL report (Haslbeck et al. 2010). In addition, the data belonging to the SCPC plant with and without capture was adopted from the same report. The present value of the equipment costs were calculated by using the Marshal & Swift (M&S) equipment cost indexes (M&S cost indexes, 2010) given in Table 4-1. It has to be noted that cost indexes can be used to give a general estimate, but no index can take into account all factors, such as special technological advancements. The M&S cost indexes permit fairly accurate estimates if the time period involved is less than 10 years (Peters and Timmerhaus 1991). In addition, the construction costs of the plants were corrected to find the equivalent cost at the present time on the basis of the Chemical Engineering plant cost indexes. The cost indexes and Pd price used in the cost estimations are given in Table 4-2. The purchased equipment cost of the water gas shift reactor shell casing and 316L PSS supports was estimated by using the six-tenths-factor rule (Peters and Timmerhaus 1991) given in Eq (4.1). The original size of the water gas shift reactor shell casing, catalyst amount and price were adopted from DOE/NETL report (Haslbeck et al. 2010) and the quote of 316L PSS supports (from Chand Eisenman, Burlington, CT and Mott Metallurgical Corporation, Farmington, CT) are also listed in Table 4-2.

$$\text{Cost of equip. a} = \text{cost of equip. b} \times \left(\frac{\text{Capacity of equip. a}}{\text{Capacity of equip. b}}\right)^{2/3} \tag{4.1}$$

Table 4-1. Annual cost indexes

M&S equipment cost indexes (M&S cost indexes, 2010)	In 2006	1302.3
	In 2010	1457.4
Chem. eng. plant cost indexes (M&S cost indexes, 2010)	In 2006	499.6
	In Oct 2009	550.8

The net power output of the IGCC-MR was fixed at 550MWe and only one stream of revenue due to electricity selling was considered while comparing the IGCC-MR plant with the competitors. The Net Present Value (NPV) framework of analysis was used in the economic assessment of the Pd-based membrane reactor integration option into IGCC power plants. The NPV of a series of future cash flows is their present value minus the initial investment required to obtain the future cash flows (Eq (4.3)). The NPV of an investment quantifies the increase in wealth that one realizes if the investment on the project is made, and mathematically represented by the following formula (Benninga 2006):

$$\text{PV} = \sum_{t=1}^{N} \frac{C_t}{(1+r_t)^t} = \frac{C_1}{1+r_1} + \frac{C_2}{(1+r_2)^2} + \frac{C_3}{(1+r_3)^3} + \cdots \tag{4.2}$$

$$NPV = C_o + PV \tag{4.3}$$

where PV given is the present value of the project, C_t is the cash flow in year t, r_t is the real discount rate in year t, N is the total plant lifetime in years, NPV is the net present value, and C_o is the initial capital investment (Brealey and Myers 1996).

Table 4-2. Economic parameters

Plant life [years]	40
Tax rate	40%
Depreciation (annual)	30%
Insurance and property tax rate	1.78%
CO_2 tax ($/ tonnes CO_2, starting in 2015)(Bohm et al. 2007)	25
CO_2 tax growth rate (Bohm 2006)	3%
CO_2 transportation & sequestration cost ($/t CO_2)(Bohm 2006)	5
Nominal discount rate	9%
Inflation rate	2.50%
Electricity selling price [cents/kWh]	9.97
Electricity selling growth rate[%]	0.5
Plant capacity factor	80%
Pd price [$/g, 10 years average]	14.2
Au price [$/g, 10 years average]	21.7
Membrane life time [years]	3
Shift catalyst price [$/kg 2006] (Haslbeck et al. 2010)	6.8
316L PSS supports (0.2 μm media grade) [$/cm^2 for a 25 cm^2 support area] 2011	4.4

In summary, an investment with a positive NPV is deemed a good investment, but an investment with a negative NPV should not be pursued. The parameters used in the NPV analysis are listed in Table 4. The assumptions made in the NPV calculations are the following: the plants are ready to operate in 2011, the life time of the gasification plant is 40 years, depreciation cost was calculated by the declining-balance method (Peters and Timmerhaus 1991), and regulatory action on carbon emissions starts in 2015 with an annual CO_2 growth rate of 3%. A representative range of the cost of abatement for conventional CO_2 capture methods (excluding transport and storage) was determined as $100-150/t$CO_2$ for a first-of-a-kind and $30-50/t$CO_2$ for an nth-of-a-kind IGCC plant with CO_2 capture in a recent comprehensive study (Al-Juaied and Whitmore 2009). Thus, the initial CO_2 tax range used in this study (with a "most likely" value: $25/t$CO_2$ and a maximum value: $75/t$CO_2$) appears to be in agreement with the aforementioned estimates.A higher discount rate of 9% for the IGCC/MR plant was used to

render the high risk associated with this relatively new technology option. In particular, the real discount rate was calculated by using a nominal discount rate along with inflation estimates followed by the appropriate calculation of all future cash flows. Moreover, the IGCC plant with an embedded Pd-based membrane reactor was assumed to achieve a 98% CO_2 capture level. Even though there is no theoretical limit of the CO_2 separation level that can be attained with the Pd-based membrane reactor, only 98% was used in order not to overestimate the membrane reactor profitability.

4.3. Economic Assessment under Uncertainty: Integration of Monte Carlo Methods into the NPV Framework of Analysis

The inherent uncertainty of the inputs of the NPV model has to be recognized and explicitly taken into account in investment decision-making; otherwise any decision based on single values/estimates of the NPV computed by using average input values often leads the investor to make the wrong decisions. Mathematically, the above is supported by the fact that using the average values of uncertain inputs in a function of random variables does not always result in the average value of the function (as a result of Jensen's inequality):

$$F\big(E(x)\big) \neq E(F(x)) \tag{4.4}$$

where x is the uncertain (random) variable(s) (in our case the NPV model's input variables), F is a nonlinear performance map/function (in our case the NPV), and E is the expected or the average value (Savage 2003).

Please notice that the NPV model introduces nonlinear terms such as annual income (Net power output × Capacity Factor × Electricity selling price), real discount rate ([1+nominal discount rate]/[1+inflation rate]-1)), etc. Eq (4.4) represents the mathematical statement of the *flaw of averages,* which states that the project value or performance indicator evaluated at average conditions is not the average project value or performance in the presence of irreducible

uncertainty, which has to be explicitly taken into account. As pointed out earlier, this task can be practically accomplished through the integration of Monte Carlo techniques into the more traditional NPV model of economic assessment (Savage 2002).

Indeed, the study of the effect of uncertain parameters on the value of the project might be rather easily conducted by integrating standard Monte Carlo (MC) simulation methods into the above NPV model. Monte Carlo simulation uses distributions of uncertain inputs, and by propagating the uncertainty through the NPV model generates a distribution of uncertain performance or equivalently a range and frequency of various economic performance outcomes (in our case an NPV distribution profile). Thus, Monte Carlo simulation provides a very effective means of identifying and probabilistically characterizing the consequences and impact on project value of uncertain futures. The particular sequence of methodological steps followed is summarized in the diagram shown in Figure 4-3. The Monte Carlo simulation generates thousands of possible "futures" (or "future states") by assigning random values to each input (sampled from a meaningful distribution through which the corresponding uncertainty is quantified), runs all these futures simultaneously through the NPV model (also known as uncertainty propagation through the NPV model), and finally generates the induced distribution of possible performance (project value) outcomes in the form of an NPV distribution profile while graphically summarizing all pertinent statistics (Savage 2003). The software XLSim was used for the Monte Carlo simulations conducted in the present study with 10^4 iterations for each run.

The most significant uncertain inputs to the NPV model considered in the present study are the following:

1. Plant capacity factor

2. Pd price

3. Au price

4. Support price

5. Membrane lifetime

6. Initial CO_2 tax

7. CO_2 tax growth rate

8. Electricity selling price

9. Nominal discount rate

10. Inflation rate

11. H_2 selling price (only for the IGCC-MR)
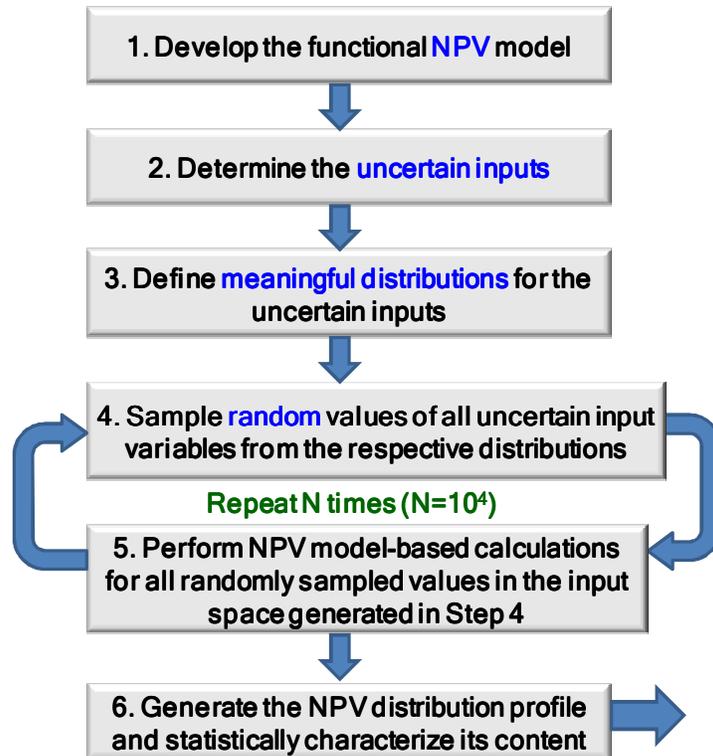
Figure 4-3. The Monte Carlo simulation procedure

The plant capacity factor plays an important role in the uncertainty analysis. The IGCC plant with an integrated Pd-based membrane reactor technology option has never been demonstrated at commercial scale. Thus, the lack of operating experience introduces significant technology risk and uncertainty reflected on the plant capacity factor. All of the uncertain parameters considered in the Monte Carlo simulations are listed with the corresponding distributions in Table 4-3.

New technology options like Pd/alloy-based membrane reactors integrated into IGCC plants that have not been demonstrated at a commercial scale pose additional challenges. As a result, any economic performance would be driven by theoretical reasonable estimates but methodologically should acknowledge the various uncertainties in an explicit manner. Within scope of the aforementioned economical analysis, the static module cost levels of the membrane reactor module and static NPV values of the power plants were assessed, followed by presentation of the Monte Carlo simulation results for the power plants comparison with and without CO_2 taxation in the Chapter 10.

Table 4-3. Probability distributions associated with the various uncertain inputs

Parameter↓	Distribution		
	Minimum	Most Likely	Maximum
CO_2 tax ($/ t CO_2), TD	0	25	75
CO_2 tax growth rate, TD	0	3	8
Nominal discount rate, TD	6	7	9
For IGCC-MR	6	8	9
For SCPC without CO_2 capture		6-fixed	
Plant capacity factor [%], TD	70	80	85
For IGCC-MR	65	70	80
For SCPC without CO_2 capture		85-fixed	
Inflation rate [%], RH	1979-2011 Historical data, U.S. Dep. of Lab. Bureau		
Electricity selling price [cents/kWh], RH	1979-2011 Historical data, U.S. Energy Inf. Adm.		
Pd price [$/g], RH	1979-2011 Historical data, www.kitco.com		
Au price[$/g], RH	1979-2011 Historical data, www.kitco.com		
Support price [$/cm^2 for lab scale], TD	2.3	5	7.5
Membrane life time [years], TD	1	3	5
H_2 selling price [$/kg] (Gray and Tomlinson 2002; 2011)	1.1	1.6	2.3

*TD: triangular distribution, RH: resample historical data

5. Experimental

5.1. Membrane fabrication

5.1.1 Porous metal supports

The synthesis of composite Pd membranes has been carried out by utilizing metal supports purchased from two different vendors, namely Chand Eisenmann (CE, Burlington, CT) and Mott Metallurgical Corporation (Farmington, CT). For permeation experiments, the porous supports consisted of 316L porous stainless steel (PSS), Inconel or Hastelloy. The chemical compositions for the metal supports used are found in Table 5-1. The supports were tubular in shape with a length with the given dimensions shown in Figure 5-1. The porous tubes were welded to non-porous 316L stainless steel at both ends with a blind cap on one end and a tube at the other.
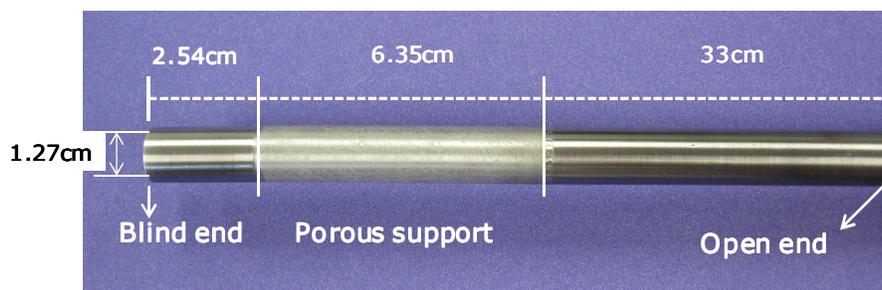
Figure 5-1. Tubular metal support[*]

---

[*] Ratios in the picture are not proportional with each other.

The support grades are specified based on the percentage of particles that are rejected during filtration with a diameter greater of equal to the corresponding grade such as 0.1, 0.2 and 0.5 µm. As an example, a 0.5 µm media grade indicates that the support rejects 95% of particles with a diameter of 0.5 µm or greater. However, mercury porosimetry analysis of the porous section of a 0.5 µm media grade cup resulted in a distribution of pores ranging in size from 1 – 12 µm diameters and few isolated large pores of 10-20 µm diameter on the porous surface (Mardilovich et al. 2002). The prices are varying with the following trend: 310 PSS > Inconel 625 > 316L PSS from CE and Inconel 600 > Hastelloy X > Hastelloy C276 > 316L PSS from Mott.

Table 5-1. Chemical compositions (wt %) and mechanical properties of porous metal supports[§]

AISI type	UNS	Composition,%†								Mechanical Properties‡				
		Cr	Ni or Ni(+Co)§	Mo	C	Si	Mn	Fe	Other	Condition	Yield Strength (MPa)	Tensile Strength (MPa)	Elongation %	Hardness HB
Inconel 600	N06600	14-17	72.	-	0.15	-	-	6-10	-	Annealed	270-345	552.690	55.35	120-170
Inconel 625	N06625	20-23	Bal.	8-10	0.10	-	-	5	3.15-4.15(Cb+Ta)	Annealed	414-655	827-1034	60-30	145-220
Hastelloy C-276	N10276	14.5-16.5	Bal.	15-17	0.02	-	-	4-7	3.0-4.5 W	Annealed	358	793	61.	194
Hastelloy X	N06002	20.5-23	Bal.	8-10	0.05-0.15	-	-	17-20	0.2-1.0 W	Annealed	386	758	45	178
316L	S31603	16-18	10-14	2.0-3.0	0.03	1.0	2.0	Bal.	-	Solution-Annealed	234	558	55	146
310	S31000	24-26	19-22	-	0.25	1.5	2	Bal.	-	Solution-Annealed	310	655	50	170

†Single numbers are maximum values.

‡Typical room temperature properties.

§Single numbers are minimum values and Ni(+Co) is valid for Inconel and Hastelloy.

[§] Perry, R. H and Green, D. W.; "Perry's Chemical Engineers Handbook", 7th Edition, Chapter 28-pp 39&42

5.1.2 Pre-treatment of porous metal supports

The first step of membrane fabrication procedure is to clean the surface of the porous metal support effectively. Failure to remove the surface contamination will result in lowered adhesive bond strength, and cause flaking or blistering of the coating during post plating heat treatments as the contaminants are baked out. Thus, the supports were cleaned to remove contaminants such as grease, oil, dirt by using an alkaline solution. The porous metal supports were submerged into alkaline solutions with the composition given in Table 5-2 at 60°C for 30 minutes in an ultrason bath.

Table 5-2. Composition of the alkaline solution

Component	Amount	Vendor
$NaPO_4 \cdot 12H_2O$, 98 wt%	45 g/l	Alfa Aesar
Na_2CO_3, 99.5 wt%	65 g/l	Alfa Aesar
NaOH, 97 wt%	45 g/l	Alfa Aesar
Industrial detergent	5 ml/l	Alconox

After alkaline solution treatment, the supports were washed sequentially with flowing pressurized tap water for 1 hour, and rinsed with DI water for 15 minutes loops in an ultrasonic bath until the water pH equals to 7 (3 loops). Then, the supports were rinsed in iso-propanol in ultrasonic bath for 15 minutes to hasten the drying of the supports and then the supports were dried at 120°C overnight in a VWR Scientific (Model 1350 FM) forced air oven.

The metal oxide layer on the support surface was used as a protective layer against the occurrence of intermetallic diffusion of support elements (Fe, Cr, Ni) during high temperature applications. Inconel and Hastelloy tubes were oxidized at 700°C and stainless steel tubes were oxidezed at 600°C for 12 hours in stagnant air using Lindberg (Blue M732) oven. A heating and cooling rate of 10°C/min was used for all.

5.1.3 Support activation

The activation layer has a structure comprising of a number of thin layers, each formed after sensitizing/activation cycle, of palladium nuclei. The induction period of the autocatalytic process at the start of the electroless palladium plating is shortened by pre-seeding the palladium nuclei. Alternatively, the palladium could be deposited on the support surface without surface activation but the nucleation process would be very slow and as a result plating rate would be slow. In either case, the growth rate of palladium on the support surface accelerates due to autocatalytic deposition once the amount of deposited palladium reaches ˜ 0.1mg/cm^2. Pd nuclei seeding on the support surface is expressed in Eq (5.1).

$$Pd^{2+} + Sn^{2+} \rightarrow Pd^0 + Sn^{4+} \tag{5.1}$$

1. The support was activated by immersing into SnCl$_2$ and PdCl$_2$ baths at room temperature. The detailed activation sequence is given below:

2. Immerse into DI water for 1 minute.

3. Immerse into acidic SnCl$_2$ solution for 5 minutes to sensitize the support and then rinse in DI water for 1 minute.

4. Immerse into acidic PdCl$_2$ solution for 5 minutes to sensitize the support, rinse in 0.01 M HCl solution for 1 minute and then rinse in DI water for 1 minute.

5. Repeat steps 2 and 3 preferably for 5 loops (until the activated layer has a uniform dark-brown color and smooth surface)

6. Dry the activated support at 120°C in the oven for at least 2 hours.

The reason of rinsing the support in DI water after SnCl$_2$ bath is to remove the byproducts of Sn^{2+} ion hydrolysis such as Sn(OH)$_{1.5}$Cl$_{0.5}$ and other more complicated hydroxyl-chlorides from the surface. In addition, rinsing in 0.01 M HCl solution after PdCl$_2$ bath is required to prevent the hydrolysis of Pd^{2+} ions (Ma et al. 2000). The compositions of the activation solutions are listed in Table 5-3.

Table 5-3. Composition of activation solutions

Component, purity	Amount	Merchant
$SnCl_2 \cdot 2H_2O$, 98 wt%	1 g/l	Aldrich
$PdCl_2$, 99.9 wt%	65 g/l	Alfa Aesar
HCl, 37 wt%	1 ml/l	Merck

5.1.4 Modification of the support surface

Plating of Pd directly on the porous support surface without modification would result in thicker Pd layers due to the Pd deposition inside the pores. Several different methods were implemented on the porous support surface in order to smooth the surface to achieve a uniform and thin Pd layer. Those grading methods are as follows and the details of the above grading techniques are explained below:

I. Al_2O_3 grading + Pd/Ag barrier

II. $Al(OH)_3$ grading

III. Sequential Al_2O_3 grading in between platings

I.   <u>Al_2O_3 grading+ Pd/Ag barrier:</u>

The composition of the Al_2O_3 grading solution is listed in Table 5-4. Before plating the dense Pd layer, 7 – 8 in Hg vacuum was applied from the tube side at and immersed in DI water for 5 minutes. Then, the first grading was performed by immersing the support in the Al_2O_3 slurry for 10 seconds. The vacuum was increased to 27 in Hg after the support was taken out of

the slurry. While still at a high vacuum of 27 in Hg, the support was immersed in DI water for 5 minutes. The vacuum was disconnected and the support was dried at 120ºC for 12 hours.

Table 5-4. Components of Al_2O_3 slurry

Al_2O_3 particle size [µm]	Amount [g/l]	Merchant, purity
1	0.14	Alfa Aesar, 99.9%
0.2 – 0.5	0.85	Alfa Aesar, 99.95%
0.01 – 0.02	0.09	Alfa Aesar, 99%

Following the grading, a short Pd plating step, namely "Pd glue" was performed to seal the Al_2O_3 particles in the pores. The particles in the support was activated once (one activation loop) under a vacuum of 10 in Hg and plated with Pd for 10 minutes.

The final step in the modification is the deposition of the porous Pd/Ag layers. The porous Pd/Ag barrier was deposited on the membrane surface to prevent intermetallic diffusion of support elements (Fe, Cr and Ni) into the membrane layer during high temperature hydrogen separation applications (Ayturk et al. 2006a). The Pd/Ag barrier was deposited with the sequence given in Table 5-5 without intermediate drying and activation steps between Pd and Ag depositions. The Pd/Ag barrier layer was lightly polished with 2400 grit SiC paper and cleaned before plating the dense Pd layer (Ma et al. 2007b).

Table 5-5. Pd/Ag barrier deposition sequence

Deposited metal	1 M - H_2NNH_2 concentration [ml/L]	Plating duration [min]
Pd	0.33	30
Ag	0.58	60
Pd	0.38	60
Ag	0.58	60
Pd	0.58	60

II. Al(OH)$_3$ grading:

The Al(OH)$_3$ grading slurry was prepared by dissolving 5 g of aluminum hydroxide powder (Al(OH)$_3$.xH$_2$O, Fisher Scientific) in 40 ml of DI H$_2$O and 1 ml of 1M HCl solution. The support was immersed into Al(OH)$_3$ grading slurry twice for 2 minutes each while applying vacuum from the tube side. Between each dipping into the slurry, the excess Al(OH)$_3$ particles was removed by wet glove and then rinsed with DI H$_2$O. It is important to note that the Al(OH)$_3$ grading did not involve the Pd glue and Pd/Ag barrier. The support was activated before Al(OH)$_3$ grading (Ayturk 2007).

III. Modified sequential Al$_2$O$_3$ grading:

The supports were graded with Al$_2$O$_3$ particles ranging from 20-50 µm to 5-3 µm in size before oxidation. The first step of sequential Al$_2$O$_3$ grading consisted of the steps listed in Table 5-6. The excess Al$_2$O$_3$ particles were removed either with wet glow or bristle brush after each grading. The composition of all of the grading slurries listed in Table 5-6 was 0.04 g/ml and grading steps were performed by applying 25 in Hg vacuum from the tube side.

Table 5-6. Sequential Al$_2$O$_3$ grading before oxidation

Step #	Al$_2$O$_3$ particle size [µm]	Merchant	Duration
1	20	Alfa Aesar	2 times× 1 min
2	10	Alfa Aesar	2 times× 1 min
3	5-3 (50-50 wt%)	Buehler	3 times× 1 min

After the oxidation of the support, the Al$_2$O$_3$ grading was combined with the Pd glue in the second stage of the modified sequential Al$_2$O$_3$ grading. The graded-oxidized support was immersed into the 20-50 µm slurry for 1 minute under 25 in Hg vacuum pressure from the tube side, excess cake was removed and the support was rinsed with DI H$_2$O. The support was

106

activated with 10 min SnCl$_2$ followed by 15 min PdCl$_2$ cycle by applying 10 in Hg vacuum pressure from the tube side before Pd glue. At last, the particles were sealed by Pd plating for 5 minutes at 60°C under 25 in Hg tube side vacuum. The latter procedure was repeated for 10 µm and 5-3 µm Al$_2$O$_3$ particles.

The final step is the grading with the activated Al$_2$O$_3$ slurry (Guazzone and Ma 2006) with the composition given in Table 5-7. The fine Al$_2$O$_3$ slurry is first mixed with SnCl$_2$ solution and stirred for 10 min, then PdCl$_2$ was added into the solution (Al$_2$O$_3$ slurry + SnCl$_2$) and stirred for 15 min. The membrane was immersed into the activated Al$_2$O$_3$ slurry at room temperature with continuous stirring for 30 minutes by applying 25 in Hg vacuum pressure from the tube side. After grading with the activated Al$_2$O$_3$ slurry, the membrane was plated with Pd for 30 minutes.

Table 5-7. Activated Al$_2$O$_3$ slurry composition

Component	Amount
1. Fine Al$_2$O$_3$ slurry	50 ml
1 µm Al$_2$O$_3$ 1 g/l	
0.3-0.5 µm Al$_2$O$_3$ 0.5 g/l	
0.01-0.02 µm Al$_2$O$_3$ 0.1 g/l	
2. SnCl$_2$ solution	50 ml
3. PdCl$_2$ solution	50 ml

5.1.5 Electroless plating

Following the activation of the support surface, the supports were plated with the desired metal (Pd, Ag, Cu, Au and etc.) with the electroless plating. Particularly, palladium plating occurs according to the following autocatalytic reaction:

$$2Pd(NH_3)_4Cl_2 + H_2NNH_2 + 4NH_4OH \rightarrow 2Pd + N_2 + 8NH_3 + 4NH_4Cl + 4H_2O \qquad (5.2)$$

or

$$2Pd(NH_3)_4Cl_2 + H_2NNH_2 + 4OH^- \rightarrow 2Pd + N_2 + 4H_2O \qquad (5.3)$$
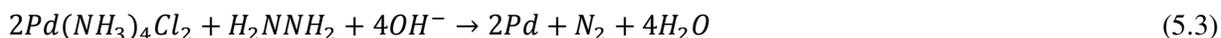
The electroless plating bath compositions are listed in Table 5-8. Care must be taken to prepare the plating solutions at least one day in advance to give enough time for the formation of stable complexes. The amount of plating solution has to be sufficient to provide approximately 3.5 cm^3 of solution per square centimeter of plating area (Ma et al. 2000).

The plating container was placed into a hot water bath (Precision) operating at 60°C to maintain the constant reaction temperature. Hydrazine was added to the plating solution when the activated support was immersed into the plating solution. The support was placed in successive Pd or Ag plating baths and the support was immersed in DI water at 60ºC for 5 minutes in between platings before immersion in a fresh Pd plating solution. The time period of the plating was adjusted based on the desired Pd thickness (typically 90 minutes for Pd and 30 minutes for Ag). Pd plating was continued until no plating solution was found in the interior of the tube indicating that the membrane was "liquid dense," usually after 2–3 plating loops. At this point, the membrane was rinsed with DI water thoroughly both from inside and outside of the membrane tube and then dried at 120°C in the oven for at least 2 hours. Additional platings were performed based on the He permeance of the membrane.

When the He permeance of the membrane was still higher than ~1 m^3/ [m^2-h.atm], the following plating loops were performed by applying vacuum at 27 in Hg (by attaching the tube side to an aspirator or vacuum pump). The latter procedure was repeated until the He leak of the membrane was below 0.01 sccm at a transmembrane pressure difference of 1 atm at room temperature.

The palladium thickness was estimated gravimetrically by measuring the weight of the membrane tube after each step by using a Sartorius LP8200S type balance (max 8.2 kg). The average estimated thickness was calculated with the Eq (5.4).

$$l = 1000. \frac{\Delta m}{A_{plating} \cdot \rho_{metal}} \tag{5.4}$$

where l is the average thickness (μm), Δm is the weight gain (mg), $A_{plating}$ is the plated area (cm^2) and ρ_{metal} is the density of the plated metal (g/cm^3).

Table 5-8. Plating bath compositions and conditions

	Pd bath	Ag bath	Purpose	(Purity) Merchant
$Pd(NH_3)_4Cl_2 \cdot H_2O$ (g/l)	4		Pd^{2+} ion source	(99 wt%) Alfa Aesar
$AgNO_3$ (g/l)		0.519	Ag^+ ion source	(99.9 wt%) Alfa Aesar
$Na_2EDTA \cdot 2H_2O$ (g/l)	40.1	40.1	complexant/stabilizer	(99 wt%) Aldrich
NH_4OH (28 %) (ml/l)	198	198	complexant/stabilizer/buffer	(28 wt%) Merck
H_2NNH_2 (98%) (ml/l)	0.19	0.19	reducing agent	(98.5 wt%) Alfa Aesar
$(C_2H_5)_2NCS_2Na \cdot 3H_2O$ (ppm)			stabilizer	(99 wt%) Alfa Aesar
pH	10 - 11	10 - 11		
Temperature (°C)	60	60		

5.1.6 Annealing and polishing

A successive application of annealing-polishing-plating was used during the fabrication of some of the membranes. The aim of successive annealing-polishing-plating method was to mitigate the leak growth. When the membrane was considered to be dense (He leak < ~0.01sccm), the membrane was placed in a furnace in which He was circulated on both the shell and tube sides of the membrane to prevent oxidation. The temperature was increased at a rate of 5°C/min and kept at 550°C for 12 hours. After the annealing was completed, the Pd layer was mechanically treated by using a mechanical lathe. Polishing was done by using 600/2400, 800/2400 and 1200/2400 grit SiC sandpaper and cleaned with acetone and DI water to remove residual SiC. The membrane was then re-plated with Pd. The He leak and the weight change were measured in between all of the steps. The sequence of annealing, polishing, and plating was repeated 2-3 times until the membrane was either dense (He leak < ~0.01sccm) or the leak was stable. Finally, the membrane synthesis steps were summarized based on the type of surface modification technique in Figure 5-2.

Al₂O₃ grading + Pd/Ag barrier

Cleaning with
alkali solution

↓

Oxidation

↓

Al_2O_3 grading

↓

Activation + Pd Glue

↓

Activation +
Pd/Ag Barrier

↓

Activation + Pd Plating
until He Leak < ~0.01 sccm

→

Anneal - Polish

Al(OH)₃ grading

Cleaning with
alkali solution

↓

Oxidation

↓

Activation + $Al(OH)_3$ grading

↓

Pd Plating

↓

Activation + Pd Plating
until He Leak < ~0.01 sccm

Sequential Al₂O₃ grading

Cleaning with
alkali solution

↓

1st step of sequential Al_2O_3 grading

↓

Oxidation

↓

2nd step of sequential
Al_2O_3 grading
20 μm Al_2O_3 grading+Activation+Pd glue
10 μm Al_2O_3 grading+Activation+Pd glue
5-3 μm Al_2O_3 grading+Activation+Pd glue

↓

3rd step of sequential
Al_2O_3 grading
Pre-activated Al_2O_3 grading

↓

Pd Plating

↓

Anneal in H_2

↓

Activation + Pd Plating
until He Leak < ~0.01 sccm

Figure 5-2. Membrane synthesis procedures based on the surface modification method

5.2. Membrane characterization

5.2.1 He leak measurements

During the synthesis of the membranes, the He permeances of the support and membrane were measured at room temperature at several different shell side pressures between 1 to 2.5 atm before and after each synthesis step. The He flow rate was measured by using three different flow meters operating at different measuring ranges, namely, GCA Wet Test Flow Meter – Precision Scientific for high flow rates of 1.5-13 l/min, Alltech 4068 digital flow mater for medium flow rates of 2-300 ml/min and a bubble flow mater for very small flow rates lower than 2 ml/min.

5.2.2 H_2 permeation apparatus

The schematic diagram of the apparatus for H_2 permeation experiments was shown in Figure 5-3. All piping and connections were 316L stainless steel. The shell casing in the H_2 test rig was a 2.54 cm OD, 50.8 cm long tube connected at the upper-end to the non-porous section of the membrane tube with 1" to ½" Swagelok reducing union, which was drilled and electrically welded to 1/8" SS tubing to allow the gas stream to exit from the shell side. The lower end of the shell casing was welded to a cap which was welded at the center to a ¼ " SS tube to allow the gas stream to enter the shell side.

The open end of the membrane tube was connected to a ½" Swagelok tee fitting, which allows the sweep gas inlet at one opening. The upper part of the ½" Swagelok tee fitting was connected to a ½" tubing which was then connected to a ½" to 1/8" Swagelok reducing union. The permeate side temperature was measured with a thermocouple connected to the 1/8" end of the ½" to 1/8" Swagelok reducing union, which was welded to a 1/8" SS tubing to allow the permeate side gas exit, He sweep or permeated H_2. The temperature of the permeate side was measured with a K-type thermocouple and the tip of the thermocouple was positioned at the center of the membrane.

The shell casing was placed in the Watlow ceramic-fiber tubular heater. The temperature of the ceramic-fiber heater was controlled by a Eurotherm 2116 temperature controller equipped with a J-type thermocouple. The J-type thermocouple was attached to the outer side of the shell casing by placing the tip of the thermocouple over the center of the membrane. The shell casing was mounted vertically into the ceramic-fiber heater and sealed properly with insulation strips from both ends of the heater.

The system pressure on the shell side was measured with the pressure transducers in the pressure range of 0-500 psig equipped with digital display indicators, purchased both from Transducer Direct. The tube side pressure was measured by the use of an MKS, Barathron pressure transducer (1000 Torr). The flow rate in the shell side was adjusted to approximately 50 sccm with the help of the needed valve at the shell side exit. The permeate side flow rate was measure with the He/H_2 mass flow meters purchased from MKS Instruments of the type M100B (max low rates of 500/1000/5000 sccm).

All of the temperature, pressure and permeate flow rate measurements were transferred to a PC by connecting the measurements equipments to a data acquisition board purchased from National Instruments and recorded continuously by the use of LabView 7.1 software.
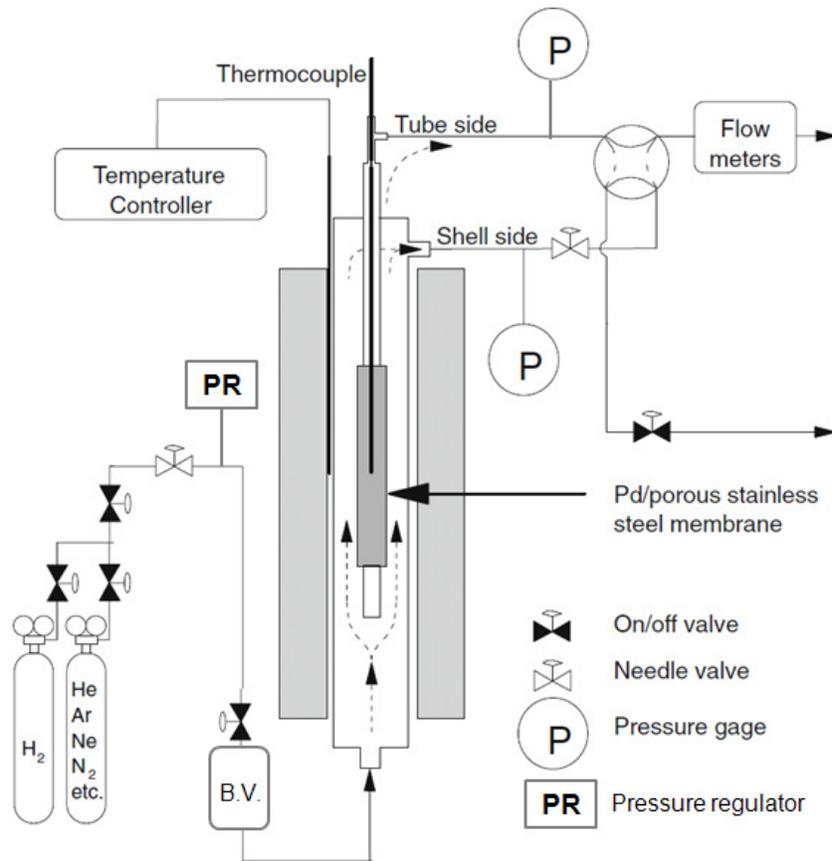
Figure 5-3. Schematic diagram of the experimental set-up for permeation measurements (Bose 2009)

5.2.3 Membrane characterization protocol

The system was flushed with He for ~1 hour at room temperature with shell side pressure of 2 atma and the permeate side pressure of 1 atma. In addition, the He sweep was on during system flushing. After system flushing, the system was heated up to 450°C with an increment of 0.5°C/min. Once the system reached the desired temperature, sweep was turned off and He leak measurement was taken at different shell side pressures between 1.2-3 atma with the permeate side pressure of 1 atma. When the inlet flow was switched from He to H_2, the smooth transition was accomplished with the use of 1L double-ended stainless steel cylinder (ballast volume, B.V. shown in Figure 5-3). At each testing temperature, the permeance of the membrane was measured at various shell side pressure from 1.2 atma to 4 atma with an increment of ~0.5 atm.

113

Linear regression was used to calculate the permeation based on the Sieverts' Law. The system was flushed with He for 2 hours while the He sweep was on. After the H_2 was totally removed from the system, the He leak was measured. Finally, the temperature was decreased to 400 °C with an increment of 0.5°C/min in He flow in both shell and permeate sides.

The same procedure was repeated for temperatures 400 and 350°C to determine H_2 permeance and He leak growth at each temperature. The H_2 permeance was measured at three different temperatures to determine the activation energy and permeability constant of the H_2 permeation which followed the Arrhenius equation.

5.3. Instrumental analysis

5.3.1 SEM and EDX

The microstructure characterization of the membranes were carried out by using the Amray 1610 Turbo Scanning Electron Microscope (SEM) equipped with a Princeton Gamma-Tech Avalon EDX light element detector and a RBA-1610 5MC type Robinson Retractable backscattered electron detector for the qualitative and quantitative analysis. The spatial resolution for the EDX anaylsis of Pd, Ag, Fe, Cr and Ni metals changes between 0.5 and 0.7 µm at an accelerating voltage of 15 keV and between 0.8 and 1.2 µm at an accelerating voltage of 20 keV (Friel 1998).

The microstructure characterization of the membrane cross-section was perfomed by using the SEM samples prepared with the following procedure. The cylindrical membrane tubes were cut through in the radial direction by using a SiC saw. The membrane pieces were rinsed with DI water and cleaned with isopropanol alcohol in ultrasonic bath for 30 min, and then they were mounted in phenolic powder with a Smithells II mounting press. The samples were ground gradually by using SiC sandpapers with increasing grid sizes from P60 to P4000 in the Metaserv 2000 grinder/polisher. Grinding of the samples was continued by using α-Al_2O_3 slurries containing 1, 0.3 and 0.05 µm particles to increase the surface smoothness. Polished sides of the SEM samples were cleaned with DI water and isopropanol. Finally, the polished samples were sputtered with a Pd target for 20 seconds using the Denton Desk II sputtering machine. The

coating thickness of a 30 seonds of preset time of the the Denton Desk II sputtering machine was reported as 100 Ang.

6. Synthesis and Characterization of Pd-Based Composite Membranes

6.1. Introduction

The main objective of the Chapter 6 is to provide a detailed fabrication and characterization summary of the Pd-based composite membranes prepared in this study. Moreover, a comparative assessment of the effectiveness of the support surface modification methods was performed to identify the important criteria of the Pd-based membrane preparation on metal supports.

Pd-based composite membranes were fabricated and characterized in pure H_2/He environment to determine H_2 permeance and final selectivity (>500 hours testing time) to be utilized in the modeling efforts and support the assumptions in the simulations. Three different surface modification/grading methods were used in this work namely, Al_2O_3 grading + Pd/Ag barrier, $Al(OH)_3$ grading and modified sequential Al_2O_3 grading to achieve maximum permeability and selectivity. For instance, a pure Pd-based composite membrane on 316PSS support with a H_2 permeance value of ˜50 m^3/[m^2.h.atm$^{0.5}$] at 450°C and an ideal H_2/He selectivity of ˜1500 (>1000 hours testing) was successfully fabricated by using the modified sequential Al_2O_3 grading method.

6.2. Fabrication history of the Pd-based composite membranes

The specifications of the membranes prepared in this study were listed in Table 6-1 up to the point when H_2 testing starts. The quality of the supports purchased from Mott and CE were different. The pore size distribution of the Mott supports were more uniform and also the surface smoothness of Mott supports were better than the CE supports. The support properties have a strong effect on the final characteristic of the Pd-based composite membranes. The thickness of the membrane and therefore the H_2 permeance was dependent of the largest pores of the support (Mardilovich et al. 2002). In addition, the media grade of the support plays a critical role in the final H_2 permeation. As the media grade of the support increases, the initial He permeance of the membrane increases. Higher initial He permeance values are desired to increase the H_2 permeation levels. The challenge at this point is to keep the He permeance of the support as high as possible after oxidation and grading steps. Both oxidation and grading steps are adding resistance to the flow of fluids through the support layer.

As seen from Table 6-1, the oxidation temperatures were changed based on the support type. As the Ni content of the metal support was increased the oxidation temperature was increased to obtain a uniform oxide layer as an effective intermetallic diffusion barrier (Ma et al. 2004). A sandwich type porous Pd/Ag layer could also be used to prevent the intermetallic diffusion of support elements (Fe, Cr and Ni) into the active Pd layer (Ayturk et al. 2006a; Ma et al. 2007b). In the fabrication method which involved the surface modification with Pd/Ag layer, an oxide layer was also applied at all times. Since the Pd/Ag layer would act as an intermetallic diffusion barrier, the additional costs related with high oxidation temperatures could be reduced. Thus, membrane RK_02 which contained a Pd/Ag layer was oxidized at 400°C to evaluate the effectiveness of the Pd/Ag layer. No sign of intermetallic diffusion, a continuous decline in H_2 permeance as a function of testing time (Ayturk et al. 2006a), was observed up to 500°C.

The thickness values reported in Table 6-1 were the total metal thickness plated on the support surface. The thickness values involved the thicknesses of the Pd glue and the final dense Pd layer (and Pd/Ag layer thickness for certain membranes). The average metal thicknesses of

the membranes were determined by measuring the weight change before and after platings. There might be inaccurate thickness measurements due to incomplete drying between steps and also weight loss due to corrosion of the support during plating in caustic plating bath. Thus, it is important to analyze the membrane cross-sections under SEM to gain better thickness measurements. Finally, the number of annealing and polishing treatments, if any, was also specified in Table 6-1.

The effect of the surface modification method on the overall membrane synthesis was shown in Figure 6-1 [a]. Since the upper left corner values of Figure 6-1 [a] were not clear due to the logarithmic scale, the initial He permeance values and the ones after oxidation were also shown in Figure 6-1 [b]. While only the oxide layer resistance was added to the mass transfer across to the metal support for the membranes RK_01, 04, 05 and 08, the He permeance values of the membranes RK_10 and 16 (were graded before oxidation) were decreased due to both grading and oxidation as shown in Figure 6-1 [b].

When the high quality supports with lower media grade (Inconel$_{0.1}$) were used, it was possible to fabricate dense membranes, like the membranes RK_01 and RK_05, by using the Al$_2$O$_3$ grading solution specified in Table 5-4 as shown in Figure 6-1. Both of the membranes RK_01 and RK_05 were fabricated by using the first Al$_2$O$_3$ grading solution (Table 5-4) and the membrane RK_05 also had the Pd/Ag layer. For the membrane reactor application areas which requires operation at elevated temperatures like steam methane reforming (700-1000°C for traditional reactors (Barelli et al. 2008) and 500°C for membrane reactor (Marigliano et al. 2001; Shu et al. 1994; Barelli et al. 2008)), the Pd/Ag barrier was not effective to prevent the intermetallic diffusion of the support elements. The most important disadvantage of the Al$_2$O$_3$ + Pd/Ag grading was the polishing step even before annealing/testing. The removal of precious metal by mechanical treatment was a waste of time and material but still an important step to smooth the surface. However, when the same grading method of Al$_2$O$_3$ grading + Pd/Ag layer was applied to the low quality CE supports (the membranes RK_08 and RK_09), the membranes were still not dense at total active layer thicknesses higher than 11 µm as presented in Table 6-1 and Figure 6-1. Thus, the synthesis of the membranes RK_08 and 09 were aborted. Even though the CE supports were told to be 0.1 µm media grade by the vendor, the pore size distribution were not uniform and there were visible defects on the support surface. The latter results indicated the need for a more efficient method for the pre-treatment of the low quality supports.

118

The second grading method originally proposed by Tong and Matsumura (2004) and slightly modified by Ayturk (2007) was applied on the membrane RK_04. The number of preparation steps of the membrane RK_04 was less compared to the ones with the first methods (RK_01 and RK_05) and also the membrane RK_04 got dense at a relatively thinner Pd layer as shown in Figure 6-1 [a]. However, there were still two important points that needed the improvement; 1) the excessive surface polishing to smooth the surface after $Al(OH)_3$ grading followed by the first Pd plating, 2) reduced H_2 permeance for the heat treated membranes at temperatures higher than 500°C. The H_2 permeance of a 3-5 μm thick Pd-based membrane prepared by using $Al(OH)_3$ grading dropped from 40 to 25 m^3 /[m^2-h-atm$^{0.5}$] at 300°C after heat treatment at 550°C due to the phase transformation of $Al(OH)_3$ (Ayturk and Ma 2008). Ayturk et al. (2007; 2008) claimed that the transformation of the $Al(OH)_3$ from Gibbsite to Boehmite and Akdalaite with increasing temperature resulted in the formation of a denser crystal structure and therefore clogging of the pores caused the decreased H_2 permeance at elevated temperatures (>400°C). Moreover, since the initial $Al(OH)_3$ grading solution was in the sol-gel form, it could go through deep in the porous structure during vacuum grading and once it was heat treated it would end up with high support resistance. This explained the great difference in H_2 permeance between the free standing Pd foil permeance with the same thickness and the membrane RK_04 (Pd foil and RK_04 permeance values are 44 and 26 m^3/ [m^2-h-atm$^{0.5}$], respectively).

Table 6-1. Specifications of the Pd-based composite membranes fabricated in this study

Label	Vendor	Support Type$_{Grade}$	Initial Pe$_{He}$ [m^3/m^2.h.atm]	Oxidation T [°C]	Grading	Pre-characterization		Anneal/Polish[†]
						Thickness [µm]	Pe$_{He}$ * [m^3/m^2.h.atm]	
RK_01	Mott	Inconel$_{0.1}$	286	700	Al$_2$O$_3$	17.94	N/D	N
RK_02	Mott	Inconel$_{0.1}$	344	400	Al$_2$O$_3$+Pd/Ag	15.56 (1.8)	N/D	N
RK_03	Mott	Inconel$_{0.1}$	312	700	Al$_2$O$_3$+Pd/Ag	10.44 (3.9)	N/D	1A/1P
RK_04	Mott	Inconel$_{0.1}$	366	800	Al(OH)$_3$	10.78	2×10^{-4}	3A/3P
RK_05	Mott	Inconel$_{0.1}$	367	700	Al$_2$O$_3$+Pd/Ag	17.27 (6.9)	1×10^{-4}	2A/2P
RK_08	CE	316L PSS$_{0.1}$	193	550	Al$_2$O$_3$+Pd/Ag	15.24	138.2	N
RK_09	CE	316L PSS$_{0.1}$	175	550	Al$_2$O$_3$+Pd/Ag	10.54	60	N
RK_10	CE	316L PSS$_{0.1}$	590	600	Seq-Al$_2$O$_3$	6.69	3×10^{-4}	1A/1P
RK_11	CE	HastelloyX$_{0.1}$	1218	650	Seq-Al$_2$O$_3$	7.63	0.025	1A/2P
RK_13	CE	310 PSS$_{0.1}$	226	600	Seq-Al$_2$O$_3$	4.78	1.5×10^{-4}	1A/NP
RK_14	CE	HastelloyX$_{0.1}$	1116	650	Seq-Al$_2$O$_3$	7.88	1.23	1A/NP
RK_15	CE	316L PSS$_{0.1}$	580	600	Seq-Al$_2$O$_3$	8.78	1.89	2A/2P
RK_16	Mott	316L PSS$_{0.2}$	418	600	Seq-Al$_2$O$_3$	5.1	N/D	2A/NP
RK_17	Mott	316L PSS$_{0.5}$	958	600	Seq-Al$_2$O$_3$	7.3	N/D	3A/NP

* N/D: Not detectable
† Number of annealing steps and polishing steps are specified, N: None, A: annealing, P:polishing

120
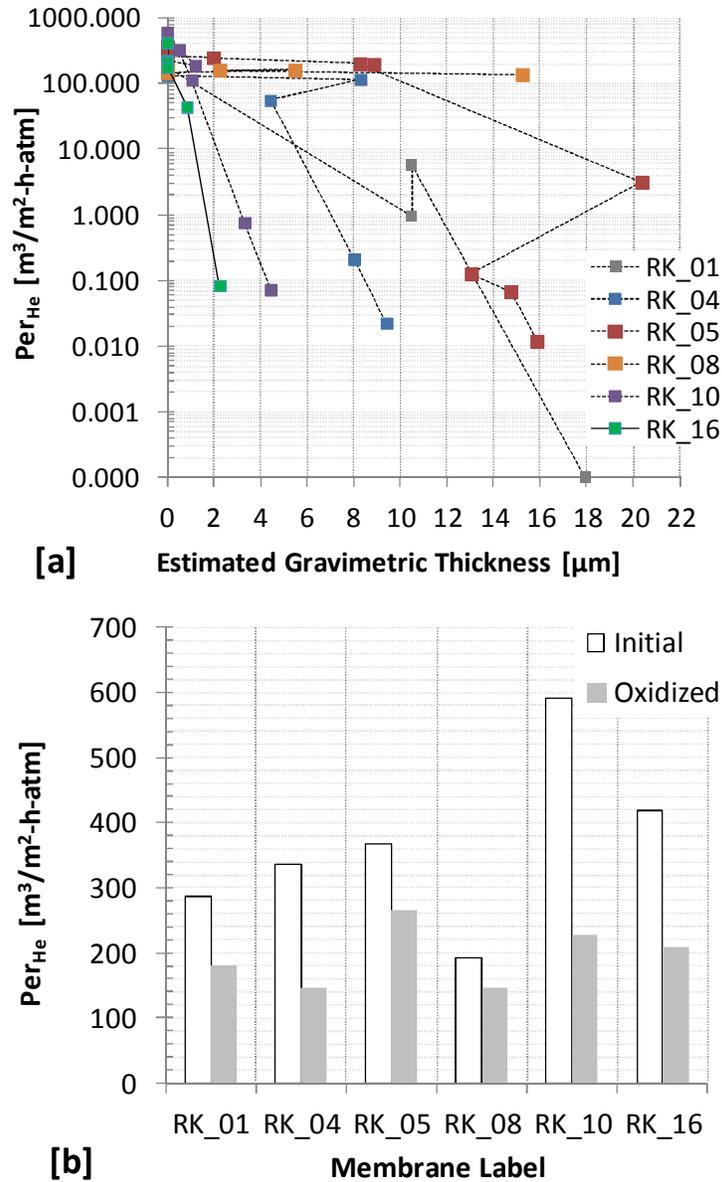
Figure 6-1. Comparison of the membrane fabrication methods

A support surface modification method which would provide less mass transfer resistance of the support, shorten the fabrication time, reduce the number of fabrication steps and decrease/eliminate the number of polishing steps was essential. The required support surface modification method would be suitable for all types of supports and it would enable the fabrication of thin (<10 µm Pd) and selective ($\alpha_{H2/He}$ >1000) membranes. The sequential Al_2O_3 grading technique which was first proposed by Ma and Guazzone (2010) was modified for the

purposes listed above. The main idea of the sequential Al_2O_3 grading technique was described in Figure 6-2. The surface modification techniques namely, Al_2O_3 + Pd/Ag grading and $Al(OH)_3$ grading contained smaller size particles and the grading was performed under vacuum which resulted in the filling of the porous structure with an uncontrolled manner. Thus, the grading material clogged most of the free space and therefore the mass transfer resistance of the support was increased as shown in Figure 6-2 [a]. In contrast, only the entrances of the surface pores were clogged step by step by using Al_2O_3 particles decreasing in size which would prevent the passage of other particles into the porous structure as shown in Figure 6-2 [b]. The support was plated with Pd for a very short time (5 min or less) after each grading to ensure the stability of the big particles (20, 10 and 5µm) in their positions. The membrane fabrication trials with the sequential Al_2O_3 grading technique were successful for various types of supports such as 316L PSS0.1/02/05, HastelloyX0.1 and 310 PSS0.1 purchased both from Chand Eisenman and Mott Metallurgical Corporation as listed in Table 6-1.

[a] Al_2O_3 grading

Al_2O_3 Particles

Metal Support

[b] Sequential Al_2O_3 grading
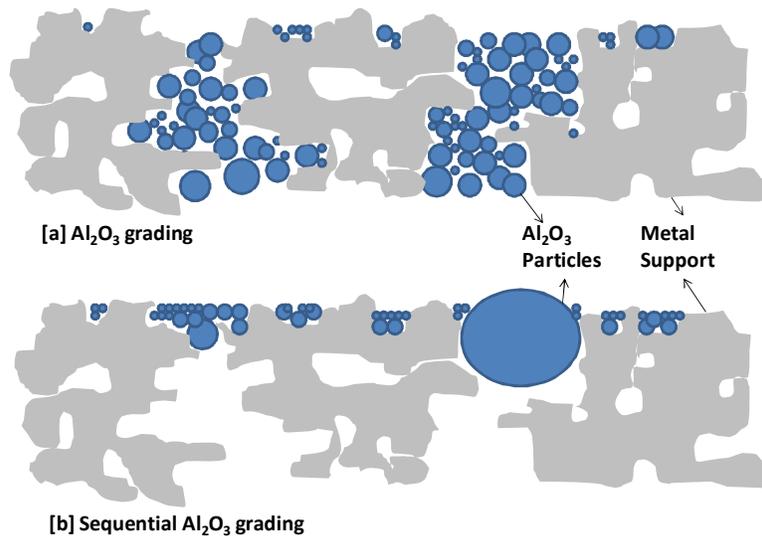
Figure 6-2. Illustration of the porous structure of the support after [a] Al_2O_3 grading (Method I) and [b] sequential Al_2O_3 grading (Method II)

The membranes prepared with the sequential Al_2O_3 grading technique namely RK_10 and 16 were compared with the ones prepared with the other two methods in Figure 6-1 [a]. As evidenced from Figure 6-1 [a], the membrane fabrication procedure was significantly improved

by using the sequential Al_2O_3 grading technique with decreased Pd thicknesses and decreased number of fabrication steps and by eliminating the polishing step. In addition, the sequential Al_2O_3 grading technique worked well on both high and low quality supports as shown with the membranes RK_10 (CE) and RK_16 (Mott) (except the CE supports which had large defects particularly on the welding areas).

6.3. Characterization of the Pd-based composite membranes

The characterization history, Sieverts' data and also leak growth history of the membrane RK_10 which was prepared with the modified sequential Al_2O_3 grading method was shown as an illustrative cas in Figure 6-3, Figure 6-4 and Figure 6-5, respectively. The membrane RK-10 was characterized in pure H_2 at 350, 400 and 450°C, and H_2 pressures up to $\Delta P = 3$ atm. In all of the annealing and characterization tests, unless the H_2 flow was on, the shell side stream was He and also the He sweep at 1 atma pressure was admitted into the tube side. The membrane RK-10 was placed into the system for the first ~24 h annealing in pure H_2 when the Pd thickness and He leak at $\Delta P = 1$ atm were 4.4 µm and 2.9 sccm, respectively. Since the He leak of the membrane RK-10 increased to 10.4 sccm at $\Delta P = 1$ atm at the end of the first annealing, the membrane RK-10 was re-plated. The total thickness of the grading + Pd layers was 6.7 µm together with a He leak of 0.06 sccm at $\Delta P = 1$ atm. The permeance and Sieverts' data of the membrane RK-10 were taken at three different temperatures of 350, 400 and 450°C for a total time of ~410 hours as shown in Figure 6-3. The temperature was increased back to 450°C to monitor the selectivity stability for additional ~600 hours as shown in Figure 6-3.

The activation energy of the membrane RK-10 was 13.5 kJ/mol by using the Sieverts' data shown in Figure 6-4. The power of H_2 partial pressure (n) was 0.5 for the both of the temperature values of 350 and 400°C, however, an n value equal to 0.62 was found for the testing temperature of 450°C. If the selectivity of a membrane was above 400, leaks did not have any significant effect on either hydrogen permeance or n-value. In other words if n value was higher than 0.5 and the selectivity was higher than 400 the reasons for n > 0.5 were due to factors other than pinholes and imperfections (Guazzone et al. 2006b).

Criscuoli et al. (2001) used palladium membranes obtained by folding Pd foils into cylindrical shape and placing a commercial porous alumina between the Pd surface and catalyst (if any) and experimentally measured H_2 flux values to determine the H_2 permeance by using Sieverts' Law. In particular, Criscuoli et al. (2001) stated that (i) Sieverts' Law yielded accurate H_2 permeance calculations for Pd thickness greater than or equal to 10 µm, (ii) both resistances in the palladium layer and on the surface were equally important if the Pd thickness was around 5 µm and standard error levels as high as 45% was made by calculating the H_2 permeance by using the Sieverts' Law, (iii) and finally, H_2 permeance calculations made for ultra thin Pd membranes (1µm) based on the the Sieverts' Law could cause large errors.

The leak growth of the membrane RK-10 was monitored for the whole testing time and the details were shown in Figure 6-5. The changes in the leak of the other membranes during testing were also measured in the same fashion. The final ideal selectivity ($\alpha_{H_2/He}$) of the membrane RK-10 was ~1000 at end of 1112 hours of testing time. The membrane RK-10 was tested in H_2 at 450°C for 360 hours in total and the He leak rate increase at t=1003 hours was 1.86×10^{-7} $m^3/[m^2\text{-h-atm}]$. A similar membrane Ma-42 reported by Guazzone and Ma (2008) with a H_2 permeance of 39 $m^3/[m^2\text{-h-atm}^{0.5}]$ at 500°C had almost two orders of magnitude higher He leak rate increase of 4.2×10^{-5} $m^3/[m^2\text{-h-atm}]$ at the end of 499 hours of testing at 450°C.
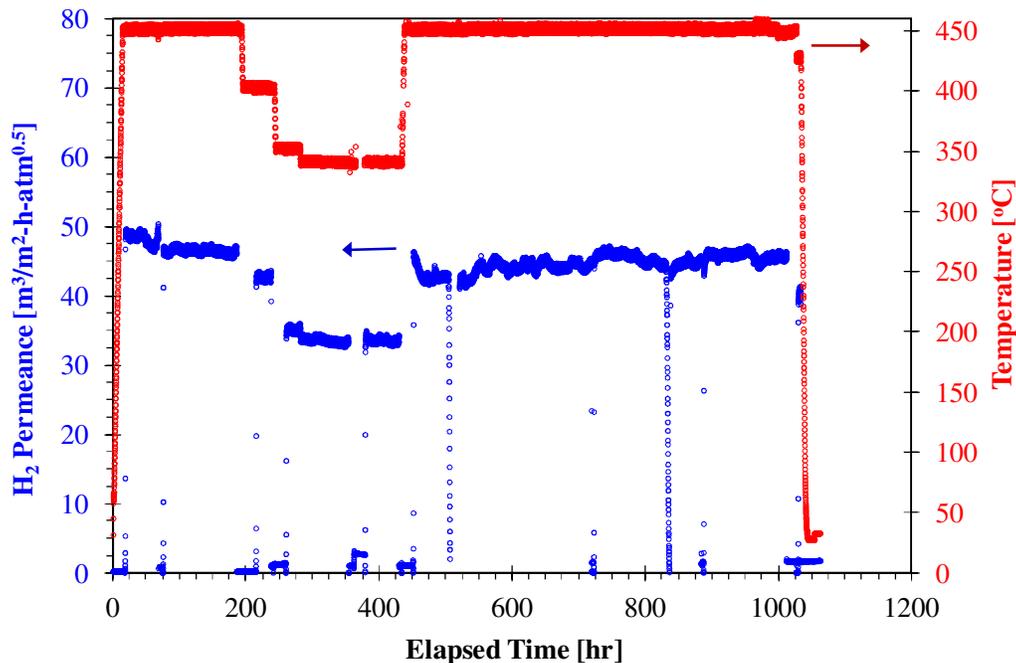
Figure 6-3. Characterization history of the membrane RK_10
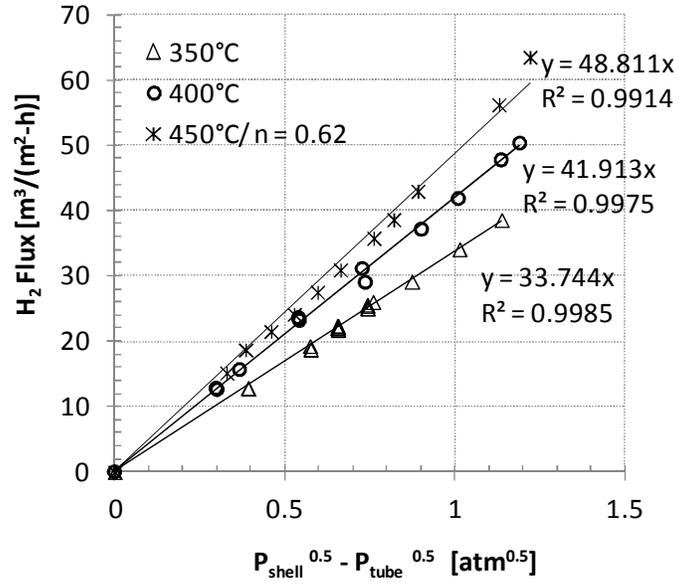
Figure 6-4. Sieverts' plot for the membrane RK_10
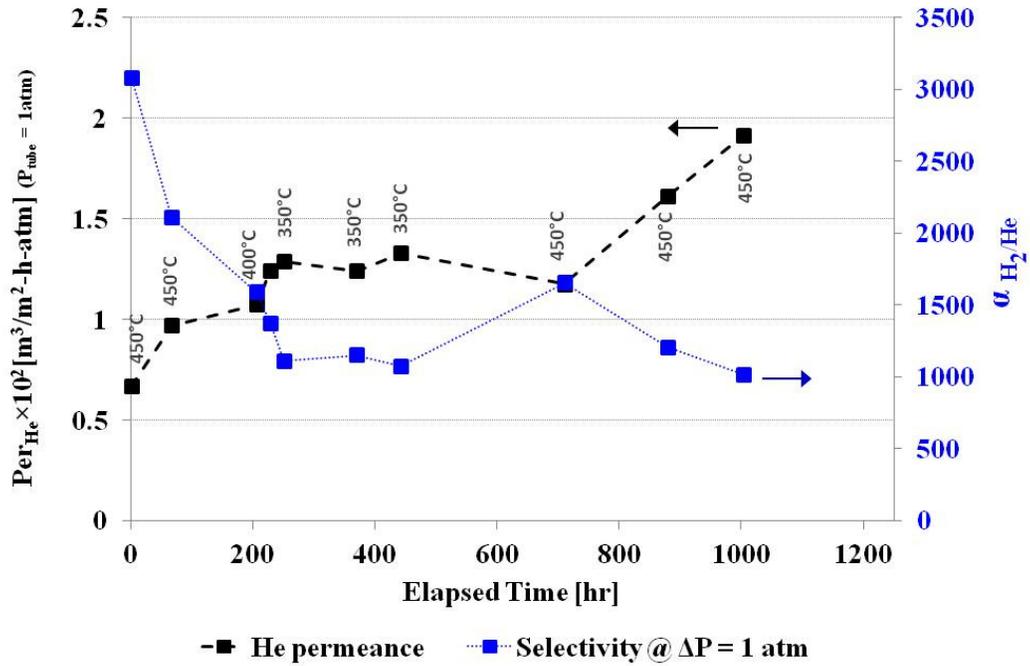
Figure 6-5. Leak growth history of the membrane RK_10 over the testing period

The important characteristics of the membranes tested throughout the present work such as activation energy for the H_2 permeation, total testing time and final He permeance of the membrane through the defects formed during H_2 testing were listed in Table 6-2. The activation energy values determined by using the Sieverts' data for all of the membranes, except the membranes RK_02 and 03, were close to the expected value of ˜15.6 kJ/mol (Guazzone 2005; Ayturk 2007). In fact, the expression for H_2 permeability was obtained by performing linear regression on the natural logarithm of H_2 permeability values of Pd foils established in the literature versus 1/temperature. The standard error calculated based on the average value of the permeability and the number of data points was 30% for Pd foil H_2 permeability (Guazzone 2005). The Ag thicknesses in the Pd/Ag layers of the membranes RK_02 and 03 could be higher than the values listed in Table 6-1 due to the inaccurate gravimetric measurements. Since the membrane RK_02 was not annealed prior to testing and RK_03 was annealed for only 12 hours, the H_2 permeation could not reach a steady value over the testing periods specified in Table 6-2. The measured H_2 permeation values were lower than the ones which should be obtained when the H_2 permeation reached a plateau, thus inaccurate activation energy values, higher than expected, were determined. The latter suggestion was supported by the results obtained with the membrane RK_05 which was annealed 3 times at 550°C. The H_2 permeation value reached its steady value in a shorter time compared to the membranes RK_02 and 03 and the determined activation energy was close to the expected value as listed in Table 6-2.

The most stable membrane in terms of ideal H_2/He selectivity was the membrane RK_01 which also had been tested at 500°C for 300 hours. Both fairly thick Pd layer (18µm) and also high quality support (Mott/Inconel$_{0.1}$) could play a role for the selectivity stability of the membrane RK_01. The characterization of the membranes RK_11, 12, 14 and 15 were stopped due to high leak growths, mostly caused by large defects on the welding area.

As the Pd thickness of the membranes was decreased, the H_2 permeation listed in Table 6-2 was increased as expected but the He leak levels were also increased. Even tough, a small He leak was detected from the membrane RK_01 at the end of 1033 hours of total testing time, the membrane RK_10 was the best performing membrane in terms of both high H_2 permeance value and at the same time low He leak as listed in Table 6-2. There was still room for improvement for the modified sequential Al_2O_3 grading method. The ideal selectivity of the membranes prepared by the sequential Al_2O_3 grading methods could be further improved by plating very thin

126

layers of other metals which has higher melting points and higher tensile strength than Pd on the outer surface of the membrane (on top of palladium). The application of a top metal layer with higher Tamman temperature such as cobalt, tungsten (Gryaznov et al. 1993) or ruthenium (Gade et al. 2009) could be effective to prevent the formation of defects in the Pd layer due to heat treatment in H_2. The activation barrier for H_2 dissociation over the metal, which would be plated on the outer surface of Pd to improve the membrane selectivity, is one of the most important criteria. Pozzo et al. (2009) investigated the H_2 dissociation and subsequent atomic hydrogen diffusion in transition metals (Ti, V, Zr, Fe, Ru, Co, Rh, Ni, Pd, Cu, Ag)-doped Mg (0001) by using an ab initio density functional theory. In Figure 6-6, the dissociation and diffusion energy barriers against the energy moment of the d-band were plotted for various doped-transition metals. It was observed that the transition metals on the left of the periodic table (Ti, V, Zr and Ru) eliminated the dissociation barrier (very low dissosication barrier as shown in Figure 6-6), however, the products were bonded so strongly to the metal that the diffusion away from the active site was hindered (high diffusion energy barrier as shown in Figure 6-6). In contrast, the bond between the transition metals on the right side of the periodic table and H atom was not too strong (Ag does not bind) and thus diffusion was easier than the previous case.
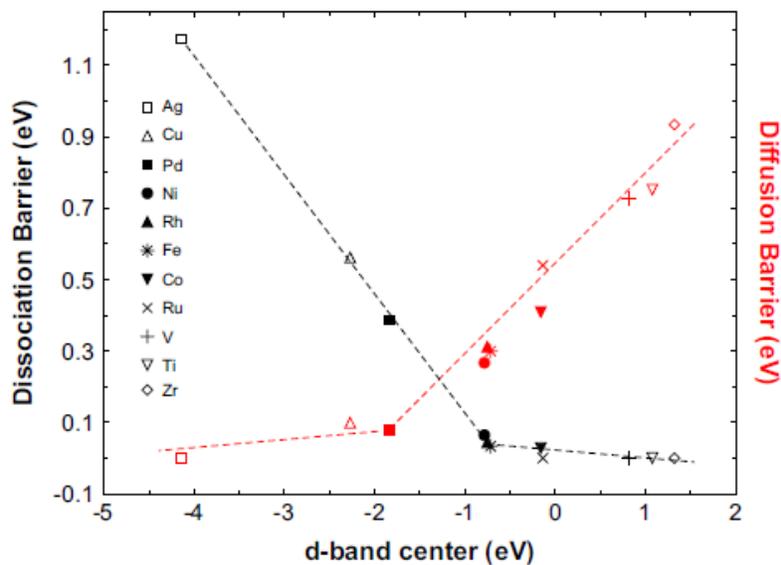
Figure 6-6. Activation energy barrier for hydrogen dissociation (black) and diffusion (red) of hydrogen on pure Mg and metal doped Mg surfaces as a function of the d-band center positions.

For instance, a 10 µm thick Pd-Ru$_{6wt\%}$ supported on porous stainless steel with a 0.8 µm tungsten as an intermetallic diffusion barrier was prepared by using magnetron sputtering by Gryaznov et al. (1993). No change in the H$_2$ permeance and selectivity of the Pd-Ru$_{6wt\%}$ membrane was observed after 1000 hours testing at 1073K (Gryaznov et al. 1993) (the value of the H$_2$ permeance was not specified). Moreover, it was claimed by Gryaznov et al. (1993) that deposition of a 100 nm Co layer on top of a Pd-Ru$_{10wt\%}$ foil, which was used for ethane/propene synthesis, improved the selectivity drastically. Both of the H$_2$ permance and long term stability (1000 hours) of a Pd-Ru$_{4.5wt\%}$ alloy was reported as better than the one for pure Pd (Gryaznov et al. 1973). Furthermore, Ryi et al. (2011) recently reported a very high H$_2$ flux of 103 m^3/m^2.h at a pressure difference of 100 kPa and at 500°C for a 6.8 µm thick non-alloy Pd-Ru membrane supported on porous Hastelloy. More importantly, there was no defect in the membrane which contained ˜85nm Ru on top of Pd layer at the end of 60 hours testing (Ryi et al. 2011). However, the authors did not explain the reasons of high permeability/selectivity of their Pd-Ru membrane. The high hydrogen permeance of the Pd-Ru membrane reported by Ryi et al. (Ryi et al. 2011) could be explained by the dissociation/diffusion energy barriers shown in Figure 6-6. The ultra thin Ru layer (˜85nm) eliminated the dissociation barrier and the permeance was still high because the Ru content was so small that the diffusion of the H atoms away from the active sites was not hindered in the Pd layer.

The high chromium and nickel content of the 310 PSS supports provides good corrosion and oxidation resistance and 310 PSS alloys are typically used for elevated temperature applications (Perry and Green 1997). More importantly, the 310 PSS supports are cheaper than the Inconel supports (Chand Eisenman and Mott Met. Cor.2011). Thus, Since the 310 PSSS supports have similar mechanical properties with Inconel and they are also cheaper, the 310 PSS supports could be used instead of Inconel supports. The membrane RK_13 was prepared by using a 310 PSS support and the highest H$_2$ permeance of 96 m^3/ [m^2-h-atm$^{0.5}$] as listed in Table 6-2, however, the selectivity of this membrane was very low due to large defects on the welding area. In summary, the promising results in terms of high H$_2$ permeation values and easiness of the fabrication obtained by using the surface modification technique namely sequential Al$_2$O$_3$ grading showed the need for further investigation to improve the efficiency of this method, particularly improvement in terms of membrane selectivity.

Table 6-2. Characteristics of the Pd-based composite membranes after H_2 testing

Label	E_A	Q_o	P_{H_2}	Testing Time	Post-Characterization Pe_{He}
	[kJ/mol]	[$m^3 \cdot \mu m/m^2 \cdot h \cdot atm^{0.5}$]	[$m^3/m^2 \cdot h \cdot atm^{0.5}$]	[h]	[$m^3/m^2 \cdot h \cdot atm$]
RK_01	13.8	2346.3	$16.16_{500°C}$	1024	N/D
RK_02	30.8	3571.8	$25_{500°C}$	336	0.095
RK_03	22.2	7237.9	$17.95_{450°C}$	1017	0.0015
RK_04	12.9	2411.9	$25.5_{450°C}$	1227	0.0057
RK_05	12.1	2419.1	$19.5_{450°C}$	223	0.0052
RK_10	13.5	8349	$49.6_{450°C}$	1033	0.019
RK_13	12.59	3838.7	$87.5_{450°C}$	405	0.22
RK_16	11	1481.9	$58.6_{450°C}$	558	0.035
RK_17	13.8	2779.4	$61.1_{450°C}$	558	0.05

6.4. Microstucture analysis of the Pd-based composite membranes prepared by Pd/Ag barrier, Al(OH)$_3$ and sequential Al$_2$O$_3$ grading surface modification techniques

A thorough microstuctre analysis was performed to reveal the differences in the characteristics of the membranes prepared by three different surface modification technique namely, Al$_2$O$_3$+Pd/Ag barrier, Al(OH)$_3$ grading and modified sequential Al$_2$O$_3$ grading (as decribed in detail in Chapter 5.1.4). The cross-section of the membrane RK_03 prepared with the Al$_2$O$_3$+Pd/Ag barrier surface modification method are shown in Figure 6-7 at three different magnifications. As depicted in the SEI micrograph in Figure 6-7 [a], the porous structure of the high quality 0.1 media grade Inconel^{Mott} support was uniform. The diameter of the pore openings on the outer surface of the Inconel^{Mott} support was ranging between approximately 0.3-1 µm as seen in Figure 6-7 [b]. The thickness of the membrane RK_03 determined via SEI micrograph

shown in Figure 6-7 [c] of ˜7.6-13 µm were consistent with the ones determined experimentally (10.44 µm as listed in Table 6-1). In addition, the porous structure of the first Pd/Ag barrier was distinguished (as also shown with the EDX line scans in Figure 6-8) with a ˜4-8 µm layer adjacent to the support as shown in Figure 6-7 [c].

To further confirm the membrane composition and the Pd/Ag barrier thickness, a cross-sectional EDX line scan of the membrane RK_03 was conducted as shown in Figure 6-8. As depicted in Figure 6-8, the membrane RK_03 consisted of an approximately 4 µm thick Pd/Ag barrier with ˜20 wt% Ag and a 6 µm thick dense Pd layer on top of the Pd/Ag barrier. Even tough the membrane was annealed at 550°C for 12 hours; there was no intermetallic diffusion of support elements into the Pd layer which proved the effectiveness of the Pd/Ag barrier. Furthermore, the support composition was varifed by taking an area X-ray scan of the cross-section of the support as listed in Table 6-3. The Inconel composition of 25 wt% Cr, 60 wt% Ni, 12 wt% Mo and 3 wt% Fe (Pd excluded) given in Table 6-3, matched well with the tabulated compositions of the Ni-rich Inconel 625 listed in Table 5-1.
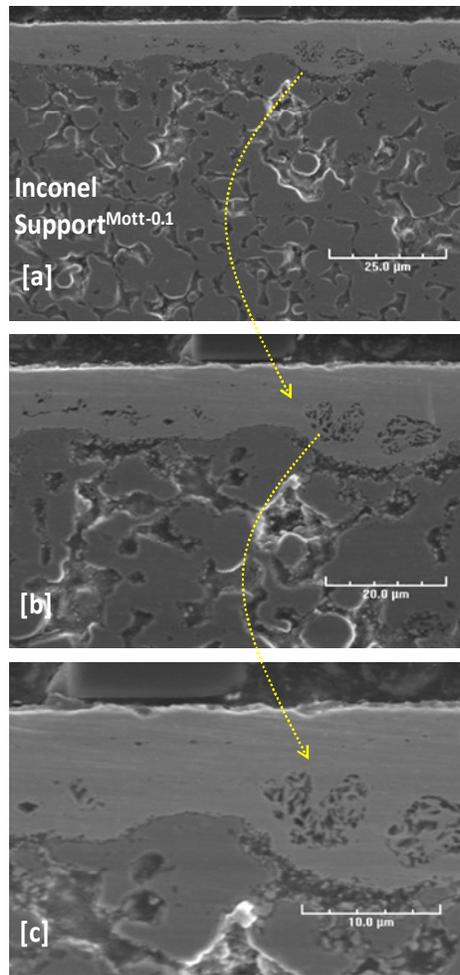
Figure 6-7. SEI Micrographs of the cross section of the membrane RK_03 with the Pd/Ag barrier [a] at 1000x, [b] 2000x, [c] 3500x

Table 6-3. Composition of the support (Inconel 625) cross- section of the membrane RK_03

Element	keV	Wt%
Pd	2.838	7.54
Fe	6.403	2.73
Ni	7.477	54.56
Cr	5.414	22.12
Mo	2.293	10.41
Al	1.487	2.65
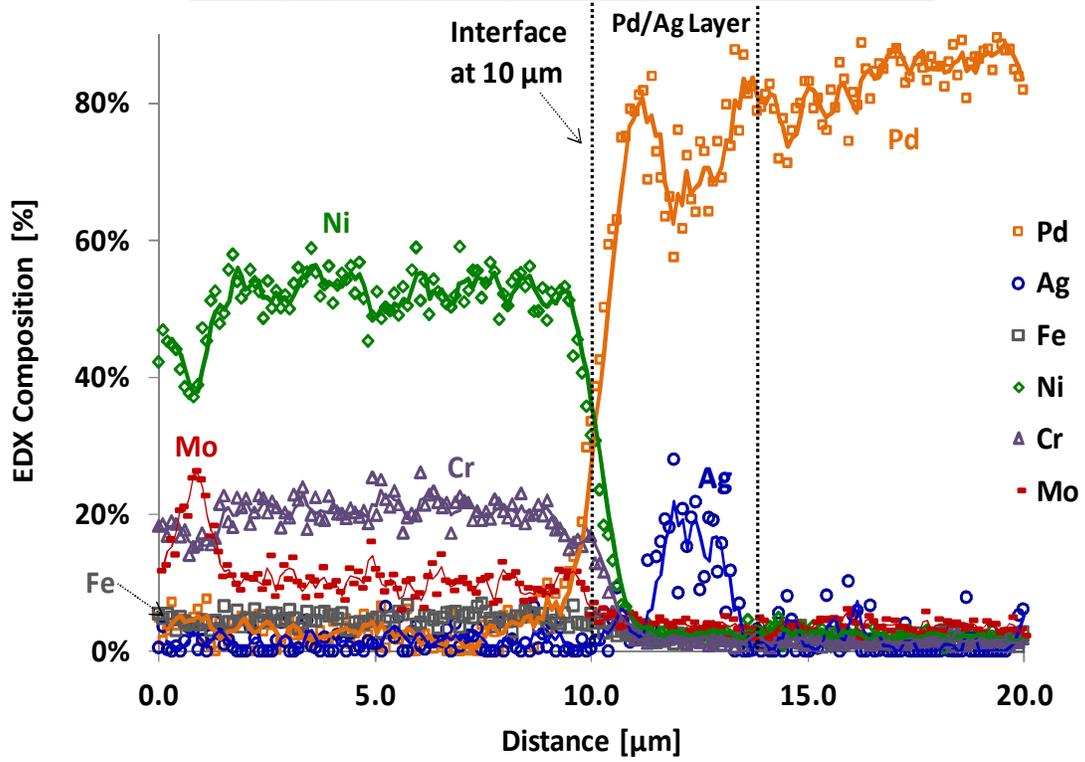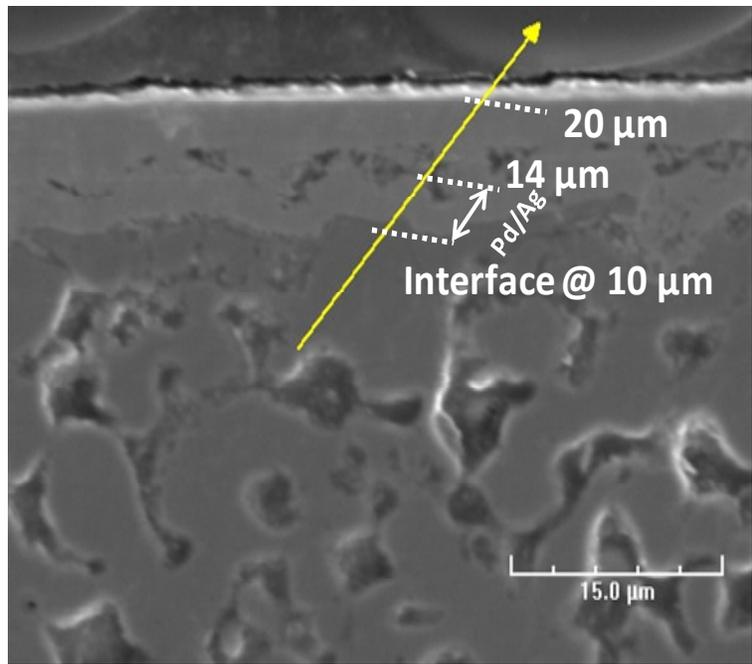
Figure 6-8. EDX cross- section line scan of the membrane RK_03

The membrane RK_05 was also synthesized with the Al_2O_3+Pd/Ag barrier surface modification method. However, the vacuum pressure applied from the tube side during the Pd glue step was 27 in Hg instead of 7 in Hg. Since the grading slurry (given in Table 5-4) consisted of mainly 0.2-0.5 µm size Al_2O_3 particles, the grading step was not effective enough to plug the pore mouths as large as 1-2µm as shown in Figure 6-9 [a] under high vacuum pressure. Thus, the application of high vacuum pressure (27 in Hg) resulted in the deposition of Pd/Ag in the pores. Even though the Pd thickness on the outer surface of the membrane was ultra thin (1-1.6 µm as shown in Figure 6-9 [b]), the H_2 permeance of the membrane RK_05 listed in Table 6-2 was low due to high Pd thickness in the pores. The membrane RK_05 could be used as an illustrative case of an undesired membrane synthesis outcome.

The aluminum hydroxide was used as the filler material for the support surface modification, which as first proposed by (Tong and Matsumura 2004) and then modified by Ayturk (Ayturk 2007; Ayturk and Ma 2008), of the membrane RK_04. The cross- sectional SEI micrographs for the $Al(OH)_3$ surface modified support of the membrane RK_04 is shown in Figure 6-10. At some locations, the $Al(OH)_3$ surface modification was very effective and resulted in the deposition of a very thin and uniform Pd layer (4 µm) as shown in Figure 6-10 [a]. Moreover, the $Al(OH)_3$ grading successfully plugged the pore mouths as large as ~30 µm in diameter as depicted in Figure 6-10 [b].

Despite the well defined Pd layer in some parts like the location shown in Figure 6-10 [a], the Pd layer thickness was changing between 7-16 µm in some other sections of the membrane cross-section as shown in Figure 6-10 [c]. Figure 6-10 [d] illustrates the overall effectiveness of the surface $Al(OH)_3$ modification method, with a thin Pd layer on top without penetration into the porous structure of the support. In spite of the good grading properties of $Al(OH)_3$, the disadvantage of decreased H_2 permeance at elevated temperatures (>400°C) caused by clogging of the pores due to phase transformation of $Al(OH)_3$ needs to be eliminated (as Chapter 6.2).
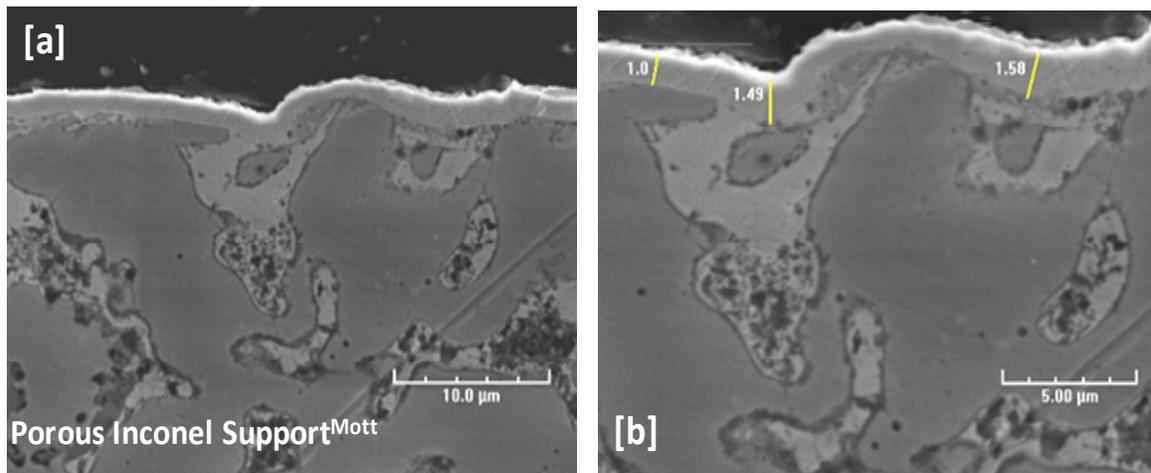
Figure 6-9. SEI Micrographs of the cross section of the membrane RK_05 with the Pd/Ag barrier [a] at 3500x, [b] 5000x
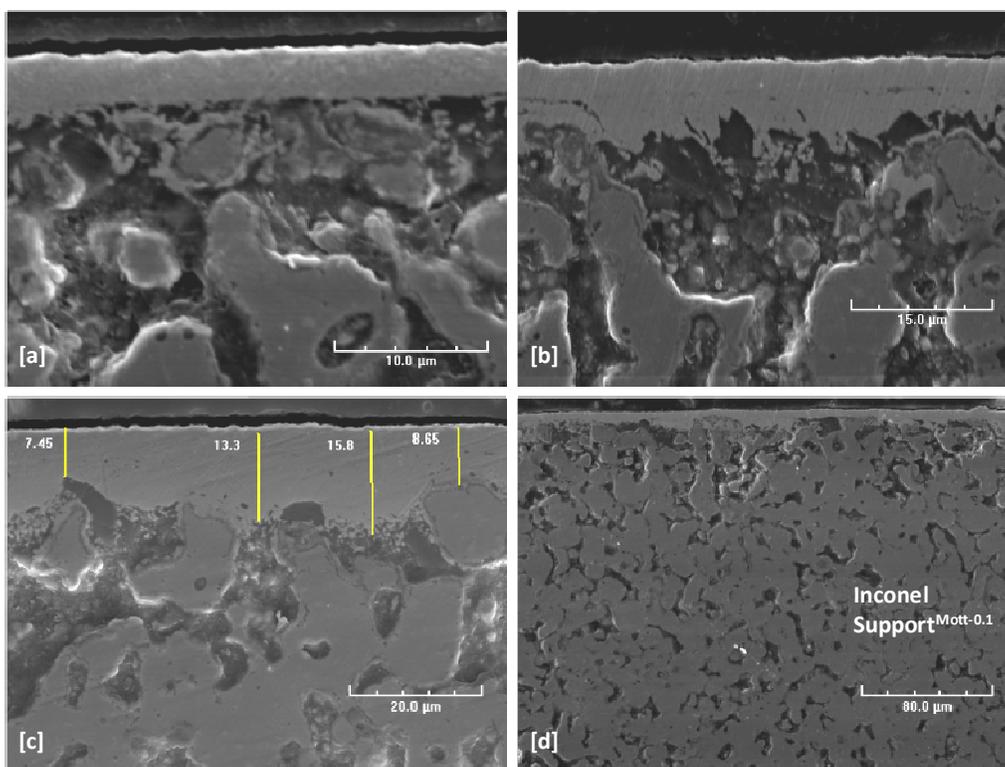
Figure 6-10. SEI Micrographs of the cross section of the membrane RK_04 prepared with $Al(OH)_3$ [a] at 3500x, [b] at 2000x, [c] at 2500x and [d] at 500x

The membranes RK_14 and 15 were prepared with the modified sequential Al_2O_3 grading surface modification method. The syntheses of these two membranes were aborted due to the defects on the welding area of the metal support. The SEI micrographs in Figure 6-11 show the cross-section details of the membrane RK_14 at various locations and at different magnifications. In Figure 6-11 [a], the diameter of the pore mouths on the outer support surface was around 2-3 µm and these pores were open to larger volumes in the porous support. The blockage of the surface pore entrances would be easirer if the pore diematers are small and at the same time the porosity of the support section after the outer surface would be high to decrease the support resistance. Thus, smaller diameter pore mouths on the support surface opening to larger porous volumes are desired. While some parts on the cross-section of the membrane RK_14 were similar to Figure 6-11 [a], wide valleys which were difficult to plug were also found at some other parts of the cross-section of the membrane RK_14 as shown in Figure 6-11 [b] and [c]. The diameters of the wide valleys on the surface were roughly 25 µm and 75 µm in Figure 6-11 [b] and [c], respectively. It is important to remind the failure of the synthesis of the membranes RK_08 and 09 which were prepared with the Al_2O_3+Pd/Ag barrier surface modification method by using the same type of support as RK_14 and 15. The size distribution of the particles in Al_2O_3 slurry as listed in Table 5-4 was not adequate to plug the surface pores resulting in the deposition of thick Pd layers without being dense.

The grading steps starting from large Al_2O_3 particles (20 µm) and continuing with smaller particles (10-5-3 µm) could be observed in Figure 6-11 [d]. Since vaccum was applied from the tube side during Pd plating after each grading step for 5 minutes, a thin Pd layer (1-2 µm) was also deposited on the support surface used as the Pd glue after the first grading with 20 µm particles as shown in Figure 6-11 [d]. In addition, one of the 20 µm diameter Al_2O_3 particle was observed as it blocked a ˜50 Al_2O_3 µm wide pore mouth opening in Figure 6-11 [e]. The modified sequential Al_2O_3 grading surface modification method was very effective in blocking even 75 µm wide pore mouths on the support surface and provided a thin Pd layer as can be seen in Figure 6-11 [f] with a larger membrane cross-section area. More importantly, the porous structure of the Hastelloy-X support provided by CE was significantly different than the Inconel ones provided by Mott as depicted in Figure 6-11 [f]. The porosity of the first 200 µm on the outer surface of the Hastelloy-X[CE] support was higher than the rest of the support as shown in Figure 6-11 [f]. The latter finding with the micrographs explained the large pore openings on the

135

support surface even though the Hastelloy-X^{CE} support was reported as 0.1 media grade by the manufacturer.

Before taking the EDX line scan of the membrane RK_14, the support composition was varifed by taking an area X-ray scan of the cross-section of the support as listed in Table 6-4. The Hastelloy-X composition of 24 wt% Cr, 44 wt% Ni, 12 wt% Mo and 19 wt% Fe (Pd, Al excluded) given in Table 6-4, was consistent with the tabulated composition of the Hastelloy-X listed in Table 5-1.

In Figure 6-12, the interfaces between the porous support metal and the Pd layer for line 1 and 2 were located at 23 µm and 21µm, respectively. The EDX scan of the first line could be distinguished by four grading/Pd platimg steps as shown in Figure 6-12. The gap between the porous support and the Pd layer was filled with Al_2O_3 in between 10 and 21 µm of the first line as shown in the EDX scan in Figure 6-12. In addition, the following grading steps together with the Pd glue steps were observed with peaks in the Al_2O_3 compositions at approximately 22, 25 and 30 µm along the length of the first line scan in Figure 6-12. Another line scan was taken at a location where the Pd layer and porous support were close to each other as shown in Figure 6-12. Similarly, the distinct Al_2O_3 peaks along the length of the second line scan in Figure 6-12 indicated the successful grading between the Pd layer and the support and the intermediate grading steps in between Pd platings as well.

Table 6-4. Composition of the support (Hastelloy X) cross-section of the membrane RK_14

Element	keV	Wt%
Al	1.487	1.86
Cr	5.414	23.09
Fe	6.403	17.92
Ni	7.477	42.33
Mo	2.293	11.38
Pd	2.838	2.06
Si	1.740	1.30
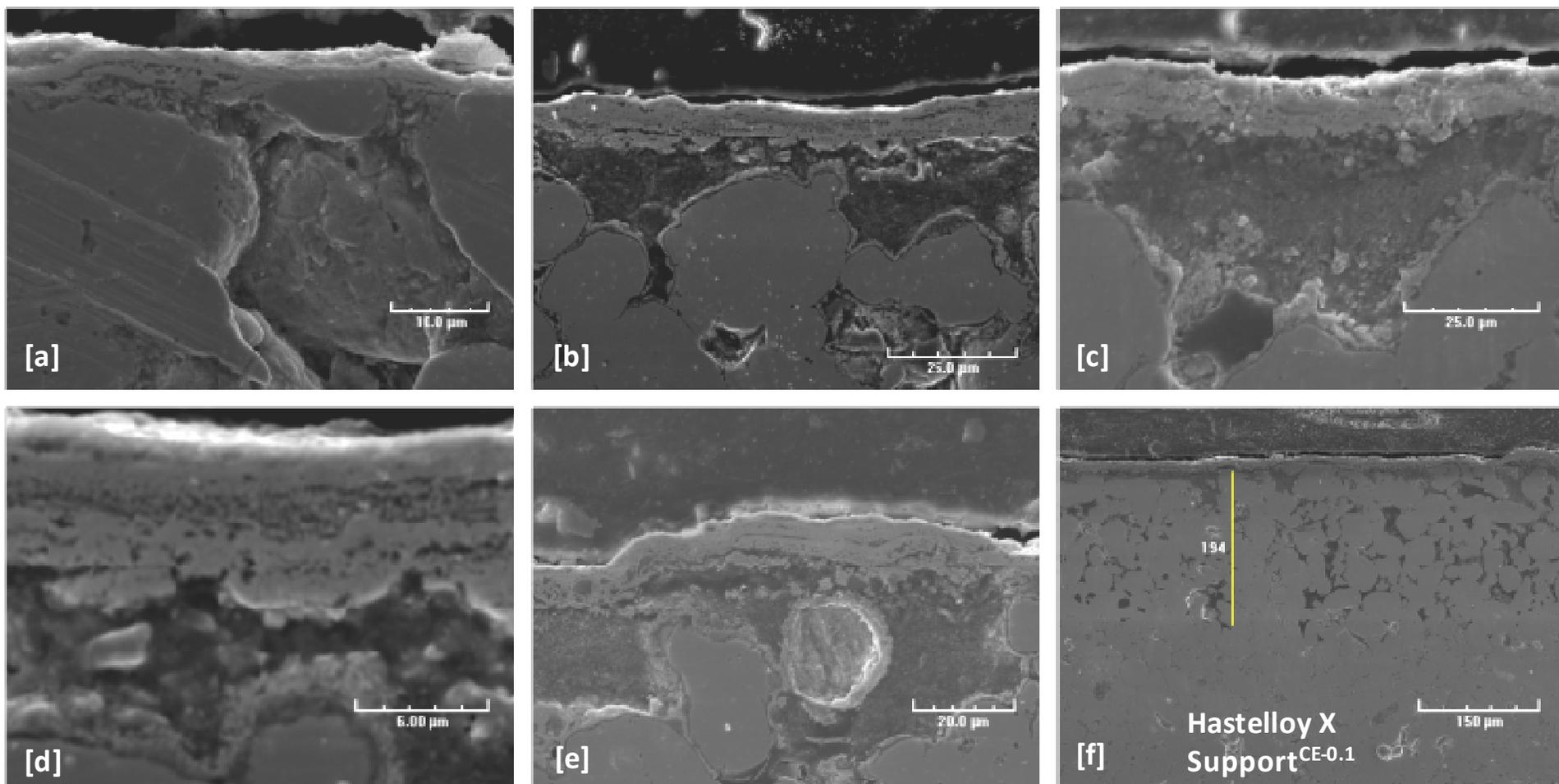
Figure 6-11. SEI Micrographs of the cross section of the membrane RK_14 prepared with the modified sequential Al_2O_3 grading [a] at 2500x, [b] at 1500x, [c] at 1000x, [d] at 5000x, [e] at 2000x and [f] at 300x
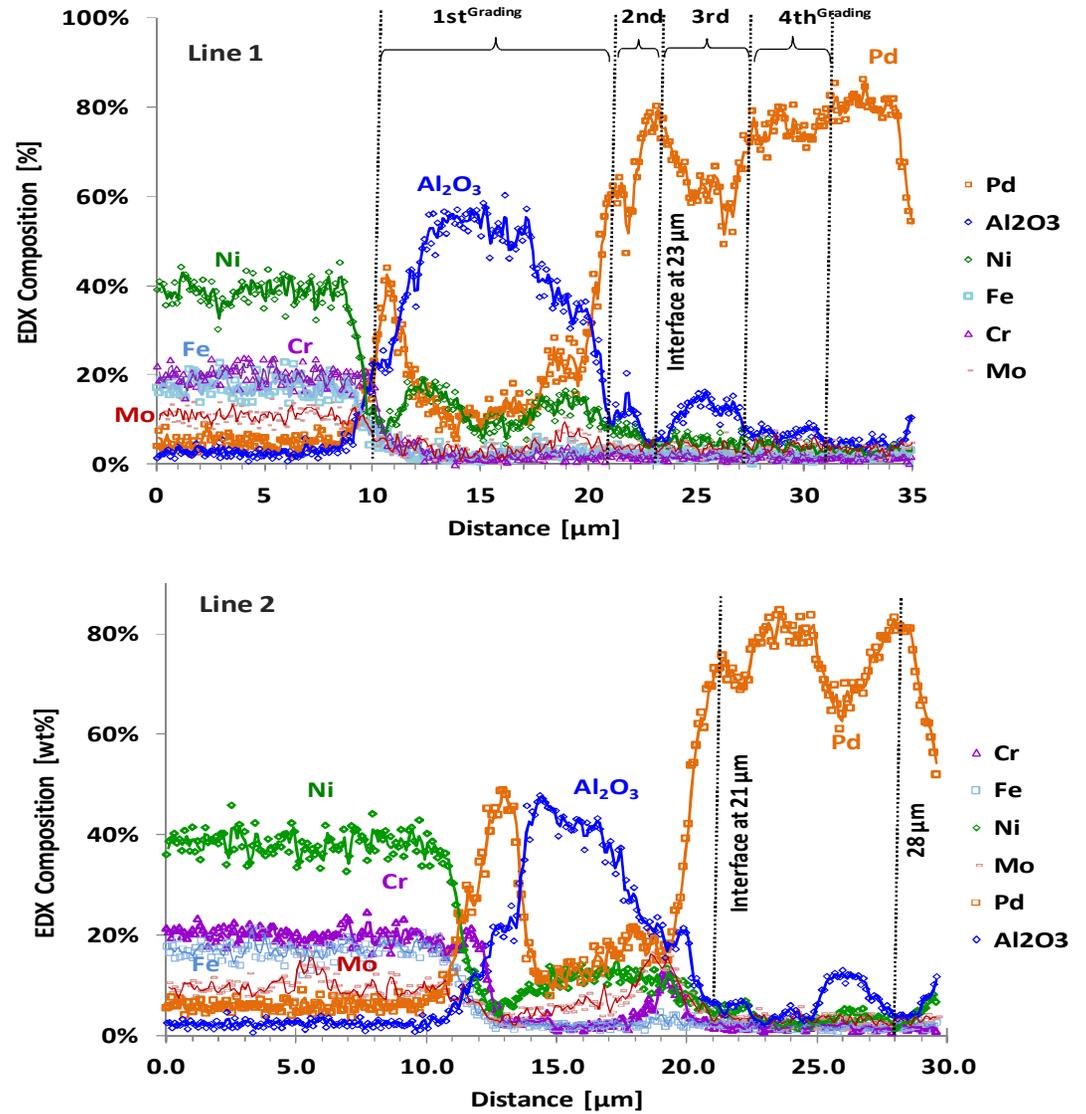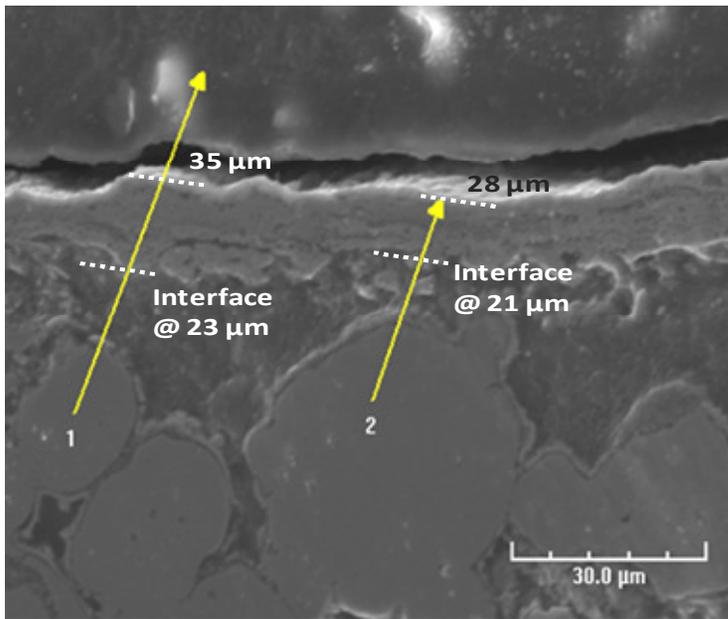
Figure 6-12. EDX cross-sectional line scans of the membrane RK_14

The same procedure was also followed with the membrane RK_15 by taking the area X-Ray scan of the 316L support before starting the microstructure analysis. The experimentally determined 316L composition of 20 wt% Cr, 9 wt% Ni, 2 wt% Mo and 69 wt% Fe (Pd, Al excluded) given in Table 6-5, was verified with the reference composition of the 316L listed in Table 5-1. The SEI micrographs shown in Figure 6-13 were taken to reveal the details of the results of the the modified sequential Al_2O_3 grading surface modification method on the microstructure of the membrane RK_15 which was prepared by using the 0.1 media grade 316L CE support.

As similar patterns were observed with the membrane RK_14 support shown in Figure 6-11, the diversity in the size and structure of the pores on the $316L^{CE-0.1}$ support was also detected as depicted in Figure 6-13. The small pore mouths (~1-3 µm in diameter) opening to large pore volumes as shown in Figure 6-13 [a], large valleys (~35 µm in diameter) opening to narrow channels (~2-5 µm in diameter) line in Figure 6-13 [b] and large valleys (~20-30 µm in diameter) proceeding to large pore volumes as shown in Figure 6-13 [c] on the outer surface of the support, demonstrated the challenge in support grading to achieve a thin Pd layer only on top of the support. The details of Pd layer and the grading efficieny beneath the Pd layer was demonstared with the SEI micrograph at a higher magnification as shown in Figure 6-13 [d]. The thin Pd layer (~5-7 µm) was successfully deposited only on top of the support without Pd deposition in the pores with the aid of the application of the modified sequential Al_2O_3 grading surface modification method on the membrane RK_15 as shown in Figure 6-13 [e]. Furthermore, Figure 6-13 [f] which included a large area of the cross-section of the $316L^{CE-0.1}$ was drastically more uniform in terms of porosity compared to the Hastelloy_$X^{CE-0.1}$ shown in Figure 6-11 [f].

Table 6-5. Composition of the support (316L) cross-section of the membrane RK_15

Element	keV	Wt%
Pd	2.838	10.82
Fe	6.403	60.32
Ni	7.477	7.71
Cr	5.414	17.36
Mo	2.293	1.97

The EDX data were collected for two lines, one for a location where the Pd layer and the 316L support were close and the second line where the line started at the Al_2O_3 graded pores and continued to Pd layer as shown in Figure 6-14. As shown in the first EDX line scan in Figure 6-14, the Fe-rich 316L support ended around at 5.2 µm where Pd glue, which was combined with the first grading, started. In Figure 6-14, the interface between the Pd layer and the graded support was located at 8.2 µm for the first line. Similarly, the successful Al_2O_3 grading was observed clearly in the second line scan in Figure 6-14. In addition, an Al_2O_3 particle was found upon at the gradeded support and Pd layer interface at 8 µm as seen in Figure 6-14. A 4 µm diameter Al_2O_3 particle was stuck at the entrance of a 25 µm wide pore as shown in Figure 6-14. Moreover, the effectiveness of the oxide layer to prevent the intermetallic diffusion of the support elements into the Pd layer was also proved with the EDX line scans shown in Figure 6-12 and Figure 6-14. Since both of the membranes RK_14 and 15 were pure Pd membranes, the only precaution against intermetallic diffusion was the oxide layer on the bare support and no intermetallic diffusion was encountered for both of the membranes prepared by using Hastelloy-X and 316L supports tested in H_2 up to 450°C.
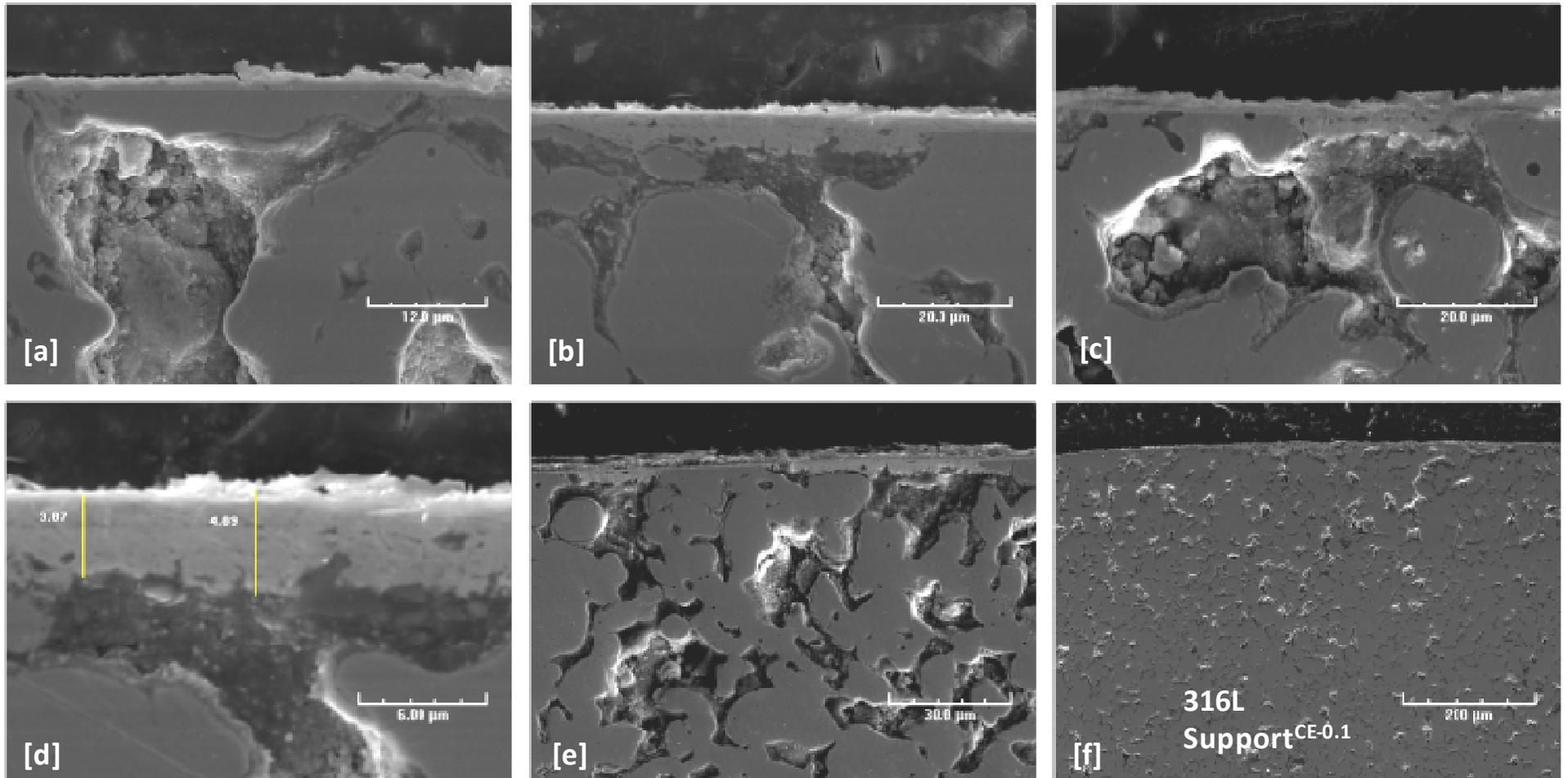
Figure 6-13. Micrographs of the cross section of the membrane RK_15 prepared with the modified sequential Al$_2$O$_3$ grading [a] at 3000x, [b] at 2000x, [c] at 1500x, [d] at 5000x, [e] at 1000x and [f] at 250x

141
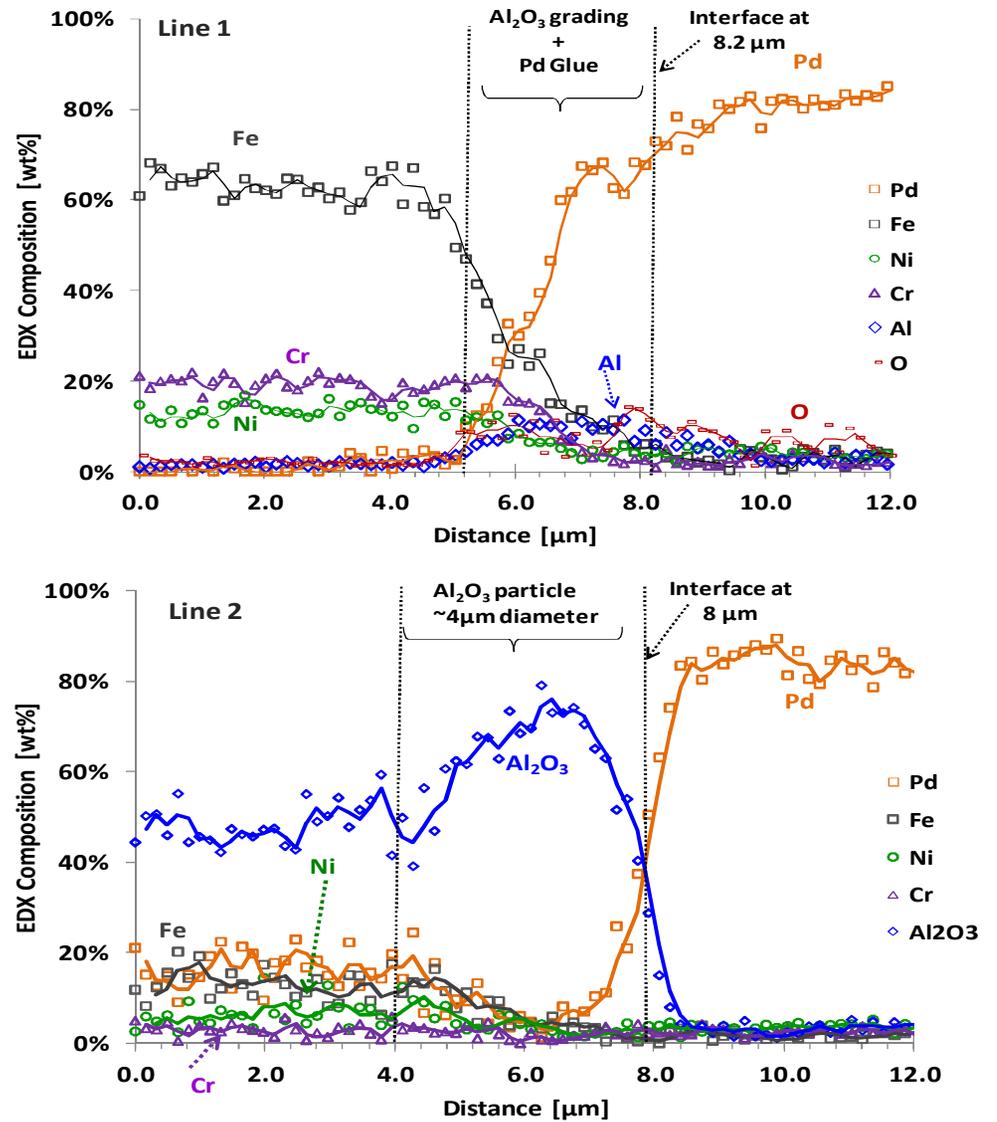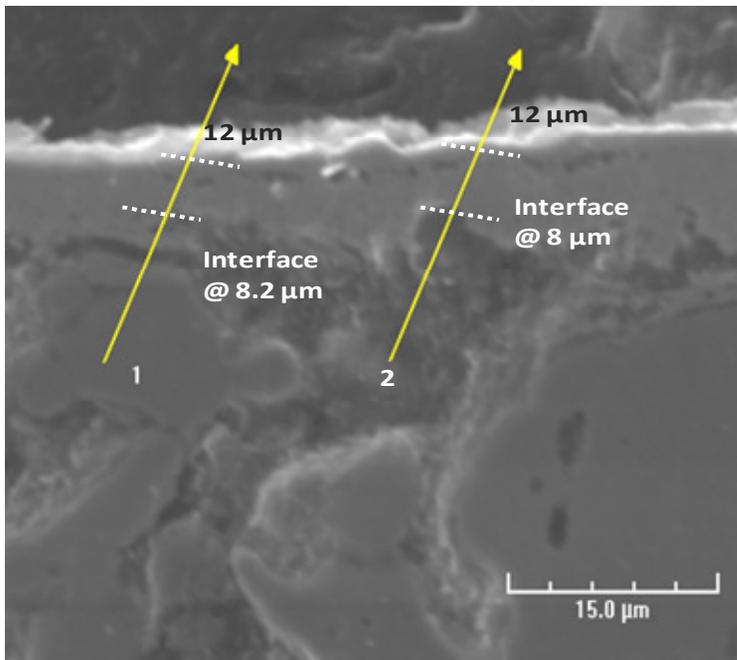
Figure 6-14 EDX cross-sectional line scans of the membrane RK_15

6.5. Conclusions

Three porous support surface modification techniques namely, Al_2O_3 grading+Pd/Ag barrier, $Al(OH)_3$ grading and modified sequential Al_2O_3 grading were applied to different quality metal supports with various compositions and porosity values. Inconel and 310 stainless steel supports with 0.1 media grade purchased from Mott Metallurgical Corporation, Farmington, CT were better in quality compared to the 0.1 media grade Hastelloy-X and 0.1, 0.2 and 0.5 media grade 316L stainless steel purchased from Chand Eisenman, Burlington, CT.

The prime purpose of the Chapter 6 was to select the most appropriate surface modification method among the aforementioned methods to achive the highest H_2 permeance and ideal (H_2/He) selectivity. The Pd-based membrane fabrication method was desired to be with the minimum number of steps and the mass production, for industrial applications such as coal gasification, to be practical. Moreover, the polishing step included in the Al_2O_3 grading+Pd/Ag barrier (Ma et al. 2007a; Ma et al. 2007b), $Al(OH)_3$ grading (Ayturk 2007; Tong and Matsumura 2004) methods could be eliminated to decrease the membrane fabrication cost. Thus, the modified sequential Al_2O_3 grading method, which was derived from the original methods proposed by Ma and Guazzone (2010), was used to accomplish the objectives mentioned above.

Coupled with the long term H_2 permeation results over the temperature range of 350-450°C and the SEI and EDX analyses of the membranes RK_01 through 17 led to a conclusion that the modified sequential Al_2O_3 grading method was the most efficient way to fabricate thin membranes (5-10 µm) with the least number of fabrication steps, by eliminating membrame polishing and without being dependent on the support quality. It should be noted that Pd/Ag barrier had to be combined with the modified sequential Al_2O_3 grading method for the high temperature applications to have extra protection against intermetallic diffusion of the support elements.

The utilization of the modified sequential Al_2O_3 grading method provided the synthesis of a pure Pd-based composite membrane on 316PSS$^{CE-0.1}$ support with a stable H_2 permeance

value of ~50 m^3/[m^2.h.atm$^{0.5}$] at 450°C and a long term stability over a period of 1000 hours with an ideal H$_2$/He selectivity of ~1500 at the end of testing.

7. A Process Dynamic Modeling and Control Framework for Performance Assessment of Pd/Alloy-Based Membrane Reactors Used in Hydrogen Production

7.1. Introduction

A practical process dynamic modeling framework was developed in order to analyze and characterize the transient behavior of a Pd/alloy-based (Pd/Au or Pd/Cu) water gas shift (WGS) membrane reactor. Furthermore, simple process control ideas were proposed aiming at enhancing process system performance by inducing the desirable dynamic characteristics in the response of the controlled process during start-up as well as in the presence of unexpected adverse disturbances (process upset episodes) or operationally favorable set-point changes that reflected new hydrogen production requirements. Finally, the proposed methods were evaluated through detailed simulation studies in an illustrative example involving a Pd/alloy-based WGS membrane reactor that exhibited complex dynamic behavior and is currently used for lab-scale pure hydrogen production and separation.

7.2. Process control framework

When a disturbance occurs in an unexpected and unpredictable manner, the process is driven away from its nominal and often operationally favorable design steady state. In such a case the primary control objective is to bring the process back to the aforementioned steady state in a fast and smooth manner, thus rejecting the disturbance effect (regulator problem). Furthermore, one may envision cases, where the control objective is to drive the process to a new

operationally favorable steady state that reflects a set of performance specifications, new production targets/requirements, process safety and process economics criteria etc. by enforcing key process variables to approach desirable set-point values (servo-mechanism problem). In both cases, the primary objectives can be typically met though the use of a feedback controller such as a Proportional Integral (PI) controller.

Indeed, a simple PI feedback control system was considered in order to meet membrane reactor performance requirements such as one casted in terms of the overall CO conversion level of the WGS reaction by controlling the CO fraction (dry basis) at the reactor exit.

In particular:

- The controlled output variable considered in the present study was the fraction of CO at the exit of the shell side which in turn dictates the overall CO conversion. The set point can be chosen depending on the desired CO conversion level. The set point was 2.32% and 1.2% for the servo and regulator problems respectively, which would be discussed next in greater detail.

- The manipulated input variable considered was the steam molar flow rate at the reactor entrance/ inlet.

In order to meet the primary control objectives, the PI controller generated an actuating signal and determined an input variable profile by processing the error between the measured output variable and its set-point value in the following fashion:

$$Error = f_{CO}^{Dry}\big|_{exit} - f_{CO}^{Set\ Point} \tag{7.1}$$

$$F_{H_2O}(t)\big|_{y=0} = F_{H_2O}(t=0)\big|_{y=0} + K_c.Error + \frac{K_c}{\tau_I}\int_0^t Error.dt \tag{7.2}$$

The process control Eq (7.1) and (7.2) were combined with the set of Eqs (3.9) through (3.14). An appropriate set of values for the integral time constant τ_I and the proportional gain K_c in Eq (7.2) had to be determined (controller tuning problem). Although there were several approaches for tuning a controller such as the one-quarter decay ratio criterion, integral performance criteria and procedures that involved semi empirical rules of limited validity, a more direct and transparent approach has been utilized in the estimation of the proper set of values for the adjustable controller parameters. These were explicitly determined on the basis of

a set of desirable dynamic characteristics of the controlled process response such as speed, smoothness and robustness in the presence of disturbances subject to process economics and energy efficiency constraints.

7.3. Results and Discussion

Table 7-1 shows the typical compositions of syngas that might be expected from different gasifiers (Hla et al. 2009; Gupta et al. 2007). In particular, the feed gas compositions listed in Table 7-1 were used in the model to determine feeding and operating conditions that led to undesirably low conversion levels, so that the process performance enhancement could be attained through feedback control action.

Table 7-1. Feed gas compositions

	A	B	C	D	E	F
CO [%]	27.50	26.28	25.15	28.38	23.78	3.81
H2O [%]	54.99	52.56	50.31	56.75	47.57	7.61
CO2 [%]	1.73	4.47	6.26	0.75	8.65	36.20
H2 [%]	15.78	16.68	18.28	14.12	20.00	52.38

*A-D (Gupta et al. 2007) / E-F (Hla et al. 2009)

Theoretically predicted results using the above dynamic process model when steady state was reached are given in Table 7-2 in terms of CO conversion and hydrogen recovery corresponding to these different feed compositions. The calculated hydrogen recovery and CO conversions were very similar except for the feed composition at the backend of the WGS reactor (F). Notice that placing the membrane reactor after the existing WGS reactors was an option, however replacing the WGS reactors with a membrane reactor would be a more efficient one. The utilization of a Pd-based membrane as an H_2 separation unit would be of course more advantageous when the syngas contained high amounts of H_2 as in the case of F. The feed with the slurry-feed coal-derived syngas composition (E) and the lowest conversion level was used in the ensuing simulation runs. An H_2O: CO ratio of 2 was used in Table 7-1, however, the original feed composition of a GE gasifier (slurry-feed coal-derived syngas) was typically associated with

higher H_2O: CO ratio values (H_2O: CO=4). Finally, it should be pointed out that integrating the WGS Pd-based membrane reactor and a CO_2 capture and sequestration system with the GE gasifier exhibited significant advantages because of the particular composition of the syngas (Maurstad, 2005).

Table 7-2. Simulation results with different feed compositions at steady state

	A	B	C	D	E	F
R_{H_2} [%]	87.6	87.2	87.3	87.3	87.2	86.6
X_{CO}[%]	97.7	97.3	97.0	97.8	96.6	17.8

The accuracy of the lumped-parameter finite-dimensional reactor modeling approach could be assessed by comparing its predictions with the exact first principle-based steady state membrane reactor model through simulation studies (Reyes and Luyben 2000). The results/predictions generated by the lumped-parameter model when there was no further change in the various concentration profiles (steady state conditions) should match those offered by the exact steady state model. Figure 7-1 shows the steady state CO conversion and H_2 recovery profiles both for the exact steady state model and for the lumped-parameter one. The CO conversion at the exit of the membrane reactor was 97%, exceeding the equilibrium conversion by 17 % under the same temperature and feed compositions as reported in Table 7-1. The lumped-parameter model was simulated for different numbers of lumps/compartments/zones (n = 5, 20 and 30). As shown in Figure 7-1 [a], increasing the number of lumps/zones led to a CO conversion profile approach to the one provided by the detailed first principle-based steady state model, suggesting that the proposed lumped-parameter finite-dimensional model approximation exhibited very satisfactory convergence properties as the number of lumps/zones was increased. Particularly for the first 10% of the reactor volume, the length increments could be decreased to obtain a better fit. Even though the overall CO conversion at the reactor exit for all values of number of lumps considered was the same, the CO conversion at any point deviated most with N=5 for z < 0.6 as shown in Figure 7-1 [a]. If additional feeds had to be added along the length of the reactor to drive the reaction and permeation rates to higher levels or segmental control strategies were applied, the partial pressures of each species at the specific location needed to be

known. Furthermore, a model conceptualization of reactors in series might be usefully employed for various design purposes. For instance, at a CO conversion target level of 90% at the first reactor exit, a model prediction made by considering N=5 could be misleading for the calculation of membrabe length and could overestimate the membrane cost. Since the closest results to the full first-principle steady state model were derived with N≥20, the minimum number of lumps with the best fit (within the aforementioned trials) to the steady state model concentration profiles was determined to be N=20 and used in all of the simulation runs/scenarios discussed next. The permeated H_2 levels in each segment (η_{H_2}) and H_2 recovery profiles shown in Figure 7-1 [b] indicated that the extents of neither the reaction nor the permeation was significant in the last 60% of the membrane reactor length, and consequently, this reactor scale would be suitable for higher feed flow rates in order to use the membrane reactor under its maximum efficiency.
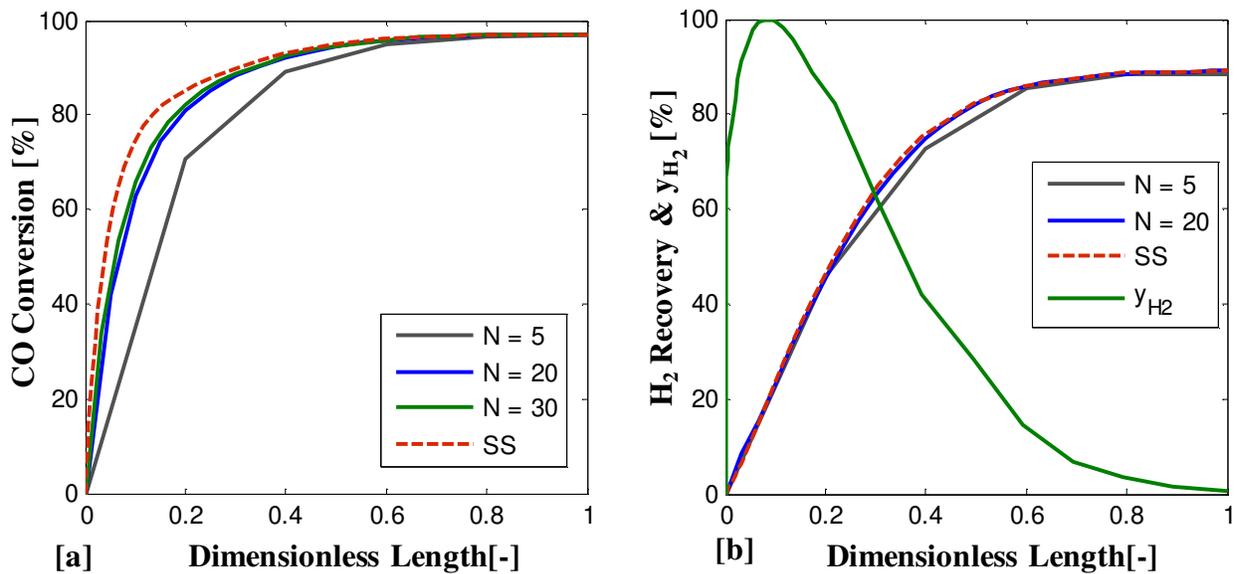
Figure 7-1. Comparison of the steady-state [a] CO conversion and [b] H_2 recovery profiles along the length of the reactor: The lumped-parameter approximation model versus the exact steady state model. (SS: steady state, $\eta_{H_2} = 100 \times \left[\nabla F_{H_2}^{Tube} / \nabla F_{H_2,max}^{Tube} \right]$ at steady state)

The simulation results were compared with the experimental results reported by Augustine et al. (2009). A 12 µm thick Pd-based membrane synthesized by electroless plating

which had an oxide layer (Ma et al. 2007a) and Pd/Ag layers as the intermetallic diffusion barriers (Ayturk et al. 2006a; Ma et al. 2007b) was tested at the same reaction conditions listed in Table 3-1. The membrane had a permeability constant (Q_0) of 6375.38 [$m^3.\mu m/(m^2.h.atm^{0.5})$], activation energy of 16.6 kJ/mol, H_2/He selectivity of greater than 1000 and the feed was 22.5% CO, 45.9% H_2O, 21.8 H_2 and 9.8% CO_2 with a total inlet flow rate of 963 sccm during the experiment. Even though the predicted CO conversion level was very close to the experimental value, there was a 10% discrepancy in the H_2 recovery level as listed in Table 7-3. Some possible reasons of the over-predicted H_2 recovery levels would be the constant H_2 partial pressure in the radial direction and/or plug flow assumption as well as a concentration polarization (Hara et al. 1999; Koukou et al. 1998; Koukou et al. 2001; Itoh et al. 1994; Mori et al. 2007; Bhattacharya and Hwang 1997). Finally, it should be pointed out that the above 1-D dynamic reactor model represented a quite useful tool for a quick, yet reliable, assessment of the overall membrane reactor performance as well as a computationally attractive option for screening the design space and thus identifying viable designs that would merit further examination through the development of higher dimensional membrane reactor models (Israni et al. 2009; Ramirez Serrano et al. 2009).

Table 7-3. Comparison with experimental results

	X_{CO}	R_{H_2}
1D Model	96.6	88
Experiment	95.4	78

7.3.1 Dynamic analysis and characterization of the membrane reactor during the start-up stage

The first task was to characterize the spatial distribution profiles of the fractions of each component as a function of time during the start-up stage of the process. The solution sought was based on the specifications given in Table 3-1 and the feed was the slurry-feed-coal-derived syngas. It was assumed that the membrane was already characterized in pure H_2. We considered

steam and H_2 (H_2O: 47.57% – H_2: 52.43%) flowing through the shell side just before the feed was admitted into the reactor. No vacuum or purge was applied on the tube side and the pressure of the permeate flow was 1atm. Figure 7-2 and Figure 7-3 show the simulation results for the start-up of the process. Figure 7-2 shows the fractions of gases as a function of time where each line corresponded to a position starting from the reactor inlet/entrance and ending at the exit of the last segment or zone. The line which appeared first on the time scale in Figure 7-2 belonged to segment 1 and the line which responded last on the time scale belonged to segment 20 (exit of the reactor). The direction of the dashed arrow lines in each figure indicated the increasing number of segments or zones (starting from the inlet and ending at the exit of the reactor).

As shown in Figure 7-2, the system reached steady state conditions in 10 seconds. If there were no reaction, the CO fraction at the exit of each segment would be expected to increase at a level higher than the inlet CO fraction corresponding to steady state. However, the consumption of CO by the WGS reaction caused the CO fraction to decrease at the exit of each segment as a function of time as shown in Figure 7-2[a]. At time equaled zero, only H_2 and H_2O was present in the reaction side. The H_2O fractions were decreasing towards the reactor exit due to the depletion of H_2. After the reaction started, the fast reaction rate at the reactor inlet caused the drop in H_2O fraction in the initial segments shown in Figure 7-2 [b]. The reason of the drastic decrease at the segments close to the exit was the increase in the CO_2 amount and the depletion of H_2 through permeation.

The forward reaction rate was faster than the backward reaction rate due to the continuous H_2 removal from the shell side to the tube side. Thus, the fraction of CO_2 at the exit of each segment in Figure 7-2 [c] exceeded the inlet fraction of CO_2 as time progressed. The H_2 fraction before the initiation of the reaction was higher than the maximum possible H_2 fraction (20% H_2 plus 23.7% CO) of the reaction feed. Consequently, the most significant decrease in H_2 fraction occurred at the first half of the reactor where the H_2 permeation was higher as shown in Figure 7-2 [d]. Furthermore, the fraction of H_2 at any time decreased as a function of the reactor length due to the permeation of H_2 as depicted in Figure 7-2 [d]. Particularly in the last 25% of the reactor length, the H_2 fraction profiles were not affected drastically because both the reaction and permeation rates were practically very low within this zone.
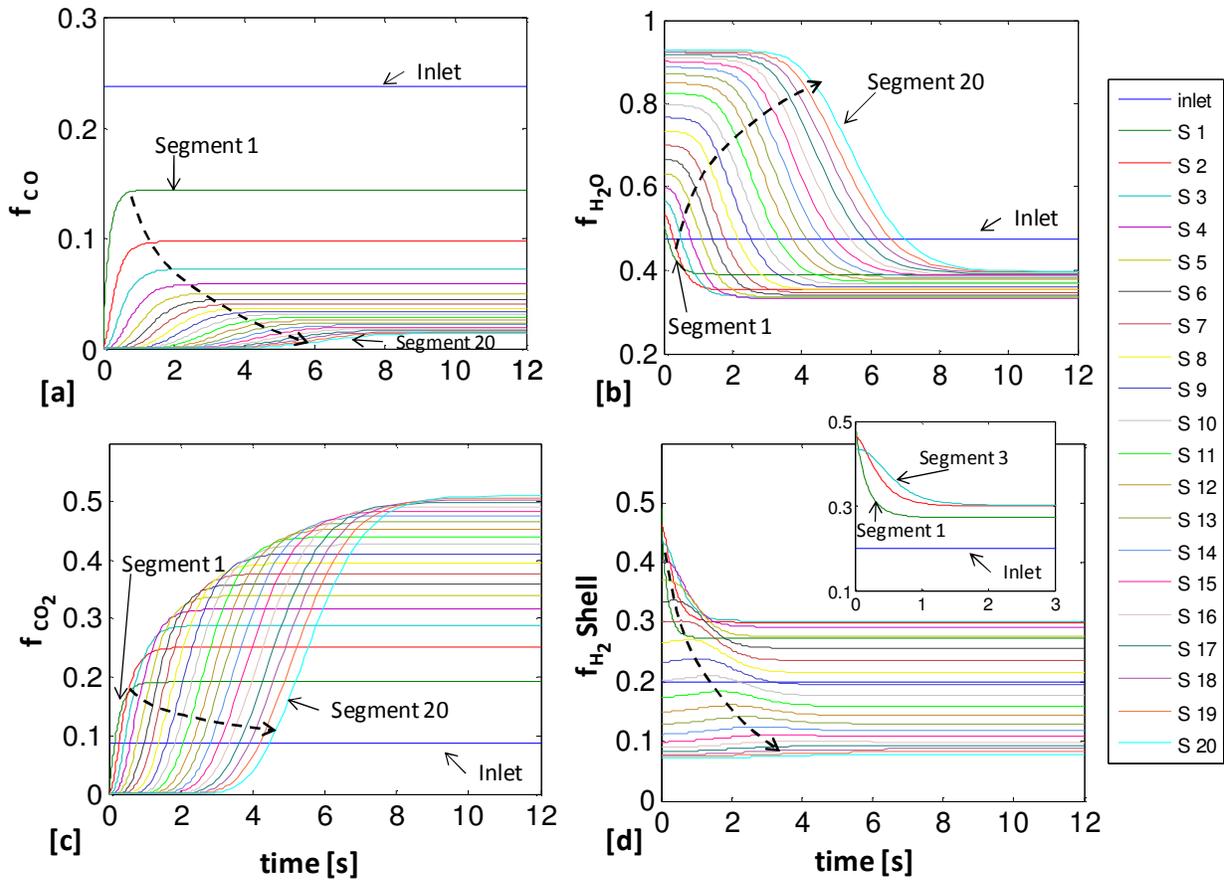
Figure 7-2. Profiles of fractions of species in each segment during start-up stage.

The time period required to obtain pure H_2 from the tube side at a certain flow rate during the start up stage was crucial because the knowledge of the starting time was required. The spatial distribution of the H_2 molar flow rate is presented in Figure 7-3 [a]; the direction of the dashed arrow line corresponded to increasing time from t= 0 to t= 12 seconds. In Figure 7-3 [a], the H_2 production rate decreased as the time progressed because of the difference in the H_2 fraction in the reaction side before and after the reaction had started, as previously stated.
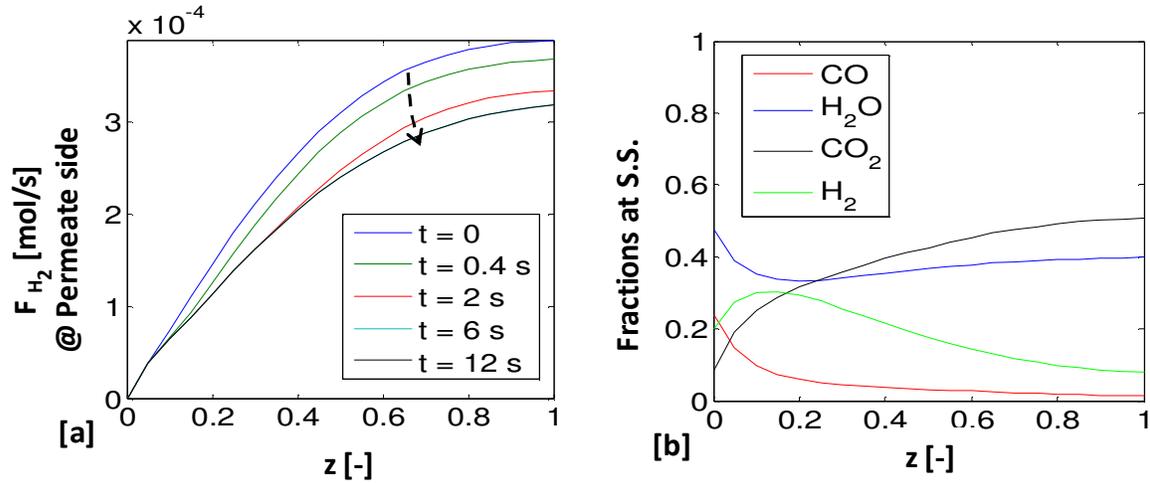
Figure 7-3. [a] H_2 flow profiles along the length of the membrane tube during the start-up stage, [b] the fractions along the length of the reactor at steady state.

Figure 7-3 [b] contains the spatial profiles of the various fractions along the length of the reactor at t = 10 (steady state). It should be noted that the minimum H_2 and CO fractions at the exit of the shell side of the reactor could reduce the cost associated with the separation units placed after (downstream) the membrane reactor. The total flow at the shell exit was composed of mainly 39.8% steam and 50.9% CO_2. The low H_2 and CO amounts at the reaction side exit (7.8 and 1.4%) could be further reduced by the application of sweep or vacuum, as discussed previously. Finally, the fractions at the final time in Figure 7-3 [b] would be used as the new "initial conditions" for the ensuing process control simulations.

The H_2 fraction in the shell side did not go down to zero in Figure 7-3 [b] because no sweep/vacuum was applied. The H_2 permeation stopped when the partial pressure of H_2 in the shell side became equal to the partial pressure of H_2 in the tube side. The fast depletion rate of H_2 by permeation would cause an increased forward reaction rate in the shell side. Vacuum or sweep flow could be applied in the tube side to maintain a lower partial pressure of H_2 in the tube side. As the rate of permeation increased due to the increased driving force, the rate of the forward reaction increased. At the same time, the consequences of the application of vacuum or sweep had to be considered. If vacuum were applied to the tube side, an extra cost would be added when the full process system economics was taken into account. The H_2 flow mixed with the He sweep had to be separated to obtain pure H_2. In light of an earlier discussion (Chapter

7.3.1), the dynamic process equations in the simulations were solved by assuming that neither a sweep flow nor vacuum was applied in the tube side. Future simulation studies will include explicit mathematical expressions for the sweep and vacuum to assess their effect on reactor performance.

The primary objective associated with the use of the Pd/alloy-based membrane reactor was to increase the forward reaction rate of the WGS reaction and also to use the membrane with its maximum efficiency to obtain pure H_2 flow from the tube side. The additional separation costs that were required in a packed bed reactor for H_2 separation could be eliminated since the membrane reactor could achieve 87% H_2 recovery (no sweep/vacuum) with the aforementioned reaction conditions and membrane properties. The CO conversion at the exit of the reactor was 97% when the system reached steady state. Even though this value of the CO conversion was much higher than the thermodynamically determined equilibrium conversion of 79.4%, it could be further enhanced through proper process re-design and adjustment of the regime of operating conditions (total molar flow rate, inlet compositions, temperature, pressure etc.) or applying a process control strategy.

7.3.2 The regulator problem: Rejecting the effect of unexpected pressure drop

In a typical regulator problem, the feedback controller is designed in order to take action and keep the process at its nominal design steady state (assuming no set point changes) by eliminating the effect of a disturbance (such as total pressure or temperature) that may occur unexpectedly and upset the process. In the specific underlying scenario considered in the present study, it was assumed that while the process system was operating at a nominal steady state, the total pressure dropped from 15 to 10 atm unexpectedly staying at 10 atm for the rest of the process operation (disturbance step-change). In this scenario, the PI controller regulated the steam flow rate (manipulated input) so that the CO fraction (process output) reverted to its original and operationally favorable nominal steady state value, thus rejecting the potentially adverse disturbance effect on process performance. The particular initial conditions for the initialization of the simulation runs corresponded to the values reported in Figure 7-3 [b]. Furthermore, all of the inlet molar flow rates of CO, CO_2 and H_2 were the same as the ones given

in Table 3-1 and the set point for the CO fraction at the exit remained the same at 2.32% CO (dry basis). Please notice that all the above values constituted and represented the nominal design steady state in the process regulation problem under consideration. Also notice that if there were no process control action, the CO fraction at the exit would change with time as shown in the dashed line in Figure 7-4 [b]. Specifically, the CO fraction at the exit would increase during the first 5 seconds and remain at the same value inevitably resulting in an undesirably low CO conversion value.

Tuning of the proportional gain (K_c) and integral time constant (τ_I) of the PI controller employed, while non-trivial, remained important from a process control quality standpoint. The first attempt to controller tuning was to find a reasonable set of initial values for τ_I and K_c without compromising process stability and robustness of the process response. The dynamic process responses generated for different K_c values with fixed τ_I (1 s) and also the responses for different τ_I values with fixed K_c (0.002) are shown in Figure 7-4.

In particular, the tuning of τ_I and K_c and their respective ranges of values considered in the simulation study, induced the following dynamic characteristics on the response of the closed-loop system:

As K_c increased, the response became faster, driving the process closer to the nominal values at the expense of occasionally introducing oscillatory dynamic behavior. The above oscillations could be satisfactorily suppressed through the appropriate tuning of τ_I (Stephanopoulos 1984). Proper values of the controller parameters during the tuning process were identified and selected by taking into account the following:

- Fast and stable responses without oscillatory characteristics.

- Minimum consumption of steam for energy efficiency and favorable process economics.

- Smooth steam flow rate profiles with no drastic excursions from operationally favorable operating conditions to facilitate physical realizability and efficiency in actuating.
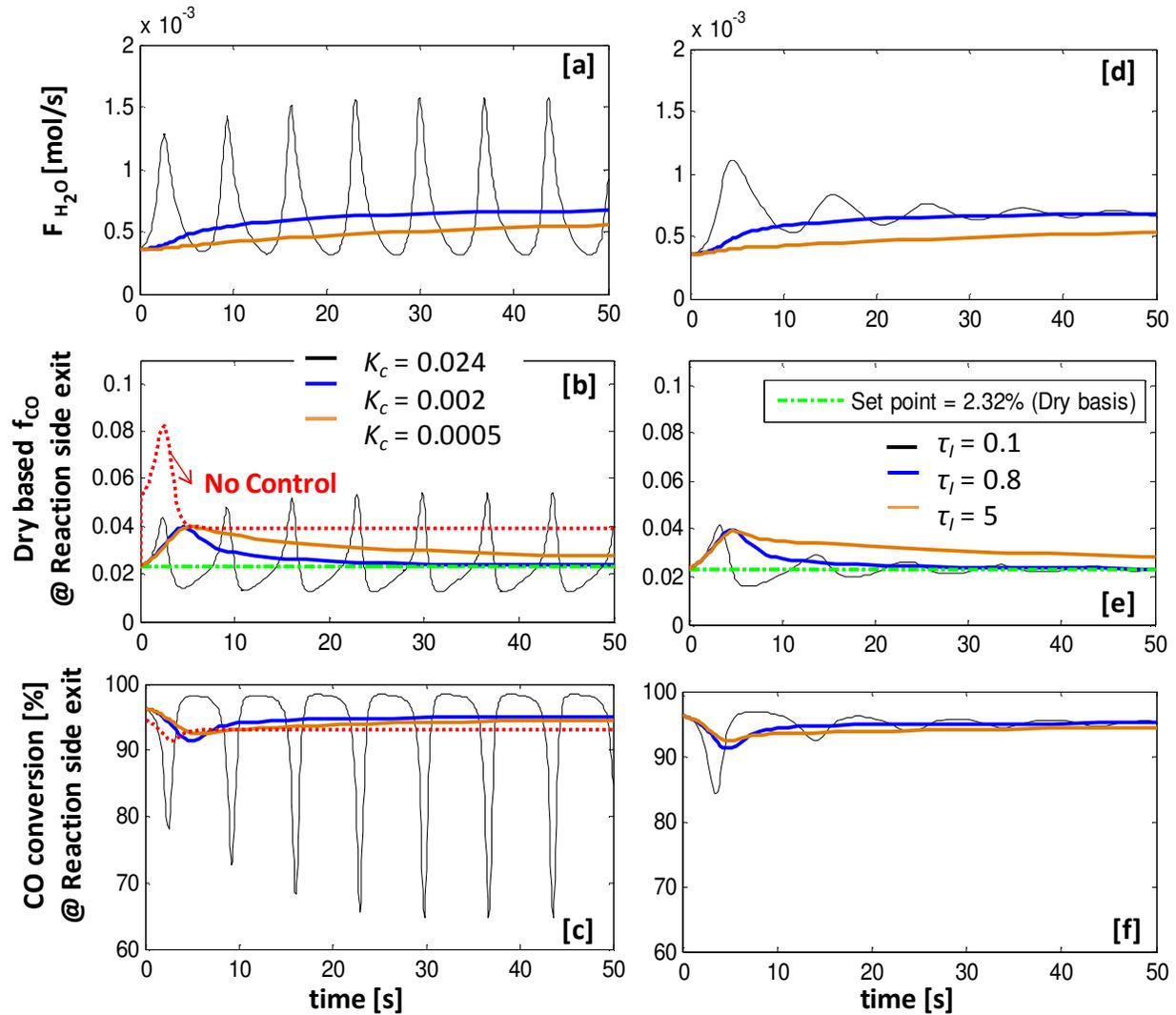
Figure 7-4. Controller tuning for [a] proportional gain and [b] integral time constant / Regulator problem.

While the steam molar flow rate shown in Figure 7-4 [a] had to be lowered by considering the energy efficiency of the system, the time required for the steam flow rate to equilibrate had to be minimized. In Figure 7-4 [b], the trends of the CO fraction at the exit for a K_c value equal to 0.028 or higher had a maximum and minimum, which was clearly undesirable. In Figure 7-4 [b], the controlled output, i.e., the CO fraction at the exit, reached the set point value at shorter times as the value of K_c increased, however, closed-loop stability was compromised when the value of K_c increased to 0.024 and higher. Closed-loop stability was restored when K_c was decreased. However, the required time to revert to the nominal steady state

value was longer. The steam flow rate reached steady state after 250 seconds when K_c was 0.0005. The best value of K_c was found to be 0.002 without inducing oscillatory behavior while at the same time enforcing a quite fast response time of 65 seconds. In Figure 7-4 [c], the overall CO conversion profile of the process passed through a minimum (91%) which could of course cause deviations from predetermined product quality specifications. The minimum in the CO conversion profile resulted from a controller delay time of approximately 3 seconds while the rate of increase in steam flow rate was slow. Figure 7-4 [d-f] shows the effect of the integral time constant, τ_I, on the process response. The fine tuning was performed by adjusting τ_I. The responses of the controlled process with varying τ_I values were similar to the trends shown in Figure 7-4 [a]. The residence time calculated based on the inlet flow rate (residence time= void volume/volumetric flow rate at the inlet) was 1.4 s. The first trial values of τ_I were chosen close to the residence time value. When τ_I was 0.1s, thus much smaller than the residence time, the controller increased the steam flow rate too fast as shown in Figure 7-4 [d]. As a result, the controlled output experienced an overshoot at 4 s and undershoot at 6 s as depicted in Figure 7-4 [e], settling down after a time period of 100 s. An appropriate value for τ_I of 0.8 s was selected for a K_c value of 0.002 so that reversion to the nominal design steady state in the presence of the above disturbance was attained within the shortest possible time (50s) in a smooth manner. Please notice that the ratio of H_2O:CO increased to 3.8 at the end of a 50 seconds period under the above values of K_c and τ_I. More importantly, the CO conversion was kept at 95% which was higher than the uncontrolled conversion with a marked difference of 15%. Those two values were then used for the evaluation of membrane reactor performance under PI-control and the pertinent closed-loop results/responses are shown in Figure 7-5 and Figure 7-6.
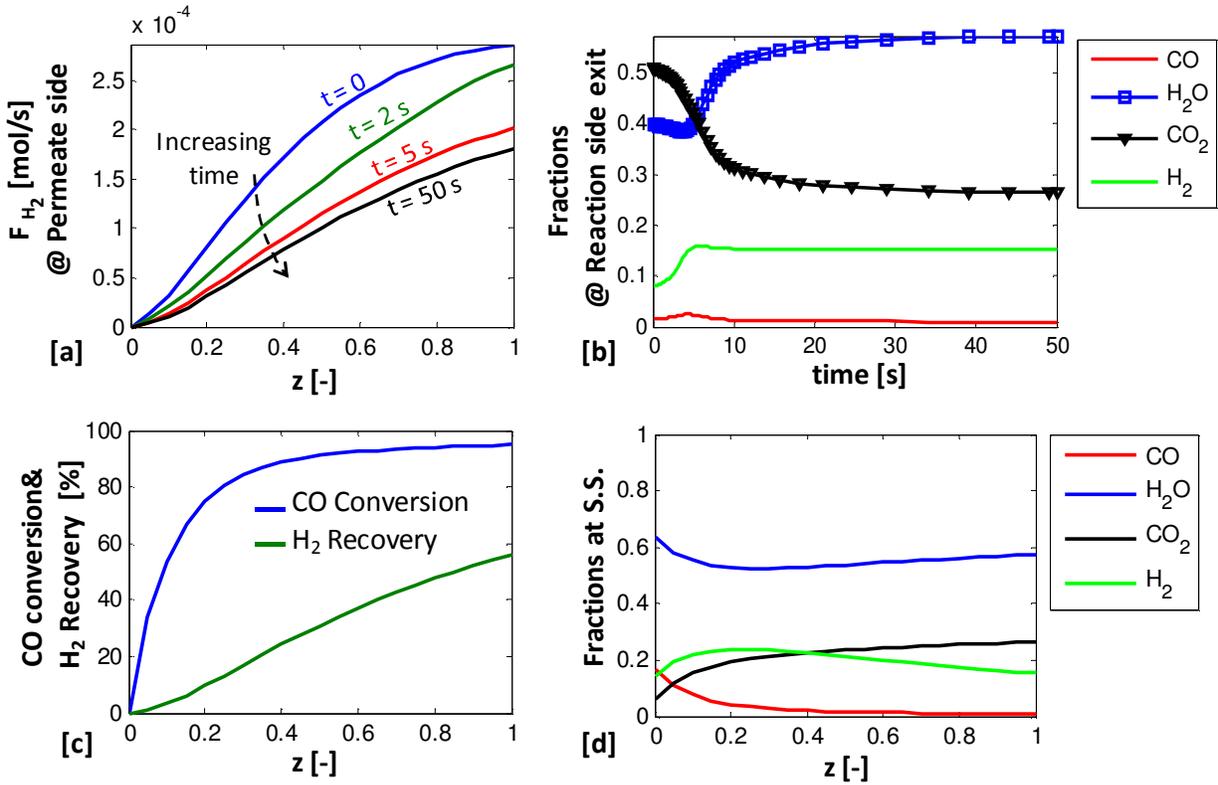
Figure 7-5. Overall performance evaluation of the controlled process system /Regulator case: $K_c = 0.002 \& \tau_I = 0.8$ s

The driving force for H_2 permeation was reduced in the presence of the disturbance considered, namely the change in the system pressure, and therefore, the declining trend in the H_2 production rate profile from the permeate side was the one intuitively expected: specifically, a 36% decrease as shown in Figure 7-5 [a]. Even though the H_2 production rate was reduced, the controller could maintain the dry based CO fraction at the reaction side exit at its nominal value of 2.32%. Notice that the retentate side stream could be processed for high pressure CO_2 sequestration without being affected by the pressure drop until the system returns to its regular operation. As shown in Figure 7-5 [b], the effect of the increased inlet steam flow rate on the retentate side stream composition started at t =4 s which was equal to the total time realized by the residence time and the delay time (dead time) associated with the controller action. The total pressure at the reaction side dropped from 15 to 10 atm and the permeation continued until the H_2 partial pressures corresponding to reaction and permeate sides equaled each other. Consequently, the 8% H_2 content of retentate stream increased to 15% as time progressed and

158

shown in Figure 7-5 [b]. The most significant change at the reaction side exit was observed in the CO_2 fractions because the retentate side stream consisted of mostly H_2O and CO_2. The increased steam fraction was of course correlated to the decrease in the CO_2 fraction at the reaction side exit. The remaining H_2 in the retentate stream could be proven quite valuable by pursuing vigorous design options: A membrane separation unit with vacuum pump on the permeate side or compressor on the membrane inlet could be utilized to further separate H_2 and concentrate CO_2 at the membrane exit if one considered the potential enhancement options for the underlying process economics.

The membrane reactor could achieve 95% CO conversion and 56% H_2 recovery with the pertinent profiles given in Figure 7-5 [c] at the end of the regulatory control action. The retentate stream contained 62% CO_2 36% H_2 (no steam) as shown in Figure 7-5 [d]. After the utilization of the energy value of H_2 and condensation of steam, the retentate side stream would be mostly CO_2. The remained H_2 in the retentate stream could be used as a fuel or purified through an additional membrane separation unit. Alternatively, vacuum could be applied on the tube side to remove almost all of the H_2 from the reaction side. The decision of course between these options needs to be done by conducting a comprehensive process economic analysis under various plant configurations.
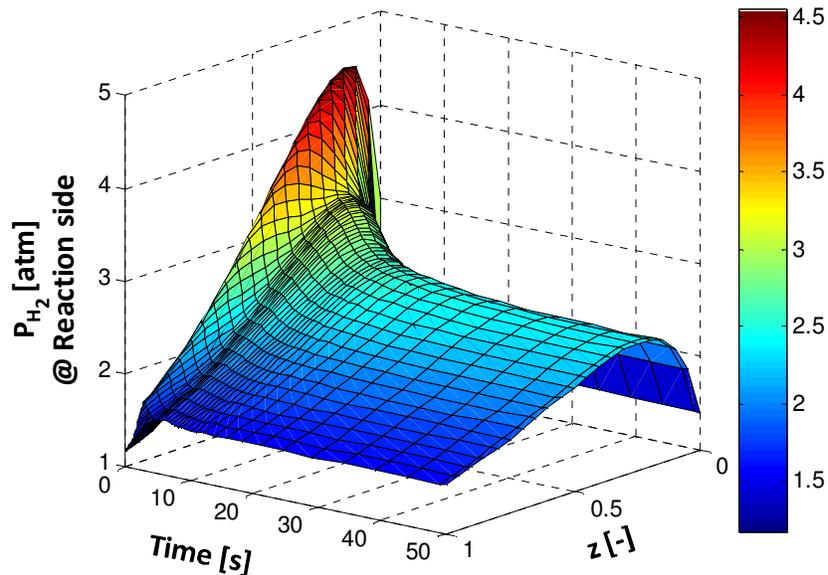
Figure 7-6. Partial pressure profiles of H_2 in the reaction side/Regulator case: $K_c = 0.002$ $\tau_I = 0.8$ s

The highest H_2 partial pressure was observed along the initial segments of the membrane reactor. The extent of produced H_2 by the forward reaction was higher than the amount of the permeated H_2 at the first 3 segments (up to 0.9 cm), resulting in a sudden increase in H_2 partial pressure observed along the initial segments of the membrane reactor and depicted in Figure 7-6. Increased steam flow rates also forced the WGS reaction to proceed towards the product side. As the controller increased the steam flow rate slowly during the first 2 seconds, the H_2 extent increased because of the increased forward reaction rate. Following that, a rather drastic H_2 pressure drop was observed in between t=2-6 s because of the unexpected drop in the total system pressure. As the controller increased the steam flow rate, the H_2 partial pressure started decreasing due to the increased H_2O fraction for t = 6-30 seconds in Figure 7-6. Additionally, Figure 7-6 indicated that the H_2 partial pressure profiles equilibrated around the steady state after 30 seconds.

7.3.3 The Servo-mechanism problem: Decreased exit CO fraction

In a typical servo-mechanism process control problem, disturbance load variables are kept constant at their nominal values while the set point undergoes a deliberate change reflecting new process performance specifications (such as new production requirements, safety and environmental regulatory ones, etc) Within this context, the feedback controller takes action in such a way that the controlled output (the CO fraction at the exit of the shell in the present study) closely tracks the new set point value in a fast and smooth manner. Notice that when the slurry-feed-derived syngas was used as the feed, the CO fraction at the reaction side exit was already too low (2.32% dry basis). However, the dry basis CO fraction of 2.32% at the reactor exit could be reduced even further (to 1.2%) under the action of a PI servo-mechanism controller in order to meet more stringent production requirements.
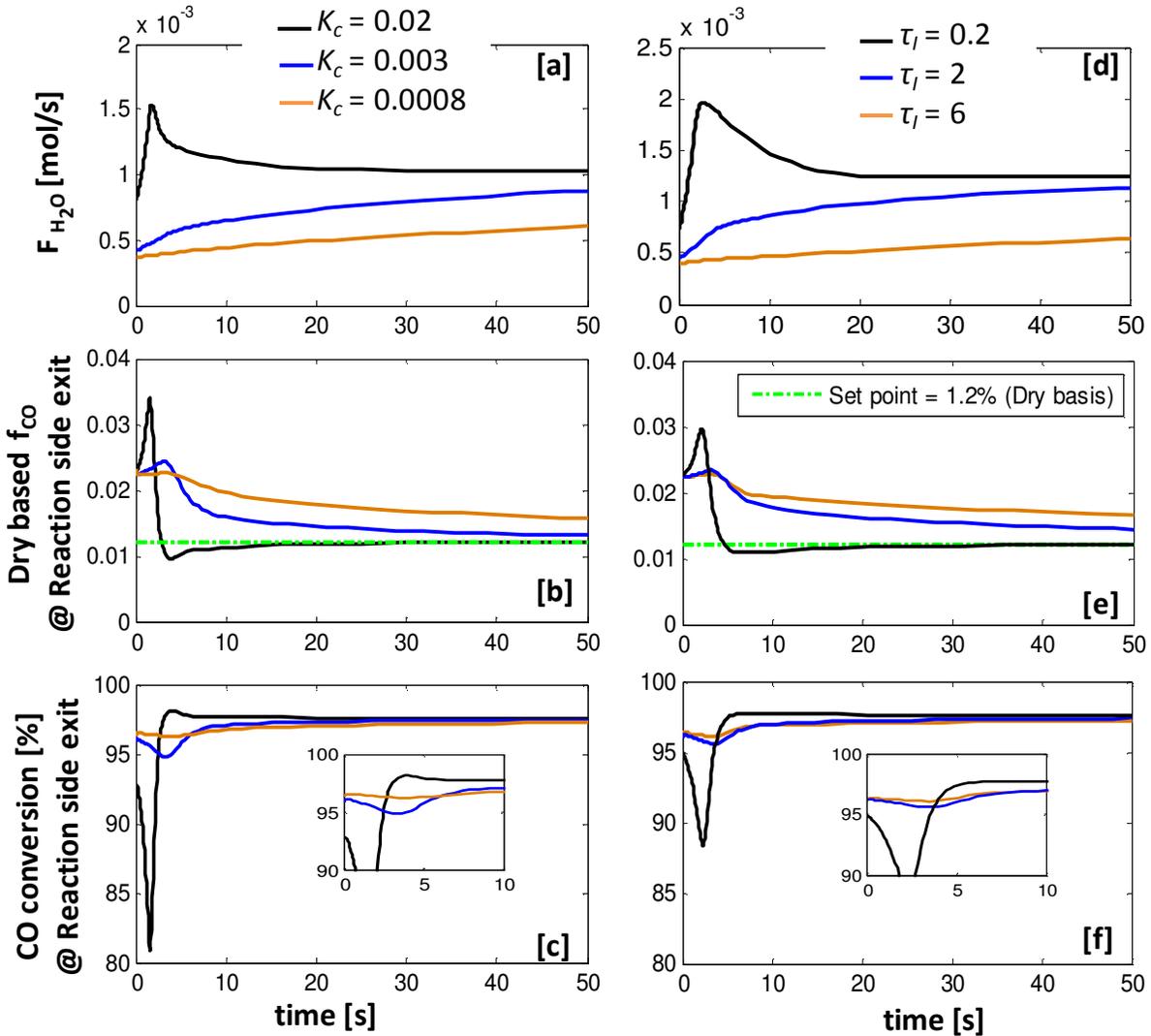
Figure 7-7. Controller tuning for [a] proportional gain and [b] integral time constant/ Servo-mechanism case.

In Figure 7-7, similar tuning guidelines to the regulator case were followed in the servo mechanism one. The closed-loop system's stability could be compromised at K_c values higher than 0.03 and τ_I values lower than 0.1 s. Furthermore, the speed of the process response and transition to the new set-point was adversely impacted by K_c values lower than 0.0008 and τ_I values higher than 6 s, and the maximum peak in the steam flow rate observed for a $K_c = 0.03$ (shown in Figure 7-7 [a]) was clearly undesirable from an energy efficiency and process economics point of view. Additionally, this observed peak of the steam flow rate and the associated residence time could cause CO conversion to decrease. Once the value of K_c was set at

0.003 providing a fast and stable response, fine tuning was performed by adjusting the value of τ_I as shown in Figure 7-7 [d] through [f]. The value of τ_I was adjusted by aiming to reduce the exit CO fraction level in Figure 7-7 [e]. The overall CO conversion decreased slightly to 95.6% during that delay time and then the conversion improved by climbing to the 97.6% level through the action of the controller with $\tau_I = 2$ as shown in Figure 7-7 [f]. The best set of values for K_c and τ_I were identified as 0.003 and 2 s respectively by ensuring that the set point was satisfactorily tracked in a fast, stable, smooth and as energy efficient manner as possible. Finally, notice that the H_2O: CO mole ratio increased from 2 to 5.8 when the new set point was reached.

Exploring the changes in the driving force for H_2 permeation would allow us to better understand and characterize the membrane reactor behavior while the process was controlled. Figure 7-8 shows the H_2 partial pressure profiles along the length of the reactor as a function of time in the reaction side. When the increase in the steam flow rate was still at a moderate level until the first 6 seconds, the H_2 partial pressure was increasing in all of the reactor segments (spatial domain) as shown in Figure 7-8. While the membrane reactor was already using the benefit of removal of H_2 from the product side, the addition of extra steam caused the WGS reaction to shift to the product side further. Thus the H_2 partial pressure increased at the first 6 seconds due to a slight increase in the inlet steam flow rate. Then, the controller continued to increase the steam flow rate to reach the new set point of 1.2% CO at the reaction side exit. Since the total pressure in the reaction side remained constant, the H_2 partial pressure decreased due to the increased steam fraction until the inlet steam flow rate reached its steady state value after 442 seconds.
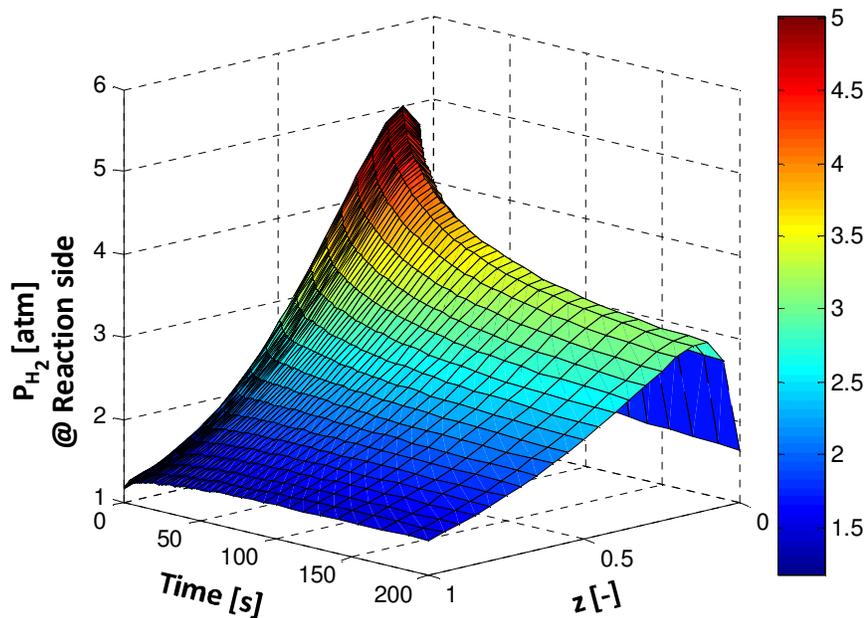
Figure 7-8. Partial pressure profiles of H_2 in the reaction side/Servo-mechanism case: $K_c = 0.003$, $\tau_I = 2$ s

The increase in the driving force for H_2 permeation (because of the increasing inlet steam flow rate during the first 6 seconds) was associated with the increased H_2 production rates during the first 6 seconds as shown in Figure 7-9 [a]. As the inlet steam flow rate continued to increase, the H_2 fraction and driving force decreased in response. In addition to the decreased driving force, the residence time was also reduced by the increased steam flow rate. The decreased driving force for H_2 permeation, together with the reduced residence time due to the higher steam flow rate caused a 24.6% decrease in the H_2 production rate depicted in Figure 7-9 [a]. In Figure 7-9 [b], the CO_2 and H_2O had the highest fractions at the reaction side exit. Therefore, as the inlet steam flow rate increased, the most drastic change observed was the one in the CO_2 fraction at the reactor exit profile during the course of the PI controller action.
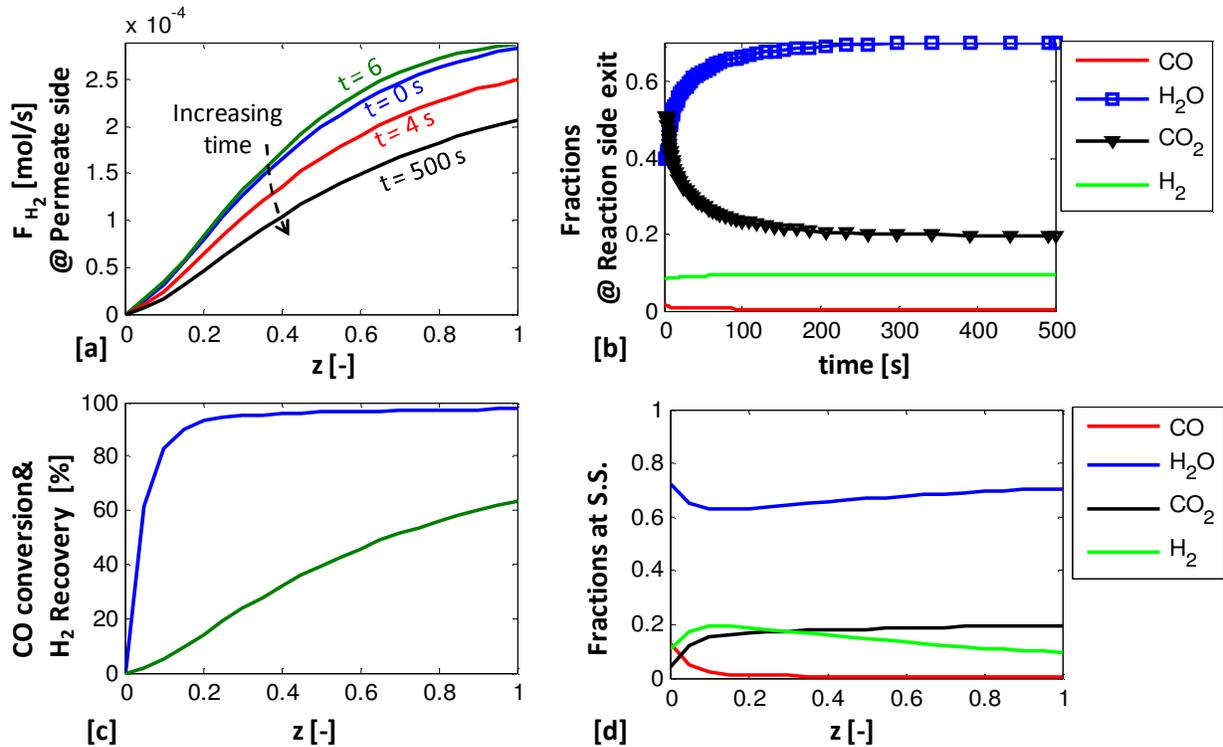
Figure 7-9. Overall performance evaluation of the process system/Servo mechanism case: $K_c = 0.003$, $\tau_I = 2$ s.

The membrane reactor attained the new steady state with 97.6% CO conversion and 63.4% H_2 recovery with the profiles graphically represented in Figure 7-9 [c]. Most of the CO was converted along the initial segments in the reactor's spatial domain. However, the rest of the reactor was used efficiently for the H_2 recovery. While the extra pure H_2 from the permeate side could be used for the processing/synthesis of other chemicals or fuel cell applications, the retentate stream consisting of 66.4% CO_2, 32.4% H_2 and 1.2% CO could be utilized as a turbine fuel with a diluent, such as nitrogen (Chiesa and Lozza, 2010; Todd and Battista, 2010) within an IGCC plant configuration.

As a final reflection, please notice that even though the CO fraction at the reaction side exit (and thus conversion) was successfully controlled in both the regulator and servo-mechanism cases, the H_2 recovery was reduced due to the decreased driving force for H_2 permeation. The same process control scenarios were repeated by using a membrane having permeance value equal to 100% of a 10µm Pd foil and compared with the above results in Table

7-4. The production rate and recovery of H_2 could be certainly improved by using a Pd-based membrane with higher permeance. Not only the H_2 recovery was improved but also the controller used less steam as the permeance increased. Moreover, it should be pointed out that the purpose of the simple process control framework developed in this work was to show the feasibility of maintaining not only a high H_2 production rate but also high levels of CO conversion in the presence of external disturbances and set-point changes. Thus, a ~20-30% decrease in H_2 recovery at the end of the process control action might be deemed acceptable until corrective action is taken and the total system pressure is restored to its original value within the shortest possible time for example. Furthermore, advanced multivariate control configurations and algorithms could potentially further enhance the quality of control by addressing the above challenges through a more sophisticated structure at the expense of higher costs and complexity in implementation, controller tuning and maintenance.

Table 7-4. Results summary

Permeance coefficient	Control type	$f_{CO,exit}$	X_{CO}	R_{H_2}	H_2O/CO
30%	Regulator	2.32	95	56	3.8
	Servo	1.2	97.6	63.4	5.8
100%	Regulator	1.8	97	82	3.2
	Servo	1	98.3	89.8	4.3

Notice also that the controller action led to an increase in the H_2O: CO ratio from 2 to 3.8 and 5.8 in the regulator and servo-mechanism cases respectively. Even though the heating cost of steam was certainly not negligible, there were other benefits that could be potentially realized through the use of optimum steam amount. It should also be kept in mind that excessive steam in the reaction side would dilute the H_2 and decrease the driving force for H_2 permeation. Moreover, if temperature control was not highly effective in the case of a non-isothermal membrane reactor, the high latent heat of steam could help decrease the temperature rise in the reaction side due to the exothermic WGS reaction. Notice that the Pd-based membrane should be protected from a possible formation of hot spots, and intermetallic diffusion and leak formation could become problematic at temperatures higher than 550°C due to decreased permeation and selectivity (Ayturk et al. 2006b; Ma et al. 2004). The temperature profile of the membrane

reactor could be thus maintained under almost isothermal conditions by proper adjustment of the pre-heater temperature and by using the benefit of excess steam to eliminate a potential temperature rise due to the exothermic reaction. Furthermore, the deactivation of catalyst and/or the deterioration membrane by coke formation could be prevented by using excess steam. Finally, it should be pointed out that a comprehensive process economics framework that explicitly acknowledged the cost of compressor for the membrane reactor and CO_2 sequestration, vacuum pump or excess steam together with the value of produced H_2 as an energy carrier should form the basis of any sound investment decision-making platform in the technology options under consideration.

7.4. Conclusions

A process dynamic modeling framework was developed and presented in order to analyze and characterize the transient phenomena of a lab-scale Pd/Alloy-based membrane (Pd/Cu or Pd/Au) reactor. Furthermore, the feasibility of a simple process control framework was examined in the presence of unexpected disturbances and operationally favorable set-point changes. Although there was, in principle, a plethora of different scenarios relevant to process control studies, two main illustrative cases were considered, namely the process regulation and servo mechanism. In both control structures, quite satisfactory process control was attained maintaining CO conversion at levels higher than 95% so that the retentate stream could become suitable for high pressure CO_2 sequestration. Finally, since the rapidly evolving field of membrane technology may facilitate the synthesis and practical utilization of membranes with higher permeance levels and resistance to impurities in hydrogen production and separation process systems, not only could the performance of such systems be further enhanced but also process control strategies could become more effective, energy efficient and economically advantageous.

8. Process Safety Aspects in Water-Gas-Shift (WGS) Membrane Reactors Used for Pure Hydrogen Production

8.1. Introduction

The syngas produced by coal gasification processes can be utilized in Pd-based water gas shift membrane reactors for the production of pure H_2. Pd/alloy composite membrane reactors exhibit comparative advantages over traditional packed bed reactors such as simultaneous reaction/separation in one compact unit and increased reaction yields. Furthermore, the development of comprehensive process intensification strategies could further enhance membrane reactor performance resulting in a substantially smaller and functional, inherently safer, environmentally friendlier and more energy efficient process.

A systematic non-isothermal modeling framework under both steady state and dynamic/transient conditions for a catalytic high temperature water-gas shift reaction in a Pd-based membrane reactor has been developed to characterize the dynamic behavior of the process system at various operating conditions from a process safety standpoint. In particular, various reaction conditions as well as key process variables such as feed temperature and flow rate, catalyst loading, driving force for H_2 permeation were considered as they were critically related to various safety aspects in the operation of a Pd-based membrane reactor. Within the proposed framework, process parameters and operating conditions which might induce hazards and compromise process safety were identified, analyzed and characterized. Finally, the proposed approach was evaluated through detailed simulation studies in an illustrative case study involving a real Pd-based membrane reactor used for pure hydrogen production and separation that exhibited complex behavior over a wide operating regime.

8.2. Results and discussion

The non-isothermal modeling framework detailed in the Chapter 3.2 for the Pd-based membrane reactor served as the basis for the identification of key process variables as well as operating conditions capable of inducing potentially hazardous situations where process safety was compromised. The standard principles of Hazard and Operability (HAZOP) analysis were followed and applied to identify and hopefully prevent potential process risks to personnel, environment, equipment integrity and/or enhance the process efficiency and economics (Chiappetta et al. 2006a). In particular, the causes and consequences for each of the hypothesized scenarios involving deviations of one of the key process variables were considered in the present study from the desirable operating conditions were determined in a systematic way within the context of HAZOP analysis. A guide word such as "MORE, LESS or NO" is normally assigned to one of the selected variables and deviations in all other process variables were identified and monitored (Basile et al. 2001; Bartolozzi et al. 2000). One of course should be mindful of the fact that an analysis involving the whole process plant is time-consuming and requires a large amount of work by a group of experts (Khan and Abbasi 1997). Throughout the conduct of the process safety analysis, only the Pd-based WGS membrane reactor unit was evaluated using HAZOP analysis. In particular, a non-isothermal model-based membrane reactor performance assessment was performed by analyzing the particular effects on process operation and performance of the feed temperature, feed flow rate, bulk catalyst density, the $H_2O:CO$ mole ratio, reaction side total pressure, membrane area and permeate side pressure on the CO conversion, H_2 recovery and reaction side temperature profile. Root causes, consequences and precautionary measures associsated with any deviations in the operating conditions from the desirable ones were identified and evaluated in order to ensure process safety while maintaining performance target levels at $X_{CO} = 98\%$ CO conversion and $R_{H2} = 95\%$ hydrogen recovery. At the same time, the objective to keep the maximum temperature in the reaction side below the safety limit of 500°C was pursued.

The simulation results of the one dimensional model at isothermal conditions were compared with the experimental ones reported by Agustine et al. (2011). The experimental and simulation results correlated very well for the CO conversion levels at 400°C and 450°C.

However, the H_2 recovery levels were overestimated in the range of 3-10% with the one-dimensional model. The over-predicted H_2 recovery levels arose from the constant H_2 partial pressure in the radial direction and/or plug flow assumptions as well as the concentration polarization (Hara et al. 1999; Koukou et al. 1998; Koukou et al. 2001; Itoh et al. 1994; Mori et al. 2007; Bhattacharya and Hwang 1997). A one-dimensional reactor model represented a quite useful tool for a quick, yet reliable, assessment of the overall membrane reactor performance as well as a computationally attractive option for screening the design space and thus identifying viable designs that would merit further examination through the development of higher dimensional membrane reactor models (Israni et al. 2009; Ramirez Serrano et al. 2009). Higher dimensional membrane reactor models however were necessary for industrial scale applications.

8.2.1 Effect of feed temperature

The characterization of the optimum feed temperature needs to be performed by considering both the efficiency of the process and integrity of the Pd-based membrane. On one hand, the feed temperature should be higher than the threshold temperature of the WGS catalyst and the reaction rate should be high enough to achieve the performance target levels. The rate of permeation is also dependent on temperature and high permeation rates are favored at high temperatures. On the other hand, if the feed temperature exceeds a certain limit, the resulting high reaction side temperature would cause a deterioration of the Pd-based membrane. Notice that pure Pd-based membranes have a minimum and maximum working temperature. The reaction side temperature should be higher than 300°C to avoid the α-β phase transition of palladium hydride. Once the palladium hydride is formed, the pure Pd membrane would lose its infinite selectivity due to significant crack and pinhole formation through the Pd layer. The critical temperature for the α-β phase transition of some of the Pd alloys is lower than in the pure Pd case. Thus, the utilization of the Pd alloy membranes would provide a wider range of operating temperatures. A well-known example of a Pd alloy membrane, namely a Pd/Ag membrane does not experience any H_2 embrittlement at temperatures below 300°C in the H_2 environment (Shu et al. 1991). Furthermore, the intermetallic diffusion of the metallic support elements to Pd layer and leak formation could be problematic at temperatures higher than 550°C due to decreased permeation and selectivity, respectively (Ayturk et al. 2006b; Ma et al. 2004).

As shown in Figure 8-1, the non-isothermal membrane reactor model was simulated using a feed temperature range of 275-400°C in order to identify reaction conditions which could eventually give rise to process hazards. The maximum temperature in the reaction side was limited to 500°C. When the feed temperature was higher than 300°C in Figure 8-1 [a], the reaction side temperature limit was exceeded starting with quite low feed flow rates at 300°C. The intermetallic diffusion of the components of porous support into the Pd/Alloy layer would decrease permeation and cause leak formation at temperatures 500°C and higher. As a consequence of leak formation, the reacting gases other than H_2 can diffuse into the permeate side. The CO conversion levels would drop due to transport of some of the unreacted CO to the permeate side. In addition, the heat carried by the gases diffusing to the permeate side for the defected membranes was found to be less than ˜5% of the heat generated by the water-gas shift reaction. If a pure Pd membrane is used, the low temperature at the reactor inlet would damage the membrane if the membrane is in H_2 flow at temperatures below 300°C (as shown earlier in Figure 2-1). Keeping the feed temperature at 300°C would be more beneficial to maintain high reaction and H_2 permeation rates without damaging the Pd-based membrane supported on metal substrates and another way for reducing the reaction side temperature, such as a higher steam flow rate, needed to be employed.
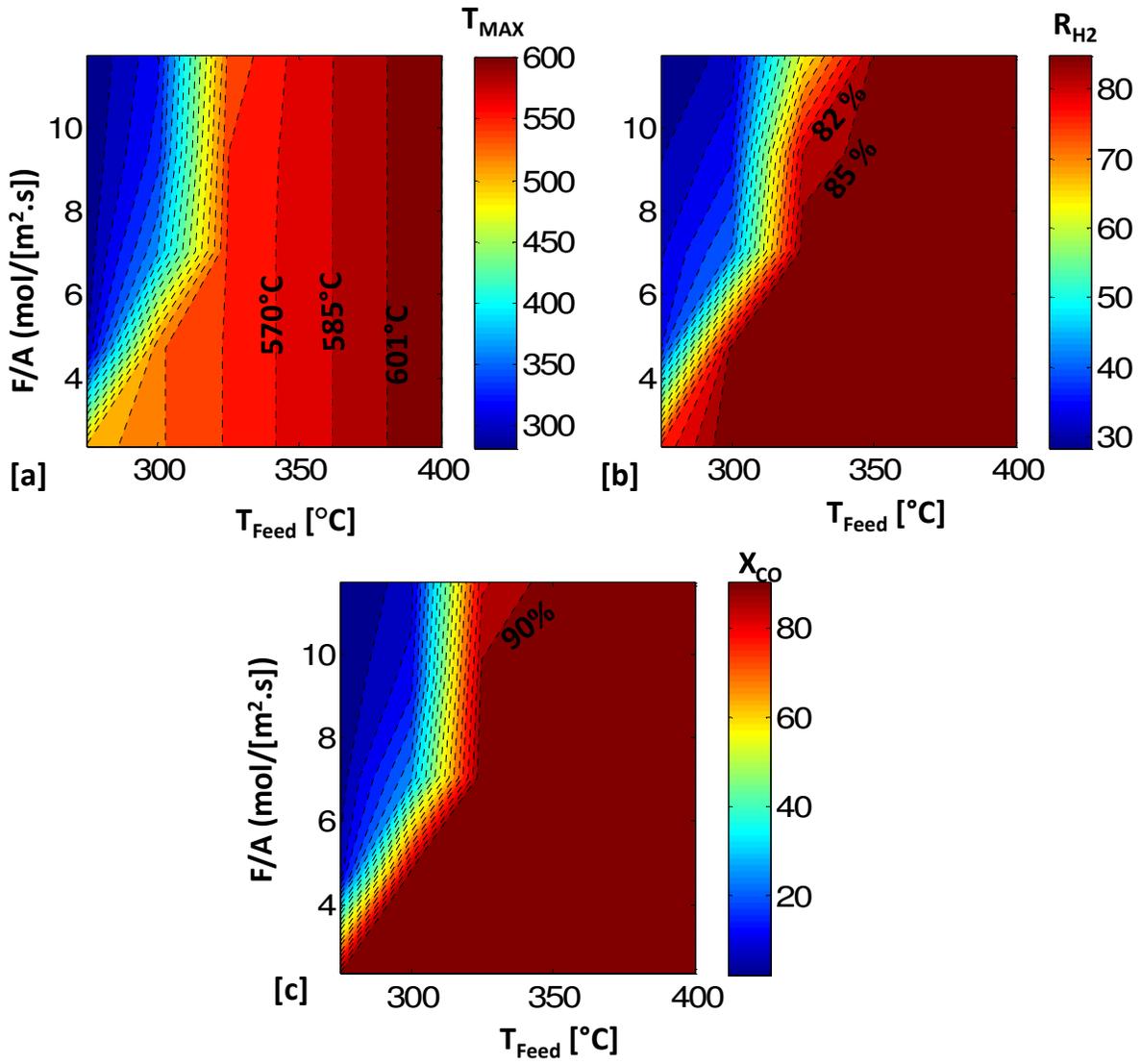
Figure 8-1. Contour plots of [a] $T_{Rxn.Max}$ [b] R_{H2} and [c] X_{CO} as a function of inlet feed flow rate and feed temperature at $P_{Total,Rxn}$ = 15 atm, P_{Tube} = 1 atm, $H_2O:CO$ = 2 and 100% $\rho_{Bulk,max}$.

The reaction rate was insignificant at feed temperatures at 280°C and lower for all flow rates as shown in Figure 8-1[c] with CO conversion levels 10% and lower. Additionally, the feed temperature should not be higher than 300°C at these reaction conditions in order not to exceed the reaction side temperature limit. Attaining the performance target levels of X_{CO} = 98% and R_{H2} = 95%, became challenging due to the limited range of feed temperatures considered. As can be seen from Figure 8-1 [b] and [c], the target levels of X_{CO} = 98% and R_{H2} = 95% were not

achieved at feed flow rates as low as 2.35 mol/[s.m^2]. Thus, the specific reaction conditions should be carefully examined to reach these levels of performance through an inherently safe process.
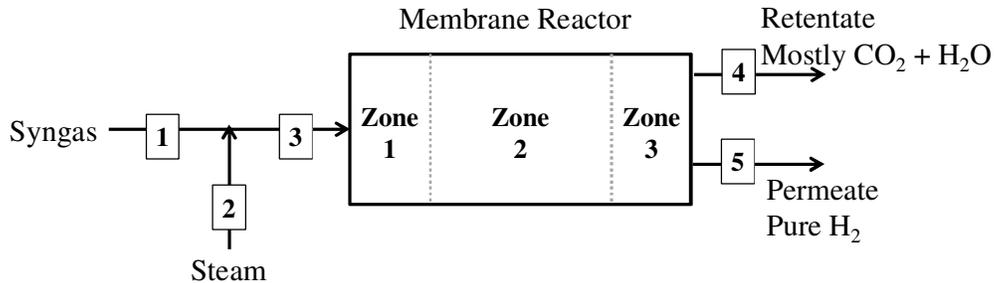
Figure 8-2. Hazard detection nodes and zones on the schematic diagram of a membrane reactor

If the feed temperature exceeds the limit of 550°C (MORE -T_{Feed}) due to overheating of the feed stream and stayed at that temperature for long times, the membrane would be damaged and the permeance would consequently decrease. The exit stream of the gasifier had to be cooled from 677°C to the feed temperature of the membrane reactor (GEE gasifier, GEE IGCC with CO_2 capture case). Additionally, if the syngas at the gasifier exit did not carry the required amount of steam, then supplemental steam had to be added to the stream at the gasifer exit. Thus, insufficient cooling of the syngas stream after the gasifier or overheating of the supplemental steam would cause an increase in the membrane reactor feed temperature. In addition, the membrane reactor has to be cooled in an actual operation at isothermal conditions to remove the extra heat generated by the water-gas shift reaction. The reaction side temperature would increase in the case of cooling water failure. In the case of a feed temperature increase, the behavior of the membrane reactor would differ within certain zones of the reactor. The CO concentration would be the highest in zone 1 and lowest in zone 3 of Figure 8-2. Similarly, the H_2 concentration would decrease from zone 1 through zone 3 due to the H_2 depletion by permeation. Thus, the highest amount of energy released by the reaction would be observed in zone 1 (Figure 8-2); zone 2 and zone 3 would sequentially follow based on the overall amount of the heat release. Positioning high temperature alarms at node 3 and zone 1 in Figure 8-2 would thus be highly recommended. If any of the detection and prevention methods could not mitigate excessive reaction side temperature rises, the un-cleaned gas containing high concentrations of

172

sulfur containing gases before the gas cleaning unit, could be admitted to the membrane reactor to kill the reaction and permeation as a last resort. Even though the economic loss would be considerable with this action, injury or loss of life and a chain of serial accidents between communicating units could be prevented.

If the required action could not be taken within a reasonable time frame, the feed flow rate could be increased by opening a valve at the membrane reactor exit to decrease the reaction rate. If no action could prevent a drastic temperature rise and/or pressure relief equipment at the reactor exit failed and an ignition source existed at the same time, isolation valves and chemical isolation had to be placed on nodes 3, 4 and 5 in Figure 8-2 to prevent passage of flames between communicating process units. These isolation vales and chemical isolation systems had to be used in conjunction with detection and control devices. Flame sensors had to be located in sufficient distance from node 3, in zone 1 and 3 in Figure 8-2 such that the valves had adequate time to close (1993a).

On the other hand; a decrease of the feed temperature (LESS-T_{Feed}) would lead to the deterioration in the membrane performance by reducing the CO conversion and H_2 production rates. In addition to low productivity caused by the decreased feed temperature, pure Pd membranes could experience H_2 embrittlement. The temperature of the heat exchangers before the membrane reactor should be monitored and the feed streams that were at undesirable temperature levels should be redirected through a backup line while the membrane reactor was being fed by inert gas at the operating temperature. The above considerations and recommendations for changes in the feed temperature are summarized in an HAZOP worksheet shown in Table 8-1.

Table 8-1. HAZOP worksheet – Parameter: feed temperature

GW	Causes	Consequences	Prevention & Repair
More ($T_{Rxn,Max}>T_{Upper}$[*])	High steam temperature at node 2 High syngas temperature at node 1 Low feed flow rate at node 3 Malfunction of the reactor heating system	Hot spots Decreased permeance & selectivity (due to Intermetallic diffusion) Catalyst sintering Increased pressure due to increased temperature if pressure relief equipment fails simultaneously	High temperature alarms on node 3 and zone 1 Fast temperature control before node 1 and 2 (in heat exchangers for syngas cooling and steam heating) Maintain/check valves and pipelines Increase feed flow rate with a valve on node 4 Membrane replacement in case of intermetallic diffusion Isolation valves and chemical isolation at nodes 3, 4 and 5 together with flame sensors Inert feed at operating temperature and backup line for the syngas feed at inadequate temperature Refer to HAZOP worksheet for reaction side pressure
Less ($T_{Rxn,Max}<T_{Lower}$[*])	Low steam temperature at node 2 Low syngas temperature at node 1 High feed flow rate at node 3 Malfunction of the reactor heating system	Decreased CO conversion and H_2 recovery Defects/cracks on the membrane surface and decreased selectivity (due to H_2 embrittlement for pure Pd membranes)	Low temperature alarm on node 3 and zone 1 Fast temperature control before node 1 and 2 Maintain/check valves and pipelines Membrane replacement/repair in case of embrittlement Inert feed at operating temperature and backup line for the syngas feed at inadequate temperature

* T_{Upper} = 500°C which equals the maximum temperature limit in the reaction side, T_{Lower} = 300°C which equals the threshold temperature

of the catalyst to maintain high CO conversion levels also to prevent H_2 embrittlement in Pure Pd membranes.

8.2.2 Effect of feed flow rate

The non-isothermal membrane reactor model was also evaluated under a wide range of feed flow rates (~0.4-33.7 mol/[s.m^2]) in order to highlight the competing effects between residence time and reaction/permeation rate on process performance enhancement. The feed temperature was fixed at 350°C and the same reaction conditions in the Chapter 8.2.1 were used; $P_{Total,Rxn}$ = 15 atm, P_{Tube} = 1 atm, H_2O:CO = 2 and 100% $\rho_{Bulk,max}$. The effect of feed flow rate at node 3 in Figure 8-2 was examined in isolation to clarify the consequences. In addition, it was assumed that the ratio controller for the addition of steam at node 2 to the syngas at node 1 worked properly and the feed composition was constant (Figure 8-2). An unplanned increase or decrease of the above process variable, depending on the extent of this change, could drive the process to undesirable operating conditions. Furthermore, the Damköhler number (Da) given Eq (8.1) in which is the ratio of the maximum reaction rate at the reactor inlet to the space velocity is a good parameter to characterize and assess the consequences of such an increase of the total feed flow rate.

$$Da = \frac{[-r_{co} \cdot \rho_{Bulk} \cdot V_{An.}]|_{y=0}}{F_{CO}|_{y=0}} \tag{8.1}$$

Two base cases with different feed flow rates, namely point A and B in Figure 8-3[a], were examined to identify the consequences of variations in the feed flow rate. For point A in Figure 8-3a], the reaction side temperature was kept at 450°C by using a high feed flow rate to produce H_2 at a high flow rate of 6.2×10^{-4}mol/s. Notice that depending on the extent of the increase of the feed flow rate two different cases: Da<0.34 or Da<< 0.34 could be considered. Even a slight increase in the feed flow rate, from Da = 0.34 to 0.31 would cause a temperature decrease of 12°C. When the feed flow rate increase was drastic, from Da = 0.34 to 0.12, the temperature decrease could be as significant as 79°C due to the low residence time which was still faster than the reaction and permeation rates as shown in Figure 8-3[a].
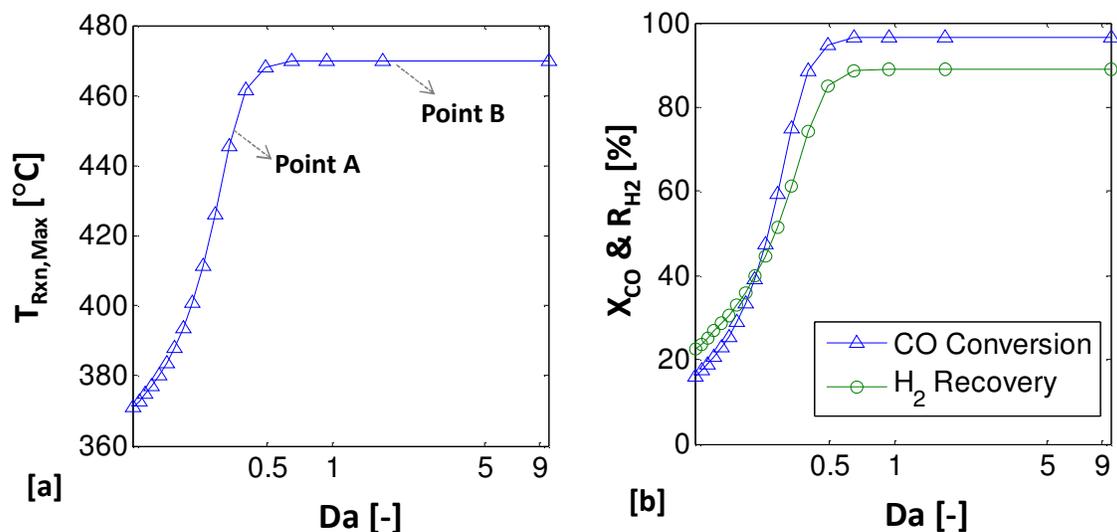
Figure 8-3 The effect of feed flow rate on [a] $T_{Rxn.Max}$ [b] R_{H2} and X_{CO} at T_{Feed} = 350°C, $P_{Total,Rxn}$ = 15 atm, P_{Tube} = 1 atm, $H_2O:CO$ = 2 and 100% $\rho_{Bulk,max}$.

A 40% decrease in the feed flow rate, Da = 0.34 to 0.57, caused the reaction side temperature to increase fast and reached a plateau as shown in Figure 8-3[a]. During the first 40% of the decrease considered, the contact time with the catalyst would be longer in order to convert more reactants than under the original operating conditions, thus, the heat produced by the reaction increased accordingly. Consequently, the CO conversion and H_2 recovery levels would be higher but the H_2 production rate would be lower compared to operation at point A.

As shown in Figure 8-3[a] and [b], the feed flow rate should be enough to achieve a Da number higher than 0.6 to maintain the CO conversion and H_2 recovery levels at ˜97% and 88%, respectively. However, the feed flow rate should not be too low either (Da>>1). If the feed flow rate decreased drastically, the membrane reactor would not be operated at the maximum capacity and insufficient H_2 would be produced.

If the membrane reactor was operated at point B with Da = 2 (Table 8-4[a]), the H_2 production of 1.5×10^{-4}mol/s would be lower compared to point A but the reactor temperature would be less benign to changes in the feed flow rate. Operating at around Da = 2 would provide time to act to prevent hazards with the aid of a broader feed flow rate range (up to 5 times higher and lower of the original feed flow rate). Moreover, the membrane reactor would be operated at a better efficiency with 96.6% CO conversion and 88.8% H_2 recovery as shown in Figure 8-3[b].

176

Table 8-2. HAZOP worksheet – Parameter: feed flow rate

GW	Causes	Consequences		Prevention & Repair
More ($\uparrow F_{Feed}$*)	Malfunction of the flow control instruments on nodes 1, 2 & 3 Inappropriate adjustment and/or failure of the valves and pressure regulators on node 4 Leaks on the pipeline on node 4 before the pressure regulator	Da<2	Insignificant changes in T_{Rxn}, CO conversion and H_2 recovery Increased H_2 production rates	Regular maintenance and inspection of the control instrument, valves and pressure regulators Fast responsive temperature recorders and controllers
		Da<<2	Decreased T_{Rxn} due to reduced ΔH_{Rxn} Decreased CO conversion and H_2 recovery Increased H_2 production rates	Backup lines before and after the reactor, on node 3 and 4 Fast responsive temperature recorders and controllers A recycle switch from node 4 to node 3 in case of very low CO conversion Monitor H_2 production rate and permeate/retentate compositions
Less ($\downarrow F_{Feed}$*)	(same causes with More and) Partial plugging of the lines before node 3 or on node 4 Partial clogging of the reactor by coke in the catalytic bed Leaks on the feed line before node 3	Da>2	Insignificant changes	Regular maintenance and inspection of the control instrument, valves and pressure regulators Fast responsive temperature recorders and controllers
		Da>>2	Membrane damage & catalyst deactivation in case of coke formation Pressure increase in the feed line due to plugging Pressure decrease due to leaks	Enclosed safety relief valves on node 3 and 4 Poisonous gas detectors on both reaction and permeate sides in case of leak Maintenance of the filter systems before node 3 Monitor H_2 production rate and permeate composition Regeneration / substitution of the membrane and/or catalyst
No ($F_{Feed}=0$)	(same causes with More and) Complete plugging of the lines before node 3 or on node 4 Complete clogging of the reactor by coke in the catalytic bed	Decreased T_{Rxn} as low as feed temperature No CO conversion and H_2 recovery Oxidation of the membrane in case of backflow		Extra feed line between node 1 and 3 Inert feed line to protect the membrane until repair Check valve on node 4 and 5 to prevent back flow Regeneration / substitution of the membrane in case of oxidation

* ↑ : Increased , ↓ : Decreased

177

In light of the above considerations, the HAZOP worksheet for the effect of feed flow rate was assessed by assuming membrane reactor operation with Da = 2 as given in Figure 8-3. In particular, an increase of the total feed flow rate (MORE-F_{Feed}) could be caused by a malfunction of the flow control instruments, inappropriate adjustment and/or failure of the valves and pressure regulators. When the unexpected increase of the total feed flow rate was minor, Da<2, the reaction side temperature, CO conversion and H_2 recovery levels would remain constant and only the H_2 production rate would increase. If the increase in the feed flow rate was more significant, Da<<2, the efficiency of both of the isothermal and non-isothermal membrane reactors, CO conversion and H_2 recovery, could deteriorate due to lower residence times. Backup lines at the inlet and outlet of the membrane reactor would provide continued operation if any problem with valves, leaks on the pipeline and pressure regulators occured. In the case of malfunction of flow controllers, recycling of the un-reacted syngas from the reactor exit to the inlet would provide valuable time for corrective action should the need arise.

In addition to a malfunction possibility of the flow control instruments, inappropriate adjustment and/or failure of the valves and pressure regulators, as well as plugging of the lines which were located before the membrane reactor and any leaks on the feed line could result in a decrease (LESS-F_{Feed}) in the total feed flow rate. Two scenarios might be evaluated in the case of a decrease of the total feed flow rate: Da>2 or Da>>2, depending on the extent of the decrease. In the case of a moderate decrease of the feed flow rate, Da>2, the heat carried by the convective flow would be reduced but the process would not be affected significantly. If the total feed flow rate approached an extremely low value leading to Da>>2, the reaction side temperature would decrease due to the decreased heat of reaction since less reactant was converted. Notice that the H_2 production rate of the membrane reactor would decline due to the lower feed flow rate. The temperature controller of the isothermal reactor had to act fast and the feed temperature of the non-isothermal reactor had to be maintained constant (at 300°C) to prevent a temperature drop inside the reactor. If the reason of the decreased flow was plugging of the lines, pressure might build up. A steady reliable operation of the filtration units had to be maintained to prevent plugging. An extra feed line might be added to the system in case of plugging to sustain the continuous operation of the process. In the case of leakage, poisonous gas detectors had to be positioned at multiple locations of the reaction and permeate sides of the reactor and an inert gas purge system should be built for the removal of potentially hazardous gases from the reactor unit

until the source of the leak was identified and repaired. Finally, the maintenance and inspection of the control instrument, valves and pressure regulators should be done on a regular basis. An alternative feed line for the wet syngas feed had to be positioned before the entrance of the reactor and the feed had to be switched to inert gas in cases where the relief valve was activated.

Similar reasons that could cause a decrease in the feed flow rate might lead to the worse case scenario of no flow (NO-F_{Feed}). The surface of the Pd-based membrane might then be oxidized by the air in the pipeline in case of back flow, and therefore, it needed to be regenerated with H_2 prior to reaction. The backflow to the reactor should be prevented by positioning check valves (one-way valve) on retentate and permeate side exits to prevent catastrophic results like internal deflagration.

More importantly, the changes in the H_2 production rate and composition at the permeate side exit were conspicuous signs of deviations in the feed flow rate or deterioration of the Pd-based membrane properties. Thus, the permeate stream had to be monitored closely to identify possible deviations from the regular operating conditions.

8.2.3 Effect of bulk catalyst density

The forward reaction rate and associated heat produced by the exothermic WGS reaction were higher in the catalytic zone close to the membrane surface where the permeation rate was the fastest. Hot spot formation on the membrane surface due to the fast forward reaction could damage the Pd membrane and also sinter the catalyst. Diluting the catalyst mass with an inert packing would not only help to prevent the formation of hazardous hot spots but also would reduce the cost of the membrane reactor. Thus, the maximum temperature in the reaction side, overall CO conversion and H_2 recovery of the membrane reactor were calculated at a feed flow rate range of ~2.3-11.7 mol/[s.m^2] and 2-100% of the maximum bulk catalyst density (weight of catalyst without inert packing/ void annulus volume). The reduction of the bulk catalyst density by distributing the catalyst weight evenly along the entire reactor length was not an effective way of decreasing the reaction side temperature. The maximum temperature in the reaction side was as high as ~575°C for all of the bulk catalyst density values at almost all feed flow rates as shown in Figure 8-4 [a]. Thus, only diluted catalyst weight was not enough to maintain the reaction side temperature below the limit. Moreover, the performance indicators, X_{CO} and R_{H2},

were not significantly affected at the feed flow rates considered for ρ_{Bulk} values higher than 50% of the $\rho_{Bulk,max}$. Thus, packing the non-isothermal membrane reactor with 50% of the $\rho_{Bulk,max}$ was selected for the ensuing simulation runs.
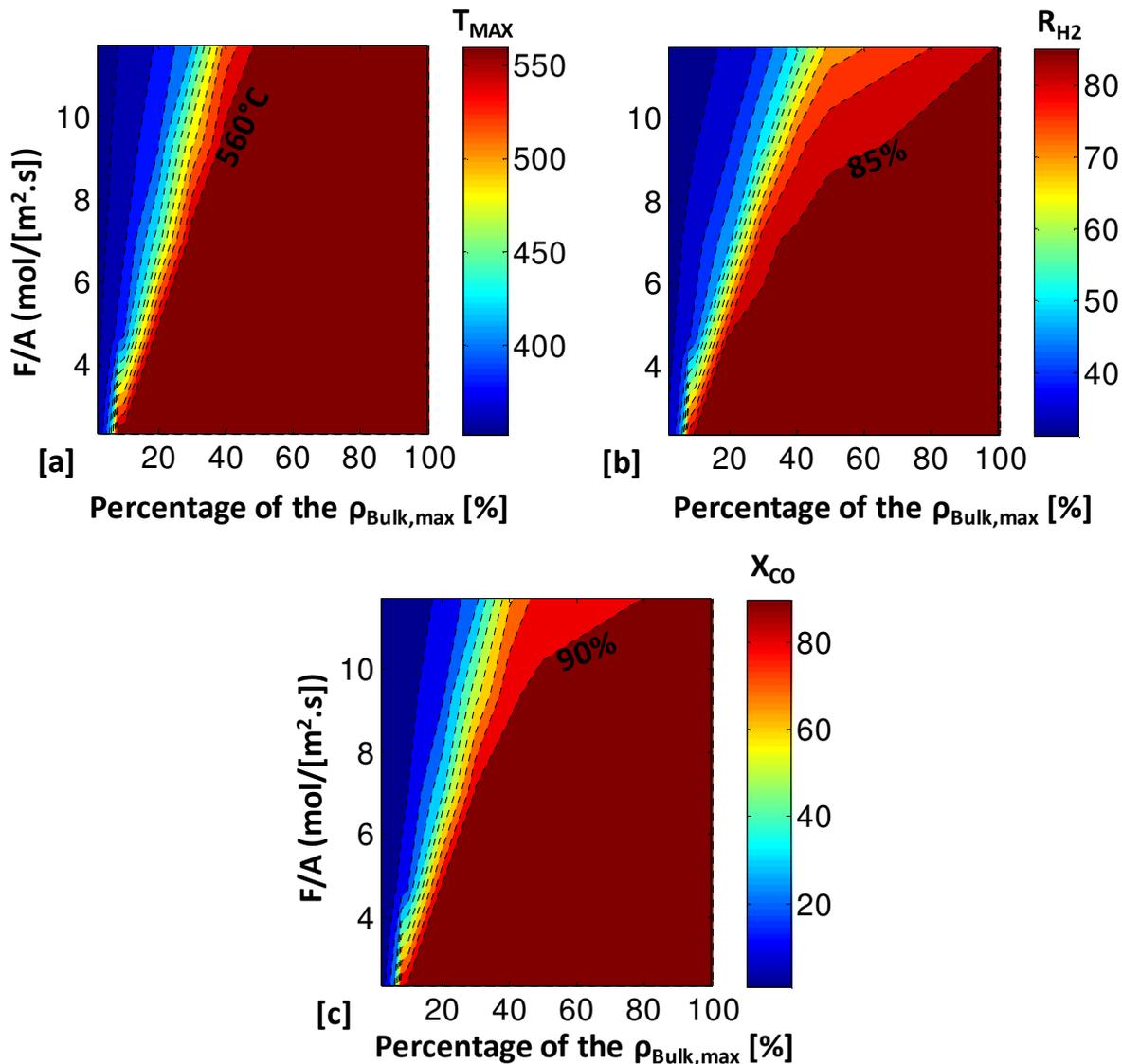
Figure 8-4. Contour plots of [a] $T_{Rxn.Max}$ [b] R_{H2} and [c] X_{CO} as a function of inlet feed flow rate and bulk catalyst density at $T_{Feed} = 350°C$, $P_{Total,Rxn} = 15$ atm, $P_{Tube} = 1$ atm, $H_2O:CO = 2$.

8.2.4 Effect of H_2O:CO mole ratio

The temperature rise due to the heat of reaction could easily cause the reaction side temperature to exceed the temperature limit of 500°C at feed temperatures above 300°C. Feed temperatures below 300°C reduced the permeation and forward reaction rates. Also, the H_2 embrittlement remained a problem for pure palladium membranes below 300°C. While the feed temperature was kept at 300°C and higher, the reaction side temperature needed to be lower than 500°C to protect the membrane. An effective way of reducing the reaction side temperature would be feeding excess steam to make use of the high sensible heat of steam. Even though the heating cost of steam would be high, the utilization of excess steam to prevent high temperature zones for the safety of the operation of the Pd-Based membrane reactor was more crucial. Moreover, the increased steam flow rate would shift the WGS reaction to the products side and increase reaction yield along with the removal of H_2.

In the simulation runs, the total feed flow rate range was kept constant and the mole ratio of H_2O:CO was changed from 1 to 8 in Figure 8-5. The mole ratio of H_2O:CO should be higher than 4.5 to avoid exceeding the reaction side temperature limit of 500°C at the specified reaction conditions as presented in Figure 8-5 [a]. The temperature rise was not at acceptable levels for all feed flow rates considered, particularly at H_2O:CO ≤ 2 and the high temperature zones could undermine process safety by causing leak formation and an undesirable productivity decline by reducing the permeance due to intermetallic diffusion. Even though an 96% CO conversion was attained with H_2O:CO = 4 in Figure 8-5 [c], the highest H_2 recovery was 81% at the corresponding conditions of Figure 8-5 [b]. The maximum of the H_2 recovery (85%) was observed with H_2O:CO =2 because of the high residence time and temperature at this zone.
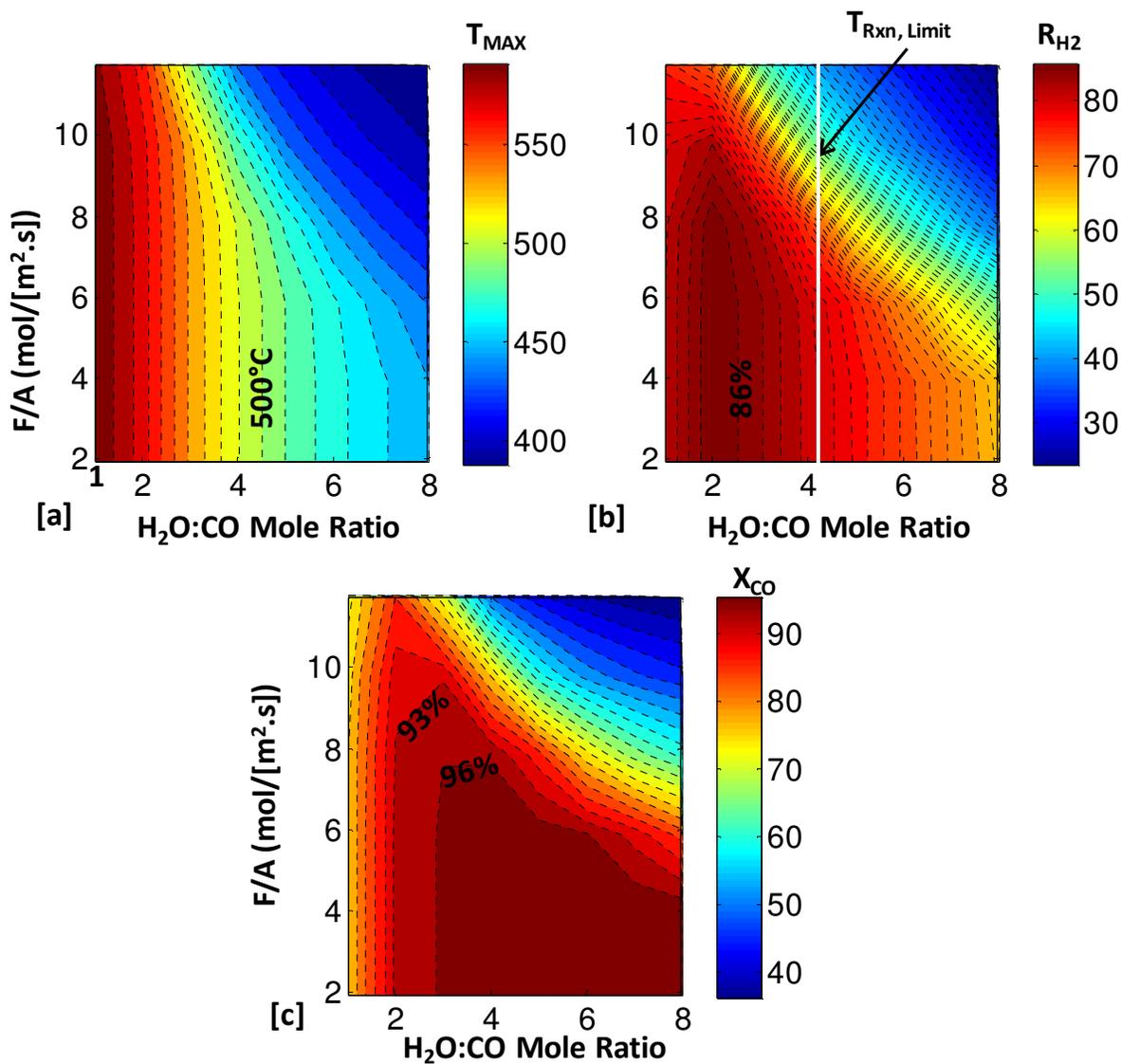
Figure 8-5. Contour plots of [a] $T_{Rxn.Max}$ [b] R_{H2} and [c] X_{CO} as a function of inlet feed flow rate and the mole ratio of $H_2O:CO$ at $T_{Feed} = 350°C$, $P_{Total,Rxn} = 15$ atm, $P_{Tube} = 1$ atm, 50% $\rho_{Bulk,max}$.

Besides the apparent advantages of using excess steam such as decreased reaction side temperatures and shift of reaction to the products side, excess steam could prevent coke formation on the catalyst and/or Pd-Based membrane. If the dry syngas composition and flow rate at the outlet of the scrubber of the gasifier was assumed constant, the variable which could affect the composition of the wet syngas was the steam flow rate at the entrance of the reactor. Note that the possible deviations in the ratio of $H_2O:CO$ might be caused by an error in the ratio controller and/or inappropriate adjustment and/or failure of the valves along the steam feed line

on node 2 in Figure 8-2. An excessive increase of the H_2O:CO ratio (MORE- F_{H_2O}) which was accompanied by an increase of the total feed flow rate, reduced the productivity of the process as mentioned earlier in Chapter 8.2.2. The decrease of the residence time and reaction side temperature below the threshold limits due to an increase in the H_2O flow rate were the main reasons for the deviations from the desired product specifications observed. The increased steam ratio would cause the reaction to proceed to the product side up to the total feed flow rate of 4 mol/[s.m^2]. Any further increase in the steam flow rate would then cause the CO conversion levels to decrease as shown in Figure 8-5 [c]. Since both the H_2 partial pressure and residence time would decrease in the case of a much higher steam flow rate, the H_2 production rate would also decrease due to the decreased driving force for H_2 permeation.

If the extent of the decrease of the H_2O:CO ratio (LESS- F_{H2O}) was drastic, lower than 1, the membrane reactor performance decreased due to the lower CO conversion and H_2 production rates. Moreover, the H_2O:CO ratio had to be kept at 3 and higher to protect the non-isothermal membrane from hot spots. If precautions were not taken in time, the problem of reduced steam flow rate, such as a potential failure of a water pump, could get worse and might end up generating a situation of no steam flow (NO- F_{H2O}). The decreased H_2O:CO ratio below ˜2 (Augustine et al. 2011) and no steam flow conditions could cause coke formation on both of the catalyst and the membrane surface (Xue et al. 1996). Augustine et al. (2011)observed severe coke formation on the first 33% of the spatial domain of the membrane reactor; on the membrane surface as well as on the high temperature Fe-Cr catalyst, with a H_2O:CO ratio of 1.1 after 5 hours of testing at 450°C, 14.4 bars reaction side and 1 bar permeate side pressures . Over the course of coke formation, the H_2 recovery level dropped gradually from 79% to 72%. Thus, monitoring the H_2 production rate closely would allow the detection of any sign of abnormality such as coke formation. Lastly, an unsteady steam feed due to an error in the heat exchanger before node 2 in Figure 8-2 would cause coke formation in the feed lines even before the reactor and clog the pipeline.

Another important point about the possibility of an unexpected decrease in the H_2O:CO ratio is the syngas composition at the gasifier exit which could of course depend on the gasifier technology. The H_2O:CO ratio of the syngas at the exit of the CO hydrolysis unit after the scrubber of the GE Energy, E-Gas and Shell gasifiers were 1.13, 0.63 and 0.03, respectively. If a

significant decrease in H_2O:CO ratio occured, the feed coming from the E-Gas and Shell gasifiers would be affected more drastically than in the GE Energy case.

In addition, plugging of the pipelines and/or the membrane reactor with the accumulation of deposited coke would eventually cause a pressure built up which was a serious safety concern. Depressuring and/or pressure relief systems needed to be placed at various locations to decrease the system pressure in the case of a pressure built up. A detailed discussion about deviations in the reaction side total pressure from normal operating conditions could be found in the following Chapter 8.2.5. Finally, the Fe-Cr based high temperature water gas shift catalyst and the Pd-based membrane had to be regenerated with H_2/steam before the process reverted to the normal operation.

Table 8-3. HAZOP worksheet – Parameter: the H_2O:CO mole ratio

GW	Causes	Consequences	Prevention & Repair
More ($\uparrow F_{H_2O}$*)	Malfunction of the ratio controller on node 2 Inappropriate adjustment and/or failure of the valves	Decreased T_{Rxn}[‡] due low residence time Increased CO conversion up to $F_{Feed} < 4$ mol/[s.m^2] Decreased CO conversion for $F_{Feed} > 4$ mol/[s.m^2] Decreased H_2 recovery and H_2 production rates	Regular maintenance and inspection of the ratio controller and valves A recycle switch from node 4 to node 3 in case of very low CO conversion and H_2 recovery Monitor H_2 production rate and permeate/retentate compositions Extra feed line to replace the line on node 2
Less ($\downarrow F_{H_2O}$*)	(same causes with More and) Leaks on the steam feed line on node 2 Failure of the water pump Error in the steam heating system before node 2	Increased T_{Rxn}[‡] Decreased CO conversion Increased H_2 recovery until H_2O:CO=2 Decreased H_2 recovery below H_2O:CO=2 Coke formation in the membrane reactor starting in zone 1 and/or in the feed line on node 3 if H_2O:CO<2	Backup line between node 1 and 3 Monitor H_2 production rate and permeate composition Inert feed at operating temperature and backup line for the syngas feed for H_2O:CO<2 Refer to HAZOP worksheet for reaction side pressure
No (F_{H_2O}=0)	Blocked outlet of the line on node 2 Complete clogging of the line on node 3 by coke deposition	Increased T_{Rxn}[‡] Decreased CO conversion and H_2 recovery Coke formation in the membrane reactor starting in zone 1 and/or in the feed line on node 3	Regular maintenance and inspection of the water pump and heat exchangers before node 2 Backup line for pipeline on node 2 Controlled release by depressuring in case of clogging on node 3 if the clogging is in the pipe, at the entrance of zone 1 and end of zone 2 if it is in the reactor Regeneration / substitution of the catalyst and/or repair/ substitution of the membrane in case of coking Refer to HAZOP worksheet for reaction side pressure

* ↑ : Increased , ↓ : Decreased

‡ Refer to Table 8-1 for changes in the reaction side temperature

8.2.5 Effect of reaction side total pressure

Since the temperature rise in the reaction zone could be eliminated by using excess steam, other parameters such as reaction and permeate side pressure could be in principle used to enhanced the H_2 recovery levels while inducing a temperature profile in compliance with process safety limits/standards. Unlike the traditional packed bed reactors, the reaction side pressure could have a dramatic effect on the performance of a Pd-based water gas shift membrane reactor. Low levels of R_{H2} and production rate of pure H_2 could be enhanced by increasing the reaction side total pressure thus increasing the driving force for H_2 permeation.

The bulk catalyst density and H_2O:CO ratio were set at 50% of the $\rho_{Bulk,max}$ and 4, respectively. The non-isothermal membrane reactor's performance was evaluated under a reaction side total pressure range of 10-70 atm. Furthermore, the maximum of the reaction side temperature was kept below ~500°C with the aid of excess steam as shown Figure 8-6 [a]. It should be noted that operating at a lower temperature than the limit of 500°C would provide the required time to take action to control the process in the case of any unexpected disturbance upsetting the process system under consideration. The performance target levels of X_{CO} = 98% and R_{H2} = 95% were attained at a reaction side pressure of 35 atm and higher by using H_2O:CO = 4.5 as depicted in Figure 8-6 [b] and [c]. However, there was no available information about how the thin (5-10µm) Pd-Based membrane reactors would behave at industrially relevant conditions for the higher amounts of the pure H_2 production. The high pressure at the reaction side might damage the thin Pd layer on the porous substrate. If the membrane was damaged under the effect of a high reaction side pressure, reactants through the permeate side could reduce conversion, purity of the permeate side and even the reaction side pressure could drop significantly.
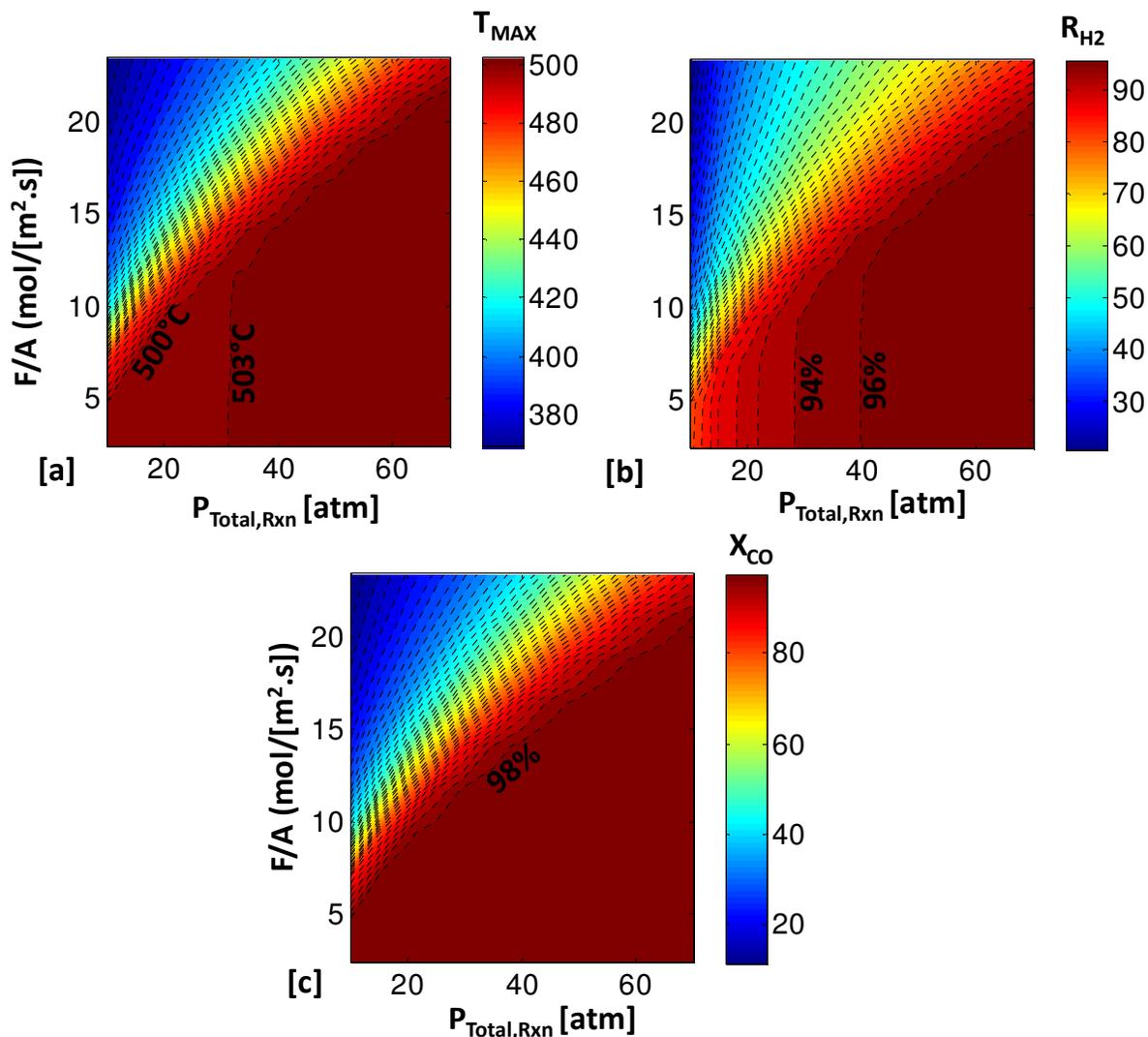
Figure 8-6. Contour plots of [a] $T_{Rxn.Max}$ [b] R_{H2} and [c] X_{CO} as a function of inlet feed flow rate and the reaction side total pressure at $T_{Feed} = 350°C$, $P_{Tube} = 1$ atm, $H_2O:CO = 4.5$ and 50% $\rho_{Bulk,max}$.

Drastic deviations associated with the reaction side total pressure, for example an increase (MORE – $P_{Total,Rxn}$), might arise from a possible malfunction of the compressor and back pressure regulators, plugging or closing of the valves as well as connections at the membrane reactor exit. The higher H_2 partial pressure led to an increase of the driving force and H_2 permeation rate. Consequently, the CO conversion increased while more heat was released from the exothermic water gas shift reaction. The increased heat of reaction at high system pressures might cause the reaction temperature to exceed the temperature limit of the non-

isothermal reactor. As already pointed out, the most effective way of reducing the temperature in the reaction side was shown to be an increase in the steam flow rate for minor and fast reversible pressure increase. In addition, the coke formation in the pipelines and/or in the reactor would cause a gradual pressure increase at the early stages of coke deposition. In such a case, the steam to CO ratio could be increased gradually by decreasing mixed gas feed before the steam addition (at node 2, in Figure 8-2) until the system pressure returned to its desired value. The rate of temperature rise especially at the reactor inlet might be faster than the speed of action of the temperature controller for the isothermal membrane reactor. In that case, hot spots might be a potential hazard for membrane integrity. Another approach to prevent undesirable outcomes would be the partitioning of the whole membrane reactor into several sections. For instance, a membrane reactor module consisting of 3 reactors in series would allow a more controlled operation than in the single reactor case.

For more severe cases such as total blockage of the pipelines or the reactor, emergency relief devices had to be explicitly integrated into the membrane reactor design. Relief systems should be used to avoid over-pressure incidences and alarm systems needed to be set up to warn the employees in the case of an adverse pressure increase. The first level of design should be depressuring to avoid large scale releases followed by pressure relief systems. Even though the pressure relief systems would not be used frequently, they had to be designed for high reliability (1993b). Details about pressure relief systems, such as sizing, installation, relieving rates, selection of disposal system can be found in the API recommended practices 520 and 521 (API 520, 1990; API RP 521, 1990).

When the process fluid was expensive and/or toxic, leakages through a safety valve were not deemed acceptable (Chung et al. 2000). The syngas contains high amounts of poisonous carbon monoxide and explosive H_2 which required usage of either a rupture disk or enclosed safety relief valves which sent the released syngas to a containment vessel instead of disposal to the process environment. In the case of actuation of the pressure relief systems, the discharged syngas should be collected and re-directed to the gas turbine without converting carbon monoxide. If the pressure rise in the membrane reactor was too rapid and the safety valves did not respond as desired then rapture disks had to be placed at the membrane reactor entrance and exit (zone 1 and 3, in Figure 8-2) instead. The combination of a rapture disk-rupture disk-safety relief valve in series (RRS) system could be installed at the latter locations. A weep hole in the

space between the disk and safety relief valve could prevent pressure buildup in the interspace if there was a pinhole on the disk (Chung et al. 2000). Sparing of the relief equipment would provide on-line maintenance of the RRS system by switching and also the process would not need to be shut down for replacement (AIChE report 1993a). Rupture disks are temperature sensitive devices. The rupture disk must operate at pre-specified temperature and pressure levels preventing it from bursting. In addition, a heat-removing device might be needed in the safety relief valve to protect the valve from the hot reaction gas coming from the membrane reactor (API 520, 1990).

Similar to the reasons of the increase of the reaction side total pressure, a possible failure of the compressor and back pressure regulators, plugging or closing of the valves and connections at the zones before the membrane entrance, as well as leakage and defects on the membrane could result in a decrease of the reaction side total pressure (LESS – $P_{Total,Rxn}$). Reduced system pressure could affect the H_2 recovery of the membrane reactor drastically. Finally, notice that the production rate of pure H_2 decreased due to the reduced H_2 driving force and the pressure controllers employed had to respond fast to keep process productivity at the desired target levels.

Table 8-4. HAZOP worksheet – Parameter: reaction side total pressure

GW	Causes	Consequences	Prevention & Repair
More ($\uparrow P_{Total,Rxn}$*)	Malfunction of the compressor and back pressure regulators, plugging or closing of the valves as well as connections at the membrane reactor exit Coke formation in the pipelines and/or in the reactor	Increased T_{Rxn}[‡] Increased CO conversion and H_2 recovery Increased H_2 production rates Runaway reactions Membrane reactor failure by explosion due to excessive pressure	Increase steam flow rate or decrease mixed gas flow rate at node 2 in case of a minor causes, such as misuse of control equipment or initial stage of coke formation Monitor H_2 production rate and permeate composition Depressuring into a containment vessel to be fed to the gas turbine directly The combination of a rapture disk-rupture disk-safety relief valve (RSS) system in series in zone 1 and 3 Use a spare RSS system in parallel with interlocked valves
Less ($\downarrow P_{Total,Rxn}$*)	Failure of the compressor and back pressure regulators, plugging or closing of the valves and connections at the zones before the membrane entrance Leakage and defects on the membrane and pipeline	Decreased CO conversion and H_2 recovery Decreased T_{Rxn}[‡] Decreased H_2 production rates Decreased H_2 purity	Regular maintenance and inspection of the compressor, back pressure regulators, valves and pipelines Monitor H_2 production rate and permeate composition Repair/substitution of the membrane in case of low selectivity

* $\uparrow$: Increased , $\downarrow$: Decreased

[‡] Refer to Table 8-1 for changes in the reaction side temperature

8.2.6 Effect of permeate side pressure

As the driving force responsible for the H_2 permeation was increased, the H_2 recovery and also CO conversion levels could be enhanced. The driving force for the H_2 permeation could be increased by several ways such as through an increase in the reaction side pressure and the application of sweep gas or vacuum on the permeate side. In the present study, neither the application of a sweep gas nor vacuum was considered up to this point. An extra separation unit would be necessary at the permeate side exit when a sweep gas was used. Moreover, the application of vacuum or using steam as the sweep gas might not be favorable in terms of energy consumption. However, the feasibility of the vacuum or sweep gas on the permeate side of the membrane reactor needed to be investigated through a detailed process economic analysis.

The application of vacuum on the permeate side was evaluated in this case to obtain directly pure H_2 without additional time and material requirements related to the use of a separation unit. The main goal was to mitigate the occurrence of any hazardous conditions in case of high reaction side pressures while maintaining high performance target levels of X_{CO} = 98% and R_{H2} = 95%. In particular, the reaction side pressure was kept at a moderately low pressure of 30 atm and the permeate side pressure was changed to fall within the range of 0.1-1 atm with the application of vacuum. The performance target levels could easily be attained by applying vacuum on the permeate side without a significant temperature rise in the reaction side as shown in Figure 8-7 [a]. If the permeate side H_2 pressure could be reduced to 0.2 atm, almost complete CO conversion and very high H_2 recovery could be achieved as depicted in Figure 8-7 [b] and [c]. However, strict caution needed to be exercised to maintain the H_2O:CO ratio of 4.5 and higher and thus kept the reaction side temperature below the maximum temperature limit. As shown in Figure 8-7 [b] and [c], the original performance target levels of X_{CO} = 98% and R_{H2} = 95% were achieved at a permeate side H_2 pressure and reaction side total pressure of 0.55 atm and 30 atm respectively.
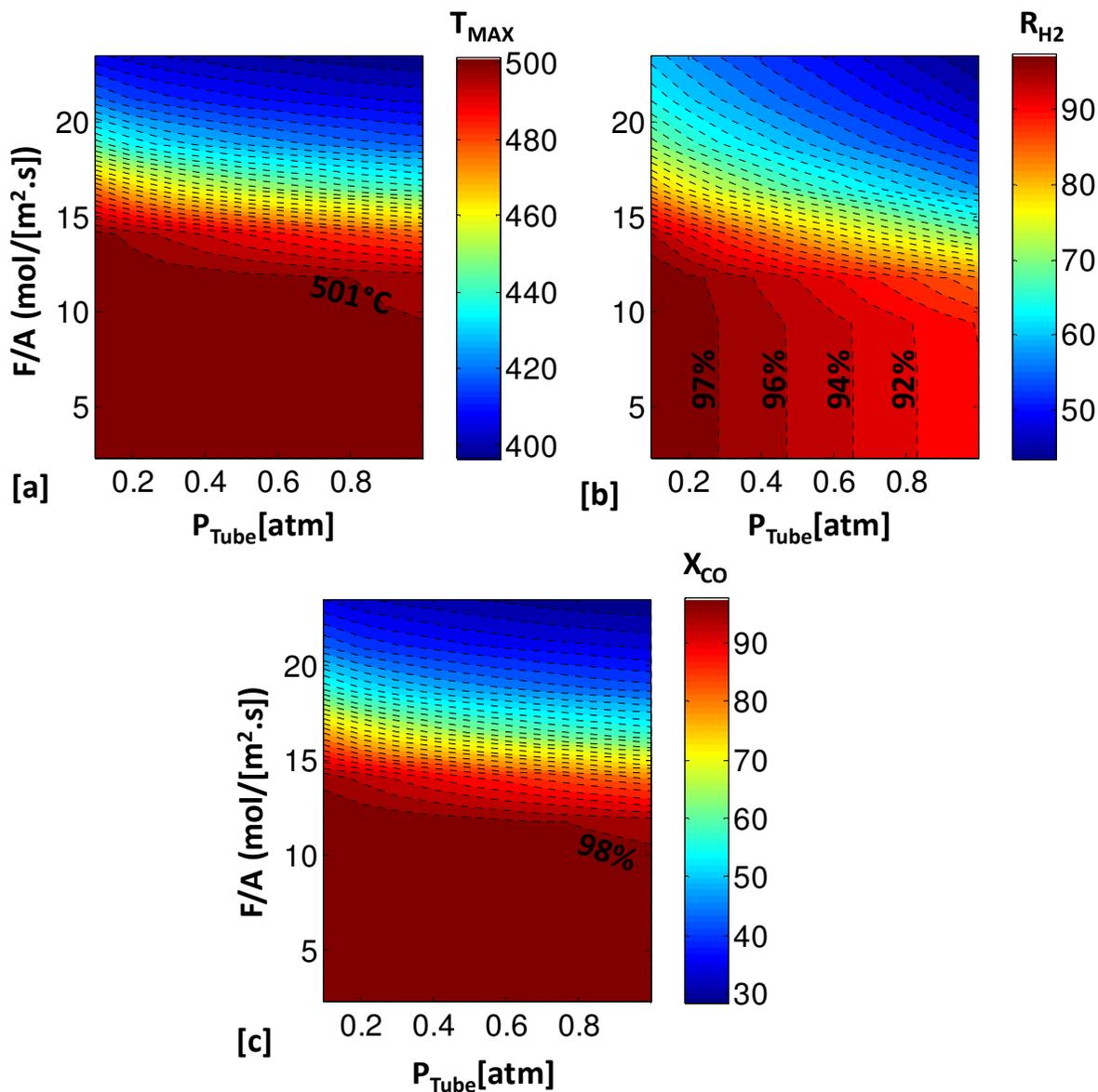
Figure 8-7. Contour plots of [a] $T_{Rxn.Max}$ [b] R_{H2} and [c] X_{CO} as a function of inlet feed flow rate and the permeate side pressure at T_{Feed} = 350°C, $P_{Total,Rxn}$ = 30 atm, $H_2O:CO$ =4.5 and 50% $\rho_{Bulk,max}$.

A blockage at the membrane tube exit would cause the permeate side pressure to reach a higher value than the vacuum pressure. In that case, the tube side pressure would increase up to the partial pressure of H_2 in the reaction side and at this point the permeation would be equal to zero. Thus, a gradual decline in the H_2 production rate without any increase in the reaction side total pressure would indicate a blockage at the membrane tube exit. Another obvious cause for

higher permeate side pressures than the set vacuum pressure would be a possible failure of the vacuum pump at the permeate side exit. Therefore, a vacuum relief valve should be positioned at the permeate side exit to protect the membrane tubes from collapse due to full or very low vacuum.

If the vacuum pump failed, the permeate side pressure would increase up to the atmospheric pressure with a relative decline in permeance, conversion and recovery, but the result would not be as serious as a blockage. The material selection and design of the membrane tubes, connections and H_2 pipeline had to be appropriate for partial and full vacuum conditions.

The extra purity H_2 from the permeate side exit had to be compressed after the membrane reactor for end-use purposes such as electricity production in a gas turbine or hydrogenation/dehydrogenation reactions. If the reaction side pressure was high enough, the permeate side pressure could be higher than the atmospheric pressure for various design purposes such as the reduction of the H_2 compression costs. A malfunction of the valves and/or pressure regulators would cause a deviation as well. The pertinent discussion and recommendations in the case of unexpected deviations in the permeate side pressure are summarized in Table 8-5.

Table 8-5. HAZOP worksheet – Parameter: permeate side pressure

GW	Causes	Consequences	Prevention & Repair
More ($\uparrow P_{Tube}$*)	Blocked outlet of the membrane tube Failure of the vacuum pump	Decreased CO conversion and H_2 recovery Decreased T_{Rxn}[‡] Decreased H_2 production rates Decreased H_2 purity	Monitor H_2 production rate and permeate composition Regular maintenance and inspection of the vacuum pump, connection points between the membrane tubes and the pipeline for the following units and valves Membrane tube and H_2 pipeline designed for partial or full vacuum condition
Less ($\downarrow P_{Tube}$*)	Malfunction of the vacuum pump Misuse of a manual/auto valve at the exit of the membrane tube exit (if any)	Increased CO conversion and H_2 recovery Increased T_{Rxn}[‡] Increased H_2 production rates Increased H_2 purity	Same with $\uparrow P_{Tube}$ and Vacuum relief valve actuates at the low pressure limit and to admit inert He into the tube side

* ↑ : Increased , ↓ : Decreased

[‡] Refer to Table 8-1 for changes in the reaction side temperature

8.2.7 Impurities in the feed stream

A possible malfunction of the gas cleaning unit located before the membrane reactor could produce unacceptable levels of impurities. Pure Pd and Pd-Alloy membranes lose their high permeance values partly or completely in the presence of impurities such as H_2S in the feed stream (MORE-F$_{Impurity}$). The formation of Pd_4S at 320°C with a concentration of 20 ppm H_2S/H_2 was observed in Pd foil experiments (Mundschau et al. 2006). Micro-defects may form on the pure palladium surface due to changes in the lattice parameter and membrane selectivity declines when Pd_4S was formed (Kulprathipanja et al. 2005; Kajiwara et al. 1999). Therefore, if a pure palladium (or Pd/Ag) membrane is utilized in the reactor and the feed steam is not H_2S free, membrane selectivity and H_2 purity of the permeate flow could decrease significantly. Chen and Ma (2010b) showed that after exposure of a pure palladium membrane to a 54.8 ppm H_2S/H_2 mixture, no permeance recovery was possible due to the irreversible formation of bulk Pd_4S. As a result, the replacement of the poisoned pure palladium membrane is necessary to maintain high productivity levels of the process. Pd-Alloy membranes, particularly Pd-Au and Pd-Cu, have the advantages of permeance recovery and selectivity stability of the Pd-based membrane after poisoning (Pomerantz and Ma 2009; Chen and Ma 2010b). Membrane reactors, in which Pd-Au and Pd-Cu membranes are utilized, should be regenerated with H_2 after exposure to H_2S to increase the permeance of the membrane. Finally, the placement of the gas composition analyzers at the entrance of the membrane reactor and at the exit of the permeate side is crucial in order to take fast action when needed and prevent potential poisoning. The summary of results related to the case of impurities in the membrane reactor feed stream can be found in Table 8-6.

The sulfur containing gases may not be the only impurities in the feed stream of the membrane reactor. The effect of other trace impurities, such as As, P, Sb, Zn, Cl, Hg, Cd and Se (Cayan et al. 2008), on the Pd/alloy-based membranes is still unknown and has to be investigated for industrial scale applications.

Table 8-6. HAZOP worksheet – Parameter: impurities

GW	Causes	Consequences	Prevention & Repair
As well as (impurities such as H_2S)	Error and/or malfunction of the gas cleaning units before the membrane reactor	Poisoning of the membrane For pure Pd membranes: decreased and even demolished selectivity and permeance For Pd/alloy membranes, particularly Pd/Au and Pd/Cu: decreased but recoverable permeance Catalyst poisoning Corrosion in the membrane reactor equipment Decreased CO conversion and H_2 recovery Decreased T_{Rxn}[‡] Decreased H_2 production rates Decreased H_2 purity	Regular maintenance and inspection of the gas cleaning unit before the membrane reactor Monitor H_2 production rate and permeate composition Gas composition analyzer before the membrane reactor inlet Substitution of the pure Pd membrane and catalyst Regeneration of the Pd/Au or Pd/Cu membrane Poisonous gas detectors outside the membrane reactor module sensitive to both CO, H_2 and sulfur containing gases for the health safety Automatically activated inert purge system with remote control

[‡] Refer to Table 8-1 for changes in the reaction side temperature

8.3. Conclusions

A standard Hazard and Operability (HAZOP) analysis was pursued to identify potential hazards as well as failure modes and hopefully prevent potential risks to personnel, environment, equipment and/or process efficiency and performance. In particular, the effect of variations (random or intentional) in the total feed flow rate and temperature, catalyst loading, $H_2O:CO$ ratio, reaction and permeate side pressures and purity of the feed on the process state in the form of possibly adverse process excursions/deviations from normal operating conditions was considered as part of a process safety analysis protocol associated with Pd-based membrane reactors. The absence of adequate control of the reactor temperature as well as the purity of the feed which might cause hot spots and decline in permeance and selectivity were identified and classified as critical for the operation of the WGS membrane reactor. The utilization of excess steam together with the application of vacuum on the permeate side were found to be the most effective method of reducing the temperature rise in the reaction zone without decreasing the overall CO conversion and H_2 recovery. Since the main advantage of the Pd/alloy based membrane reactor technology was the high-quality H_2 separation driven by the H_2 partial pressure difference between the reaction and permeate sides, operation at high reaction side pressure was desirable. Therefore, the high pressure reactor operation represented a process safety challenge. Proper material selection, stringent process monitoring and control together with multiple pressure relief systems had to be explicitly integrated into process system design as a part of a comprehensive process intensification strategy. If the suggested precautionary measures were taken by considering the possible consequences of the aforementioned deviations from normal operating conditions as identified through the proposed membrane reactor modeling framework, the membrane reactor could be operated safely without compromising high performance at 98% CO conversion and 95% recovery of extra pure (99.9999%) H_2.

9. A Dusty Gas-Based Modeling Framework to Characterize the Selectivity of Pd/Alloy-Based Membrane Reactors

9.1. Introduction

Primary desired features of Pd or Pd/alloy membranes include sulfur tolerance, easy fabrication independent of geometry, as well as thin and highly selective Pd layers. In particular, selectivity of Pd-based membranes is critically linked to PEM fuel cell applications. Furthermore, low selectivity values may decrease CO conversion and H_2 purity on the permeate side. In light of the above considerations, the objective of the the Chapter 9 was to develop a systematic and insightful membrane reactor modeling framework that explicitly took into account the multi-component gas diffusion through the defects in the membrane. Within the proposed framework, the detailed mass balance equations of an isothermal steady state mathematical model for Pd-based membrane reactors were coupled with the equations of a multi-component gas diffusion model through the defects of the membrane. In particular, the proposed multi component gas diffusion model through the membrane defects was structurally realized through the Dusty Gas Model (DGM) (Mason and Malinauskas 1983) and had the capacity to quantitatively characterize the H_2 purity of the permeate flow. The permeation of H_2 was described by two transport mechanisms; the diffusion in the porous parts of the Pd layer (defects) and the solution diffusion in the dense Pd layer.

To account for the leak growth in the dense Pd layer, the proposed modeling framework was appropriately modified by the addition of a new permeation model based on an integration of the Dusty Gas Model (DGM) with a standard solution diffusion model. The modified model had the capacity to characterize the mass fluxes of all components (CO, H_2O, CO_2 and H_2) in the permeate side as well as the H_2 separation factor profile along the length of the reactor.

9.2. Results and discussion

The low selectivity values may decrease the CO conversion and H_2 purity from the permeate side. Thus, the objective was to develop a mathematical model which took the multi-component gas diffusion through the defects in the membrane into account. The one dimensional isothermal steady state mathematical model for the Pd-based membrane reactors was enhanced with the addition of the multi-component gas diffusion through the defects on the membrane. The multi component gas diffusion through the defects was described by the Dusty Gas Model and the model was able to predict the H_2 purity of the permeate flow. The permeation of H_2 was described by two transport mechanisms; the diffusion in the porous parts of the Pd layer (defects) and the solution diffusion in the dense Pd layer.

The current Pd-based membrane fabrication technique had limitations. For instance, as the Pd thickness was decreased the H_2 permeances were increased and, in contrast the ideal selectivity was decreased resulting into lower H_2 purity as shown in Figure 9-1. One should keep in mind that the US DOE target levels were set for fuel cell grade H_2 (99.99%) production. The H_2 product of the water-gas shift membrane reactor could also be used for electricity production and a H_2 purity level higher than 94% to be sent to the gas turbine (Haslbeck et al. 2010) would be sufficient. Thus, the membrane reactor model with the multi-component gas diffusion through the defects could help to screen the fabricated membrane for their end use.
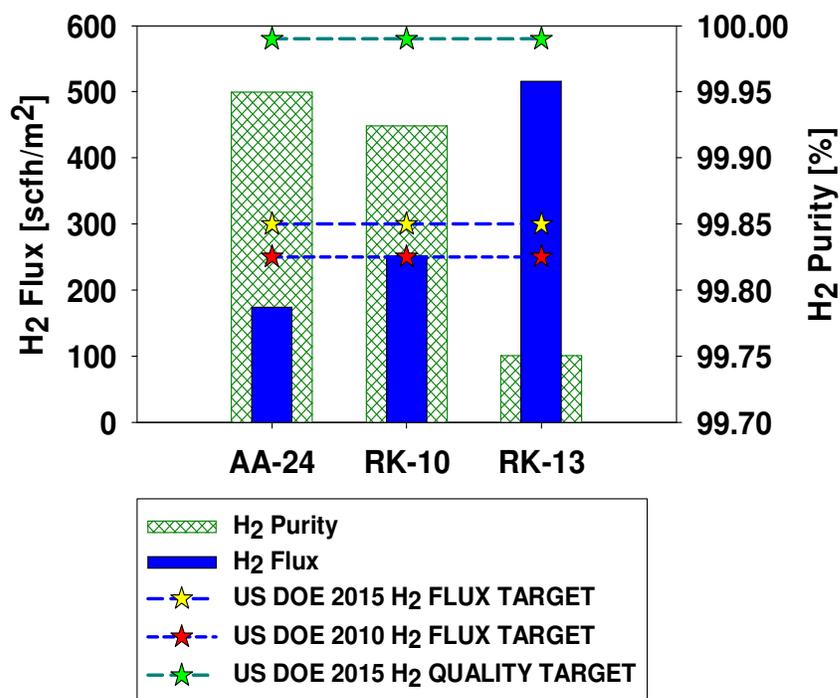
Figure 9-1. H_2 flux and purity comparison with the US DOE target levels[*]

The theory of the Dusty Gas Model built on a surprisingly simple idea was used in the following simulations. The matrix particles (porous media) were assumed to be giant gas molecules ('dust') in an ideal gas mixture. The thermal motion of the dust particles were assumed to be negligible because they were so large. The multicomponent gas transport in porous media is a complex phenomenan which may involve the following mechanisms:

- Knudsen flow (free-molecular): the collision of the molecules with each other compared to the collision of molecules with the walls of the porous structure might be ignored when the gas density is low enough. The Knudsen equation describes the diffusion in solids where the pores are smaller than the mean free path of the gas.

- Viscous flow (convective flow): the gas flows continuously and the driving force for the flow is the pressure gradient. In convective flow, the effect of molecule-molecule

---

[*] The properties of the membrane AA-24 which were tested under water-gas shift reaction conditions were taken from Augustine et al. {{270 Augustine,Alexander S.; }}.

collisions is more significant than the molecule-wall collisions. The viscous velocity is decribed by the Poiseuille equation and it is very small in narrow pores.

- Continuum diffusion: concentration gradient (molecular diffusion) and/or temperature gradients (thermal diffusion) are the cause of movement of different species relative to each other.

- Surface flow/diffusion: molecules move olang the along the surface due to adsorption.

During membrane fabrication, as the number of pores are decreased and the pores get narrow, both of the Knudsen and viscous flow diminishes. As the membrane gets dense, viscous flow approaches zero earlier than the Knudsen flow due to decreasing pore size on the membrane surface. In contrast, the number and size of the pores of the defects get larger as the tesing time increases for membranes with leaks. For instance, the difference in the ideal selectivity and pore diameter reported in Table 9-2 for RK_10 reflected the change in Knudsen/viscous flow at two different testing times. The He permeance of 0.0022 m^3/[m^2-h-atm] with $\alpha_{H2/He}$ = 7704 included only Knudsen flow whereas the He permeance of 0.013 m^3/[m^2-h-atm] with $\alpha_{H2/He}$ = 1320 was the combination of both viscous and Knudsen flow because of the enlargening of the pores due to leak growth. The DGM model simulation results were compared with the experimental results of the two membranes at different sizes, one was a lab-scale membrane (AA_24) with a surface area of 25 cm^2.The details of the characteristics of the membrane AA_30 and also water-gas shift reaction conditions were listed in Table 9-1.

The defects in the Pd layer were assumed as cylindirical pores and the physical properties of the defects were determined by measuring the He, N_2 and Ar permeance of the defected Pd-based membranes at various transmembrane pressure differences. The ratio of α/β was used to determine pore diameter of the defect by using Eq (3.37) and then the ratio of porosity over tortuosity was determined by using the pore diameter of the defect and the α value. The experimental results to determine the DGM parameters such as pore diameter and effective Knudsen diffusion coefficient were listed in Table 9-2.

Table 9-1. Water-gas shift membrane reactor parameters for the DGM

Parameter ↓	AA_30 (Augustine et al. 2010)
I.D. of the shell casing, x_2 [cm]	2.54
O.D. of the membrane tube, x_1 [cm]	1.27
The total length of the membrane [cm]	6.35
Wall thickness of the membrane tube [mm]	1.5
H_2 permeance $m^3/[m^2\text{-}h\text{-}atm^{0.5}]$	$28_{@400°C}$
Reaction side P [atm]	15
Permeate side P [atm]	1
Reaction T [°C]	400
GHSV [h^{-1}]	1375
Syngas composition [%]	19 CO
	55 H_2O
	8 CO_2
	18 H_2

The membrane AA_30 (Augustine et al. 2010) was tested under water –gas shift conditions for ˜1000 hours. The He permeance of the membrane was taken twice at time equaled 400 hours and 1000 hours and the corresponding leak data were listed inTable 9-2. The membranes RK_10 and 13 were not tested under water-gas shift conditions; however, their properties were used to estimate the permeate compositions if they would have been used under under reaction conditions. The values of porosity over turtuosity (ε/τ) for the defected Pd layer was changing between 4.42×10^{-6} and 1.97×10^{-3} for the membranes RK_10 with an ideal H_2/He selectivity of 7700 and the membrane RK_13 with an ideal H_2/He selectivity of 414 at $\Delta P = 1$ bara, respectively. The value of the ε/τ for the high selectivity membrane RK_10 was compatable with the literature data of 5.11×10^{-8} for a 20 µm thick Pd based membrane with an ideal H_2/N_2 selectivity of 4200 at $\Delta P = 1$ bara (Mardilovich et al. 1997). Moreover, the pinhole diameters listed in Table 9-2 were compared with the data reported by Guazzone et al. (2008) for a wide range of selectivity values. The pinhole diameters of the defects on the same type of Pd based membranes supported on porous stainless steel substrates were changing between 2.7 and 0.04µm with a standard error of 20% (Guazzone and Ma 2008).

Pure Pd based membranes may have leaks in two major forms: (1) large and sudden leak growth due to H_2 emmbrittlement when the membrane is exposed to H_2 at temperatures lower than 300°C and (2) small and gradual leak growth due to incoherent sintering of the ultrafine (100 nm Pd cristallites) which leads to micropore formation in the Pd layer because of local densification of differential shrinkage (Guazzone and Ma 2008). None of the membranes listed in Table 9-2 have experienced H_2 emmbrittlement and thus, the gradual leak growth was the cause of the He permeances of the membranes listed in Table 9-2.

The leak measurements were taken twice at testing times of ~30-406 hours and 67-1003 hours for the membranes RK_10 and 13, respectively. Since both of the defect ratios (ρ_{defect}) and pinhole diameters increased with testing time as listed in Table 9-2 for RK_10 and 13, the increase in the He permeance values of the membranes RK_10 and 13 listed in Table 9-2 could be caused by the enlargement of the pinhole diameters and the increase of the number of pinholes on the membrane surface, which was reflected by ρ_{defect}. For the membrane AA_30, since the pinhole diameter was decreased as the defect ratio was increased with testing time, the cause of increased He leak could be the increase in the number of smaller pinholes compared to the pinhole diameter at the beginning of the test.

The detailed results of the DGM simulation are given in Table 9-3 in terms of permeate composition, hydrogen recovery (R_{H2}) and CO conversion. In addition, the results tabulated in Table 9-3 were plotted as a function of $D_{knudsen,effective} \times \rho_{defect}$ at 400°C for He as shown in Figure 9-2. Since most of the CO was converted in the first 30% of the volume of the membrane reactor, the concentration of the CO_2 and H_2O were much higher than CO in the shell side, and as a result, the permeate concentration of the CO_2 and H_2O were higher than the ones for CO as listed in Table 9-3. More importantly, the membrane selectivity did not influence the overall CO conversion and H_2 recovery levels significantl, whereas the H_2 purity levels in the permeate side was decreased drastically with the decreased He permeance values of the defected membranes.

A good match was obtained between the CO concentrations calculated by the use of membrane reactor simulation with the DGM and the ones determined experimentally (the long term water-gas shift membrane reactor experiments performed with the membrane AA-30 (Augustine et al. 2010), as shown in Figure 9-2 [a]. The experimentally determined CO levels in the permeate flow were higher than the simulated values. The DGM model was implemented in

the one dimensional water-gas shift membrane model as explained in Chapter 3.3. In the one dimensional model, the radial concentration gradient in the reaction side was neglected, thus the H_2 concentration on the membrane surface was higher than its actual value and consequently, the concentration of CO, CO_2 and H_2O were lower than their actual values. Therefore, the lower driving force for CO, CO_2 and H_2O in the DGM explains the lower values of the simulated results compared to the experimentally measured values shown in Figure 9-2 [a].

Even the membranes with comparatively low selectivity values (RK_13, $\alpha_{H2/He}$ = ~118 and $D_{knudsen,effective} \times \rho_{defect}$ = 3.5×10^{-8} m^2/s) was shown to have the potential to be used for the electricity production in power plant application with an H_2 purity of 96% (F-Class Gas turbine H_2 purity limit = 94% (Haslbeck et al. 2010)) as shown in Figure 9-2 [b]. More importantly, both H_2 purity of 99.99% for fuel cell grade H_2 production and flux target of 250 scfh/m^2 specified by the DOE could be easily achieved by using a Pd-based membrane having ~39 m^3/[m^2-h-atm$^{0.5}$] H_2 permeance and ~8000 ideal H_2/He selectivity.

Table 9-2. Parameters used in the DGM

Membrane Label	T [°C]	Pe_{He} [m³ / (m².h.atm)]	Pe_{H2} [m³ / (m².h.atm$^{0.5}$)]	Ideal Selectivity @ΔP = 1 atm	Pinhole diameter, d_p [μm]	ρ_{defect} [-]	$D_{knudsen,effective}$ [m²/s] He at 400°C
RK_10	400	0.0022	41.3	7703.8	1.032774	0.0085	2.88E-09
RK_10	400	0.0129	41.3	1320.3	1.876621	0.049	5.23E-09
RK_13	450	0.0874	87	414.3	0.043865	0.134	5.46E-08
RK_13	350	0.217	62.1	118	0.144805	0.332	1.05E-07
AA_30	400	0.0049	28.57	2415.1	1.99	0.094	5.54E-09
AA_30	400	0.024	28.57	493.1	0.428	0.46	1.37E-08

*Leak measurements for the membrane M-06 was taken after the membrane was removed from the reactor at the end of water-gas shift reaction.

The He leak during the water-gas shift reaction test was reported as 0.0168[m³ / (m².h.atm)] at 400°C at ΔP=1bara.

Table 9-3. The DGM simulation results

Label ↓	Permeate composition CO	H_2O	CO_2	H_2	Dry H_2 purity	X_{CO}	R_{H2}
RK_10	0.0009%	0.02%	0.01%	99.97%	99.99%	98.57%	87.05%
RK_10	0.0157%	0.35%	0.24%	99.40%	99.75%	98.55%	87.08%
RK_13	0.1304%	1.38%	0.80%	97.69%	99.05%	98.36%	87.06%
RK_13	0.3233%	6.73%	4.35%	88.59%	94.98%	98.03%	87.52%
AA_30	0.0355% (0.0371%$_{Exp}$)	0.73%	0.50%	98.74%	99.46%	98.52% (98.1%$_{Exp}$)	87.10% (88.6%$_{Exp}$)
AA_30	0.1974% (0.2597%$_{Exp}$)	2.43%	1.63%	95.74%	98.13%	98.25% (97.2%$_{Exp}$)	87.14% (86.9%$_{Exp}$)
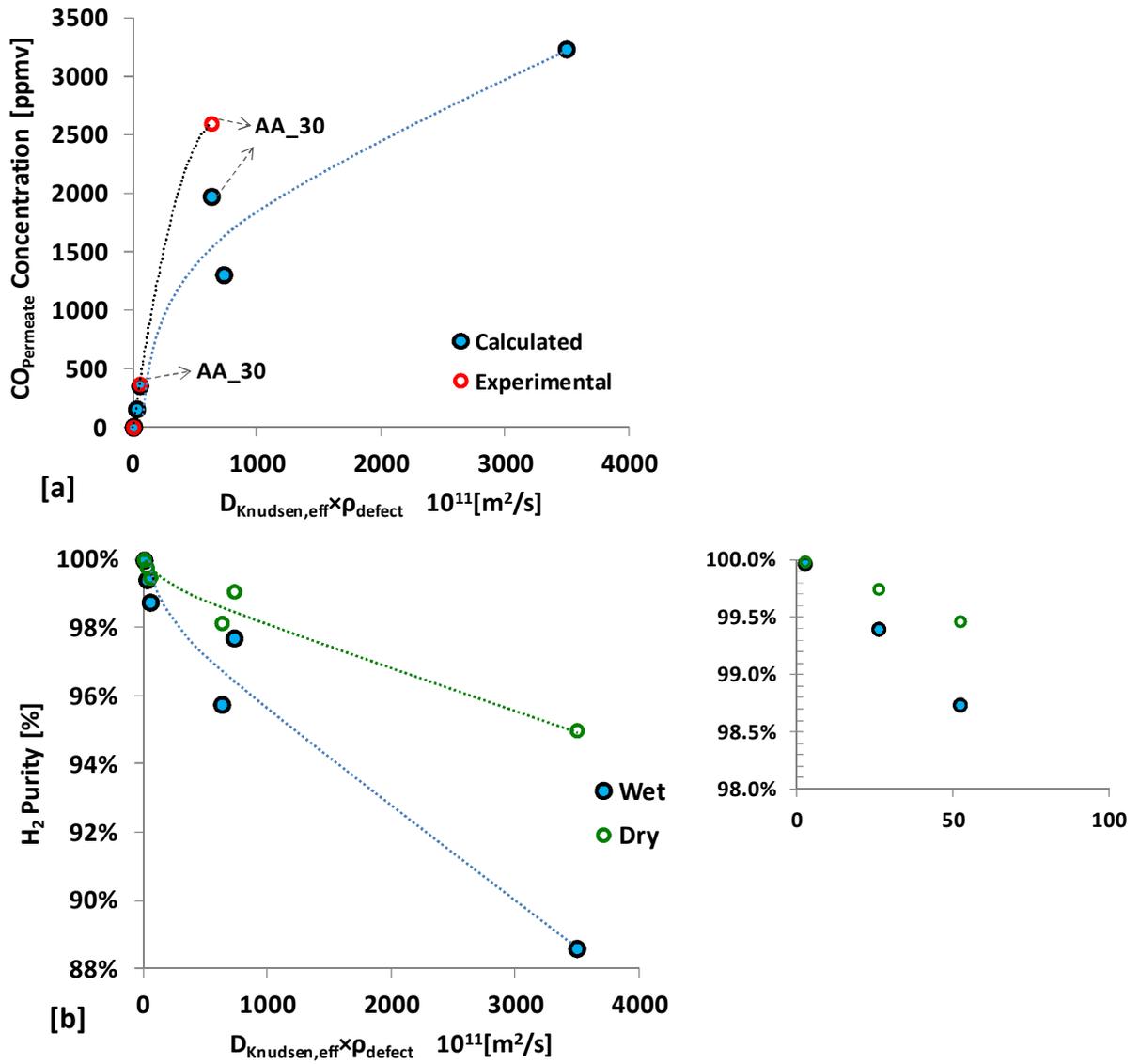
Figure 9-2. [a] CO concentration levels in the permeate flow [b] H_2 purity levels of the Pd-based membranes in the ideal selectivity range of ~118-7700 for reaction conditions of AA_30 (The dashed lines was drawn for eye guidance)

9.3. Conclusions

To account for the leak growth in the dense Pd layer, the one dimensional steady state model was modified by the addition of a new permeation model which is based on the combination of the Dusty Gas Model and the solution diffusion model. The modified model was able to predict the mass fluxes of all components (CO, H_2O, CO_2 and H_2) in the permeate side and the H_2 separation factor along the length of the reactor. Even though the membrane selectivity did not affect the CO conversion significantly, it had a strong effect on the purity levels of the separated H_2 for the membranes having ideal H_2/He selectivity values between 118 and 7700. The membranes having low ideal selectivity values (~100) could still be used to produce H_2 for electricity production and fuel cell grade H_2 could be produced through the use of highly selective membrane with ideal selectivity values higher than ~7000.

10. Pd/Au-Based Membrane Reactor Technology Option Integrated into IGCC Power Plants: An Economic Evaluation in the Presence of Uncertainty

10.1. Introduction

A comprehensive economical analysis was performed for the Pd/Au-based membrane reactor integrated into an Integrated Gasification Combined Cycle (IGCC) plants (IGCC-MR). In particular, a detailed Net Present Value (NPV) model has been developed to evaluate the economic viability of an IGCC-MR plant. The project value of the IGCC-MR was compared with the other options such as Supercritical Pulverized coal, baseline IGCC and IGCC with traditional shift reactors with and without CO_2 capture systems. Moreover, sources of irreducible uncertainty (market, regulatory and technological) are explicitly recognized such as the power plant capacity factor, Pd price, membrane life time and CO_2-taxes due to future regulatory policies. The effect of the above uncertainty drivers on the project's/plant's value was carefully taken into account by a Monte-Carlo simulation technique that enabled the propagation of the above uncertain inputs through the NPV-model, and therefore, generated a more realistic distribution of the plant's value rather than a single-point/estimate that overlooked these uncertainties. In the presence of 11 uncertain inputs, Monte-Carlo techniques suggested that regulatory action on CO_2 emissions would induce a more appealing NPV-profile for the IGCC-MR technology option.

In addition, the economic viability of an IGCC-MR plant, where the membrane reactor module design conformed to basic inherent safety principles, was evaluated with a detailed Net Present Value (NPV) model. The simulation results suggested that process safety investments on

concrete safety risk-reducing measures might result in enhanced IGCC-MR economic performance in the presence of irreducible uncertainties

.

10.2.   Results and Discussion

A comprehensive two-dimensional (2D) membrane reactor modeling framework has been developed to take into account the radial concentration gradients and pressure drop of the Pd-based membrane reactors (Adams and Barton 2009; De Falco et al. 2007; Tiemersma et al. 2006; Boon et al. 2011). The main objective of the 2D model was to assess the membrane reactor performance in a better fashion than the one-dimensional model in which the H_2 recovery levels were overestimated and the calculated membrane areas were less than the actually required. The main structure of the 2D membrane reactor model was presented in the 3rd Chapter. The composite Pd/Alloy-based membrane was assumed to be mounted at the center of a stainless steel shell casing. The Pd/Alloy-based membrane was on one side of the inner stainless steel tube and the entrance of the inner tube at the membrane side was blocked with a cap, while the other side was located at the reactor exit. The annular space between the shell casing and the membrane was assumed to be filled with high temperature water gas shift catalyst.

As mention earlier, Pd/Au alloy composite membranes have increased resistance against sulfur poisoning. Pd/Au alloys showed higher hydrogen permeability than pure Pd for Au contents below 20 wt% and also higher sulfur tolerance compared to other Pd alloys (Knapton 1977a; McKinley 1967; Gryaznov 2000). Chen and Ma (2010b) conducted poisoning experiments by using an 18.1 µm thick Pd/Au composite membrane with 8 wt% Au in 54.8 ppm H_2S/H_2 at 400°C for 4 hours and managed to recover essentially 100% of the permeance in H_2 at 500°C. Furthermore, the optimum Au composition to attain maximum performance in the presence of H_2S up to 5 ppmv was determined to be in the range of 10 – 30 wt% by Chen and Ma (2010a). In addition, a 17 µm thick Pd- based membrane lost 15% of the permeance after alloying the pure Pd with an 12.3 wt% Au layer and, then the same membrane retained ~80% of its permeance after exposure to 1 ppmv H_2S for 24 hours. Furthermore, 100% of the H_2

permeance of the Pd/Au$_{12.3wt\%}$ membrane was recovered in H$_2$ flow at 500°C (Chen and Ma 2010b) after exposure to H$_2$S.

Pd/Au composite membranes were used in the economic analysis for two reasons: 1) to retain high permeance in the presence of trace amount of sulfur containing gases, 2) to have the flexibility to recover the membrane permeance in the occurrence of feeding with high sulfur concentration. The H$_2$ flux of the membrane was assumed to follow Sieverts' Law (Sieverts 1907) and expressed with the Eq (8.2) by considering the permeance loss due to Au alloying and 1 ppm H$_2$S poisoning effect.

$$J_{H_2} = \Phi_{\text{Au Alloying}} \cdot \Phi_{H_2 \text{S poisoning}} \frac{Q \cdot \Delta P_{H_2}^{0.5}}{l} \tag{8.2}$$

where Q is the permeability (m^3.µm/[m^2.h.atm$^{0.5}$]), $\Phi_{\text{Au Alloying}}$ is the permeance decline coefficient due to alloying 12%wt Au (85%), $\Phi_{H_2 \text{S poisoning}}$ is the permeance decline coefficient due to exposure to 1 ppm H$_2$S at 450°C (80%) and l is the membrane thickness (µm).

Table 10-1. Feed specifications, reaction conditions and membrane permeance

Total inlet flow rate to the MR [mol/s](Haslbeck et al. 2010)	9575.2 (8191 w/o CO$_2$ comp.)
Feed composition [%]	CO: 23 - CO$_2$:9 - H$_2$:22 - H$_2$O: 46
Reaction temperature [°C]	400
Reaction side pressure [atm]	50
Permeate side pressure [atm]	1
Permeance [m^3 /[m^2.h.atm$^{0.5}$]	38.94
Bulk catalyst density [kg/m^3]	990.4

Quite promising simulation results were found in satisfactory agreement with experimental findings involving both a lab-scale (0.5"OD$_M$×1"OD$_S$×2.5"L) membrane reactor (Augustine et al. 2011) and a pilot scale (1"OD$_M$×2"OD$_S$×10"L) membrane reactor within the GHSV range of ~1000-6000 h^{-1} as shown in the Figure 10-1. The 2D membrane reactor model was operated under the feed specifications, reaction conditions and permeation properties given in Table 10-1. The solid catalyst density of the high temperature shift catalyst was 2476 kg/m^3

(Adams and Barton 2009) and the void fraction of the catalytic bed was assumed to be 0.5. The minimum amount of catalyst, which would still be enough to achieve the target CO conversion and H_2 recovery levels, was also determined through the modeling efforts. The catalytic bed was assumed to be filled with 80 wt% catalyst and 20 wt% inert packing such as quartz sand.
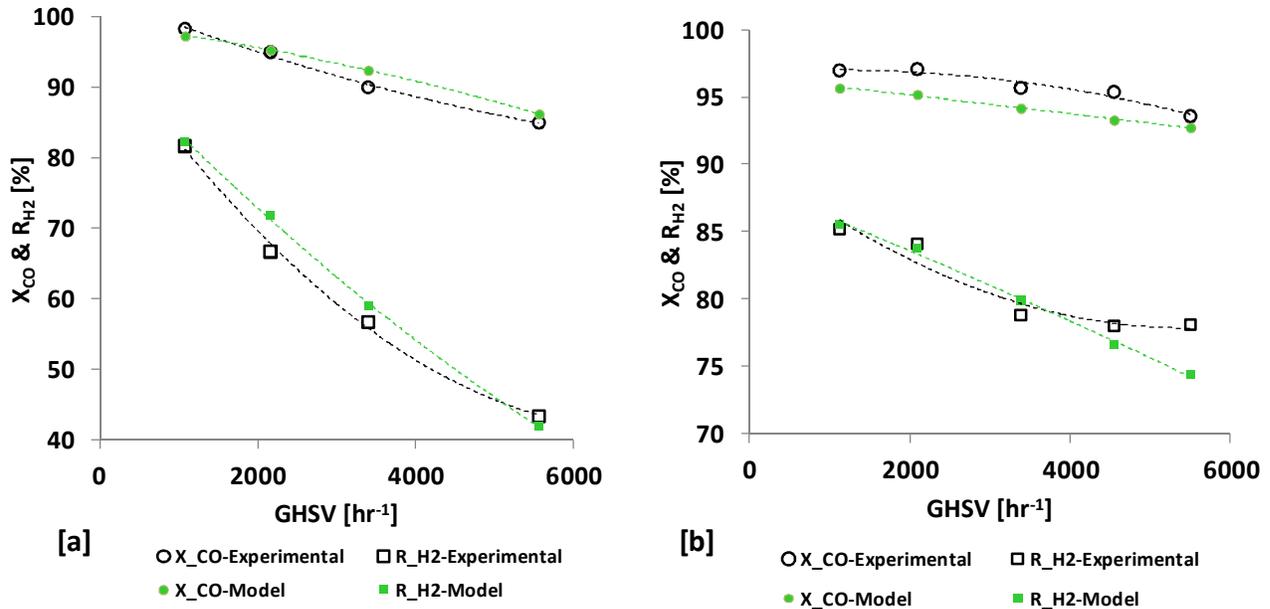
Figure 10-1. Comparison of the simulation results with the experimental data for [a] a lab-scale membrane reactor with a surface area of 0.0024 m^2 (Augustine et al. 2011)and for [b] a pilot scale membrane reactor with a surface area of 0.02 m^2(Catalano et al. 2011).

The dimensions, total feed flow rates and exit flow rates of the single membrane tube and also the whole water gas shift membrane reactor, which also conformed to the industrial scale IGCC plant load specifications, are provided in Table 10-2. Since the total number of Pd-based membrane tubes was quite high, the membrane reactor module was assumed to consist of 8 bundle reactors in parallel, each having 1073 membrane tubes (with CO_2 compression case). Based on the 2D membrane reactor model calculations, the Pd-based membrane reactor with the aforementioned dimensions was able to achieve ~98% CO conversion and 95% H_2 recovery. Since the membranes were assumed to have infinite selectivity, pure H_2 at a flow rate of 0.48 mol/s (from each tube) could be produced. The retentate stream (membrane reactor exit) composition was calculated as 0.84% CO, 41.08% H_2O, 55.14% CO2 and 2.94% H_2 with a total

flow rate of 0.64 mol/s from each tube. The H_2 composition of the retentate stream could be reduced with the application of either vacuum from the permeate side or sweep gas.

Table 10-2. Industrial scale membrane reactor specifications used for cost analysis

Single membrane tube		Water gas shift membrane reactor module		
			w CO_2 comp.	w/o CO_2 comp.
Pd thickness [μm]	6.8	Total Pd weight [kg]	1064	910
Au thickness [μm]	0.58	Total Au weight [kg]	145	124
OD of the membrane, x_1 [cm]	5.08	No of membrane tubes	8584	7343
ID of the shell casing, x_2 [cm]	7.62	# of bundle MR in series	8	8
Length of the membrane, L [m]	9.525	Total V_{shell} [m^3]	372	319
Membrane area [m^2]	1.52	Total area [m^2]	13043	11157
$V_{annulus}$ [m^3]	0.02	Total $V_{annulus}$ [m^3]	207	177
$F_{total, in}$ [mol/s]	1.12	Total $F_{total, in}$ [mol/s]	9575	8191
$F_{CO_2, exit}$ [mol/s]	0.35	Total $F_{CO_2, exit}$ [Mtonne/year]	4.2	3.6
$F_{H_2, exit}$ [mol/s]	0.48	Total $F_{H_2, exit}$ [kg/s]	8.2	7
$W_{catalyst}$ [kg]	23.89	Total $W_{catalyst}$ [tonne]	205	175

10.2.1 Membrane Reactor Module Cost

The cost analysis of the industrial scale Pd/alloy-based composite membrane reactor was conducted by considering capital-investment costs, manufacturing costs and general expenses. The details of the fixed-capital investment and total product cost calculations (Peters and Timmerhaus 1991) for the Pd/alloy-based water gas shift membrane reactor are detailed in Table 10-3 and Table 10-4, respectively.

The cost of the Pd-based membranes supported on 316L PSS supports was mainly dependent on the support, Pd cost and thickness for this particular case. A fairly thick Pd/Au layer of ~7.4 μm was used in the calculations and the cost could be reduced further by decreasing

the Pd/Au thickness. It should be pointed out that the support cost would be much higher than the 316L PSS supports if the Pd-based membranes were required to be used for other applications such as steam methane reforming, in which Inconel supports are preferred. More importantly, the Pd thickness contributed the highest portion of the membrane equipment cost in Table 10-3 when the six-tenths-factor rule was applied to the support price (Chand Eisenman and Mott Met. Cor.2011). If the support price could not be further reduced through relatively large-scale purchases, the support cost would have a stronger effect on the equipment cost than the Pd thickness. Similarly, as the Pd/Pd-alloy thickness gets thinner (< 5µm) with the fast developing advances in the inorganic membrane reactor technology, the support price would start to dominate. Since the components of the fixed-capital investment, such as installation and engineering & supervision, were all dependent on the equipment cost of the Pd-based membranes, the fixed-capital investment of the membrane reactor module would increase directly proportional to the equipment cost of the membrane bundle.

In addition, membrane replacement cost was included in the variable operating costs of the IGCC-MR and calculated by dividing the equipment cost of the membrane bundle by the life-time of the Pd-based membrane (i.e. US M$ 25.8/ 3 years). Of course it is desirable to extend the membrane lifetime, so as to reduce replacement costs. Membrane replacement-related costs were also included into the operating and maintenance costs of the IGCC-MR plant. Finally, it should be pointed out that the membrane could be repaired through re-plating in order to increase its life time or Pd could be recovered from the membrane tube, and therefore, the cost associated with these processing steps could also explicitly be taken into account in the total product cost calculation. Please notice, that even though such a detailed cost assessment pertaining to the aforementioned membrane processing steps has not been pursued yet in the pertinent body of literature due primarily to the absence of reliable data, it does represent a meaningful future research endeavor.

Table 10-3. Estimation of capital investment cost for the membrane reactor module (for IGCC-MR w CO_2 comp.)

I. Direct Costs				
A. Equipment + installation + instrumentation + piping + electrical + insulation + painting				
1. Purchased equipment	Reactor	HTS catalyst	Pd Membrane	
	$28,758.4	$1,756,783.8	Pd Cost	$17,346,343.1
			Au Cost	$3,622,542.1
			Support [316L SS]	$3,094,501.4
			Total	$24,063,386.6
Total membrane module	$25,848,928.8			
2. Installation (%40 of A1.)	$10,339,571.5			
3. Instrumentation and controls, installed (%18 of A1.)	$4,652,807.2			
4. Piping installed (%45 of A1.)	$11,632,017.9			
5. Electrical, installed (%25 of A1.)	$6,462,232.2			
Equipment total	$58,935,557.6			
B. Buildings, process and auxilary (20% of A1)	$5,169,785.75			
C. Service facilities and yard improvements (40% of A1)	$10,339,571.51			
D. Land (4% of A1)	$1,033,957.15			
Sub-total	$75,478,872.02			
II. Indirect Costs				
A. Engineering and supervision (%17.5 of direct cost)	$13,208,802.6			
B. Construction expense and supervision (18% of direct cost)	$13,586,197.0			
C. Contingency (%10 of Fixed-capital investment)	$11,363,763.5			
Sub-total	$38,158,763.1			
III. Fixed-capital investment = direct + indirect costs	$113,637,635.1			
IV. Working capital (15% of V)	$20,053,700.3			
V. Total capital investment = III + IV	$133,691,335.4			

Table 10-4. Estimation of total product cost for the membrane reactor module

(for IGCC-MR w CO_2 comp.)

I. Manufacturing cost = direct production cost + fixed charges		
A. Direct production costs		
1. Raw materials (30% of total product cost)		$86,772,567.99
2. Operating labor (15% of total product cost)		$43,386,283.99
3. Direct supervisory and clerical labor (17.5% of operating labor)		$7,592,599.70
4. Utilities (15% of total product cost)		$43,386,283.99
5. Maintanence (6% fixed-capital in.)		$6,818,258.11
6. Operating supplies (0.75% of fixed-capital in.)		$852,282.26
7. Laboratory charges (15% of operating labor)		$6,507,942.60
8. Patents and loyalties (3% of total product cost)		$8,677,256.80
	Sub-total	$203,993,475.44
B. Fixed charges		
1. Depriciation (assumed 10% of fixed-capital in.)		$11,363,763.51
2. Local taxes (4% of fixed-capital in.)		$4,545,505.40
3. Insurance (0.7% of fixed-capital in.)		$795,463.45
Subtotal		$16,704,732.36
II. General expenses = administrative + distribution & selling + R&D costs		
A. Administrative costs (4% of total product cost)		$11,569,675.73
B. Distribution & selling costs (11% of total product cost)		$31,816,608.26
C. R&D costs (5% total product cost)		$14,462,094.66
D. Financing (interest - 8% of total capital investment)		$10,695,306.83
	Subtotal	$68,543,685.49
III. Total product cost		
Membrane replacement		$8,616,309.59
Manufacturing cost + general expenses		$289,241,893.29
	Total	$297,858,202.88

The target cost of membrane module in the "Fuel cell technologies program multi-year research, development and demonstration plan" by the US Department of Energy was set as 1000 US$/ft^2 for 2010 (1500 US$/ft^2 for 2006 status, <500 US$/ft^2 for 2015). The cost levels of the water gas shift membrane reactor were summarized in Table 10-5. It is important to note that the US Department of Energy cost targets were specified for H_2 usage for fuel cells. Even though the cost levels listed in Table 10-5 were derived for industrial scale water gas shift Pd/Au-based membrane reactor, they were still competitive with the high standards of the US-DOE target

levels. As mentioned earlier, single membrane reactor cost numbers would not be enough to make an investment decision and revenues depending on the use of membrane reactor had to be taken into account to reveal the profitability of the project.

Table 10-5. Static membrane reactor module cost summary

	w CO_2 comp	w/o CO_2 comp
Fixed-capital investment [$\$/ft^2$]	705	708
Total capital investment [$\$/ft^2$]	829	833
Total product cost [$\$/ft^2$]	1795	1802

10.2.2 Plant Costs and Operating & Maintenance Costs

The total plant costs and also operating/maintenance (O&M) costs for six different plants listed below were estimated by using the data provided by DOE/NETL report (Haslbeck et al. 2010). All of the plants except IGCC-MR cases were resized to attain the net energy output of 550 MWe. The capacity and availability of the plants were assumed as equal.

Cases without CO_2 capture:

1. IGCC Baseline

2. IGCC-MR without CO_2 compression/transport/sequestration

3. SCPC

Cases with CO_2 capture:

4. IGCC-PBR (with traditional packed bed reactors)

5. IGCC-MR

6. SCPC with CO_2 capture

The plant cost of the IGCC-MR was determined by using the IGCC baseline. Since there was no COS hydrolysis unit in the IGCC-MR it was subtracted from the total plant cost. The

IGCC-MR case included CO_2 compression system and a bigger size heat recovery steam generator (HRSG). Therefore, the corresponding cost differences were added. More importantly, the cost of membrane reactor module listed in Table 10-4 was also included into the plant cost.

The annual operating labor cost of the membrane reactor was added into the fixed O&M costs of the IGCC-MR. The operating labor for the membrane reactor was determined as ˜55 employee hours/day/processing steps and two major steps were assumed to be involved in the membrane reactor (heat transfer and reaction/separation) (Peters and Timmerhaus 1991). The product capacity of 718 tonnes H_2 per day was used by assuming 80% plant capacity for the IGCC-MR. The hourly labor rate of 24$/h (Monthly Labor Review, 2011) was used in the calculations and the resulting annual labor cost for the membrane reactor was approximately US M$ 0.7. In addition, the membrane replacement cost was included in the variable O&M cost of the IGCC-MR.

The auxiliary power load of the IGCC-MR case was found by including the energy requirements to reheat the feed steam to the membrane reactor, cooling the retentate stream before CO_2 compression, the H_2 compression of the permeate stream prior to the gas turbine and CO_2 compression. The power requirements for the H_2 compression was calculated by assuming multi-stage intercooled compressor (7 stages, cooling down to 196°C which was the inlet temperature of the gas turbine). The energy requirements and gains for the heating and cooling steps were determined by assuming 40% efficiency to convert thermal energy to electric power, and vice versa.

The O&M costs and the plant costs for the six cases listed above are shown in Figure 10-2 [a]. The plant capacity factor (CF) for SCPC was assumed as 85% and the rest of the plants shown in Figure 10-2 were all assumed to have 80% CF. The number of units in a SCPC plant is significantly lower than the one in an IGCC plant and also there was extensive operational experience with pulverized coal power plants since 1920s (Yeh and Rubin 2007). Thus, not surprisingly the O&M costs for the SCPC (without CO_2 capture) was the lowest one due to the simplicity of the process and accumulated operational experience. As expected, the O&M costs of the IGCC-MR, IGCC-PBR and SCPC with CO_2 capture cases were higher than the ones without capture. The common reason of higher O&M costs for cases with CO_2 capture was the significant energy and material need for CO_2 compression unit. The use of a less efficient CO_2

removal system (Econamine, 90% CO_2 recovery) due to the operating pressure of the SCPC resulted in higher O&M costs. The Selexol system used in the IGCC-PBR was more efficient (92% CO_2 recovery) than the Econamine system for CO_2 removal, however additional costs related with the packed bed reactor and the differences of the IGCC technology from the pulverized coal boiler caused the O&M costs of the IGCC-PBR to be higher than the one for the SCPC with CO_2 capture. The IGCC-MR had the highest O&M costs as shown in Figure 10-2. The most important differences of the O&M costs of the IGCC-MR case were the additional costs included in the O&M with the membrane replacement and also additional labor costs of the membrane reactor added in the fixed O&M costs.

The plant costs of the IGCC baseline and SCPC without CO_2 capture cases were the lowest as shown in Figure 10-2 [b] as expected due to the less smaller size plants with less coal feed listed in Table 10-6 and no additional units for CO_2 capture/compression. In contrast, SCPC with CO_2 capture case had the highest total plant cost because of the larger plant size and costly CO_2 removal/compression units. The removal and compression units in the SCPC with CO_2 capture case constituted a remarkable portion of the total plant cost, 29%. In addition, the required coal feed for the SCPC with CO_2 capture was the highest of all as listed in Table 10-6 to compensate the higher energy need for CO_2 removal and compression.

The total plant cost of IGCC-MR and IGCC-PBR were very similar with membrane reactor case having a slightly lower value. The energy need for isothermal H_2 compression before directing the H_2 flow to the gas turbine was 40% of the total auxiliary power need. Innovative membrane reactor design options were essential at this point to reduce the H_2 compression costs, such as membrane reactors in series; one operating at a higher permeate side pressure and the next one with a lower permeate side to remove as much H_2 as possible. If the H_2 compression costs could be reduced, the size of the IGCC-MR could be smaller to achieve the same amount of the net power output.

Another parameter worth mentioning is the amount of CO_2 product listed in Table 10-6. The extents of CO_2 product for all of the cases except the IGCC-MR were adopted from the DOE/NETL report (Haslbeck et al. 2010). The total CO_2 product for the IGCC-MR was determined based on the retentate composition of the membrane reactor which was calculated

with the 2D model. The differences in the extent of CO_2 product could vary due to the type of gasifiers and also the amount of coal feed.
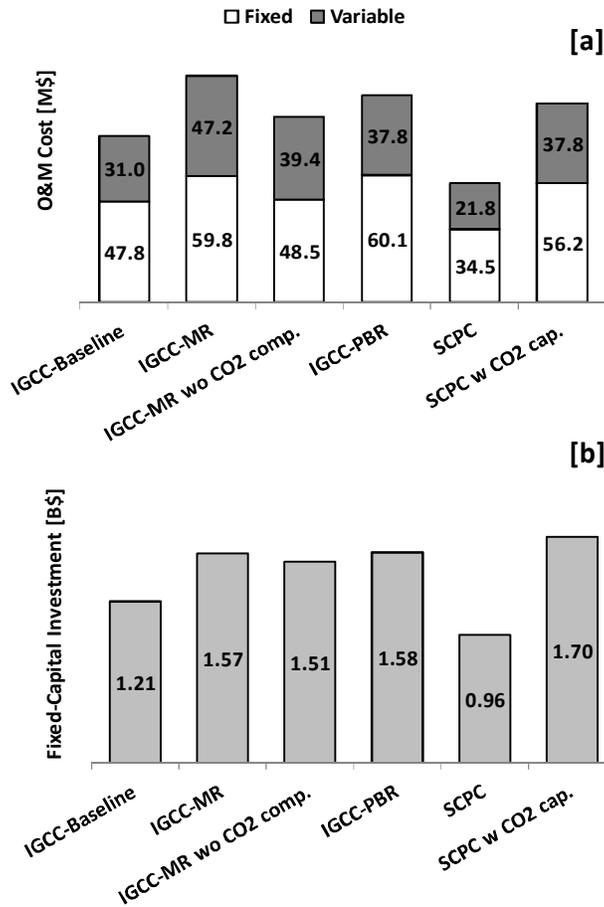
Figure 10-2. [a] O&M and [b] Plant costs for the listed coal-fired power plants

Table 10-6. Coal feed and CO_2 product levels

Power Plant Type	Coal Feed [Mtonne/year]	Captured CO_2 [Mtonne/year]	Released CO_2 [Mtonne/year]
SCPC	1.4	0.0	3.3
SCPC w CO_2 Capture	1.8	3.8	0.4
IGCC/PBR w CO_2 capture	1.6	4.1	0.4
IGCC-MR w/o CO_2 comp.	1.5	0.0	4.3
IGCC-MR	1.7	4.7	0.1
IGCC Baseline	1.3	0	3.0

10.2.3 Static NPV Results without Uncertainty Drivers and Sensitivity Analysis with the Initial CO_2 Tax

Many Scientists, policy makers and business leaders have been concentrating on actions that address increasing greenhouse gas (GHG) emissions. The discussion is now focused on answering more practical questions such as how emission reductions can be best achieved, at what costs, and over what periods of time. As McKinsey reports, a composite of official US government agency projections indicates that, if unchecked, annual greenhouse gas emissions will increase from 7.2 gigatons of carbon-dioxide equivalent to 9.7 gigatons by 2030 (Creyts et al. 2007). No action will be taken to capture CO_2 from power plants unless governments set definite incentives to prompt power plants owners. Two powerful examples of incentives are taxes on carbon emissions or regulatory action on carbon emissions such as cap and trade scheme (Bohm 2006). In this research study, carbon tax was used as a carbon emission control mechanism.

Sensitivity analysis on initial CO_2 tax was performed to evaluate the influence of CO_2 taxes on the NPVs of all six power plant options. The single point projected NPV results presented in Figure 10-3 were all based on the current market conditions or best guesses without risk assessment.

For the zero CO_2 tax scenario, the overwhelming NPV result of the SCPC without CO_2 capture plant made it a preferred option as shown in Figure 10-3 [a]. Even though all of the plant options had the same net power output of 550 MWe and same revenues, the resulting NPV values of the IGCC baseline and IGCC-MR were lower than SCPC due to their higher plant and O&M costs as shown in Figure 10-3. The IGCC-MR case, having the 3rd highest NPV, stands as a strong candidate even without any regulatory action on carbon emissions with a positive NPV result. One should keep in mind that IGCC-MR has the strongest advantage of producing extra purity H_2 and, thus the IGCC-MR could compete with the SCPC without CO_2 capture if the net plant efficient could be increased from 40% to 60%.

As shown in Figure 10-3, the SCPC without CO_2 capture stayed as the most profitable option as long as the initial CO_2 tax was below 30$/tonnes CO_2. Consequently, SCPC plants could still be operated by paying the taxes without capturing the CO_2 product if the taxes stays

below 30$/tonnes CO_2 level (with 3% growth rate). For initial CO_2 taxes higher than 30$/tonnes CO_2, the IGCC-MR attained the highest NPV value which indicated that membrane reactor technology had the best investment potential as evidenced in Figure 10-3 [d].

As expected, the power plants with CO_2 capture capability were less benign to increased CO_2 taxes compared to non-capture options. In the presence of CO_2 taxes shown in Figure 10-3 [b] through [d], the IGCC-MR plant was the least affected by increased CO_2 taxes mainly because of the higher CO_2 recovery level. In addition, the negative NPV values of the baseline IGCC plant for initial CO_2 taxes higher than 15$/tonnes CO_2 indicated that the baseline IGCC could not compete with SCPC if CO_2 capture was not provided.
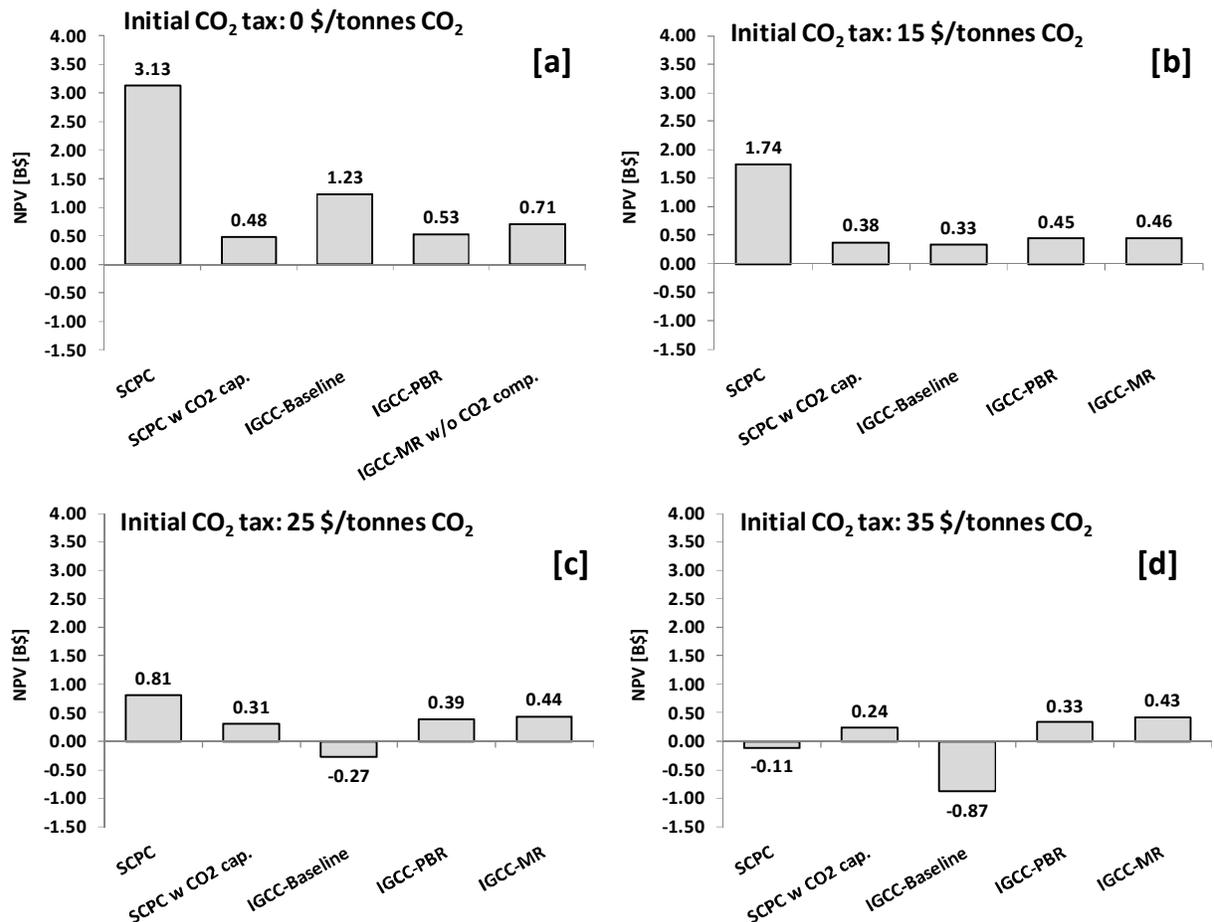
Figure 10-3. Sensitivity analysis on initial CO_2 tax

10.2.4 Economic Assessment under Uncertainty: Membrane Reactor Module Cost Distribution Profiles

The Monte Carlo simulation was first applied to the membrane reactor module cost analysis. Pd, Au, support prices and membrane life time were the uncertainties considered in order to determine the fixed-capital, total capital (fixed-capital + working capital) and total product cost including the manufacturing cost and general expenses. The probability distribution of the membrane reactor module cost is shown in Figure 10-4. In addition to the module cost distribution profiles, the average values of all of the outcomes, maximum and minimum cost results are also listed in Table 10-7. The upper right zone of Figure 10-4 is called risk zone and corresponded to higher Pd, Au and support prices and shorter membrane lifetime. Similarly, the lower left zone of Figure 10-4 is called reward zone and corresponded to lower Pd, Au and support prices and longer membrane lifetime. The average value of the total product cost for the water-gas shift membrane reactor was determined as 1464 US$/ft^2 which was over the target value of the DOE for 2010 (DOE-Fuel Cell Program, 2011). As mentioned earlier, the DOE targets were set for fuel cell grade H_2 production and did not include costs related with the water-gas shift reaction. Thus, the total product cost of 1464 US$/ft^2 for the water-gas shift membrane reactor module stood as a quite promising result. Moreover, since the cost criterion of the DOE was not specified in detail, the fixed-capital and total capital for the membrane reactor module listed in Table 10-7 could also be compared with the DOE target level. The average fixed-capital investment of 575 US$/ft^2 and the average total capital investment of 677 US$/ft^2 were very close to the 2015 DOE target level of < 500 US$/ft^2.

The membrane module cost could be decreased by using thinner Pd-based membranes, alloying with cheaper metals such as Cu or decreasing the required membrane area with the application of vacuum from the permeate side.
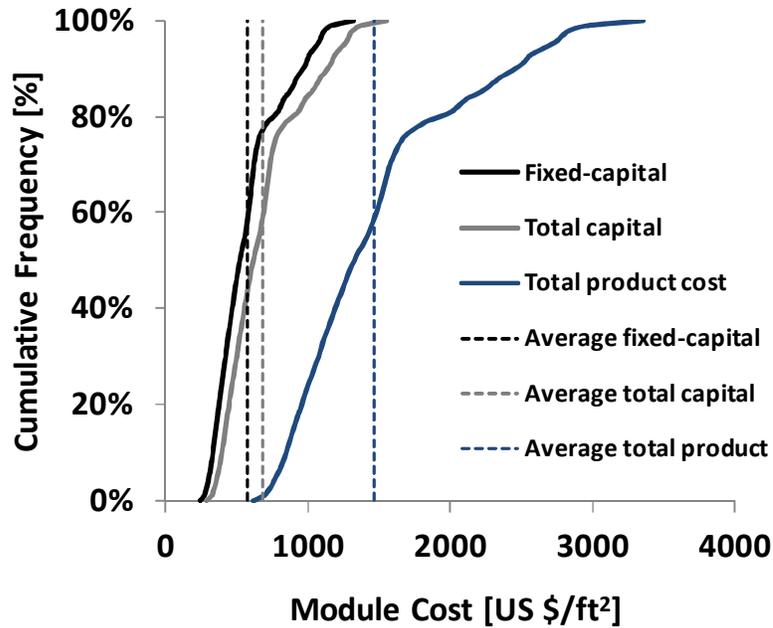
Figure 10-4. Membrane reactor module cost distributions

Table 10-7. Membrane reactor module cost summary

	Fixed-capital investment [US$]	Total capital investment [US$]	Total product cost [US$]
Average	575	677	1464
Max	1318	1549	3353
Min	244	287	621

10.2.5 Economic assessment under uncertainty: Integration of Monte Carlo methods into the NPV framework of analysis

As explained earlier, the Net Present Value (NPV) framework of analysis as a tool-of-choice, to determine which investment project on a specific technology option to undertake, was used in the economic assessment. The Monte Carlo simulation technique was easily incorporated

into the NPV model to determine and compare the NPV profiles of SCPC, IGCC baseline, IGCC-PBR and IGCC-MR power plants. The Monte Carlo simulation was applied to the NPV model with three different representative cases:

- No CO_2 tax legislation in the future

- CO_2 tax legislation in the future starting in year 2015

- Potential improvements for profitability of the membrane reactor technology

10.2.5.1 No CO_2 tax in the future

The CO_2 tax was not included into the uncertainty analysis for the first scenario to evaluate the current competitiveness of the membrane reactor technology with the well known options and the results were presented in Figure 10-5. The interpretation of Figure 10-5 is as follows: the y axis is the cumulative probability of achieving the corresponding NPV value on the x axis. This shows the percentage of times that profit was less than or equal to the amount shown on the horizontal axis. The likelihood of losing money may be determined by locating zero on the horizontal axis, then going up to the curve to determine the percent of trials that are less than zero, about 13% for IGCC-MR without CO_2 compression/transportation/sequestration and 1% for IGCC baseline as shown in Figure 10-5 [a].

Since the pulverized coal power plants has been operated for almost a century, the nominal discount rate and plant capacity values were fixed at 6% and 85%, respectively. Under no CO_2 tax condition, SCPC without CO_2 capture plant achieved the best profile with the highest NPV range and also no risk of losing money as shown in Figure 10-5 [a]. The profit of the baseline IGCC plant could not be as high as that of the SCPC, however, the baseline IGCC plant was also found to be a quite attractive investment option with a very low chance of losing money. In addition, the baseline IGCC plants could be competitive with the SCPC plants when their superior environmental performance was considered. The NPV profile of the IGCC plant with an embedded membrane reactor indicated why investors hesitate to decide on the option of IGCC-MR under the current conditions without any CO_2 tax. The capacity factor and also the nominal discount rate for the IGCC-MR case were assumed to be worse than the other cases in order not to overestimate the potential of the new membrane reactor technology option. As

shown in Figure 10-5 [a], the IGCC plant with the membrane reactor technology could lose almost one billion dollar in the worst case scenario or less, mostly due to the risk in unknown total plant operation time (capacity factor) and also higher interest rates paid.

The maximum NPV range of the plants with CO_2 capture capability shown in Figure 10-5 [b] namely, SCPC with capture, IGCC with traditional packed bed reactors and with membrane reactor, were drastically lower than those without capture due to the higher plant costs and O&M costs related with CO_2 capture units and also expenses for CO_2 transportation and sequestration. The NPV profile of the IGCC-MR plant under no CO_2 tax condition was not better than the IGCC-PBR and SCPC with capture, but the difference was not as significant as the results without capture cases shown in Figure 10-5 [a]. It is important to note that even though the membrane reactor technology brought a high risk due to the lack of operational experience, the IGCC-MR was still capable of producing a significant range of positive NPV outcomes as shown in both Figure 10-5 [a] and [b].

An immediate result of a MC simulation was the calculation of the expected NPV (ENPV) from the corresponding distribution profile in the presence of uncertainty. ENPV is simply the average of all the NPV realizations associated with each of the thousands of simulated possibilities and represents the average value of the project (de Neufville et al. 2011). The results presented in Figure 10-5 were summarized with the ENPV, maximum and minimum of the NPV distributions in Table 10-8. The simplest conclusion for the no CO_2 tax scenario drawn from Table 10-8 was that the investment on the most profitable SCPC plant with an ENPV of US B\$ 3.1 could be preferable if the future would be similar to the current condition without CO_2 tax.

Table 10-8. NPV results summary under no CO_2 tax condition [US B\$]

	No CO_2 capture			With CO_2 capture		
	SCPC	IGCC Baseline	IGCC-MR wo CO_2 comp.	SCPC w CO_2 cap.	IGCC-PBR	IGCC-MR
ENPV	3.1	1.7	0.93	0.83	0.87	0.64
Max	5.2	4.1	3.5	3.2	3.0	2.9
Min	0.58	-0.3	-0.8	-1.0	-0.9	-1.1
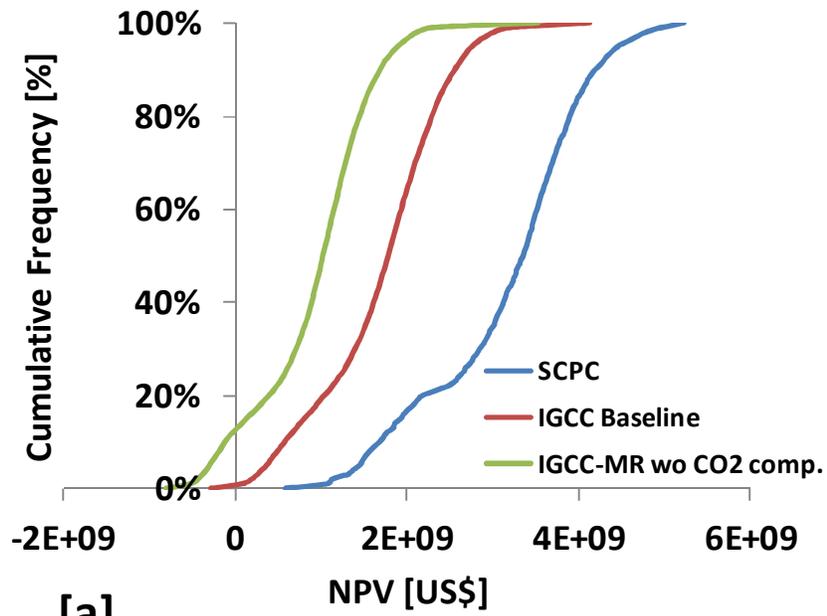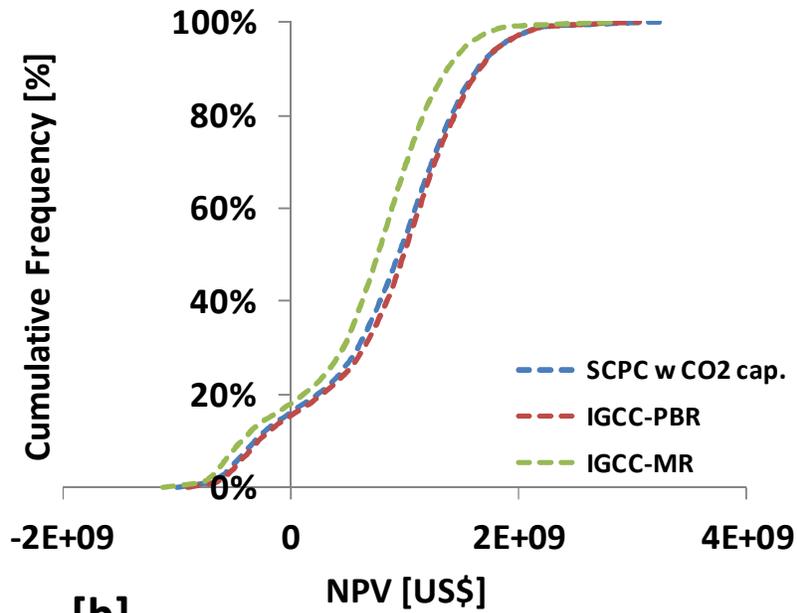
Figure 10-5. NPV distributions under no CO_2 tax condition for plants [a] without and [b] with CO_2 capture

10.2.5.2 CO_2 tax included in the future

The following risk analysis was conducted by comparatively assessing the economic performance results of the IGCC baseline, IGCC-MR and SCPC cases by considering all of the uncertainties listed in Table 4-3, except the H_2 selling price. The Monte Carlo simulation results clearly proved the strong effect of CO_2 taxes on the economics of the power plant options as shown in Figure 10-6. The difference between Figure 10-5 [a] and Figure 10-6 [a] demonstrated undesired consequences of any future CO_2 taxes on the economics of the power plants which were not equipped with CO_2 capture and sequestration units. Since the chances of obtaining zero profit or losing money were extremely high for SCPC (55%) and baseline IGCC (78%) without CO_2 capture under CO_2 taxes, the SCPC and baseline IGCC would not be able to survive under CO_2 taxation.

Even though the NPV profiles of the cases with CO_2 capture were decreased (shifted downwards) compared to Figure 10-5 [b], the power plants with the capture ability namely, SCPC with CO_2 capture, IGCC-PBR and IGCC-MR shown in Figure 10-6 [b] were slightly affected with the carbon taxes. The IGCC-MR plant had the highest level of CO_2 recovery, 98%, compared to the CO_2 recovery levels of SCPC and IGCC-PBR, 90% and 92% respectively. Thus IGCC-MR got influenced least with the CO_2 taxes and had the lowest negative NPV zone shown in Figure 10-6 [b]. The lower percentage of losing money (17%) and the highest ENPV value of 0.8 US B\$ listed in Table 10-9 for the IGCC plant with embedded Pd/Au-based membrane reactor indicated that membrane reactor technology could be a promising option as a future investment choice under CO_2 taxation.

Table 10-9. NPV results summary with CO_2 taxes [US B\$]

	No CO_2 capture			With CO_2 capture		
	SCPC	IGCC Baseline	IGCC-MR wo CO_2 comp.	SCPC w CO_2 cap.	IGCC-PBR	IGCC-MR
ENPV	-0.6	-1.5	-2.9	0.58	0.68	0.78
Max	4.9	3.1	1.8	2.9	3.3	3.4
Min	-15.0	-15.30	-16.1	-1.9	-1.7	-1.1
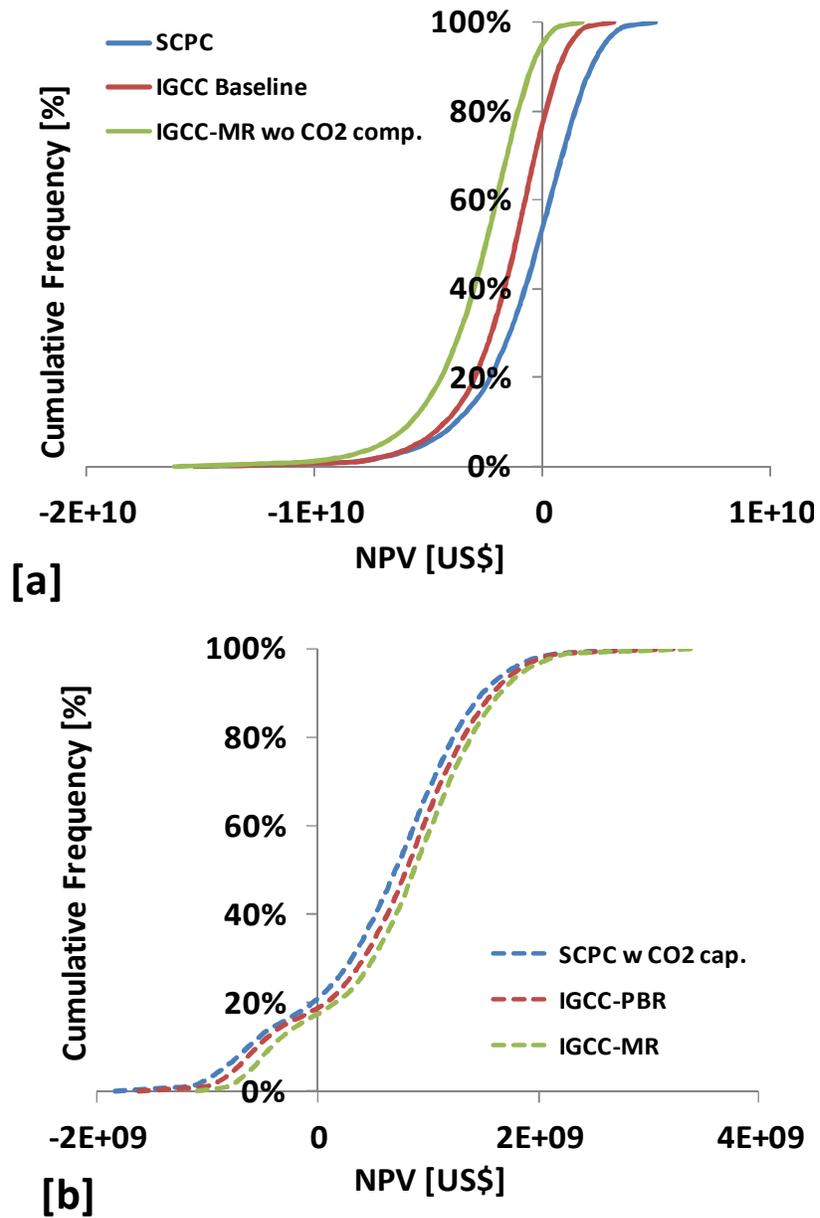
Figure 10-6. NPV distributions with the effect of CO_2 tax legislation for plants [a] without and [b] with CO_2 capture

10.2.6 Potential improvements for profitability of the membrane reactor technology

The main objective of the Chapter 10 is to improve the risk-reward (NPV-distribution) profile for the IGCC-MR technology option through the use of creative economy tools namely, "Technology-Push" and "Market-Pull". Technology-push policy incites the accumulation of operational experience through demonstration plants and a reduction in the uncertainty in the availability factor (or CF). Market-pull policy stimulates the reduction of the cost of the capital through carefully structured financing mechanism, and thus the cost of electric energy production. The method of "3 Party Covenant Financing" (Rosenberg et al. 2005), which was proposed by the Energy Technology Innovation Project Group, J.F. Kennedy School of Government, Harvard University, was used to improve the IGCC-MR profitability even more with a well defined plan.

The primary objective of the 3 party covenant financing (3PCF) method is to stimulate the deployment of IGCC demonstration plants at the commercial scale to establish technical feasibility and potential economic viability. The main participants of the 3PCF method are government, state/regional utility rate selling body and equity investor. Government provides loan guarantees at low budget cost and AAA credit rating on project debt financing. State/regional utility rate selling body provides assured revenue and establishes cost recovery mechanisms while closely monitoring the plant performance. Equity investor, electric utility or independent power producer, provides project equity financing and know-how with guarantees from an EPC firm.

The main idea behind the 3PCF is to lower the cost of debt through the government loan guarantee from 6.5% (mid-grade utility bond) to 5.5% and to increase debt to equity project financing ratio from 55/45 (traditional utility financing) to 80/20 as shown in Figure 10-7. Consequently, the outcome is a reduction of the nominal weighted-average cost of capital and the cost of electricity production.
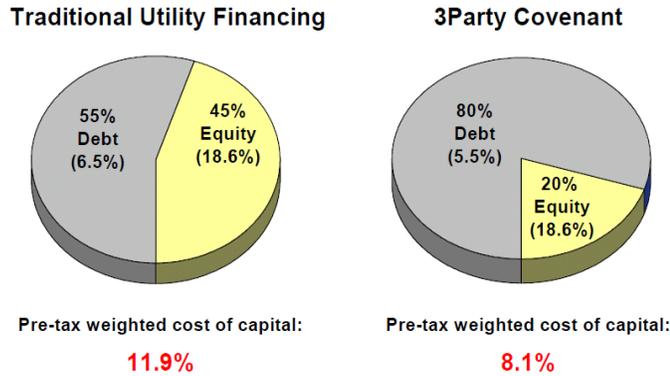
Figure 10-7. 3 Party Covenant Financing mechanism (Rosenberg et al. 2005)

In addition to the technology-push and 3 PCF methods, the IGCC-MR technology option has the advantage of producing extra purity H_2 which could be sold together with electricity. The NPV profile of the IGCC-MR was evaluated in the following sequence and the results are shown in Figure 10-8:

- Eliminate the uncertainty in the capacity factor (technology-push), CF = 85%

- Eliminate the uncertainty in the nominal discount rate (3PCF), r = 7%, CF = 85%

- Include H_2 selling into the revenues

Electricity will certainly be produced in an IGCC-MR through the use of steam turbines in addition to the H_2 production. The remaining electricity after subtracting the net auxiliary power needed for the IGCC-MR and all of the produced H_2 was assumed to be sold and included in the revenues. The amount of sold H_2 was not investigated in this study; however the relative extents of electricity and H_2 selling had to be adjusted based on the market demand. The IGCC-MR product could be switched between electricity and H_2 to achieve the maximum NPV based on the need.

The NPV profile of the IGCC-MR plant got better and better as the planned strategy was applied step by step starting from technology-push followed by 3 PCF and increased revenues by H_2 selling as shown in Figure 10-8. Fixed and improved capacity factor and nominal discount rate resulted in decreased risk of losing money from 17% to 12% by shifting the NPV profile towards the positive NPV region. Moreover, the most significant benefit of revenues coming

from H_2 selling was the decreased chance of obtaining zero or negative NPV from 12% to 2% as shown in Figure 10-8. The price of extra purity H_2 which could be used in hydrogenation/dehydrogenation reactions for the production of other valuable chemicals was higher than the electricity price. Thus, the economic performance of the IGCC-MR which sold H_2 was better than that which sold only electricity. The electricity selling price annual growth rate was adopted from the historical data, however one should keep in mind that CO_2 taxes had not ever been applied in the past. Thus, electricity selling price might be higher than the values predicted in this study if any CO_2 tax legislation was initiated in the future.

The most important outcome of the results presented in Figure 10-8 was the competitive economic performance of the IGCC-MR even with CO_2 capture and heavy CO_2 tax legislations compared to the economic performance of the SCPC without CO_2 capture and no CO_2 tax application. The ENPV of the IGCC-MR with CO_2 capture and tax and SCPC without capture and tax were US B\$ 1.5 and 3.1 as listed in Table 10-10 and Table 10-8, respectively. If the membrane reactor technology could increase the project value significantly even with all of the economical conditions weighed against the IGCC-MR, the profitability of the IGCC-MR could be easily improved with the aid of improved net thermal efficiency and better membrane reactor integration. As stated earlier, the membrane reactor either had to be implemented together with gas cleaning units (sulfur and mercury removal) operating at high temperatures to decrease the amount of waste heat or the Pd-based membranes should tolerate sulfur and mercury contents to perform gas cleaning post-combustion instead of pre-combustion. Not only the waste heat had to be reduced, but also the energy need for the H_2 compression needed to be decreased. Innovative design options for the Pd-based membrane reactors could easily provide decreased auxiliary power needs for the H_2 compression.
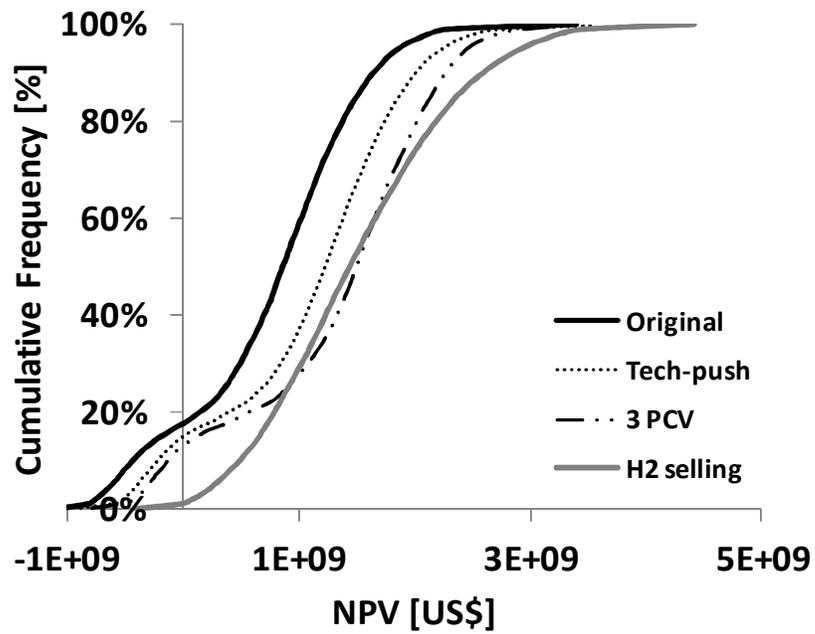
Figure 10-8. The effect of Tech-push, 3 Party Covenant Financing mechanisms and H2 selling on the NPV profiles of the IGCC-MR plant.

Table 10-10. NPV results summary of the IGCC-MR with tech-push, 3 PCF and H_2 selling

	Original	Tech-push	3 PCF	H_2 selling
ENPV	0.78	1.10	1.33	1.5
Max	3.40	3.55	3.34	4.42
Min	-1.10	-0.87	-0.79	-0.42

10.3.   Conclusions

The integration of the membrane reactor technology into IGCC power plants offered a promising prospect of supporting energy security and environmental policy objectives when comparatively assessed against traditional technology options and evaluated on three levels:

- Technical performance: Overall efficiency, co-production of H_2

- Environmental performance: Significant reductions of air pollutants and greenhouse gas emissions

- Economic performance: Assessment conducted in the presence of market, regulatory uncertainties and technology risk by implementing the Monte Carlo simulations into a Net Present Value analysis.

The NPV profile of the IGCC plant with embedded Pd/Au-based membrane reactor was compared with the super critical pulverized, baseline IGCC and IGCC plants with the traditional packed bed power plants. In the absence of regulatory action on CO_2 emissions or stringent regulatory standards on overall environmental performance, IGCC could not be easily justified as a viable option on purely economic grounds. SCPC plant with an expected NPV of US B\$ 3.1 was found to be more profitable if the future would be similar to the current condition without CO_2 tax. However, there is a window of opportunity for IGCC-MR in the presence of regulatory action on CO_2 emissions. If CO_2 emissions were regulated through taxation, an IGCC plant with embedded Pd-based membrane reactors, with a stream of revenues coming from electricity selling, would be shown as the economically advantageous option against its rivals namely, IGCC plant with shift reactors and double stage Selexol units as well as the more traditional supercritical pulverized coal power plant option with an Econamine unit installed for CO_2 capture purposes.

A creatively structured portfolio of technology-push and market-pull policy incentives could lead to more attractive risk-reward profiles for the IGCC-MR technology option for the co-production of electric power and high-purity hydrogen. Even in the presence of the CO_2 taxation, a stream of revenues gained by both electricity and H_2 selling could lead to the IGCC-MR technology to be preferable with an expected NPV value of US B\$ 1.5. Adjustable electricity and

H$_2$ selling option based on the market demand will be included into the NPV model as a future work. In addition, the economic performance of the IGCC-MR with hot gas cleaning units will also be investigated in the future work to reach net plant thermal efficiency level of 60%.

11. Economic Rationale for Safety Investment in IGCC-MR Power Plants

11.1.   Introduction

The economic viability of Pd/Au-based membrane reactor modules whose design conformed to inherently safe design principles and intended to allow their incorporation into Integrated Gasification Combined Cycle (IGCC) plants was evaluated within the Net Present Value (NPV) framework explained in detail in Chapter 10. Sources of irreducible uncertainty (market, technological, operational) as well as safety risk were explicitly recognized, such as the Pd/Au prices, membrane life-time and loss in the power plant capacity factor due to possible accidents. Moreover, the effect of the above uncertainty drivers on the membrane module cost along with production disruption and associated revenue losses was elucidated using Monte-Carlo simulation techniques.

The derived simulation results suggested that in the presence of (operational, economic and regulatory) uncertainties, inherently safe membrane reactor technology options integrated into IGCC plants could become economically viable even in the absence of any valuation being placed on human life or quality of life by considering only equipment damage and interruption of business/lost production cost. The pre-investment on risk reducing measures, such as spare safety relief systems (cautionary redundancy) for membrane reactor modules operating at high pressures (e.g. 50 atm), was shown to be economically more attractive than cases where analogous safety measures were not implemented. Comparatively more attractive NPV distribution profiles were obtained when concrete safety risk-reducing measures were taken into account through pre-investment in process safety (equipment) in a pro-active manner, giving further credence to the thesis that process safety investments might result in enhanced economic performance in the presence of irreducible uncertainties.

11.2. Results and Discussion

Since coal-fired power plants have being operating since 1920s (WRI-Pulverized Coal Power, 2011), significant operating experience has been accumulated and sound safety procedures have been established. Therefore, in the case of Pd-based membrane reactor technology options integrated into coal-fired power plants the membrane reactor module needs to be considered as a new "node" and HAZOP analysis to be updated in light of this recognition. Since the integration of Pd-based membrane reactors into coal-fired power plant represents a new technology option which has neither been fully tested nor yet demonstrated at a commercial scale, and given the operating and structural characteristics of membrane reactors, conditions are perhaps favorable to evaluate inherent safety design prospects and hopefully demonstrate that inherent process safety does not undermine the economic viability of such a plant, but in an uncertain world it actually enhances the value of engineering design and the project itself in concrete economic terms (Mannan, 2011).

The first systematic attempt to analyze and understand the issues and challenges related to Pd-based membrane reactor safety aspects was made by Chieppetta et al. (2006a). Following a methodologically similar approach, HAZOP analysis was performed by Koc et al. (2011) for WGS Pd/Pd-alloy based membrane reactors. The absence of an adequate control of the reactor temperature as well as the purity of the feed which might cause hot spots and a decline in permeance and selectivity were identified and classified as critical for the operation of the WGS membrane reactor. Since the main advantage of the Pd/alloy-based membrane reactor technology was the high-quality H_2 separation driven by the H_2 partial pressure difference between the reaction and permeate sides, the operation at high reaction side pressure was identified as a key process safety challenge. It was also shown that proper material selection, stringent process monitoring and control together with multiple pressure relief systems had to be explicitly integrated into process system design as a part of a comprehensive process intensification strategy (Koc et al. 2011). However, the primary challenge in explicitly incorporating and implementing carefully designed process safety strategies and thoughtful approaches such as inherently safe process system design depended on the development of a transparent and sound economic justification. One would argue that historical experience and empirical evidence would

advance the argument that investments in process safety do make economic sense in an uncertain world where relatively low probability-major consequences events do happen. However, significant progress in process safety also introduced a sense of complacency by facilitating rationalizations that major catastrophic events could be averted, their consequences minimized due to "superior" existing process knowledge and availability of technological means, and as a result reinforcing resistances against sustained investments in process safety (Pasman 2000). The objective of Chapter 11 was to show that if the required process safety investment was made (as part of the initial capital expenditure) at the construction stage of an IGCC plant, process safety investment strategies could save money by preventing or minimizing the effects of accidents and possibly catastrophic events, demonstrating that in an uncertain world they might actually enhance the value of the engineering project.

11.2.1 Economic assessment of inherently safe membrane reactor technology options integrated into IGCC power plants

From an inherent process safety point of view in particular, the following conditions needed to be satisfied by designing and operating the Pd/alloy-based WGSMR in a safety-constrained regime, thus preventing the development and occurrence of hazards to personnel as well as process performance (loss of efficiency, deterioration of process economics, etc), as identified in Chapter 8:

- The membrane reactor and feed stream had to be pre-heated to 300°C before syngas was admitted to the reactor. Pre-heating was necessary to maintain sufficient WGS reaction rates and to prevent H_2 embrittlement of pure Pd-based membranes.
- The extra heat of the WGS reaction (above 450°C) needed to be removed with the aid of a heat exchanger to maintain the isothermal operation of the WGSMR and to prevent potential hazards which could compromise the safety of the WGSMR.
- The main advantage of the Pd/alloy-based membrane reactor technology was the high-quality H_2 separation driven by the H_2 partial pressure difference between the reaction and permeate sides, and therefore, operation at a high reaction side

pressure was necessary. Thus, the high pressure operation of the WGSMR represents a safety challenge. As proposed in Chapter 8.2.5, the combination of a disk-rupture safety relief valve in series system (RRS) could be installed at the membrane reactor entrance and exit as a safety measure. In addition, sparing of the relief equipment would provide an on-line maintenance option of the RRS system through switching and also the process would not necessarily need to be shut down for replacement purposes (1993a).

All safety measures listed above required an initial up-front capital investment in process safety associated with the integration of the membrane reactor into IGCC power plants so as to mitigate potential risks to personnel, the environment, equipment and/or process efficiency and performance.

In particular, a potential investor in this new technology and engineering project had two options: one was to make no or minor effort to prevent accidents by taking a chance and paying for the consequences should any accident happen; the other was to act proactively by investing on plant safety in advance and thus potentially reduce the economic damage and cost of an accident. One is reminded that accidents are costly due to lost working days, but also due to lost production, damage to equipment and plant, investigation time, liability claims and loss of human life (Pasman 2000; Kletz 1990).

Within the above economic assessment framework, two cases were evaluated and analyzed in this study:

A minor leak incident under

- No initial action at start-up
- A pre-investment in plant safety

A major leak and potentially quite hazardous incident under

- No initial action at start-up
- A pre-investment in plant safety

The uncertainty related to the possible occurrence of an industrial accident was represented in our NPV-model with integrated Monte Carlo through a simple Bernoulli

distribution assigned to the 11th additional uncertain value driver. The modified formula for the NPV is given in Eq (11.1) encompassing both the initial investment in equipment to enhance plant safety as well as the total cost incurred in case the accident occurs:

$$NPV = (C_o - C_{safety}) - (pr \times D_0)DF + PV \tag{11.1}$$

where $DF = \sum_{t=1}^{N} \frac{1}{(1+r_t)^t}$ is the so-called unit annuity present value factor (a constant for a fixed discount rate), C_{safety} is the safety pre-investment amount, pr is the probability of occurrence of the accident (associated with a Bernoulli distribution) and D_0 is the expected loss or a monetary measure of damage (total cost incurred) due to the occurrence of the accident.

The amount of investment in safety is directly proportional to the magnitude of the accident: a relatively small investment would be required to reduce the risk and the associated cost of a minor leak whereas the amount of investment in plant safety needs to be larger in the case of a major accident for the attainment of the above objectives. Representative values of the investment in safety (C_{safety}), probability of accidents (pr) and expected loss (D_0) were adopted from Pasman (2000) and listed in Table 11-1.

The orders of magnitudes for the safety investments were matched with the Pasman's study (2000) and the amount of safety investments on the membrane reactor unit were set as the half and full of the total capital investment (listed in Table 10-3) for the minor and major leak cases, respectively.

Table 11-1. Decision matrix for risk reduction measures

Options of risk reduction		C_{safety} [k\$]	pr [year^{-1}]	D_0[k\$]
Minor leak	No measure	0	10^{-1}	10^6
	Safety investment action	6.5×10^4	10^{-4}	10^3
Major leak	No measure	0	10^{-3}	10^8
	Safety investment action	13×10^4	10^{-6}	10^6

The NPV distribution (risk-reward) profile for IGCC-MR is given in Figure 11-1 by considering the 10 uncertain value drivers plus the uncertainty and risk of a minor leak. Figure 11-1 being a graph of a cumulative distribution function allowed a probabilistic/statistical

characterization of the entire range of possible economic performance outcomes in the presence of uncertainty. The upper-right positive NPV zone of Figure 11-1 was associated with quite favorable economic outcomes due to high plant capacity factor, low nominal discount rate, low Pd price and so on; the lower-left negative NPV zone of Figure 11-1 was associated with undesirable economic performance outcomes (possibly due to low capacity factor, high nominal discount rate, high Pd price, etc). According to the NPV distribution profile in Figure 11-1, the risk of generating a negative NPV was 62% if no measure was taken against the possibility of a minor leak. If the required investment were made during the construction period, the risk-reward profile could be shifted to the right and the risk of generating a negative NPV was reduced to 19%.

The risk associated with a major leak together with the other 9 uncertain value drivers was even more significant from an economic performance standpoint as shown in Figure 11-1. While the probability of losing money was 66% without any pre-investment in plant safety, the risk reward profile of the IGCC-MR plant was successfully shifted to the right reducing the probability of generating negative NPV to 24% after investing in plant safety at the construction stage.

Interesting findings and results for both case studies could be found in both Figure 11-1 [a] and [b] as well as those tabulated in Table 11-2. No matter the size of the leak, the project might end up with negative expected NPV values if no safety measures were taken for the membrane reactor technology in an IGCC plant with a net power output of 550MWe. The negative NPV zones of the cases without safety measure could be reduced by increasing the net power output. However, their NPV profiles would still stay lower than the cases with pre-safety investment as evidenced from Figure 11-1. The requisite safety investments could lead the IGCC-MR to a more profitable zone with the ENPV values of US B$ 0.6 and 0.4 for the cases with minor and major risk of leak, respectively.

The expected value of NPV (ENPV) generated through the Monte Carlo simulations in the case of pre-investment in process safety and risk reduction measures was considerably higher than the ENPV without any action against hazards given the conditions that were considered in the present study. Therefore, the analysis conducted suggested that under the above conditions, an initial investment in plant safety at the initial stage of the IGCC power plant could actually

improve the project's economic value. Summarizing, the two case studies considered offered credence to the thesis that in an uncertain world (where accidents happen, market conditions change and the regulatory   environment evolves) process safety investment strategies might actually enhance overall economic performance.

Table 11-2. The expected NPV (ENPV) results for all 4 cases

	Minor Leak		Major Leak	
	No Measure Taken	With Pre-Investment in Process Safety	No Measure Taken	With Pre-Investment in Process Safety
Average (ENPV) [$US]	-2.37E+08	5.79E+08	-3.11E+08	4.44E+08
Max[$US]	2.72E+09	2.94E+09	1.93E+09	3.06E+09
Min[$US]	-2.79E+09	-1.21E+09	-2.46E+09	-1.32E+09
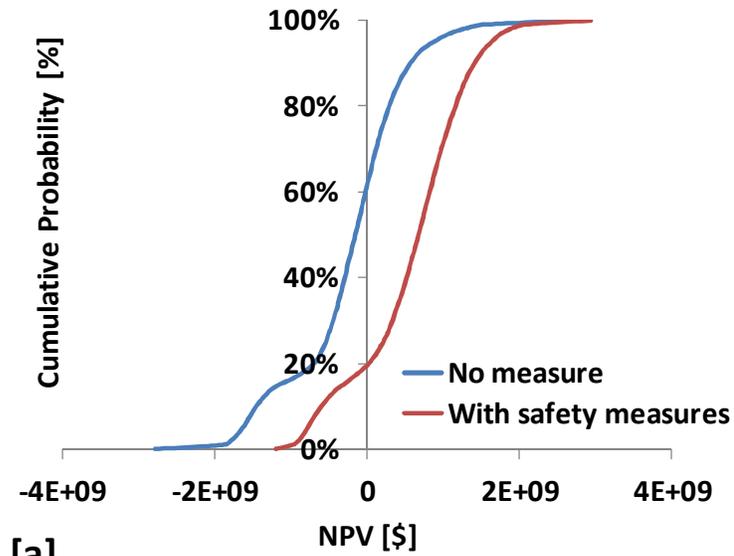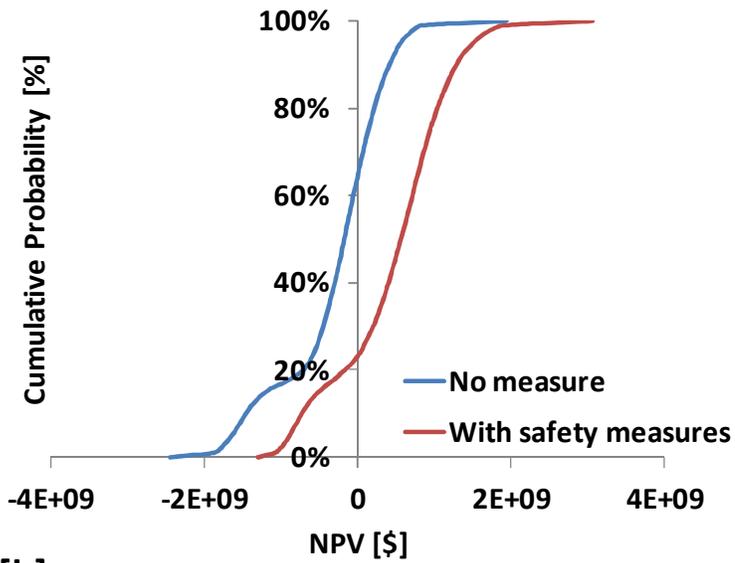
Figure 11-1. NPV distribution profile considering 10 uncertain inputs plus the risk of a [a] minor and [b] major leak

11.2.2 Economic evaluation framework for inherently safe membrane reactor modules in the presence of uncertainty

The main advantage of the Pd/alloy-based membrane reactor technology is the high-quality H_2 separation driven by the H_2 partial pressure difference between the reaction and permeate sides, and therefore, operation at a high reaction side pressure is necessary. Thus, the high pressure operation of the WGSMR represents a safety challenge. As proposed in Chapter 8.2.5, the combination of a disk-rupture safety relief valve in series system (RRS) could be installed at the membrane reactor entrance and exit as a safety measure. In addition, sparing of the relief equipment would provide an on-line maintenance option of the RRS system through switching. Furthermore, the process would not necessarily need to be shut down for replacement purposes (1993a; 1993a) .

In this chapter, a potential overpressure incidence in a WGSMR was considered as a case study in order to demonstrate the economic benefits of pre-investment on safety. The material, maintenance and replacement costs of safety relief valve and rupture disc equipment could be expensive and even sparing of these safety measures could cause concern to the investor from an economic perspective. In general, blocked discharge, fire exposure, check valve failure, thermal expansion, etc. could cause overpressure in process equipment (Ling 2007). A possible sequence of events in a WGSMR which might cause the system pressure to exceed the set limit could be exemplified in the following scenario: An additional steam feed could be supplied to the membrane reactor at the reactor inlet via a high pressure water pump to achieve optimum CO conversion for syngas mixtures with a high steam/CO ratio, to prevent coke formation or to control the reaction side temperature. A blocked discharge might be caused by plugging of the lines at the reactor exit, closed valves due to human error, or failure of the automated control systems. Moreover, the steam amount and pressure could increase unintentionally due to a check valve failure of the water pump, malfunction of the H_2O/CO ratio controller or water pump. The combination of a blocked discharge and a malfunction in the high pressure water pump might lead to overpressure. Finally, since the contact of oxygen and hydrogen in the reactor was unlikely, an explosion could be considered as a low probability event due to overpressure.

A safety relief system consisting of a rupture disc-rupture disc-safety relief valve (RRS) could be used at two locations in the WGSMR: one at the end of the first 1/3 of the reactor and the other at the beginning of the 2/3 of the reactor as explained in Chapter 8.2.5. The cost structure of a membrane reactor module with a single RRS system as well as a spare RRS system to prevent interruption of the process operation was evaluated in the following section through the development of a comprehensive Net Present Value framework of economic assessment with an integrated Monte Carlo simulator in order to explicitly take into account key uncertain cost/value drivers.

Monte Carlo simulations were performed to propagate the uncertainty of the seven system value drivers given in Table 11-3 through the NPV model. Moreover, another random variable related to the possible occurrence of an overpressure incident was incorporated into the above NPV-Monte Carlo economic evaluation framework as shown in the sequel. Please notice that overpressure incidents might lead to catastrophic events if precautionary or mitigating measures were not effective and pertinent accidents could be particularly costly due to lost working days, but also due to lost production, damage to equipment and plant, investigation time as well as liability claims (Pasman 2000; Kletz 1990; Pasman and Rogers 2010).

Table 11-3. Probability distributions associated with the uncertain inputs in the module cost

Parameter↓	Distribution		
	Minimum	Most Likely	Maximum
Loss in plant CF [%], TD	1	5	20
Electricity selling price [cents/kWh], RH	1979-2011 Historical data, U.S. Energy Inf. Adm.		
Pd price [$/g], RH	1979-2011 Historical data, www.kitco.com		
Au price[$/g], RH	1979-2011 Historical data, www.kitco.com		
Support price [$/cm^2 for lab scale], TD	2.3	5	7.5
Membrane life time [years], TD	1	3	5
Risk of an overpressure incident	Bernoulli distribution		

Within the context of the present study in particular, one considers two possibilities were considered:

i. Place a single relief system at the designated two locations and pay less at the process start-up stage, essentially taking a chance and accepting the cost of possible consequences should a process shutdown occur.

ii. Exercise caution and introduce an additional spare safety relief system (cautionary redundancy) to ensure continuity in system operation. Such a risk reducing measure requires higher pre-investment on safety but could potentially also prevent, mitigate or minimize the costs associated with the loss of plant capacity in the presence of an adverse overpressure incident.

Similar to the Chapter 11.2.1, the uncertainty related to the possible occurrence of an industrial accident such as the above was probabilistically represented in our NPV-Monte Carlo model through a simple Bernoulli distribution assigned to the 7th additional uncertain value driver (risk of overpressure incident). Since the focus of the present study was placed on the economic assessment of an inherently safe membrane reactor module in the presence of uncertainty and in particular the possibility of an industrial accident, and the revenue stream generated through the sales of electricity was fixed (the same positive additive term in the cash flows of the NPV-model Eqs (4.3) and (4.2) under all scenarios considered), the NPV-Monte Carlo analysis is performed on the cost component of the cash flows in the NPV-model Eqs (4.3)and (4.2) (where all the uncertain inputs appear). Hence, the modified formula for the NPV-cost (NPVC) is given in Eq encompassing both the initial investment in equipment to enhance process safety as well as the total cost incurred in case the accident does occur:

$$NPVC = (C_o - C_{safety}) - (pr \times D_0)DF + PV \tag{11.2}$$

where $DF = \sum_{t=1}^{N} \frac{1}{(1+r_t)^t}$ is unit annuity present value factor, C_{safety} is the safety pre-investment amount, pr is the probability of occurrence of the overpressure/accident (associated with a Bernoulli distribution) and D_0 is the expected loss or a monetary measure of damage (total cost incurred) due to the occurrence of the accident. The probability was assumed to be 10^{-1} year^{-1} which equaled the probability of a minor accident reported by Pasman (2000). The specific safety pre-investment amount (C_{safety}) was the initial investment on the RRS systems. The

expected loss (D_o) for the first case corresponds to the cost of ruptured discs (should any overpressure incident happen) plus the cost associated with the loss in revenues for the time period the system was shut down and remained idle. Finally, the expected loss (D_o) corresponded to the replacement cost of rupture discs in the second case.

Table 11-4. Stream specifications at the pressure relief system locations

Location→	1	2
Composition		
CO	0.0963	0.0547
H_2O	0.3499	0.3318
CO_2	0.2501	0.3237
H_2	0.3038	0.2898
# Tubes	1231.9	1231.9
$MW_{mix,dry}$ [g/mol]	14.3084	16.354
C_p [j/mol.K]	24.07	26.01
C_v [j/mol.K]	15.75	17.70
$k = C_p/C_v$	1.528	1.469
$F_{retentate,dry}$		
Single tube [mol/s]	0.59	0.55
Single tube [g/s]	8.43	9.06
Total [kg/s]	10.38	11.16
Total [lb/h]	82416.68	88605.76
F_{steam}		
Single tube [mol/s]	0.317	0.275
Single tube [g/s]	5.707	4.959
Total [kg/s]	7.031	6.101
Total [lb/h]	55803.3	48426.2

The gas composition, flow rate, temperature and pressure values were required in the selection of the proper size and type of the pressure relief system. Thus, the gas properties at the aforementioned two locations were determined by using the 2D membrane reactor model as described in Table 11-4. A combined rupture disc and safety relief valve were selected for the membrane reactor as explained in detail in Appendix A along with the pertinent decision tree for pressure relief systems (API 520, 1990; Ling 2007; Mukherjee 2008; Brazier 2009). The required discharge area had to be calculated also in order to estimate the cost of the RRS system. The guidelines presented in the API Recommended Practice 520 (API 520, 1990) were utilized in order to determine the discharge areas as summarized below. In the discharge area calculations, the design case corresponded to a blocked discharge and the related safety relief valve and rupture disc design parameters are listed in Table 11-5.

Table 11-5. Safety relief valve/rupture disc design parameters

Location→	1	2
Back P [psia]	14.7	14.7
Set P [psig]	793.8	867.3
Offset [%]	10	10
P_1 [psia]	873.2	954.0
P_{cf} [psia]	443.3	493.1
C	367	362
K_d	0.975	0.975
K_b	1	1
T (F+460) [R]	1212	1212

- Step 1. Determine the flow characteristic (API 520, 1990)

The critical flow throat pressure was used as an indicator to determine if the flow was critical or subcritical. The critical flow pressure ratio was estimated using the ideal gas relationship in Eq (11.3).

$$\frac{P_{cf}}{P_1} = \left[\frac{2}{k+1}\right]^{k/(k-1)} \tag{11.3}$$

where P_{cf} is the critical flow throat pressure (psia), P_1 is the upstream relieving pressure (psia), k is the ratio of specific heats for any ideal gas (heat capacity at constant pressure/heat capacity at constant volume).

Critical flow would occur if the pressure downstream of the throat was less than or equal to the critical flow pressure (P_{cf}). If the downstream pressure exceeded the critical flow pressure, then subcritical flow would occur.

Table 11-6. Relief requirements

Relief valve set pressure [psig]	793.8
Permitted accumulation [%]	10
Back pressure [psig]	0
C_p [J/mol.K]	24.07
C_v [J/mol.K]	15.76
k (C_p/C_v)	1.53

Upstream relieving pressure (P1)

$$= \text{set pressure } + \text{ allowable overpressure } + \text{ atmospheric pressure}$$
$$= 793.8 \times 1.1 + 14.7$$

The critical flow pressure was calculated as 443 psia by using the the upstream relieving pressure (P_1) and Table 11-6. Since the back pressure (0 psig) was less than the critical flow pressure (443 psig), the relief valve area calculations were based on the critical flow equation.

- Step 2. Determine if the safety relief device system needed to be independent or combined

The decision tree method (Chung et al. 2000; Parry 1992) to select between safety valve, rupture disc or a combination of the two was used as a guide to design the most appropriate relief system for the WGSMR. The direction designated with the blue arrows in Figure 11-2 was

followed for the membrane reactor and a bursting disc upstream and downstream of safety valve configuration was selected.

The discharge area of a rupture disc could be calculated in the same fashion as the safety relief valve with the only difference being in the value of K_d. The value of the effective coefficient of discharge (K_d) for rupture discs was 0.62.
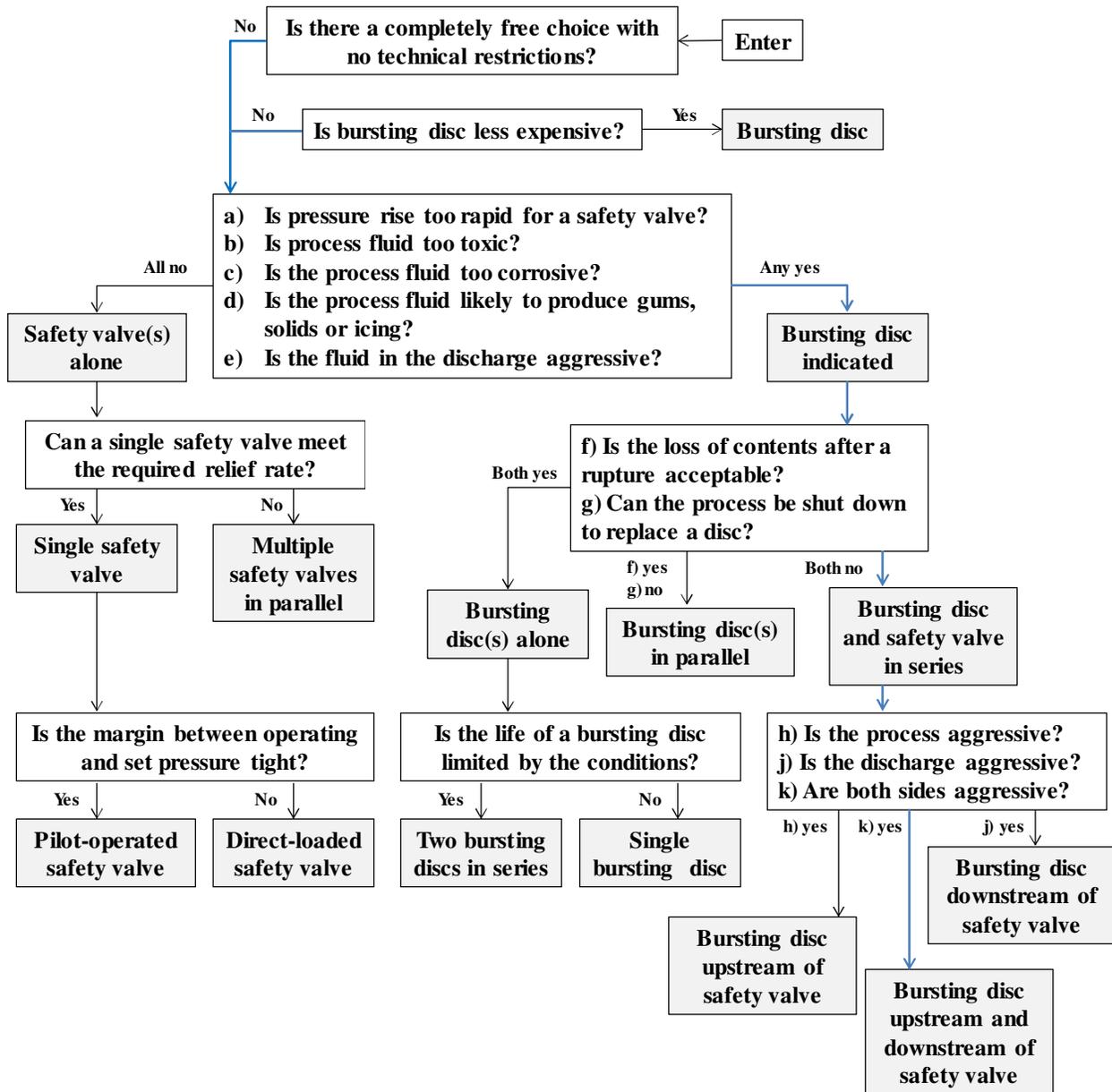
Figure 11-2. Decision tree for selection of relief devices (Parry 1992)

- Step 3. Determine the appropriate type of equation (API 520, 1990)

Since the syngas mixture in the membrane reactor consisted of hydrogen, carbon monoxide, carbon dioxide and steam, the required areas for the safety valve and rupture disc were calculated separately for the dry gas mixture and steam. The rupture disk and safety valves were assumed to be heated to 260°C to prevent the two phase flow due to steam condensation. Otherwise, the discharge area calculations could be performed by using equations related to the two-phase liquid/vapor relief. A valve, which had an effective discharge area equal to or greater than the calculated area, had to be chosen. The minimum discharge area for the dry gas mixture was calculated using Eq (11.4).

$$A_g = \frac{W}{C K_d P_1 K_b} \sqrt{\frac{TZ}{M}}$$ (11.4)

here A_g is the required effective discharge area of the valve (in^2), W is the required flow through the valve (lb/h), C is the coefficient determined from an expression which is dependent on specific heats of the gas/vapor at the standard conditions (obtained from Table 9 of (API 520, 1990), C = 325, K_d is the effective coefficient of discharge (K_d = 0.975), K_b is the capacity correction factor due to back pressure, applied only to balanced-bellows valves, T is the relieving temperature of the inlet gas/vapor (Rankine), Z is the compressibility factor evaluated at the inlet conditions, M is the molecular weight of the gas/vapor.

Since the gas mixture in the membrane reactor contained steam, the sizing of the relief valve for the portion of the steam was calculated separately using Eq (11.5) given below below:

$$A_s = \frac{W}{51.5\, K_d P_1 K_N K_{SH}}$$ (11.5)

where K_{SH} is the superheated steam correction factor (K_{SH} = 1 for saturated steam at any pressure), K_N is the correction factor for Napier equation:

K_N = 1 where $P_1 \leq$ 1515 psia

K_N = (0.1906P1-1000)/(0.2292P_1-1061) where P_1 >1515 psia and $\leq$ 3215 psia.

The final effective discharge area of the safety relief valve for the wet syngas mixture was found by using Eq (11.6):

$$A = A_s + A_g \tag{11.6}$$

The discharge areas for the safety relief valve and rupture disc were calculated as shown in Table 11-7. The required discharge areas were calculated separately for the dry gas and steam compositions of the syngas as explained earlier. The recommended sizes were adopted from the API Standard 526 based on the calculated discharge area and listed in Table 11-7. An Austenitic stainless steel (body/bonnet) spring-loaded pressure relief valve with a high-temperature alloy steel spring having the dimensions of 4M6 (inlet by orifice by outlet) could be used (API Standard 526, 2002). The recommended sizes by the manufacturer (Fike Corp., Pressure Relief Systems 2012; Sentrol Sensor & Control Solutions, Plymouth-MA 2012) were used for the rupture disc (3 in). The associated prices were found in the literature for safety relief valves (4P6) (Hellemans 2009) and the quotes from the manufacturer (Fike Corp., Pressure Relief Systems 2012) were used to calculate the price of the RRS system for the membrane reactor module. It is important to point out that the intent of this study was not to produce exact cost numbers, but rather to develop inherently safe membrane reactor module cost profiles and ranges of economic performance outcomes in order to demonstrate the inherent cost efficiency and prudential aspects of safety pre-investment strategies when even standard techno-economic performance metrics were considered in the presence of uncertainty. The RRS system cost estimate results calculated with the aforementioned method is listed in Table 11-8. The cost estimates were included in the total product cost for the membrane reactor module.

The NPVC distribution (risk-reward) profile for the Pd/Au-based membrane module is given in Figure 11-3 [a] by considering the 7 uncertain value drivers including the uncertainty and risk of an overpressure incident. The cumulative distribution function given in Figure 11-3[a] allowed a probabilistic/statistical characterization of the entire range of possible economic performance outcomes in the presence of uncertainty. The upper-right positive NPVC zone of Figure 11-3[a] was associated with quite favorable economic outcomes due to low Pd/Au price, low support price, longer membrane lifetime, etc; the lower-left negative NPVC zone of Figure 11-3[a] was associated with undesirable economic performance outcomes (possibly due to a relatively short membrane life time, high Pd price, etc). The NPVC profile which is closer to the y axis is preferable due to lower capital investment or lower revenue loss attributed to an accident. The NPVC profiles of the membrane module with and without the spare RRS pressure

relief system was shown in Figure 11-3[a]. Starting with the single RRS system option two likely values of the capacity factor distribution profile; namely 5 and 10% were considered.

Table 11-7. Calculated discharge area values

Safety Relief Valve		
Location→	1	2
A_g [in^2]	2.43	2.27
A_s [in^2]	1.27	1.01
A_{total} [in^2]	3.70	3.27
Rupture disc		
A_g [in^2]	3.75	3.50
A_s [in^2]	2.37	1.88
$A_{total} \times Kc^{\ddagger}$ [in^2]	4.9	4.31

$^{\ddagger}K_c$ is the capacity coefficient for rupture disc in combination with safety relief valve (K_c =0.8).

Table 11-8. RRS system cost estimates

	Spared RRS	Single RRS
# SRV	32	16
# RD	64	32
SRV [$]	92572	46286
RD [$]	143802	71901

When only one safety relief system was used (absence of precautionary redundancy), the operation might be stopped to replace the parts for an uncertain period of time which depends on the mounting procedure of the parts and manufacturer-related time delays. Even though the components of the safety relief system such as a rupture disc might be still in good condition, this type of equipment does need routine maintenance. Thus, the process might have to be shut down to perform the maintenance if there is no spare safety relief system. Consequently, the capacity factor of the plant will decrease due to a shut down (resulting also in a loss of revenues).

If the maximum capacity factor for an IGCC plant with embedded WGSMR was 85%, a 5% capacity factor loss corresponds to 2 weeks of operation-hour loss and a total of 41 weeks per year. The NPVC-profile of the membrane module with a spare RRS system was shown to move to the right and closer to the y axis, thus becoming more attractive than the one without a spare relief system (Figure 11-3[a]). The NPVC profile of such a WGSMR module would be thus preferred because the loss in revenues would have been significantly higher than the cost of introducing a spare RRS system. The values of key statistical performance indicators associated with the above NPVC profiles were also summarized in Table 11-9, namely the average, maximum and minimum values for all economic outcomes generated by the Monte Carlo simulator. The observed difference in the cost figure (of almost US$ 27 million) between the case with a spare RRS system and the one involving a single RRS system with a capacity factor centered at 10% did not obviously correspond to a minor loss in revenues.

Table 11-9. The expected NPVC results (for Figure 11-3[a])

NPVC [US M$] ↓	Spared	Single ML: 5%	Single ML: 10%
Average	-133.8	-156.4	-160.7
Max	-66.3	-67.1	-66.9
Min	-262.1	-310.8	-302.0
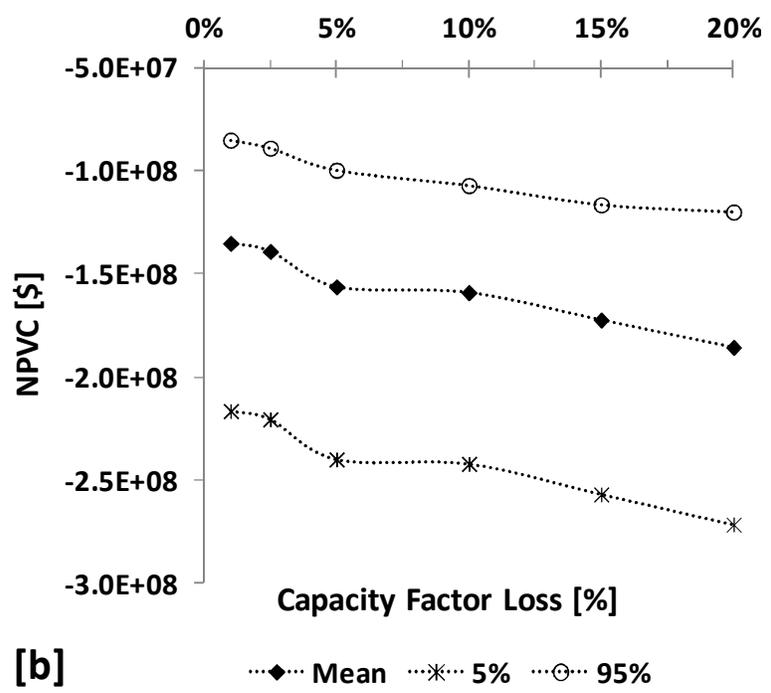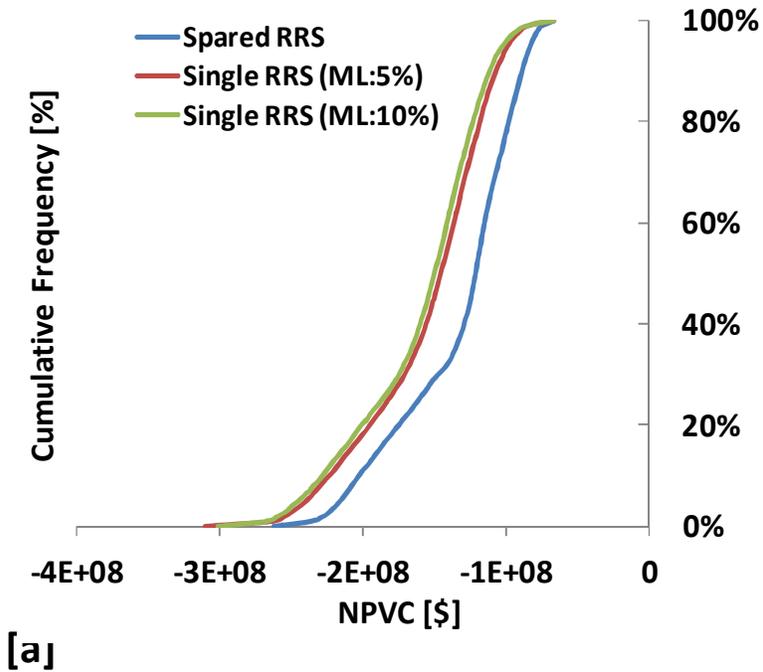
Figure 11-3. NPVC profile for the Pd/Au-based membrane reactor module [a], seeding on the capacity factor loss [b].

The uncertainty in the capacity factor loss was incorporated into the NPVC model by assigning a triangular probability distribution. However, the most likely value of the capacity factor loss might change the average of all possible economic performance outcomes. Thus, a parameterized simulation was run by changing the value of the capacity factor loss as shown in Figure 11-3[b]. The NPVC profiles for each value of the capacity factor loss were determined, and then the results were presented in Figure 11-3[b] by using the mean of all 10^4 outcomes together with the average of the outcomes within the 5% and 95% of all outcomes. As shown in Figure 11-3 [b], a steep increase was observed twice in the NPVC profile as the capacity factor loss increased from 2.5% to 5% and at capacity factor loss values higher than 10%. Based on the economic conditions considered, a week of working hour loss would result in an annual loss of US$ 7.4 million for an IGCC power plant with a net plant output of 550 MWe. Notice that even a week of difference in working hours resulting from a 2.5% to 5% difference in capacity loss caused a drastic increase in revenue loss. Therefore, pre-investment on safety measures, such as safety relief systems to prevent overpressure incidents, not only helped to mitigate or minimize the effects of accidents and possibly catastrophic events, but might also significantly improve the economics of the process.

11.3.   Conclusions

An economic performance assessment of inherently safe Pd/alloy-based membrane reactor technology option integrated into IGCC power plants in the presence of market and regulatory uncertainty as well as technology and safety risks has been performed.

The uncertainty in key inputs to the NPV- model (plant capacity factor, nominal discount rate, inflation rate, CO_2 tax, CO_2 tax growth rate, electricity selling price, Pd price, support price and membrane lifetime) and also the uncertainty/risk in plant safety (realized as an additional random variable that follows a simple Bernoulli distribution to describe the possibility of the occurrence of an industrial accident) were explicitly considered for an IGCC-MR plant. A comparatively more attractive NPV distribution profile was obtained when concrete safety risk-reducing measures were taken into account through pre-investment in process safety, giving credence to the thesis that process safety investments might result in enhanced economic performance in the presence of irreducible uncertainties.

A basic approach has been proposed to show the economic benefits of pre-investment on membrane reactor safety in the presence of irreducible uncertainties. In particular, the cost related to a spare safety relief system consisting of two rupture discs and a safety relief valve and the cost associated with revenue loss due to a process system shut-down in the absence of a backup safety relief system were compared. The NPV-cost distribution profiles of an inherently safe membrane reactor module which was designed to be integrated into an IGCC power plant with a net power output of 550 MWe endowed with a spare safety relief system was found to be more attractive than the one endowed with a single safety relief system under the conditions of the accident scenario considered in the present study. Therefore, concrete safety risk-reducing measures through pre-investment in process safety were shown to be value-enhancing in the presence of uncertainty.

12. Conclusions

The main conclusions could be listed briefly as follows:

- A process intensification methodology for the water-gas shift membrane reactor, in four main areas namely process enhancement, control, safety and economics was proposed. The reaction conditions, reactor dimensions and safe operation guidelines were determined to achieve cost effective operation of an inherently safe Pd-based water-gas shift membrane reactor.

- A feedback controller with proportional and integral action (PI controller) was considered and implemented to the water-gas shift membrane reactor. The controlled and manipulated variables were chosen as the CO fraction at the shell exit and the steam molar flow rate at the inlet, respectively. The objective of the controller was to keep the overall CO conversion (>95%) at the desired value (set-point) in the presence of disturbances.

- Two control strategies namely regulatory control where an unexpected membrane reactor total pressure drop occurred and servo mechanism control where the set level of CO conversion was increased to 98%. In both cases, quite satisfactory process control was attained maintaining CO conversion at levels higher than 95% so that the retentate stream could become suitable for high pressure CO_2 sequestration.

- The absence of adequate control of the reactor temperature as well as the purity of the feed which might cause hot spots and decline in permeance and selectivity were identified and classified as critical for the operation of the WGS membrane reactor.

- Utilization of excess steam together with the application of vacuum on the permeate side were found to be the most effective method of reducing the temperature rise in the reaction zone without decreasing the overall CO conversion and H_2 recovery.

- Since the main advantage of the Pd/alloy based membrane reactor technology is the high-quality H_2 separation driven by the H_2 partial pressure difference between the reaction and permeate sides, operation at high reaction side pressure is inevitable. Therefore, high pressure reactor operation represents a process safety challenge.

- Under safe operation zone, the total reaction side pressure was determined to be at least 35 atm at a fixed permeate side pressure of 1 atm to attain the target performance levels. Alternatively, the permeate side pressure has to equal or be lower than 0.6 atm (with vacuum) at a fixed total reaction side pressure of 30 atm, to attain the performance target levels of $X_{CO} = 98\%$ and $R_{H2} = 95\%$, by using a feed temperature of 350°C, permeate pressure of 1 atm, H_2O:CO ratio of 4.5 and 50% $\rho_{Bulk,max}$ for an adiabatic membrane reactor.

- The purity levels of the separated H_2 by using membranes having various selectivity values were successfully assessed through the use of a membrane reactor model including multi-component gas diffusion through the defects. The simulation results supported with the experimental findings showed that H_2 purity of 99.99% and flux target of 250 scfh/m^2 specified by the DOE could be easily achieved by using a Pd-based membrane having ~39 m^3/[m^2-h-atm$^{0.5}$] H_2 permeance and ~8000 ideal H_2/He selectivity, prepared through the current membrane synthesis technology developed in the CIMS laboratory, WPI.

- The single estimate/projection NPV results showed that the IGCC-MR was an economically attractive technology option generating a positive NPV in a scenario with a 25 \$/tonne CO_2 tax starting in 2015. The negative NPV values of IGCC-PBR and SC-PC with CO_2 capture plants would possibly preclude these options from investment consideration in the presence of regulatory action on carbon emissions.

- The average total product cost of an industrial scale water-gas shift membrane reactor module was determined as 1464 US\$/ft^2 in the presence uncertainties in Pd/Au, support prices and membrane life time (maximum = 3353 US\$/ft^2 and minimum = 621 US\$/ft^2).

- The uncertainty in nine key inputs of the NPV/Cost model was considered for IGCC-MR, IGCC-PBR and SC-PC with capture options producing the same amount of net power

output, 550 MWe. A comparatively more attractive NPV/Cost distribution profile obtained in the IGCC-MR case assessed against the ones in the IGCC-PBR and SC-PC cases in the presence of regulatory action on CO_2 emissions makes the Pd-based membrane reactor technology option integrated into an IGCC power plant a promising investment choice.

- The uncertainty in plant safety (with a simple Bernoulli distribution to describe the possibility of the occurrence of an industrial accident) was included in the Monte Calo simutaltion to identify the NPV distribution of an inherently safe IGCC-MR plant. A comparatively more attractive NPV distribution profile was obtained when concrete safety risk-reducing measures were taken into account through pre-investment in process safety, giving credence to the thesis that process safety investments might result in enhanced economic performance in the presence of irreducible uncertainties.

13. Recommendations

In the economic analysis section;

- The economic analysis of the IGCC power plant with embedded membrane reactors could be updated to take into account the adjustable revenues coming from H_2 and electricity selling based on the market demand. The relative amounts of the H_2 and electricity selling can be changed whichever is more profitable during the corresponding market environment.

- Since the cost figures of the DOE/NETL report (Haslbeck et al. 2010) were directly used in the economic analysis, a verification of the cost and performance analysis of the IGCC-MR could be performed by rebuilding the system by using the ASPEN modeling tool. Particularly, the IGCC-MR could be updated by including the hot-gas desulfurization unit instead of Selexol unit.

- The configuration possibilities of membrane reactors integrated into coal gasification plants needs to be investigated in order to identify the ones with enhanced performance prospects based on production target levels and process economics. Three illustrative configuration examples could be examined: 1) a membrane separation unit (P_{tube}=1 atm) to remove the H_2 content of the syngas and the membrane reactor connected in series (P_{tube}=0.5 atm); 2) a membrane reactor operating at a high permeate side pressure to reduce the compression costs of H_2 (P_{tube}=10 atm) followed by a second membrane reactor (P_{tube}=0.5 atm); 3) a combined-membrane reactor representing a single reactor unit whose first 70% of its spatial domain is filled with catalyst and the remaining part is used merely for H_2 separation purposes (P_{tube}=0.5 atm) in order to utilize both the membrane and catalyst under maximum efficiency.

- The flexibility analysis proposed by de Neufville and Scholtes (de Neufville et al. 2011) could be included into the economic analysis. It is possible to increase the profitability of

the membrane reactor technology option significantly by designing it cleverly to deal with future eventualities. Both membrane reactor configuration possibilities mentioned and adjustable revenues by H_2 and electricity selling are flexible design options. In addition, hybrid systems in the IGCC power plants could be designed such as combination of Selexol units, packed bed reactors and polymer membranes (operating at low temperatures such as polybenzimidazole (PBI) membranes which can achive the optimum performance in terms of permeability and H_2/CO_2 selectivity between 200 and 270°C (Li et al. 2008)) together with the Pd-based membrane reactors.

The present research study was centered at the integration of the Pd-Pd/alloy based composite membranes supported on metal substares ino coal fired power plants. Therefore, a comprehensive process intenficiation methodology was followed to achieve an efficient, safe and economical membrane reactor operation. The same type of methodology could be applied to any type of specific innovation related with the fields in the Chemical Engineering world such as manufacturing, pharmaceuticals, healthcare, pulp and paper, petrochemicals, food processing, polymers, biotechnology, and environmental health and safety industries ans so on. The main steps pursued in the present study are followings:

The application areas of the specific innovation (Pd-based membrane reactors) were investigated. The advantages and disadvantages related with the application area were identified to find solutions to overcome the challenge. For instance, the high pressure operation of the water-gas shift membrane reactor was a safety challenge.

The fabrication and characterization procedures of the product have to be established. In addition, the fabrication technique of the product at laboratory scale as well as large scale should be feasible. The knowledge obtained from fabrication/characterization history should be used to further improve/enhance the product features. The Pd thickness levels as low as 5-10 µm with high ideal H_2/He selectivity values >1000 is a good example. The selection of the most appropriate surface modification way among the method namely, Al_2O_3+Pd/Ag barrier, $Al(OH)_3$ grading and modified sequential Al_2O_3 grading, could be shown as an illustrative case.

When the lab-scale results are promising, the utilization of modeling tools might help to save time and money before jumping the next stage, pilot scale operation. Thus, performance evaluation at the desired conditions could be done by using simulation tools in advance. In the present study, the CO conversion, H_2 recovery and purity levels for both lab-scale and industrial scale applications were identified by using simulations based on the mass and energy balances for a Pd-based water-gas membrane reactor using MATLAB. If available, the pilot scale and larger scale test results has to be compared with the simulation results inorder to verify and/or eliminate the drawbacks.

At startup, the design should be made not only to provide the highest yield, conversion, profit and so on, but also the process has to be inherently safe. Since safety comes first, the high performance levels and economics advantages of certain operating regimes could be sacrificed in certain conditions. The water-gas shift membrane reactor case, the HAZOP analysis was performed by using the membrane reactor as a node and the HAZOP worksheets were tabulated for reaction parameters such as feed temperature, reaction side pressure, etc.

No engineering project can survive if it is not economically viable. Thus, the technical aspects of any new engineering idea have to be considered together with the related costs. The project value has to be estimated in advance by using economy tools such as paypack method, average retun on book value, internal rate of return and net preset value. Investors seek for solid results to choose between options and a high level of profit represetnted by economy tools such as net present value for a new engineering project could eliminate idea of risk in an investor's mind. The Net Present Value (NPV) method was used for Pd-based membrane reactor integration into IGCC coal-fired power plants due to its more reliable nature compared to others (Brealey and Myers 1996).

The dynamic and active nature of the economy in an uncertain world hinders the use of simple and static economic tools and more representative methods are required in the reacl world. The integration of Pd-based membrane reactors into coal-fired power plants represents a new technology option which has neither been fully tested nor yet demonstrated at a commercial scale. The lack of operating experience associated with membrane reactor technology options integrated into IGCC power plants on the commercial scale inevitably

produces a lack of real data pertinent to process economics. Consequently, any economic performance evaluation at this early stage would be driven by reasonable yet theoretical estimates, but methodologically should acknowledge irreducible (market, regulatory, technological) uncertainties in an explicit manner (Savage 2002). Thsu, the Monte Carlo simulations was used in order to provide NPV distributions rather than using single point NPV values.

Last but not the least, any engineering project based on absolute technical paramaters would fail if not accompanied by the social, economic and regulatory factors. As de Neufville and Scholtes (de Neufville et al. 2011) emphasized, we need "d*ynamic socio-technical"* models to evaluate the project value. Design engineers could benefit from socio-technical models by exploring alternative configuration options of a process and by selecting the preferred solution. Thus, the NPV model built for the IGCC power plant with an embedded membrane reactor could be updated by considering some of the socio-technical parameters such as CO_2 capture and co-production of electricity and H_2 in a flexible manner based on the future eventualities.

References

Fike corp., Pressure Relief Systems, http://www.fike.com/pressurerelief.html.

Sentrol sensor & control solutions, Personal communication, Plymouth-MA.

Annual energy outlook 2011, carbon dioxide emissions by sector and source, united states. Accessed year: 2011. http://www.eia.gov/forecasts/aeo/MT_coal.cfm#lto.

Chand Eisenman, Burlington, CT and Mott Metallurgical Corporation, Farmington, CT.

DOE-Hydrogen and clean fuels, system studies. Accessed year: 2012. http://www.netl.doe.gov/technologies/hydrogen_clean_fuels/systems_studies.html.

EIA 2010- U.S. Coal reserves current and back issues. Accessed year: 2012. http://www.eia.gov/cneaf/coal/reserves/reserves.html.

Fuel cell technologies program multi-year research, development and demonstration plan. Accessed year: 2011. http://www1.eere.energy.gov/hydrogenandfuelcells/mypp/.

Hydrogen from coal R&D plan. Accessed year: 2012. http://fossil.energy.gov/programs/fuels/hydrogen/Hydrogen_from_Coal_R%26D.html.

NIST chemistry WebBook. Accessed year: 2012. http://webbook.nist.gov/chemistry/.

Pulverized coal power. Accessed year: 2012. http://www.wri.org/publication/content/10338.

US DOL. Accessed year: 2011. http://www.bls.gov/opub/mlr/2011/09/mlr201109.pdf.

Marshall & swift cost indexes. Accessed year: 2012. http://www.che-digital.com/che/201001?pg=90#pg90.

Mathworks. Accessed year: 2012. http://www.mathworks.com/.

Cost and performance baseline for fossil energy plants. Accessed year: 2007. http://www.netl.doe.gov/energy-analyses/pubs/Bituminous%20Baseline_Final%20Report.pdf.

Flanged steel pressure relief valves. API Standard 526, Fifth Edition: 2002.

Guide for pressure-relieving and depressuring systems. API Recommended Practice 521, Third Edition: 1990.

Sizing, selection, and installation of pressure-relieving devices in refineries, part 1-sizing and selection.API Recommended Practice 520, Fifth Edition: 1990.

Aasberg-Petersen, K., Nielsen, C. S., Jørgensen, S. L. , 1998. Membrane reforming for hydrogen. *Catalysis Today* 46 (2–3): 193-201.

Abdollahi, M., Yu, J., Liu, P. K. T., Ciora, R., Sahimi, M., Tsotsis, T. T. , 2010. Hydrogen production from coal-derived syngas using a catalytic membrane reactor based process. *Journal of Membrane Science* 363 (1-2): 160-9.

Adams, T. A., Barton, P. I. , 2009. A dynamic two-dimensional heterogeneous model for water gas shift reactors. *International Journal of Hydrogen Energy* 34 (21): 8877-91.

Adrover, M. E., López, E., Borio, D. O., Pedernera, M. N. , 2009a. Simulation of a membrane reactor for the WGS reaction: Pressure and thermal effects. *Chemical Engineering Journal* 154 (1-3): 196-202.

Adrover, M. E., López, E., Borio, D. O., Pedernera, M. N. , 2009b. Theoretical study of a membrane reactor for the water gas shift reaction under nonisothermal conditions. *AICHE Journal* 55 (12): 3206-13.

Cambridge, Mass.: Belfer Center for Science and International Affairs, Al-Juaied, M. A., Whitmore, A. , 2009. *Realistic costs of carbon capture.* Discussion Paper 2009-08.

TDA Research, Inc.,Alptekin, G., Lind, J., Amalfitano, R. and Copeland, R. , 1917. *Sorbents for Mercury Removal from Coal-Derived Synthesis Gas*TDA Research, Inc.

Amelio, M., Morrone, P., Gallucci, F., Basile, A. , 2007. Integrated gasification gas combined cycle plant with membrane reactors: Technological and economical analysis. *Energy Conversion and Management* 48 (10): 2680-93.

Andrés, M., Boyd, T., Grace, J. R., Lim, C. J., Gulamhusein, A., Wan, B., Kurokawa, H., Shirasaki, Y. , 2011. In-situ CO_2 capture in a pilot-scale fluidized-bed membrane reformer for ultra-pure hydrogen production. *International Journal of Hydrogen Energy* 36 (6): 4038-55.

Armor, J. N. , 1998. Applications of catalytic inorganic membrane reactors to refinery products. *J.Membr.Sci.* 147 : 217,217-223.

Arstad, B., Venvik, H., Klette, H., Walmsley, J. C., Tucho, W. M., Holmestad, R., Holmen, A., Bredesen, R. , 2006. Studies of self-supported 1.6 μm Pd/23 wt.% ag membranes during

and after hydrogen production in a catalytic membrane reactor. *Catalysis Today* 118 (1-2): 63-72.

Augustine, A. S., Ma, Y. H., Kazantzis, N. K. , 2011. High pressure palladium membrane reactor for the high temperature water–gas shift reaction. *International Journal of Hydrogen Energy* 36 (9): 5350.

Augustine,A. S., Ayturk, M. E., Kazantzis, N. K., Ma, Y. H., "Composite Palladium Membrane Reactor for Hydrogen Production with Syngas Feed" (Presentation, , 2010).

———. "Composite Palladium Membrane Reactor for the Water Gas Shift Reaction" (Presentation, , 2009).

Ayturk, M. E. , 2007. Synthesis, annealing strategies and *in-situ* characterization of thermally stable composite thin Pd/Ag alloy membranes for H_2 separation.Worcester Polytechnic Institute.

Ayturk, M. E., Augustine, A. S., Ma, Y. H. , 2009. Long-term selectivity stability and high-pressure mixed gas hydrogen permeation testing of composite Pd/Inconel membranes. Paper presented at AICHE 09, Nashville TN, .

Ayturk, M. E., Engwall, E. E., Ma, Y. H. , 2007. Microstructure analysis of the intermetallic diffusion-induced alloy phases in composite Pd/Ag/Porous stainless steel membranes. *Industrial & Engineering Chemistry Research* 46 (12): 4295-306.

Ayturk, M. E., Ma, Y. H. , 2009. Electroless pd and ag deposition kinetics of the composite pd and Pd/Ag membranes synthesized from agitated plating baths. *Journal of Membrane Science* 330 (1-2): 233-45.

———. "Synthesis and Characterization of Pd-Based Composite Membranes by $Al(OH)_3$ Grading" (DOE_Project_07NT43058, , 2008).

Ayturk, M. E., Payzant, E. A., Speakman, S. A., Ma, Y. H. , 2008. Isothermal nucleation and growth kinetics of Pd/Ag alloy phase via in situ time-resolved high-temperature X-ray diffraction (HTXRD) analysis. *Journal of Membrane Science* 316 (1-2): 97-111.

Ayturk, M. E., Kazantzis, N. K., and Ma, Y. H. , 2009. Modeling and performance assessment of pd- and Pd/Au-based catalytic membrane reactors for hydrogen production. *Energy & Environmental Science* 2 : 430,430-438.

Ayturk, M. E., Mardilovich, I. P., Engwall, E. E., Ma, Y. H. , 2006a. Synthesis of composite pd-porous stainless steel (PSS) membranes with a Pd/Ag intermetallic diffusion barrier. *Journal of Membrane Science* 285 (1-2): 385-94.

Ayturk, M. E., Mardilovich, I. P., Engwall, E. E., Ma, Y. H. , 2006b. Synthesis of composite pd-porous stainless steel (PSS) membranes with a Pd/Ag intermetallic diffusion barrier. *Journal of Membrane Science* 285 (1-2): 385-94.

Barbieri, G., Brunetti, A., Granato, T., Bernardo, P., Drioli, E. , 2005. Engineering evaluations of a catalytic membrane reactor for the water gas shift reaction. *Industrial & Engineering Chemistry Research* 44 (20): 7676-83.

Barbieri, G., Brunetti, A., Tricoli, G., Drioli, E. , 2008a. An innovative configuration of a pd-based membrane reactor for the production of pure hydrogen: Experimental analysis of water gas shift. *Journal of Power Sources* 182 (1): 160-7.

Barbieri, G., Scura, F., Lentini, F., De Luca, G., Drioli, E. , 2008b. A novel model equation for the permeation of hydrogen in mixture with carbon monoxide through Pd–Ag membranes. *Separation and Purification Technology* 61 (2): 217-24.

Barelli, L., Bidini, G., Gallorini, F., Servili, S. , 2008. Hydrogen production through sorption-enhanced steam methane reforming and membrane technology: A review. *Energy* 33 (4): 554-70.

Bartolozzi, V., Castiglione, L., Picciotto, A., Galluzzo, M. , 2000. Qualitative models of equipment units and their use in automatic HAZOP analysis. *Reliability Engineering & System Safety* 70 (1): 49-57.

Basile, A., Chiappetta, G., Tosti, S., Violante, V. , 2001. Experimental and simulation of both pd and Pd/Ag for a water gas shift membrane reactor. *Separation and Purification Technology* 25 (1-3): 549-71.

Basile, A., Criscuoli, A., Santella, F., Drioli, E. , 1996a. Membrane reactor for water gas shift reaction. *Gas Separation & Purification* 10 (4): 243-54.

Basile, A., Drioli, E., Santell, F., Violante, V., Capannelli, G., Vitulli, G. , 1996b. A study on catalytic membrane reactors for water gas shift reaction. *Gas Separation & Purification* 10 (1): 53-61.

Beér, J. M. , 2000. Combustion technology developments in power generation in response to environmental challenges. *Progress in Energy and Combustion Science* 26 (4-6): 301-27.

Benninga, S. , 2006. *Principles of finance with excel*. New York: Oxford University Press.

Bhat, S. A., Sadhukhan, J. , 2009. Process intensification aspects for steam methane reforming: An overview. *AICHE Journal* 55 (2): 408-22.

Bhattacharya, S., Hwang, S. , 1997. Concentration polarization, separation factor, and peclet number in membrane processes. *Journal of Membrane Science* 132 (1): 73-90.

Bird, R. B., Stewart, W. E., Lightfoot, E. N. , 1990. *Transport phenomena*. New York, NY: John Wiley & Sons, Inc.

Bohlbro, H. , 1970. Catalysts for the conversion of carbon monoxide. *Chem. Eng. World* 5 (8): 46.

———. , 1963. The kinetics of the water gas conversion. III. influence of H2S on the rate equation. *ACTA CHEM SCAND* 17 (4): 1001.

———. , 1961. The kinetics of the water gas conversion at atmospheric pressure. *ACTA CHEM SCAND* 15 : 502,502-520.

Bohm, M. C., Herzog, H. J., Parsons, J. E., Sekar, R. C. , 2007. Capture-ready coal plants—Options, technologies and economics. *International Journal of Greenhouse Gas Control* 1 (1): 113-20.

Bohm, M. C. , 2006. Capture-ready power plants - options, technologies and economics.Massachusetts Institute of Technology.

Boon, J., Dijk, E. v., Pirgon-Galin, O., Haije, W., Brink, R. v. d. , 2009. Water-gas shift kinetics over FeCr-based catalyst: Effect of hydrogen sulphide. *Catal. Lett.* 131 : 406,406-412.

Boon, J., Li, H., Dijkstra, J. W., Pieterse, J. A. Z. , 2011. 2-dimensional membrane separator modelling: Mass transfer by convection and diffusion. *Energy Procedia* 4 (0): 699-706.

Bose, A. C. , 2009. Chapter 13. composite pd and Pd/Alloy membranes. In *Inorganic membranes for energy and environmental applications*. NY, USA: Springer Science+Business Media.

Bracht, M., Alderliesten, P. T., Kloster, R., Pruschek, R., Haupt, G., Xue, E., Ross, J. R. H., Koukou, M. K., Papayannakos, N. , 1997. Water gas shift membrane reactor for CO2 control in IGCC systems: Techno-economic feasibility study. *Energy Conversion and Management* 38 (Supplement 1): S159-64.

Chemical Engineering, Brazier, G. , 2009. *Combining rupture disks with safety relief valves.*

Brealey, R. A., Myers, S. C. , 1996. *Principles of corporate finance*. 5th edition ed. USA: The McGraw-Hill Componies, Inc.

Bredesen, R., Jordal, K., Bolland, O., 2004. High-temperature membranes in power generation with CO_2 capture. *Chemical Engineering and Processing* 43 (9): 1129-58.

Brunetti, A., Barbieri, G., Drioli, E., 2011. Integrated membrane system for pure hydrogen production: A Pd–Ag membrane reactor and a PEMFC. *Fuel Processing Technology* 92 (1): 166-74.

———. , 2009a. Pd-based membrane reactor for syngas upgrading. *Energy & Fuels* 23 (10): 5073-6.

———. , 2009b. Upgrading of a syngas mixture for pure hydrogen production in a Pd–Ag membrane reactor. *Chemical Engineering Science* 64 (15): 3448-54.

Brunetti, A., Caravella, A., Barbieri, G., Drioli, E. , 2007. Simulation study of water gas shift reaction in a membrane reactor. *Journal of Membrane Science* 306 (1-2): 329-40.

Bryden, K. J., Ying, J. Y. , 1995. Nanostructured palladium membrane synthesis by magnetron sputtering. *Materials Science and Engineering A* 204 (1-2): 140-5.

Bunshah, R. F. , 1994. *Handbook of Deposition Technologies for Films and Coatings - Science, Technology and Applications (2nd Edition)*William Andrew Publishing/Noyes, http://www.knovel.com/web/portal/browse/display?_EXT_KNOVEL_DISPLAY_bookid=57.

Callaghan, C. A. , 2006. Kinetics and catalysis of the water-gas-shift reaction:A microkinetic and graph theoretic approach.Worcester Polytechnic Institute.

Callaghan, C., Fishtik, I., Datta, R., Carpenter, M., Chmielewski, M., Lugo, A. , 2003. An improved microkinetic model for the water gas shift reaction on copper. *Surface Science* 541 (1-3): 21-30.

Caravella, A., Barbieri, G., Drioli, E. , 2008. Modelling and simulation of hydrogen permeation through supported pd-alloy membranes with a multicomponent approach. *Chemical Engineering Science* 63 (8): 2149-60.

Caravella, A., Scura, F., Barbieri, G., Drioli, E. , 2010a. Inhibition by CO and polarization in pd-based membranes: A novel permeation reduction coefficient. *The Journal of Physical Chemistry B* 114 (38): 12264-76.

———. , 2010b. Sieverts law empirical exponent for pd-based membranes: Critical analysis in pure H2 permeation. *The Journal of Physical Chemistry B* 114 (18): 6033-47.

Catalano, J., Guazzone, F., Mardilovich, I. P., Kazantzis, N. K., Ma, Y. H. , 2011. Hydrogen production in a large scale water-gas shift pd-based catalytic membrane reactor. *Industrial & Engineering Chemistry Research*.

Cayan, F. N., Zhi, M., Pakalapati, S. R., Celik, I., Wu, N., Gemmen, R. , 2008. Effects of coal syngas impurities on anodes of solid oxide fuel cells. *Journal of Power Sources* 185 (2): 595-602.

Center for Chemical Process Safety/AIChE. , 1993a. Chapter 14. pressure relief systems. In *Guidelines for engineering design for process safety.*Center for Chemical Process Safety/AIChE.

———. , 1993b. Chapter 17. explosion protection. In *Guidelines for engineering design for process safety.*Center for Chemical Process Safety/AIChE.

Chapel, D. G., Mariz, C.L and Ernest, J. , 1999. Recovery of CO_2 from flue gases: Commercial trends. *Presented at the Canadian Society of Chemical Engineers Annual Meeting, October 4-6, 1999, Saskatoon, Saskatchewan, Canada.*

Checchetto, R., Bazzanella, N., Patton, B., Miotello, A. , 2004. Palladium membranes prepared by r.f. magnetron sputtering for hydrogen purification. *Surface and Coatings Technology* 177-178 : 73-9.

Chen,C., Ma, Y. H., "The Effect of Au Content in Composite Pd/Au Membranes Prepared by Galvanic Displacement on Hydrogen Permeance and H_2S Resistance " (Presentation, , 2010a).

———. , 2010b. The effect of H_2S on the performance of pd and Pd/Au composite membrane. *Journal of Membrane Science* 362 (1-2): 535-44.

Chen, C., Rubin, E. S. , 2009. CO_2 control technology effects on IGCC plant performance and cost. *Energy Policy* 37 (3): 915-24.

Chen, S. C., Hung, C. C. Y., Tu, G. C., Rei, M. H. , 2008a. Perturbed hydrogen permeation of a hydrogen mixture—New phenomena in hydrogen permeation by pd membrane. *International Journal of Hydrogen Energy* 33 (7): 1880-9.

Chen, S. C., Tu, G. C., Hung, C. C. Y., Huang, C. A., Rei, M. H. , 2008b. Preparation of palladium membrane by electroplating on AISI 316L porous stainless steel supports and its use for methanol steam reformer. *Journal of Membrane Science* 314 (1-2): 5-14.

Chervotkin, V., Bokovikov, B. A., Gogolev, Y. F. , 1969. Privalov SI. sb nauch tr. *Vses Nauch-Issled Inst Met Teplotek* 16 : 108,108–118.

Chiappetta, G., Clarizia, G., Drioli, E. , 2006. Improvement of membrane reactor performance in hydrogen production. *Desalination* 200 (1-3): 695-6.

Chiappetta, G., Clarizia, G., Drioli, E. , 2008. Theoretical analysis of the effect of catalyst mass distribution and operation parameters on the performance of a pd-based membrane reactor for water–gas shift reaction. *Chemical Engineering Journal* 136 (2-3): 373-82.

———. , 2006a. Analysis of safety aspects in a membrane reactor. *Desalination* 193 (1-3): 267-79.

Chiappetta, G., Clarizia, G., Drioli, E. , 2006b. Design of an integrated membrane system for high level hydrogen purification. *Desalination* 200 (1-3): 267-8.

Chiesa, P., Lozza, G. Using hydrogen as gas turbine fuel. [Accessed Year 2012]. Available from http://www.netl.doe.gov/technologies/coalpower/turbines/refshelf/igcc-h2-sygas/Using%20H2%20as%20a%20GT%20Fuel.pdf.

Chung, P. W. H., Yang, S., He, C. , 2000. Conceptual design of pressure relief systems. *Journal of Loss Prevention in the Process Industries* 13 (6): 519-26.

Chvatal, V. , 1965. Hutnicke listy. 19 : 466,466–474.

Collins, J. P., Way, J. D. , 1993. Preparation and characterization of a composite palladium-ceramic membrane. *Industrial & Engineering Chemistry Research* 32 (12): 3006-13.

McKinsey&Company - U.S. Greenhouse Gas Abatement Mapping Initiative, Creyts, J., Derkach, A., Nyquist, S., Ostrowski, K. and Stephenson, J. , 2007. *Reducing U.S. greenhouse gas emissions: How much at what cost?* .

Criscuoli, A., Basile, A., Drioli, E. , 2000. An analysis of the performance of membrane reactors for the water–gas shift reaction using gas feed mixtures. *Catalysis Today* 56 (1-3): 53-64.

Criscuoli, A., Basile, A., Drioli, E., Loiacono, O. , 2001. An economic feasibility study for water gas shift membrane reactor. *Journal of Membrane Science* 181 (1): 21-7.

Cunningham, R. E., Williams, R. J. J. , 1980. *Diffusion in gases and porous media*. New York: Plenum Press.

Damle, A., Richardson, C., Powers, T., Love, C. and Acquavivab, J. , 2008. Demonstration of a Pilot–Scale membrane reactor process for hydrogen production. *ECS Transactions* 12 (1): 499-510.

De Falco, M., Di Paola, L., Marrelli, L., Nardella, P. , 2007. Simulation of large-scale membrane reformers by a two-dimensional model. *Chemical Engineering Journal* 128 (2-3): 115-25.

de Neufville, R and Scholtes, S. , 2011. *Flexibility in engineering design*Massachusetts Institute of Technology.

Dijkstra, J. W., Pieterse, J. A. Z., Li, H., Boon, J., van Delft, Y. C., Raju, G., Peppink, G., van den Brink, R. W., Jansen, D. , 2011. Development of membrane reactor technology for power production with pre-combustion CO_2 capture. *Energy Procedia* 4 : 715-22.

Diniz da Costa, J. C., Reed, G. P., Thambimuthu, K. , 2009. "High temperature gas separation membranes in coal gasification". *Energy Procedia* 1 (1): 295-302.

Dixon, A. G. , 2003. Recent research in catalytic inorganic membrane reactors. *Int J Chem React Eng* Vol 1 .

———. , 1996. An improved equation for the overall heat transfer coefficient in packed beds. *Chemical Engineering and Processing* 35 (5): 323-31.

Dixon, A. G., Cresswell, D. L. , 1979. Theoretical prediction of effective heat transfer parameters in packed beds. *AIChE Journal* 25 : 663,663-672.

Dolan, M. D., Donelson, R., Dave, N. C. , 2010. Performance and economics of a pd-based planar WGS membrane reactor for coal gasification. *International Journal of Hydrogen Energy* 35 (20): 10994-1003.

Doyle, M. L., Harris, I. R. , 1988. Palladium-rare earth alloys: Their order-disorder transformations and behavior with hydrogen. *Plat. Metals Rev.* 32 : 130-140.

Foggler, H. S. , 1999. *Elements of chemical reaction engineering*. 3rd Edition ed. New Jersey: Printice-Hall International, Inc.

Fort, D., Farr, J. P. G., Harris, I. R. , 1975. A comparison of palladium-silver and palladium-yttrium alloys as hydrogen separation membranes. *Journal of the Less Common Metals* 39 (2): 293-308.

Frey, H. C., Rubin, E. S. and Diwekar, U. M. , 1994. Modeling uncertainties in advanced technologies: Application to a coal gasification system with hot-gas cleanup. *Energy* 19 : 449-463.

Friel, J. J. , 1998. *X-ray and image analysis in electron microscopy*. Princeton, NJ: Princeton-Gamma Tech.

Frieske, H., Wicke, E. , 1973. Magnetic susceptibility and equilibrium diagram of palladium hydride. *Berichte Der Bunsen-Gesellschaft* 77 : 48,48-52.

Fu, C., Wu, J. C. S. , 2008. A transient study of double-jacketed membrane reactor via methanol steam reforming. *International Journal of Hydrogen Energy* 33 (24): 7435-43.

Gabitto, J., Tsouris, C. , 2008. Hydrogen transport in composite inorganic membranes. *Journal of Membrane Science* 312 (1-2): 132-42.

Gade, S. K., Keeling, M. K., Davidson, A. P., Hatlevik, O., Way, J. D. , 2009. Palladium–ruthenium membranes for hydrogen separation fabricated by electroless co-deposition. *International Journal of Hydrogen Energy* 34 (15): 6484-91.

Gallucci, F., De Falco, M., Tosti, S., Marrelli, L., Basile, A. , 2007. The effect of the hydrogen flux pressure and temperature dependence factors on the membrane reactor performances. *International Journal of Hydrogen Energy* 32 (16): 4052-8.

Research Triangle Institute, Gangwal, S. K., Portzer, J. W., Roberts, G.W. and Kozup, S.C. , 1998. *Engineering evaluation of hot-gas desulfurization with sulfur recovery.* Contract No. DE-AC21-94MC31258.

Gielens, F. C., Knibbeler, R. J. J., Duysinx, P. F. J., Tong, H. D., Vorstman, M. A. G., Keurentjes, J. T. F. , 2006. Influence of steam and carbon dioxide on the hydrogen flux through thin Pd/Ag and pd membranes. *Journal of Membrane Science* 279 (1-2): 176-85.

Gokhale, A. A., Dumesic, J. A., Mavrikakis, M. , 2008. On the mechanism of low-temperature water gas shift reaction on copper. *Journal of the American Chemical Society* 130 (4): 1402-14.

Graham, T. , 1866. On the absorption and dialytic separation of gases by colloid septa. *Phil. Trans. R. Soc.* 156 : 399,399-439.

Mitretek technical paper, Gray, D., Tomlinson, G. , 2002. *Hydrogen from coal.* MTR 2002–31.

Grekov, E. A. , 1970. Sb tr tsent nauch. *Issled Inst Chern Met* 75 : 77,77-84.

Gryaznov, V. , 2000. Metal containing membranes for the production of ultrapure hydrogen and the recovery of hydrogen isotopes. *SEPAR PURIF METHOD* 29 (2): 171,171-187.

Gryaznov, V. M., Mischenko, A. P., Polyakova, V. P., Roshan, N. R., Savitsky, E. M., Smirnov, V. S., Khrapova, E. V., Shimulis, V. I. , 1973. Palladium-ruthenium alloys as membrane catalysts. *Dokl.Acad.Nauk SSSR* 211 : 624.

Gryaznov, V. M., Vedernikov, V. I., Gul'yanova, S. G. , 1986. *Kinet. Katal.* 27 : 142.

Gryaznov, V. M., Serebryannikova, O. S., Serov, Y. M., Ermilova, M. M., Karavanov, A. N., Mischenko, A. P., Orekhova, N. V. , 1993. Preparation and catalysis over palladium composite membranes. *Applied Catalysis A: General* 96 (1): 15-23.

Guazzone, F. , 2005. Engineering of substrate surface for the synthesis of ultra-thin composite pd and pd-cu membranes for H_2 separation.Worcester Polytechnic Institute.

Guazzone, F., Ma, Y. H. , 2006. *Composite gas separation modules having A layer of particles with A uniform binder metal distribution.* Patent WO 2006/019805 A2, filed 2006.

Guazzone, F., Payzant, E. A., Speakman, S. A., Ma, Y. H. , 2006a. Microstrains and stresses analysis in electroless deposited thin pd films. *Industrial & Engineering Chemistry Research* 45 (24): 8145-53.

Guazzone, F., Engwall, E. E., Ma, Y. H. , 2006b. Effects of surface activity, defects and mass transfer on hydrogen permeance and n-value in composite palladium-porous stainless steel membranes. *Catalysis Today* 118 (1-2): 24-31.

Guazzone, F., Ma, Y. H. , 2008. Leak growth mechanism in composite pd membranes prepared by the electroless deposition method. *AICHE Journal* 54 (2): 487-94.

Gupta, P., Velazquez-Vargas, L. G., Fan, L. , 2007. Syngas redox (SGR) process to produce hydrogen from coal derived syngas. *Energy & Fuels* 21 (5): 2900-8.

Hara, S., Sakaki, K., Itoh, N. , 1999. Decline in hydrogen permeation due to concentration polarization and CO hindrance in a palladium membrane reactor. *Industrial & Engineering Chemistry Research* 38 (12): 4913-8.

DOE/NETL, Haslbeck, J. L., Kuehn, N. J., Lewis, E. G., Pinkerton, L. L., Simpson, J., Turner, M. J., Varghese, E., Woods, M. C. , 2010. *Cost and performance baseline for fossil energy plants volume 1: Bituminous coal and natural gas to electricity.* 2011.

Hatlevik, Ø., Gade, S. K., Keeling, M. K., Thoen, P. M., Davidson, A. P., Way, J. D. , 2010. Palladium and palladium alloy membranes for hydrogen separation and production: History, fabrication strategies, and current performance. *Separation and Purification Technology* 73 (1): 59-64.

Hellemans, M. , 2009. *Safety relief valve handbook - design and use of process safety valves to ASME and international codes and standards*Elsevier.

Hermann, C., Quicker, P., Dittmeyer, R. , 1997. Mathematical simulation of catalytic dehydrogenation of ethylbenzene to styrene in a composite palladium membrane reactor. *Journal of Membrane Science* 136 (1-2): 161-72.

Hla, S. S., Park, D., Duffy, G. J., Edwards, J. H., Roberts, D. G., Ilyushechkin, A., Morpeth, L. D., Nguyen, T. , 2009. Kinetics of high-temperature water-gas shift reaction over two iron-based commercial catalysts using simulated coal-derived syngases. *Chemical Engineering Journal* 146 (1): 148-54.

Holleck, G. L. , 1970. Diffusion and solubility of hydrogen in palladium and palladium-silver alloys. *J. Phys. Chem.* 74 : 503-511.

Huang, Y., Dittmeyer, R. , 2007. Preparation of thin palladium membranes on a porous support with rough surface. *Journal of Membrane Science* 302 (1-2): 160-70.

Hughes, R. , 2001. Composite palladium membranes for catalytic membrane reactors. *Membrane Technology* 2001 (131): 9-13.

Hyatt, N. , 2003. Identification of hazards and structured hazards analysis tools. In *Guidelines for process hazards analysis (PHA, HAZOP), hazards identification, and risk analysis.*, 5-1-5-20CRC Press.

Israni, S. H., Nair, B. K. R., Harold, M. P. , 2009. Hydrogen generation and purification in a composite pd hollow fiber membrane reactor: Experiments and modeling. *Catalysis Today* 139 (4): 299-311.

Itoh, N., Xu, W. C., Haraya, K. , 1994. Radial mixing diffusion of hydrogen in a packed-bed type of palladium membrane reactor. *Industrial & Engineering Chemistry Research* 33 (2): 197-202.

Iwuchukwu, I. J., Sheth, A. , 2008. Mathematical modeling of high temperature and high-pressure dense membrane separation of hydrogen from gasification. *Chemical Engineering and Processing: Process Intensification* 47 (8): 1292-304.

Jewett, D. N., Makrides, A. C. , 1965.
Diffusion of hydrogen through palladium and palladium-silver alloys. *Trans Faraday Soc* 61 : 932,932-939.

Jun, C., Lee, K. , 2000. Palladium and palladium alloy composite membranes prepared by metal-organic chemical vapor deposition method (cold-wall). *Journal of Membrane Science* 176 (1): 121-30.

Kajiwara, M., Uemiya, S., Kojima, T. , 1999. Stability and hydrogen permeation behavior of supported platinum membranes in presence of hydrogen sulfide. *International Journal of Hydrogen Energy* 24 (9): 839-44.

Kajiwara, M., Uemiya, S., Kojima, T., Kikuchi, E. , 2000a. Hydrogen permeation properties through composite membranes of platinum supported on porous alumina. *Catalysis Today* 56 (1-3): 65-73.

———. , 2000b. Rhodium- and iridium-dispersed porous alumina membranes and their hydrogen permeation properties. *Catalysis Today* 56 (1-3): 83-7.

Karpova, R. A., Tverdovskii, I. P. , 1959. Hydrogen sorption in the dispersed palladium-copper alloys. *Zhurnal Fizicheskoi Khimii* 33 : 1393,1393-400.

Keiski, R. L., Salmi, T., Niemistö, P., Ainassaari, J., Pohjola, V. J. , 1996. Stationary and transient kinetics of the high temperature water-gas shift reaction. *Applied Catalysis A: General* 137 (2): 349-70.

Keiski, R. L., Salmi, T., Pohjola, V. J. , 1992. Development and verification of a simulation model for a non-isothermal water-gas shift reactor. *The Chemical Engineering Journal* 48 (1): 17-29.

Khan, F. I., Abbasi, S. A. , 1997. Mathematical model for HAZOP study time estimation. *Journal of Loss Prevention in the Process Industries* 10 (4): 249-57.

Kikuchi, E., Uemiya, S., Sato, N., Inoue, H., Ando, H., and Matsuda, T. , 1989. Membrane reactor using micro-porous glass-supported thin film of palladium. application to the water gas shift reaction. *Chemistry Letters* 18 (3): 489.

Kikuchi, E., Nemoto, Y., Kajiwara, M., Uemiya, S., Kojima, T. , 2000. Steam reforming of methane in membrane reactors: Comparison of electroless-plating and CVD membranes and catalyst packing modes. *Catalysis Today* 56 (1-3): 75-81.

Kleemann, G., Hartmann, K., Wiss, Z. , 1978. *Tech Hochsch "Carl Schorlemmer" Leuna-Merseburg* 20 : 417,417–425.

Kletz, T. A. , 1990. *Improving chemical engineering practicesnew , A look at old myths of the chemical industry*. Second Edition ed. USA: Hemisphere Publishing Corporation.

Knapton, A. G. , 1977a. Palladium alloys for hydrogen diffusion membranes. *Plat. Metals Rev.* 21 (2): 44,44-50.

Knapton, A. G. , 1977b. Palladium alloys for hydrogen diffusion membranes: A review of high permeability materials. *Plat. Metals Rev.*: 44,44-50.

Koc, R., Kazantzis, N. K., Ma, Y. H. , 2011. A process dynamic modeling and control framework for performance assessment of Pd/alloy-based membrane reactors used in hydrogen production. *International Journal of Hydrogen Energy* 36 (8): 4934-51.

Kolpakov, S. V., Frantsenyuk, I. V., Teder, L. I. , 1971. Beremblyum GB. stal' 1971. 31 : 401,401–402.

Koros, W. J., Ma, Y. H., Shimidzu, T. , 1996. Terminology for membranes and membrane processes. *Pure & Appl. Chem* 68 (No 7): 1479-1489.

Kothari, R., Buddhi,D., Sawhney,R. L. , 2008a. Comparison of environmental and economic aspects of various hydrogen production methods. *Renewable and Sustainable Energy Reviews* 12 : 31 July 2006,553–563.

Kothari, R., Buddhi, D., Sawhney, R. L. , 2008b. Comparison of environmental and economic aspects of various hydrogen production methods. *Renewable and Sustainable Energy Reviews* 12 (2): 553-63.

Koukou, M. K., Papayannakos, N., Markatos, N. C. , 2001. On the importance of non-ideal flow effects in the operation of industrial-scale adiabatic membrane reactors. *Chemical Engineering Journal* 83 (2): 95-105.

Koukou, M. K., Papayannakos, N., Markatos, N. C., Bracht, M., Alderliesten, P. T. , 1998. Simulation tools for the design of industrial-scale membrane reactors. *Chemical Engineering Research and Design* 76 (8): 911-20.

Krishna, R. , 1987. Diffusion in multicomponent electrolyte systems. *The Chemical Engineering Journal* 35 (1): 19-24.

Kulprathipanja, A., Alptekin, G. O., Falconer, J. L., Way, J. D. , 2005. Pd and Pd–Cu membranes: Inhibition of H_2 permeation by H_2S. *Journal of Membrane Science* 254 (1-2): 49-62.

Leszczynski, Z. , 1973. *Przem Chem* 52 : 161,161-163.

Lewis, F. A. , 1967. *The palladium hydrogen system*. NY, USA: Academic Press Inc.

Li, H., Dijkstra, J. W., Pieterse, J. A. Z., Boon, J., van den Brink, R. W., Jansen, D. , 2010. Towards full-scale demonstration of hydrogen-selective membranes for CO2 capture: Inhibition effect of WGS-components on the H2 permeation through three pd membranes of 44 cm long. *Journal of Membrane Science* 363 (1-2): 204-11.

Li, N. N.; Fane, A. G.; Ho, W.S.W.; Matsuura, T. (2008). Advanced Membrane Technology and Applications.. John Wiley & Sons. Online version available at: http://www.knovel.com/web/portal/browse/display?_EXT_KNOVEL_DISPLAY_bookid= 2935&VerticalID=0

Li, H., Pieterse, J. A. Z., Dijkstra, J. W., Haije, W. G., Xu, H. Y., Bao, C., van den Brink, R. W., Jansen, D. , 2011. Performance test of a bench-scale multi-tubular membrane reformer. *Journal of Membrane Science* 373 (1–2): 43-52.

KLM Technology Group, Ling, A. L. , 2007. *Pressure relief valve selection and sizing (engineering design guideline)*.

Lloyd, L., Ridler, D. E., Twigg, M. V. , 1989. Chapter 6. In *Catalyst handbook.*, ed. M. V. Twigg. 2nd Edition ed. Wolfe, London: CRC Press, Boca Raton, Fla.

Lu, G. Q., Diniz da Costa, J. C., Duke, M., Giessler, S., Socolow, R., Williams, R. H., Kreutz, T. , 2007. Inorganic membranes for hydrogen production and purification: A critical review and perspective. *Journal of Colloid and Interface Science* 314 (2): 589-603.

Lukyanov, B. N., Andreev, D. V., Parmon, V. N. , 2009. Catalytic reactors with hydrogen membrane separation. *Chemical Engineering Journal* 154 : 258,258-266.

DOE, Lund, C. R. F. , 2001. *Water-gas shift kinetics over iron oxide catalysts at membrane reactor conditions.* DE-FG2699-FT40590.

Lywood, W. J., Twigg, M. V. , 1990. European Patent Appl. Patent W0361648, filed 1990.

Ma, D., Lund, C. R. F. , 2003. Assessing high-temperature water gas shift membrane reactors. *Industrial & Engineering Chemistry Research* 42 (4): 711-7.

Ma, Y. H., Akis, B. C., Ayturk, M. E., Guazzone, F., Engwall, E. E., Mardilovich, I. P. , 2004. Characterization of intermetallic diffusion barrier and alloy formation for Pd/Cu and Pd/Ag porous stainless steel composite membranes. *Industrial & Engineering Chemistry Research* 43 (12): 2936-45.

Ma, Y. H., Engwall, E. E., Mardilovich, I. P. , 2003. Composite palladium and palladium -alloy membranes for high temperature hydrogen separations. *Fuel Chemistry Division Preprints* 48 : 333-4.

Ma, Y. H., Guazzone, F. , 2010. *Method for fabricating a composite gas separation module.* Worcester MA, USA Patent 7727596, filed 2010.

Ma, Y. H., Mardilovich, P. P., Engwall, E. , 2007. *Method for curing defects in the fabrication of a composite gas separation module.* US Patent 7172644, filed 2007.

Ma, Y. H., Mardilovich, P. P., She, Y. , 2000. *Hydrogen gas-extraction module and method of fabrication.* Worcester MA, USA Patent 6152987, filed 2000.

Ma, Y. H., Mardilovich, I. P., Engwall, E. E. , 2007a. *Composite gas separation modules having high tamman temperature intermediate layers.* Worcester MA, USA Patent 7255726 B2, filed 2007a.

———. , 2007b. *Composite gas separation modules having intermediate porous layers.* Worcester MA, USA Patent 7175694 B2, filed 2007b.

DOE Scientific and Technical Information, Ma, Y. H., Pomerantz, N. a. C.,Chao-Huang. , 2008. *Sulfur tolerant Pd/Cu and Pd/Au alloy membranes for H_2 separation with high pressure CO_2 for sequestration.* Contract No. FG26-04NT42194.

Ma, Y. H., Mardilovich, I. P., Engwall, E. E. , 2003. Thin composite palladium and Palladium/Alloy membranes for hydrogen separation. *Annals of the New York Academy of Sciences* 984 (1): 346-60.

Madia, G. S., Barbieri, G., Drioli, E. , 1999. Theoretical and experimental analysis of methane steam reforming in a membrane reactor. *The Canadian Journal of Chemical Engineering* 77 (4): 698-706.

Mannan, M. S. White paper on *challenges in implementing inherent safety principles in new and existing chemical processes*, Mary Kay O'Connor Process Safety Center, Chemical Engineering Dep.. [Accessed Year 2012]. Available from http://psc.tamu.edu/library/center-publications/white-papers-and-position-statements.

Mardilovich, P. P., She,Y., and Ma,Y. H. , 1997. Defect-free palladium membranes on porous stainless-steel support. *AIChE Journal* 44 (2): 16 Apr 2004,310 - 322.

Mardilovich, I. P., Engwall, E., Ma, Y. H. , 2002. Dependence of hydrogen flux on the pore size and plating surface topology of asymmetric pd-porous stainless steel membranes. *Desalination* 144 (1-3): 85-9.

Marigliano, G., Barbieri, G., Drioli, E. , 2001. Effect of energy transport on a palladium-based membrane reactor for methane steam reforming process. *Catalysis Today* 67 (1-3): 85-99.

Mason, E. A., Malinauskas, A. P. , 1983. *Gas transport in porous media: The dusty-gas model*. Amsterdam: Elsevier.

Maurstad, O. An overview of coal based integrated gasification combined cycle (IGCC) technology. [Accessed Year 2005]. Available from http://sequestration.mit.edu/pdf/LFEE_2005-002_WP.pdf.

McKinley, D. L. , 1967. *Metal alloy for hydrogen separation and purification.* West Virginia, USA Patent 3350845, filed 1967.

McKinley, D. L. , 1966. *Method for hydrogen separation and purification.* West Virginia, USA Patent 3247648, filed 1966.

Mejdell, A. L., Chen, D., Peters, T. A., Bredesen, R., Venvik, H. J. , 2010. The effect of heat treatment in air on CO inhibition of a ∼3 μm Pd–Ag (23 wt.%) membrane. *Journal of Membrane Science* 350 (1-2): 371-7.

Middleton, P., Solgaard-Andersen, H., Rostrup-Nielsen, T. , 2002. Hydrogen production with CO2 capture using membrane reactors. Paper presented at 14th World Hydrogen Energy Conference, .

Miller, C. L., Cicero, D. C., Mark, A. Hydrogen from coal multi-year RD&D plan. [Accessed Year 2012]. Available from http://fossil.energy.gov/programs/fuels/publications/programplans/2009_Draft_H2fromCoal_Sept30_web.pdf.

Moe, J. M. , 1962. Design of water gas shift reactors. *CHEM ENG PROG* 58 (3): 33,33-36.

Mori, N., Nakamura, T., Noda, K., Sakai, O., Takahashi, A., Ogawa, N., Sakai, H., Iwamoto, Y., Hattori, T. , 2007. Reactor configuration and concentration polarization in methane steam reforming by a membrane reactor with a highly hydrogen-permeable membrane. *Industrial & Engineering Chemistry Research* 46 (7): 1952-8.

Mukherjee, S. , 2008. Pressure-relief system design. *Chemical Engineering* 115 (12): 40-5.

Mundschau, M. V., Xie, X., Evenson IV, C. R., Sammells, A. F. , 2006. Dense inorganic membranes for production of hydrogen from methane and coal with carbon dioxide sequestration. *Catalysis Today* 118 (1-2): 12-23.

Nam, S., Lee, K. , 2000. A study on the palladium/nickel composite membrane by vacuum electrodeposition. *Journal of Membrane Science* 170 (1): 91-9.

Nam, S., Lee, S., Lee, K. , 1999. Preparation of a palladium alloy composite membrane supported in a porous stainless steel by vacuum electrodeposition. *Journal of Membrane Science* 153 (2): 163-73.

Newsome, D. S. , 1980. The water-gas shift reaction. *Catalysis Reviews: Science and Engineering* 21 (2) : 275,275-318.

Nguyen, T. H., Mori, S., Suzuki, M. , 2009. Hydrogen permeance and the effect of H2O and CO on the permeability of $Pd_{0.75}Ag_{0.25}$ membranes under gas-driven permeation and plasma-driven permeation. *Chemical Engineering Journal* 155 (1-2): 55-61.

Nolan, D. P. , 1994. *Application of HAZOP and what-if safety reviews to the petroleum, petrochemical and chemical industries* William Andrew Publishing/Noyes.

Oki, S. and Mezaki, R. , 1973. Identification of rate-controlling steps for the water-gas shift reaction over an iron oxide catalyst. *J PHYS CHEM-US* 77 (4): 447,447-452.

Ovesen, C. V., Clausen, B. S., Hammershøi, B. S., Steffensen, G., Askgaard, T., Chorkendorff, I., Nørskov, J. K., Rasmussen, P. B., Stoltze, P., Taylor, P. , 1996. A microkinetic analysis of the Water–Gas shift reaction under industrial conditions. *Journal of Catalysis* 158 (1): 170-80.

Ovesen, C. V., Stoltze, P., Nørskov, J. K., Campbell, C. T. , 1992. A kinetic model of the water gas shift reaction. *Journal of Catalysis* 134 (2): 445-68.

Parry, C. F. , 1992. *Relief systems handbook* Institution of Chemical Engineers.

Parvasi, P., Khosravanipour Mostafazadeh, A., Rahimpour, M. R. , 2009. Dynamic modeling and optimization of a novel methanol synthesis loop with hydrogen-permselective membrane reactor. *International Journal of Hydrogen Energy* 34 (9): 3717-33.

Pasman, H. J. , 2000. Risk informed resource allocation policy: Safety can save costs. *Journal of Hazardous Materials* 71 : 375-394.

Pasman, H. J., Rogers, W. J. , 2010. Safety challenges in view of the upcoming hydrogen economy: An overview. *Journal of Loss Prevention in the Process Industries* 23 (6): 697-704.

Perry, R. H., Green, D. W. , 1997. *Perry's chemical engineers handbook*. 7th International Edition ed. USA: McGraw Hill.

Peschka, w., Wilhelm, E. A., Wilhelm, U. , 1992. *Liquid hydrogen: Fuel of the future*. Verlag: Springer.

Peters, M. S., Timmerhaus, K. D. , 1991. *Plant design and economics for chemical engineers.* 4th edition ed. USA: McGraw Hill, Inc.

Podolski, W. F., Kim, Y. G. , 1974. Modeling the water-gas shift reaction. *Industrial & Engineering Chemistry Process Design and Development* 13 (4): 415-21.

Pomerantz, N., Ma, Y. H. , 2009. Effect of H_2S on the performance and long-term stability of Pd/Cu membranes. *Industrial & Engineering Chemistry Research* 48 (8): 4030-9.

Pomerantz, N., Ma, Y. H., Payzant, E. A. , 2010a. Isothermal solid-state transformation kinetics applied to Pd/Cu alloy membrane fabrication. *AICHE Journal*: n/a,n/a.

Pomerantz, N., Meyer, N., Chen, C., Ma, Y. H. , 2010b. Sulfur poisoning of high permeance Pd/Cu alloy membranes for H_2 separation from coal gas. *NAMS Annual Meting, Washington, D.C. 2010.*

Pozzo, M., Alfè, D. , 2009. Hydrogen dissociation and diffusion on transition metal (= Ti, zr, V, fe, ru, co, rh, ni, pd, cu, ag)-doped mg(0001) surfaces. *International Journal of Hydrogen Energy* 34 (4): 1922-30.

Rahimpour, M. R., Behjati, H. E. , 2009. Dynamic optimization of membrane dual-type methanol reactor in the presence of catalyst deactivation using genetic algorithm. *Fuel Processing Technology* 90 (2): 279-91.

Raich, B. A., Foley, H. C. , 1995. Supra-equilibrium conversion in palladium membrane reactors: Kinetic sensitivity and time dependence. *Applied Catalysis A: General* 129 (2): 167-88.

Ramirez Serrano, A., Tiscareno Lechuga, F., Ochoa Tapia, J. A. , 2009. *Industrial & Engineering Chemistry Research* 48 (3): 1134-9.

Ramshaw, C. , 1983. *Chem Engr (London)* 389 : 13,13-14.

Ratafia-Brown, J. A., Manfredo, L. M., Hoffmann, J. W., Ramezan, M. and Stiegel, G.J. , 2002. An environmental assessment of IGCC power systems. *Nineteenth Annual Pittsburgh Coal Conference, September 23 – 27.*

Rei, M. H. , 2009. A decade's study and developments of palladium membrane in Taiwan. *Journal of the Taiwan Institute of Chemical Engineers* 40 (3): 238-45.

Reid, R. C., Prausnitz, J. M., Poling, B. E. , 1987. *The properties of Gases&Liquids.* 4th Edition ed. USA: McGraw-Hill.

Reyes, F., Luyben, W. L. , 2000. Steady-state and dynamic effects of design alternatives in heat-Exchanger/Furnace/Reactor processes. *Industrial & Engineering Chemistry Research* 39 (9): 3335-46.

Rezvani, S., Huang, Y., McIlveen-Wright, D., Hewitt, N., Mondol, J. D. , 2009. Comparative assessment of coal fired IGCC systems with CO2 capture using physical absorption, membrane reactors and chemical looping. *Fuel* 88 (12): 2463-72.

Rhodes, C., Hutchings, G. J., Ward, A. M. , 1995. Water-gas shift reaction: Finding the mechanistic boundary. *Catalysis Today* 23 (1): 43-58.

Rhodes, C., Peter Williams, B., King, F., Hutchings, G. J. , 2002. Promotion of Fe_3O_4/Cr_2O_3 high temperature water gas shift catalyst. *Catalysis Communications* 3 (8): 381-4.

Roa, F., Way, J. D. , 2005. The effect of air exposure on palladium–copper composite membranes. *Applied Surface Science* 240 (1-4): 85-104.

Roa, F., Way, J. D., McCormick, R. L., Paglieri, S. N. , 2003. Preparation and characterization of Pd–Cu composite membranes for hydrogen separation. *Chemical Engineering Journal* 93 (1): 11-22.

Rosenberg, W. G., Alpern, D. C., Walker, M. R. , 2005. *"Deploying IGCC technology in this decade with 3 party covenant financing: Volume I" ENRP discussion paper.* John F. Kennedy School of Government Harvard University, Cambridge, MA: Belfer Center for Science and International Affairs, Kennedy School of Government, Harvard University: Discussion Paper 2004-07.

Roy, S., Cox, B. G., Adris, A. M., Pruden, B. B. , 1998. Economics and simulation of fluidized bed membrane reforming. *International Journal of Hydrogen Energy* 23 (9): 745-52.

Ryi, S., Li, A., Lim, C. J., Grace, J. R. , 2011. Novel non-alloy Ru/Pd composite membrane fabricated by electroless plating for hydrogen separation. *International Journal of Hydrogen Energy* 36 (15): 9335-40.

Salmi, T., Bostrom, S., Lindfords, L. E. , 1988. Dynamic study of the water-gas shift reaction over an industrial ferrochrome catalyst. *J. Catal.* 112 : 345.

Satterfield, C. N. , 1996. Chapter 10-synthesis gas and associated processes. In *Heterogeneous catalysis in industrial practice.* Synthesis Gas and Associated Processes ed. Malabar, Fla. : Krieger Pub.

Savage, S. L. , 2003. *Decision making with insight*. USA: Brooks/Cole.

———. , 2002. The flaw of averages. *Harvard Business Review*: 20-22.

Schechter, S., Wise, H. , 1979. Phase boundaries for the C-H-O system in equiblibrium with carbides and oxides of iron and nickel. *J. Phys. Chem.* 83 (16): 2107,2107-2111.

Schramm, O., Seidel-Morgenstern, A. , 1999. Comparing porous and dense membranes for the application in membrane reactors. *Chemical Engineering Science* 54 (10): 1447-53.

Scura, F., Barbieri, G., De Luca, G., Drioli, E. , 2008. The influence of the CO inhibition effect on the estimation of the H2 purification unit surface. *International Journal of Hydrogen Energy* 33 (15): 4183-92.

Seshan, K. , 2002. *Handbook of Thin-Film Deposition Processes and Techniques - Principles, Methods, Equipment and Applications (2nd Edition)*William Andrew Publishing/Noyes, http://www.knovel.com/web/portal/browse/display?_EXT_KNOVEL_DISPLAY_bookid=459.

Shafiee, S., Topal,E. , 2009. When will fossil fuel reserves be diminished? *Energy Policy* 37 : 181-9.

Shirasaki, Y., Tsuneki, T., Ota, Y., Yasuda, I., Tachibana, S., Nakajima, H., Kobayashi, K. , 2009. Development of membrane reformer system for highly efficient hydrogen production from natural gas. *International Journal of Hydrogen Energy* 34 (10): 4482-7.

Shu, J., Grandjean, B. P. A., Neste, A. V., Kaliaguine, S. , 1991. Catalytic palladium-based membrane reactors: A review. *The can. J. Chem. Eng.* 69 : 1036-60.

Shu, J., Grandjean, B. P. A., Kaliaguine, S. , 1994. Methane steam reforming in asymmetric pd- and pd-Ag/porous SS membrane reactors. *Applied Catalysis A: General* 119 (2): 305-25.

Sieverts, A. , 1907. Zur kenntnis der okklusion und diffusion von gasen in metalle. *Z. Phys. Chem.* 2 : 129,129-201.

Silva, L. C., Murata, V. V., Hori, C.E. and Assis, A.J. , 2008. Optimization of a membrane reactor for hydrogen production through methane steam reforming using experimental design techniques and NPSOL. *EngOpt2008-International Conference on Engineering Optimization*.

Sirikitputtisak, T., Mirzaesmaeeli, H., Douglas, P. L., Croiset, E., Elkamel, A., Gupta, M. , 2009. A multi-period optimization model for energy planning with CO2 emission considerations. *Energy Procedia* 1 (1): 4339-46.

Sonwane, C. G., Wilcox, J., Ma, Y. H. , 2006a. Solubility of hydrogen in PdAg and PdAu binary alloys using density functional theory. *The Journal of Physical Chemistry B* 110 (48): 24549-58.

Sonwane, C. G., Wilcox, J., Ma, Y. H. , 2006b. Achieving optimum hydrogen permeability in PdAg and PdAu alloys. *The J. Chem. Phys.* 125 (18): 184714.

Stankiewicz, A. I., Moulijn, J. A. , 2004. *Re-engineering the chemical processing plant process intensification*New York : M. Dekker.

Stephanopoulos, G. , 1984. *Chemical process control :An introduction to theory and practice /George stephanopoulos*. Prentice-hall international series in the physical and chemical engineering sciences. Vol. 21. Englewood Cliffs, N.J. : Prentice-Hall.

Sun, Y. M., Khang, S. J. , 1990. A catalytic membrane reactor: Its performance in comparison with other types of reactors. *Industrial & Engineering Chemistry Research* 29 (2): 232-8.

Takht Ravanchi, M., Kaghazchi, T., Kargari, A. , 2009. Application of membrane separation processes in petrochemical industry: A review. *Desalination* 235 (1-3): 199-244.

Tarun, C. B., Croiset, E., Douglas, P. L., Gupta, M., Chowdhury, M. H. M. , 2007. Techno-economic study of CO2 capture from natural gas based hydrogen plants. *International Journal of Greenhouse Gas Control* 1 (1): 55-61.

Taylor, P., Krishna, R. , 1993. *Multicomponent mass transfer*. Canada: John Wiley & Sons, Inc.

Tiemersma, T. P., Patil, C. S., Sint Annaland, M. v., Kuipers, J. A. M. , 2006. Modelling of packed bed membrane reactors for autothermal production of ultrapure hydrogen. *Chemical Engineering Science* 61 (5): 1602-16.

Tinkle, M., Dumesic, J. A. , 1987. Isotopic exchange measurements of the rates of Adsorption/Desorption and interconversion of CO and CO2 over chromia-promoted magnetite: Implications for water-gas shift. *J. Catal.* 103 : 65,65-78.

Todd, D. M., Battista, R. A. Demonstrated applicability of hydrogen fuel for gas turbines. [Accessed Year 2010]. Available from http://www.netl.doe.gov/technologies/coalpower/turbines/refshelf/GE%20Hydrogen-Fueled%20Turbines.pdf.

Tong, J., Matsumura, Y. , 2004. Thin pd membrane prepared on macroporous stainless steel tube filter by an in-situ multi-dimensional plating mechanism. *Chemical Communications*(21): 2460-1.

Tosti, S., Basile, A., Chiappetta, G., Rizzello, C., Violante, V. , 2003. Pd–Ag membrane reactors for water gas shift reaction. *Chemical Engineering Journal* 93 (1): 23-30.

Tosti, S., Bettinali, L., Castelli, S., Sarto, F., Scaglione, S., Violante, V. , 2002. Sputtered, electroless, and rolled palladium–ceramic membranes. *Journal of Membrane Science* 196 (2): 241-9.

Tosti, S., Bettinali, L., Violante, V. , 2000. Rolled thin pd and Pd–Ag membranes for hydrogen separation and production. *International Journal of Hydrogen Energy* 25 (4): 319-25.

Tucho, W. M., Venvik, H. J., Stange, M., Walmsley, J. C., Holmestad, R., Bredesen, R. , 2009. Effects of thermal activation on hydrogen permeation properties of thin, self-supported Pd/Ag membranes. *Separation and Purification Technology* 68 (3): 403-10.

Twigg, M. V. , 1989. *Catalyst handbook*. 2nd edition, London: Wolfe publishing.

Uemiya, S., Sato, N., Ando, H., Kikuchi, E. , 1991a. The water gas shift reaction assisted by a palladium membrane reactor. *Industrial & Engineering Chemistry Research* 30 (3): 585-9.

Uemiya, S., Sato, N., Ando, H., Kikuchi, E. , 1991b. The water gas shift reaction assisted by a palladium membrane reactor. *Industrial & Engineering Chemistry Research* 30 (3): 585-9.

Uemiya, S., Matsuda, T., Kikuchi, E. , 1991c. Hydrogen permeable palladium-silver alloy membrane supported on porous ceramics. *Journal of Membrane Science* 56 (3): 315-25.

Uemiya, S., Sato, N., Ando, H., Kude, Y., Matsuda, T., Kikuchi, E. , 1991d. Separation of hydrogen through palladium thin film supported on a porous glass tube. *Journal of Membrane Science* 56 (3): 303-13.

Uhlhorn, R. J. R., Keizer, K., Burggraaf, A. J. , 1989. Gas and surface diffusion in modified γ-alumina systems. *Journal of Membrane Science* 46 (2–3): 225-41.

Van Natter, R. M., Coleman, J. S., Lund, C. R. F. , 2008. DFT models for active sites on high temperature water-gas shift catalysts. *Journal of Molecular Catalysis A: Chemical* 292 (1-2): 76-82.

Veziroglu, T. N., Barbir, F. , 1998. *HYDROGEN ENERGY TECHNOLOGIES. EMERGING TECHNOLOGY SERIES*. Vienna: UNIDO.

Ward, T. L., Dao, T. , 1999. Model of hydrogen permeation behavior in palladium membranes. *Journal of Membrane Science* 153 (2): 211-31.

Way, J. D., Lusk, M., Thoen, P. , 2008. *Sulfur-resistant composite metal membranes*. Patent US Patent 20080038567, filed 2008.

Wen, C. Y., Fan, L. T. , 1975. *Models for flow systems and chemical reactors*. New York: Marcel Dekker, Inc..

Wicke, E., Nernst, G. H. , 1964.
Phase diagram and thermodynamic behavior of the systems Pd/H_2 and Pd/D_2 at normal temperatures; H/D separation effects. *Berichte Der Bunsen-Gesellschaft* 68 (3): 224,224-235.

Wieland, S., Melin, T., Lamm, A. , 2002. Membrane reactors for hydrogen production. *Chemical Engineering Science* 57 (9): 1571-6.

Winter, C. , 2009. Hydrogen energy — abundant, efficient, clean: A debate over the energy-system-of-change. *International Journal of Hydrogen Energy* 34 (14, Supplement 1): S1-S52.

Xomeritakis, G., Lin, Y. S. , 1996. Fabrication of a thin palladium membrane supported in a porous ceramic substrate by chemical vapor deposition. *Journal of Membrane Science* 120 (2): 261-72.

Xue, E., O'Keeffe, M., Ross, J. R. H. , 1996. Water-gas shift conversion using a feed with a low steam to carbon monoxide ratio and containing sulphur. *Catalysis Today* 30 (1-3): 107-18.

Yeh, S., Rubin, E. S. , 2007. A centurial history of technological change and learning curves for pulverized coal-fired utility boilers. *Energy* 32 (10): 1996-2005.

Yun, S., Oyama, S. T. , 2011. Correlations in palladium membranes for hydrogen separation: A review. *Journal of Membrane Science* 375 (1–2): 28-45.

Yur'eva, T. M., Boreskov, G.K. and Gruver, V. S. , 1969. *Kinet. Katal.* 10 : 862.

Zhao, H., Xiong, G., Stroh, N., Brunner, H. , 1999. Preparation and characterization of pd-ag alloy composite membrane with magnetron sputtering. *Science in China, Series B: Chemistry* 42 (6): 581,581-588.

Zhao, H. -., Xiong, G. -., Baron, G. V. , 2000. Preparation and characterization of palladium-based composite membranes by electroless plating and magnetron sputtering. *Catalysis Today* 56 (1-3): 89,89-96.

Nomenclature

A : surface or cross sectional area (m^2)

C   : concentration (mol/m^3)

C_t : cash flow in year t

C_0 : initial capital investment

C_p : molar heat capacity at constant pressure (J/[mol.K])

$d_{particle}$: particle diameter (m)

D   : diffusion coefficient (m^2/s), D_{i-mix}^e : effective diffusion coefficient of the *ith* species in the gas mixture, D_{ij}^e : effective binary diffusion coefficient, D_{ij} : binary diffusion coefficient

E   : activation energy (J/mol)

f : mole fraction

F   : molar flow rate (mol/s)

G   : mass specific gas flow rate (kg/[m^2.s])

H   : enthalpy (J/mol)

ID   : inside diameter (m)

J : flux (mol /[m^2. S])

k : Boltzmann's constant, 1.3805×10^{-23} J/K

l : Pd thickness of the membrane (μm)

L   : reactor length (m)

MW   : molecular weight

n : number of moles (mol)

N : total number of lumps/segments

NPV : net present value

OD : outside diameter (m)

Pe : Peclet number

P : pressure (atm)

PV : present value

r : reaction rate (mol /[kg cat. s])

r_t :real discount rate in year t (%)

Re : Reynolds number

R_{H2} : hydrogen recovery (%)

Sc : Schmidt number

Q : permeability of the membrane (mol H_2.µm/ [m^2. s. $atm^{0.5}$])

Q_o : permeability constant of the membrane (m^3 H_2.µm/ [m^2. s. $atm^{0.5}$])

t : time (s)

S.S. : steady state

T : temperature (K), T_b: normal boiling point (@ 1 atm), (K), T_c : critical temperature (K), T_r : reduced temperature

u : gas velocity (m/s)

U : overall heat transfer coefficient (W/[m^2.K])

V : volume (m^3)

V_b : liquid molar volume at the normal boiling point, cm^3/mol

V_c : critical volume, cm^3/mol

$\bar{V}$: volumetric flow rate (m^3/s)

W : cumulative weight of catalyst (kg)

x : radial coordinate

X_{CO} : CO conversion (%)

y : spatial coordinate (m)

$\bar{y}$: dimensionless spatial coordinate (y/L)

Greek symbols

ε   : void fraction of the catalytic bed

ρ   : density (kg/m^3) $\rho_{Bulk,Cat.}$: Bulk catalyst density =weight of catalyst/ annular reactor volume, $\rho_{Bulk,Cat}$: gas mixture density

Φ   : permeance decline coefficient

η : viscosity (μP)

Ω   : collision integral, Ω_v: Viscosity collision integral, Ω_D : Diffusion collision integral, $\Omega_{D,p}$: Polar diffusion collision integral

ω : acentric factor

μ_r : dimensionless dipole moment

μ : dipole moment (debyes)

η : viscosity (μP), η_m: viscosity of the mixture (μP), $\eta_{i\ or\ j}$: pure component viscosity (μP)

δ : polar parameter

κ : association factor

σ : characteristic length parameter (Å); σ_i , for pure i; σ_{ij}, for an i-j interaction

ϵ : characteristic energy parameter; ϵ_i, for pure i; ϵ_{ij}, for an i-j interaction

τ : tortuosity, dimensionless

Δv : volume of each segment (m^3)

Δw : weight of catalyst for each segment (g)

Δy : length of each segment (m)

Subscripts

An.   : the annular space between the shell casing and membrane

c   : cross section

HF   : heat flow

i   : ith species

m   : membrane

p   : permeation

Rxn : reaction

shell   : shell side of the membrane module where reaction is taking place (Reaction side)

s   : shaft

tube   : tube side of the membrane module where permeated H_2 is flowing through (Permeate side)

Subscripts

Annulus: the annular space between the shell casing and membrane

g   : gas

i/j   : i/jth species

mix   : mixture

m   : membrane

 p   : polar

Rxn   : reaction

Superscripts

e   : effective

Shell   : shell side of the membrane module where reaction is taking place (Reaction side)

Tube : tube side of the membrane module where permeated H_2 is flowing through (Permeate side)

0 : inlet condition

Abbreviations

ASU : air separation unit

B : billion

BC : boundary condition

CLC : chemical looping combustion cycle

DGM : dusty gas model

ENPV : expected net present value

GE : General Electric

GEE : General Electric Energy

GEE IGCC : An IGCC plant with uses GE gasifier

GHSV : gas hourly space velocity

HAZOP : hazard and operability analysis

HRSG : heat recovery steam generator

IGCC : integrated gasification combined cycle

IGCC-MR : an IGCC plant with embedded membrane reactor

IGCC-PBR : an IGCC plant with traditional shift reactors

M : million

MC : Monte Carlo

MR : membrane reactor

M&S : Marshall and Swift Cost Indexes

NPV : net present value

OTM   : oxygen transport membrane

PC   : pulverized coal

PSA   : pressure swing adsorption

PSS   : porous stainless steel

PV   : present value

RRS   : rupture disk-rupture disk-safety relief valve

RH   : resample historical data

TD   : triangular distribution

w   : with

w/o   : without

WGSMR   : water-gas shift membrane reactor

Appendix A

Thermodynamic Equilibrium Constant for the Water-gas Shift Reaction

All of the constants used in the thermodynamics equilibrium constant calculation were taken from the NIST chemistry Webbook (NIST Chemistry WebBook, 2011).

CO:

				Temperature (K) =	298. - 1300.
$\Delta fH°gas$	-110.53	kJ/mol			
S°gas,1 bar	197.66	J/mol*K		A	25.56759
				B	6.09613
				C	4.054656
Gas Phase Heat Capacity (Shomate Equation)				D	-2.671301
$Cp° = A + B*t + C*t2 + D*t3 + E/t2$				E	0.131021
$H° − H°298.15 = A*t + B*t2/2 + C*t3/3 + D*t4/4 − E/t + F − H$				F	-118.0089
$S° = A*ln(t) + B*t + C*t2/2 + D*t3/3 − E/(2*t2) + G$				G	227.3665
Cp = heat capacity (J/mol*K)				H	-110.5271

H° = standard enthalpy (kJ/mol)

S° = standard entropy (J/mol*K)

t = temperature (K) / 1000.

H₂O:

			Temperature (K) =	500. - 1700.
ΔfH°gas	-241.83	kJ/mol		
S°gas,1 bar	188.84	J/mol*K	A	30.092
			B	6.832514
			C	6.793435
Gas Phase Heat Capacity (Shomate Equation)			D	-2.53448
Cp° = A + B*t + C*t2 + D*t3 + E/t2			E	0.082139
H° − H°298.15= A*t + B*t2/2 + C*t3/3 + D*t4/4 − E/t + F − H			F	-250.881
S° = A*ln(t) + B*t + C*t2/2 + D*t3/3 − E/(2*t2) + G			G	223.3967
Cp = heat capacity (J/mol*K)			H	-241.8264

H° = standard enthalpy (kJ/mol)

S° = standard entropy (J/mol*K)

t = temperature (K) / 1000.

CO₂:

			Temperature (K) =	298. - 1200.
ΔfH°gas	-393.52	kJ/mol		
S°gas,1 bar	213.79	J/mol*K	A	24.99735
			B	55.18696
			C	-33.69137
Gas Phase Heat Capacity (Shomate Equation)			D	7.948387
Cp° = A + B*t + C*t2 + D*t3 + E/t2			E	-0.136638
H° − H°298.15= A*t + B*t2/2 + C*t3/3 + D*t4/4 − E/t + F − H			F	-403.6075
S° = A*ln(t) + B*t + C*t2/2 + D*t3/3 − E/(2*t2) + G			G	228.2431
Cp = heat capacity (J/mol*K)			H	-393.5224

H° = standard enthalpy (kJ/mol)

S° = standard entropy (J/mol*K)

t = temperature (K) / 1000.

H₂:

ΔfH°gas   0   kJ/mol

S°gas,1
bar   130.68   J/mol*K

Gas Phase Heat Capacity (Shomate Equation)

$Cp° = A + B*t + C*t2 + D*t3 + E/t2$

$H° − H°298.15 = A*t + B*t2/2 + C*t3/3 + D*t4/4 − E/t + F − H$

$S° = A*ln(t) + B*t + C*t2/2 + D*t3/3 − E/(2*t2) + G$

Cp = heat capacity (J/mol*K)

H° = standard enthalpy (kJ/mol)

S° = standard entropy (J/mol*K)

t = temperature (K) / 1000.

Temperature (K) =	298. - 1000.
A	33.066178
B	-11.363417
C	11.432816
D	-2.772874
E	-0.158558
F	-9.980797
G	172.707974
H	0

Table A-1. Equilibrium constants for the water-gas shift reaction

T (K)	ΔH(T) (J/mol)	ΔS(T) (J/mol*K)	ΔG(T) (J/mol)	K (Eq. Cons.)
503.15	-39798.27914	-38.66437868	-20344.29701	129.456672
513.15	-39708.8031	-38.48829527	-19958.53439	107.5710564
523.15	-39618.06246	-38.31316935	-19574.52791	90.05681365
533.15	-39526.13349	-38.13910916	-19192.26745	75.9283552
543.15	-39433.08876	-37.9662099	-18811.74185	64.44470604
553.15	-39338.99736	-37.7945553	-18432.9391	55.04376722
563.15	-39243.92517	-37.6242188	-18055.84635	47.29548367
573.15	-39147.93509	-37.45526472	-17680.45011	40.86815025

583.15	-39051.08723	-37.28774924	-17306.73626	35.50394252
593.15	-38953.43913	-37.12172125	-16934.69017	31.00098732
603.15	-38855.04587	-36.95722313	-16564.29674	27.20011341
613.15	-38755.96024	-36.79429138	-16195.54048	23.97498069
623.15	-38656.2329	-36.63295726	-15828.40558	21.22466945
633.15	-38555.91246	-36.47324732	-15462.87592	18.86807521
643.15	-38455.04561	-36.3151838	-15098.93515	16.83963909
653.15	-38353.67722	-36.15878515	-14736.5667	15.08607352
663.15	-38251.85042	-36.00406631	-14375.75385	13.56383473
673.15	-38149.6067	-35.8510391	-14016.47973	12.23715976
683.15	-38046.98597	-35.69971246	-13658.7274	11.0765326
693.15	-37944.02662	-35.5500928	-13302.47979	10.05747886
703.15	-37840.76562	-35.40218414	-12947.71984	9.159613328
713.15	-37737.23853	-35.25598841	-12594.4304	8.365883479
723.15	-37633.47961	-35.11150557	-12242.59436	7.661965392
733.15	-37529.5218	-34.96873384	-11892.19459	7.03577915
743.15	-37425.39682	-34.82766982	-11543.21399	6.477098188
753.15	-37321.13517	-34.68830865	-11195.63551	5.97723295
763.15	-37216.76622	-34.55064412	-10849.44216	5.528773604
773.15	-37112.31819	-34.41466881	-10504.617	5.12537991
783.15	-37007.81821	-34.28037417	-10161.14318	4.761608886
793.15	-36903.29235	-34.14775061	-9819.003946	4.432772925

803.15	-36798.76563	-34.01678764	-9478.182634	4.134822538
813.15	-36694.26207	-33.88747387	-9138.662696	3.864249088
823.15	-36589.80471	-33.75979713	-8800.4277	3.618003827
833.15	-36485.4156	-33.63374454	-8463.46134	3.393430261
843.15	-36381.11586	-33.50930252	-8127.747441	3.188207474
853.15	-36276.92569	-33.38645692	-7793.269968	3.000302472
863.15	-36172.86435	-33.26519298	-7460.01303	2.827929994
873.15	-36068.95024	-33.14549546	-7127.960887	2.669518508
883.15	-35965.20088	-33.02734861	-6797.097952	2.523681369
893.15	-35861.63289	-32.91073626	-6467.408799	2.389192275
903.15	-35758.26208	-32.79564183	-6138.878167	2.264964324
913.15	-35655.10342	-32.68204836	-5811.49096	2.150032107
923.15	-35552.17102	-32.56993854	-5485.232254	2.04353634

Appendix B

Estimation of gas mixture diffusivity and viscosity values:

All of the constants and equations used in order to estimate the diffusivity and viscosity values of the gas mixture were adopted from "The Properties of Gases & Liquids" (Reid et al. 1987).

Estimation of single gas viscosity:

$$\eta = 40.785 \frac{F_c (MW.T)^{1/2}}{V_c^{2/3} \Omega_v} \tag{A.1}$$

$$F_c = 1 - 0.2756\omega + 0.059035\mu_r^4 + \kappa \tag{A.2}$$

$$\kappa = 0.0682 + 0.2767[(17)(number\ of - OH\ groups)/MW] \tag{A.3}$$

$$\mu_r = 131.3 \frac{\mu}{(V_c T_c)^{1/2}} \tag{A.4}$$

Collision integral:

$$\Omega_v = [a_1(T^*)^{-b_1}] + c_1[exp(-d_1 T^*)] + e_1[exp(-f_1 T^*)] \tag{A.5}$$

$$T^* = 1.2593 T_r \text{ and } T_r = T/T_c \tag{A.6}$$

a_1 = 1.16145, b_1=0.14874, c_1=0.52487, d_1=0.77320, e_1=2.16178, and f_1=2.43787

Estimation of the viscosities of gas mixtures:

$$\eta_{mix} = \sum_{i=1}^{n} \frac{f_i \eta_i}{\sum_{j=1}^{n} f_j \phi_{ij}} \tag{A.7}$$

$$\phi_{ij} = \frac{[1 + (\eta_i/\eta_j)^{1/2} (MW_j/MW_i)^{1/4}]^2}{[8(1 + MW_i/MW_j)]^{1/2}}$$ (A.8)

Diffusion coefficients for binary gas systems:

$$D_{ij} = \frac{0.00266\, T^{3/2}}{P.MW_{ij}^{1/2}.\sigma_{ij}^2.\Omega_D}$$ (A.9)

$$MW_{ij} = 2[(1/MW_i) + (1/MW_j)]^{-1}$$ (A.10)

Diffusion collision integral (Ω_D):

$$\Omega_D = \frac{a_2}{(T_D^*)^{b_2}} + \frac{c_2}{exp\,(d_2 T_D^*)} + \frac{e_2}{exp\,(f_2 T_D^*)} + \frac{g_2}{exp\,(h_2 T_D^*)}$$ (A.11)

$$T_D^* = kT/\epsilon_{ij}$$ (A.12)

$$\epsilon_{ij} = (\epsilon_i \epsilon_j)^{1/2}$$ (A.13)

$$\sigma_{ij} = \frac{\sigma_i + \sigma_j}{2}$$ (A.14)

$a_2 = 1.06036$, $b_2 = 0.15610$, $c_2 = 0.19300$, $d_2 = 0.47635$, $e_2 = 1.03587$, $f_2 = 1.52996$, $g_2 = 1.76474$, and $h_2 = 3.89411$.

For polar gases (CO and H_2O):

$$\Omega_{D,p} = \Omega_D + \frac{0.19\, \delta_{ij}^2}{T_D^*}$$ (A.15)

$$\delta = \frac{1940\mu_p^2}{V_b T_b}$$ (A.16)

$$V_b = 0.285\, V_c^{1.048} \tag{A.17}$$

$$\frac{\epsilon}{k} = 1.18\, (1 + 1.3\delta^2)T_b \tag{A.18}$$

$$\sigma = \left(\frac{1.585 V_b}{1 + 1.3\delta^2}\right)^{1/3} \tag{A.19}$$

$$\delta_{ij} = (\delta_i \delta_j)^{1/2} \tag{A.20}$$

$$\frac{\epsilon_{ij}}{k} = \left(\frac{\epsilon_i}{k}\frac{\epsilon_j}{k}\right)^{1/2} \tag{A.21}$$

$$\sigma_{ij} = (\sigma_i \sigma_j)^{1/2} \tag{A.22}$$

Effective binary diffusion coefficient:

$$D_{ij}^e = D_{ij}\frac{\varepsilon}{\tau} \tag{A.23}$$

Table B-1. Property data for the viscosity and diffusion coefficient calculations

Species→ Parameter↓	CO	H_2O	CO_2	H_2
σ	3.69	2.641	3.941	2.827
ϵ/k	91.7	809.1	195.2	59.7
T_b	81.7	373.2	-	20.4
T_c	132.9	647.3	304.1	33.2
P_c	35	221.2	73.8	13
V_c	93.2	57.1	93.9	65.1
κ	0.0682	0.076	0.0682	0.0682
μ	0.1	1.8	0	0
ω	0.066	0.344	0.239	-0.218

Appendix C

1. One dimensional membrane reactor model at steady state conditions

a. Isothermal conditions

m.file:

```
% 1-D Steady State WGS Simulation - Isothermal

% x(1) : Fco
% x(2) : Fh2o
% x(3) : Fco2
% x(4) : Fh2
% x(5) : H2 permeate

function dxdz = Iso_MR_2(z,x)
global Dim Rxn_Con Memb ro_b Pp

Patm = 101325; % Atm pressure - tube side pressure (Pa)
To = Rxn_Con(1); Pp2= Rxn_Con(2); Pp1 = Rxn_Con(3); rxnc1 = Rxn_Con(4);
perc1= Rxn_Con(5);
ko1 = 10^(2.845); ko2 = 10^(0.659);
Pp = Pp1*Patm; PT = Pp2*Patm;
E1 = 111*10^3; E2 = 88*10^3; % Activation Energy j/mol
Rg = 8.314; % Ideal gas constant j/(mol/K) or m3?Pa?/K mol

Cto = PT/(Rg*To); % Total concentration (mol/m3)
ft = x(1) + x(2) + x(3) + x(4);
C1 = Cto*(x(1)/ft); % C : Concentration of each gas mol/m3
C2 = Cto*(x(2)/ft);
C3 = Cto*(x(3)/ft);
C4 = Cto*(x(4)/ft);

% K = exp(4577.8/x(5) - 4.33); Moe et al.1962

P1 = C1*Rg*To; % P partial pressure of each gas (pa)
P2 = C2*Rg*To;
P3 = C3*Rg*To;
P4 = C4*Rg*To;

L1 = Dim(1); r2 = Dim(2); r1 = Dim(3); e = Dim(4); cof1 = Dim(5);
V1 = pi*(r2^2-r1^2)*L1;
Ac = pi*(r2^2-r1^1)*e;
Am = 2*pi*r1*L1; % membrane area m^2
```

```
Qo = Memb(1); th = Memb(2); Ep = Memb(3); p_cof = Memb(4);
Q= perc1*p_cof*Qo*exp(-Ep/(Rg*To)); % mol.micron/(m2.s.pa^0.5)

% Cns - Constants for Cp CO H2O CO2 H2; Cp = heat capacity (J/mol*K)
% t = temperature (K) / 1000.
t = To/1000;
%        A       B        C        D         E         F         G          H
Cns = [ 25.56759 6.09613 4.054656 -2.671301 0.131021 -118.0089 227.3665 -
110.5271;
        30.092 6.832514 6.793435 -2.53448 0.082139 -250.881 223.3967 -
241.8264;
        24.99735 55.18696 -33.69137 7.948387 -0.136638 -403.6075 228.2431 -
393.5224;
        33.066178 -11.363417 11.432816 -2.772874 -0.158558 -9.980797
172.707974 0 ];

% dfH°gas for each gas CO H2O CO2 H2
Hf = [ -110.53; -241.83; -393.52; 0 ];

%CO -  H° ? H°298.15= A*t + B*t2/2 + C*t3/3 + D*t4/4 ? E/t + F ? H
H1 = Hf(1) +  Cns(1,1)*t + Cns(1,2)*(t^2)/2 + Cns(1,3)*(t^3)/3 +
Cns(1,4)*(t^4)/4 - Cns(1,5)/t + Cns(1,6) - Cns(1,8);
%H2O -  H° ? H°298.15= A*t + B*t2/2 + C*t3/3 + D*t4/4 ? E/t + F ? H
H2 = Hf(2) +  Cns(2,1)*t + Cns(2,2)*(t^2)/2 + Cns(2,3)*(t^3)/3 +
Cns(2,4)*(t^4)/4 - Cns(2,5)/t + Cns(2,6) - Cns(2,8);
%CO2 -  H° ? H°298.15= A*t + B*t2/2 + C*t3/3 + D*t4/4 ? E/t + F ? H
H3 = Hf(3) +  Cns(3,1)*t + Cns(3,2)*(t^2)/2 + Cns(3,3)*(t^3)/3 +
Cns(3,4)*(t^4)/4 - Cns(3,5)/t + Cns(3,6) - Cns(3,8);
%H2 -  H° ? H°298.15= A*t + B*t2/2 + C*t3/3 + D*t4/4 ? E/t + F ? H
H4 = Hf(4) +  Cns(4,1)*t + Cns(4,2)*(t^2)/2 + Cns(4,3)*(t^3)/3 +
Cns(4,4)*(t^4)/4 - Cns(4,5)/t + Cns(4,6) - Cns(4,8);

% dH_Rxn
dHrxn = H4+H3-(H1+H2);

%CO Cp° = A + B*t + C*t2 + D*t3 + E/t2
Cp1 = Cns(1,1) + Cns(1,2)*t + Cns(1,3)*(t^2) + Cns(1,4)*(t^3) +
Cns(1,5)/(t^2);
%H2O Cp° = A + B*t + C*t2 + D*t3 + E/t2
Cp2 = Cns(2,1) + Cns(2,2)*t + Cns(2,3)*(t^2) + Cns(2,4)*(t^3) +
Cns(2,5)/(t^2);
%CO2 Cp° = A + B*t + C*t2 + D*t3 + E/t2
Cp3 = Cns(3,1) + Cns(3,2)*t + Cns(3,3)*(t^2) + Cns(3,4)*(t^3) +
Cns(3,5)/(t^2);
%H2 Cp° = A + B*t + C*t2 + D*t3 + E/t2
Cp4 = Cns(4,1) + Cns(4,2)*t + Cns(4,3)*(t^2) + Cns(4,4)*(t^3) +
Cns(4,5)/(t^2);

%S° = A*ln(t) + B*t + C*t2/2 + D*t3/3 ? E/(2*t2) + G
S1 = Cns(1,1)*log(t) + Cns(1,2)*t + Cns(1,3)*(t^2)/2 + Cns(1,4)*(t^3)/3 -
Cns(1,5)/(2*t^2) + Cns(1,7);
S2 = Cns(2,1)*log(t) + Cns(2,2)*t + Cns(2,3)*(t^2)/2 + Cns(2,4)*(t^3)/3 -
Cns(2,5)/(2*t^2) + Cns(2,7);
S3 = Cns(3,1)*log(t) + Cns(3,2)*t + Cns(3,3)*(t^2)/2 + Cns(3,4)*(t^3)/3 -
Cns(3,5)/(2*t^2) + Cns(3,7);
```

```
S4 = Cns(4,1)*log(t) + Cns(4,2)*t + Cns(4,3)*(t^2)/2 + Cns(4,4)*(t^3)/3 -
Cns(4,5)/(2*t^2) + Cns(4,7);
dS = S4 + S3 - S2 - S1;


K = exp(dS/Rg)*exp(-dHrxn*10^3/(Rg*To));


% R : mol/g cat. s     rco = mol/m^3. s
beta = P3*P4/(P1*P2*K); % reversibility factor
%R1 = ko1*exp(-E1/(Rg*To))*(P1)*(P3^(-0.36))*(P4^(-0.09))*(1-beta); %
reaction rate 1  of co mol/kg.s
R1 = (ko1/(1000^0.55))*exp(-E1/(Rg*To))*(P1)*(P3^(-0.32))*(P4^(-0.083))*(1-
beta); % reaction rate 1  of co mol/kg.s
R2 = (ko2/(1000^1.004))*exp(-E2/(Rg*To))*(P1^0.9)*(P2^0.31)*(P3^(-
0.156))*(P4^(-0.05))*(1-beta); % reaction rate 2  of co mol/kg.s
R3 = 469.44*4.48*exp(-
E2/(Rg*To))*((x(1)/ft)^0.9)*((x(2)/ft)^0.31)*((x(3)/ft)^(-
0.156))*((x(4)/ft)^(-0.05))*(1-beta);
R4 = (6*10^11)*exp(-26800/(1.987*To))*(PT/1000)*(1-
e)*Cto*(((x(1)/ft)*(x(2)/ft))-(x(4)/ft)*(x(3)/ft)/K)/((2.5*10^9)*exp(-
21500/(1.987*To))+(x(3)/ft));
rco = rxnc1*-R1 % or R2


FH2 = Am*Q*(sqrt(P4)-sqrt(Pp))/th;
rco
dxdz = zeros(5,1);
dxdz(1,:) = rco*(V1*e*ro_b);
dxdz(2,:) = rco*(V1*e*ro_b);
dxdz(3,:) = -rco*(V1*e*ro_b);
dxdz(4,:) = -rco*(V1*e*ro_b)-FH2;
dxdz(5,:) =FH2;


end
```

Run file:

```
clear
clc
Rg = 8.314; % Ideal gas constant m^3.Pa/(mol/K)
Ps = 101325 ;Ts = 273.15;% Ps (Pa)  Ts (K)   standard temp-press
Patm = 101325; % Atm pressure - tube side pressure (Pa)

global Dim Rxn_Con Memb ro_b
% Dim has the reactor dimensions, L1 = Length of the shell (m)
% r2 = inside radius of shell (m), r1 = outside radious of membrane tube
% e = porosity of the packed bed , V1 = annulus volume
% cof1 is the percentage of the maximum bulk catalyst density

Dim = [60*0.0635 0.8*20*0.0204/2 20*0.0127/2 1 0.5]; % M1 of M1-MR1
%Dim = input('enter [ L; r_shell; r_membrane; %ro_bulk; bed porosity]');
L1 = Dim(1); r2 = Dim(2); r1 = Dim(3); cof1 = Dim(4); e = Dim(5);
V1 = pi*(r2^2-r1^2)*L1;
Rxn_Con = [723 50 1 1 0];
To = Rxn_Con(1); Pp2= Rxn_Con(2); Pp1 = Rxn_Con(3); rxnc1 = Rxn_Con(4);
perc1= Rxn_Con(5);
```

```
% Inlet composition
% Dry_Feed has the dry based feed composition and H2O/CO ratio
% cof2 is the  H2O/CO ratio
% Vol is the inlet total feed flow rate (together with steam) sccm
%Dry_Feed = [41.6/100 40.3/100 18.1/100 2.04 1165.6];%A
% 220.44 411.05 664.47 892.77 1.0800e+003 inlet flow rates sccm
Dry_Feed = [41.58/100 40.29/100 18.13/100 2.0 5*10^7]; % M1 of M1-MR1
X_COi= Dry_Feed(1); X_H2i= Dry_Feed(2) ; X_CO2i= Dry_Feed(3);
cof2 =Dry_Feed(4) ; Vol =Dry_Feed(5) ;
Vol1 = (60/(30.48^3))*Vol; % scfh
GHSV1 = Vol*60/(V1*e*(10^6));


% Permeation properties
% Qo is the permeability constant, mol.micron/(m2.s.pa^0.5)
% th is the Pd thickness, micron
% Ep is the activation energy for h2 permeation, kJ/mol
Memb = [ 6375.38*Patm/(Rg*273.15*3600*sqrt(Patm)) 12 16.623*10^3 1]; % Exp
Qo = Memb(1); th = Memb(2); Ep = Memb(3); p_cof = Memb(4);


vexp = pi*((0.021/2)^2-(0.0127/2)^2)*2.5*0.0254; % annulus volume used in the
experiment = fits 15 gr catalyst
% w = (V1/vexp)*15; % g catalyst for the current reactor
% ro_b =cof1*w/V1; % bulk catalyst density g/m^3
ro_b =15/vexp;


Pp = Pp1*Patm;
FTi = Vol*Ps/(Rg*Ts*(10^6)*60); % Total inlet flow rate mol/s
Fdry = FTi/(X_COi + X_COi*cof2 + X_H2i + X_CO2i);


COi = Fdry*X_COi; % mol/s
H2Oi = Fdry*X_COi*cof2; % mol/s
CO2i = Fdry*X_CO2i;
H2i = Fdry*X_H2i;


X_COif= COi/FTi;X_H2Oif = H2Oi/FTi;
X_CO2if= CO2i/FTi;X_H2if= H2i/FTi;


ic=[COi;H2Oi;CO2i;H2i;0]; vspan=[0 1];
[z,x]=ode23s('Iso_MR_2',vspan,ic);


nn = length(z);

% fr is the fraction of each gas
fr = zeros(nn,4);
for k = 1:4
    for l = 1:nn
        fr(l,k) = x(l,k)/(x(l,1)+x(l,2)+x(l,3)+x(l,4));
    end
end

Conv = zeros(nn,1);
HRI = zeros(nn,1);
for i = 1:nn
    Conv(i) = 100*(x(1,1)-x(i,1))/x(1,1);
    HRI(i) = 100*x(i,5)/(x(1,4)+x(1,1));
```

```matlab
    %HRI(i) = 100*x(i,5)/(x(1,4));
end


figure (1)
plot(z,HRI,z,ref_h2,'LineWidth',2);
% xlabel('Dimensionless Length [-]','fontsize',14,'fontweight','b');
% ylabel('dF_H_2/dz & F_H _2 Tube side
[mol/s]','fontsize',14,'fontweight','b');

figure (2)
plot(z,HRI,z,Conv,'LineWidth',2);
% xlabel('Dimensionless Length [-]','fontsize',14,'fontweight','b');
% ylabel('Con & HR ','fontsize',12);

figure (3)
plot(z,d_Conv);
% xlabel('Dimensionless Length [-]','fontsize',12);
% ylabel('dFco/dz ','fontsize',12);

figure (4)
plot(z,Pp2*fr(:,4));
% xlabel('Dimensionless Length [-]','fontsize',12);
% ylabel('dFh2/dz ','fontsize',12);
figure (5)
plot(z,14.7*Pp2*fr(:,4));
% xlabel('Dimensionless Length [-]','fontsize',12);
% ylabel('dFh2/dz ','fontsize',12);

FR_dry = zeros(1,4);
   for k= 1:4
      FR_dry(k)=100*fr(end,k)/(1-fr(end,2));
   end
F_retmol =sum(x(end,1:4))
F_retsccm = sum(x(end,1:4))/(Ps/(Rg*Ts*(10^6)*60))
Frac_ret = 100*fr(end,:)
Frac_dry = FR_dry
Fh2_mol= x(end,5)
Fh2_lbday = x(end,5)*2*60*60*24/453.6
```

b. Non-isothermal conditions

m.file:

The m.file was written for two loops, one loop for total inlet flow rate and the other for the H2O:CO mole ratio. The derivatives of the m.files for the other combinations such as bulk catalyst density, reactor length, feed temperature, etc. could be written in the same fashion.

```matlab
% 1-D Steady State WGS Simulation - Adiabatic

% x(1) : Fco
% x(2) : Fh2o
% x(3) : Fco2
% x(4) : Fh2
% x(5) : T
% x(6) : Q
% x(7) : H2 permeate

function dxdz = NonIso_Allh2o_Ed(z,x)
global cof1 ro_b T TF

Patm = 101325 ; % Atm pressure - tube side pressure (Pa)
PT = 15*Patm ; % Total pressure 15 atm (Pa)
%Us = 219.5; Um = 53.68;
Us = 0; Um = 53.68;

ko1 = 10^(2.845); ko2 = 10^(0.659);ko1k = 2.623; E1k =79802;
E1 = 111*10^3; E2 = 88*10^3; % Activation Energy j/mol
Rg = 8.314; % Ideal gas constant j/(mol/K) or m3?Pa?/K mol

% To Initial Temperature (K)
Cto = PT/(Rg*T); % Total concentration (mol/m3)
Ct = PT/(Rg*x(5));

ft = x(1) + x(2) + x(3) + x(4);
C1 = Cto*(x(1)/ft)*(T/x(5)); % C : Concentration of each gas mol/m3
C2 = Cto*(x(2)/ft)*(T/x(5));
C3 = Cto*(x(3)/ft)*(T/x(5));
C4 = Cto*(x(4)/ft)*(T/x(5));

P1 = PT*x(1)/ft; % P partial pressure of each gas (pa)
P2 = PT*x(2)/ft;
P3 = PT*x(3)/ft;
P4 = PT*x(4)/ft;

% K = P3*P4/(P1*P2);
r1 = 0.0127/2; % Radius of inner porous tube (m)
r2 = 0.0254/2; % Radius of shell (m)
L1 = 0.0635; % Length of the shell (m)
L2 = 0.0635;
e = 0.5;
V1 = pi*(r2^2-r1^2)*L1;
```

```
V2 = pi*(r2^2-r1^2)*L2*e;
Ashell=2*pi*r2*L1;


Am = 2*pi*r1*L2; % membrane area m^2
Qo = 1*6322.7*Patm/(Rg*273.15*3600*sqrt(Patm)); % mol.micron/(m2.s.pa^0.5)
th = 10; % Pd thickness 10 micron
Ep = 15.6*10^3;
Q= Qo*exp(-Ep/(Rg*x(5))); % mol.micron/(m2.s.pa^0.5)
% Cns - Constants for Cp CO H2O CO2 H2; Cp = heat capacity (J/mol*K)
% t = temperature (K) / 1000.
t = x(5)/1000;
%       A        B        C        D        E         F        G          H
Cns = [ 25.56759 6.09613 4.054656 -2.671301 0.131021 -118.0089 227.3665 -
110.5271;
        30.092 6.832514 6.793435 -2.53448 0.082139 -250.881 223.3967 -
241.8264;
        24.99735 55.18696 -33.69137 7.948387 -0.136638 -403.6075 228.2431 -
393.5224;
        33.066178 -11.363417 11.432816 -2.772874 -0.158558 -9.980797
172.707974 0 ];


% dfH°gas for each gas CO H2O CO2 H2
Hf = [ -110.53; -241.83; -393.52; 0 ];


%CO -  H° ? H°298.15= A*t + B*t2/2 + C*t3/3 + D*t4/4 ? E/t + F ? H
H1 = Hf(1) +  Cns(1,1)*t + Cns(1,2)*(t^2)/2 + Cns(1,3)*(t^3)/3 +
Cns(1,4)*(t^4)/4 - Cns(1,5)/t + Cns(1,6) - Cns(1,8);
%H2O -  H° ? H°298.15= A*t + B*t2/2 + C*t3/3 + D*t4/4 ? E/t + F ? H
H2 = Hf(2) +  Cns(2,1)*t + Cns(2,2)*(t^2)/2 + Cns(2,3)*(t^3)/3 +
Cns(2,4)*(t^4)/4 - Cns(2,5)/t + Cns(2,6) - Cns(2,8);
%CO2 -  H° ? H°298.15= A*t + B*t2/2 + C*t3/3 + D*t4/4 ? E/t + F ? H
H3 = Hf(3) +  Cns(3,1)*t + Cns(3,2)*(t^2)/2 + Cns(3,3)*(t^3)/3 +
Cns(3,4)*(t^4)/4 - Cns(3,5)/t + Cns(3,6) - Cns(3,8);
%H2 -  H° ? H°298.15= A*t + B*t2/2 + C*t3/3 + D*t4/4 ? E/t + F ? H
H4 = Hf(4) +  Cns(4,1)*t + Cns(4,2)*(t^2)/2 + Cns(4,3)*(t^3)/3 +
Cns(4,4)*(t^4)/4 - Cns(4,5)/t + Cns(4,6) - Cns(4,8);


% dH_Rxn
dHrxn = H4+H3-(H1+H2);


%CO Cp° = A + B*t + C*t2 + D*t3 + E/t2
Cp1 = Cns(1,1) + Cns(1,2)*t + Cns(1,3)*(t^2) + Cns(1,4)*(t^3) +
Cns(1,5)/(t^2);
%H2O Cp° = A + B*t + C*t2 + D*t3 + E/t2
Cp2 = Cns(2,1) + Cns(2,2)*t + Cns(2,3)*(t^2) + Cns(2,4)*(t^3) +
Cns(2,5)/(t^2);
%CO2 Cp° = A + B*t + C*t2 + D*t3 + E/t2
Cp3 = Cns(3,1) + Cns(3,2)*t + Cns(3,3)*(t^2) + Cns(3,4)*(t^3) +
Cns(3,5)/(t^2);
%H2 Cp° = A + B*t + C*t2 + D*t3 + E/t2
Cp4 = Cns(4,1) + Cns(4,2)*t + Cns(4,3)*(t^2) + Cns(4,4)*(t^3) +
Cns(4,5)/(t^2);


% Tube side
tt = x(8)/1000;
```

```
Cp4t = Cns(4,1) + Cns(4,2)*tt + Cns(4,3)*(tt^2) + Cns(4,4)*(tt^3) +
Cns(4,5)/(tt^2);
H4t = Hf(4) +  Cns(4,1)*tt + Cns(4,2)*(tt^2)/2 + Cns(4,3)*(tt^3)/3 +
Cns(4,4)*(tt^4)/4 - Cns(4,5)/tt + Cns(4,6) - Cns(4,8);

%S° = A*ln(t) + B*t + C*t2/2 + D*t3/3 ? E/(2*t2) + G
S1 = Cns(1,1)*log(t) + Cns(1,2)*t + Cns(1,3)*(t^2)/2 + Cns(1,4)*(t^3)/3 -
Cns(1,5)/(2*t^2) + Cns(1,7);
S2 = Cns(2,1)*log(t) + Cns(2,2)*t + Cns(2,3)*(t^2)/2 + Cns(2,4)*(t^3)/3 -
Cns(2,5)/(2*t^2) + Cns(2,7);
S3 = Cns(3,1)*log(t) + Cns(3,2)*t + Cns(3,3)*(t^2)/2 + Cns(3,4)*(t^3)/3 -
Cns(3,5)/(2*t^2) + Cns(3,7);
S4 = Cns(4,1)*log(t) + Cns(4,2)*t + Cns(4,3)*(t^2)/2 + Cns(4,4)*(t^3)/3 -
Cns(4,5)/(2*t^2) + Cns(4,7);

dS = S4 + S3 - S2 - S1;

K = exp(dS/Rg)*exp(-dHrxn*10^3/(Rg*x(5)));

% R : mol/g cat. s    rco = mol/m^3. s
beta = P3*P4/(P1*P2*K); % reversibility factor
R1 = ko1*exp(-E1/(Rg*x(5)))*(P1)*(P3^(-0.36))*(P4^(-0.09))*(1-beta); %
reaction rate 1  of co mol/kg.s
R2 = ko2*exp(-E2/(Rg*x(5)))*(P1^0.9)*(P2^0.31)*(P3^(-0.156))*(P4^(-0.05))*(1-
beta); % reaction rate 2  of co mol/kg.s
R3 = ko1k*exp(-E1k/(Rg*x(5)))*(P1)*(P3^(-0.36))*(P4^(-0.09))*(1-beta);
rco = -R1/(1000^0.55); % or R2
kc = (6*10^11)*exp(-26800/(1.987*x(5))); ak = (2.5*10^9)*exp(-
21500/(1.987*x(5)));

dxdz = zeros(8,1);
dxdz(1,:) = rco*(ro_b*V1);
dxdz(2,:) = rco*(ro_b*V1);
dxdz(3,:) = -rco*(ro_b*V1);
dxdz(4,:) = -rco*(ro_b*V1) - Am*Q*(sqrt(P4)-sqrt(Patm))/th;
dxdz(5,:) = (Us*Ashell*(TF-x(5))-Um*Am*(x(5)-x(8))+(-dHrxn)*(10^3)*(-
rco)*(ro_b*V1))/(x(1)*Cp1 + x(2)*Cp2 + x(3)*Cp3 + x(4)*Cp4);
dxdz(6,:) = -dHrxn*(10^3)*(-rco)*(ro_b*V1);
dxdz(7,:) = Am*Q*(sqrt(P4)-sqrt(Patm))/th;
dxdz(8,:) =(Um*Am*(x(5)-x(8))+ (Am*Q*(sqrt(P4)-sqrt(Patm))/th)*(Cp4*x(5)-
Cp4t*x(8)))/(x(7)*Cp4t);

end
```

Run.file:

```
clear
clc
Rg = 8.314; % Ideal gas constant m^3.Pa/(mol/K)
Ps = 101325 ;% Ps (Pa)  Ts (K)   standard temp-press
Ts = 273.15;

r1 = 0.0127/2; % Radius of inner porous tube (m)
```

```matlab
r2 = 0.0254/2; % Radius of shell (m)
L1 = 0.0635; % Length of the shell (m)
e = 0.5; %void fraction
V1 = pi*(r2^2-r1^2)*L1;
A1 = pi*(r2^2-r1^2);

global cof1 ro_b T TF

cof = [1:1:8]; % H2O:CO ratio

Vol = 500:500:2000; % sccm
Vol1 = (60/(30.48^3))*Vol; % scfh
GHSV1 = Vol*60/(V1*e*(10^6));

T =(350+Ts);
TF = T;
P = zeros(length(T),4);
AlldCon = zeros(88,length(T));
Allz =  zeros(87,length(T)); AllCon = zeros(88,length(T));
AllHR = zeros(88,length(cof)); All_Fh2 = zeros(1,length(cof));
All_Trxn= zeros(88,length(cof));All_Tper= zeros(88,length(cof));

for m = 1:length(Vol)
for j = 1:length(cof)

% Inlet compositions
X_COi= 45.4/100;
X_H2i= 38.2/100;
X_CO2i= 16.4/100;
FTi(m) = Vol(m)*Ps/(Rg*Ts*(10^6)*60); % Total inlet flow rate mol/s
flux_t(m)=FTi(m)/(e*A1);

Fdry(m) = FTi(m)/(X_COi + X_COi*cof(j) + X_H2i + X_CO2i);

COi = Fdry(m)*X_COi; % mol/s
H2Oi = Fdry(m)*X_COi*cof(j); % mol/s
CO2i = Fdry(m)*X_CO2i;
H2i = Fdry(m)*X_H2i;

X_COif= COi/FTi(m);X_H2Oif = H2Oi/FTi(m);
X_CO2if= CO2i/FTi(m);X_H2if= H2i/FTi(m);

Ti = T;
cof1 = 0.5;
w = cof1*15; % g catalyst
ro_b =w/V1; % bulk catalyst density g/m^3

ic=[COi;H2Oi;CO2i;H2i;Ti;0;10^-10;Ti]; vspan=[0 1];
[z,x]=ode23s('NonIso_Allh2o_Ed',vspan,ic);

nn = length(z);

figure (1)
plot(z,x(:,5));
```

```matlab
xlabel('Dimensionless Length [-]');
ylabel('T_R_x_n [^0C]');
legend('300^o', '350^o','400^o','450^o');
hold on

figure (5)
plot(z,x(:,7));
xlabel('Dimensionless Length [-]');
ylabel('F _H _2 Tube side [mol/s]');
legend('300^o', '350^o','400^o','450^o');
hold on

% fr is the fraction of each gas
fr = zeros(nn,4);
for k = 1:4
    for l = 1:nn
        fr(l,k) = x(l,k)/(x(l,1)+x(l,2)+x(l,3)+x(l,4));
    end
end
Pi = fr.*15;

Conv = zeros(nn,1);
HRI = zeros(nn,1);
for i = 1:nn
    Conv(i) = 100*(x(1,1)-x(i,1))/x(1,1);
    HRI(i) = x(i,7)/(x(1,1)+x(1,4));
end

d_Conv = zeros(nn-1,1);
for i = 1:nn-1
    d_Conv(i) = 100*(x(i,1)-x(i+1,1))/x(1,1);
end

AllCon(1:length(Conv),j) = Conv;
AllHR(1:length(HRI),j) = HRI;
AlldCon(1:length(d_Conv),j) = d_Conv;
Allz(1:length(z),j)= z;
All_Fh2(j) = Rg*Ts*(3.28^3)*3600*x(end,7)/Ps;
All_Trxn(1:length(x),j)= x(:,5);
All_Tper(1:length(x),j)= x(:,8);

OverallCO(m,j) = max(Conv);
OverallHR(m,j) = 100*max(HRI);
OverallFh2(m,j) = All_Fh2(j);
Tmax(m,j) = max(x(:,5)); Tmaxp(m,j) = max(x(:,8));
end
end
hold off

figure (2)
plot(Allz(1:67,1),AlldCon(1:67,1),'k',Allz(1:74,2),AlldCon(1:74,2),'b',Allz(1
:87,3),AlldCon(1:87,3),'g',Allz(1:82,4),AlldCon(1:82,4),'r');
xlabel('Dimensionless Length [-]');
ylabel('Delta CO Conversion [%]');
ylim([0 inf]);
```

```matlab
legend('300^o', '350^o','400^o','450^o');

figure (3)
plot(T,P)

figure (4)
plot(Allz(1:67,1),AllCon(1:67,1),'k',Allz(1:74,2),AllCon(1:74,2),'b',Allz(1:8
7,3),AllCon(1:87,3),'g',Allz(1:82,4),AllCon(1:82,4),'r');
xlabel('Dimensionless Length [-]');
ylabel('CO Conversion [%]');
legend('300^o', '350^o','400^o','450^o');

figure(4)
X = ones(length(Vol),1)*cof;
Y = flux_t'*ones(1,length(cof));
Z1 = OverallCO;
[C,h] = contourf(X,Y,Z1,20);
clabel(C,h);

figure(5)
Z2 = Tmax-273.15;
[C,h] = contourf(X,Y,Z2,20);
clabel(C,h);

figure(6)
Z3 =OverallHR;
[C,h] = contourf(X,Y,Z3,50);
clabel(C,h);
```

2. Two dimensional-isothermal membrane reactor model at steady state conditions

a. for Re>1000:

```
clear
clc
% CO   H2O   CO2   H2
% 1    2     3     4
% Viscosity Calculation
nz = 8001; nr=11;
MW = [ 28.0101; 18.0153; 44.0095; 2.01588];
Rg = 8.314; % gas constant j/mol-K
Ts = 273.15; % Standard Temperature (K)
Ps = 101325; % pa
T = (400.0 + Ts); % Temperature (K)
P = 50; pt = 10; % atm
Pt = P*Ps; Ptt = pt*Ps;
PT= zeros(1,nz);PT(1)= Pt;
dp = 10*0.4*10^-3; % m
% e: porosity - to: tortuosity - dp:average particle diameter
to = 1.5; % tortuosity
po = 0.50;% porosity
Rxncof = 0.3; % dilution coefficient for catalytic bed, weight of catalyst/
weight of inert packing

r1 = 4*0.0127/2; % Radius of inner porous tube (m)
r2 = 1.5*r1; % Radius of shell (m)
L1 = 2.5*60*0.0635; % Length of the shell (m)
A1 = pi*(r2^2-r1^2);
V1 = pi*(r2^2-r1^2)*L1;
Am = 2*pi*r1*L1;

%ro_b =we/V1; % `1bulk catalyst density g/m^3
ro_cat = 2476*10^3; % solid cat density g/m3
ro_b = ro_cat*po;  %

% k : interval in length, h: interval in radius
k = L1/(nz-1); h=(r2-r1)/(nr-1);

rd=zeros(nr,1);
rd(1)=r1;
for m=2:nr
    rd(m)=rd(m-1)+h;
end


% permeance parameters
% Qo is the permeability constant, th: Pd thickness, Ep:  activation energy
for permeation, Q: permeability
Qo = 6322.7*Ps/(Rg*273.15*3600*sqrt(Ps)); % mol.micron/(m2.s.pa^0.5)
th = 10; % Pd thickness 10 micron
```

```matlab
Ep = 15630;
Q= Qo*exp(-Ep/(Rg*T)); % mol.micron/(m2.s.pa^0.5)


% reaction rate parameters
%ko1 = 725; ko2 = 10^(0.659);
ko1 = 10^(2.845); ko2 = 10^(0.659); ko1k = 2.623; E1k =79802;
E1 = 111*10^3; E2 = 88*10^3; % Activation Energy j/mol
Rg = 8.314; % Ideal gas constant j/(mol/K)


% Inlet compositions
X_COi= 23.8/100;
X_H2i= 20/100;
X_CO2i= 8.7/100;
X_H2Oi=47.6/100;


% In: total inlet flow rate, sccm
In=1.5*10^6;
In_scfh = In*60*(0.0328)^3;
GHSV=In*60/((10^6)*V1); % gas hourly space velocity


FTi = In*Ps/(Rg*Ts*(10^6)*60); % Total inlet flow rate mol/s
COi = FTi*X_COi; % mol/s
H2Oi = FTi*X_H2Oi ; % mol/s
CO2i = FTi*X_CO2i;
H2i = FTi*X_H2i;


t = T/1000;
%        A        B        C         D         E        F        G         H
Cns = [ 25.56759 6.09613 4.054656 -2.671301 0.131021 -118.0089 227.3665 -
110.5271;
    30.092 6.832514 6.793435 -2.53448 0.082139 -250.881 223.3967 -241.8264;
    24.99735 55.18696 -33.69137 7.948387 -0.136638 -403.6075 228.2431 -
393.5224;
    33.066178 -11.363417 11.432816 -2.772874 -0.158558 -9.980797 172.707974 0
];


% dfH°gas for each gas CO H2O CO2 H2
Hf = [ -110.53; -241.83; -393.52; 0 ];


%CO -  H° ? H°298.15= A*t + B*t2/2 + C*t3/3 + D*t4/4 ? E/t + F ? H
H1 = Hf(1) +  Cns(1,1)*t + Cns(1,2)*(t^2)/2 + Cns(1,3)*(t^3)/3 +
Cns(1,4)*(t^4)/4 - Cns(1,5)/t + Cns(1,6) - Cns(1,8);
%H2O -  H° ? H°298.15= A*t + B*t2/2 + C*t3/3 + D*t4/4 ? E/t + F ? H
H2 = Hf(2) +  Cns(2,1)*t + Cns(2,2)*(t^2)/2 + Cns(2,3)*(t^3)/3 +
Cns(2,4)*(t^4)/4 - Cns(2,5)/t + Cns(2,6) - Cns(2,8);
%CO2 -  H° ? H°298.15= A*t + B*t2/2 + C*t3/3 + D*t4/4 ? E/t + F ? H
H3 = Hf(3) +  Cns(3,1)*t + Cns(3,2)*(t^2)/2 + Cns(3,3)*(t^3)/3 +
Cns(3,4)*(t^4)/4 - Cns(3,5)/t + Cns(3,6) - Cns(3,8);
%H2 -  H° ? H°298.15= A*t + B*t2/2 + C*t3/3 + D*t4/4 ? E/t + F ? H
H4 = Hf(4) +  Cns(4,1)*t + Cns(4,2)*(t^2)/2 + Cns(4,3)*(t^3)/3 +
Cns(4,4)*(t^4)/4 - Cns(4,5)/t + Cns(4,6) - Cns(4,8);


% dH_Rxn
dHrxn = H4+H3-(H1+H2);
```

```matlab
%CO Cp° = A + B*t + C*t2 + D*t3 + E/t2
Cp1 = Cns(1,1) + Cns(1,2)*t + Cns(1,3)*(t^2) + Cns(1,4)*(t^3) +
Cns(1,5)/(t^2);
%H2O Cp° = A + B*t + C*t2 + D*t3 + E/t2
Cp2 = Cns(2,1) + Cns(2,2)*t + Cns(2,3)*(t^2) + Cns(2,4)*(t^3) +
Cns(2,5)/(t^2);
%CO2 Cp° = A + B*t + C*t2 + D*t3 + E/t2
Cp3 = Cns(3,1) + Cns(3,2)*t + Cns(3,3)*(t^2) + Cns(3,4)*(t^3) +
Cns(3,5)/(t^2);
%H2 Cp° = A + B*t + C*t2 + D*t3 + E/t2
Cp4 = Cns(4,1) + Cns(4,2)*t + Cns(4,3)*(t^2) + Cns(4,4)*(t^3) +
Cns(4,5)/(t^2);


%S° = A*ln(t) + B*t + C*t2/2 + D*t3/3 ? E/(2*t2) + G
S1 = Cns(1,1)*log(t) + Cns(1,2)*t + Cns(1,3)*(t^2)/2 + Cns(1,4)*(t^3)/3 –
Cns(1,5)/(2*t^2) + Cns(1,7);
S2 = Cns(2,1)*log(t) + Cns(2,2)*t + Cns(2,3)*(t^2)/2 + Cns(2,4)*(t^3)/3 –
Cns(2,5)/(2*t^2) + Cns(2,7);
S3 = Cns(3,1)*log(t) + Cns(3,2)*t + Cns(3,3)*(t^2)/2 + Cns(3,4)*(t^3)/3 –
Cns(3,5)/(2*t^2) + Cns(3,7);
S4 = Cns(4,1)*log(t) + Cns(4,2)*t + Cns(4,3)*(t^2)/2 + Cns(4,4)*(t^3)/3 –
Cns(4,5)/(2*t^2) + Cns(4,7);


dS = S4 + S3 – S2 – S1;

% K: water gas shift reaction equilibrium constant
K = exp(dS/Rg)*exp(-dHrxn*10^3/(Rg*T));

% Lennard-Jones parameters
LJ1 = [ 3.69; 2.641; 3.941; 2.827]; % unit: Amstrong
LJ2 = [ 91.7; 809.1; 195.2; 59.7]; % unit: Kelvin
Tb = [ 81.7; 373.2; 1; 20.4];
Tc = [ 132.9; 647.3; 304.1; 33.2];
Pc = [ 35; 221.2; 73.8; 13];
Vc = [ 93.2; 57.1; 93.9; 65.1];
Vb = 0.285*(Vc.^1.048);
ka = [ 0.0682; 0.076; 0.0682; 0.0682];
dip = [ 0.1; 1.8; 0; 0];
w = [0.066; 0.344; 0.239; -0.218];


ks1 = T./LJ2;
ks2 = 1.2593*(T./Tc);


% coefficients for the calculation of the collosion integral
om_c = [ 1.16145; 0.14874; 0.52487; 0.7732; 2.16178; 2.43787];
%          A       B        C        D       E        F
%         The properties of  gases and liquids book by Reid et al page 393

om1 = zeros(4,1);om2 = zeros(4,1);om3 = zeros(4,1);Fc = zeros(4,1);% the
collosion integral of pure compounds
vis2_p= zeros(4,1); % viscosity of a single gas
for i=1:length(ks1)
    teta(i)=Tb(i)/Tc(i);
    mu_r(i)=131.3*dip(i)/(sqrt(Vc(i)*Tc(i)));
```

```matlab
    % w(i)=3*teta(i)*log(Pc(i))/(7*(1-teta(i)))-1;
    Fc(i)= 1 - 0.2756*w(i) + 0.059035*(mu_r(i)^4) + ka(i);
    om1(i) = om_c(1)*ks1(i)^(-om_c(2)) + om_c(3)*exp(-om_c(4)*ks1(i)) +
om_c(5)*exp(-om_c(6)*ks1(i));
    om2(i) = om_c(1)*ks2(i)^(-om_c(2)) + om_c(3)*exp(-om_c(4)*ks2(i)) +
om_c(5)*exp(-om_c(6)*ks2(i));
    om3(i) = (0.427*ks1(i)^3 +58.13*ks1(i)^2 + 55.89*ks1(i))/(ks1(i)^3 +
73.3*ks1(i)^2 -4.765*ks1(i)+2.754);
    vis1_p(i) = 26.69*sqrt(MW(i)*T)/((LJ1(i)^2)*om1(i));
    vis2_p(i) = 40.785*Fc(i)*sqrt(MW(i)*T)/((Vc(i)^(2/3))*om2(i));
    vis3_p(i) = 26.67*sqrt(MW(i)*T)/((LJ1(i)^2)*om3(i));

end


%Diffusivity Calculation
% H2: A - CO: B1 - H2O: B2 - CO2: B3
pp=zeros(4,1);LJ1p=zeros(4,1); LJ2p=zeros(4,1);
for i=1:4
    pp(i) = 1940*dip(i)^2/(Vb(i)*Tb(i));
    LJ1p(i) = (1.585*Vb(i)/(1+1.3*pp(i)^2))^(1/3);
    LJ2p(i) = 1.18*(1+1.3*pp(i)^2)*Tb(i);
end

% Correction for CO2 since it does not have normal boiling point
LJ1p(3) = LJ1(3); LJ2p(3) = LJ2(3);


om_cof = [ 1.06036; 0.15610; 0.193; 0.47635; 1.03587; 1.52996; 1.76474;
3.89411];
LJ1p_ab = zeros(4,4);LJ2p_ab = zeros(4,4); MW_ab= zeros(4,4);
pp_ab=zeros(4,4);T_st= zeros(4,4);om_p= zeros(4,4);D_BA= zeros(4,4);

for i= 1:4
    for j = 1:4
        LJ1p_ab(i,j) = sqrt(LJ1p(i)*LJ1p(j));
        LJ2p_ab(i,j) = sqrt(LJ2p(i)*LJ2p(j));
        MW_ab(i,j) = 2/(1/MW(i) + 1/MW(j));
        pp_ab(i,j) = sqrt(pp(i)*pp(j));
        T_st(i,j) = T./LJ2p_ab(i,j);
        om_p(i,j)= om_cof(1)/(T_st(i,j)^om_cof(2)) +
om_cof(3)/(exp(om_cof(4)*T_st(i,j))) + om_cof(5)/(exp(om_cof(6)*T_st(i,j))) +
om_cof(7)/(exp(om_cof(8)*T_st(i,j)))+ 0.19*pp_ab(i,j)^2/T_st(i,j);
        D_BA(i,j) =
(0.00266*T^(3/2))/(P*sqrt(MW_ab(i,j))*(LJ1p_ab(i,j)^2)*om_p(i,j));
    end
end

% CO2 (3) non-polar
LJ1_B3A = (LJ1(3)+LJ1(4))/2;
LJ2_B3A = sqrt(LJ2(3)*LJ2(4));

ks_B3A = T/LJ2_B3A;
```

```matlab
om_B3A = om_cof(1)/(ks_B3A^om_cof(2)) + om_cof(3)/(exp(om_cof(4)*ks_B3A)) + om_cof(5)/(exp(om_cof(6)*ks_B3A)) + om_cof(7)/(exp(om_cof(8)*ks_B3A));
M_B3A = 2/(1/MW(3) + 1/MW(4));


D_B3A = (0.00266*T^(3/2))/(P*sqrt(M_B3A)*(LJ1_B3A^2)*om_B3A);


D_BA(3,4)=D_B3A;
D_BA(3,4)=D_BA(4,3);


D_BA_ef=zeros(4,4);
% Effective binary diffusion coefficients
for i=1:4
    for j=1:4
        D_BA_ef(i,j) =(10^-4)*(po/to)*D_BA(i,j);
    end
end


% at z=0 all r
P1=zeros(nr,nz);P2=zeros(nr,nz);P3=zeros(nr,nz);P4=zeros(nr,nz);
UT=zeros(nr,nz);Re_p=zeros(nr,nz);
U1=zeros(nr,nz);U2=zeros(nr,nz);U3=zeros(nr,nz);U4=zeros(nr,nz);
X1=zeros(nr,nz);X2=zeros(nr,nz);X3=zeros(nr,nz);X4=zeros(nr,nz);
Sch1=zeros(nr,nz);Sch2=zeros(nr,nz);Sch3=zeros(nr,nz);Sch4=zeros(nr,nz);
Pe_r1=zeros(nr,nz);Pe_r2=zeros(nr,nz);Pe_r3=zeros(nr,nz);Pe_r4=zeros(nr,nz);
Np=zeros(nz+1,1); Np2=zeros(nz,1);
U5=zeros(nz,1);L=zeros(nz,1);Aa1=zeros(nz,1);


int_1 = zeros(1,nr-1);int_2 = zeros(1,nr-1);int_3 = zeros(1,nr-1);int_4 = zeros(1,nr-1);


U1(:,1)= ones(nr,1)*(COi/((1-po)*A1));U2(:,1)= ones(nr,1)*(H2Oi/((1-po)*A1));
U3(:,1)= ones(nr,1)*(CO2i/((1-po)*A1));U4(:,1)= ones(nr,1)*(H2i/((1-po)*A1));
UT(:,1)= U1(:,1)+U2(:,1)+U3(:,1)+U4(:,1);
FTt = zeros(1,nz); FTt(1) = FTi;
us = zeros(1,nz); us(1) = (In/(60*10^6))/((1-po)*A1);
Vv = zeros(1,nz); Vv(1) = (In/(60*10^6));
MW_m=zeros(nr,nz); ro_m=zeros(nr,nz);


C1=zeros(nr,nz);C2=zeros(nr,nz);C3=zeros(nr,nz);C4=zeros(nr,nz);
CT=zeros(nr,nz);


for z= 1:nz-1
    % Average density of the gas mixture
    % Ui = Fi/A mol/s/m2; Xi : mol fraction;
    %MW_m : molecular weight of the gas mixture
    % ro_m: density of the gas mixture
    UT(1,z)=(U1(1,z)+U2(1,z)+U3(1,z)+U4(1,z));
    us(z)=UT(1,z)*Rg*T/PT(z);

C1(1,z)=U1(1,z)*us(z);C2(1,z)=U2(1,z)*us(z);C3(1,z)=U3(1,z)*us(z);C4(1,z)=U4(1,z)*us(z);
    CT(1,z)=C1(1,z)+C2(1,z)+C3(1,z)+C4(1,z);
    X1(1,z)=C1(1,z)/CT(1,z);X2(1,z)=C2(1,z)/CT(1,z);
    X3(1,z)=C3(1,z)/CT(1,z);X4(1,z)=C4(1,z)/CT(1,z);
```

```matlab
    MW_m(1,z)=X1(1,z)*MW(1)+X2(1,z)*MW(2)+X3(1,z)*MW(3)+X4(1,z)*MW(4);
    ro_m(1,z)= PT(z)*(10^-3)*MW_m(1,z)/(Rg*T);


    part=zeros(4,1); s=zeros(4,4);
    y = [X1(1,z) X2(1,z) X3(1,z) X4(1,z)];
    for i = 1:length(ks1)
        for j = 1:length(ks1)
            s(i,j)= (1+ sqrt(vis1_p(i)/
vis1_p(j))*((MW(j)/MW(i))^(1/4)))^2/(sqrt(8*(1+MW(i)/MW(j))));
        end
    end

    for i=1:4

part(i)=(y(i)*vis2_p(i))/(y(1)*s(i,1)+y(2)*s(i,2)+y(3)*s(i,3)+y(4)*s(i,4));
    end
    vis_mix=sum(part);

    vis_mix = vis_mix*10^-7; % viscosity of the gas mix in Pa.s

    % D_m(i)Diffusivity in mixture
    D_m1(1)=(1-y(1))/(y(2)/D_BA_ef(1,2)+y(3)/D_BA_ef(1,3)+y(4)/D_BA_ef(1,4));
    D_m1(2)=(1-y(2))/(y(1)/D_BA_ef(1,2)+y(3)/D_BA_ef(2,3)+y(4)/D_BA_ef(2,4));
    D_m1(3)=(1-y(3))/(y(1)/D_BA_ef(1,3)+y(2)/D_BA_ef(2,3)+y(4)/D_BA_ef(3,4));
    D_m1(4)=(1-y(4))/(y(1)/D_BA_ef(1,4)+y(3)/D_BA_ef(3,4)+y(2)/D_BA_ef(2,4));

    PT(z+1) = -k*(150*((1-po)^2)*us(z)*vis_mix/((po^3)*(dp^2)) + 1.75*(1-
po)*us(z)*ro_m(1,z)/((po^3)*dp)) + PT(z);

P1(1,z)=X1(1,z)*PT(z);P2(1,z)=X2(1,z)*PT(z);P3(1,z)=X3(1,z)*PT(z);P4(1,z)=X4(
1,z)*PT(z);

    %us(z)=UT(1,z)*Rg*T/((1-po)*PT(z));

    Re_p(1,z) = ro_m(1,z)*us(z)*dp/(vis_mix);

    %R : mol/g cat. s     rco = mol/m^3. s
    beta(1,z) = P3(1,z)*P4(1,z)/(P1(1,z)*P2(1,z)*K); % reversibility factor
    R1(1,z) = ko1*exp(-E1/(Rg*T))*(P1(1,z))*(P3(1,z)^(-0.36))*(P4(1,z)^(-
0.09))*(1-beta(1,z)); % reaction rate 1  of co mol/kg.s
    %R2(1,z) = ko2*exp(-E2/(Rg*T))*(P1(1,z)^0.9)*(P2(1,z)^0.31)*(P3(1,z)^(-
0.156))*(P4(1,z)^(-0.05))*(1-beta(1,z)); % reaction rate 2  of co mol/kg.s
    rco(1,z) = -Rxncof*R1(1,z)*ro_b/(1000^0.55); % or R2

    %     %Keiski
    %     beta(1,z) = P3(1,z)*P4(1,z)/(P1(1,z)*P2(1,z)*K); % reversibility
factor
    %     R1(1,z) = ko1k*exp(-
E1k/(Rg*T))*((P1(1,z)/(Rg*T))^0.74)*((P3(1,z)/(Rg*T))^(-
0.18))*((P2(1,z)/(Rg*T))^(0.47))*(1-beta(1,z)); % reaction rate 1  of co
mol/kg.s
    %     rco(1,z) = -R1(1,z)*ro_b; % or R2

    Pe = 8.8*(2-(1-2*dp/(r2-r1))^2);
    a1(1) = (1-2*dp*k/(Pe*h^2));
```

```matlab
    b1(1) = 2*dp*k/(Pe*(h^2));
    U1(1,z+1)= a1(1)*U1(1,z)+ b1(1)*U1(2,z) + k*rco(1,z);


    a1(2) = (1-2*dp*k/(Pe*h^2));
    b1(2) = 2*dp*k/(Pe*h^2);
    U2(1,z+1)= a1(2)*U2(1,z)+ b1(2)*U2(2,z) + k*rco(1,z);


    a1(3) = (1-2*dp*k/(Pe*h^2));
    b1(3) = 2*dp*k/(Pe*h^2);
    U3(1,z+1)= a1(3)*U3(1,z)+ b1(3)*U3(2,z) - k*rco(1,z);



    if P4(1,z) > Ptt
        Np(z+1)=Q*(sqrt(P4(1,z))-sqrt(Ptt))/th;
    else
        Np(z+1) = 0;
    end



    if P4(1,z) > Ptt
        Np2(z+1)=(Am/(nz-1))*Q*(sqrt(P4(1,z))-sqrt(Ptt))/th;
    else
        Np2(z+1) = 0;
    end

    a1(4) = 2*dp*k/(Pe*(h^2));
    b1(4) = (1-2*dp*k/(Pe*h^2));
    c1(4) = (dp*k/(Pe*h))*(1/h - 1/(2*rd(1)));
    U4(1,z+1)= b1(4)*U4(1,z)+ a1(4)*U4(2,z) - c1(4)*2*h*Np(z)*Pe/dp -
k*rco(1,z);
    a11=(dp*k/(Pe_r2(1,z)*h))*(1/(2*rd(1))+ 1/h);

    L(z+1)=L(z)+k;
    Aa1(z+1)=2*pi*r1*L(z+1);
    %U5(z+1) = k*Aa1(z+1)*Np(z)+U5(z);
    U5(z+1) = 2*pi*r1*k*Np(z)+U5(z);

    % at r = nr
    UT(nr,z)=(U1(nr,z)+U2(nr,z)+U3(nr,z)+U4(nr,z));


C1(nr,z)=U1(nr,z)*us(z);C2(nr,z)=U2(nr,z)*us(z);C3(nr,z)=U3(nr,z)*us(z);C4(nr
,z)=U4(nr,z)*us(z);
    CT(nr,z)=C1(nr,z)+C2(nr,z)+C3(nr,z)+C4(nr,z);
    X1(nr,z)=C1(nr,z)/CT(nr,z);X2(nr,z)=C2(nr,z)/CT(nr,z);
    X3(nr,z)=C3(nr,z)/CT(nr,z);X4(nr,z)=C4(nr,z)/CT(nr,z);

    MW_m(nr,z)=X1(nr,z)*MW(1)+X2(nr,z)*MW(2)+X3(nr,z)*MW(3)+X4(nr,z)*MW(4);
    ro_m(nr,z)= PT(z)*(10^-3)*MW_m(nr,z)/(Rg*T);

    part=zeros(4,1); s=zeros(4,4);
    y = [X1(nr,z) X2(nr,z) X3(nr,z) X4(nr,z)];
    for i = 1:length(ks1)
```

318

```matlab
        for j = 1:length(ks1)
            s(i,j)= (1+ sqrt(vis1_p(i)/
vis1_p(j))*((MW(j)/MW(i))^(1/4)))^2/(sqrt(8*(1+MW(i)/MW(j))));
        end
    end

    for i=1:4

part(i)=(y(i)*vis2_p(i))/(y(1)*s(i,1)+y(2)*s(i,2)+y(3)*s(i,3)+y(4)*s(i,4));
    end
    vis_mix=sum(part);

    vis_mix = vis_mix*10^-7; % viscosity of the gas mix in Pa.s

    % D_m(i)Diffusivity in mixture
    D_m2(1)=(1-y(1))/(y(2)/D_BA_ef(1,2)+y(3)/D_BA_ef(1,3)+y(4)/D_BA_ef(1,4));
    D_m2(2)=(1-y(2))/(y(1)/D_BA_ef(1,2)+y(3)/D_BA_ef(2,3)+y(4)/D_BA_ef(2,4));
    D_m2(3)=(1-y(3))/(y(1)/D_BA_ef(1,3)+y(2)/D_BA_ef(2,3)+y(4)/D_BA_ef(3,4));
    D_m2(4)=(1-y(4))/(y(1)/D_BA_ef(1,4)+y(3)/D_BA_ef(3,4)+y(2)/D_BA_ef(2,4));




    Re_p(nr,z) = ro_m(nr,z)*us(z)*dp/(vis_mix);


P1(nr,z)=X1(nr,z)*PT(z);P2(nr,z)=X2(nr,z)*PT(z);P3(nr,z)=X3(nr,z)*PT(z);P4(nr
,z)=X4(nr,z)*PT(z);


    % R : mol/g cat. s    rco = mol/m^3. s
    beta(nr,z) = P3(nr,z)*P4(nr,z)/(P1(nr,z)*P2(nr,z)*K); % reversibility
factor
    R1(nr,z) = ko1*exp(-E1/(Rg*T))*(P1(nr,z))*(P3(nr,z)^(-0.36))*(P4(nr,z)^(-
0.09))*(1-beta(nr,z)); % reaction rate 1  of co mol/kg.s
    rco(nr,z) = -Rxncof*R1(nr,z)*ro_b/(1000^0.55); % or R2


    a2(1) = (1-2*dp*k/(Pe*h^2));
    b2(1) = 2*dp*k/(Pe*h^2);
    U1(nr,z+1)= a2(1)*U1(nr,z)+ b2(1)*U1(nr-1,z) + k*rco(nr,z);

    a2(2) = (1-2*dp*k/(Pe*h^2));
    b2(2) = 2*dp*k/(Pe*h^2);
    U2(nr,z+1)= a2(2)*U2(nr,z)+ b2(2)*U2(nr-1,z) + k*rco(nr,z);

    a2(3) = (1-2*dp*k/(Pe*h^2));
    b2(3) = 2*dp*k/(Pe*h^2);
    U3(nr,z+1)= a2(3)*U3(nr,z)+ b2(3)*U3(nr-1,z) - k*rco(nr,z);

    a2(4) = (1-2*dp*k/(Pe*h^2));
    b2(4) = 2*dp*k/(Pe*h^2);
    U4(nr,z+1)= a2(4)*U4(nr,z)+ b2(4)*U4(nr-1,z) - k*rco(nr,z);

    for r=2:nr-1
```

```matlab
        % Average density of the gas mixture
        % Ui = Fi/A mol/s/m2; Xi : mol fraction;
        %MW_m : molecular weight of the gas mixture
        % ro_m: density of the gas mixture
        UT(r,z)=(U1(r,z)+U2(r,z)+U3(r,z)+U4(r,z));


C1(r,z)=U1(r,z)*us(z);C2(r,z)=U2(r,z)*us(z);C3(r,z)=U3(r,z)*us(z);C4(r,z)=U4(
r,z)*us(z);
    CT(r,z)=C1(r,z)+C2(r,z)+C3(r,z)+C4(r,z);
    X1(r,z)=C1(r,z)/CT(r,z);X2(r,z)=C2(r,z)/CT(r,z);
    X3(r,z)=C3(r,z)/CT(r,z);X4(r,z)=C4(r,z)/CT(r,z);

        MW_m(r,z)=X1(r,z)*MW(1)+X2(r,z)*MW(2)+X3(r,z)*MW(3)+X4(r,z)*MW(4);
        ro_m(r,z)= PT(z)*(10^-3)*MW_m(r,z)/(Rg*T);

        part=zeros(4,1);s=zeros(4,4);
        y = [X1(r,z) X2(r,z) X3(r,z) X4(r,z)];
        for i = 1:length(ks1)
            for j = 1:length(ks1)
                s(i,j)= (1+ sqrt(vis1_p(i)/
vis1_p(j))*((MW(j)/MW(i))^(1/4)))^2/(sqrt(8*(1+MW(i)/MW(j))));
            end
        end
        for i=1:4

part(i)=(y(i)*vis2_p(i))/(y(1)*s(i,1)+y(2)*s(i,2)+y(3)*s(i,3)+y(4)*s(i,4));
        end
        vis_mix1=sum(part);

        vis_mix = vis_mix1*10^-7; % viscosity of the gas mix in Pa.s

        % D_m(i)Diffusivity in mixture
        D_m(1)=(1-
y(1))/(y(2)/D_BA_ef(1,2)+y(3)/D_BA_ef(1,3)+y(4)/D_BA_ef(1,4));
        D_m(2)=(1-
y(2))/(y(1)/D_BA_ef(2,1)+y(3)/D_BA_ef(2,3)+y(4)/D_BA_ef(2,4));
        D_m(3)=(1-
y(3))/(y(1)/D_BA_ef(3,1)+y(2)/D_BA_ef(3,2)+y(4)/D_BA_ef(4,3));
        D_m(4)=(1-
y(4))/(y(1)/D_BA_ef(4,1)+y(3)/D_BA_ef(4,3)+y(2)/D_BA_ef(4,2));



        Re_p(r,z) = ro_m(r,z)*us(z)*dp/(vis_mix);


P1(r,z)=X1(r,z)*PT(z);P2(r,z)=X2(r,z)*PT(z);P3(r,z)=X3(r,z)*PT(z);P4(r,z)=X4(
r,z)*PT(z);


        % R : mol/g cat. s     rco = mol/m^3. s
```

```matlab
        beta(r,z) = P3(r,z)*P4(r,z)/(P1(r,z)*P2(r,z)*K); % reversibility
factor
        R1(r,z) = ko1*exp(-E1/(Rg*T))*(P1(r,z))*(P3(r,z)^(-0.36))*(P4(r,z)^(-
0.09))*(1-beta(r,z)); % reaction rate 1  of co mol/kg.s
        rco(r,z) = -Rxncof*R1(r,z)*ro_b/(1000^0.55); % or R2


        a(1) = (dp*k/(Pe*h))*(1/(2*rd(r))+ 1/h);
        b(1) = (1- 2*dp*k/(Pe*(h^2)));
        c(1) = (dp*k/(Pe*h))*(1/h - 1/(2*rd(r)));
        U1(r,z+1)= a(1)*U1(r+1,z)+ b(1)*U1(r,z) + c(1)*U1(r-1,z) +
k*rco(r,z);

        a(2) = (dp*k/(Pe*h))*(1/(2*rd(r))+ 1/h);
        b(2) = (1- 2*dp*k/(Pe*(h^2)));
        c(2) = (dp*k/(Pe*h))*(1/h - 1/(2*rd(r)));
        U2(r,z+1)= a(2)*U2(r+1,z)+ b(2)*U2(r,z) + c(2)*U2(r-1,z) +
k*rco(r,z);

        a(3) = (dp*k/(Pe*h))*(1/(2*rd(r)) + 1/h);
        b(3) = (1 - 2*dp*k/(Pe*(h^2)));
        c(3) = (dp*k/(Pe*h))*(1/h - 1/(2*rd(r)));
        U3(r,z+1)= a(3)*U3(r+1,z)+ b(3)*U3(r,z)  + c(3)*U3(r-1,z) -
k*rco(r,z);

        a(4) = (dp*k/(Pe*h))*(1/(2*rd(r)) + 1/h);
        b(4) = (1 - 2*dp*k/(Pe*(h^2)));
        c(4) = (dp*k/(Pe*h))*(1/h - 1/(2*rd(r)));
        U4(r,z+1)= a(4)*U4(r+1,z)+ b(4)*U4(r,z)  + c(4)*U4(r-1,z) -
k*rco(r,z);

    end

end

UT(:,end)=(U1(:,end)+U2(:,end)+U3(:,end)+U4(:,end));
X1(:,end)=U1(:,end)./UT(:,end);X2(:,end)=U2(:,end)./UT(:,end);X3(:,end)=U3(:,
end)./UT(:,end);X4(:,end)=U4(:,end)./UT(:,end);
%(FTt(1)-FTt(end))/(COi+H2i)
F_con = (sum(U1(:,1))-sum(U1(:,end)))/sum(U1(:,1))
F_HR = (sum(UT(:,1))-sum(UT(:,end)))/(sum(U1(:,1))+sum(U4(:,1)))
f_h2 = F_HR*(H2i+COi)
f_ret = FTi-f_h2
f_retcm =(f_ret*Rg*Ts*60*10^6)/Ps
Frac_exit = [sum(U1(:,end))/sum(UT(:,end)) sum(U2(:,end))/sum(UT(:,end))...
    sum(U3(:,end))/sum(UT(:,end)) sum(U4(:,end))/sum(UT(:,end))]

for z=1:nz
    F_HR(z) = 100*(sum(UT(:,1))-sum(UT(:,z)))/(sum(U1(:,1))+sum(U4(:,1)));
    %F_HR(z) = 100*(sum(UT(:,1))-sum(UT(:,z)))/(sum(U4(:,1)));
    F_con(z) = 100*(sum(U1(:,1))-sum(U1(:,z)))/sum(U1(:,1));
    H2per(z) = F_HR(z)*(H2i+COi);
end
```

b. for Re<1000:

```
clear
clc
% CO   H2O  CO2   H2
% 1    2    3     4
% Viscosity Calculation
MW = [ 28.0101; 18.0153; 44.0095; 2.01588];
Rg = 8.314; % gas constant j/mol-K
Ts = 273.15; % Standard Temperature (K)
Ps = 101325; % pa
T = (450.0 + Ts); % Temperature (K)
P = 15; % bar
PT = P*Ps;
dp = 0.43*10^-3; % m
% e: porosity - to: tortuosity - dp:average particle diameter
to = 1.5; % tortuosity
po = 0.53;% porosity
%Fpres correction factor for pressure in the reaction rate
if P>30
    Fpres = P^(0.5-P/250);
else
    Fpres = P^(0.5-P/500);
end
%Fpres=1;
r1 = 0.0128/2; % Radius of inner porous tube (m)
r2 = 0.020/2; % Radius of shell (m)
L1 = 0.0635; % Length of the shell (m)
A1 = pi*(r2^2-r1^2);
V1 = pi*(r2^2-r1^2)*L1;
Am = 2*pi*r1*L1;

we = 15; % g catalyst
ro_b =we/V1; % `1bulk catalyst density g/m^3
%ro_b = (10^3)*2628*po; %2628*po; 6782% instaed of 0.2 g catalyst
(2628kg/m3), 0.3 g is used (3937.5kg/m3)
% ro_cat = 2476*10^3; % solid cat density g/m3 - ro_b = 1.0753e+006;
% ro_b = ro_cat*(1-po); %

nz = 5001; nr =31;
k = L1/(nz-1); h=(r2-r1)/(nr-1);

rd=zeros(nr,1);
rd(1)=r1;
for m=2:nr
    rd(m)=rd(m-1)+h;
end


Qo = 6322.7*Ps/(Rg*273.15*3600*sqrt(Ps)); % mol.micron/(m2.s.pa^0.5)
th = 10; % Pd thickness 10 micron
Ep = 15630;
Q= Qo*exp(-Ep/(Rg*T)); % mol.micron/(m2.s.pa^0.5)
```

```
ko1 = 10^(2.845); ko2 = 10^(0.659); ko1k = 2.623; E1k =79802;
E1 = 111*10^3; E2 = 88*10^3; % Activation Energy j/mol
Rg = 8.314; % Ideal gas constant j/(mol/K) or m3?Pa?/K mol


% Inlet compositions
X_COi= 23.78/100;
X_H2i= 20/100;
X_CO2i= 8.65/100;
X_H2Oi=47.57/100;

GHSV = 2000;
In=GHSV*((10^6)*V1)/60;
FTi = In*Ps/(Rg*Ts*(10^6)*60); % Total inlet flow rate mol/s
COi = FTi*X_COi; % mol/s
H2Oi = FTi*X_H2Oi ; % mol/s
CO2i = FTi*X_CO2i;
H2i = FTi*X_H2i;



t = T/1000;
%        A        B        C        D        E        F        G        H
Cns = [ 25.56759 6.09613 4.054656 -2.671301 0.131021 -118.0089 227.3665 -
110.5271;
    30.092 6.832514 6.793435 -2.53448 0.082139 -250.881 223.3967 -241.8264;
    24.99735 55.18696 -33.69137 7.948387 -0.136638 -403.6075 228.2431 -
393.5224;
    33.066178 -11.363417 11.432816 -2.772874 -0.158558 -9.980797 172.707974 0
];

% dfH°gas for each gas CO H2O CO2 H2
Hf = [ -110.53; -241.83; -393.52; 0 ];

%CO -  H° ? H°298.15= A*t + B*t2/2 + C*t3/3 + D*t4/4 ? E/t + F ? H
H1 = Hf(1) +  Cns(1,1)*t + Cns(1,2)*(t^2)/2 + Cns(1,3)*(t^3)/3 +
Cns(1,4)*(t^4)/4 - Cns(1,5)/t + Cns(1,6) - Cns(1,8);
%H2O -  H° ? H°298.15= A*t + B*t2/2 + C*t3/3 + D*t4/4 ? E/t + F ? H
H2 = Hf(2) +  Cns(2,1)*t + Cns(2,2)*(t^2)/2 + Cns(2,3)*(t^3)/3 +
Cns(2,4)*(t^4)/4 - Cns(2,5)/t + Cns(2,6) - Cns(2,8);
%CO2 -  H° ? H°298.15= A*t + B*t2/2 + C*t3/3 + D*t4/4 ? E/t + F ? H
H3 = Hf(3) +  Cns(3,1)*t + Cns(3,2)*(t^2)/2 + Cns(3,3)*(t^3)/3 +
Cns(3,4)*(t^4)/4 - Cns(3,5)/t + Cns(3,6) - Cns(3,8);
%H2 -  H° ? H°298.15= A*t + B*t2/2 + C*t3/3 + D*t4/4 ? E/t + F ? H
H4 = Hf(4) +  Cns(4,1)*t + Cns(4,2)*(t^2)/2 + Cns(4,3)*(t^3)/3 +
Cns(4,4)*(t^4)/4 - Cns(4,5)/t + Cns(4,6) - Cns(4,8);

% dH_Rxn
dHrxn = H4+H3-(H1+H2);


%CO Cp° = A + B*t + C*t2 + D*t3 + E/t2
Cp1 = Cns(1,1) + Cns(1,2)*t + Cns(1,3)*(t^2) + Cns(1,4)*(t^3) +
Cns(1,5)/(t^2);
%H2O Cp° = A + B*t + C*t2 + D*t3 + E/t2
Cp2 = Cns(2,1) + Cns(2,2)*t + Cns(2,3)*(t^2) + Cns(2,4)*(t^3) +
Cns(2,5)/(t^2);
```

```matlab
%CO2 Cp° = A + B*t + C*t2 + D*t3 + E/t2
Cp3 = Cns(3,1) + Cns(3,2)*t + Cns(3,3)*(t^2) + Cns(3,4)*(t^3) +
Cns(3,5)/(t^2);
%H2 Cp° = A + B*t + C*t2 + D*t3 + E/t2
Cp4 = Cns(4,1) + Cns(4,2)*t + Cns(4,3)*(t^2) + Cns(4,4)*(t^3) +
Cns(4,5)/(t^2);


%S° = A*ln(t) + B*t + C*t2/2 + D*t3/3 ? E/(2*t2) + G
S1 = Cns(1,1)*log(t) + Cns(1,2)*t + Cns(1,3)*(t^2)/2 + Cns(1,4)*(t^3)/3 -
Cns(1,5)/(2*t^2) + Cns(1,7);
S2 = Cns(2,1)*log(t) + Cns(2,2)*t + Cns(2,3)*(t^2)/2 + Cns(2,4)*(t^3)/3 -
Cns(2,5)/(2*t^2) + Cns(2,7);
S3 = Cns(3,1)*log(t) + Cns(3,2)*t + Cns(3,3)*(t^2)/2 + Cns(3,4)*(t^3)/3 -
Cns(3,5)/(2*t^2) + Cns(3,7);
S4 = Cns(4,1)*log(t) + Cns(4,2)*t + Cns(4,3)*(t^2)/2 + Cns(4,4)*(t^3)/3 -
Cns(4,5)/(2*t^2) + Cns(4,7);


dS = S4 + S3 - S2 - S1;


K = exp(dS/Rg)*exp(-dHrxn*10^3/(Rg*T));


% Lennard-Jones parameters
LJ1 = [ 3.69; 2.641; 3.941; 2.827]; % unit: Amstrong
LJ2 = [ 91.7; 809.1; 195.2; 59.7]; % unit: Kelvin
Tb = [ 81.7; 373.2; 1; 20.4];
Tc = [ 132.9; 647.3; 304.1; 33.2];
Pc = [ 35; 221.2; 73.8; 13];
Vc = [ 93.2; 57.1; 93.9; 65.1];
Vb = 0.285*(Vc.^1.048);
ka = [ 0.0682; 0.076; 0.0682; 0.0682];
dip = [ 0.1; 1.8; 0; 0];
w = [0.066; 0.344; 0.239; -0.218];


ks1 = T./LJ2;
ks2 = 1.2593*(T./Tc);


% coefficients for the calculation of the collosion integral
om_c = [ 1.16145; 0.14874; 0.52487; 0.7732; 2.16178; 2.43787];
%        A        B        C        D        E        F
%        The properties of  gases and liquids book by Reid et al page 393


om1 = zeros(4,1);om2 = zeros(4,1);om3 = zeros(4,1);Fc = zeros(4,1);% the
collosion integral of pure compounds
vis2_p= zeros(4,1); % viscosity of a single gas
for i=1:length(ks1)
    teta(i)=Tb(i)/Tc(i);
    mu_r(i)=131.3*dip(i)/(sqrt(Vc(i)*Tc(i)));

    % w(i)=3*teta(i)*log(Pc(i))/(7*(1-teta(i)))-1;
    Fc(i)= 1 - 0.2756*w(i) + 0.059035*(mu_r(i)^4) + ka(i);
    om1(i) = om_c(1)*ks1(i)^(-om_c(2)) + om_c(3)*exp(-om_c(4)*ks1(i)) +
om_c(5)*exp(-om_c(6)*ks1(i));
    om2(i) = om_c(1)*ks2(i)^(-om_c(2)) + om_c(3)*exp(-om_c(4)*ks2(i)) +
om_c(5)*exp(-om_c(6)*ks2(i));
```

```matlab
    om3(i) = (0.427*ks1(i)^3 +58.13*ks1(i)^2 + 55.89*ks1(i))/(ks1(i)^3 +
73.3*ks1(i)^2 -4.765*ks1(i)+2.754);
    vis1_p(i) = 26.69*sqrt(MW(i)*T)/((LJ1(i)^2)*om1(i));
    vis2_p(i) = 40.785*Fc(i)*sqrt(MW(i)*T)/((Vc(i)^(2/3))*om2(i));
    vis3_p(i) = 26.67*sqrt(MW(i)*T)/((LJ1(i)^2)*om3(i));


end


%Diffusivity Calculation
% H2: A - CO: B1 - H2O: B2 - CO2: B3
pp=zeros(4,1);LJ1p=zeros(4,1); LJ2p=zeros(4,1);
for i=1:4
    pp(i) = 1940*dip(i)^2/(Vb(i)*Tb(i));
    LJ1p(i) = (1.585*Vb(i)/(1+1.3*pp(i)^2))^(1/3);
    LJ2p(i) = 1.18*(1+1.3*pp(i)^2)*Tb(i);
end

% Correction for CO2 since it does not have normal boiling point
LJ1p(3) = LJ1(3); LJ2p(3) = LJ2(3);


om_cof = [ 1.06036; 0.15610; 0.193; 0.47635; 1.03587; 1.52996; 1.76474;
3.89411];
LJ1p_ab = zeros(4,4);LJ2p_ab = zeros(4,4); MW_ab= zeros(4,4);
pp_ab=zeros(4,4);T_st= zeros(4,4);om_p= zeros(4,4);D_BA= zeros(4,4);

for i= 1:4
    for j = 1:4
        LJ1p_ab(i,j) = sqrt(LJ1p(i)*LJ1p(j));
        LJ2p_ab(i,j) = sqrt(LJ2p(i)*LJ2p(j));
        MW_ab(i,j) = 2/(1/MW(i) + 1/MW(j));
        pp_ab(i,j) = sqrt(pp(i)*pp(j));
        T_st(i,j) = T./LJ2p_ab(i,j);
        om_p(i,j)= om_cof(1)/(T_st(i,j)^om_cof(2)) +
om_cof(3)/(exp(om_cof(4)*T_st(i,j))) + om_cof(5)/(exp(om_cof(6)*T_st(i,j))) +
om_cof(7)/(exp(om_cof(8)*T_st(i,j)))+ 0.19*pp_ab(i,j)^2/T_st(i,j);
        D_BA(i,j) =
(0.00266*T^(3/2))/(P*sqrt(MW_ab(i,j))*(LJ1p_ab(i,j)^2)*om_p(i,j));
    end
end

% CO2 (3) non-polar
LJ1_B3A = (LJ1(3)+LJ1(4))/2;
LJ2_B3A = sqrt(LJ2(3)*LJ2(4));


ks_B3A = T/LJ2_B3A;

om_B3A = om_cof(1)/(ks_B3A^om_cof(2)) + om_cof(3)/(exp(om_cof(4)*ks_B3A)) +
om_cof(5)/(exp(om_cof(6)*ks_B3A)) + om_cof(7)/(exp(om_cof(8)*ks_B3A));
M_B3A = 2/(1/MW(3) + 1/MW(4));


D_B3A = (0.00266*T^(3/2))/(P*sqrt(M_B3A)*(LJ1_B3A^2)*om_B3A);
```

```matlab
D_BA(3,4)=D_B3A;
D_BA(3,4)=D_BA(4,3);

D_BA_ef=zeros(4,4);
% Effective binary diffusion coefficients
for i=1:4
    for j=1:4
        D_BA_ef(i,j) = (10^-4)*(po/to)*D_BA(i,j);
    end
end

% at z=0 all r
P1=zeros(nr,nz);P2=zeros(nr,nz);P3=zeros(nr,nz);P4=zeros(nr,nz);
UT=zeros(nr,nz);us=zeros(nr,nz);Re_p=zeros(nr,nz);
U1=zeros(nr,nz);U2=zeros(nr,nz);U3=zeros(nr,nz);U4=zeros(nr,nz);
X1=zeros(nr,nz);X2=zeros(nr,nz);X3=zeros(nr,nz);X4=zeros(nr,nz);
Sch1=zeros(nr,nz);Sch2=zeros(nr,nz);Sch3=zeros(nr,nz);Sch4=zeros(nr,nz);
Pe_r1=zeros(nr,nz);Pe_r2=zeros(nr,nz);Pe_r3=zeros(nr,nz);Pe_r4=zeros(nr,nz);
Np=zeros(nz+1,1);
U5=zeros(nz,1);

U1(:,1)= ones(nr,1)*(COi/(po*A1));U2(:,1)= ones(nr,1)*(H2Oi/(po*A1));
U3(:,1)= ones(nr,1)*(CO2i/(po*A1));U4(:,1)= ones(nr,1)*(H2i/(po*A1));
UT(:,1)= U1(:,1)+U2(:,1)+U3(:,1)+U4(:,1);

MW_m=zeros(nr,nz); ro_m=zeros(nr,nz);

for z= 1:nz-1
    % Average density of the gas mixture
    % Ui = Fi/A mol/s/m2; Xi : mol fraction;
    %MW_m : molecular weight of the gas mixture
    % ro_m: density of the gas mixture
    UT(1,z)=(U1(1,z)+U2(1,z)+U3(1,z)+U4(1,z));
    X1(1,z)=U1(1,z)/UT(1,z); X2(1,z)=U2(1,z)/UT(1,z);
X3(1,z)=U3(1,z)/UT(1,z); X4(1,z)=U4(1,z)/UT(1,z);
    MW_m(1,z)=X1(1,z)*MW(1)+X2(1,z)*MW(2)+X3(1,z)*MW(3)+X4(1,z)*MW(4);
    ro_m(1,z)= PT*(10^-3)*MW_m(1,z)/(Rg*T);

    part=zeros(4,1); s=zeros(4,4);
    y = [X1(1,z) X2(1,z) X3(1,z) X4(1,z)];
    for i = 1:length(ks1)
        for j = 1:length(ks1)
            s(i,j)= (1+ sqrt(vis1_p(i)/
vis1_p(j))*((MW(j)/MW(i))^(1/4)))^2/(sqrt(8*(1+MW(i)/MW(j))));
        end
    end

    for i=1:4

part(i)=(y(i)*vis2_p(i))/(y(1)*s(i,1)+y(2)*s(i,2)+y(3)*s(i,3)+y(4)*s(i,4));
    end
    vis_mix=sum(part);

    vis_mix = vis_mix*10^-7; % viscosity of the gas mix in Pa.s
```

```matlab
    % D_m(i)Diffusivity in mixture
    D_m1(1)=(1-y(1))/(y(2)/D_BA_ef(1,2)+y(3)/D_BA_ef(1,3)+y(4)/D_BA_ef(1,4));
    D_m1(2)=(1-y(2))/(y(1)/D_BA_ef(1,2)+y(3)/D_BA_ef(2,3)+y(4)/D_BA_ef(2,4));
    D_m1(3)=(1-y(3))/(y(1)/D_BA_ef(1,3)+y(2)/D_BA_ef(2,3)+y(4)/D_BA_ef(3,4));
    D_m1(4)=(1-y(4))/(y(1)/D_BA_ef(1,4)+y(3)/D_BA_ef(3,4)+y(2)/D_BA_ef(2,4));


    us(1,z)=UT(1,z)*Rg*T/PT;


    Re_p(1,z) = ro_m(1,z)*us(1,z)*dp/(vis_mix);



P1(1,z)=X1(1,z)*PT;P2(1,z)=X2(1,z)*PT;P3(1,z)=X3(1,z)*PT;P4(1,z)=X4(1,z)*PT;


%      Keiski
    beta(1,z) = P3(1,z)*P4(1,z)/(P1(1,z)*P2(1,z)*K); % reversibility factor
    R1(1,z) = ko1k*exp(-
E1k/(Rg*T))*((P1(1,z)/(Rg*T))^0.74)*((P3(1,z)/(Rg*T))^(-
0.18))*((P2(1,z)/(Rg*T))^(0.47))*(1-beta(1,z)); % reaction rate 1  of co
mol/kg.s
    rco(1,z) = -Fpres*R1(1,z)*ro_b; % or R2


    Sch1(1,z)= vis_mix/(ro_m(1,z)*D_m1(1));
    Pe_r11(1,z)=0.4/((Re_p(1,z)*Sch1(1,z))^0.8) +
0.09/(1+10/(Re_p(1,z)*Sch1(1,z)));
    Pe_r1(1,z)=1/Pe_r11(1,z);
    a1(1) = (1-2*dp*k/(Pe_r1(1,z)*h^2));
    b1(1) = 2*dp*k/(Pe_r1(1,z)*(h^2));
    U1(1,z+1)= a1(1)*U1(1,z)+ b1(1)*U1(2,z) + k*rco(1,z);


    Sch2(1,z)= vis_mix/(ro_m(1,z)*D_m1(2));
    Pe_r22(1,z)=0.4/((Re_p(1,z)*Sch2(1,z))^0.8) +
0.09/(1+10/(Re_p(1,z)*Sch2(1,z)));
    Pe_r2(1,z)=1/Pe_r22(1,z);
    a1(2) = (1-2*dp*k/(Pe_r2(1,z)*h^2));
    b1(2) = 2*dp*k/(Pe_r2(1,z)*h^2);
    U2(1,z+1)= a1(2)*U2(1,z)+ b1(2)*U2(2,z) + k*rco(1,z);


    Sch3(1,z)= vis_mix/(ro_m(1,z)*D_m1(3));
    Pe_r33(1,z)=0.4/((Re_p(1,z)*Sch3(1,z))^0.8) +
0.09/(1+10/(Re_p(1,z)*Sch3(1,z)));
    Pe_r3(1,z)=1/Pe_r33(1,z);
    a1(3) = (1-2*dp*k/(Pe_r3(1,z)*h^2));
    b1(3) = 2*dp*k/(Pe_r3(1,z)*h^2);
    U3(1,z+1)= a1(3)*U3(1,z)+ b1(3)*U3(2,z) - k*rco(1,z);



    if P4(1,z) >= Ps
        Np(z)=Q*(sqrt(P4(1,z))-sqrt(Ps))/th;
    else
        Np(z) = 0;
    end


    Sch4(1,z)= vis_mix/(ro_m(1,z)*D_m1(4));
    Pe_r44(1,z)=0.4/((Re_p(1,z)*Sch4(1,z))^0.8) +
0.09/(1+10/(Re_p(1,z)*Sch4(1,z)));
```

```matlab
    Pe_r4(1,z)=1/Pe_r44(1,z);
    a1(4) = 2*dp*k/(Pe_r4(1,z)*(h^2));
    b1(4) = (1-2*dp*k/(Pe_r4(1,z)*h^2));
    c1(4) = (dp*k/(Pe_r4(1,z)*h))*(1/h - 1/(2*rd(1)));
    U4(1,z+1)= b1(4)*U4(1,z)+ a1(4)*U4(2,z) - c1(4)*2*h*Np(z)*Pe_r4(1,z)/dp -
k*rco(1,z);
    a11=(dp*k/(Pe_r2(1,z)*h))*(1/(2*rd(1))+ 1/h);
    %U4(1,z+1)= a11*U4(2,z) + (1+c1(4))*U4(1,z) - c1(4)*h*Np(z)*Pe_r4(1,z)/dp
- k*rco(1,z);

    b1(4)*U4(1,z)
    a1(4)*U4(2,z)
    -c1(4)*2*h*Np(z)*Pe_r4(1,z)/dp
    - k*rco(1,z)


    % at r = nr
    UT(nr,z)=(U1(nr,z)+U2(nr,z)+U3(nr,z)+U4(nr,z));
    X1(nr,z)=U1(nr,z)/UT(nr,z); X2(nr,z)=U2(nr,z)/UT(nr,z);
X3(nr,z)=U3(nr,z)/UT(nr,z); X4(nr,z)=U4(nr,z)/UT(nr,z);
    MW_m(nr,z)=X1(nr,z)*MW(1)+X2(nr,z)*MW(2)+X3(nr,z)*MW(3)+X4(nr,z)*MW(4);
    ro_m(nr,z)= PT*(10^-3)*MW_m(nr,z)/(Rg*T);

    part=zeros(4,1); s=zeros(4,4);
    y = [X1(nr,z) X2(nr,z) X3(nr,z) X4(nr,z)];
    for i = 1:length(ks1)
        for j = 1:length(ks1)
            s(i,j)= (1+ sqrt(vis1_p(i)/
vis1_p(j))*((MW(j)/MW(i))^(1/4)))^2/(sqrt(8*(1+MW(i)/MW(j))));
        end
    end

    for i=1:4

part(i)=(y(i)*vis2_p(i))/(y(1)*s(i,1)+y(2)*s(i,2)+y(3)*s(i,3)+y(4)*s(i,4));
    end
    vis_mix=sum(part);

    vis_mix = vis_mix*10^-7; % viscosity of the gas mix in Pa.s

    % D_m(i)Diffusivity in mixture
    D_m2(1)=(1-y(1))/(y(2)/D_BA_ef(1,2)+y(3)/D_BA_ef(1,3)+y(4)/D_BA_ef(1,4));
    D_m2(2)=(1-y(2))/(y(1)/D_BA_ef(1,2)+y(3)/D_BA_ef(2,3)+y(4)/D_BA_ef(2,4));
    D_m2(3)=(1-y(3))/(y(1)/D_BA_ef(1,3)+y(2)/D_BA_ef(2,3)+y(4)/D_BA_ef(3,4));
    D_m2(4)=(1-y(4))/(y(1)/D_BA_ef(1,4)+y(3)/D_BA_ef(3,4)+y(2)/D_BA_ef(2,4));

    us(nr,z)=UT(nr,z)*Rg*T/PT;

    Re_p(nr,z) = ro_m(nr,z)*us(nr,z)*dp/(vis_mix);


P1(nr,z)=X1(nr,z)*PT;P2(nr,z)=X2(nr,z)*PT;P3(nr,z)=X3(nr,z)*PT;P4(nr,z)=X4(nr
,z)*PT;

%Keiski
```

```matlab
    beta(nr,z) = P3(nr,z)*P4(nr,z)/(P1(nr,z)*P2(nr,z)*K); % reversibility
factor
    R1(nr,z) = ko1k*exp(-
E1k/(Rg*T))*((P1(nr,z)/(Rg*T))^0.74)*((P3(nr,z)/(Rg*T))^(-
0.18))*((P2(nr,z)/(Rg*T))^(0.47))*(1-beta(nr,z)); % reaction rate 1  of co
mol/kg.s
    rco(nr,z) = -Fpres*R1(nr,z)*ro_b; % or R2


    Sch1(nr,z)= vis_mix/(ro_m(nr,z)*D_m2(1));
    Pe_r11(nr,z)=0.4/((Re_p(nr,z)*Sch1(nr,z))^0.8) +
0.09/(1+10/(Re_p(nr,z)*Sch1(nr,z)));
    Pe_r1(nr,z)=1/Pe_r11(nr,z);
    a2(1) = (1-2*dp*k/(Pe_r1(nr,z)*h^2));
    b2(1) = 2*dp*k/(Pe_r1(nr,z)*h^2);
    U1(nr,z+1)= a2(1)*U1(nr,z)+ b2(1)*U1(nr-1,z) + k*rco(nr,z);

    Sch2(nr,z)= vis_mix/(ro_m(nr,z)*D_m2(2));
    Pe_r22(nr,z)=0.4/((Re_p(nr,z)*Sch2(nr,z))^0.8) +
0.09/(1+10/(Re_p(nr,z)*Sch2(nr,z)));
    Pe_r2(nr,z)=1/Pe_r22(nr,z);
    a2(2) = (1-2*dp*k/(Pe_r2(nr,z)*h^2));
    b2(2) = 2*dp*k/(Pe_r2(nr,z)*h^2);
    U2(nr,z+1)= a2(2)*U2(nr,z)+ b2(2)*U2(nr-1,z) + k*rco(nr,z);

    Sch3(nr,z)= vis_mix/(ro_m(nr,z)*D_m2(3));
    Pe_r33(nr,z)=0.4/((Re_p(nr,z)*Sch3(nr,z))^0.8) +
0.09/(1+10/(Re_p(nr,z)*Sch3(nr,z)));
    Pe_r3(nr,z)=1/Pe_r33(nr,z);
    a2(3) = (1-2*dp*k/(Pe_r3(nr,z)*h^2));
    b2(3) = 2*dp*k/(Pe_r3(nr,z)*h^2);
    U3(nr,z+1)= a2(3)*U3(nr,z)+ b2(3)*U3(nr-1,z) - k*rco(nr,z);

    Sch4(nr,z)= vis_mix/(ro_m(nr,z)*D_m2(4));
    Pe_r44(nr,z)=0.4/((Re_p(nr,z)*Sch4(nr,z))^0.8)+
0.09/(1+10/(Re_p(nr,z)*Sch4(nr,z)));
    Pe_r4(nr,z)=1/Pe_r44(nr,z);
    a2(4) = (1-2*dp*k/(Pe_r4(nr,z)*h^2));
    b2(4) = 2*dp*k/(Pe_r4(nr,z)*h^2);
    U4(nr,z+1)= a2(4)*U4(nr,z)+ b2(4)*U4(nr-1,z) - k*rco(nr,z);


    for r=2:nr-1

        % Average density of the gas mixture
        % Ui = Fi/A mol/s/m2; Xi : mol fraction;
        %MW_m : molecular weight of the gas mixture
        % ro_m: density of the gas mixture
        UT(r,z)=(U1(r,z)+U2(r,z)+U3(r,z)+U4(r,z));
        X1(r,z)=U1(r,z)/UT(r,z); X2(r,z)=U2(r,z)/UT(r,z);
X3(r,z)=U3(r,z)/UT(r,z); X4(r,z)=U4(r,z)/UT(r,z);
        MW_m(r,z)=X1(r,z)*MW(1)+X2(r,z)*MW(2)+X3(r,z)*MW(3)+X4(r,z)*MW(4);
        ro_m(r,z)= PT*(10^-3)*MW_m(r,z)/(Rg*T);

        part=zeros(4,1);s=zeros(4,4);
        y = [X1(r,z) X2(r,z) X3(r,z) X4(r,z)];
        for i = 1:length(ks1)
```

```matlab
        for j = 1:length(ks1)
             s(i,j)= (1+ sqrt(vis1_p(i)/
vis1_p(j))*((MW(j)/MW(i))^(1/4)))^2/(sqrt(8*(1+MW(i)/MW(j))));
        end
    end
    for i=1:4

part(i)=(y(i)*vis2_p(i))/(y(1)*s(i,1)+y(2)*s(i,2)+y(3)*s(i,3)+y(4)*s(i,4));
    end
    vis_mix1=sum(part);

    vis_mix = vis_mix1*10^-7; % viscosity of the gas mix in Pa.s

    % D_m(i)Diffusivity in mixture
    D_m(1)=(1-
y(1))/(y(2)/D_BA_ef(1,2)+y(3)/D_BA_ef(1,3)+y(4)/D_BA_ef(1,4));
    D_m(2)=(1-
y(2))/(y(1)/D_BA_ef(2,1)+y(3)/D_BA_ef(2,3)+y(4)/D_BA_ef(2,4));
    D_m(3)=(1-
y(3))/(y(1)/D_BA_ef(3,1)+y(2)/D_BA_ef(3,2)+y(4)/D_BA_ef(4,3));
    D_m(4)=(1-
y(4))/(y(1)/D_BA_ef(4,1)+y(3)/D_BA_ef(4,3)+y(2)/D_BA_ef(4,2));

    us(r,z)=UT(r,z)*Rg*T/PT;

    Re_p(r,z) = ro_m(r,z)*us(r,z)*dp/(vis_mix);


P1(r,z)=X1(r,z)*PT;P2(r,z)=X2(r,z)*PT;P3(r,z)=X3(r,z)*PT;P4(r,z)=X4(r,z)*PT;

%Keiski
    beta(r,z) = P3(r,z)*P4(r,z)/(P1(r,z)*P2(r,z)*K); % reversibility factor
    R1(r,z) = (ko1k)*exp(-
E1k/(Rg*T))*((P1(r,z)/(Rg*T))^0.74)*((P3(r,z)/(Rg*T))^(-
0.18))*((P2(r,z)/(Rg*T))^(0.47))*(1-beta(r,z)); % reaction rate 1  of co
mol/kg.s
    rco(r,z) = -Fpres*R1(r,z)*ro_b; % or R2

    Sch1(r,z)= vis_mix/(ro_m(r,z)*D_m(1));
    Pe_r11(r,z)=0.4/((Re_p(r,z)*Sch1(r,z))^0.8) +
0.09/(1+10/(Re_p(r,z)*Sch1(r,z)));
    Pe_r1(r,z)=1/Pe_r11(r,z);
    a(1) = (dp*k/(Pe_r1(r,z)*h))*(1/(2*rd(r))+ 1/h);
    b(1) = (1- 2*dp*k/(Pe_r1(r,z)*(h^2)));
    c(1) = (dp*k/(Pe_r1(r,z)*h))*(1/h - 1/(2*rd(r)));
    U1(r,z+1)= a(1)*U1(r+1,z)+ b(1)*U1(r,z) + c(1)*U1(r-1,z) +
k*rco(r,z);

    Sch2(r,z)= vis_mix/(ro_m(r,z)*D_m(2));
    Pe_r22(r,z)=0.4/((Re_p(r,z)*Sch2(r,z))^0.8) +
0.09/(1+10/(Re_p(r,z)*Sch2(r,z)));
    Pe_r2(r,z)=1/Pe_r22(r,z);
    a(2) = (dp*k/(Pe_r2(r,z)*h))*(1/(2*rd(r))+ 1/h);
    b(2) = (1- 2*dp*k/(Pe_r2(r,z)*(h^2)));
    c(2) = (dp*k/(Pe_r2(r,z)*h))*(1/h - 1/(2*rd(r)));
```

```matlab
        U2(r,z+1)= a(2)*U2(r+1,z)+ b(2)*U2(r,z) + c(2)*U2(r-1,z) +
k*rco(r,z);

        Sch3(r,z)= vis_mix/(ro_m(r,z)*D_m(3));
        Pe_r33(r,z)=0.4/((Re_p(r,z)*Sch3(r,z))^0.8) +
0.09/(1+10/(Re_p(r,z)*Sch3(r,z)));
        Pe_r3(r,z)=1/Pe_r33(r,z);
        a(3) = (dp*k/(Pe_r3(r,z)*h))*(1/(2*rd(r)) + 1/h);
        b(3) = (1 - 2*dp*k/(Pe_r3(r,z)*(h^2)));
        c(3) = (dp*k/(Pe_r3(r,z)*h))*(1/h - 1/(2*rd(r)));
        U3(r,z+1)= a(3)*U3(r+1,z)+ b(3)*U3(r,z) + c(3)*U3(r-1,z) -
k*rco(r,z);

        Sch4(r,z)= vis_mix/(ro_m(r,z)*D_m(4));
        Pe_r44(r,z)=0.4/((Re_p(r,z)*Sch4(r,z))^0.8) +
0.09/(1+10/(Re_p(r,z)*Sch4(r,z)));
        Pe_r4(r,z)=1/Pe_r44(r,z);
        a(4) = (dp*k/(Pe_r4(r,z)*h))*(1/(2*rd(r)) + 1/h);
        b(4) = (1 - 2*dp*k/(Pe_r4(r,z)*(h^2)));
        c(4) = (dp*k/(Pe_r4(r,z)*h))*(1/h - 1/(2*rd(r)));
        U4(r,z+1)= a(4)*U4(r+1,z)+ b(4)*U4(r,z) + c(4)*U4(r-1,z) -
k*rco(r,z);

    end

end

UT(:,end)=(U1(:,end)+U2(:,end)+U3(:,end)+U4(:,end));
X1(:,end)=U1(:,end)./UT(:,end);X2(:,end)=U2(:,end)./UT(:,end);X3(:,end)=U3(:,
end)./UT(:,end);X4(:,end)=U4(:,end)./UT(:,end);

F_con = (sum(U1(:,1))-sum(U1(:,end)))/sum(U1(:,1))
F_HR = (sum(UT(:,1))-sum(UT(:,end)))/(sum(U1(:,1))+sum(U4(:,1)))
f_h2 = F_HR*(H2i+COi)
f_ret = FTi-f_h2
f_retcm =(f_ret*Rg*Ts*60*10^6)/Ps
Frac_exit = [sum(U1(:,end))/sum(UT(:,end)) sum(U2(:,end))/sum(UT(:,end))...
    sum(U3(:,end))/sum(UT(:,end)) sum(U4(:,end))/sum(UT(:,end))]

for z=1:nz
    F_HR(z) = 100*(sum(UT(:,1))-sum(UT(:,z)))/(sum(U1(:,1))+sum(U4(:,1)));
    F_con(z) = 100*(sum(U1(:,1))-sum(U1(:,z)))/sum(U1(:,1));
end
```

3. One dimensional-isothermal membrane reactor model at transient conditions:

a. Membrane reactor startup

m.file:

```
% CSTRs in Series_with Reaction – SWEEP STOPS AT t=0
% x(1) : co
% x(2) : h2o
% x(3) : co2
% x(4) : h2
% x(5) : N2
% x(6) : H2 permeate

function dfdt = Startup_syn(t,x)

nn = 20; % number of cstrs in series
e = 0.5; % void fraction of the fixed bed
Rg = 8.314; % Ideal gas constant m^3.Pa/(mol/K)
Ps = 101325 ;% Ps (Pa)  Ts (K)  standard temp-press
Ts = 273.15;
T = (450+273.15); % Kelvin
Patm = 101325; % Pa, Tube side pressure equals to 1 atm
PT = 15*Patm ; % (Pa) % Total pressure in shell side 15 atm
r1 = 0.0127/2; % Radius of inner porous tube (m)
r2 = 0.0254/2; % Radius of shell (m)
As = pi*(r2^2-r1^2); % cross sectional area in the shell side(m^2)
At = pi*r1^2; % cross sectinal area of the tube
L = 0.0635; % Length of the shell (m)
Vs = As*L*e; % Total void volume in the shell side (m^3)
vs = Vs/nn; % Void volume of each cstr
Vt = At*L;
vt = Vt/nn;
w = 15/nn; % g catalyst
Am = 2*pi*r1*L/nn; % membrane area m^2
CTs = PT/(T*Rg); % Total concentration in shell side (mol/m^3) Constant all
the time, P =15 atm, T = 627 K
CTt = Patm/(T*Rg);
ko1 = 10^(2.845); ko2 = 10^(0.659);
E1 = 111*10^3; E2 = 88*10^3; % Activation Energy for water gas shift reaction
j/mol

% INLET specifications
COin = 237.8*Ps/(Rg*Ts*(10^6)*60); % mol/s
H2Oin = 475.7*Ps/(Rg*Ts*(10^6)*60); % mol/s
CO2in =  86.5*Ps/(Rg*Ts*(10^6)*60);
H2in =  200*Ps/(Rg*Ts*(10^6)*60);
N2in = 0;
Fo =[COin;H2Oin;CO2in;H2in;0;0];
fto = Fo(1) + Fo(2) + Fo(3) + Fo(4)+ Fo(5);
ft_t = 0;
X_co = COin/fto;
X_h2o = H2Oin/fto;
X_co2 = CO2in/fto;
X_h2s = H2in/fto ; % shell
```

```matlab
X_n2 = N2in/fto;


X_h2t = 0; % tube
X_he = 1;


P = zeros(nn,5);
for i =1:nn
    for j =1:5;
        k = (i-1)*6+j;
        P(i,j) = PT*x(k);
    end
end

% Qo = 1935.1;  RK_01 permeability constant m3.micron/(m2.h.atm0.5)
Qo = 0.3*6322.7*Patm/(Rg*273.15*3600*sqrt(Patm)); % mol.micron/(m2.s.pa^0.5)
th = 10; % Pd thickness 10 micron
Ep = 15.6*10^3;
Q= Qo*exp(-Ep/(Rg*T)); % mol.micron/(m2.s.pa^0.5)


FT = zeros(nn+1,1);
FTt = zeros(nn+1,1);
Per = zeros(nn+1,1);


FT(1) = fto;
FTt(1) = ft_t;
Per(1) = 0;


Pas = zeros(nn,1); % P average shell
Pas(1) = (P(1,4)+PT*X_h2s)/2;
for i = 2:nn
    Pas(i) = (P(i,4)+P(i-1,4))/2;
end


Pat = zeros(nn,1); % P average tube
Pat(1) = Patm*(x(6)+X_h2t)/2;
for i = 2:nn
    Pat(i) = Patm*(x(i*6-6)+ x(i*6))/2;
end


for i = 1:nn
    if Pas(i) <= Pat(i)
        Per(i+1)=0;
    else
    Per(i+1) = Am*Q*(sqrt(Pas(i))-sqrt(Pat(i)))/th;
    end
end


for i = 1:nn
    FT(i+1) = FT(i) - Per(i+1);
    FTt(i+1) = FTt(i) + Per(i+1);
end
```

```matlab
% Cns – Constants for Cp CO H2O CO2 H2; Cp = heat capacity (J/mol*K)
% t = temperature (K) / 1000.
t = T/1000;
%        A         B         C         D         E          F         G           H
Cns = [ 25.56759 6.09613 4.054656 -2.671301 0.131021 -118.0089 227.3665 -
110.5271;
        30.092 6.832514 6.793435 -2.53448 0.082139 -250.881 223.3967 -241.8264;
        24.99735 55.18696 -33.69137 7.948387 -0.136638 -403.6075 228.2431 -
393.5224;
        33.066178 -11.363417 11.432816 -2.772874 -0.158558 -9.980797 172.707974 0
];

% dfH°gas for each gas CO H2O CO2 H2
Hf = [ -110.53; -241.83; -393.52; 0 ];

%CO -  H° ? H°298.15= A*t + B*t2/2 + C*t3/3 + D*t4/4 ? E/t + F ? H
H1 = Hf(1) +  Cns(1,1)*t + Cns(1,2)*(t^2)/2 + Cns(1,3)*(t^3)/3 +
Cns(1,4)*(t^4)/4 - Cns(1,5)/t + Cns(1,6) - Cns(1,8);
%H2O -  H° ? H°298.15= A*t + B*t2/2 + C*t3/3 + D*t4/4 ? E/t + F ? H
H2 = Hf(2) +  Cns(2,1)*t + Cns(2,2)*(t^2)/2 + Cns(2,3)*(t^3)/3 +
Cns(2,4)*(t^4)/4 - Cns(2,5)/t + Cns(2,6) - Cns(2,8);
%CO2 -  H° ? H°298.15= A*t + B*t2/2 + C*t3/3 + D*t4/4 ? E/t + F ? H
H3 = Hf(3) +  Cns(3,1)*t + Cns(3,2)*(t^2)/2 + Cns(3,3)*(t^3)/3 +
Cns(3,4)*(t^4)/4 - Cns(3,5)/t + Cns(3,6) - Cns(3,8);
%H2 -  H° ? H°298.15= A*t + B*t2/2 + C*t3/3 + D*t4/4 ? E/t + F ? H
H4 = Hf(4) +  Cns(4,1)*t + Cns(4,2)*(t^2)/2 + Cns(4,3)*(t^3)/3 +
Cns(4,4)*(t^4)/4 - Cns(4,5)/t + Cns(4,6) - Cns(4,8);

% dH_Rxn
dHrxn = H4+H3-(H1+H2);

%S° = A*ln(t) + B*t + C*t2/2 + D*t3/3 ? E/(2*t2) + G
S1 = Cns(1,1)*log(t) + Cns(1,2)*t + Cns(1,3)*(t^2)/2 + Cns(1,4)*(t^3)/3 -
Cns(1,5)/(2*t^2) + Cns(1,7);
S2 = Cns(2,1)*log(t) + Cns(2,2)*t + Cns(2,3)*(t^2)/2 + Cns(2,4)*(t^3)/3 -
Cns(2,5)/(2*t^2) + Cns(2,7);
S3 = Cns(3,1)*log(t) + Cns(3,2)*t + Cns(3,3)*(t^2)/2 + Cns(3,4)*(t^3)/3 -
Cns(3,5)/(2*t^2) + Cns(3,7);
S4 = Cns(4,1)*log(t) + Cns(4,2)*t + Cns(4,3)*(t^2)/2 + Cns(4,4)*(t^3)/3 -
Cns(4,5)/(2*t^2) + Cns(4,7);

dS = S4 + S3 - S2 - S1;

K = exp(dS/Rg)*exp(-dHrxn*10^3/(Rg*T));
% K = exp(4577.8/x(5) - 4.33); Moe

% R : mol/g cat. s    rco = mol/m^3. s

R = zeros(nn,1);
rco = zeros(nn,1);
for i = 1:nn

    beta = P(i,3)*P(i,4)/(P(i,1)*P(i,2)*K); % reversibility factor
    R(i) = ko1*exp(-E1/(Rg*T))*(P(i,1))*(P(i,3)^(-0.36))*(P(i,4)^(-0.09))*(1-
beta); % reaction rate 1  of co mol/kg.s
```

```matlab
    %R(i) = ko2*exp(-E2/(Rg*T))*(P(i,k+1)^0.9)*(P(i,k+2)^0.31)*(P(i,k+3)^(-
0.156))*(P(i,k+4)^(-0.05))*(1-beta); % reaction rate 2  of co mol/kg.s
    rco(i) = -R(i)*w/(1000^0.55);
end


%% 1
dfdt = zeros(6*nn,1);
dfdt(1,:) = (X_co*FT(1) - x(1)*FT(2) + rco(1))/(CTs*vs);
dfdt(2,:) = (X_h2o*FT(1) - x(2)*FT(2) + rco(1))/(CTs*vs);
dfdt(3,:) = (X_co2*FT(1) - x(3)*FT(2) - rco(1))/(CTs*vs);
dfdt(4,:) = (X_h2s*FT(1) - x(4)*FT(2) - rco(1) - Per(2))/(CTs*vs);
dfdt(5,:) = (X_n2*FT(1) - x(5)*FT(2) )/(CTs*vs);
dfdt(6,:) = (X_h2t*FTt(1) - x(6)*FTt(2) + Per(2))/(CTt*vt);
%% 2
dfdt(7,:) = (x(1)*FT(2) - x(7)*FT(3) + rco(2))/(CTs*vs);
dfdt(8,:) = (x(2)*FT(2) - x(8)*FT(3) + rco(2))/(CTs*vs);
dfdt(9,:) = (x(3)*FT(2) - x(9)*FT(3) - rco(2))/(CTs*vs);
dfdt(10,:) = (x(4)*FT(2) - x(10)*FT(3) - rco(2) - Per(3))/(CTs*vs);
dfdt(11,:) = (x(5)*FT(2) - x(11)*FT(3) )/(CTs*vs);
dfdt(12,:) = (x(6)*FTt(2) - x(12)*FTt(3) + Per(3))/(CTt*vt);
%% 3
dfdt(13,:) = (x(7)*FT(3) - x(13)*FT(4) + rco(3))/(CTs*vs);
dfdt(14,:) = (x(8)*FT(3) - x(14)*FT(4) + rco(3))/(CTs*vs);
dfdt(15,:) = (x(9)*FT(3) - x(15)*FT(4) - rco(3))/(CTs*vs);
dfdt(16,:) = (x(10)*FT(3) - x(16)*FT(4) - rco(3) - Per(4))/(CTs*vs);
dfdt(17,:) = (x(11)*FT(3) - x(17)*FT(4) )/(CTs*vs);
dfdt(18,:) = (x(12)*FTt(3) - x(18)*FTt(4) + Per(4))/(CTt*vt);
%% 4
dfdt(19,:) = (x(13)*FT(4) - x(19)*FT(5) + rco(4))/(CTs*vs);
dfdt(20,:) = (x(14)*FT(4) - x(20)*FT(5) + rco(4))/(CTs*vs);
dfdt(21,:) = (x(15)*FT(4) - x(21)*FT(5) - rco(4))/(CTs*vs);
dfdt(22,:) = (x(16)*FT(4) - x(22)*FT(5) - rco(4) - Per(5))/(CTs*vs);
dfdt(23,:) = (x(17)*FT(4) - x(23)*FT(5) )/(CTs*vs);
dfdt(24,:) = (x(18)*FTt(4) - x(24)*FTt(5) + Per(5))/(CTt*vt);
%% 5
dfdt(25,:) = (x(19)*FT(5) - x(25)*FT(6) + rco(5))/(CTs*vs);
dfdt(26,:) = (x(20)*FT(5) - x(26)*FT(6) + rco(5))/(CTs*vs);
dfdt(27,:) = (x(21)*FT(5) - x(27)*FT(6) - rco(5))/(CTs*vs);
dfdt(28,:) = (x(22)*FT(5) - x(28)*FT(6) - rco(5) - Per(6))/(CTs*vs);
dfdt(29,:) = (x(23)*FT(5) - x(29)*FT(6) )/(CTs*vs);
dfdt(30,:) = (x(24)*FTt(5) - x(30)*FTt(6) + Per(6))/(CTt*vt);
%% 6
dfdt(31,:) = (x(25)*FT(6) - x(31)*FT(7) + rco(6))/(CTs*vs);
dfdt(32,:) = (x(26)*FT(6) - x(32)*FT(7) + rco(6))/(CTs*vs);
dfdt(33,:) = (x(27)*FT(6) - x(33)*FT(7) - rco(6))/(CTs*vs);
dfdt(34,:) = (x(28)*FT(6) - x(34)*FT(7) - rco(6) - Per(7))/(CTs*vs);
dfdt(35,:) = (x(29)*FT(6) - x(35)*FT(7) )/(CTs*vs);
dfdt(36,:) = (x(30)*FTt(6) - x(36)*FTt(7) + Per(7))/(CTt*vt);
%% 7
dfdt(37,:) = (x(31)*FT(7) - x(37)*FT(8) + rco(7))/(CTs*vs);
dfdt(38,:) = (x(32)*FT(7) - x(38)*FT(8) + rco(7))/(CTs*vs);
dfdt(39,:) = (x(33)*FT(7) - x(39)*FT(8) - rco(7))/(CTs*vs);
dfdt(40,:) = (x(34)*FT(7) - x(40)*FT(8) - rco(7) - Per(8))/(CTs*vs);
dfdt(41,:) = (x(35)*FT(7) - x(41)*FT(8) )/(CTs*vs);
dfdt(42,:) = (x(36)*FTt(7) - x(42)*FTt(8) + Per(8))/(CTt*vt);
%% 8
dfdt(43,:) = (x(37)*FT(8) - x(43)*FT(9) + rco(8))/(CTs*vs);
```

```
dfdt(44,:) = (x(38)*FT(8) - x(44)*FT(9) + rco(8))/(CTs*vs);
dfdt(45,:) = (x(39)*FT(8) - x(45)*FT(9) - rco(8))/(CTs*vs);
dfdt(46,:) = (x(40)*FT(8) - x(46)*FT(9) - rco(8) - Per(9))/(CTs*vs);
dfdt(47,:) = (x(41)*FT(8) - x(47)*FT(9) )/(CTs*vs);
dfdt(48,:) = (x(42)*FTt(8) - x(48)*FTt(9) + Per(9))/(CTt*vt);
%% 9
dfdt(49,:) = (x(43)*FT(9) - x(49)*FT(10) + rco(9))/(CTs*vs);
dfdt(50,:) = (x(44)*FT(9) - x(50)*FT(10) + rco(9))/(CTs*vs);
dfdt(51,:) = (x(45)*FT(9) - x(51)*FT(10) - rco(9))/(CTs*vs);
dfdt(52,:) = (x(46)*FT(9) - x(52)*FT(10) - rco(9) - Per(10))/(CTs*vs);
dfdt(53,:) = (x(47)*FT(9) - x(53)*FT(10) )/(CTs*vs);
dfdt(54,:) = (x(48)*FTt(9) - x(54)*FTt(10) + Per(10))/(CTt*vt);
%% 10
dfdt(55,:) = (x(49)*FT(10) - x(55)*FT(11) + rco(10))/(CTs*vs);
dfdt(56,:) = (x(50)*FT(10) - x(56)*FT(11) + rco(10))/(CTs*vs);
dfdt(57,:) = (x(51)*FT(10) - x(57)*FT(11) - rco(10))/(CTs*vs);
dfdt(58,:) = (x(52)*FT(10) - x(58)*FT(11) - rco(10) - Per(11))/(CTs*vs);
dfdt(59,:) = (x(53)*FT(10) - x(59)*FT(11) )/(CTs*vs);
dfdt(60,:) = (x(54)*FTt(10) - x(60)*FTt(11) + Per(11))/(CTt*vt);
%% 11
dfdt(61,:) = (x(55)*FT(11) - x(61)*FT(12) + rco(11))/(CTs*vs);
dfdt(62,:) = (x(56)*FT(11) - x(62)*FT(12) + rco(11))/(CTs*vs);
dfdt(63,:) = (x(57)*FT(11) - x(63)*FT(12) - rco(11))/(CTs*vs);
dfdt(64,:) = (x(58)*FT(11) - x(64)*FT(12) - rco(11) - Per(12))/(CTs*vs);
dfdt(65,:) = (x(59)*FT(11) - x(65)*FT(12) )/(CTs*vs);
dfdt(66,:) = (x(60)*FTt(11) - x(66)*FTt(12) + Per(12))/(CTt*vt);
%% 12
dfdt(67,:) = (x(61)*FT(12) - x(67)*FT(13) + rco(12))/(CTs*vs);
dfdt(68,:) = (x(62)*FT(12) - x(68)*FT(13) + rco(12))/(CTs*vs);
dfdt(69,:) = (x(63)*FT(12) - x(69)*FT(13) - rco(12))/(CTs*vs);
dfdt(70,:) = (x(64)*FT(12) - x(70)*FT(13) - rco(12) - Per(13))/(CTs*vs);
dfdt(71,:) = (x(65)*FT(12) - x(71)*FT(13) )/(CTs*vs);
dfdt(72,:) = (x(66)*FTt(12) - x(72)*FTt(13) + Per(13))/(CTt*vt);
%% 13
dfdt(73,:) = (x(67)*FT(13) - x(73)*FT(14) + rco(13))/(CTs*vs);
dfdt(74,:) = (x(68)*FT(13) - x(74)*FT(14) + rco(13))/(CTs*vs);
dfdt(75,:) = (x(69)*FT(13) - x(75)*FT(14) - rco(13))/(CTs*vs);
dfdt(76,:) = (x(70)*FT(13) - x(76)*FT(14) - rco(13) - Per(14))/(CTs*vs);
dfdt(77,:) = (x(71)*FT(13) - x(77)*FT(14) )/(CTs*vs);
dfdt(78,:) = (x(72)*FTt(13) - x(78)*FTt(14) + Per(14))/(CTt*vt);
%% 14
dfdt(79,:) = (x(73)*FT(14) - x(79)*FT(15) + rco(14))/(CTs*vs);
dfdt(80,:) = (x(74)*FT(14) - x(80)*FT(15) + rco(14))/(CTs*vs);
dfdt(81,:) = (x(75)*FT(14) - x(81)*FT(15) - rco(14))/(CTs*vs);
dfdt(82,:) = (x(76)*FT(14) - x(82)*FT(15) - rco(14) - Per(15))/(CTs*vs);
dfdt(83,:) = (x(77)*FT(14) - x(83)*FT(15) )/(CTs*vs);
dfdt(84,:) = (x(78)*FTt(14) - x(84)*FTt(15) + Per(15))/(CTt*vt);
%% 15
dfdt(85,:) = (x(79)*FT(15) - x(85)*FT(16) + rco(15))/(CTs*vs);
dfdt(86,:) = (x(80)*FT(15) - x(86)*FT(16) + rco(15))/(CTs*vs);
dfdt(87,:) = (x(81)*FT(15) - x(87)*FT(16) - rco(15))/(CTs*vs);
dfdt(88,:) = (x(82)*FT(15) - x(88)*FT(16) - rco(15) - Per(16))/(CTs*vs);
dfdt(89,:) = (x(83)*FT(15) - x(89)*FT(16) )/(CTs*vs);
dfdt(90,:) = (x(84)*FTt(15) - x(90)*FTt(16) + Per(16))/(CTt*vt);
%% 16
dfdt(91,:) = (x(85)*FT(16) - x(91)*FT(17) + rco(16))/(CTs*vs);
dfdt(92,:) = (x(86)*FT(16) - x(92)*FT(17) + rco(16))/(CTs*vs);
```

```matlab
dfdt(93,:) = (x(87)*FT(16) - x(93)*FT(17) - rco(16))/(CTs*vs);
dfdt(94,:) = (x(88)*FT(16) - x(94)*FT(17) - rco(16) - Per(17))/(CTs*vs);
dfdt(95,:) = (x(89)*FT(16) - x(95)*FT(17) )/(CTs*vs);
dfdt(96,:) = (x(90)*FTt(16) - x(96)*FTt(17) + Per(17))/(CTt*vt);
%% 17
dfdt(97,:) = (x(91)*FT(17) - x(97)*FT(18) + rco(17))/(CTs*vs);
dfdt(98,:) = (x(92)*FT(17) - x(98)*FT(18) + rco(17))/(CTs*vs);
dfdt(99,:) = (x(93)*FT(17) - x(99)*FT(18) - rco(17))/(CTs*vs);
dfdt(100,:) = (x(94)*FT(17) - x(100)*FT(18) - rco(17) - Per(18))/(CTs*vs);
dfdt(101,:) = (x(95)*FT(17) - x(101)*FT(18) )/(CTs*vs);
dfdt(102,:) = (x(96)*FTt(17) - x(102)*FTt(18) + Per(18))/(CTt*vt);
%% 18
dfdt(103,:) = (x(97)*FT(18) - x(103)*FT(19) + rco(18))/(CTs*vs);
dfdt(104,:) = (x(98)*FT(18) - x(104)*FT(19) + rco(18))/(CTs*vs);
dfdt(105,:) = (x(99)*FT(18) - x(105)*FT(19) - rco(18))/(CTs*vs);
dfdt(106,:) = (x(100)*FT(18) - x(106)*FT(19) - rco(18) - Per(19))/(CTs*vs);
dfdt(107,:) = (x(101)*FT(18) - x(107)*FT(19) )/(CTs*vs);
dfdt(108,:) = (x(102)*FTt(18) - x(108)*FTt(19) + Per(19))/(CTt*vt);
%% 19
dfdt(109,:) = (x(103)*FT(19) - x(109)*FT(20) + rco(19))/(CTs*vs);
dfdt(110,:) = (x(104)*FT(19) - x(110)*FT(20) + rco(19))/(CTs*vs);
dfdt(111,:) = (x(105)*FT(19) - x(111)*FT(20) - rco(19))/(CTs*vs);
dfdt(112,:) = (x(106)*FT(19) - x(112)*FT(20) - rco(19) - Per(20))/(CTs*vs);
dfdt(113,:) = (x(107)*FT(19) - x(113)*FT(20) )/(CTs*vs);
dfdt(114,:) = (x(108)*FTt(19) - x(114)*FTt(20) + Per(20))/(CTt*vt);
%% 20
dfdt(115,:) = (x(109)*FT(20) - x(115)*FT(21) + rco(20))/(CTs*vs);
dfdt(116,:) = (x(110)*FT(20) - x(116)*FT(21) + rco(20))/(CTs*vs);
dfdt(117,:) = (x(111)*FT(20) - x(117)*FT(21) - rco(20))/(CTs*vs);
dfdt(118,:) = (x(112)*FT(20) - x(118)*FT(21) - rco(20) - Per(21))/(CTs*vs);
dfdt(119,:) = (x(113)*FT(20) - x(119)*FT(21) )/(CTs*vs);
dfdt(120,:) = (x(114)*FTt(20) - x(120)*FTt(21) + Per(21))/(CTt*vt);
end
```

Run.file:

```matlab
clear
clc
xi = "Get no reaction results"

% ns: number of species, nn: % number of cstrs in series
ns =6;nn = 20;
ic=xi; tspan=[0 12];
[t,x]=ode23s('Startup_syn',tspan,ic);
```

b. Regulator problem: pressure drop

m.file:

```
function dfdt = RP_P_syntune(t,x)
global Kc to
ns = 6; % number of equations in each segment
nn = 20; % number of cstrs in series
e = 0.5; % void fraction of the fixed bed

Rg = 8.314; % m3 Pa/ K mol
T = (450+273.15); % Kelvin
Patm = 101325; % Pa, Tube side pressure equals to 1 atm
PT = 10*Patm ; % (Pa) % Total pressure in shell side 15 atm

Ps = 101325 ;% Ps (Pa)  Ts (K)  standard temp-press
Ts = 273.15;

r1 = 0.0127/2; % Radius of inner porous tube (m)
r2 = 0.0127; % Radius of shell (m)
As = pi*(r2^2-r1^2); % cross sectional area in the shell side(m^2)
At = pi*r1^2; % cross sectinal area of the tube
L = 0.0635; % Length of the shell (m)
Vs = As*L*e; % Total void volume in the shell side (m^3)
vs = Vs/nn; % Void volume of each cstr
Vt = At*L;
vt = Vt/nn;
w = 15/nn; % g catalyst
Am = 2*pi*r1*L/nn; % membrane area m^2

CTs = PT/(T*Rg); % Total concentration in shell side (mol/m^3) Constant all
the time, P =15 atm, T = 627 K
CTt = Patm/(T*Rg);

ko1 = 10^(2.845); ko2 = 10^(0.659);
E1 = 111*10^3; E2 = 88*10^3; % Activation Energy j/mol

%% Inlet Flow Rates
F_CO = (237.8*Ps/(Rg*Ts*(10^6)*60)); % *** Disturbance *** % mol/s
Fo_H2O = (475.7*Ps/(Rg*Ts*(10^6)*60)); % mol/s
F_CO2 = (86.5*Ps/(Rg*Ts*(10^6)*60));
F_H2 = (200*Ps/(Rg*Ts*(10^6)*60));
F_N2 = 0;
%% P.C.
% Xco_sp = 0.001;
% error = (x((nn-1)*ns+1)-Xco_sp);
sp = 2.32/100;
%sp = 1.8/100;
c_o= x(115)/(x(115)+x(117)+x(118));
error = (c_o - sp);
% Kc = 0.02;
% to = 1;
F_H2O = Fo_H2O + Kc*error + Kc*x(nn*ns+1)/to;
```

338

```matlab
Fo =[F_CO;F_H2O;F_CO2;F_H2;F_N2;0];
fto = Fo(1) + Fo(2) + Fo(3) + Fo(4)+ Fo(5);
ftt= 0;

%% INLET specifications
X_CO = F_CO/fto;
X_H2O = F_H2O/fto;
X_CO2 = F_CO2/fto;
X_H2S = F_H2/fto; % shell
X_N2 = F_N2/fto;


X_H2T = 1; % tube
X_HE = 0;


%% Membrane Properties
Qo = 0.3*6322.7*Patm/(Rg*273.15*3600*sqrt(Patm)); % mol.micron/(m2.s.pa^0.5)
th = 10; % Pd thickness 10 micron
Ep = 15.6*10^3;
Q= Qo*exp(-Ep/(Rg*T)); % mol.micron/(m2.s.pa^0.5)
%%
FT = zeros(nn+1,1);
FTt = zeros(nn+1,1);
Per = zeros(nn+1,1);


FT(1) = fto;
FTt(1) = ftt;
Per(1) = 0;


Pas = zeros(nn,1); % P average shell
Pas(1) = (x(4)+PT*X_H2S)/2;
for i = 2:nn
    k = (i-1)*ns+4;
    Pas(i) = (x(k)+x(k-ns))/2;
end

Pat = zeros(nn,1); % P average tube
Pat(1) = (x(6)+Patm*X_H2T)/2;
for i = 2:nn
    k2 = i*6;
    Pat(i) = (x(k2-ns)+ x(k2))/2;
end


for i = 1:nn
    if Pas(i)<=Pat(i)
        Per(i+1)=0;
    else
        Per(i+1) = Am*Q*(sqrt(Pas(i))-sqrt(Pat(i)))/th;
    end
end

for i = 1:nn
    FT(i+1) = FT(i) - Per(i+1);
    FTt(i+1) = FTt(i) + Per(i+1);
```

```matlab
    end

%% Thermodynamic Properties

% Cns - Constants for Cp CO H2O CO2 H2; Cp = heat capacity (J/mol*K)
% t = temperature (K) / 1000.
t = T/1000;
%        A         B         C         D         E         F         G         H
Cns = [ 25.56759 6.09613 4.054656 -2.671301 0.131021 -118.0089 227.3665 -
110.5271;
    30.092 6.832514 6.793435 -2.53448 0.082139 -250.881 223.3967 -241.8264;
    24.99735 55.18696 -33.69137 7.948387 -0.136638 -403.6075 228.2431 -
393.5224;
    33.066178 -11.363417 11.432816 -2.772874 -0.158558 -9.980797 172.707974 0
];

% dfH°gas for each gas CO H2O CO2 H2
Hf = [ -110.53; -241.83; -393.52; 0 ];

%CO -  H° ? H°298.15= A*t + B*t2/2 + C*t3/3 + D*t4/4 ? E/t + F ? H
H1 = Hf(1) +  Cns(1,1)*t + Cns(1,2)*(t^2)/2 + Cns(1,3)*(t^3)/3 +
Cns(1,4)*(t^4)/4 - Cns(1,5)/t + Cns(1,6) - Cns(1,8);
%H2O -  H° ? H°298.15= A*t + B*t2/2 + C*t3/3 + D*t4/4 ? E/t + F ? H
H2 = Hf(2) +  Cns(2,1)*t + Cns(2,2)*(t^2)/2 + Cns(2,3)*(t^3)/3 +
Cns(2,4)*(t^4)/4 - Cns(2,5)/t + Cns(2,6) - Cns(2,8);
%CO2 -  H° ? H°298.15= A*t + B*t2/2 + C*t3/3 + D*t4/4 ? E/t + F ? H
H3 = Hf(3) +  Cns(3,1)*t + Cns(3,2)*(t^2)/2 + Cns(3,3)*(t^3)/3 +
Cns(3,4)*(t^4)/4 - Cns(3,5)/t + Cns(3,6) - Cns(3,8);
%H2 -  H° ? H°298.15= A*t + B*t2/2 + C*t3/3 + D*t4/4 ? E/t + F ? H
H4 = Hf(4) +  Cns(4,1)*t + Cns(4,2)*(t^2)/2 + Cns(4,3)*(t^3)/3 +
Cns(4,4)*(t^4)/4 - Cns(4,5)/t + Cns(4,6) - Cns(4,8);

% dH_Rxn
dHrxn = H4+H3-(H1+H2);

%S° = A*ln(t) + B*t + C*t2/2 + D*t3/3 ? E/(2*t2) + G
S1 = Cns(1,1)*log(t) + Cns(1,2)*t + Cns(1,3)*(t^2)/2 + Cns(1,4)*(t^3)/3 -
Cns(1,5)/(2*t^2) + Cns(1,7);
S2 = Cns(2,1)*log(t) + Cns(2,2)*t + Cns(2,3)*(t^2)/2 + Cns(2,4)*(t^3)/3 -
Cns(2,5)/(2*t^2) + Cns(2,7);
S3 = Cns(3,1)*log(t) + Cns(3,2)*t + Cns(3,3)*(t^2)/2 + Cns(3,4)*(t^3)/3 -
Cns(3,5)/(2*t^2) + Cns(3,7);
S4 = Cns(4,1)*log(t) + Cns(4,2)*t + Cns(4,3)*(t^2)/2 + Cns(4,4)*(t^3)/3 -
Cns(4,5)/(2*t^2) + Cns(4,7);

dS = S4 + S3 - S2 - S1;

K = exp(dS/Rg)*exp(-dHrxn*10^3/(Rg*T));
% K = exp(4577.8/x(5) - 4.33); from Moe

%% Reaction Rate from Hla et al
% R : mol/g cat. s    rco = mol/m^3. s
R = zeros(nn,1);
rco = zeros(nn,1);
for i = 1:nn
```

```matlab
    k3 = i*ns;
    beta =x(k3-3)*x(k3-2)/(x(k3-5)*x(k3-4)*K);
%P(i,3)*P(i,4)/(P(i,1)*P(i,2)*K); % reversibility factor
    R(i) = ko1*exp(-E1/(Rg*T))*(x(k3-5)*x(k3-3)^(-0.36))*(x(k3-2)^(-
0.09))*(1-beta);%(P(i,1))*(P(i,3)^(-0.36))*(P(i,4)^(-0.09))*f % reaction rate
1  of co mol/kg.s
    %R(i) = ko2*exp(-E2/(Rg*T))*(P(i,k+1)^0.9)*(P(i,k+2)^0.31)*(P(i,k+3)^(-
0.156))*(P(i,k+4)^(-0.05))*(1-beta); % reaction rate 2  of co mol/kg.s
    rco(i) = -R(i)*w/(1000^0.55);
end


%% 1
dfdt = zeros(6*nn+1,1);
dfdt(1,:) = (PT*X_CO*FT(1) - x(1)*FT(2) + PT*rco(1))/(CTs*vs);
dfdt(2,:) = (PT*X_H2O*FT(1) - x(2)*FT(2) + PT*rco(1))/(CTs*vs);
dfdt(3,:) = (PT*X_CO2*FT(1) - x(3)*FT(2) - PT*rco(1))/(CTs*vs);
dfdt(4,:) = (PT*X_H2S*FT(1) - x(4)*FT(2) - PT*rco(1) - PT*Per(2))/(CTs*vs);
dfdt(5,:) = (PT*X_N2*FT(1) - x(5)*FT(2) )/(CTs*vs);
dfdt(6,:) = (Patm*X_H2T*FTt(1) - x(6)*FTt(2) + Patm*Per(2))/(CTt*vt);
%% 2
dfdt(7,:) = (x(1)*FT(2) - x(7)*FT(3) + PT*rco(2))/(CTs*vs);
dfdt(8,:) = (x(2)*FT(2) - x(8)*FT(3) + PT*rco(2))/(CTs*vs);
dfdt(9,:) = (x(3)*FT(2) - x(9)*FT(3) - PT*rco(2))/(CTs*vs);
dfdt(10,:) = (x(4)*FT(2) - x(10)*FT(3) - PT*rco(2) - PT*Per(3))/(CTs*vs);
dfdt(11,:) = (x(5)*FT(2) - x(11)*FT(3) )/(CTs*vs);
dfdt(12,:) = (x(6)*FTt(2) - x(12)*FTt(3) + Patm*Per(3))/(CTt*vt);
%% 3
dfdt(13,:) = (x(7)*FT(3) - x(13)*FT(4) + PT*rco(3))/(CTs*vs);
dfdt(14,:) = (x(8)*FT(3) - x(14)*FT(4) + PT*rco(3))/(CTs*vs);
dfdt(15,:) = (x(9)*FT(3) - x(15)*FT(4) - PT*rco(3))/(CTs*vs);
dfdt(16,:) = (x(10)*FT(3) - x(16)*FT(4) - PT*rco(3) - PT*Per(4))/(CTs*vs);
dfdt(17,:) = (x(11)*FT(3) - x(17)*FT(4) )/(CTs*vs);
dfdt(18,:) = (x(12)*FTt(3) - x(18)*FTt(4) + Patm*Per(4))/(CTt*vt);
%% 4
dfdt(19,:) = (x(13)*FT(4) - x(19)*FT(5) + PT*rco(4))/(CTs*vs);
dfdt(20,:) = (x(14)*FT(4) - x(20)*FT(5) + PT*rco(4))/(CTs*vs);
dfdt(21,:) = (x(15)*FT(4) - x(21)*FT(5) - PT*rco(4))/(CTs*vs);
dfdt(22,:) = (x(16)*FT(4) - x(22)*FT(5) - PT*rco(4) - PT*Per(5))/(CTs*vs);
dfdt(23,:) = (x(17)*FT(4) - x(23)*FT(5) )/(CTs*vs);
dfdt(24,:) = (x(18)*FTt(4) - x(24)*FTt(5) + Patm*Per(5))/(CTt*vt);
%% 5
dfdt(25,:) = (x(19)*FT(5) - x(25)*FT(6) + PT*rco(5))/(CTs*vs);
dfdt(26,:) = (x(20)*FT(5) - x(26)*FT(6) + PT*rco(5))/(CTs*vs);
dfdt(27,:) = (x(21)*FT(5) - x(27)*FT(6) - PT*rco(5))/(CTs*vs);
dfdt(28,:) = (x(22)*FT(5) - x(28)*FT(6) - PT*rco(5) - PT*Per(6))/(CTs*vs);
dfdt(29,:) = (x(23)*FT(5) - x(29)*FT(6) )/(CTs*vs);
dfdt(30,:) = (x(24)*FTt(5) - x(30)*FTt(6) + Patm*Per(6))/(CTt*vt);
%% 6
dfdt(31,:) = (x(25)*FT(6) - x(31)*FT(7) + PT*rco(6))/(CTs*vs);
dfdt(32,:) = (x(26)*FT(6) - x(32)*FT(7) + PT*rco(6))/(CTs*vs);
dfdt(33,:) = (x(27)*FT(6) - x(33)*FT(7) - PT*rco(6))/(CTs*vs);
dfdt(34,:) = (x(28)*FT(6) - x(34)*FT(7) - PT*rco(6) - PT*Per(7))/(CTs*vs);
dfdt(35,:) = (x(29)*FT(6) - x(35)*FT(7) )/(CTs*vs);
dfdt(36,:) = (x(30)*FTt(6) - x(36)*FTt(7) + Patm*Per(7))/(CTt*vt);
%% 7
dfdt(37,:) = (x(31)*FT(7) - x(37)*FT(8) + PT*rco(7))/(CTs*vs);
dfdt(38,:) = (x(32)*FT(7) - x(38)*FT(8) + PT*rco(7))/(CTs*vs);
```

```
dfdt(39,:) = (x(33)*FT(7) - x(39)*FT(8) - PT*rco(7))/(CTs*vs);
dfdt(40,:) = (x(34)*FT(7) - x(40)*FT(8) - PT*rco(7) - PT*Per(8))/(CTs*vs);
dfdt(41,:) = (x(35)*FT(7) - x(41)*FT(8) )/(CTs*vs);
dfdt(42,:) = (x(36)*FTt(7) - x(42)*FTt(8) + Patm*Per(8))/(CTt*vt);
%% 8
dfdt(43,:) = (x(37)*FT(8) - x(43)*FT(9) + PT*rco(8))/(CTs*vs);
dfdt(44,:) = (x(38)*FT(8) - x(44)*FT(9) + PT*rco(8))/(CTs*vs);
dfdt(45,:) = (x(39)*FT(8) - x(45)*FT(9) - PT*rco(8))/(CTs*vs);
dfdt(46,:) = (x(40)*FT(8) - x(46)*FT(9) - PT*rco(8) - PT*Per(9))/(CTs*vs);
dfdt(47,:) = (x(41)*FT(8) - x(47)*FT(9) )/(CTs*vs);
dfdt(48,:) = (x(42)*FTt(8) - x(48)*FTt(9) + Patm*Per(9))/(CTt*vt);
%% 9
dfdt(49,:) = (x(43)*FT(9) - x(49)*FT(10) + PT*rco(9))/(CTs*vs);
dfdt(50,:) = (x(44)*FT(9) - x(50)*FT(10) + PT*rco(9))/(CTs*vs);
dfdt(51,:) = (x(45)*FT(9) - x(51)*FT(10) - PT*rco(9))/(CTs*vs);
dfdt(52,:) = (x(46)*FT(9) - x(52)*FT(10) - PT*rco(9) - PT*Per(10))/(CTs*vs);
dfdt(53,:) = (x(47)*FT(9) - x(53)*FT(10) )/(CTs*vs);
dfdt(54,:) = (x(48)*FTt(9) - x(54)*FTt(10) + Patm*Per(10))/(CTt*vt);
%% 10
dfdt(55,:) = (x(49)*FT(10) - x(55)*FT(11) + PT*rco(10))/(CTs*vs);
dfdt(56,:) = (x(50)*FT(10) - x(56)*FT(11) + PT*rco(10))/(CTs*vs);
dfdt(57,:) = (x(51)*FT(10) - x(57)*FT(11) - PT*rco(10))/(CTs*vs);
dfdt(58,:) = (x(52)*FT(10) - x(58)*FT(11) - PT*rco(10) -
PT*Per(11))/(CTs*vs);
dfdt(59,:) = (x(53)*FT(10) - x(59)*FT(11) )/(CTs*vs);
dfdt(60,:) = (x(54)*FTt(10) - x(60)*FTt(11) + Patm*Per(11))/(CTt*vt);
%% 11
dfdt(61,:) = (x(55)*FT(11) - x(61)*FT(12) + PT*rco(11))/(CTs*vs);
dfdt(62,:) = (x(56)*FT(11) - x(62)*FT(12) + PT*rco(11))/(CTs*vs);
dfdt(63,:) = (x(57)*FT(11) - x(63)*FT(12) - PT*rco(11))/(CTs*vs);
dfdt(64,:) = (x(58)*FT(11) - x(64)*FT(12) - PT*rco(11) -
PT*Per(12))/(CTs*vs);
dfdt(65,:) = (x(59)*FT(11) - x(65)*FT(12) )/(CTs*vs);
dfdt(66,:) = (x(60)*FTt(11) - x(66)*FTt(12) + Patm*Per(12))/(CTt*vt);
%% 12
dfdt(67,:) = (x(61)*FT(12) - x(67)*FT(13) + PT*rco(12))/(CTs*vs);
dfdt(68,:) = (x(62)*FT(12) - x(68)*FT(13) + PT*rco(12))/(CTs*vs);
dfdt(69,:) = (x(63)*FT(12) - x(69)*FT(13) - PT*rco(12))/(CTs*vs);
dfdt(70,:) = (x(64)*FT(12) - x(70)*FT(13) - PT*rco(12) -
PT*Per(13))/(CTs*vs);
dfdt(71,:) = (x(65)*FT(12) - x(71)*FT(13) )/(CTs*vs);
dfdt(72,:) = (x(66)*FTt(12) - x(72)*FTt(13) + Patm*Per(13))/(CTt*vt);
%% 13
dfdt(73,:) = (x(67)*FT(13) - x(73)*FT(14) + PT*rco(13))/(CTs*vs);
dfdt(74,:) = (x(68)*FT(13) - x(74)*FT(14) + PT*rco(13))/(CTs*vs);
dfdt(75,:) = (x(69)*FT(13) - x(75)*FT(14) - PT*rco(13))/(CTs*vs);
dfdt(76,:) = (x(70)*FT(13) - x(76)*FT(14) - PT*rco(13) -
PT*Per(14))/(CTs*vs);
dfdt(77,:) = (x(71)*FT(13) - x(77)*FT(14) )/(CTs*vs);
dfdt(78,:) = (x(72)*FTt(13) - x(78)*FTt(14) + Patm*Per(14))/(CTt*vt);
%% 14
dfdt(79,:) = (x(73)*FT(14) - x(79)*FT(15) + PT*rco(14))/(CTs*vs);
dfdt(80,:) = (x(74)*FT(14) - x(80)*FT(15) + PT*rco(14))/(CTs*vs);
dfdt(81,:) = (x(75)*FT(14) - x(81)*FT(15) - PT*rco(14))/(CTs*vs);
dfdt(82,:) = (x(76)*FT(14) - x(82)*FT(15) - PT*rco(14) -
PT*Per(15))/(CTs*vs);
dfdt(83,:) = (x(77)*FT(14) - x(83)*FT(15) )/(CTs*vs);
```

```
dfdt(84,:) = (x(78)*FTt(14) - x(84)*FTt(15) + Patm*Per(15))/(CTt*vt);
%% 15
dfdt(85,:) = (x(79)*FT(15) - x(85)*FT(16) + PT*rco(15))/(CTs*vs);
dfdt(86,:) = (x(80)*FT(15) - x(86)*FT(16) + PT*rco(15))/(CTs*vs);
dfdt(87,:) = (x(81)*FT(15) - x(87)*FT(16) - PT*rco(15))/(CTs*vs);
dfdt(88,:) = (x(82)*FT(15) - x(88)*FT(16) - PT*rco(15) -
PT*Per(16))/(CTs*vs);
dfdt(89,:) = (x(83)*FT(15) - x(89)*FT(16) )/(CTs*vs);
dfdt(90,:) = (x(84)*FTt(15) - x(90)*FTt(16) + Patm*Per(16))/(CTt*vt);
%% 16
dfdt(91,:) = (x(85)*FT(16) - x(91)*FT(17) + PT*rco(16))/(CTs*vs);
dfdt(92,:) = (x(86)*FT(16) - x(92)*FT(17) + PT*rco(16))/(CTs*vs);
dfdt(93,:) = (x(87)*FT(16) - x(93)*FT(17) - PT*rco(16))/(CTs*vs);
dfdt(94,:) = (x(88)*FT(16) - x(94)*FT(17) - PT*rco(16) -
PT*Per(17))/(CTs*vs);
dfdt(95,:) = (x(89)*FT(16) - x(95)*FT(17) )/(CTs*vs);
dfdt(96,:) = (x(90)*FTt(16) - x(96)*FTt(17) + Patm*Per(17))/(CTt*vt);
%% 17
dfdt(97,:) = (x(91)*FT(17) - x(97)*FT(18) + PT*rco(17))/(CTs*vs);
dfdt(98,:) = (x(92)*FT(17) - x(98)*FT(18) + PT*rco(17))/(CTs*vs);
dfdt(99,:) = (x(93)*FT(17) - x(99)*FT(18) - PT*rco(17))/(CTs*vs);
dfdt(100,:) = (x(94)*FT(17) - x(100)*FT(18) - PT*rco(17) -
PT*Per(18))/(CTs*vs);
dfdt(101,:) = (x(95)*FT(17) - x(101)*FT(18) )/(CTs*vs);
dfdt(102,:) = (x(96)*FTt(17) - x(102)*FTt(18) + Patm*Per(18))/(CTt*vt);
%% 18
dfdt(103,:) = (x(97)*FT(18) - x(103)*FT(19) + PT*rco(18))/(CTs*vs);
dfdt(104,:) = (x(98)*FT(18) - x(104)*FT(19) + PT*rco(18))/(CTs*vs);
dfdt(105,:) = (x(99)*FT(18) - x(105)*FT(19) - PT*rco(18))/(CTs*vs);
dfdt(106,:) = (x(100)*FT(18) - x(106)*FT(19) - PT*rco(18) -
PT*Per(19))/(CTs*vs);
dfdt(107,:) = (x(101)*FT(18) - x(107)*FT(19) )/(CTs*vs);
dfdt(108,:) = (x(102)*FTt(18) - x(108)*FTt(19) + Patm*Per(19))/(CTt*vt);
%% 19
dfdt(109,:) = (x(103)*FT(19) - x(109)*FT(20) + PT*rco(19))/(CTs*vs);
dfdt(110,:) = (x(104)*FT(19) - x(110)*FT(20) + PT*rco(19))/(CTs*vs);
dfdt(111,:) = (x(105)*FT(19) - x(111)*FT(20) - PT*rco(19))/(CTs*vs);
dfdt(112,:) = (x(106)*FT(19) - x(112)*FT(20) - PT*rco(19) -
PT*Per(20))/(CTs*vs);
dfdt(113,:) = (x(107)*FT(19) - x(113)*FT(20) )/(CTs*vs);
dfdt(114,:) = (x(108)*FTt(19) - x(114)*FTt(20) + Patm*Per(20))/(CTt*vt);
%% 20
dfdt(115,:) = (x(109)*FT(20) - x(115)*FT(21) + PT*rco(20))/(CTs*vs);
dfdt(116,:) = (x(110)*FT(20) - x(116)*FT(21) + PT*rco(20))/(CTs*vs);
dfdt(117,:) = (x(111)*FT(20) - x(117)*FT(21) - PT*rco(20))/(CTs*vs);
dfdt(118,:) = (x(112)*FT(20) - x(118)*FT(21) - PT*rco(20) -
PT*Per(21))/(CTs*vs);
dfdt(119,:) = (x(113)*FT(20) - x(119)*FT(21) )/(CTs*vs);
dfdt(120,:) = (x(114)*FTt(20) - x(120)*FTt(21) + Patm*Per(21))/(CTt*vt);
dfdt(121,:) = (c_o - sp);
end
```

Run.file:

```
clear
clc
```

```matlab
%% ODE Solution Method
global Kc to
% to = 1;
% Kcall = [0.024 0.002 0.0005];% 0.024 0.005 0.001 Kc-highest is the value
with the constant oscillation with to=0/ take the half
 toall = [0.8];% 0.1 0.8 5
 Kc = 0.002;
%for m = 1:length(Kcall)
for m = 1:length(toall)
    ns = 6; % number of equations in each segment
    nn = 20; % number of segments
    sp = 2.32/100;
    %sp = 1.8/100;
    %Xco_sp = 0.001;
    %Kc = Kcall(m);
    to = toall(m);

    xi = "Get the start-up result"
    xi(6:6:(nn-1)*6+6)= 101325;

    c_oi = xi(115)/(xi(115)+xi(117)+xi(118));
    xi(nn*ns+1) = (c_oi - sp);
    %xi(nn*ns+1) = xi((nn-1)*ns+1)-Xco_sp;
    ic=xi; tspan=[0 100];
    [t,x]=ode23s('RP_P_syntune',tspan,ic);


    %%
    Rg = 8.314; % Ideal gas constant m^3.Pa/(mol/K)
    Ps = 101325;% Ps (Pa)  Ts (K)  standard temp-press
    Ts = 273.15;

    Patm = 101325; % Pa, Tube side pressure equals to 1 atm
    PT = 10*Patm ; % (Pa) % Total pressure in shell side 15 atm
    T = (450+273.15); % Kelvin

    %Qo = 1935.1*Patm/(Rg*273.15*3600*sqrt(Patm)); % mol.micron/(m2.s.pa^0.5)
    %th = 10; % Pd thickness 10 micron
    %Ep = 12.89*10^3;
    %Q= Qo*exp(-Ep/(Rg*T)); % mol.micron/(m2.s.pa^0.5)
    Qo = 0.3*6322.7*Patm/(Rg*273.15*3600*sqrt(Patm)); %
mol.micron/(m2.s.pa^0.5)
    th = 10; % Pd thickness 10 micron
    Ep = 15.6*10^3;
    Q= Qo*exp(-Ep/(Rg*T)); % mol.micron/(m2.s.pa^0.5)

    r1 = 0.0127/2; % Radius of inner porous tube (m)
    L = 0.0635; % Length of the shell (m)
    Am = 2*pi*r1*L/nn; % membrane area m^2

    % Q_inlet = 1000 sccm, Fh20_inlet / Fco_inlet = 2
    F_CO = (237.8*Ps/(Rg*Ts*(10^6)*60)); % *** Disturbance *** % mol/s
    Fo_H2O = (475.7*Ps/(Rg*Ts*(10^6)*60)); % mol/s
    F_CO2 = (86.5*Ps/(Rg*Ts*(10^6)*60));
    F_H2 = (200*Ps/(Rg*Ts*(10^6)*60));
```

```matlab
    F_N2 = 0;
    %% P.C.
    % Kc = 0.02;
    % to = 1;
    error = zeros(length(t),1);
    F_H2O = zeros(length(t),1);
    fso = zeros(length(t),1);
    c_oo = zeros(length(t),1);
    for i = 1:length(t)
        c_oo(i)= x(i,115)/(x(i,115)+x(i,117)+x(i,118));
        error(i) = (c_oo(i) - sp);
        F_H2O(i) = (Fo_H2O + Kc*error(i) + Kc*x(i,nn*ns+1)/to);
        fso(i) = (F_CO + F_CO2 + F_H2 + F_N2 + F_H2O(i));
    end


    %% INLET specifications

    X_co = zeros(length(t),1);X_h2o= zeros(length(t),1);X_co2=
zeros(length(t),1);X_h2s= zeros(length(t),1);X_n2= zeros(length(t),1);
    for i = 1:length(t)
        X_co(i) = F_CO/fso(i);
        X_h2o(i) = F_H2O(i)/fso(i);
        X_co2(i) = F_CO2/fso(i);
        X_h2s(i) = F_H2/fso(i); % shell
        X_n2(i) = F_N2/fso(i);
    end
    X_h2t = 1; % tube
    X_he = 0;

   Pco_i = [X_co(1)*15*Patm; X_co(2:end)*10*Patm];
   Ph2o_i = [X_h2o(1)*15*Patm; X_h2o(2:end)*10*Patm];
   Pco2_i = [X_co2(1)*15*Patm; X_co2(2:end)*10*Patm];
   Ph2s_i = [X_h2s(1)*15*Patm; X_h2s(2:end)*10*Patm];
   Pn2_i = [X_n2(1)*15*Patm; X_n2(2:end)*10*Patm];

    %%
    X1 = [Pco_i x(:,1:6:(nn-1)*ns+1)];
    X2 = [Ph2o_i x(:,2:6:(nn-1)*ns+2)];
    X3 = [Pco2_i x(:,3:6:(nn-1)*ns+3)];
    X4 = [Ph2s_i x(:,4:6:(nn-1)*ns+4)];
    X5 = [Pn2_i x(:,5:6:(nn-1)*ns+5)];
    X6 = [Patm*ones(length(t),1) x(:,6:6:(nn-1)*ns+6)];
    %X6 = [zeros(length(t),1) x(:,6:6:(nn-1)*ns+6)];

    co_dry = zeros(length(t),1);
    for i = 1:length(t)
        co_dry(i) = X1(i,end)/(X1(i,end)+X3(i,end)+X4(i,end));
    end

    % Partial Pressures (atm)
    X1_1 = X1./Patm;X2_2 = X2./Patm;X3_3 = X3./Patm;X4_4 = X4./Patm;
    X5_5 = X5./Patm;X6_6 = X6./Patm;

    % Partial Pressures vs time (s)
```

```matlab
figure (1)
subplot 221
plot(t,X1_1);
ylim([0 1]);
%xlabel('time (s)','fontsize',12,'fontweight','b');
ylabel('f_C_O','fontsize',12,'fontweight','b');

subplot 222
plot(t,X2_2);
% ylim([0.17 0.25]);
%xlabel('time (s)','fontsize',12,'fontweight','b');
ylabel('f_H_2_O','fontsize',12,'fontweight','b');

subplot 223
plot(t,X3_3);
ylim([0 inf]);
%xlabel('time (s)','fontsize',12,'fontweight','b');
ylabel('f_C_ _O_2','fontsize',12,'fontweight','b');

subplot 224
plot(t,X4_4);
ylim([0 inf]);
%xlabel('time (s)','fontsize',12,'fontweight','b');
ylabel('f_H_2 Shell','fontsize',12,'fontweight','b');

%%
PAS = zeros(length(t),nn); % Average of H2 partial pressure shell side
PAT = zeros(length(t),nn); % Average of H2 partial pressure tube side
for i = 1:length(t)
    PAS(i,1) = (X4(i,1) + PT.*X_h2s(i))/2;
    PAT(i,1) = (X6(i,1) + Patm.*X_h2t)/2;
end


for i = 1:length(t)
    for j = 2:nn
        PAS(i,j) = (X4(i,j) + X4(i,j-1))/2;
        PAT(i,j) = (X6(i,j) + X6(i,j-1))/2;
    end
end

per = zeros(length(t),nn+1); % Permeance
for i = 1:length(t)
    for j = 1:nn
        if PAS(i,j) <= PAT(i,j)
            per(i,j+1) = 0;
        else
            per(i,j+1) = Am*Q*(sqrt(PAS(i,j))-sqrt(PAT(i,j)))/th;
        end
    end
end

fts = zeros(length(t),nn+1);
fts(:,1) = fso; % shell side total molar flow rate
for i = 1:length(t)
    for j = 1:nn
```

```matlab
            fts(i,j+1) = fts(i,j)- per(i,j+1);
        end
    end


ftt = zeros(length(t),nn+1);


for i = 1:length(t)
    for j = 1:nn
        ftt(i,j+1) = ftt(i,j)+ per(i,j+1);
    end
end
FR1=zeros(length(t),nn+1); FR2=zeros(length(t),nn+1);
FR3=zeros(length(t),nn+1); FR4=zeros(length(t),nn+1);
FR5=zeros(length(t),nn+1); FR6=zeros(length(t),nn+1);
% Fractions


for i = 1:length(t)
    for j = 1:nn+1
        FR1(i,j)= X1(i,j)/(X1(i,j)+X2(i,j)+X3(i,j)+X4(i,j));
        FR2(i,j)= X2(i,j)/(X1(i,j)+X2(i,j)+X3(i,j)+X4(i,j));
        FR3(i,j)= X3(i,j)/(X1(i,j)+X2(i,j)+X3(i,j)+X4(i,j));
        FR4(i,j)= X4(i,j)/(X1(i,j)+X2(i,j)+X3(i,j)+X4(i,j));
    end
end


FR6= X6_6;


fco = fts.*(FR1); fh2o = fts.*(FR2);
fco2 = fts.*(FR3); fh2s = fts.*(FR4);
fh2t = ftt.*(FR6);

%
con = zeros(length(t),nn+1);
for i = 1:length(t)
    for j = 1:nn+1
        con(i,j) = 100*(fco(i,1)-fco(i,j))/fco(i,1);
    end
end

HRI = zeros(length(t),nn+1);
for i = 1:length(t)
    for j = 1:nn+1
        HRI(i,j) = 100*ftt(i,j)/(fco(i,1)+fh2s(i,1));
    end
end

Fh2end = 60*(0.0328^3)*ftt(end,end)/(Ps/(Rg*Ts*(10^6)*60)); % scfh
ratio = F_H2O(end)/fco(end,1);


%%
DryCO = FR1(:,end)./(1-FR2(:,end));

figure (2)
subplot 311
```

```matlab
    plot(t,F_H2O,'LineWidth',2)
    %xlabel('time','fontsize',12,'fontweight','b');
    ylabel('F H_2O inlet (mol/s)','fontsize',12,'fontweight','b');
    legend('to = 0.5','5','1.25');
    %legend('K_c = 0.028','0.0117','0.001','0.006');
    hold on
    subplot 312
    plot(t,ones(length(t),1)*sp,'-.g',t,co_dry,'LineWidth',2);
    legend('f_ _C_ _O (t)', 'f_ _C_ _O Set Point');
    %xlabel('time','fontsize',12,'fontweight','b');
    ylabel('f_ _C_ _O at the exit','fontsize',12,'fontweight','b');
    legend('Set point = 1.89% (Dry basis)');
    hold on
    subplot 313
    plot(t,con(:,end),'LineWidth',2)
    xlabel('time [s]','fontsize',12,'fontweight','b');
    ylabel('CO Conversion at the exit','fontsize',12,'fontweight','b');
    hold on

%%
    a = (Ps/(Rg*Ts*(10^6)*60));
    figure (7)
    subplot 221
    plot(0:nn,fh2t(1:20:end,:),0:nn,fh2t(end,:),'k','LineWidth',2);
    ylim([0 inf]);
    xlabel('Segment No','fontsize',12,'fontweight','b');
    ylabel('F  H_2 tube [mol/s]','fontsize',12,'fontweight','b');
    legend('t = 0 s','2.2','6.2','14','40');

    subplot 222

plot(t,fco(:,end)./a,t,fh2o(:,end)./a,t,fco2(:,end)./a,t,fh2s(:,end)./a,t,fh2
t(:,end)./a,'LineWidth',2);
    xlabel('time [s]','fontsize',12,'fontweight','b');
    ylabel('F_ _i at the exit [sccm]','fontsize',12,'fontweight','b');
    ylim([0 inf]);
    legend('CO','H_2O','CO_2','H_2 Shell side','H_2 Tube Side');

    subplot 223
    x1 = t;y1 = con(:,end);
    x2 = 0:nn;y2 = con(end,:);
    hl1 = line(x1,y1,'Color','k','LineWidth',2);
    xlabel('time [s]','fontsize',12,'fontweight','b');
    ylabel('CO Conversion the exit [%]','fontsize',12,'fontweight','b');
    ax1 = gca;
    set(ax1,'XColor','k','YColor','k')
    ax2 = axes('Position',get(ax1,'Position'),...
        'XAxisLocation','top',...
        'YAxisLocation','right',...
        'Color','none',...
        'XColor','r','YColor','r');
    hl2 = line(x2,y2,'Color','r','Parent',ax2,'LineWidth',2);
    xlabel('Segment No','fontsize',12,'fontweight','b');
    ylabel('Overall CO Conversion [%]','fontsize',12,'fontweight','b');
    %ylim([90 inf]);
```

```matlab
    subplot 224
plot(0:nn,X1_1(end,:),'r',0:nn,X2_2(end,:),'b',0:nn,X3_3(end,:),'k',0:nn,X4_4
(end,:),'g',0:nn,X6_6(end,:),'m','LineWidth',2);
    legend('CO','H_2O','CO_2','H_2 Shell','H_2 Tube');
    ylim([0 inf]);
    xlabel('Segment No','fontsize',12,'fontweight','b');
    ylabel('Fraction of each gas at t_S_S','fontsize',12,'fontweight','b');

    figure(8)
    surf(X4/Patm);
    zlim([0 inf]);
    xlim([1 21]);
    xlabel('Segment No','fontsize',12,'fontweight','b');
    ylabel('Time [s]','fontsize',12,'fontweight','b');
    zlabel('Partial Pressure of H_2 [atm]','fontsize',12,'fontweight','b');

    figure (9)
    subplot 221
    plot(0:1/nn:1,fh2t(1:20:end,:),0:1/nn:1,fh2t(end,:),'k','LineWidth',2);
    ylim([0 inf]);
    xlabel('Reactor Length [cm]','fontsize',12,'fontweight','b');
    ylabel('F  H_2 tube [mol/s]','fontsize',12,'fontweight','b');
    legend('t = 0 s','2.2','6.2','14','50');

    subplot 222
    plot(t,FR1(:,end),'r',t,FR2(:,end),'-bs',t,FR3(:,end),'-
kv',t,FR4(:,end),'g','LineWidth',2,'MarkerSize',5);
    xlabel('time [s]','fontsize',12,'fontweight','b');
    ylabel('F_ _i at the exit [sccm]','fontsize',12,'fontweight','b');
    ylim([0 inf]);
    legend('CO','H_2O','CO_2','H_2 Shell');

    subplot 223
    plot(0:1/nn:1,con(end,:),0:1/nn:1,HRI(end,:),'LineWidth',2);
    xlabel('Reactor Length [cm]','fontsize',12,'fontweight','b');
    ylabel('CO Conversion & HR','fontsize',12,'fontweight','b');
    ylim([0 inf]);

    subplot 224
plot(0:1/nn:1,FR1(end,:),'r',0:1/nn:1,FR2(end,:),'b',0:1/nn:1,FR3(end,:),'k',
0:1/nn:1,FR4(end,:),'g','LineWidth',2);
    legend('CO','H_2O','CO_2','H_2 Shell','H_2 Tube');
    ylim([0 inf]);
    xlabel('Reactor Length [cm]','fontsize',12,'fontweight','b');
    ylabel('Fraction of each gas at t_S_S','fontsize',12,'fontweight','b');

    figure (10)
    xxx = 0:1/nn:1;
    yyy = t;
    surf(xxx,yyy,X4_4);

end
```

c. Servo-mechanism problem: increased CO conversion

m.file:

```matlab
% CSTRs in Series_with Reaction - SWEEP STOPS AT t=0
% x(1) : co
% x(2) : h2o
% x(3) : co2
% x(4) : h2
% x(5) : N2
% x(6) : H2 permeate


function dfdt = same_fco_syntune(t,x)
global Kc to
ns = 6; % number of equations in each segment
nn = 20; % number of cstrs in series
e = 0.5; % void fraction of the fixed bed


Rg = 8.314; % m3 Pa/ K mol
T = (450+273.15); % Kelvin
Patm = 101325; % Pa, Tube side pressure equals to 1 atm
PT = 15*Patm ; % (Pa) % Total pressure in shell side 15 atm


Ps = 101325 ;% Ps (Pa)  Ts (K)  standard temp-press
Ts = 273.15;


r1 = 0.0127/2; % Radius of inner porous tube (m)
r2 = 0.0127; % Radius of shell (m)
As = pi*(r2^2-r1^2); % cross sectional area in the shell side(m^2)
At = pi*r1^2; % cross sectinal area of the tube
L = 0.0635; % Length of the shell (m)
Vs = As*L*e; % Total void volume in the shell side (m^3)
vs = Vs/nn; % Void volume of each cstr
Vt = At*L;
vt = Vt/nn;
w = 15/nn; % g catalyst
Am = 2*pi*r1*L/nn; % membrane area m^2


CTs = PT/(T*Rg); % Total concentration in shell side (mol/m^3) Constant all
the time, P =15 atm, T = 627 K
CTt = Patm/(T*Rg);


ko1 = 10^(2.845); ko2 = 10^(0.659);
E1 = 111*10^3; E2 = 88*10^3; % Activation Energy j/mol

%% Inlet Flow Rates

F_CO = (237.8*Ps/(Rg*Ts*(10^6)*60)); % *** Disturbance *** % mol/s
Fo_H2O = (475.7*Ps/(Rg*Ts*(10^6)*60)); % mol/s
F_CO2 = (86.5*Ps/(Rg*Ts*(10^6)*60));
F_H2 = (200*Ps/(Rg*Ts*(10^6)*60));
F_N2 = 0;
%% P.C.
```

```matlab
% Xco_sp = 0.001;
% error = (x((nn-1)*ns+1)-Xco_sp);
sp = 1.2/100; % 1.2 for 30% permeance
c_o= x(115)/(x(115)+x(117)+x(118));
error = (c_o - sp);
% Kc = 0.02;
% to = 1;
F_H2O = Fo_H2O + Kc*error + Kc*x(nn*ns+1)/to;



Fo =[F_CO;F_H2O;F_CO2;F_H2;F_N2;0];
fto = Fo(1) + Fo(2) + Fo(3) + Fo(4)+ Fo(5);
ftt= 0;



%% INLET specifications

X_co = F_CO/fto;
X_h2o = F_H2O/fto;
X_co2 = F_CO2/fto;
X_h2s = F_H2/fto; % shell
X_n2 = F_N2/fto;

X_h2t = 1; % tube
X_he = 0;

%%
% P partial pressure of each gas (pa)
P = zeros(nn,5);
for i =1:nn
    for j =1:5;
        k = (i-1)*6+j;
        P(i,j) = PT*x(k);
    end
end

%% Membrane Properties
Qo = 0.3*6322.7*Patm/(Rg*273.15*3600*sqrt(Patm)); % mol.micron/(m2.s.pa^0.5)
th = 10; % Pd thickness 10 micron
Ep = 15.6*10^3;
Q= Qo*exp(-Ep/(Rg*T)); % mol.micron/(m2.s.pa^0.
%%
FT = zeros(nn+1,1);
FTt = zeros(nn+1,1);
Per = zeros(nn+1,1);

FT(1) = fto;
FTt(1) = ftt;
Per(1) = 0;

Pas = zeros(nn,1); % P average shell
Pas(1) = (P(1,4)+PT*X_h2s)/2;
for i = 2:nn
    Pas(i) = (P(i,4)+P(i-1,4))/2;
end
```

351

```matlab
Pat = zeros(nn,1); % P average tube
Pat(1) = Patm*(x(6)+X_h2t)/2;
for i = 2:nn
    Pat(i) = Patm*(x(i*6-6)+ x(i*6))/2;
end


for i = 1:nn
    if Pas(i)<=Pat(i)
        Per(i+1)=0;
    else
        Per(i+1) = Am*Q*(sqrt(Pas(i))-sqrt(Pat(i)))/th;
    end
end

for i = 1:nn
    FT(i+1) = FT(i) - Per(i+1);
    FTt(i+1) = FTt(i) + Per(i+1);
end

%% Thermodynamic Properties

% Cns - Constants for Cp CO H2O CO2 H2; Cp = heat capacity (J/mol*K)
% t = temperature (K) / 1000.
t = T/1000;
%       A        B         C         D         E          F         G          H
Cns = [ 25.56759 6.09613 4.054656 -2.671301 0.131021 -118.0089 227.3665 -
110.5271;
    30.092 6.832514 6.793435 -2.53448 0.082139 -250.881 223.3967 -241.8264;
    24.99735 55.18696 -33.69137 7.948387 -0.136638 -403.6075 228.2431 -
393.5224;
    33.066178 -11.363417 11.432816 -2.772874 -0.158558 -9.980797 172.707974 0
];

% dfH°gas for each gas CO H2O CO2 H2
Hf = [ -110.53; -241.83; -393.52; 0 ];

%CO -  H° ? H°298.15= A*t + B*t2/2 + C*t3/3 + D*t4/4 ? E/t + F ? H
H1 = Hf(1) +  Cns(1,1)*t + Cns(1,2)*(t^2)/2 + Cns(1,3)*(t^3)/3 +
Cns(1,4)*(t^4)/4 - Cns(1,5)/t + Cns(1,6) - Cns(1,8);
%H2O -  H° ? H°298.15= A*t + B*t2/2 + C*t3/3 + D*t4/4 ? E/t + F ? H
H2 = Hf(2) +  Cns(2,1)*t + Cns(2,2)*(t^2)/2 + Cns(2,3)*(t^3)/3 +
Cns(2,4)*(t^4)/4 - Cns(2,5)/t + Cns(2,6) - Cns(2,8);
%CO2 -  H° ? H°298.15= A*t + B*t2/2 + C*t3/3 + D*t4/4 ? E/t + F ? H
H3 = Hf(3) +  Cns(3,1)*t + Cns(3,2)*(t^2)/2 + Cns(3,3)*(t^3)/3 +
Cns(3,4)*(t^4)/4 - Cns(3,5)/t + Cns(3,6) - Cns(3,8);
%H2 -  H° ? H°298.15= A*t + B*t2/2 + C*t3/3 + D*t4/4 ? E/t + F ? H
H4 = Hf(4) +  Cns(4,1)*t + Cns(4,2)*(t^2)/2 + Cns(4,3)*(t^3)/3 +
Cns(4,4)*(t^4)/4 - Cns(4,5)/t + Cns(4,6) - Cns(4,8);

% dH_Rxn
dHrxn = H4+H3-(H1+H2);

%S° = A*ln(t) + B*t + C*t2/2 + D*t3/3 ? E/(2*t2) + G
```

```
S1 = Cns(1,1)*log(t) + Cns(1,2)*t + Cns(1,3)*(t^2)/2 + Cns(1,4)*(t^3)/3 -
Cns(1,5)/(2*t^2) + Cns(1,7);
S2 = Cns(2,1)*log(t) + Cns(2,2)*t + Cns(2,3)*(t^2)/2 + Cns(2,4)*(t^3)/3 -
Cns(2,5)/(2*t^2) + Cns(2,7);
S3 = Cns(3,1)*log(t) + Cns(3,2)*t + Cns(3,3)*(t^2)/2 + Cns(3,4)*(t^3)/3 -
Cns(3,5)/(2*t^2) + Cns(3,7);
S4 = Cns(4,1)*log(t) + Cns(4,2)*t + Cns(4,3)*(t^2)/2 + Cns(4,4)*(t^3)/3 -
Cns(4,5)/(2*t^2) + Cns(4,7);


dS = S4 + S3 - S2 - S1;


K = exp(dS/Rg)*exp(-dHrxn*10^3/(Rg*T));
% K = exp(4577.8/x(5) - 4.33); from Moe


%% Reaction Rate from Hla et al
% R : mol/g cat. s    rco = mol/m^3. s
R = zeros(nn,1);
rco = zeros(nn,1);
for i = 1:nn
    beta = P(i,3)*P(i,4)/(P(i,1)*P(i,2)*K); % reversibility factor
    R(i) = ko1*exp(-E1/(Rg*T))*(P(i,1))*(P(i,3)^(-0.36))*(P(i,4)^(-0.09))*(1-
beta); % reaction rate 1  of co mol/kg.s
    %R(i) = ko2*exp(-E2/(Rg*T))*(P(i,k+1)^0.9)*(P(i,k+2)^0.31)*(P(i,k+3)^(-
0.156))*(P(i,k+4)^(-0.05))*(1-beta); % reaction rate 2  of co mol/kg.s
    rco(i) = -R(i)*w/(100^0.55);
end


%% 1
dfdt = zeros(6*nn+1,1);
dfdt(1,:) = (X_co*FT(1) - x(1)*FT(2) + rco(1))/(CTs*vs);
dfdt(2,:) = (X_h2o*FT(1) - x(2)*FT(2) + rco(1))/(CTs*vs);
dfdt(3,:) = (X_co2*FT(1) - x(3)*FT(2) - rco(1))/(CTs*vs);
dfdt(4,:) = (X_h2s*FT(1) - x(4)*FT(2) - rco(1) - Per(2))/(CTs*vs);
dfdt(5,:) = (X_n2*FT(1) - x(5)*FT(2) )/(CTs*vs);
dfdt(6,:) = (X_h2t*FTt(1) - x(6)*FTt(2) + Per(2))/(CTt*vt);
%% 2
dfdt(7,:) = (x(1)*FT(2) - x(7)*FT(3) + rco(2))/(CTs*vs);
dfdt(8,:) = (x(2)*FT(2) - x(8)*FT(3) + rco(2))/(CTs*vs);
dfdt(9,:) = (x(3)*FT(2) - x(9)*FT(3) - rco(2))/(CTs*vs);
dfdt(10,:) = (x(4)*FT(2) - x(10)*FT(3) - rco(2) - Per(3))/(CTs*vs);
dfdt(11,:) = (x(5)*FT(2) - x(11)*FT(3) )/(CTs*vs);
dfdt(12,:) = (x(6)*FTt(2) - x(12)*FTt(3) + Per(3))/(CTt*vt);
%% 3
dfdt(13,:) = (x(7)*FT(3) - x(13)*FT(4) + rco(3))/(CTs*vs);
dfdt(14,:) = (x(8)*FT(3) - x(14)*FT(4) + rco(3))/(CTs*vs);
dfdt(15,:) = (x(9)*FT(3) - x(15)*FT(4) - rco(3))/(CTs*vs);
dfdt(16,:) = (x(10)*FT(3) - x(16)*FT(4) - rco(3) - Per(4))/(CTs*vs);
dfdt(17,:) = (x(11)*FT(3) - x(17)*FT(4) )/(CTs*vs);
dfdt(18,:) = (x(12)*FTt(3) - x(18)*FTt(4) + Per(4))/(CTt*vt);
%% 4
dfdt(19,:) = (x(13)*FT(4) - x(19)*FT(5) + rco(4))/(CTs*vs);
dfdt(20,:) = (x(14)*FT(4) - x(20)*FT(5) + rco(4))/(CTs*vs);
dfdt(21,:) = (x(15)*FT(4) - x(21)*FT(5) - rco(4))/(CTs*vs);
dfdt(22,:) = (x(16)*FT(4) - x(22)*FT(5) - rco(4) - Per(5))/(CTs*vs);
dfdt(23,:) = (x(17)*FT(4) - x(23)*FT(5) )/(CTs*vs);
dfdt(24,:) = (x(18)*FTt(4) - x(24)*FTt(5) + Per(5))/(CTt*vt);
```

```
%% 5
dfdt(25,:) = (x(19)*FT(5) - x(25)*FT(6) + rco(5))/(CTs*vs);
dfdt(26,:) = (x(20)*FT(5) - x(26)*FT(6) + rco(5))/(CTs*vs);
dfdt(27,:) = (x(21)*FT(5) - x(27)*FT(6) - rco(5))/(CTs*vs);
dfdt(28,:) = (x(22)*FT(5) - x(28)*FT(6) - rco(5) - Per(6))/(CTs*vs);
dfdt(29,:) = (x(23)*FT(5) - x(29)*FT(6) )/(CTs*vs);
dfdt(30,:) = (x(24)*FTt(5) - x(30)*FTt(6) + Per(6))/(CTt*vt);
%% 6
dfdt(31,:) = (x(25)*FT(6) - x(31)*FT(7) + rco(6))/(CTs*vs);
dfdt(32,:) = (x(26)*FT(6) - x(32)*FT(7) + rco(6))/(CTs*vs);
dfdt(33,:) = (x(27)*FT(6) - x(33)*FT(7) - rco(6))/(CTs*vs);
dfdt(34,:) = (x(28)*FT(6) - x(34)*FT(7) - rco(6) - Per(7))/(CTs*vs);
dfdt(35,:) = (x(29)*FT(6) - x(35)*FT(7) )/(CTs*vs);
dfdt(36,:) = (x(30)*FTt(6) - x(36)*FTt(7) + Per(7))/(CTt*vt);
%% 7
dfdt(37,:) = (x(31)*FT(7) - x(37)*FT(8) + rco(7))/(CTs*vs);
dfdt(38,:) = (x(32)*FT(7) - x(38)*FT(8) + rco(7))/(CTs*vs);
dfdt(39,:) = (x(33)*FT(7) - x(39)*FT(8) - rco(7))/(CTs*vs);
dfdt(40,:) = (x(34)*FT(7) - x(40)*FT(8) - rco(7) - Per(8))/(CTs*vs);
dfdt(41,:) = (x(35)*FT(7) - x(41)*FT(8) )/(CTs*vs);
dfdt(42,:) = (x(36)*FTt(7) - x(42)*FTt(8) + Per(8))/(CTt*vt);
%% 8
dfdt(43,:) = (x(37)*FT(8) - x(43)*FT(9) + rco(8))/(CTs*vs);
dfdt(44,:) = (x(38)*FT(8) - x(44)*FT(9) + rco(8))/(CTs*vs);
dfdt(45,:) = (x(39)*FT(8) - x(45)*FT(9) - rco(8))/(CTs*vs);
dfdt(46,:) = (x(40)*FT(8) - x(46)*FT(9) - rco(8) - Per(9))/(CTs*vs);
dfdt(47,:) = (x(41)*FT(8) - x(47)*FT(9) )/(CTs*vs);
dfdt(48,:) = (x(42)*FTt(8) - x(48)*FTt(9) + Per(9))/(CTt*vt);
%% 9
dfdt(49,:) = (x(43)*FT(9) - x(49)*FT(10) + rco(9))/(CTs*vs);
dfdt(50,:) = (x(44)*FT(9) - x(50)*FT(10) + rco(9))/(CTs*vs);
dfdt(51,:) = (x(45)*FT(9) - x(51)*FT(10) - rco(9))/(CTs*vs);
dfdt(52,:) = (x(46)*FT(9) - x(52)*FT(10) - rco(9) - Per(10))/(CTs*vs);
dfdt(53,:) = (x(47)*FT(9) - x(53)*FT(10) )/(CTs*vs);
dfdt(54,:) = (x(48)*FTt(9) - x(54)*FTt(10) + Per(10))/(CTt*vt);
%% 10
dfdt(55,:) = (x(49)*FT(10) - x(55)*FT(11) + rco(10))/(CTs*vs);
dfdt(56,:) = (x(50)*FT(10) - x(56)*FT(11) + rco(10))/(CTs*vs);
dfdt(57,:) = (x(51)*FT(10) - x(57)*FT(11) - rco(10))/(CTs*vs);
dfdt(58,:) = (x(52)*FT(10) - x(58)*FT(11) - rco(10) - Per(11))/(CTs*vs);
dfdt(59,:) = (x(53)*FT(10) - x(59)*FT(11) )/(CTs*vs);
dfdt(60,:) = (x(54)*FTt(10) - x(60)*FTt(11) + Per(11))/(CTt*vt);
%% 11
dfdt(61,:) = (x(55)*FT(11) - x(61)*FT(12) + rco(11))/(CTs*vs);
dfdt(62,:) = (x(56)*FT(11) - x(62)*FT(12) + rco(11))/(CTs*vs);
dfdt(63,:) = (x(57)*FT(11) - x(63)*FT(12) - rco(11))/(CTs*vs);
dfdt(64,:) = (x(58)*FT(11) - x(64)*FT(12) - rco(11) - Per(12))/(CTs*vs);
dfdt(65,:) = (x(59)*FT(11) - x(65)*FT(12) )/(CTs*vs);
dfdt(66,:) = (x(60)*FTt(11) - x(66)*FTt(12) + Per(12))/(CTt*vt);
%% 12
dfdt(67,:) = (x(61)*FT(12) - x(67)*FT(13) + rco(12))/(CTs*vs);
dfdt(68,:) = (x(62)*FT(12) - x(68)*FT(13) + rco(12))/(CTs*vs);
dfdt(69,:) = (x(63)*FT(12) - x(69)*FT(13) - rco(12))/(CTs*vs);
dfdt(70,:) = (x(64)*FT(12) - x(70)*FT(13) - rco(12) - Per(13))/(CTs*vs);
dfdt(71,:) = (x(65)*FT(12) - x(71)*FT(13) )/(CTs*vs);
dfdt(72,:) = (x(66)*FTt(12) - x(72)*FTt(13) + Per(13))/(CTt*vt);
%% 13
```

```
dfdt(73,:) = (x(67)*FT(13) - x(73)*FT(14) + rco(13))/(CTs*vs);
dfdt(74,:) = (x(68)*FT(13) - x(74)*FT(14) + rco(13))/(CTs*vs);
dfdt(75,:) = (x(69)*FT(13) - x(75)*FT(14) - rco(13))/(CTs*vs);
dfdt(76,:) = (x(70)*FT(13) - x(76)*FT(14) - rco(13) - Per(14))/(CTs*vs);
dfdt(77,:) = (x(71)*FT(13) - x(77)*FT(14) )/(CTs*vs);
dfdt(78,:) = (x(72)*FTt(13) - x(78)*FTt(14) + Per(14))/(CTt*vt);
%% 14
dfdt(79,:) = (x(73)*FT(14) - x(79)*FT(15) + rco(14))/(CTs*vs);
dfdt(80,:) = (x(74)*FT(14) - x(80)*FT(15) + rco(14))/(CTs*vs);
dfdt(81,:) = (x(75)*FT(14) - x(81)*FT(15) - rco(14))/(CTs*vs);
dfdt(82,:) = (x(76)*FT(14) - x(82)*FT(15) - rco(14) - Per(15))/(CTs*vs);
dfdt(83,:) = (x(77)*FT(14) - x(83)*FT(15) )/(CTs*vs);
dfdt(84,:) = (x(78)*FTt(14) - x(84)*FTt(15) + Per(15))/(CTt*vt);
%% 15
dfdt(85,:) = (x(79)*FT(15) - x(85)*FT(16) + rco(15))/(CTs*vs);
dfdt(86,:) = (x(80)*FT(15) - x(86)*FT(16) + rco(15))/(CTs*vs);
dfdt(87,:) = (x(81)*FT(15) - x(87)*FT(16) - rco(15))/(CTs*vs);
dfdt(88,:) = (x(82)*FT(15) - x(88)*FT(16) - rco(15) - Per(16))/(CTs*vs);
dfdt(89,:) = (x(83)*FT(15) - x(89)*FT(16) )/(CTs*vs);
dfdt(90,:) = (x(84)*FTt(15) - x(90)*FTt(16) + Per(16))/(CTt*vt);
%% 16
dfdt(91,:) = (x(85)*FT(16) - x(91)*FT(17) + rco(16))/(CTs*vs);
dfdt(92,:) = (x(86)*FT(16) - x(92)*FT(17) + rco(16))/(CTs*vs);
dfdt(93,:) = (x(87)*FT(16) - x(93)*FT(17) - rco(16))/(CTs*vs);
dfdt(94,:) = (x(88)*FT(16) - x(94)*FT(17) - rco(16) - Per(17))/(CTs*vs);
dfdt(95,:) = (x(89)*FT(16) - x(95)*FT(17) )/(CTs*vs);
dfdt(96,:) = (x(90)*FTt(16) - x(96)*FTt(17) + Per(17))/(CTt*vt);
%% 17
dfdt(97,:) = (x(91)*FT(17) - x(97)*FT(18) + rco(17))/(CTs*vs);
dfdt(98,:) = (x(92)*FT(17) - x(98)*FT(18) + rco(17))/(CTs*vs);
dfdt(99,:) = (x(93)*FT(17) - x(99)*FT(18) - rco(17))/(CTs*vs);
dfdt(100,:) = (x(94)*FT(17) - x(100)*FT(18) - rco(17) - Per(18))/(CTs*vs);
dfdt(101,:) = (x(95)*FT(17) - x(101)*FT(18) )/(CTs*vs);
dfdt(102,:) = (x(96)*FTt(17) - x(102)*FTt(18) + Per(18))/(CTt*vt);
%% 18
dfdt(103,:) = (x(97)*FT(18) - x(103)*FT(19) + rco(18))/(CTs*vs);
dfdt(104,:) = (x(98)*FT(18) - x(104)*FT(19) + rco(18))/(CTs*vs);
dfdt(105,:) = (x(99)*FT(18) - x(105)*FT(19) - rco(18))/(CTs*vs);
dfdt(106,:) = (x(100)*FT(18) - x(106)*FT(19) - rco(18) - Per(19))/(CTs*vs);
dfdt(107,:) = (x(101)*FT(18) - x(107)*FT(19) )/(CTs*vs);
dfdt(108,:) = (x(102)*FTt(18) - x(108)*FTt(19) + Per(19))/(CTt*vt);
%% 19
dfdt(109,:) = (x(103)*FT(19) - x(109)*FT(20) + rco(19))/(CTs*vs);
dfdt(110,:) = (x(104)*FT(19) - x(110)*FT(20) + rco(19))/(CTs*vs);
dfdt(111,:) = (x(105)*FT(19) - x(111)*FT(20) - rco(19))/(CTs*vs);
dfdt(112,:) = (x(106)*FT(19) - x(112)*FT(20) - rco(19) - Per(20))/(CTs*vs);
dfdt(113,:) = (x(107)*FT(19) - x(113)*FT(20) )/(CTs*vs);
dfdt(114,:) = (x(108)*FTt(19) - x(114)*FTt(20) + Per(20))/(CTt*vt);
%% 20
dfdt(115,:) = (x(109)*FT(20) - x(115)*FT(21) + rco(20))/(CTs*vs);
dfdt(116,:) = (x(110)*FT(20) - x(116)*FT(21) + rco(20))/(CTs*vs);
dfdt(117,:) = (x(111)*FT(20) - x(117)*FT(21) - rco(20))/(CTs*vs);
dfdt(118,:) = (x(112)*FT(20) - x(118)*FT(21) - rco(20) - Per(21))/(CTs*vs);
dfdt(119,:) = (x(113)*FT(20) - x(119)*FT(21) )/(CTs*vs);
dfdt(120,:) = (x(114)*FTt(20) - x(120)*FTt(21) + Per(21))/(CTt*vt);
dfdt(121,:) = (c_o - sp);
end
```

Run file:

```
clear
clc
%% ODE Solution Method
global Kc to
% to = 1;%
% Kcall = [0.02 0.003 0.0008]; %0.03 0.003 0.0008 and up gives negative
conversion
toall = [2];% [6 2 0.2]
Kc = 0.003;
%for m = 1:length(Kcall)
for m = 1:length(toall)
    ns = 6; % number of equations in each segment
    nn = 20; % number of segments
    sp = 1.2/100; % 1.2 for 30% permeance
    %Xco_sp = 0.001;
    %Kc = Kcall(m);
    to = toall(m);

    xi = "Get the data from start-up
    c_oi = xi(115)/(xi(115)+xi(117)+xi(118));
    xi(nn*ns+1) = (c_oi - sp);
    %xi(nn*ns+1) = xi((nn-1)*ns+1)-Xco_sp;
    ic=xi; tspan=[0 500];
    [t,x]=ode23s('same_fco_syntune',tspan,ic);


        %%
    Rg = 8.314; % Ideal gas constant m^3.Pa/(mol/K)
    Ps = 101325;% Ps (Pa)  Ts (K)  standard temp-press
    Ts = 273.15;

    Patm = 101325; % Pa, Tube side pressure equals to 1 atm
    PT = 15*Patm ; % (Pa) % Total pressure in shell side 15 atm
    PTs = 15; %atm
    T = (450+273.15); % Kelvin

    %%% Free standing Pd foil
%     Qo = 6322.7*Patm/(Rg*273.15*3600*sqrt(Patm)); %
mol.micron/(m2.s.pa^0.5)
%     Ep = 15.6*10^3;
 Qo = 0.3*6322.7*Patm/(Rg*273.15*3600*sqrt(Patm)); % mol.micron/(m2.s.pa^0.5)
th = 10; % Pd thickness 10 micron
Ep = 15.6*10^3;
Q= Qo*exp(-Ep/(Rg*T)); % mol.micron/(m2.s.pa^0.

    r1 = 0.0127/2; % Radius of inner porous tube (m)
    L = 0.0635; % Length of the shell (m)
    Am = 2*pi*r1*L/nn; % membrane area m^2

    % Q_inlet = 1000 sccm, Fh20_inlet / Fco_inlet = 2
    F_CO = (237.8*Ps/(Rg*Ts*(10^6)*60)); % *** Disturbance *** % mol/s
    Fo_H2O = (475.7*Ps/(Rg*Ts*(10^6)*60)); % mol/s
    F_CO2 = (86.5*Ps/(Rg*Ts*(10^6)*60));
    F_H2 = (200*Ps/(Rg*Ts*(10^6)*60));
```

```matlab
    F_N2 = 0;
%% P.C.
% Kc = 0.02;
% to = 1;

    error = zeros(length(t),1);
    F_H2O = zeros(length(t),1);
    fso = zeros(length(t),1);
    c_oo = zeros(length(t),1);
    for i = 1:length(t)
        c_oo(i)= x(i,115)/(x(i,115)+x(i,117)+x(i,118));
        error(i) = (c_oo(i) - sp);
        F_H2O(i) = Fo_H2O + Kc*error(i) + Kc*x(i,nn*ns+1)/to;
        fso(i) = F_CO + F_CO2 + F_H2 + F_N2 + F_H2O(i);
    end


%% INLET specifications

    X_co = zeros(length(t),1);X_h2o= zeros(length(t),1);X_co2=
zeros(length(t),1);X_h2s= zeros(length(t),1);X_n2= zeros(length(t),1);
    for i = 1:length(t)
        X_co(i) = F_CO/fso(i);
        X_h2o(i) = F_H2O(i)/fso(i);
        X_co2(i) = F_CO2/fso(i);
        X_h2s(i) = F_H2/fso(i); % shell
        X_n2(i) = F_N2/fso(i);
    end
    X_h2t = 1; % tube
    X_he = 0;

%%
    X1 = [X_co x(:,1:6:(nn-1)*ns+1)];
    X2 = [X_h2o x(:,2:6:(nn-1)*ns+2)];
    X3 = [X_co2 x(:,3:6:(nn-1)*ns+3)];
    X4 = [X_h2s x(:,4:6:(nn-1)*ns+4)];
    X5 = [X_n2 x(:,5:6:(nn-1)*ns+5)];
    X6 = [ones(length(t),1)*X_h2t x(:,6:6:(nn-1)*ns+6)];

    co_dry = zeros(length(t),1);
    for i = 1:length(t)
        co_dry(i) = X1(i,end)/(X1(i,end)+X3(i,end)+X4(i,end));
    end


%%
    PAS = zeros(length(t),nn); % Average of H2 partial pressure shell side
    PAT = zeros(length(t),nn); % Average of H2 partial pressure tube side
    for i = 1:length(t)
        PAS(i,1) = (X4(i,1) + X_h2s(i))*PT/2;
        PAT(i,1) = (X6(i,1) + X_h2t)*Patm/2;
    end

    for i = 1:length(t)
        for j = 2:nn
```

```matlab
            PAS(i,j) = (X4(i,j) + X4(i,j-1))*PT/2;
            PAT(i,j) = (X6(i,j) + X6(i,j-1))*Patm/2;
        end
end


per = zeros(length(t),nn+1); % Permeance
for i = 1:length(t)
    for j = 1:nn
        if PAS(i,j) <= PAT(i,j)
            per(i,j+1) = 0;
        else
            per(i,j+1) = Am*Q*(sqrt(PAS(i,j))-sqrt(PAT(i,j)))/th;
        end
    end
end


% Partial Pressures (atm)
X1_1 = X1*PTs;X2_2 = X2*PTs;X3_3 = X3*PTs;X4_4 = X4*PTs;
X5_5 = X5*PTs;X6_6 = X6*PTs;


fts = zeros(length(t),nn+1);
fts(:,1) = fso; % shell side total molar flow rate
for i = 1:length(t)
    for j = 1:nn
        fts(i,j+1) = fts(i,j)- per(i,j+1);
    end
end


fco = X1.*fts;  % shell side CO molar flow rate
fh2s = fts.*X4; fco2 = X3.*fts; fh2o = X2.*fts;


ftt = zeros(length(t),nn+1); % tube side total molar flow rate

for i = 1:length(t)
    for j = 1:nn
        ftt(i,j+1) = ftt(i,j)+ per(i,j+1);
    end
end


fh2t = ftt;

% CO Conversion along the length of the reactor with time
con = zeros(length(t),nn+1); HRI = zeros(length(t),nn+1);
for i = 1:length(t)
    for j = 1:nn+1
        con(i,j) = 100*(fco(i,1)-fco(i,j))/(fco(i,1));
        HRI(i,j) = 100*ftt(i,j)/(fco(i,1)+fh2s(i,1));
    end
end

figure (1)
subplot 221
plot(t,X1_1);
ylim([0 1]);
%xlabel('time (s)','fontsize',12,'fontweight','b');
```

```matlab
ylabel('f_C_O','fontsize',12,'fontweight','b');

subplot 222
plot(t,X2_2);
% ylim([0.17 0.25]);
%xlabel('time (s)','fontsize',12,'fontweight','b');
ylabel('f_H_2_O','fontsize',12,'fontweight','b');

subplot 223
plot(t,X3_3);
ylim([0 inf]);
%xlabel('time (s)','fontsize',12,'fontweight','b');
ylabel('f_C_ _O_2','fontsize',12,'fontweight','b');

subplot 224
plot(t,X4_4);
ylim([0 inf]);
%xlabel('time (s)','fontsize',12,'fontweight','b');
ylabel('f_H_2 Shell','fontsize',12,'fontweight','b');


%%

figure (2)
subplot 311
plot(t,F_H2O,'LineWidth',2)
%xlabel('time','fontsize',12,'fontweight','b');
ylabel('F H_2O inlet (mol/s)','fontsize',12,'fontweight','b');
%legend('K_c = 0.028','0.0117','0.001','0.006');
hold on
subplot 312
plot(t,ones(length(t),1)*sp,'-.g',t,co_dry,'LineWidth',2);
legend('f_ _C_ _O (t)', 'f_ _C_ _O Set Point');
%xlabel('time','fontsize',12,'fontweight','b');
ylabel('f_ _C_ _O at the exit','fontsize',12,'fontweight','b');
legend('Set point = 2.32% (Dry basis)');
hold on
subplot 313
plot(t,con(:,end),'LineWidth',2)
xlabel('time [s]','fontsize',12,'fontweight','b');
ylabel('CO Conversion at the exit','fontsize',12,'fontweight','b');
hold on

figure (7)
subplot 221
plot(0:nn,fh2t(20,:),'k','LineWidth',2);
ylim([0 inf]);
xlabel('Segment no','fontsize',12,'fontweight','b');
ylabel('F  H_2 tube (mol/s)','fontsize',12,'fontweight','b');
legend('0','0.1','0.4','0.8','1.4','2.3','3.4','4.8','8.3','12');

subplot 222
plot(t,fh2s(:,end),'b',t,fh2t(:,end),'g','LineWidth',2);
ylim([0 inf]);
legend('Shell side','Tube side');
xlabel('time (s)','fontsize',12,'fontweight','b');
```

```
    ylabel('F  H_2 at the exit (mol/s)','fontsize',12,'fontweight','b');

    subplot 223
    plot(0:1:nn,con(1:40:end,:),'LineWidth',2)
    xlabel('Segment no','fontsize',12,'fontweight','b');
    ylabel('CO Conversion','fontsize',12,'fontweight','b');

    subplot 224

plot(0:nn,X1(end,:),'r',0:nn,X2(end,:),'b',0:nn,X3(end,:),'k',0:nn,X4(end,:),
'g',0:nn,X6(end,:),'m','LineWidth',2);
    legend('CO','H_2O','CO_2','H_2 Shell','H_2 Tube');
    ylim([0 1]);
    xlabel('Segment No','fontsize',12,'fontweight','b');
    ylabel('Fraction of each gas at t_S_S','fontsize',12,'fontweight','b');

    figure (8)
    subplot 221

plot(0:1/nn:1,fh2t(31,:),0:1/nn:1,fh2t(1:50:end,:),0:1/nn:1,fh2t(end,:),'k','
LineWidth',2);
    ylim([0 inf]);
    xlabel('Reactor Length [cm]','fontsize',12,'fontweight','b');
    ylabel('F  H_2 tube [mol/s]','fontsize',12,'fontweight','b');
    legend('t = 0 s','0.5','1.5','3','5','20');

    subplot 222
    plot(t,X1(:,end),'r',t,X2(:,end),'-bs',t,X3(:,end),'-
kv',t,X4(:,end),'g','LineWidth',2,'MarkerSize',5);
    xlabel('time [s]','fontsize',12,'fontweight','b');
    ylabel('F_ _i at the exit [sccm]','fontsize',12,'fontweight','b');
    ylim([0 inf]);
    legend('CO','H_2O','CO_2','H_2 Shell');

    subplot 223
    plot(0:1/nn:1,con(end,:),0:1/nn:1,HRI(end,:),'LineWidth',2);
    xlabel('Reactor Length [cm]','fontsize',12,'fontweight','b');
    ylabel('CO Conversion & HR','fontsize',12,'fontweight','b');
    ylim([0 inf]);

    subplot 224
plot(0:1/nn:1,X1(end,:),'r',0:1/nn:1,X2(end,:),'b',0:1/nn:1,X3(end,:),'k',0:1
/nn:1,X4(end,:),'g','LineWidth',2);
    legend('CO','H_2O','CO_2','H_2 Shell','H_2 Tube');
    ylim([0 inf]);
    xlabel('Reactor Length [cm]','fontsize',12,'fontweight','b');
    ylabel('Fraction of each gas at t_S_S','fontsize',12,'fontweight','b')
    figure (9)
    xxx = 0:1/nn:1;
    yyy = t;
    surf(xxx,yyy,X4_4);

end
```